JPL SP 43-40

PROCEEDINGS

PRE RELEASE

CONFERENCE ON CHARGE-COUPLED DEVICE TECHNOLOGY AND APPLICATIONS

Nov. 30 - Dec. 2, 1976

Sheraton Park Hotel
Washington, D. C.

Sponsored by

National Aeronautics and Space Administration
Office of Aeronautics and Space Technology and
Jet Propulsion Laboratory
California Institute of Technology

JPL SP 43-40

PROCEEDINGS

CONFERENCE ON CHARGE-COUPLED DEVICE TECHNOLOGY AND APPLICATIONS

Nov. 30 - Dec. 2, 1976

Sheraton Park Hotel
Washington, D. C.

Sponsored by

National Aeronautics and Space Administration
Office of Aeronautics and Space Technology and
Jet Propulsion Laboratory
California Institute of Technology

CONFERENCE ON CHARGE-COUPLED DEVICE TECHNOLOGY AND APPLICATIONS

CONFERENCE CHAIRMAN

David D. Norris
Jet Propulsion Laboratory
Pasadena, California

CONFERENCE CO-CHAIRMAN

Dr. Bernard Rubin
National Aeronautics and Space Administration
Washington, D.C.

CHAIRMAN, SESSION 1 - DATA PROCESSING

Charles E. Pontious
National Aeronautics and Space Administration
Washington, D.C.

CHAIRMAN, SESSION 2 - INFRARED

Marvin S. Maxwell
Goddard Space Flight Center
Greenbelt, Maryland

CHAIRMAN, SESSION 3 - DEVICES AND TESTING

Herbert D. Hendricks
Langley Research Center
Hampton, Virginia

CHAIRMAN, SESSION 4 - ELECTRON-IN, X-RAY, RADIATION

Dr. David F. Barbe
Naval Research Laboratory
Washington, D.C.

CHAIRMAN, SESSION 5 - APPLICATIONS

Dr. Dean R. Collins
Texas Instruments, Inc.
Dallas, Texas

BANQUET SPEAKER

Donald Looft
Deputy Director
DARPA
Arlington, Virginia

CONFERENCE COORDINATOR

Nancy Evans
Jet Propulsion Laboratory
Pasadena, California

ABSTRACT

These Proceedings present the papers given at the Conference on Charge-Coupled Device Technology and Applications held at the Sheraton Park Hotel, Washington, D.C., November 30 through December 2, 1976. Conference sessions were devoted to the following topics: Data Processing; Infrared; Devices and Testing; Electron-In, X-Ray, Radiation; and Applications. The conference was jointly sponsored by the Office of Aeronautics and Space Technology, National Aeronautics and Space Administration, and the Jet Propulsion Laboratory, California Institute of Technology.

OBJECTIVES

The objective of this conference is to provide a forum for the interchange of information on recent advances in the development, evaluation, application, and system implementation of CCD's and related devices. The emphasis will be on advances of mutual relevance and potential significance both to industry and NASA's current and future requirements in all fields of imaging, signal processing and memory.

CONTENTS

DATA PROCESSING

INFRARED

DEVICES AND TESTING

CONTENTS (Continued)

ELECTRON-IN, X-RAY, RADIATION

APPLICATIONS

CCD FILTER AND TRANSFORM TECHNIQUES FOR INTERFERENCE EXCISION

G. M. Borsuk
R. N. DeWitt

ITT Avionics Division, Electro-Physics Laboratories
Columbia, Maryland

ABSTRACT

The theoretical and some experimental results of a study aimed at applying CCD filter and transform techniques to the problem of interference excision within communications channels are presented. Adaptive noise (interference) suppression can be achieved by the modification of received signals such that they are orthogonal to the recently measured noise field. This technique does not require real-time signal processing but does require a stationary spectral distribution to achieve good performance. On the other hand, real-time excision or limiting of noise can yield the best performance because a stationary noise spectrum is not assumed. However, the implementation of real-time spectrum processing with conventional components can be impracticable. Consequently, CCD techniques have been examined to develop real-time noise excision processing. They are recursive filters, circulating filter banks, transversal filter banks, an optical implementation of the chirp Z transform, and a CCD analog FFT.

I. INTRODUCTION

The purpose of the work presented here was to determine the utility of charge-coupled devices for a signal-to-noise enhancing process here referred to as interference excision. In this introductory section, we will describe the interference excision process, discuss practical considerations that limit its applicability, and describe the role that CCDs can play in extending the range of practicable applicability of the process. In subsequent sections, several different implementations of interference excision processes will be discussed, both analytically and in terms of experimental results. Finally, a section is devoted to intercomparing the various implementations of interference excision, particularly with regard to the range of bandwidths and to the dimensionality of the signal space to which the various processing techniques can be applied.

A. ADAPTIVE NOISE SUPPRESSION

In the presence of stationary white Gaussian noise, the optimum filter that can be used to separate signal from noise is the matched filter which has an equivalent embodiment in the cross-correlation receiver. The specification of such a filter can be derived completely from the known signalling waveform. However, if the noise field in which the signal is immersed is non-white in a way which is in some sense predictable, then there are other forms of filtering which will better serve to improve signal-to-noise ratios than does the matched filter. Generally, these filters will be designed such as to reject some signal energy if by doing so they can be made to reject a disproportionately greater amount of noise energy. Usually, the noise field cannot be sufficiently predicted beforehand to permit optimization of a determined filter. Instead, some form of adaptation of the filter to the realized noise environment is attempted.

There are two general strategies that are employed to effect this adaptation. In the first, a set of m observations are in some sense statistically analyzed for a persistent characteristic that can be used to reject the noise. Most commonly, this characteristic will be the noise's spectral distribution (or in the case of adaptive arraying, the angular distribution). On the basis of these observed characteristics, the filter is optimized using some quantity such as SNR as the measure of performance.

Alternatively, a second strategy can be used. Sets of signal samples are transformed into a representation in which the signal energy is spread among many degrees of freedom of the representation, while the interference is spread among a relatively small subset of the degrees of freedom. Limiting or excising is performed on the data in this representation so that the total noise energy is greatly reduced, while the highly diluted signal is left little affected because none of the excised degrees of freedom contains a significant fraction of the signal energy.

There are some examples where this form of processing has successfully been implemented. The most familiar involves the rejection of impulsive atmospheric noise that occurs in the presence of desired narrow-band signals. In this case, the "excision" is often accomplished by limiting the time samples of the signal space (time domain representation). The bandwidth of the system at the clipping point must be as wide as it can possibly be without including other narrow-band interference that may be present at nearby frequencies. In such a representation, the narrow-band signal of interest is greatly diluted (No one time sample contains a large amount of signal energy.) while the impulsive atmospherics are confined to a relatively small number of the time samples, so excision or clipping in this domain has a disproportionally large effect on eliminating noise energy and

relatively little effect on the signal.

Some experimentation has also been carried out with converse processes in which wideband signals are to be extracted from an interference environment comprising many narrow-band interferers. Now the representation for the limiting or exciser process must be that in which the interferers affect a minimal number of degrees of freedom, i.e., a frequency domain representation in which the analysis bandwidth is comparable to the bandwidth of the interfering signals. However, in order that the desired signal not be rejected, it must be distributed more or less uniformly over much of the analyzed band; i.e., it must be a spread-spectrum signal. For example, the above procedure would be applicable were the system being designed to detect and measure the kind of atmospheric impulses that were being discriminated against in the first example.

This second form of real-time noise excision is somewhat less familiar for two reasons. First, signals of interest have usually been relatively narrow in bandwidth. This is because current allocation of the frequency spectrum largely restrict signals to such a form. Secondly, it is only recently that advances in signal processing techniques have made it possible to even consider processing of this kind except for specialized applications. It is the purpose of this paper to present such considerations.

B. PRACTICAL CONSIDERATIONS LIMITING REAL-TIME ADAPTATION

The present discussion will concern itself with the real-time excision of narrow-band interference from a spread-spectrum space. For an example, we will consider the noise and interference that typically appear in the HF bands. Observations and analyses carried out in the band indicate that the benefits of the excision process improves with increased frequency resolution down to bandwidths as little as a few hundred cycles (Ref. 1). Consequently, the representation desired for the excision process is one in which time is divided into resolvable units measuring 5 to 10 ms and for each resolvable time cell there exists a set of 100 to 200 Hz resolution cells for frequency, respectively. Suppose that a 100 kHz band is to be so resolved into 100 Hz subbands. Then the transformation from the observed time series to the excision representation involves 1000 points. The processor must be capable of performing the transformation in 10 ms.

A transform of this size requires about 20,000 complex multiplies; therefore, a complex multiply must be performed in about 500 nanoseconds. This is faster than can be accomplished with present-day microprocessors, although it is not beyond the reach of some form of processor designed specifically for the function. Furthermore, several less powerful processors can accomplish the task by dividing it up in such a way that they work in parallel. Such a division of labor could take the form of having the processors "leap frog" in time or might involve assigning different processors to operate on portions of the overall frequency passband so that each processor would have a smaller sized transform to perform.

It is the purpose of the present study to attempt to fit such a processing task to the capabilities of a particular kind of processor. Specifically, we will attempt to determine the capability of charge-coupled devices to perform the function, operating in an analog-sampled data mode. Such devices, although not unlimited in dynamic range, may nonetheless be quite suitable for the noise excision processing, and their use would permit considerable simplification of the processor by eliminating the need for analog-to-digital converters, digital multipliers, etc.

Much of the following discussion deals with the implementation of various forms of the Fourier transform. For the purpose at hand, noise excision, it is necessary that the transform process be capable of inversion. This implies that phase information be retained for the various frequency components and precludes the use of some methods, notably the sliding chirped Z algorithm, which for other applications has many attractive features for its implementation with CCDs.

In the discussions of the various spectral analysis techniques that follow, emphasis is placed on the sizes of the transforms that can be accomplished within the current state-of-the-art of CCDs. Generally, the size of the transform will be limited by the number of transfers which can be carried out without suffering significant degradation of the signal from charge transfer inefficiency. This limitation proves to be the one that most severely imposes a limit on transform size. To some extent, the effects of charge transfer inefficiency can be mitigated by techniques such as carrying the signal in two or more adjacent CCD memory locations and by providing vacant cells between the signal bearing cells. However, the use of these methods require the use of longer CCDs clocked at higher rates, and ultimately these magnitudes reach an upper limit which in turn imposes a limit on the transform size.

II. ANALYSES AND RESULTS

A. METHODS USING UNTAPPED CCDs

The simplest form of CCD and that which at this time is most readily available is the untapped analog shift register. Although the output of such a device is nothing more than a delayed version of what was earlier entered into it, these devices constitute a memory that can be

used to perform a spectral analysis.

In this section we treat three different forms of filters implemented with untapped CCDs. There are (1) th· recursive filter, (2) the circulating fi ter bank and the similar coherent memory filter (CMF), and (3) the analog FFT.

Since transformation from the time to frequency domain involves a many-to-one and, conversely, a one-to-many relationship between the input and output of the transformation process, it may be anticipated that access to each data point must be repeated. To accomplish this with an untapped delay line requires that the data be circulated repeatedly through the device. As a consequence, the number of CCD transfers required to accomplish the transformation can be large, and so in the following discussion considerable attention is paid to overcoming the deleterious effects of charge transfer inefficiency.

1. Recursive Filters

Perhaps the simplest form of filtering that can be implemented with CCDs is the recursive filter. Such filters can be implemented with an untapped delay line, so the simplest devices are suitable components of such filters. However, the recursive filter does not provide a full transformation to the frequency domain of the kind required for real-time adaptation. Instead, it provides a single bandpass or bandstop filter. It is possible that such filtering can be adapted to suppress individual strong interferers; because of the potential benefit of this mode of operation under some circumstances, recursive filters are treated here in some detail.

Using a single stage of delay, either a feedback or a bilinear recursive filter can be implemented (Ref. 2). This delay can be implemented with a CCD. If the CCD has n stages, the delay T through the device will be $T = n/f_c$ where f_c is the clocking rate through the CCD, i.e, the clocking rate at which the signal transits from stage to stage. Fig. 1 shows the configuration of the bilinear recursive filter with the various feed-back gains indicated.

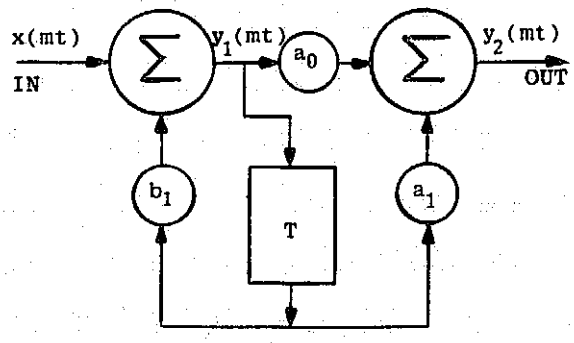

Fig. 1. Canonical form of a recursive filter

If either a_0 or a_1 is set equal to zero, the filter is equivalent to the standard recursive filter. Consequently, the more general bilinear configuration is treated and used to derive the response of the standard filter by setting the appropriate parameter equal to zero.

The response of the filter in Fig. 1 to an input x(mT) is given by a pair of difference equations. Thus,

$$y_1(mT) = x(mT) + b_1 y_1(mT-T) \qquad (1)$$

$$y_2(mT) = a_0 y_1(mT) + a_1 y_1(mT-T) \qquad (2)$$

A solution for the output can be obtained by taking the Z transform, solving for Y (Z) when the input function is a complex exponential, and inverting the transform by the method of residues. The result of this, for the steady state solution, is

$$Y(nT) = \frac{a_0 e^{j\omega T} + a_1}{e^{j\omega T} - b_1} e^{jn\omega T} = H(\omega) e^{j\omega nT} \qquad (3)$$

By suitable choice of the quantities a_0, a_1, and b_1, the transfer function $H(\omega)$ can be made to be that of a low-pass filter, high-pass filter, bilinear low- or high-pass filter, a low-pass canceller, or a high-pass canceller. In Table 1 these quantities are related to the frequency of the peak filter response and the 3 dB corner frequency for the 6 kinds of filters mentioned above.

Feed-back and bilinear recursive filters were designed and tested using the Fairchild CCD-311 and CCD-321 devices. The CCD-311 is a 260-stage two-phase buried channel serial in/serial out device. The CCD-321 consists of two independent 455 stage buried channel serial in/serial out shift registers (Ref. 3). Both types of CCDs were characterized in non-recursive circuits before their use as recursive filter elements. Second harmonic distortion of the CCD-311 was measured at -42 dB for a 945 kHz tone at a clock frequency of 10 MHz while a similar test using the CCD-321 showed second harmonic distortion to be -52 dB.

Fig. 2 shows the swept frequency response of a feed-back low-pass integrator and of the corresponding bilinear integrator using the CCD-311. The total time delay of 51.28 μs (obtained by clocking the CCD at 5.07 MHz) results in poles at frequency intervals of 19.5 kHz. The 3-dB bandwidth of the passband response was measured as 150 Hz, indicating a quality factor, Q, of 130. Fig. 3 shows similar swept frequency results obtained using one serial shift register of the CCD-321.

The harmonic content of single tones applied to both CCD-311 and 321 recursive circuits were studied. Although the plots

of Figs. 2 and 3 show peak to null ratios of ~40 dB for the feed-back circuit, we noted substantial relative increase in harmonic distortion when a single tone was placed exactly at a pole frequency. For example, second harmonic distortion increased 13 dB to a level of -25 dB of the fundamental for a signal of 39 kHz applied to the CCD-311 feed-back filter clocked at 5.07 MHz. Similar results were obtained using the CCD-321 circuit. This non-linear increase in harmonic distortion at the poles can be attributed to the finite linearity of the CCDs themselves. All measurements were made with input signals which were kept small compared to the absolute signal handling capability of the devices. Distortion due to filling the CCD potential wells to a point that interaction occurred with the interface were thus avoided, as were non-linear responses of the input and output stages.

The effects of transfer inefficiency are to shift the position of the pole frequencies from their ideal values (Ref. 4) and to cause the transfer frunction to be nonuniform in frequency. The transfer efficiency of the CCD-321 can be manipulated by changing the voltage of the static electrode set. We were therefore able to demonstrate a shift in the pole frequencies with a change in the transfer efficiency. This shift can be interpreted in terms of a non-linearity of the CCD's phase response with frequency. This increases with increased charge transfer inefficiency, and consequently, the frequency at which there occurs a particular phase shift through the device changes as the charge transfer efficiency changes.

A second effect of charge transfer inefficiency is a diminished amplitude of the device's transfer function as the Nyquist frequency is approached. Not surprisingly, this same diminuition of gain appears in the filter circuits implemented with CCDs. The amplitude of the transfer function of the CCD-311 feed-back low-pass integrator is shown for the frequency range zero to 5 MHz in Fig. 4. In Fig. 5 is shown the change of the transfer function of the CCD-311 bilinear low-pass integrator that results as the relative values of the feed forward coefficients a_0 and a_1 are changed.

2. The Circulating Filter Bank

Although the recursive filter is not suitable for transforming a data set into a representation suitable for narrow-band interference excision, there is another technique somewhat similar to recursive filtering which does provide a full transformation that may be suitable for narrow-band excision and which has an easily implemented inverse transformation. We here refer to the technique as the circulating filter bank. A block diagram of this method is shown in Fig. 6.

The circulating filter bank produces a spectral measure of the form

$$F_k(i) = \sum_{j=0}^{\infty} W^{k(i-j)} e^{-\alpha j} f_{i-j} \qquad (4)$$

where f_j is the input signal and

$$W^{jk} = e^{i2\pi jk/N} \qquad (5)$$

We wish to regard this as a transform and to determine an inverse transformation that permits restoration of the signal in the time domain. We consider the operation

$$g_i = \sum_{k=0}^{N} F_k(i)\, W^{-ki} \qquad (6)$$

$$= \sum_{j=0}^{\infty} f_{i-j}\, e^{-\alpha j} \sum_{k=0}^{N} W^{-ki}\, W^{k(i-j)}$$

$$= \sum_{j=0}^{\infty} f_{i-j}\, e^{-\alpha j}\, N\, \delta_{i,i-j} = N f_i$$

and find it is the desired inverse transform.

To implement this, the output of the filter is multiplied by the kernel function W^{ij} and summed. This can readily be done using an "integrate and dump" scheme shown below in Fig. 7

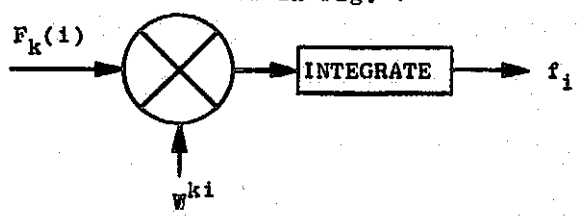

Fig. 7. Inverse transform of circulating filter bank

Note that the sum is only over a single set of N coefficients. Therefore, the dumping can be performed at the end of each circulation of the filter.

The circulating filter bank, shown in Fig. 8, is related to an older spectrum analysis technique which appears in the literature under the name coherent memory filter (CMF). To show their relationship, let the transform computed by the circulating filter be denoted $F_k(i)$ where k is the frequency index and i is the time index. Then we have

$$F_k(i) = \sum_{j=0}^{\infty} W^{k(i-j)} e^{-\alpha j} f_{i-j} \qquad (7)$$

The sum is over j, so the kernal $W^{k(i-j)}$ may be factored into $W^{ki}\, W^{-kj}$ and the first term taken out of the sum and transposed to the left hand side of the equation. Thus, we have

$$W^{-ki} F_k(i) = \sum_{j=0}^{\infty} (W^{-k} e^{-\alpha})^j f_{i-j} \qquad (8)$$

The right hand side of the above equation describes the processing done by the CMF analyzer. That the mixing and single sideband filtering is equivalent to multiplication by W^{-k} may be seen from

$$S(t) \cos 2\pi \frac{k}{N} = S(t) \left(\frac{e^{i2\pi k/N} + e^{-i2\pi k/N}}{2}\right) \qquad (9)$$

The single sideband filtering eliminates the left hand term in parenthesis,

$$\left[S(t) \cos \frac{k}{N}\right]_{\text{filtered}} = \begin{matrix} S(t)\, \frac{e^{i2\pi k/N}}{2} \\ S(t)\, W^{-k}/2 \end{matrix} \qquad (10)$$

In both the CMF and circulating filters, the CCD is required to circulate the information once for each time sample. The number of transfers required then increases as N^2 where N is the size of the transform, if the device can be tailored to the function, or as nN if an available delay of n stages is used (where $n > N$). Because charge-coupled devices are not perfect in their ability to transfer charge, the cumulative effect of many such transfers can be a gradual dispersion of the charge packet representing a signal into following charge packets. This effect places an upper limit on the size of the transformation that can be accomplished. Techniques for increasing the number of filters implementable with a single device are considered next.

Typical charge-transfer devices operate with a charge transfer efficiency of approximately 0.99995. That is to say, each time a charge packet is transferred from one well to another, there is a probability $\varepsilon = 0.00005$ that any given charge quanta will fail to transfer and so will remain in a well where it will serve to corrupt the signal respresented by a succeeding charge packet.

The transfer of charge from one cell to another may be treated as a Bernoulli process with a probability η of success and a probability $\varepsilon = 1 - \eta$ that the charge element will not transfer. If it is attempted to transfer the charge N positions along the device, after the Nth clock cycle, the charge that was initially within a single packet will be distributed among the initial cell, the intended final cell, and the various intervening cells according to the binomial distribution, which may be written

$$p(i,N) = \binom{N}{i} \eta^{N-i} \varepsilon^i \qquad (11)$$

where $\binom{N}{i}$ is the binomial coefficient:

$$\binom{N}{i} = \frac{N!}{(N-i)!\,i!} \qquad (12)$$

The laggard charge is sensed only after it has completely traveled through the device to the output point. The probability that it will require N+k attempted transfers before the specified N successful transfers occur may be written in terms of the binomial distribution as

$$p(N,N+k) = \binom{N+k}{N} \eta^N \varepsilon^k \qquad (13)$$

Parametric computations showing how $p(N,N+k)$ varies with N and k have been made. They show that if it is desired to keep the effects of charge transfer inefficiency to within a few percent, the number of transfers cannot much exceed 1024, nor the number of implemented filters, 32, if this simple mode of operation is to be utilized.

Better performance can be achieved if a cluster of adjacent cells are used to represent each signal sample. The extra cells of each cluster are zeroed with each circulation so that laggard charge is disposed of before it can corrupt the succeeding signal bearing cell, except in the relatively unlikely event that the charge falls far enough behind in a single circulation to reach the following signal sample. This method can provide good isolation of the signal samples, but it suffers from a deterioration of the samples themselves because the laggard charge is lost. To overcome this effect, a second use can be found for the multiple cells of a cluster. In this technique, the signal bearing cell is preceded by one or more cells that are filled to the same level as the signal bearing cell. Then the charge that is lost from the signal bearing cell to the following insulating cells is partially compensated by the charge it gains from the preceding cells.

The effective charge transfer efficiency that can be achieved by these methods can be computed by regarding the lagging of charge during a single pass through the CCD as a transition in a Markov process. Where k-1 preceding cells are filled to the same level as the signal bearing cell, the probability of no transition (no lag) is enhanced by the next k-1 transition probabilities. However, the probability that a signal cell is corrupted by laggard charge from a preceding signal sample must also be increased by summing over k appropriately chosen transition probabilities.

Table 2 shows the transition probabilities that result when a CCD is used in the above described way. The number of signal bearing cells is k; and the number of cells in a cluster is m; so m-k is the number of insulating cells. The transition probabilities are for the specified number of circulations, the number being appropriate for use of the device as a circulating filter bank or coherent memory filter.

The sinusoidal portion of a thirty-two point circulating filter bank has been designed and tested using the CCD-311. The diagram of the analyzer is as shown in Fig. 6. The analyzer was implemented using the techniques addressed above for increasing effective transfer efficiency. Control of the CCD was accomplished by digital logic. Accumulated signals spanned four CCD clock cycles (i.e., four samples) followed by four zeroed reference signals (except for the thirty-second element which consisted of eight zeroes). The fourth sample of each signal set from the CCD output was used to set the signal level for the four new samples taken into the CCD. The algorithm described by equation (5) was implemented using digital shift registers. The computed coefficients were then applied to an analog multiplier after digital-to-analog conversion. Fig. 8 shows several of the initial kernel functions thus generated. Figure 9 shows a complete 32 x 32 data set. Some preliminary experimental results obtained from the analyzer for three different input tones are shown in Fig. 10. The CCD clock rate was 5.1 MHz corresponding to an analysis bandwidth of 5 kHz. A future implementation of this technique is planned using the CCD-321. In this case, one of the 455 bit registers will be used to perform in-phase processing while the other register will be processing the quadrature channel. A ninty-one point transform will be implemented.

3. Analog FFT

Although the recursive filter and the circulating filter discussed above are relatively simple and straightforward to implement, they suffer from a common shortcoming when implemented in so simple a form: there is little control of the window function used in computing the transforms, with the resulting lack of control of sidelobe levels. This shortcoming can be overcome by employing additional delay elements to implement a higher order recursive filter, or to approximate more desirable weighting functions in the circulating filter. This process carried to its logical extreme would require CCDs with as many taps as those required for the implementation of transversal filters of the kind to be discussed in a subsequent section.

There exists at least one other method that can be used to compute Fourier transforms of arbitrarily windowed functions using CCDs that are not tapped. This method derives from the Fast Fourier Transform that is a well known technique in digital signal processing. The following discussion of this method assumes some familiarity with the Fast Fourier Transform, and no effort will here be made to justify or derive the algorithm.

A typical form of the algorithm used in the digital computation of the FFT is called the "in place" transform. Its advantage for this purpose lies in the fact that the results of each butterfly operation can be stored in the same memory locations as were the input data to the butterfly operation. The replaced data are the only data required for that particular operation, and these data are needed nowhere else in the calculation. This property of the algorithm has two advantages: it minimizes the amount of memory required, and it obviates the need to compute more than a single pair of addresses for each butterfly operation. However, for our purpose, where the memory is to be a charge-coupled device operated as an analog shift register, these advantages are not realized. The CCD is not a random access memory but a circulating serial memory. Therefore, a considerable advantage is realized if the FFT algorithm can be implemented in a modified form which assures that the data to be read are immediately available from the circulating memory, and the results of a calculation can be immediately stored into the first available memory locations. The tree graph for such an algorithm is shown in Fig. 11 (Ref. 5). numbers in the vertical columns indicate the positions which the corresponding data points would have taken had the "in place" algorithm been used. The mathematical process (butterfly operation) would, of course, have to be the same as that in the "in place" algorithm. Note the important property of the form of the algorithm for our purpose. Data are taken from "addresses" at the output of the circulating memory and from the midpoint of the memory, and the results of the butterfly operation are stored in adjacent memory locations (of a second memory). The same addressing scheme applies to all levels of the computation, although the arrows indicating the flow of data are shown only for the first level.

Fig. 12 is a block diagram of an analog processor implemented according to this scheme. All arithmetic operations are complex. The weights necessary at each point in the process can be stored in digital form and applied to a digital-to-analog converter before undergoing multiplication. If this procedure were used, the weights could be computed by digital logic as shown in Figure 13.

As described earlier for the other techniques, transfer inefficiency is the limiting physical process here. The effect places an upper limit on the number of transfers which can be performed and, consequently, to the size of the transform. If N is the greatest number of transforms which can be performed, then the largest transform which can be performed by the direct computation of a Fourier transform is $\sqrt{N}$. In comparison, the fast transform algorithm allows an n point transform to be computed with only $n \log_2 n$ transfers, so the upper limit on the size of the transform is governed by the equation

$$n \log_2 n \leq N \qquad (14)$$

The difference can be significant. For example, if 10^4 transfers can be performed, the direct algorithm would be limited to a 100 point transform while a 1000 point transform could be computed by the fast transform method.

C. SPECTRAL ANALYSIS METHODS UTILIZING TAPPED DELAY LINES

A tapped CCD, in which the individual analog samples are accessible for processing, permits the implementation of a transversal filter. We here consider two techniques involving transversal filters: the direct filtering of the signal into bandpass frequency components and the chirped Z transform method. The former technique leads to the signal being distributed on many lines on the basis of frequency but still in a time domain representation. These separated spectral components can be separately limited or excised, and the residuals can be summed back together to reconstitute the desired time series representation of signal and residual noise. The chirped Z transform results in an actual change of representation to the frequency domain, and there is required an inverse transformation if a return to the time domain is necessary.

1. Transversal Filter Bank

By means of a tapped CCD delay line, it is possible to compute the convolution of a discretely sampled signal, f_i, with a stored reference function, g_i. For example, with a device having N taps, the convolution

$$F(m) = \sum_{j=1}^{N} f_{m-j}\, g_j \qquad (15)$$

can be computed. If the function g_i is made to be the discrete Fourier kernel function

$$W^{-jk} = (e^{-i2\pi/N})^{jk} \qquad (16)$$

the result of the convolution is the kth coefficient of the discrete Fourier transform of f_j.

If I and Q phase references are used to reduce the signal to baseband, the signal may be written

$$f_j = \alpha_j + i\,\beta_j \qquad (17)$$

and this expansion may be used to obtain the convolution function in terms of real quantities. Thus

$$F_k(m) = \sum_{j=i}^{N} (\alpha_{m-j} + i\beta_{m-j})\,(C_{jk} + i\,S_{jk}) \qquad (18)$$

$$= \sum_{j=1}^{N} \alpha_{m-j}\, C_{jk} - \sum_{j=1}^{N} \beta_{m-j}\, S_{jk} + i \sum_{j=1}^{N} \alpha_{m-j}\, S_{jk} + i \sum_{j=1}^{N} \beta_{m-j}\, C_{jk}$$

Thus, four convolutions are required to compute each complex Fourier coefficient. The first and third terms can be derived from different weights applied to the taps of the same CCD, and similarly the second and fourth terms can be derived from a second CCD's taps.

A method for implementing this approach by means of multiplicative conductive elements only using two identical tapped CCDs is shown in Figure 14. Here, the signal inputs to the tapped CCDs are in phase quadrature. (This condition is assured by using quadrature phase local oscillator injection voltages in the last mixer circuits.) The in-phase and quadrature phase time delayed signals can be separately weighted and combined to synthesize the desired filters. It is to be observed that the two, n tap each, delay lines allow for the generation of n orthogonal filters, since the in-phase and quadrature partial resultants can, themselves, be combined by either addition or subtraction to result in response to either an upper or lower sideband. (For the upper and lower sideband synthesized filter set to be contiguous in frequency, the time delays must be operated at baseband; otherwise, the sideband filter sets will be separated in the manner of hetrodyne images.) Thus, if the latter practice is followed, no penalty in capacity has been paid for the engineering convenience of resistive-only weighting; the number of filters synthesized is equal to one-half the total number of taps.

Alternatively, a relatively high frequency IF can be employed so that image response can be suppressed by conventional filtering at the stage preceding the mixer. A CCD with n taps can then be used to generate n/2 bandpass filters.

A method for cascading filters of this kind has been suggested by White (Ref. 6). In effect, this permits relatively large transforms to be implemented with a common building block--a bank of N filters implemented in the manner discussed above. By this means, N+1 such filter banks can be used to implement a bank of N^2 filters, and a $N^2 + N + 1$ filter bank can implement N^3 filters, etc. It should be noted that each successive level of these CCDs are clocked at a rate of 1/N that of the preceding level, so while the first such CCD may be required to process signals at its maximum clock rate, the subsequent CCDs operate rather below their maximum rates.

The experimental properties of bandpass filters simultaneously synthesized using tapped CCDs have been studied. The device used to perform these experiments was a Westinghouse designed and fabricated twenty tap, four phase, surface channel CCD (Ref. 7). The device has been described in detail elsewhere (Ref. 8). In the following examples, only a single device was used resulting in baseband processing of up to ten independent filters,

(i.e., we assume all image frequencies have been removed) as shown in Fig. 15. As in the case of recursive filter implementations, the eventual need for analog pre- and post-filtering of sampled signals is recognized although not specifically addressed here. Each independent filter consisted of twenty variable resistors operating as the conductances of a current summing differential amplifier. Provision for negative weights was made by providing a negative summing bus which was subtracted from the positive bus at the output of each filter. A sample and hold was used at the output of these differential amplifiers. Each CCD tap output was buffered by a low output impedance, high current gain, line driver to minimize cross coupling between resistor weights of different filters. The uniform weighted impulse response of a filter whose bandpass occurs at 0.1 fc is shown in Fig. 16. The frequency response of the filter is shown centered at 2 kHz when clocked at 20 kHz in Fig. 17. The impulse of this filter when a Hamming window is impassed upon the tap weights is shown in Fig. 18. The impulse response of two adjacent filters, the first centered at 0.1 fc and the second centered at .15 fc are shown in Fig. 19. Fig. 20 shows the frequency response of these filters clock at 20 kHz independently in (a) and (b) and summed together in (c). Besides the Hamming weighting, each set of filter tap weights has imposed upon it a relative uniform weighting to account for the differences in amplitude response between filters that otherwise would occur.

The viability of using this externally weighted approach in a system application depends largely upon the capability of implementing the resistor array as a reproduceable thick or thin film hybrid with sufficient resistor value accuracy. To obtain peak to sidelobe ratios of -40 dB, which is within the capabiltiy of the particular device tested, requires setting tap weights to an accuracy of <1%. This proved to be a formidable task when more than one filter was being synthesized.

2. Optically Tapped Chirped Z Transform

The transversal filters discussed in the preceding section requires the use of a CCD having each stage provided with an output tap. This electrical output can be divided to provide multiple weighted sums. However, it is also possible to employ a delay line that is provided with input taps at each stage. Now, however, there is only a single weighting function that can be applied, i.e., the data set can be convolved only with a single stored function rather than with the multiple functions of the prior case. Nevertheless, there exists a technique whereby the required spectral analysis can be accomplished through convolution with a single stored function, i.e., can be performed with a single transversal filter. In the following discussion, we consider how this single transversal filter canbe implemented with a line imaging CCD of the kind now commercially available. Of course, output taps of the kind discussed above could be used as well.

The discrete Fourier transform may be defined as

$$F_k = \sum_{n=0}^{N-1} f_n \, e^{-2\pi ink/N} \qquad (19)$$

If the substitution is made,

$$2nk = n^2 + k^2 - (n-k)^2 \qquad (20)$$

equation ( ) can be put into the form

$$F_k = e^{-\pi ik^2/N} \sum_{n=0}^{N-1} (f_n \, e^{-\pi in^2/N}) e^{\pi i(n-k)^2/N} \qquad (21)$$

If the signals are to be represented as real analog voltages, currents, or quantities of charge, it must be broken into two parallel channels, one representing the reals and the other, the imaginaries. Thus, for example, the set of real data samples $\{f_n\}$ must be multiplied by sinusoidal and cosinusoidal chirps, yielding

$$c_n = f_n \text{ cosine } (\pi n^2/N) = f_n C_n \quad \text{and} \qquad (22)$$

$$s_n = f_n \text{ sine } (\pi n^2/N) = f_n S_n$$

These must be convolved with the function

$$e^{\pi i(n-k)^2/N} = C_{n-k} + i\, S_{n-k} \qquad (23)$$

We here encounter the problem of having to represent a complex function in terms of real physical quantities since we are performing the convolution function by a light sensing CCD utilizing the technique first described by Lagnado and Whitehouse (Ref. 9). A light signal, varying as S_n or C_n is propagated through a mask having a transmission that is proportional to the real or imaginary parts of $e^{\pi i(n-k)^2/N}$. Transmission can be controlled either by graded optical density or by varying the area of transmission in an otherwise opaque mask. However, now both the light intensity, representing S_n or C_n and the mask transmission, representing the Re $e^{\pi i(n-k)^2/N}$ or Im $e^{\pi i(n-k)^2/N}$ are unipolar signals while the functions to be represented by them are bipolar.

One approach is to carry the bipolar signal on a pedestal. The bias levels for the premultipled signal and the convolution kernel may be denoted A and B, respectively. Then, a convolution such as

$$R_k = (A + s_n) * (B + C_{n-k}) \qquad (24)$$

$$= \sum_{n=0}^{N-1} (A + s_n)(B + C_{n-k})$$

is computed. Four resulting terms may be identified:

$$R_k = NAB + A \sum_{n=0}^{N-1} C_{n-k} + B \sum_{n=0}^{N-1} s_n + \sum_{n=0}^{N-1} s_n C_{n-k} \qquad (25)$$

Only the last of these is the desired result, the rest being the spurious result of placing the signals on a pedestal.

Of these extraneous terms, the first is constant, and the second will vary predictably with k. However, the third term

$$B \sum_{n=0}^{N-1} s_n = B \sum_{n=0}^{N-1} f_n S_n \qquad (26)$$

will be a random variable having zero mean and an rms fluctuation determined by the mean temperature of the passband under analysis. This result is undesirable inasmuch as it represents an inability of the spectrum analyzer completely to resolve the band into frequency components. In order to avoid this problem, it is necessary to at least provide parallel convolvers so that, in effect, the mask function can be made to be positive and negative (i.e., the light can be assigned to either the positive or negative channel). The two channels can then be differenced to provide the desired result. Fig. outlines the arrangement of the CCDs and their illuminators.

This technique is being implemented using 256 x 1 linear imagers. To reduce the number of components and the optical complexity, a mask has been developed which spatially multiplexes the chirp waveform corresponding to sine +, cosine +, sine -, and cosine - functions. A computer generated plot of this mask function is shown in Fig.

The practical result that light incident upon one photosite will contaminate its adjacent neighbors either because of diffraction or poor optics has been analyzed. Table lists the computed results of the expected sidelobe response of the analyzer for various operating conditions.

At this time we have not yet demonstrated experimentally this analyzer technique. However, we have demonstrated (as have others, Ref. 9) the convolution properties of a 256 x 1 CCD imager. We obtained the impulse response and autocorrelation of a mask function which consisted of a 127-bit PN sequence.

III. INTERCOMPARISON OF TECHNIQUES

In the preceding sections, we have discussed five methods for transforming in real time from a time series to a relatively narrow band (approximately 100 Hz) frequency representation where effective interference excision can be performed. We here make comparisons among the various methods on the basis of the experimentation and analysis of the study.

Three methods were considered for implementing filters with untapped CCDs. The first of those was the simple recursive filter and various variations of it (e.g., bilinear and canceller forms). This method requires a single CCD delay line for each subband filter to be implemented, and in each such filter there are two or more gains that must be adjusted if the filter is to conform with other such filters. Also, each CCD requires a different clock rate which at the least is an inconvenience (however, recursive filter techniques have been developed which allow a single delay line or two to synthesize more than a single filter (Ref. 10)). Consequently, it seems unlikely that such an approach will be practicable except in cases where the suppression of a relatively small number of interferers offers significant improvement in system performance. In such an application the ability to dither the passband of the filter by control of the CCD clock is an advantage. The effective window of such a filter can be altered in its duration by adjusting the feed-back gain, but any control of the passband beyond that can only be achieved by a multipole filter.

The circulating filter bank, and similar coherent memory filter (CMF), have properties akin to those of the recursive filter except that now it is attempted to implement many filters in time multiplex form. Because the delay is the same for all filters in the set, it is necessary to make a correction of phase from frequency to frequency--in the feed-back loop for the CMF and at the input for the circulating filter bank. However, these methods suffer the same disadvantages as the recursive filter in that the time window is not easily controlled and thus neither are the analyzers' sidelobe responses. Also, unlike the recursive filter, the circulating filter bank requires that the signal at independent degrees of freedom be represented as charge in adjacent cells of the CCD. This places a high premium on the transfer efficiency of the device in order that the signal represented by charge in one cell does not badly corrupt that in another. Techniques were developed to mitigate this problem by representing the signal as one of a cluster of m cells which permitted insulation between adjacent signal cells and some compensation for the charge lost in the transfer process. These methods may permit filter banks numbering into the hundreds but at the cost of aggravating a second limitation--that of the clocking frequency. CCDs usually operate at clock rates to ≈ 15 MHz with a few having been tested at >100 MHz. Because the CCD must circulate once between each pair of samples, a bank of N filters, implemented with m cell clusters, can only process samples at a rate $f_c/(NM)$. For N=100 and m=3, a CCD clocked at 6 MHz would permit sampling at only a 20-kHz rate, corresponding to Nyquist bandwidth of 10 Hz. Attempts to implement larger banks of filters with the same resolution would require clocking rates that increase with at least the square of their number.

The analog FFT provides a means for circumventing many of the problems associated

with recursive filters and the circulating filter bank. First, it would not be difficult to introduce arbitrary window functions as the data are initially stored in the CCD analog memory. Because the number of transfers necessary increases only as N log N with the size of the transform, less severe demands are placed on the device's charge transfer efficiency and on the clocking rate. Also, the method requires no more elaborate components in its implementation than do the circulating filter bank and the CMF. Both require a memory for storage of the kernel functions (sines and cosines) and an analog multiplier. The greatest difference is that a more sophisticated control logic is required in the case of the analog FFT. It is projected that 1024 point transforms could be implemented by the FFT approach with currently available serial in/serial out CCDs. Such a transform would require on the order of 10^4 transfers, which at a rate of one MHz, could be completed in .01 seconds--which is approximately the time aperture required for 200 Hz resolution. Such an analysis would handle a sampling rate of 10^5 Hz.

Two methods were considered that made use of tapped CCD delay lines. Because there is no need to circulate the data in these methods, the signal sampling is the same as the CCD's clock rate. However, in the case of the externally tapped delay line filter bank, a point is quickly reached in which the number of pinouts becomes a practical limitation. For example, the device tested had twenty taps. If the technique of cascading is employed as described by White, et al., (Ref. 6), up to one hundred filters could be synthesized by eleven devices. However, unless the weighting array corresponding to the twenty taps of one device were contained in a package approximatley the same size as the device itself (or possibly on a common substrate) the implementation of this many filters would be ungainly.

The chirped Z method is very powerful because a single convolution (transversal filter) serves to analyze an entire set of signal samples. These samples can be taken at the clocking rate, so passbands measured in MHz can be processed by this method. The limitation on the size of the transform is imposed only by the limits in the size of the CCD and associated taps and summing circuitry that can be fabricated. When the convolution is performed by an electrically accessed CCD, the weights for the filter can readily be implemented by the split electrode technique. One advantage that an optically implemented CZT processor could have over its electrically implemented analog is the capability of tailoring a mask to compensate for the effects of charge transfer inefficiency.

There is one respect in which a tradeoff between the chirped Z method and the analog FFT may exist. This is in respect to the precision with which the weights can be implemented. The analog FFT is implemented with untapped CCDs that treat all samples identically, and so while it is necessary to match the performance of pairs of CCDs, the problem of cell-to-cell inqualities is obviated. Such inequalities must be kept rather low in the methods employing tapped delay lines. For example, if the peak response of each filter is to exceed the mean sidelobe level by a factor R, it is necessary that the tap weights be within $\sqrt{N/R}$ units of the correct weights.

IV. CONCLUSIONS

We have analyzed and demonstrated several CCD techniques which may find application in electronic systems which require excision of unwanted interferers (natural or otherwise). Depending upon the relative number of interferers expected in a particular application, a hierarchy of the filter techniques studies here can easily be made in which the complexity of implementation is weighted against the density of excisions required. In the case of just a few interferers, a CCD implemented recursive filter is justified. When a greater number of excisions are required, transform techniques become viable. The circulating filter bank is probably the easiest to implement but also the most limited from the standpoint of transform length. On the other hand, the analog CCD FFT has some attractive features which make it a competitor of the electrical implemented chirp Z technique when the total analysis bandwidth is less than one MHz. The analog CCD FFT uses similar hardware to the circulating filter bank and should not be difficult for us to demonstrate.

V. ACKNOWLEDGEMENT

We would like to cite Mr. Jim Taylor for his expert help in implementing the circulating filter bank and Mr. Joseph Green for his analyses of the transversal filter bank technique. We wish to thank Dr. Dean Baker of NRL for furnishing the tapped CCD. This work has been funded by the Defense Advanced Research Projects Agency under ONR Contract No. N00014-76-C-0496.

VI. REFERENCES

1. Wheeler, J., "Analysis of Noise Measured in the Upper MF-Lower MF Regime in the North Atlantic," ITT-EPL Project Report No. 255, ONR Contract N00014-76-C-0441, June, 1974. (U)

2. Tao, T. F., et al., "Sampled Analog CCD Recursive Comb Filters," Proc. International Conference of Charge-Coupled Devices," pp. 257-266, October, 27, 1975.

3. Wen, D., "A CCD Video Delay Line," Proc. ISSCC, pp. 204-205, February 18-20, 1976.

4. Sequin, C., and Tompsett, M., Charge Transfer Devices, Academic Press, Inc., New York, 1975, p. 216.

5. An Algorithm with similar properties can be found in: Gold, B., and Rader, C., Digital Processing of Signals, McGraw-Hill, New York, 1969, p. 183.

6. White, M., and Webb, W., "Study of the Use of Charge-Coupled Devices in Analog Signal Processing Systems," Final Report, NRL Contract N00014-75-C-0069, May, 1974.

7. White, M., et al., "An Analog CCD Transversal Filter with Floating Clock Electrode Sensor and Variable Tap Gains," Proc. ISSCC, pp. 194-195, February 18 - 20, 1976.

8. White, et al., "Charge-Coupled Device Analog Signal Processing," Final Report, NRL Contract N00014-75-C-0283, February, 1976.

9. Lagnado, I., and Whitehouse, "Signal Processing Image Sensor Using Charge-Coupled Devices," Proc. Int., Conf. Tech. and Appl. of CCD, Edinburgh, September, 1974, p. 198.

10. Mattern, J., and Lampe, D., "A Reprogrammable Filter Bank Using CCD Discrete Analog Signal Processin," Proc. ISSCC, February 12-14, 1975, p. 148.

Table 1. Design Equations for Recursive Filters

	K	a_0	a_1	ω_{peak}	G_p	
STANDARD LOW PASS	$e^{-\omega_x T}$	1	0	0	$\lvert\frac{a_0}{1-K}\rvert^2$	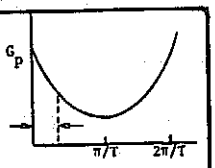
STANDARD HIGH PASS	$-e^{-\omega_x T}$	1	0	π/T	$\lvert\frac{a_0}{1+K}\rvert^2$	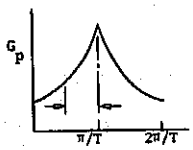
BILINEAR LOW PASS	$(\frac{1-\sin \omega_x T}{\cos \omega_x T})$	1	1	0	$\lvert\frac{2a_0}{1-K}\rvert^2$	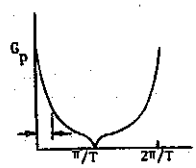
BILINEAR HIGH PASS	$-(\frac{1-\sin \omega_x T}{\cos \omega_x T})$	1	-1	π/T	$\lvert\frac{2a_0}{1+K}\rvert^2$	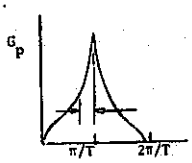
	K	a_0	a_1	ω_{peak}	G_p	
LOW PASS CANCELLER	$-(\frac{1-\sin \omega_\delta T}{\cos \omega_\delta T})$	1	1	0	$\lvert\frac{2a_0}{1-K}\rvert^2$	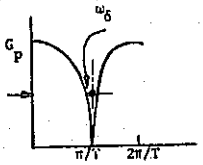
HIGH PASS CANCELLER	$(\frac{1-\sin \omega_\delta T}{\cos \omega_\delta T})$	1	-1	π/T	$\lvert\frac{2a_0}{1+K}\rvert^2$	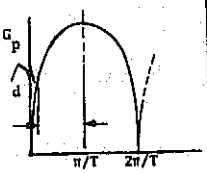

NOTATION:

G_p	peak gain
ω_x	frequency interval between frequency of peak response and 3 dB corner frequency
ω_δ	frequency interval between cancelled frequency and 3 dB corner frequency $\omega_\delta = \pi/T - x$
T	delay time. For CCD delay $T = f_c/N$
f_c	CCD clock frequency
N	number of CCD stages

Table 2. Transition Probability

NO. OF CIRCULATIONS	k	m	N	π_0	π_1	π_2	π_3	π_4
128	2	3	384	0.983	1.47×10^{-4}	1.12×10^{-8}	5.54×10^{-13}	2.05×10^{-17}
256	2	3	768	0.842	1.99×10^{-3}	2.35×10^{-6}	1.84×10^{-9}	1.08×10^{-12}
512	2	3	1536	0.243	8.93×10^{-3}	1.64×10^{-4}	2.00×10^{-6}	1.82×10^{-8}
512	3	3	1536	0.989	3.624×10^{-2}	6.627×10^{-4}	8.066×10^{-6}	7.350×10^{-8}
512	3	4	2048	0.992	2.047×10^{-3}	2.219×10^{-6}	1.601×10^{-9}	8.644×10^{-13}

Table 3. Effects of Optical Diffraction and Distortion Upon Optical CZT Performance

	QUANTIZING LEVELS				
	3	10	20	30	100
UNIFORM					
No Pedestal					
0 Spill				-13.291	-13.473
0.1 Spill					-13.291
0.2 Spill					
Pedestal					
0 Spill				-13.291	-13.382 (-13.324)
0.1 Spill					
0.2 Spill					
HAMMING					
No Pedestal					
0 Spill	-12.83	-27.943	-33.04	-37.688	-42
0.1 Spill	-12.56	-27.310	-29.131	-32.317	-33.592
0.2 Spill		-24.579			-27.674
Pedestal					
0 Spill				-25.945	
0.1 Spill		-25.581		-24.761	-24.761
0.2 Spill		-24.306			

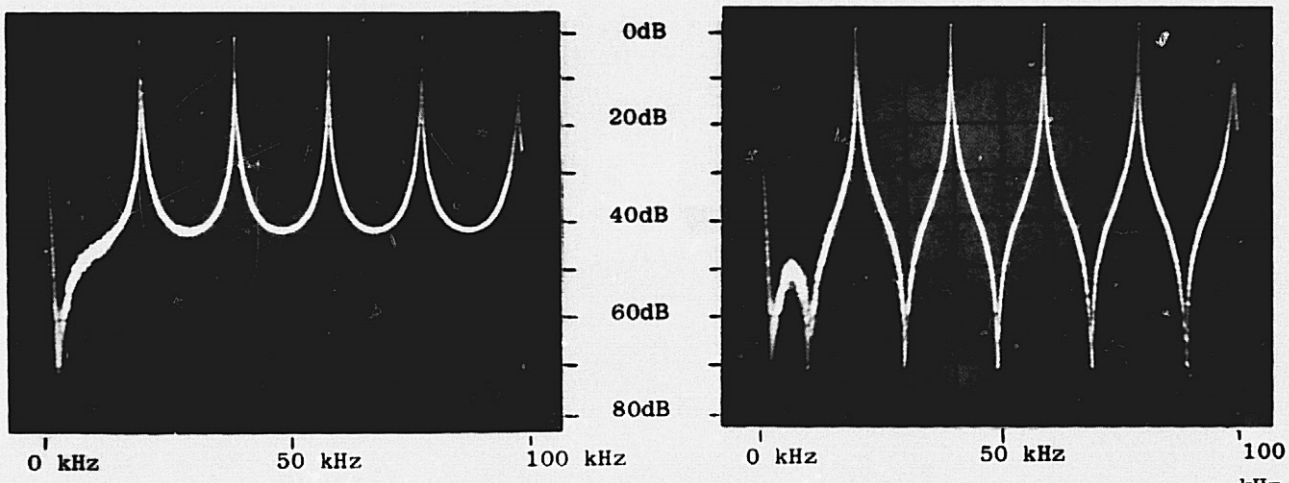

STANDARD Z

$a_1=1$
$a_0=0$
$0< b_1 \leq 1$

Vertical =10 dB/ div
Horizontal =10 kHz/div
$f_{\text{sample rate CCD}}=5.07$ MHz

BILINEAR Z

$a_0= 1$
$a_1= 1$
$b_1 \leq 1$

Fig. 2. Swept Frequency Response of Recursive Filters Using the CCD-311

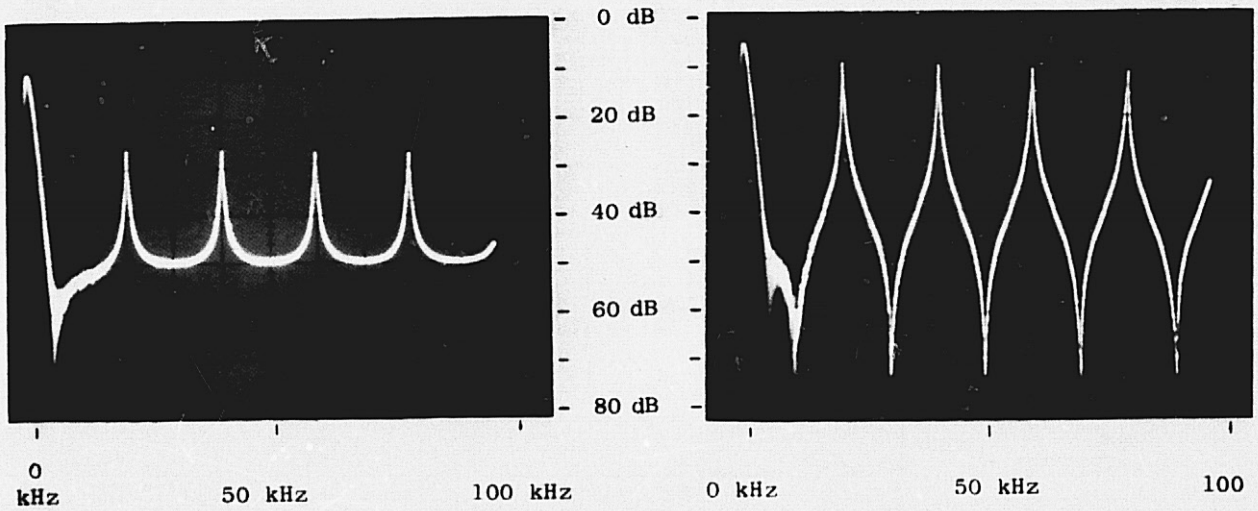

STANDARD Z

$a_1 = 1$
$a_0 = 0$
$0< b_1 \leq 1$

Vertical = 10 dB/div
Horizontal = 10 kHz/div
f_{clock} = 9.1 MHz

BILINEAR Z

$a_0 = 1$
$a_1 = 1$
$0< b_1 \leq 1$

Fig. 3. Swept Frequency Response of Recursive Filters Using the CCD-321

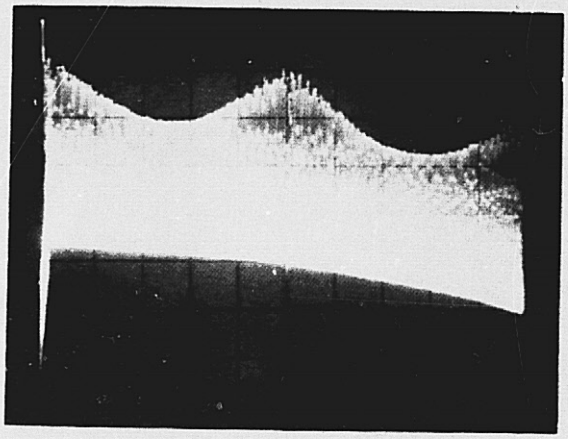

Fig. 4. Zero to 5 MHz Frequency Response of CCD-311 Feed-back Filter

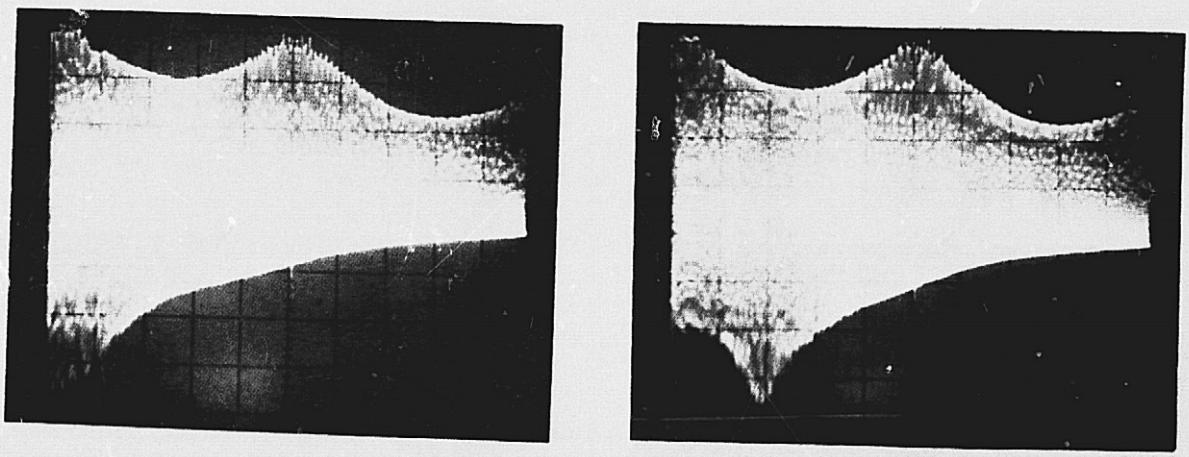

5(a) 5(b)

Fig. 5. Zero to 5 MHz Frequency Responses of CCD-311 Bilinear Filter for Several Relative Values of a_0 and a_1

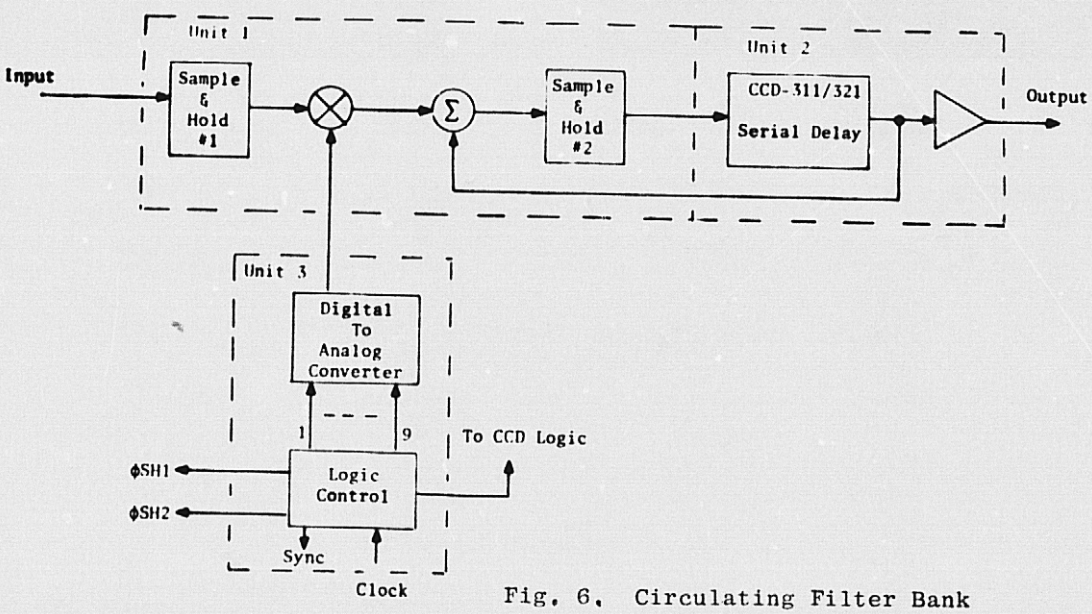

Fig. 6. Circulating Filter Bank

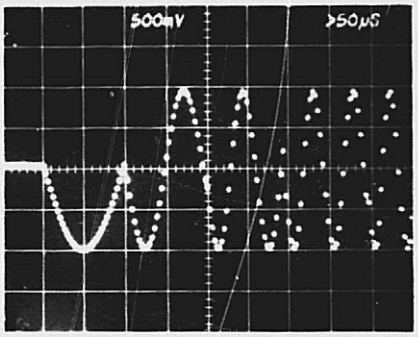

Fig. 8. DAC Output Showing Several Kernels

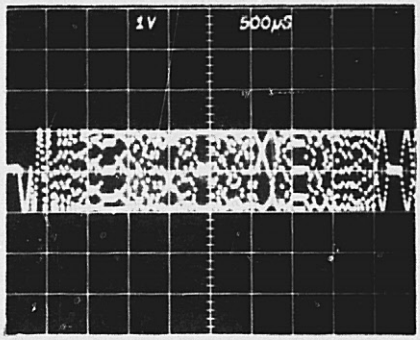

Fig. 9. The Kernel Function

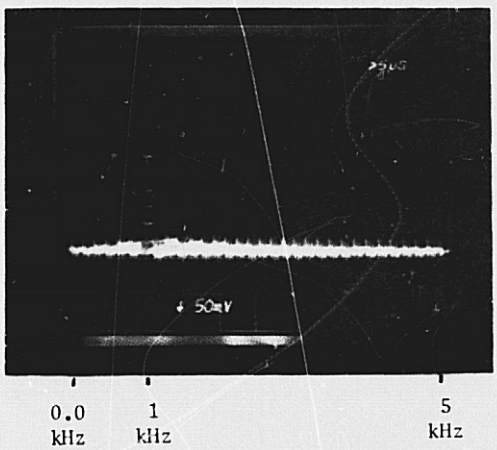

10(a)

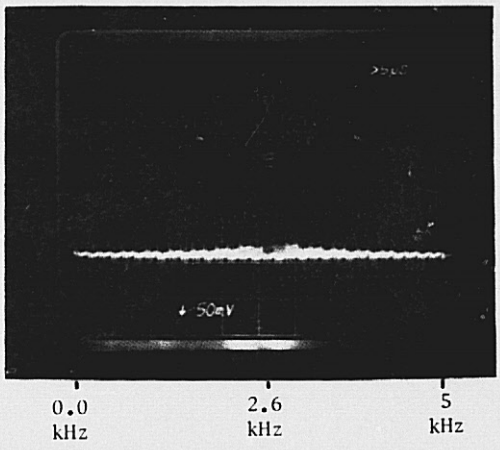

10(b)

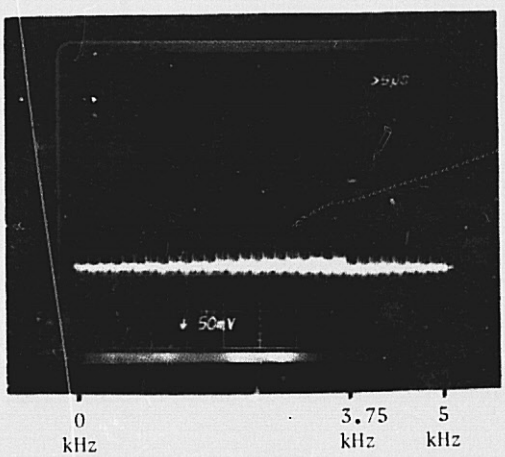

10(c)

Fig. 10. Circulating Filter Bank Using the CCD-311

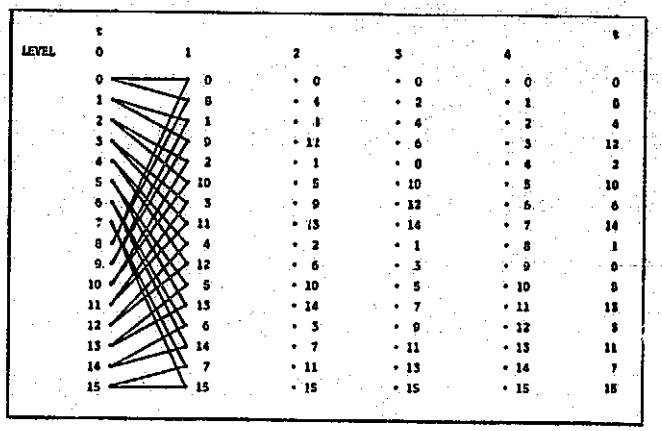

Fig. 11. Modified Tree Graph

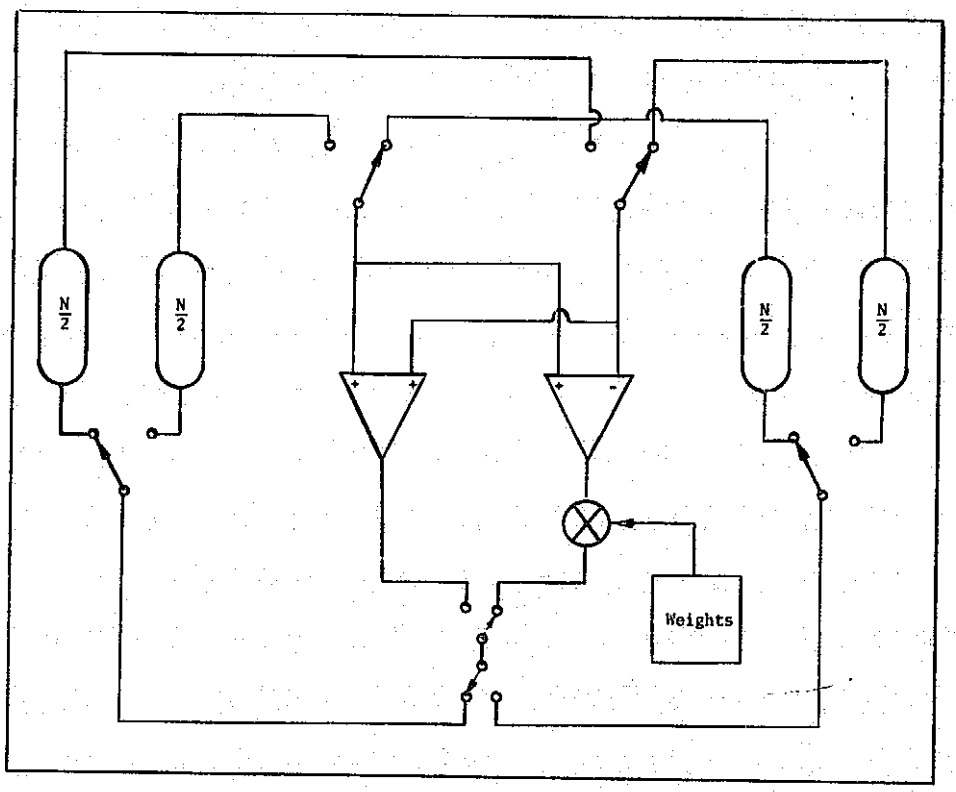

Fig. 12. Analog FFT Implemented with CCDs

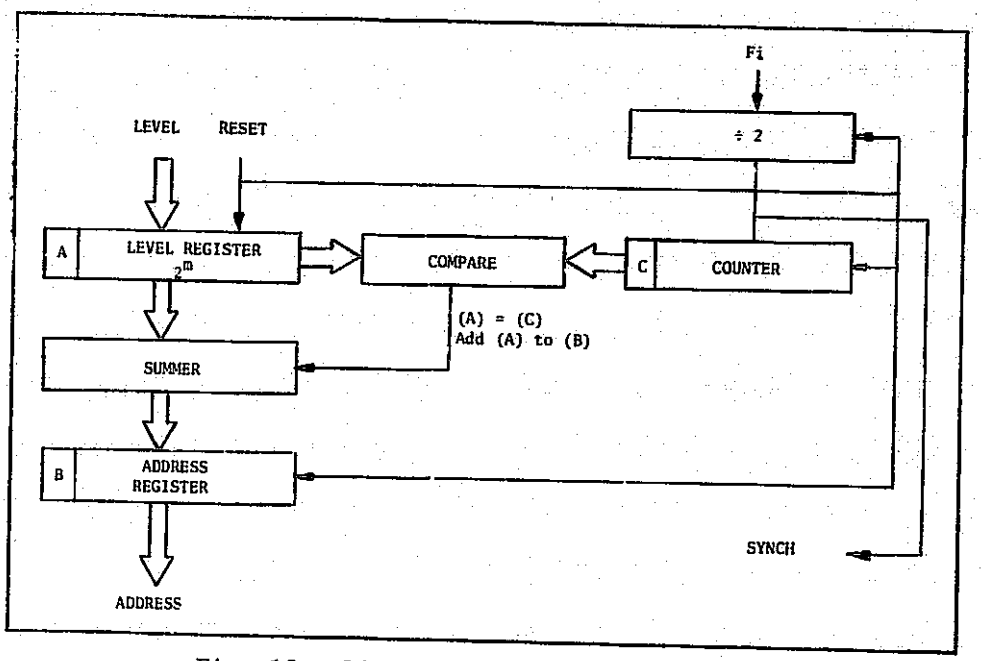

Fig. 13. Digital Logic for Generating Weight Addresses for Analog FFT

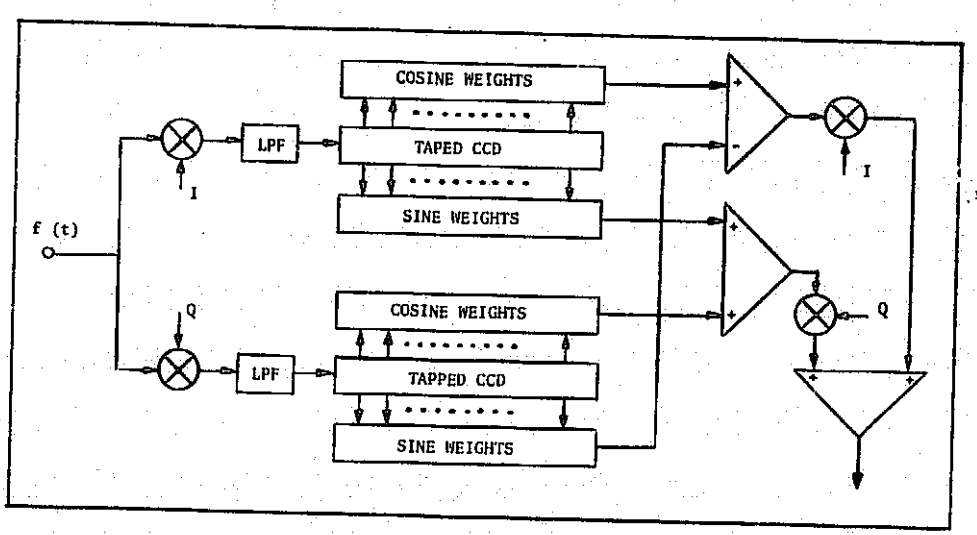

Fig. 14. Implementation of Transversal Filters Using Tapped CCDs

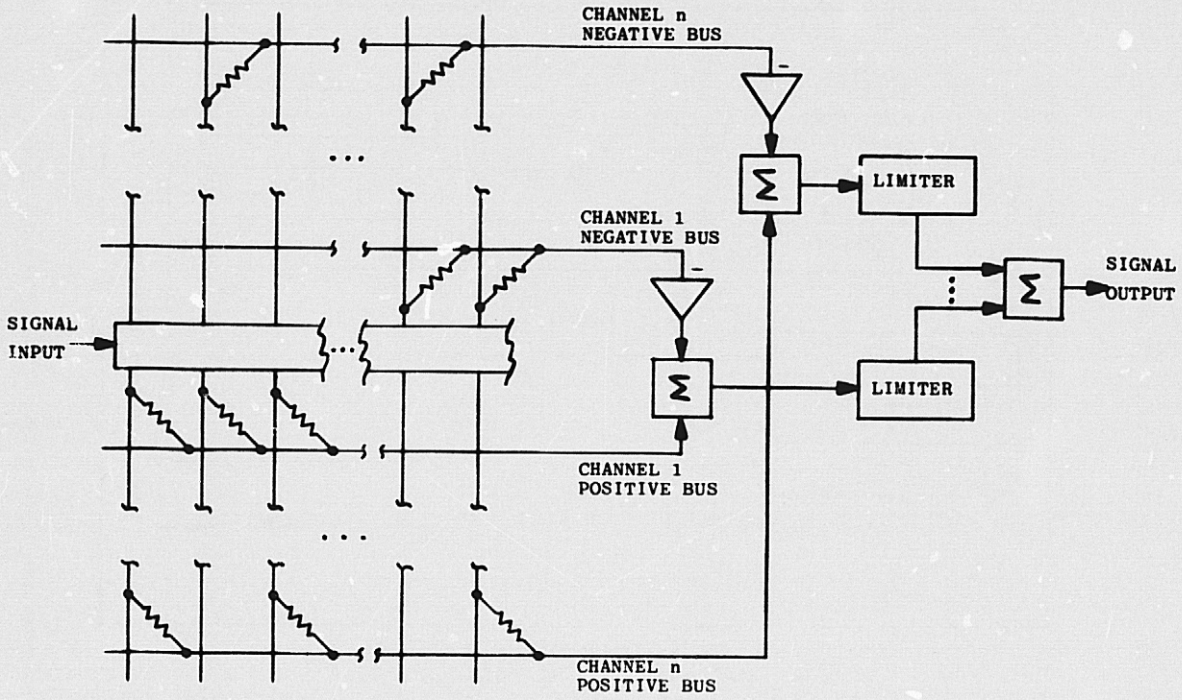

Fig. 15. Implementation of Transversal Filter Bank With Resistive Components

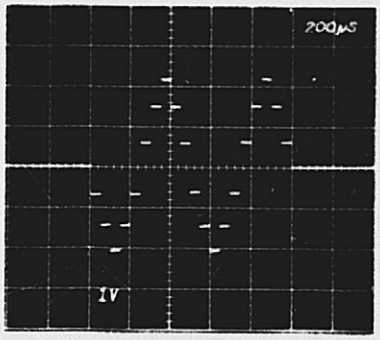

Fig. 16. Impulse Response of a Uniformly Weighted Transversal Filter for a Passband at 0.1 f_c

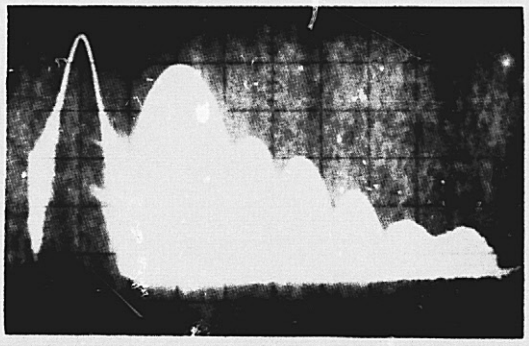

Fig. 17. Frequency Transfer Function for Uniformly Weighted Transversal Filter at 0.1 f_c

Fig. 18. Impulse Response of Transversal Filter with Hamming Window

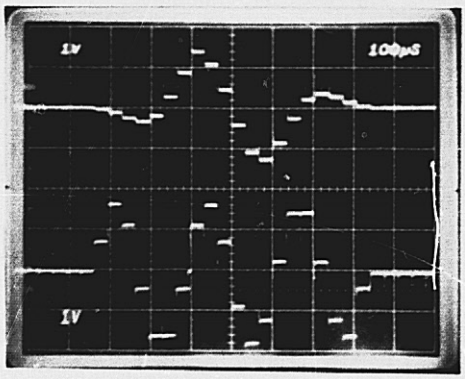

Fig. 19. Impulse Response of Two Simultaneously Synthesized Filters

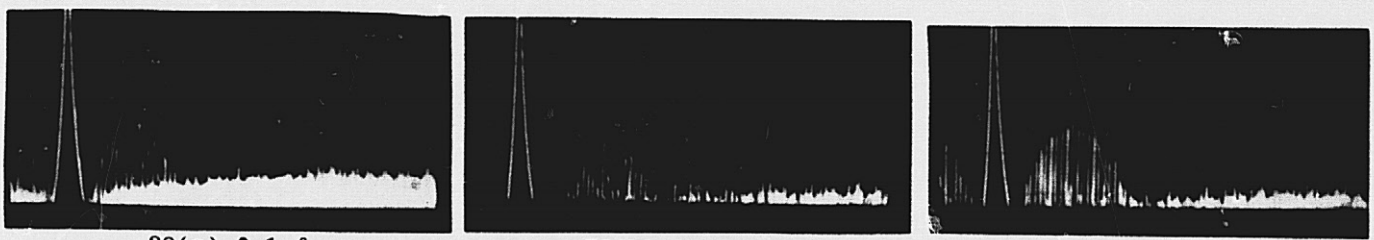

20(a) 0.1 f_c 20(b) 0.15 f_c 20(c) combined

Fig. 20. Transfer Functions of Adjacent Transversal Filters
f_c = 20 kHz

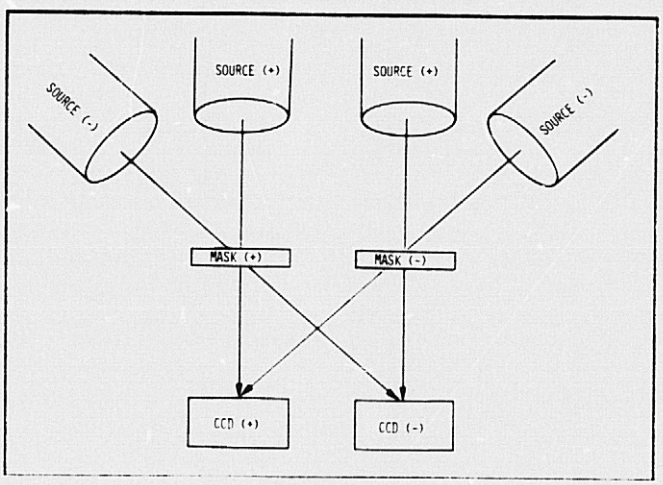

Fig. 21. Arrangement of Illuminators for Optically Implemented CZT-Diagonal Illuminators Can Be Eliminated if Pedestal on Mask Function is Tolerable

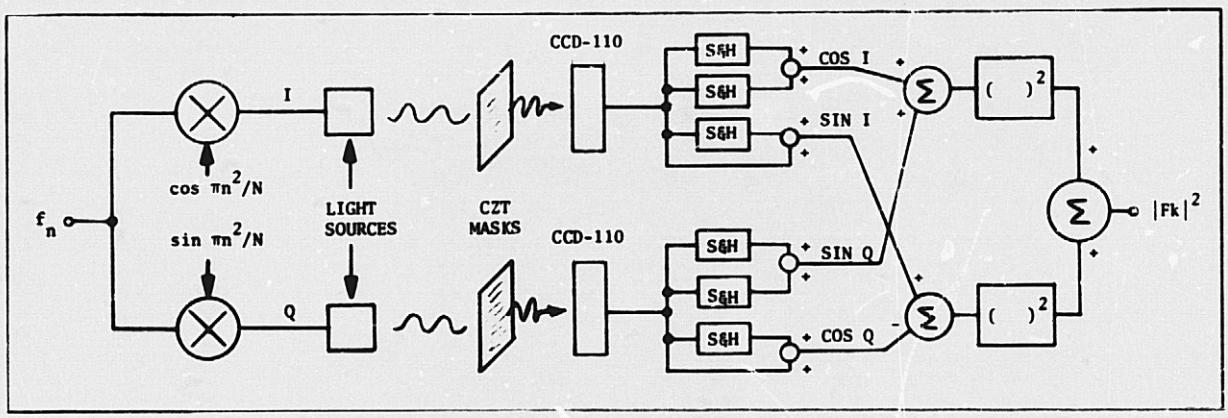

Fig. 22. Block Diagram of Circuit for Optically Implemented CZT

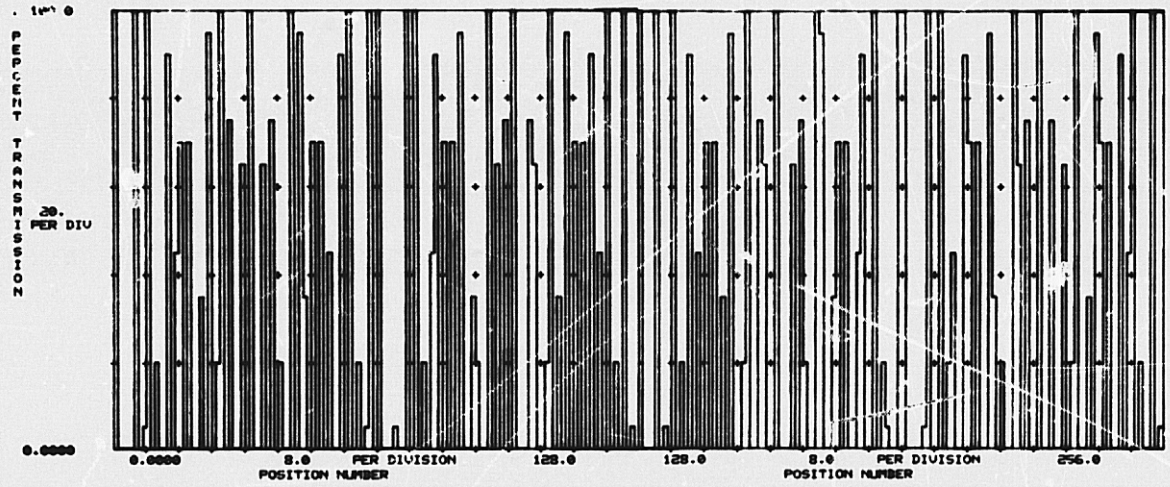

Fig. 23. Mask Function for Optical CZT

A SYNTHETIC APERTURE PROCESSOR USING CCD SIGNAL PROCESSING TECHNIQUES

By

W.H. Bailey, M.S. Bergath, J.F. DuBose
W.L. Eversole, J.H. McGehee, R.V. Ridings,
and D.C. Young

Texas Instruments Incorporated

ABSTRACT. The synthetic aperture concept has been known since the early 1950's. Application of the concept has been quite limited due to practical implementation difficulties. Early techniques relied upon photographic film for storage. This exposed film was subsequently developed and used in conjunction with an optical correlator which produced the imagery. The development of integrated circuit technology has made it possible to perform the convolution and storage functions in alternate ways. Only in this decade has it been possible to perform real time SAR processing on board an aircraft. Further reductions are still required in order to meet size, weight, and power objectives for most aircraft and satellite applications. The application of charge coupled devices offers significant advantages in these areas in addition to providing a capability to perform operations in an analog domain.

I. INTRODUCTION

Synthetic aperture radar (SAR) imaging appears to be the most suitable technique for achieving high resolution imagery through atmospheric cloud cover. This feature is important for planetary as well as earth orbiting satellite systems, and for military aircraft applications. Such applications require onboard data processing or wide-band data transmission systems in order to handle the large amounts of raw data produced by such systems. Onboard optical correlators of the conventional nature are unattractive for such applications due to size, mechanical stability problems, and long term operational objectives. Digital techniques offer some hope for onboard processing. However, size and power limitations for this approach currently exist. The charge coupled device promises important reductions in size, power, and weight in the implementation of onboard processors.

One of the first scheduled uses of a satellite borne SAR will be SEASAT-A which is to be launched in 1978. The mission of the SAR will be all-weather imaging of the sea for weather forecasting purposes.

A number of techniques have been utilized in implementing SAR processors. Frequency filtering and Fourier transform operations using both optical and digital techniques have been utilized in SAR processing.[1,2] Most approaches store the data in range lines and read the accumulated data from a given range bin into either a filter or transforming equipment which selectively passes the energy within a selected doppler frequency range. The zero doppler frequency generally corresponds to the point broadside a moving aircraft for clutter locked systems, and is the most commonly utilized frequency component analyzed. Optimal detection criterion would require pulse compression of the doppler chirp waveform found along the azimuthal direction.[3]

Generally speaking, when an image of some physical characteristic is needed, the resolution in the two orthogonal directions should be approximately equivalent. This presents a problem to conventional radar sets which could be used to produce an image of the radar cross section of a section of terrain. The resolution of the conventional radar in the radial direction depends directly on signal bandwidth. Pulse-compression techniques permit signal bandwidth to be expanded with negligible sensitivity loss so that adequate range resolution may be realized for many imaging applications.

Azimuth resolution is a more difficult matter, however. Conventional radar azimuth resolution depends ultimately upon the antenna beamwidth.[1] The antenna beamwidth is reduced by increasing the size of the aperture, increasing the carrier frequency, or both. For long-range imaging, however, this approach cannot provide an azimuth resolution that can be realized easily with modern pulse-compression techniques.

The solution to this dilemma is provided by SAR's in which data processing capability is traded for aperture size. In principle, there is no difference between:

An extremely large real antenna, and

A small real antenna that successively occupies all the positions that would be occupied simultaneously by the large real antenna, provided

The data that are successively collected by the small antenna are properly stored and subsequently combined in a simulation of the large real antenna.

Assuming this condition is satisfied, it is possible for a small antenna to move past a scene and record echo data to permit comparable range and azimuth resolution to be realized in an image of the scene after the recorded data have been properly processed, as indicated in Figure 1.

II. DESIGN CONSIDERATIONS

The use of charge coupled device transversal filters provides a very powerful computational tool in the implementation of the correlators required in a SAR processor.

The CCD filters utilized in these experiments are four-phase surface channel devices having split electrode weighting.[4] Initial device concerns were CTE effects, leakage current, and high frequency operation. Early measurements and analysis[5] indicated these effects are minimal for this

application. The laboratory feasibility breadboard utilized existing chirp filter designs having time bandwidth (TW) products of 62 and 16 for the range and azimuth correlators, respectively. Table 1 indicates the system parameters of the breadboard. Representative system parameters derived from these filter characteristics are indicated in Table 1 using the procedure outlined in Reference 5. The filters for the engineering model were designed using this procedure to be compatable with the system parameters for an existing JPL radar used for flight experiments. The key parameters for this system are indicated in Table 2.

Table 1. Breadboard Radar/Platform Parameters

Altitude	5.0 km
Slant Range	10.0 km
Nadir angle	60.0 degrees
Velocity	320.0 m/s
Wavelength	32.0 cm
Frequency	936.84 MHz
Transmitted pulse duration	3.58 μs
Transmitted signal bandwidth	17.32 MHz
Slant-range resolution	8.66 m
Along-track ground resolution	10.0 m
Cross-track ground resolution	10.0 m
Range time bandwidth product	62
Range correlation time	0.47 ms
Azimuth time bandwidth product	16
Azimuth correlation time	0.5 s

Table 2. Engineering Model Radar/Platform Parameters

Altitude	10.058 km
Slant range	15.5 m
Nadir angle	39 degrees
Velocity	257 m/s
Wavelength	24.7 cm
Frequency	1215 MHz
Transmitted pulse duration	1.25 μs
Transmitted signal bandwidth	10 MHz
Slant range resolution	15.5 m
Along-track ground resolution	25.1 m
Cross-track ground resolution	24.7 m
Range time bandwidth product	12.5
Range correlation time	58.9 μs
Azimuth time-bandwidth product	2.7
Azimuth correlation time	25.6 μs

Some limitations in the use of CCD transversal filters do exist. Peripheral circuitry limitations such as amplifier slew rates and sampling feedthrough currently limit useable data rates to less than 5 MHz. Practical filter lengths are presently limited to less than 1000 stages[6], although some flexibility exists in trading bar size for filter lengths. Several techniques, such as time expansion and presumming may be utilized to extend the operation of a processor utilizing CCD transversal filters.

The achievement of high range resolution implies the use of wideband chirp signals for a pulse compression radar. The use of a surface wave device range chirp correlation filter is an alternative capable of accommodating the required bandwidths. However, the time windows commensurate with the achievable range resolution are typically tens of nanoseconds, and are difficult to handle with A/D conversions and digital techniques.

The use of a modular processor concept in which each module processes on the order of 200 range cells, makes it possible to sample the radar video at a high rate during a small time window corresponding to the module's swath width once each PRI. The number of samples to be stored is the number of samples required to cover the swath plus the number of bits in the range correlator. While the input sampling rate is constrained by Nyquist considerations, the output data rate is constrained by the PRI making time expansion of the video possible in order to reduce the processor module's data rate to one commensurate with CCD transversal filter operation. Subsequent processing speeds may easily be handled with present CCD technology. Another advantage of such a buffering technique is that radar data from an appropriate range swath may be recorded on a conventional instrumentation tape recorder having a few hundred kilohertz bandwidth.

Presumming is an attractive alternative to minimizing the filter lengths and data rates required in the azimuth correlators. Presumming is the process whereby several consecutive samples from a given range bin are combined into one sample for subsequent processing. Presumming ahead of the azimuth correlator is possible in most cases, since the PRF greatly exceeds the azimuth time bandwidth product resulting in considerable oversampling.

Aliasing in the presum operation is a significant potential problem. Aliasing of the doppler components about harmonics of the PRF is inherent since the radar system is a sampled-data system. The antenna characteristics form a filter for the doppler returns due to the geometrical relationship between the antenna pattern and the locations of sources of higher doppler frequencies. However, the relatively large antenna beamwidth again causes ineffective filtering of the higher frequency components. Since presumming amounts to resampling the data at a lower data rate, these higher aliased frequencies must be removed by filtering in order that the new sampling operation not fold them into the video band of interest. This may be accomplished by incorporating a low pass filter into the presum operation.

Focusing is an important consideration in SAR's which involves degradation of resolution as a function of range. It is convenient in Figure 2 to think of a stationary radar with target motion being a straight line as shown. Using conventional terminology, time t is zero when the target is at the point of closest approach. This minimum range value is called R_0.

Data are assumed to be available from the time that the target enters the 3-dB beamwidth point of the real aperture until it leaves the 3-dB beamwidth point on the other side.

At time t, the target is seen in Figure 2 to

be displaced a distance Vt from the point of closest approach. The range as a function of time is given by

$$R(t) = (R_o^2 + V^2t^2)^{\frac{1}{2}} \quad (1)$$

For most cases of interest, the distance Vt in Figure 2 is much less than R_o, so that

$$R(t) \cong R_o \quad (2)$$

Degradation in resolution occurs when this assumption becomes invalid.

The effects of defocusing can be analyzed in terms of chirp slope mismatch degradation as outlined by Cook and Bernfeld.[7] The time bandwidth product of the azimuth chirp waveform for the unweighted case may be determined from[6]

$$TW_{AZ} = \frac{0.405\ \lambda R_o}{\delta_{AZ}^2} \quad (3)$$

where λ is the radar carrier wavelength, R_o is the range in meters, and δ_{AZ} is the azimuth resolution in meters.

If the filters are assumed matched at the center of the swath, the above equations may be used to determine the differences in time bandwidth products between the nominal value at the center of the range swath, and the near and far extremities of the swath. Analysis of the SEASAT geometries indicate a focusing degradation of approximately 2% could be anticipated over the 100 km swath width for 50 m resolution.

III. LABORATORY BREADBOARD

The first of the two breadboard SAR processors constructed at Texas Instruments in conjunction with this effort is a laboratory model which was developed around existing CCD filter designs. This breadboard simulates the operation of a filter bank approach to the azimuth correlators.[8] A block diagram of the laboratory breadboard is shown in Figure 5.

A single azimuth correlator was constructed which is sequentially stepped through the 200 range bins with a minicomputer in order to minimize hardware construction. The radar/platform parameters for this breadboard system shown in Table 1, are relatively representative of an aircraft radar environment. Range and azimuth correlation is accomplished with Hamming weighted linear FM complex filter pairs having TW products of 62 and 16, respectively. Range and azimuth correlation times are 0.47 ms and 0.5 s, respectively.

In order to form a 200-by-200-element picture with this breadboard, a TI 960A computer with 28K memory used in conjunction with a 1,100,000 word disk memory and a nine-track, 800-BPI magnetic tape unit were used. The simulated radar echo pulses were transferred from the tape to the disk. The simulated radar bursts correspond to radar returns from a swath of interest at sequential azimuthal locations. By recirculating this sequence of bursts to the breadboard while sliding the azimuth read-in time window across the swath time, a complete picture can be processed an azimuth column at a time. To reconstruct the picture, the output of the azimuth correlator is digitized and stored in memory. The memory can then be used much as a scan converter to refresh a CRT display.

The time required to process a 200 x 200 element picture is 1 1/3 hours due to the long azimuth correlation time. Real time processing could be accomplished by expanding the system to 200 azimuth correlators.

A number of test images have been processed with this breadboard. Two of the more significant images are shown in Figures 3 and 4. The upper photographs of Figure 3 indicate a portion of the uncompressed video signal corresponding to 48 point targets arranged in four rows in the range dimension. The point targets have a random signal phase and increase in intensity along the azimuth direction in 2-, 4-, 6-, and 8-percent increments for each of the range rows. Since the range and azimuth TW products are different, each point target's uncompressed video appears as a set of concentric ellipses. Compressing this video with the breadboard reconstructs the point targets as shown in the lower portion of Figure 3.

A second image was processed from an ERTS photograph, which was optically scanned with a microdensitometer, with the resulting picture element intensities stored on a computer tape. A decompression operation was then carried out on the minicomputer which convolved each picture element with a two dimensional chirp similar to that corresponding to a point target in Figure 3, and superimposed the resultant waveforms from picture elements having overlapping correlation functions. These decompressed data were then compressed utilizing the CCD breadboard and a compression program written for the minicomputer. Figure 4 reveals a 400 x 400 image which was processed as four 200 x 200 images.

A few subtle problem areas have been discovered in the process of evaluating this breadboard. The processed picture of Figure 4 indicates an intensity shading from left to right which is due to insufficient low frequency response in the ac coupling network at the squaring converter input. Efforts to direct couple this node were unsuccessful due to the thermal drift problems associated with the prior circuitry and the sensitivity of the analog multiplier to a precise null. An additional problem concerning dynamic range was encountered in processing the simulated pictures. A normalized 8 bit encoding scheme was used in the minicomputer data handling hardware. Since the point target test pattern of Figure 3 has non-overlapping correlation functions, the input waveforms are similarly non-overlapping, resulting in minimal amplitude reduction in the normalization process. However, the composite decompressed waveforms from the ERTS photograph of Figure 4 are formed by the superposition of two dimensional chirp waveforms from a large number of adjacent point targets. Normalization of this composite waveform to 8 bits makes the quantization error significant relative to the maximum chirp amplitude from a single picture element. As a result, the signal-to-noise ratio of many of the picture elements is relatively low. The dynamic range goal in the design of this breadboard was approximately 40 dB and was crudely based upon conventional TV grey scale detectability. The dynamic range of the breadboard was limited by the analog multipliers which perform the squaring function to approximately 40 dB. Additional dynamic range for the processor and test system would be desirable, but the desired increase is difficult to quantitatively assess.

IV. AIRCRAFT ENGINEERING MODEL

The aircraft engineering model, indicated in Figure 6 which is currently being constructed, is designed to match the system parameters of a radar utilized for SAR experiments on a CV-990 aircraft. This breadboard will be capable of real time SAR processing onboard the aircraft. The architecture of this breadboard differs from that of the earlier version by utilizing a digital "corner-turning" memory as opposed to the filter bank approach previously simulated. The primary justification for this choice was a short term economic consideration.

This breadboard utilizes a CCD delay line time expander to acquire approximately 500 range samples at a 25 MHz rate from the appropriate range swath each PRI. These samples are unloaded at a relatively slow rate (543 KHz) reducing the speed requirements of the remainder of the processor and making it possible to record unprocessed data from the desired swath on a conventional instrumentation tape recorder. This input sampler and recorder have been flown and data recorded for laboratory test purposes. This data will be played back into the range correlator which requires only a I and Q filter, since this radar system utilizes a frequency offset linear FM waveform. The output of this correlator is then digitized. The signals subsequently enter presum filters having 2nd order Butterworth low pass responses and presum numbers of 8. The data are then stored in the "corner-turning" memory in range lines (constant azimuth) and are read out in range bins (constant range). The "corner-turning" memory's outputs drive digital to analog converters which supply inputs to the azimuth correlator producing a compressed image line along the azimuth direction. This output is again digitized and subsequently applied to a digital scan converter which stores the data and uses it to refresh the CRT display.

The CCD correlators for the aircraft engineering model utilize a weighting coefficient modification of an existing bar design to produce a 32 stage frequency offset chirp and chirp-through-zero filter pairs for the range and azimuth correlators, respectively. The filter characteristics utilized in the design of these devices were derived from the parameters of the CV-990 radar to be utilized in the flight experiments. Table 2 lists many of the important system parameters. Figure 7 indicates the impulse and correlation characteristics of these filters. System operating frequencies for these correlators were 543 KHz and 1.25 MHz for the range and azimuth correlators, respectively.

V. CONCLUSIONS

The use of CCD's in onboard SAR processors appears to offer tremendous advantages through the powerful computational equivalency of transversal filters and the high density achievable with either analog or digital memories.

The two architectural approaches considered in this paper have numerous advantages and disadvantages. The filter bank processor utilizes CCD filters for both signal storage and convolution calculation eliminating the need for a large memory. CCD data rates with this configuration are minimal, since data is transferred at the PRF (or lower if presumming is utilized). Many filters are required to implement a system covering a large number of range bins. However, the feasibility of integrating multiple complex correlators on a single chip has been demonstrated.[8] Storage times and gain uniformity are additional concerns for the filter bank approach.

The "corner-turning" memory approach requires only a single azimuth correlator through which data is multiplexed. Storage time in the correlator becomes inconsequential, but operating speeds may become quite high for some systems. Redundant memories are likely to be required due to load/unload difficulties. Storage times within the memory may be a concern with this architecture. Although this configuration appears quite simple in block diagram form, control and addressing logic may become significant relative to the remainder of the system.

Improvements in SAR processors may be expected in the areas of improved resolution, multiple look imagery, focusing, motion compensation, and wider dynamic range. Techniques for accomplishing these improvements will likely influence the architecture of future processors.

ACKNOWLEDGEMENT

The authors gratefully acknowledge the support of the Jet Propulsion Laboratory through contract numbers 953954, 954087, and 954340 monitored by Wayne Arens.

REFERENCES

1. Brown, W.M., and Porcello, L.T., "An Introduction to Synthetic Aperture Radar," IEEE Spectrum, pp. 52-62, September, 1969.

2. Kirk, J.C., Jr., "A Discussion of Digital Processing in Synthetic Aperture Radar," IEEE Transactions on Aerospace and Electronic Systems, Vol. AES-11, No. 3, pp. 326-337, May 1975.

3. Harger, R.O., Synthetic Aperture Radar Systems: Theory and Design, New York Academic Press, 1970.

4. Buss, D.D., Collins, D.R., Bailey, W.H., and Reeves, C.R., "Transversal Filtering Using Charge Transfer Devices," IEEE J. Solid State Circuits, SC-8, pp. 134-146, April, 1973.

5. Bailey, W.H., Eversole, W., Holmes, J., Arens, W., Hoover, W., McGehee, J., and Ridings, R., "CCD Applications to Synthetic Aperture Radar," Proc. of CCD Applications Conference, San Diego, pp. 301-308, October 1975.

6. Hewes, C.R., "A Self Contained 800 Stage CCD Transversal Filter," Proc. of CCD Applications Conference, San Diego, pp. 309-318, October, 1975.

7. Cook, C.E., and Bernfeld, M., Radar Signals: An Introduction to Theory and Application, New York: Academic Press, pp. 152, 1967.

8. Bailey, W.H., Buss, D.D., Hite, L.R., and Whatley, M.W., "Radar Video Processing Using the CCD Chirp Z Transform," Proc. of CCD Applications Conference, San Diego, pp. 283-290, October 1975.

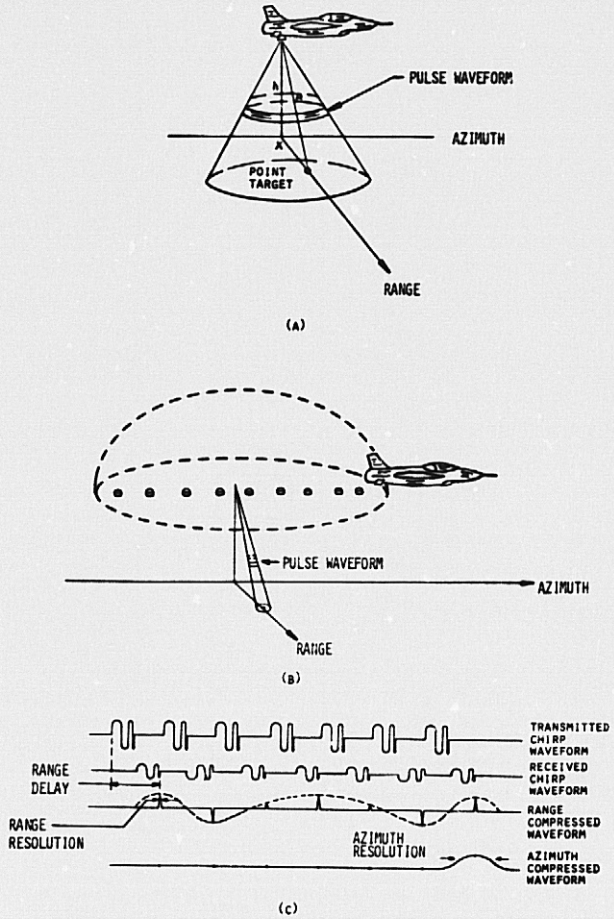

FIGURE 1. SYNTHETIC APERTURE RADAR PROCESSING CONCEPT, SHOWING:
(A) REAL ANTENNA PATTERN, (B) SYNTHETIC ANTENNA PATTERN, AND (C) WAVEFORM PROCESSING.

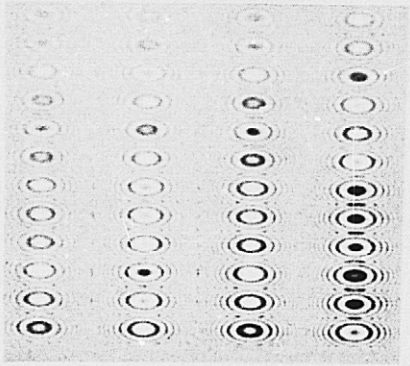

I INPUT

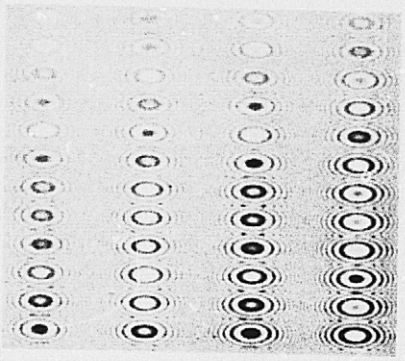

Q INPUT

CCD PROCESSED OUTPUT

FIGURE 3. POINT TARGET AMPLITUDE TEST (48 POINT TARGETS WITH LINEARLY INCREASING INTENSITY, AND RANDOM PHASE)

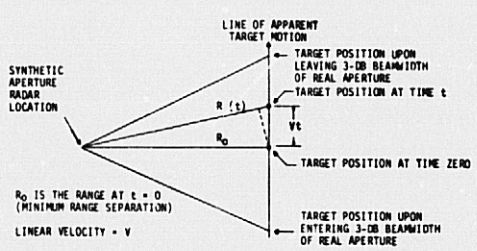

FIGURE 2. BASIC SAR AZIMUTH GEOMETRY

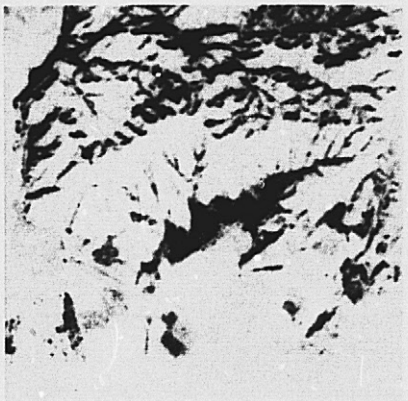

SCANNED IMAGE

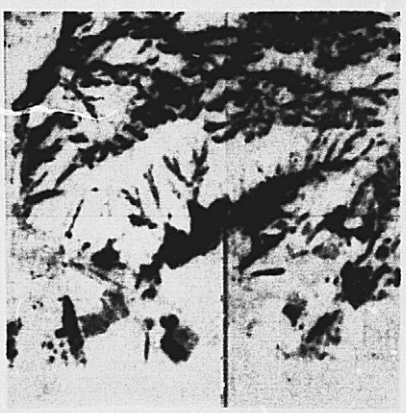

DIGITALLY PROCESSED IMAGE

CCD PROCESSED IMAGE

FIGURE 4. IMAGING RADAR MOUNTAIN SCENE (400 x 400)

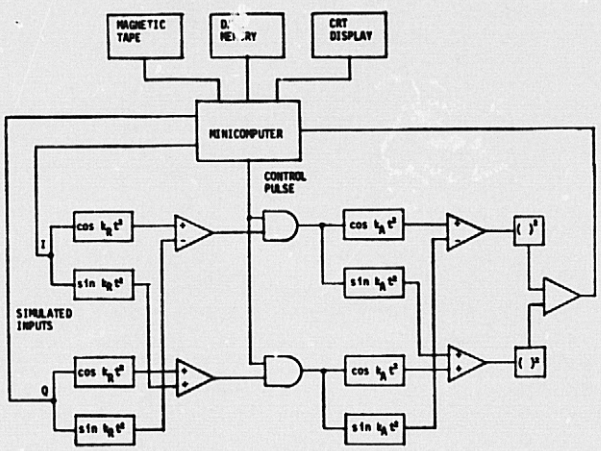

FIGURE 5. LABORATORY BREADBOARD BLOCK DIAGRAM

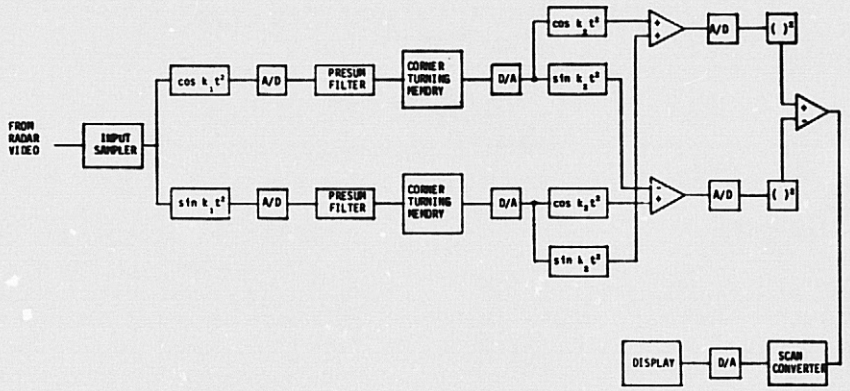

FIGURE 6. ENGINEERING MODEL BLOCK DIAGRAM

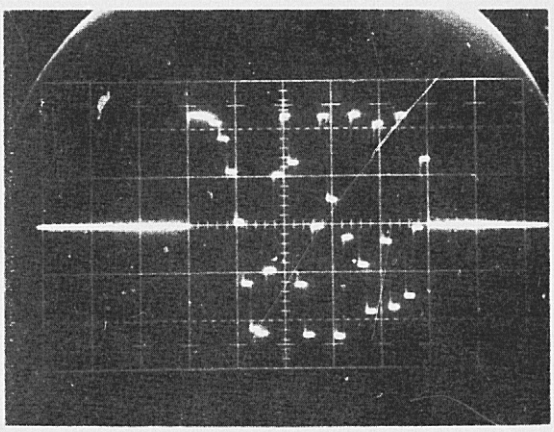

(A)

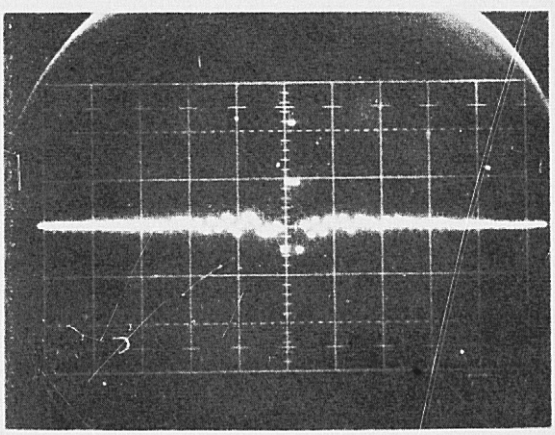

(B)

FIGURE 7. RANGE FILTER CHARACTERISTICS SHOWING:
(A) INPUT AND (B) OUTPUT

SAMPLED-DATA PROCESSING WITH CHARGE TRANSFER DEVICES

Gene P. Weckler

Reticon Corporation
Sunnyvale, California

ABSTRACT

Charge transfer devices employing both the charge-coupled and bucket-brigade principles are now available to the design engineer. These devices provide the designer with a relatively simple, cost-effective way of obtaining and controlling the delay of an analog signal with negligible degradation. The area of signal processing most suited for exploitation by charge-transfer devices will be discussed.

Charge-transfer devices will be reviewed describing not only the basic functional differences that may be employed but also showing the practical range of applications for devices of varying architectures. Also, a family of devices designed to perform correlation between either two analog signals or between an analog signal and a binary sequence will be described. The ability to field program, i. e., change the correlation sequence, greatly expands the variety of applications for which these devices are useable.

I. INTRODUCTION

Until recently, signal processing involving successive time delays was implemented either by use of physical analog delay elements, such as acoustic or electric transmission-line delay elements, or by conversion to digital format for processing, then reconverting the processed results to an analog output. Wholly analog systems are cumbersome, expensive, and sensitive to environmental factors. On the other hand, conversion to wholly digital format is often unnecessary and penalizes the system in terms of cost, complexity, speed, and power.

A very attractive alternative is discrete-time processing of analog samples. Time is quantized, but relative amplitudes are preserved. Delay is accomplished by transferring samples from cell to cell in shift-register fashion, while preserving relative amplitudes. Discrete-time systems combine many of the best features of both digital and analog systems: speed as well as the freedom from quantization effects of analog systems are combined with the time precision and flexibility of digital systems.

II. THE TAPPED ANALOG DELAY

The Tapped Analog Delay is the basic building block of the transversal filter. The transversal filter represents one of the most effective applications of charge transfer devices to sampled-data signal processing. The signals that appear at each tap of the TAD are weighted and summed by the technique shown in Figure 1. The ability to control externally the weight on each tap allows the user to design a wide variety of filter functions all based on the same basic component, and by switching in different tap-weight functions it becomes possible to program in a predetermined way a desired set of filters. For example, a time-multiplexed filter bank could be realized using one TAD and multiplexing the taps to several tap-weight functions, each derived with resistors.

Figure 2 shows the performance of a 32-tap TAD (TAD-32) operated as a low-pass filter. The impulse response of this filter is very nearly a Hamming window; therefore, one would expect the peak side lobes to be suppressed by -43dB relative to the center lobe or passband. The experimental results of Figure 2 for a sample rate of 120KHz indicate that -41dB was achieved. The width of the main lobe at -20dB is 12KHz, which compares favorably with theory. It is apparent that band edge rates in excess of 80dB/octave are possible.

This picture shows the spectral response or filter characteristic obtained for two inputs differing by 40dB. The background response curve is for an input level 20dB below the maximum level, thus from this picture one must conclude that nearly 60dB of input dynamic range is possible while still realizing a -40dB stopband to passband ratio. From this we must agree that the performance attainable from the TAD-32 exceeds by far most other approaches.

III. WHY BUCKET BRIGADE

This devices uses a bucket-brigade structure. We have all known that charge-transfer devices are very suitable for analog signal processing. However, most people immediately conclude that using charge-coupled devices is the only way to do the job. If you say that you are going to use a bucket-brigade device, immediately they ask: "Why not use charge-coupled?" Well, probably the most important single reason is that bucket-brigade devices use standard MOS processing. This means that they can be processed on a standard production line using existing technology, which in turn results in higher yield, and more cost-effective components. Another advantage, which is often overlooked, is that being compatible with existing MOS processes means that a wealth of circuitry used in making ROM's, RAM's, PROM's, and micro-processors is all available to the charge-transfer device designer. This allows the designer to build such things as flip-flops, clock drivers, shift registers, and even programmable memory onto the same chip with the

charge-transfer device. Another advantage of bucket-brigade devices is the ease with which the clocks may be generated. There are no tricky multi-phase clocks; a simple two-phase complementary square-wave clock is all that is required. The output circuitry is equally simple, allowing one to do either capacitive sampling of the bucket such as in a split electrode transversal filter, or to use source followers which are directly driven by the buckets and in turn act as current sources to the outside world. Modern n-channel bucket-brigades are capable of sampling at rates up to 5MHz. Contrary to popular belief, bucket-brigades can be made with transfer efficiency equal to surface channel CCD. Transfer inefficiency curves are shown in Figure 3 for two n-channel structures using a two layer poly-silicon MOS technology. A commercially available p-channel device is shown as a comparison.

Bucket-brigade devices are most suitable for sample rates below 5MHz, for delays not exceeding 5,000 transfers (2,500 stages), or when simplicity of associated circuitry for peripherals, etc., is a major consideration. There is also no advantage to using the alternative CCD (which does allow higher packing density) when packing density is only secondary, such as when peripheral circuitry or when pads determine the size of the chip and not the charge-transfer device itself. In such cases no real advantage can be obtained by using charge-coupled devices. Bucket-brigade devices are a natural in audio delays up to about 2,000 stages. For more than 2,000 stages one runs into transfer-efficiency problems, as well as into an increasing noise floor, both functions of the number of stages in a bucket brigade.

With the addition of some on-chip circuitry the tapped analog delay can be made into a binary analog correlator, as shown in Figure 4. This device has an on-chip static shift register which may be loaded with any desired binary sequence which then controls the (positive or negative, one or zero) tap weights from the BBD delay-line taps. This device permits 32-point real-time binary (or P-N) sequence correlation with an analog input signal. It may be used in applications requiring correlation, convolution, code generation, decoding, filtering, or other types of signal processing where an analog signal operates on a variable binary pattern or where two continuous signals - one analog, the other binary - operate on each other.

Figure 5 shows 29-bit P-N sequence correlation as performed with a 32-point binary-analog correlator (BAC-32).

Figure 6 shows a schematic representation of a 32-point analog-analog convolver (AAC-32) which uses two of the 32-tap lines with adjacent pairs of taps connected to four-quadrant multipliers whose outputs are summed in a common output line. This device will perform real convolution between two analog signals, a function which is fundamental to all time invariant linear systems.

IV. TRANSVERSAL FILTERS

The three devices which have been discussed may be considered programmable since the impulse response of each is under the control of the user. This external control requires accessory components and becomes a disadvantage if one develops a large volume requirement for devices all possessing the same impulse response. This requirement can be better satisfied by a mask programmable structure such as the split electrode structure. A 64-tap transversal filter which can be programmed at the mask level by modifying a single layer of the structure has been developed. A tap accuracy of 0.5% is attained at the mask level and the structure is completely insensitive to mask alignment. Furthermore, the sensing structure is unclocked and "full wave", therefore eliminating the need for additional signal processing in order to extract a useful signal from the clock noise. Figure 7 shows the raw output from a low-pass filter with only a differential amplifier (ua 733) as the output circuit.

This split-electrode structure has been used to produce a family of filter functions. Figure 8 shows the spectral characteristics of three general-purpose linear-phase filters, a low-pass and two band-pass filters. The low-pass filter has a corner frequency which is 10% of the sampling frequency, and a stop-band rejection of 45dB. The edge rate is about 100dB/octave. The two band-pass filters have similar edge rates and stop-band rejection; however, their pass bands are different, one having a narrow pass band 2% of the sampling frequency centered at 25% of the sampling frequency, the other having a wide band of 15% f_s centered at 17.5% f_s.

Other tap weight functions have been implemented using this structure. These include a set of linear fm chirps for implementing the chirp Z transform algorithm and a Hilbert Transform pair for broad band quadrature generation.

V. CONCLUSION

In the discussion of the TAD-32 it was demonstrated how novel discrete-time analog signal devices of this type are opening new and exciting possibilities in the area of signal processing. Complex tasks like convolution, matched filtering, correlation, etc., may be done with these large-scale integrated devices at a high speed. Signal processors, so far only realizable with complex, power consuming digital computers, can now be built on one board. Thus, sophisticated equipment may be constructed with the new devices at reduced size and power consumption, leading to higher reliability. The low cost will also enable the hobbyist to realize many of his ideas with the novel approach.

Among other discrete time analog devices, the TAD and the BAC are unique in the respect that their

window function may be changed at a high rate. This makes them useful in adaptive type applications requiring real-time alteration of the window function. These devices also allow one to experiment with different operations and patterns, making it useful as an educational tool. Concepts expressed with complicated formulas or simulated on digital computers may be demonstrated, requiring only a simple TAD or BAC and some peripheral circuitry and one oscilloscope.

For large quantity requirements of a fixed filter function, the mask programmed structure offers the additional advantage of lower cost through volume production.

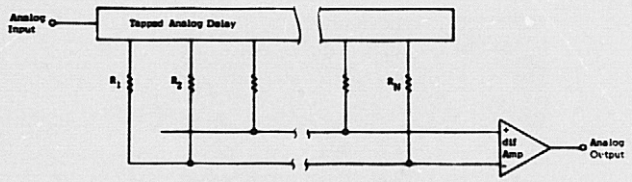

Figure 1. Block diagram representation of a transversal filter using a Tapped Analog Delay and resistor weighting of the taps.

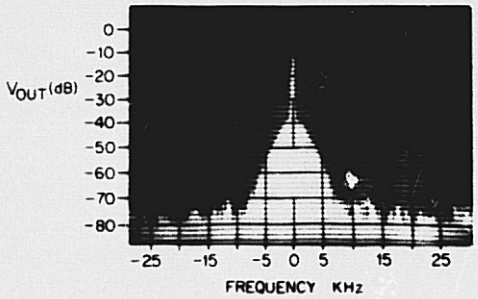

Figure 2. Spectrums obtained at two input levels from a 32-tap transversal filter whose impulse response was a Hamming window function.

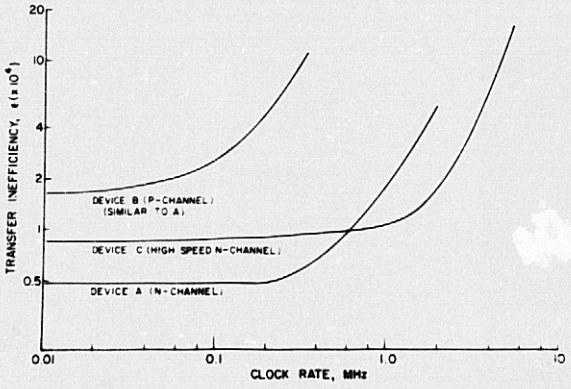

Figure 3. Transfer inefficiency versus sample rate of a modern n-channel bucket brigade device.

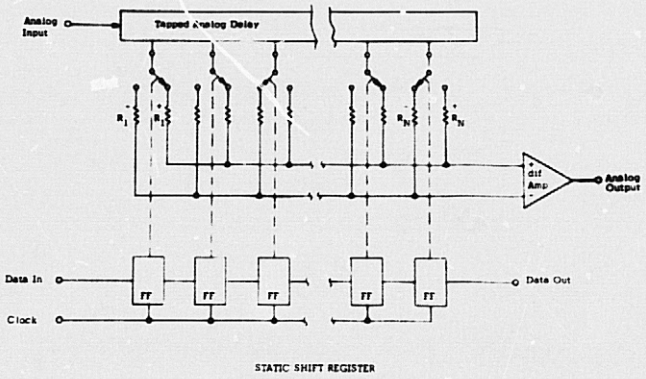

Figure 4. Block diagram representation of a Binary-Analog Correlator.

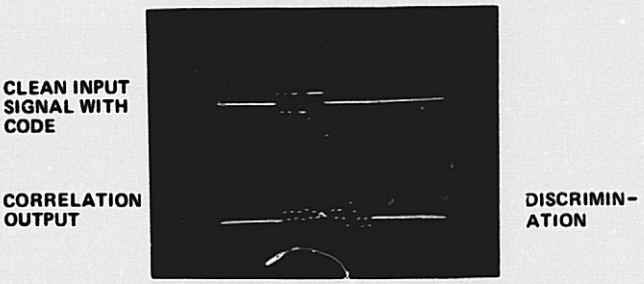

a) Input Signal Contains Code Only

b) Code In Input Signal Is Buried In Noise

Figure 5. Correlation Output obtained by correlating signal with high discrimination code with some code stored in digital shift register.

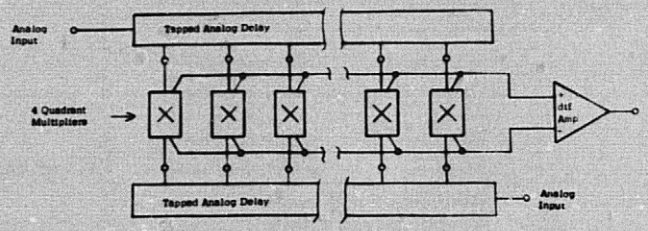

Figure 6. Block representation of an Analog-Analog Convolver.

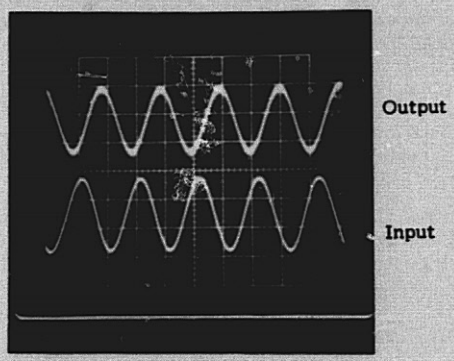

Figure 7. Waveforms showing the input and the unfiltered output from a 64-tap BBD transversal filter.

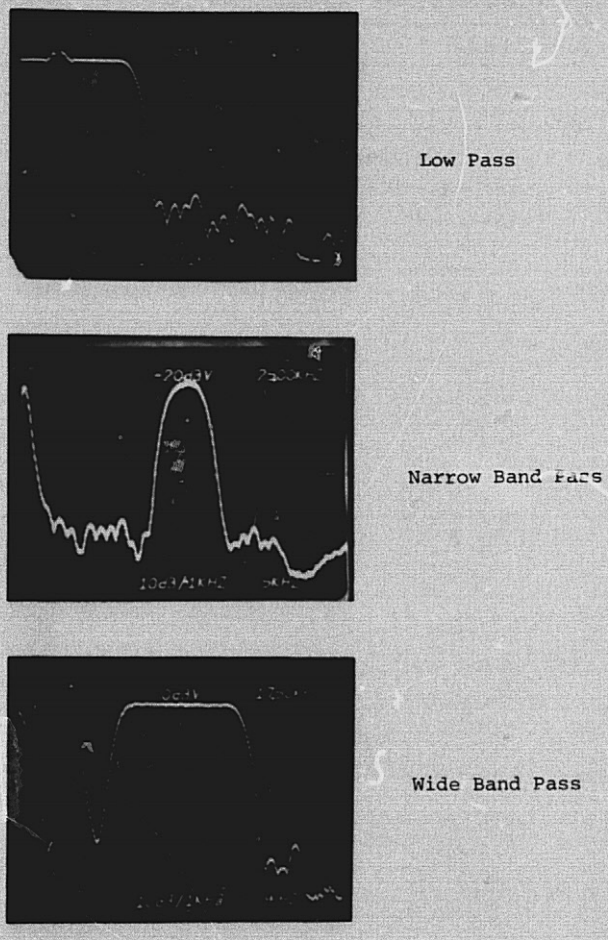

Figure 8. Spectral responses from three 64-tap transversal filters implemented by a BBD structure.

FOURIER ANALYSIS COMPUTER-AIDED DESIGN OF CCD SIGNAL PROCESSING ANALOG MULTIPLIER ARRAYS

H. C. Lin

University of Maryland
College Park, Md.

D. R. Lampe
M. H. White
I. A. Mack

Westinghouse Electric Corp.
Baltimore, Md.

ABSTRACT

When a CCD is used for signal processing, multipliers are required to multiply two signals or multiply the signal with a weight. The desired features of a multiplier are (a) low harmonic distortion, (b) wide dynamic range, (c) compatible signal levels, (d) small size, (e) low power dissipation, and (f) compatible with the CCD processing. From the design standpoint, many of these requirements are conflicting. This paper is a study of the design of MOS multipliers with CAD. In particular we use the Fourier analysis capability of the CAD program to analyze the harmonic distortion rejection, DR, of the multiplier.

I. INTRODUCTION

The multiplication function can be performed with MOS transistors operating in the triode region. The drain current I_D of an MOS transistor can be approximated as

$$I_D = \alpha \left(V_{GS} - V_T\right) V_{DS} + \beta V_{DS}^2 \qquad (1)$$

where V_{GS} is the gate to source voltage, V_T is the threshold voltage, V_{DS} is the drain to source voltage and (α, β) are physical parameters proportional to the width to length ratio and mobility of the channel. When the drain to source voltage is low, i.e. near the origin of the output characteristics, the square term in Eq. (1) is small and

$$I_D \approx \alpha \left(V_{GS} - V_T\right) V_{DS} \qquad (2)$$

If V_{GS} and V_{DS} represent two signals, then the drain current has a term ($\alpha V_{GS} V_{DS}$), which is proportional to the product of the two signals. If the two signals represented by V_{GS} and V_{DS} are substituted in Eq. (1) or Eq. (2), there are terms other than the desired multiplied outputs such as $\alpha V_{DS} V_T$ or $\beta V_{DS}^2/2$. These extraneous components of the drain current can be reduced in a balanced multiplier[1] as shown in Figure 1. But the signals may contain dc bias which must eventually be eliminated. One signal is given as $V_x \sin\theta$ with a dc offset V_X. The other signal is $V_y \sin\phi$ with a dc offset V_Y. The signal $V_X + V_x \sin\theta$ is applied to the common drain of Q_3 and Q_4. The signal $V_Y + V_y \sin\phi$ is applied to the gate of Q3, but only the offset voltage V_Y is applied to the gate of Q4. The currents of Q_3 and Q_4 can be obtained by substituting in Eq. (1) $V_X + V_x \sin\theta$ as V_{DS} and $V_Y + V_y \sin\phi$ as V_{GS} for Q_3 and V_Y as V_{GS} for Q_4.

$$I_{D3} = \alpha_3 \left[(V_Y + V_y \sin\phi - V_{T_3})(V_X + V_x \sin\theta)\right] + \beta_3 \left[(V_X + V_x \sin\theta)^2\right] \qquad (3)$$

$$I_{D4} = \alpha_4 \left[(V_Y - V_{T4})(V_X + V_x \sin\phi)\right] + \beta_4 \left[(V_X + V_x \sin\theta)^2\right] \qquad (4)$$

The differential output current I_{D0} is obtained by subtracting Eq. (4) from Eq. (3), assuming identical thresholds ($V_{T3} = V_{T4}$) and physical parameters ($\alpha_3 = \alpha_4$, $\beta_3 = \beta_4$):

$$I_{D0} = I_{D3} - I_{D4} = \alpha V_x V_y \sin\theta \sin\phi + \alpha V_X V_y \sin\phi \qquad (5)$$

But in a typical MOS array needed for a CCD correlator the assumptions used to give Eq. (5) are invalid, so that a four-quadrant sequential multiplication operation[2] is needed to eliminate terms due to array non-uniformities which degrade rejection of the two input frequencies. CAD Fourier analysis, however, facilitates evaluation of the susceptibility of various candidate circuits to degradation of distortion rejection due to MOS array nonuniformities.

II. EFFECTS OF DRIVING IMPEDANCES ON THE MULTIPLIER

For the proper operation of the multiplier, the driving point impedance should be low. Otherwise, the product current will develop a voltage across this impedance which would multiply with the voltage at the gate and cause distortion.

Since the impedance of a floating gate, from which the signal is derived is high compared with the channel resistance of the multiplier, a buffer must be placed between the floating gate and the

drain of the multiplier. A balanced multiplier can be used in conjunction with a source follower buffer as shown in figure 2.

Let R_{OB} be the output impedance of the buffer, then a voltage $I_{xy} R_{OB}$ would appear at the drain.

$$I_{xy} R_{ob} = \alpha V_x V_y R_{ob} \tag{6}$$

When multiplied by the gate signal V_y, an undesired product current I' is produced

$$I' = \alpha V_y (\alpha V_x V_y R_{OB}) \tag{7}$$

This current should be much less than the desired product current $\alpha V_x V_y$. Let the rejection ratio be DR. Then,

$$DR = \frac{\alpha V_x V_y}{\alpha V_y (\alpha V_x V_y R_{OB})} = \frac{1}{R_{OB} \alpha V_y} \tag{8}$$

where $\alpha = \mu C_{ox} W_x/L_x$ μ= mobility, W_x/L_x is the width to length ratio of the channel of the multiplier transistor. For the buffer

$$R_{ob} = \frac{L_B}{\mu C_{ox} W_B (V_{GS_B} - V_{T_B})} \tag{9}$$

where L_B, W_B are the length and width of the buffer.

Combining these three equations, we have this limitation from the drain buffer

$$\frac{(W_B/L_B)(V_{GS_B} - V_{T_B})}{W_x/L_x \quad V_y} = DR\Big]_{DB} \tag{10}$$

In a similar fashion, any impedance in series with the gate of the multiplier can develop a voltage by virtue of the feed-through capacitance from the drain of the multiplier transistor.[3] If the multiplier gate signal is directly derived from the floating gate of a CCD with sensing capacitance, C_{FG}, the impedance of the driver is the impedance of the capacitance C_{FG}. The voltage feedthrough is equal to $V_x C_{gdy}/C_{FG}$. If the desired signal is V_y, the rejection ratio limited by gate interaction is simply

$$\frac{V_y C_{FG}}{V_x C_{gdy}} = DR\Big]_G \tag{11}$$

One way to reduce the adverse effect of the feedthrough from the drain to the gate of the multiplier transistor is to place a buffer between the floating gate of the CCD and the gate of the multiplier. Because the gate of the multiplier should be more negative than the drain for p-channel transistors, it is easier to derive the proper d-c voltage with an inverter than a source follower. The schematic diagram for an inverter buffer at the gate is shown in Figure 3, complete with "dummy" sensing circuits for automatic multiplier biasing and clock feed-through cancellation (using small resistors in lieu of a differential current meter to facilitate CAD modeling).

Besides a lower impedance, it is also possible to increase the voltage gain. The output impedance is the source impedance of the load device, Q2:

$$\frac{1}{g_m} = \frac{1}{\alpha_2 (V_{GS2} - V_{T2})} \tag{12}$$

where V_{GS2} is the gate to source voltage of Q_2. The feedthrough signal from the drain now becomes

$$\frac{V_x}{\frac{1}{j\omega C_{gdy}} + \frac{1}{g_m}} \times \frac{1}{g_m} = \frac{V_x}{1 + \frac{\alpha_2 (V_{GS2} - V_T)}{j\omega C_{gdy}}} \tag{13}$$

The rejection ratio now becomes

$$DR\Big]_G = \frac{V_y}{V_x} \left[1 + \frac{\alpha_2 (V_{GS2} - V_T)}{j\omega C_{gdy}}\right] \tag{14}$$

III. ANALYSIS OF THE MULTIPLIER WITH A DRAIN BUFFER ONLY

For the proper operation of the multiplier in Figure2 the drain of the multiplier transistor Q_3 should be driven from a voltage source; i.e., the output conductance of the source follower (Q_1, Q_2), should be larger than the conductance of the multiplier Q_3. If the current source Q_2, is operating in the pentode region, the output conductance, Q_1 should be operating as a pentode. The output conductance is then equal to

$$\frac{dI_{D1}}{dV_{GS1}} = \alpha_1 (V_{GS1} - V_{T1}) = g_{m1} \tag{15}$$

where α_1 is a geometry constant, V_{GS1} is the gate to source voltage, V_{T1} is the threshold voltage, and g_{m1} is the transconductance. If V_X is the d-c voltage of the first signal appearing at the gate of Q_1 and V_3 is the d-c source voltage then source-follower operation gives:

$$V_{GS1} = V_X - V_3 \tag{16}$$

The drain voltage of Q_2 is also V_3 and the gate voltage should be chosen to operate in the pentode region. One convenient way is to make the gate

voltage of Q_2 equal to V_3. For equal geometry of Q_1 and Q_2,

$$V_X - V_3 = V_{T1} = V_3 - V_{T2} \tag{17}$$

If the self-biasing effect is small, $V_{T1} \cong V_{T2}$

$$V_3 = V_X/2 \tag{18}$$

Combining (15), (16), (18)

$$g_{m1} = \alpha_1 (V_X/2 - V_{T1}) \tag{19}$$

This conductance should be larger than the conductance of the multiplier:

$$g_3 = \frac{dI_{D3}}{dV_{DS}} = \alpha_3 (V_{GS} - V_{T3}) \tag{20}$$

or

$$g_{m1} \geq g_3 \tag{21}$$

If the two signals are at the same d-c level then

$$V_{GS1} = V_{GS3} = V_X/2 \tag{22}$$

Equation (21) can be satisfied if

$$\alpha_1 (V_X/2 - V_{T1}) \geq \alpha_3 (V_X/2 - V_{T3}) \tag{23}$$

If all the transistors have the same threshold voltage, then

$$\alpha_1 \geq \alpha_3 \tag{24}$$

Since α_1 and α_3 are proportional to the width to length ratios, it is desirable to have

$$\frac{W_1}{L_1} \geq \frac{W_3}{L_3} \tag{25}$$

Meanwhile, the multiplier transistor must not be cut off, i.e. (from eqn. 22)

$$V_X > 2V_{T3}. \tag{26}$$

From the standpoint of linearity, it is desirable to use a large amplitude V_X; because the linear triode region, where the linear multiplication function is performed, should be large compared to the signal. Thus, the larger the dc signal level V_X, the closer the multiplier approximates operation near the origin of eqn 1 and the better is the harmonic distortion rejection. On the other hand, a large value of V_X gives rise to large dissipation, and the choice of V_X is a compromise between distortion and dissipation.

The dissipation of the drain-buffered multiplier is essentially due to the buffer and is equal to

$$P_d \cong \alpha_2 (V_X/2 - V_{T2})^2 V_X \tag{27}$$

If, to satisfy Eqn (26), one chooses

$$V_X = 2 (V_{T2} + V^*) \tag{28}$$

Then from Eq. (27),

$$P_d \cong 2 \alpha_2 (V^*)^2 (V_{T2} + V^*) \tag{29}$$

From Eq. (29), we can see that a lower V_T reduces the power dissipation. Therefore, a <100> crystal orientation with a low threshold voltage should give reduced power consumption. A depletion mode transistor should help similarly.

Another consideration in designing a multiplier is the output current,

$$I = \alpha_3 \left[(V_X + V_x \sin\theta) \left(\frac{g_{m1}}{g_{m1} + g_{m2} + g_3} \right) (V_Y + V_y \sin\phi - V_{T3}) \right] \tag{30}$$

The desired output is the product term,

$$\frac{\alpha_3 g_{m1}}{g_{m1} + g_{m2} + g_3} (V_x V_y \sin\theta \sin\phi)$$

From (19) and (20)

$$\frac{\alpha_3 g_{m1}}{g_{m1} + g_{m2} + g_3} = \frac{\alpha_1 \alpha_3 \left(\frac{V_X}{2} - V_{T1} \right)}{\alpha_1 \left(\frac{V_X}{2} - V_{T1} \right) + \alpha_2 \left(\frac{V_X}{2} - V_{T2} \right) + \alpha_3 \left(\frac{V_X}{2} - V_{T3} \right)} \tag{31}$$

Here we see that larger geometry multipliers increase the desired output signal current but only up to the point where buffer loading occurs. This is in concert with equation (10), which shows that distortion rejection performance requires very limited loading by the multiplier on the drain buffer.

IV. THE FULLY BUFFERED MULTIPLIER

With a single (source-follower) buffer to drive the multiplier drain, the signal for the gate of the multiplier is assumed to be directly derived from the floating clock of a CCD. There are some advantages if an inverter is placed between the floating clock and the gate of the multiplier. a) Voltage

gain achieved for the signal. b) Reduced capacitive feed through from the signal at the drain of the multiplier to the gate of the multiplier. While the inverter lowers the driving point impedance, gain may reduce the d-c voltage developed at the multiplier gate and simultaneously increase the ac signal voltage there.

In Figure 3, if the amplifying transistor Q_1 and the load device Q_2 are of the same minimum geometry and both transistors are operating in the pentode region; then the voltage gain is unity, and the output conductance is the transconductance of the load device. To operate Q_1 in the pentode region, the following condition should be satisfied:

$$V_{DS1} = V_3 \geq V_Y - V_{T1} \tag{32}$$

Since the same current must flow in both Q_1 and Q_2, for pentode operation we must have

$$I_1 \cong \frac{\alpha_1}{2} (V_{GS1} - V_{T1})^2 = I_2 \cong \frac{\alpha_2}{2} (V_{GS2} - V_{T2})^2$$

or

$$V_{DD} - V_3 - V_{T2} = (V_Y - V_{T1}) \cdot \left(\frac{\alpha_1}{\alpha_2}\right)^{1/2} \tag{33}$$

But the unloaded voltage gain, A_v, of such an inverter may be approximated by:

$$A_v = g_m Z_L = \frac{g_{m1}}{g_{m2}} = \frac{\alpha_1 (V_{GS1} - V_{T1})}{\alpha_2 (V_{GS2} - V_{T_2})} = \left(\frac{\alpha_1}{\alpha_2}\right)^{1/2} \cdot \left(\frac{I_1}{I_2}\right)^{1/2} = \left(\frac{\alpha_1}{\alpha_2}\right)^{1/2} \tag{34}$$

Combing (32), (33), and (34) gives: $V_{DD} \geq (1 + A_v)(V_Y - V_{T1}) + V_{T2}$ (35)

For the case of unity gain and comparable threshold voltages, the minimum V_{DD} becomes $(2 V_Y - V_T)$. Also equation (35) indicates that the power dissipation of the multiplier gate buffer, P_g, increases directly with the voltage gain:

$$P_g \cong \alpha_1 (V_Y - V_{T1})^2 (1 + A_V) (V_Y) \tag{36}$$

Application of eqn (27) to Figure 3 gives

$$P_d \cong \alpha_{16} (V_X/2 - V_{T16})^2 V_X \tag{37}$$

Again invoking the requirement that the multiplier not be cut-off for the dual buffered circuit of Figure 3, we find

$$V_{GS4} = (V_Y - V_X/2) > V_{T4} \tag{38}$$

To simplify the operation of the two CCD's, it is desireable to use common clock and bias levels, so that one may again want to apply

$$V_X \simeq V_Y \simeq 2(V_T + V^*) , \tag{39}$$

yielding a combined power per multiplier stage of

$$P = P_d + P_g = 2(V_T + V^*) \left[\alpha_{16} (V^*)^2 + \alpha_1 (1 + A_V) (2V^* + V_T)^2\right] \tag{40}$$

The benefits of low threshold and operating voltages are certainly apparent to minimize on-chip heat generation.

V. THE FOURIER ANALYSIS BY CAD

The distortion error of a multiplier can best be determined by Fourier analysis as shown in Eq. (5), the desired term is the product term. If the two input signals are harmonically related say $\phi = N\theta$, where N is an integer, then the desired output is $^{\alpha} V_x V_y \sin\theta \sin N\theta$. From trigonometry, this product term can be resolved as a sum and difference frequency terms.

$$\sin\theta \sin N\theta = 1/2 \left[\text{Cos}\,(N-1)\,\theta - \text{Cos}\,(N+1)\theta\right] \tag{41}$$

All other frequency components are undesirable. The distortion rejection ratio can be defined as

$$DR = \frac{V^2 (f_G - f_D) + V^2 (f_G + f_D)}{(\text{NYQUIST})}$$

$$\sum_{(m,\ p)} = \sum_2 \left[V^2 (mf_D - f_G) + V^2 (pf_G - f_D) + V^2 (f_D) + V^2 (f_G) + V^2 (pf_G \pm mf_D)\right] \tag{42}$$

The different frequency components of a Fourier Analysis can readily be obtained with a CAD program.

VI. RESULTS OF CAD FOURIER ANALYSIS

Many circuit configurations were considered and evaluated by means of CAD Fourier analysis, including (i) MOSFET circuits consisting of all the same type devices requiring no extra fabrication steps beyond those needed to make CCD's, (ii) circuits incorporating depletion mode devices, (iii) complementary MOSFET circuits, (iv) combined MOS and bipolar circuits, and (v) permutations of all the preceeding. The MSINC CAD program developed by Standord University was used for all non-bipolar circuits. To best illustrate important aspects of the CAD Fourier analysis technique, we have selected one of the many circuit configurations studied: in particular, a fully buffered MOSFET circuit fabricated completely

within a typical CCD manufacturing sequence, featuring complementary operation as shown in Figure 3. Most of the significant data from four different computer runs for the selected circuit (PCWCO = PMOS correlator with complimentary operation) are presented in Tables 1 through 4, where the bottom-most harmonic listing describes the single multiplier current (I_4 =(V8, 17)÷ 10 ohms) while the harmonics above that give the differential output current. A summary of the CAD data is then listed in Table 5, to facilitate comparison with the preceeding general analysis. For the purpose of the CAD Fourier analysis, all other CCD clocks and switches (like the floating clock switch) are assumed to be in the state they would occupy at the time of anlalog readout. Furthermore, although the a-c-signal surface potential variations in a CCD typically exceed one volt amplitude, considerable attenuation of that amplitude due to parasitic capacitive loading has been incorporated into the model by setting the applied sine-wave signals at one-quarter volt peak-to-peak. (Tabulated amplitudes are from center to peak.) Both the ac and dc conditions used in the model closely approximate those observed in our own non-destructive parallel read-out CCD[4].

Run PCWCO-4-3, shown in Table 1, describes a PERFECTLY UNIFORM array with the CCD operated to give an ac "Fat Zero" level of about ten volts on the floating clock. In Table 2 (Run PCWCO-4-5) a nonuniform multiplier threshold offset of 0.25 V. is introduced, and the effects are comparable to such an offset in the floating clock/gate buffer circuit. A 0.25V. threshold offset nonuniformity in a floating clock/drain buffer is contained in Table 3 (PCWCO-4-6). The final run (PCWCO-4-2) shown in Table 4 is again a perfectly uniform array but with higher voltage operation. The summary of results (Table 5) accentuates the following conclusions:

(1) The theory of the SEQUENTIAL four-quadrant multiplier nominally requires only a single transistor, not a differential matched pair. Table 5, however, shows that rejection of the input drain signal would be substantially more difficult by around 80 dB. (i.e., the sequential cancellation of two extremely large quantities is required.)

(2) The differential circuit enhances the rejection of the drain signal second harmonic by at least 20 dB over the single FET multiplier.

(3) An increase from 10V. to 12V. for the ac Fat Zero level nearly doubled the power consumption per multiplier but did not proportionately improve the distortion rejection, due to the resultant loading (see #7 below).

(4) Two identical minimum-geometry devices as biased in the inverter give a gain around half; while two identical larger devices give a slightly larger gain as source followers. The inverter was just barely into the pentode region, which may be cured by a larger V_{DD} bias, that increases power consumption.

(5) Array nonuniformities which introduce multiplier source-drain offsets will degrade rejection of the input gate frequency and the intermodulation of the gate frequency with the second harmonic of the drain signal as well as the drain signal and its second harmonic to a smaller extent.

(6) Array nonuniformities which introduce multiplier differential gate offsets degrade rejection of the input drain signal and its second harmonic.

(7) The limited range tabulated for loading (λ) by the multiplier on the drain buffer falls totally within the region that the source-follower buffer gain (A_D) is being degraded by the multiplier load:

$$A_D = \frac{g_m R_s}{1 + g_m R_s} = \frac{1}{1 + g_{ds}/g_m} = \frac{1}{1 + \lambda^{-1}} \quad (43)$$

This equation describes the tabulated correlation between A_D, λ, and, consequently, the desired output signal via eqn (31). Since this group of runs does not involve greatly reduced loading, there is no apparent relationship between distortion rejection and λ; and eqn (10) is not truly applicable.

Some of the more promising configurations are now undergoing experimental hybrid-device laboratory evaluation. The observed characteristics closely match the CAD Fourier Analysis predictions like those exhibited in Tables 1 through 5. Figure 4 illustrates the typical output of a minimum geometry PMOSFET pair with

V_{DS} = 51 mV. DC and 0.2 V_{pp} at 1 KHz

V_{GS} = 3.962 V. DC and 0.2 V_{pp} at 5 KHz

V_{SB} = 11.78 V. DC and ΔV_G = 142 mV.

VII. SUMMARY/CONCLUSIONS

CAD Fourier analysis of analog multiplier arrays for CCD signal processing facilitates comprehensive study of most practical device configurations before commitment to mask layout is required. The CAD Fourier analysis technique helps evaluate many trade-off options and

interactions between the following: (1) Device technology such as simple MOS, MOS with depletion mode FET's, CMOS, and MOS with bipolar. (2) Area and complexity of each buffered multiplier circuit. (3) Circuit performance to include drive and signal compatibility with the associated CCD's, power consumption, output signal amplitude and distortion rejection, and susceptibility of circuit performance to array nonuniformities.

Computer predictions and laboratory multichip hybrid models agree reasonably when such comparisons are possible.

REFERENCES

1. J.G. Harp, G.F. Vanstone, D.J. MacLennan, J. Mavor, "Analog Correlators using Charge Coupled Devices," 1975 International Conference on the Applications of CCD Proceedings, pp. 229.

2. D.R. Lampe, M.H. White, I.A. Mack, H.C. Lin "Four Quadrant Analog Multiplier for CCD Signal Processing," 1976 GOMAC Digest

3. P. Bosshart, "An Integrated Analog Correlator using Charge-Coupled Devices," 1976 ISSCC Digest of Technical Papers, XIX, pp 198-199, Feb. 1976.

4. M.H. White, et al, "An Analog CCD Transversal Filter With Floating Clock Electrode Sensor and Variable Tap Gains" IEEE ISSCC Digest of Technical Papers, Feb. 1976, pp 194-95.

ACKNOWLEDGEMENT

This work is supported in part by the NASA Langley Research Center in a contract awarded to Westinghouse (NAS-1-13674).

Table 1. Perfect Uniform Array, No Offsets (PCWCO-4-3)

```
TIME 1U 200U
RA 8 17 10
RB 9 17 10
C8 8 0 5P
C9 9 0 5P
C16 16 0 .5P
C17 17 0 5800U
C10 10 0 .5P
Q1 BP1 3 2 6 0 .7M .7M 0 0 .07P .07P
Q2 BP1 4 4 3 0 .7M .7M 0 0 .07P .07P
Q4 BP1 16 3 8 0 2.8M .7M 0 0 .28P .28P
Q5 BP1 16 10 9 0 2.8M .7M 0 0 .28P .28P
Q3 BP1 10 7 0 0 .7M .7M 0 0 .07P .07P
Q6 BP1 4 4 10 0 .7M .7M 0 0 .07P .07P
Q14 BP1 16 17 0 0 14M .7M 0 0 .07P .07P
Q15 BP1 17 17 0 0 14M .7M 0 0 .07P .07P
Q16 BP1 7 6 16 0 14M .7M 0 0 .07P .07P
Q17 BP1 7 7 17 0 14M .7M 0 0 .07P .07P
BP1 PMO VTO=-2 UB=250.6E4+.15 COX=23N DNB=1E15 XJD=.3M GDS=2 CSS=.5P
BP2 PMO VTO=-2.25 UB=250.6E4+.15 COX=23N DNB=1E15 XJD=.3M GDS=2 CSS=.5P
V4 4 0 -20
V7 7 0 -10
VSIN 6 0 .125V 6KHZ 0 -10
VSIN 2 0 .125V 30KHZ 0 -10
PLOT VOUT 8 9
PLOT VD 16 0
PLOT V3 3 0
PLOT V8 8 17
PLOT VG 3 10
PLOT V17 17 0
FOR 30U 196.667U 20
END
```

NODE VOLTAGES --

(0)	.0000	(2)	-10.0000	(3)	-8.7846	(4)	-20.0000
(6)	-10.0000	(7)	-10.0000	(8)	-4.4624	(9)	-4.4624
(10)	-8.7846	(16)	-4.4624	(17)	-4.4624		

TRANSISTOR OP. PT. --

NAME	TP	VGS	VDS	VSB	IDS(MA)
Q1	P	-10.0000	-8.7846	.0000	-.1291
Q2	P	-11.2154	-11.2154	-8.7846	-.1291
34	P	-4.3221	-.0000	-4.4624	-.0000
Q5	P	-4.3221	-.0000	-4.4624	-.0000
G3	P	-10.0000	-8.7846	.0000	-.1291
Q6	P	-11.2154	-11.2154	-8.7846	-.1291
Q14	P	-4.4624	-4.4624	.0000	-.3026
Q15	P	-4.4624	-4.4624	.0000	-.3026
Q16	P	-5.5376	-5.5376	-4.4624	-.3026
Q17	P	-5.5376	-5.5376	-4.4624	-.3026

ORDER	HARM	DSINE	COSINE	MAGNITUDE	REL MAG	PHASE
V89:	0	.0000	-.1267-10	.1267-10	5.3795	180.0000
	1	.2022-09	.1209-09	.2356-09	100.0000	-59.1188
	2	.3119-09	.6844-11	.3120-09	132.4361	-88.7430
	3	-.2942-08	-.1109-08	.3145-08	1334.8697	110.6585
	4	-.4767-06	-.8919-07	.4840-06	205439.9595	-100.6191
	5	-.7262-08	.1737-08	.7467-08	3169.5422	76.5503
	6	.2264-06	-.4069-06	.4656-06	197655.0427	-150.9082
	7	-.1645-09	.2663-08	.2668-08	1132.3948	3.5362
	8	-.2496-09	-.7649-09	.8046-09	341.5345	161.9263
	9	-.1008-09	-.4966-09	.5067-09	215.0972	168.5307
	10	-.1678-09	-.3498-09	.3879-09	164.6712	154.3725
	11	-.2007-09	-.3724-09	.4230-09	179.5752	151.6917
	12	-.7872-10	-.3059-09	.3158-09	134.0631	165.5675
	13	-.5805-10	-.3812-09	.3856-09	163.6592	171.3406
	14	-.2275-10	-.3482-09	.3489-09	148.1193	176.2024
	15	-.6252-10	-.3593-09	.3647-09	154.8230	170.1300
	16	-.2663-10	-.3775-09	.3784-09	160.6288	175.9849
	17	-.4544-10	-.3532-09	.3561-09	151.1591	172.6681
	18	-.2519-10	-.3951-09	.3959-09	168.0653	176.3528
	19	-.2114-10	-.3737-09	.3743-09	158.8854	176.7619
	20	-.3655-10	-.4156-09	.4172-09	177.0943	174.9741
V817:	0	.0000	.2722-06	.2722-06	1.5494	.0000
	1	.7466-05	.1590-04	.1757-04	100.0000	-25.1475
	2	.2073-06	.1723-06	.2695-06	1.5341	-50.2653
	3	-.6232-08	-.1670-08	.6451-08	.0367	105.0009
	4	.4447-06	-.8296-07	.4524-06	2.5747	-100.5674
	5	-.8786-08	.2834-08	.9232-08	.0525	72.1299
	6	.2117-06	-.3800-06	.4350-06	2.4758	-150.8732
	7	-.1684-09	.3758-08	.3762-08	.0214	2.5658
	8	-.1496-09	-.4339-09	.4590-09	.0026	160.9762
	9	-.7467-10	-.1873-09	.2017-09	.0011	158.2671
	10	-.1028-09	-.5846-10	.1183-09	.0007	119.6193
	11	-.1747-09	-.5412-10	.1829-09	.0010	107.2119
	12	-.6024-10	-.2233-10	.6425-10	.0004	110.3359
	13	-.4383-10	-.6039-10	.7462-10	.0004	144.0303
	14	-.3691-10	-.4635-10	.5926-10	.0003	141.4682
	15	-.5933-10	-.4428-10	.7403-10	.0004	126.7346
	16	-.5602-10	-.5300-10	.7712-10	.0004	133.4104
	17	-.6512-10	-.3799-10	.7539-10	.0004	120.2508
	18	-.6212-10	-.5262-10	.8141-10	.0005	130.2676
	19	-.6883-10	-.4481-10	.8213-10	.0005	123.0663
	20	-.8110-10	-.6068-10	.1013-09	.0006	126.8057

Table 2. An Offset (0.25V) Multiplier Threshold (or Floating Clock/Gate Buffer) (PCWCO-4-5)

```
TIME 1U 200U
RA 8 17 10
RB 9 17 10
C8 8 0 5P
C9 9 0 5P
C16 16 0 .5P
C17 17 0 5800U
C10 10 0 .5P
Q1 BP1 3 2 0 0 .7M .7M 0 0 .07P .07P
Q2 BP1 4 4 3 0 .7M .7M 0 0 .07P .07P
Q4 BP2 16 3 8 0 2.8M .7M 0 0 .28P .28P
Q5 BP1 16 10 9 0 2.8M .7M 0 0 .28P .28P
Q3 BP1 10 7 0 0 .7M .7M 0 0 .07P .07P
Q6 BP1 4 4 10 0 .7M .7M 0 0 .07P .07P
Q14 BP1 16 17 0 0 14M .7M 0 0 .07P .07P
Q15 BP1 17 17 0 0 14M .7M 0 0 .07P .07P
Q16 BP1 7 6 16 0 14M .7M 0 0 .07P .07P
Q17 BP1 7 7 17 0 14M .7M 0 0 .07P .07P
BP1 PMO VTO=-2 UB=250.6E4.15 COX=23N DNB=1E15 XJD=.3M GDS=2 CSS=.5P
BP2 PMO VTO=-2.25 UB=250.6E4.15 COX=23N DNB=1E15 XJD=.3M GDS=2 CSS=.5P
V4 4 0 -20
V7 7 0 -10
VSIN 6 0 .125V 6KHZ 0 -10
VSIN 2 0 .125V 30KHZ 0 -10
PLOT VOUT 8 9
PLOT VD 16 0
PLOT V3 3 0
PLOT V8 8 17
PLOT VG 3 10
PLOT V17 17 0
FOR 30U 196.667U 20
END
```

NODE VOLTAGES --

(0)	.0000	(2)	-10.0000	(3)	-8.7846	(4)	-20.0000
(6)	-10.0000	(7)	-10.0000	(8)	-4.4624	(9)	-4.4624
(10)	-8.7846	(16)	-4.4624	(17)	-4.4624		

TRANSISTOR OP. PT. --

NAME	TP	VGS	VDS	VSB	IDS(MA)
Q1	P	-10.0000	-8.7846	.0000	-.1291
Q2	P	-11.2154	-11.2154	-8.7846	-.1291
Q4	P	-4.3221	-.0000	-4.4624	-.0000
Q5	P	-4.3221	-.0000	-4.4624	-.0000
Q3	P	-10.0000	-8.7846	.0000	-.1291
Q6	P	-11.2154	-11.2154	-8.7846	-.1291
Q14	P	-4.4624	-4.4624	.0000	-.3026
Q15	P	-4.4624	-4.4624	.0000	-.3026
Q16	P	-5.5376	-5.5376	-4.4624	-.3026
Q17	P	-5.5376	-5.5376	-4.4624	-.3026

ORDER	HARM	DSINE	CODSINE	MAGNITUDE	REL MAG	PHASE
V89:	0	.0000	.2281-07	.2281-07	.6164	.0000
	1	-.1572-05	-.3350-05	.3701-05	100.0000	154.8649
	2	.1780-07	.1443-07	.2292-07	.6192	-50.9759
	3	-.3536-08	-.1335-08	.3779-08	.1021	110.6825
	4	.5000-06	-.9383-07	.5088-06	13.7477	-100.6284
	5	-.7884-08	.2166-08	.8176-08	.2209	74.6347
	6	.2380-06	-.4278-08	.4895-06	13.2278	-150.9148
	7	-.2014-09	.2978-08	.2985-08	.0807	3.8695
	8	-.2840-09	-.8711-09	.9163-09	.0248	161.9435
	9	-.2433-10	-.4964-09	.4970-09	.0134	177.1941
	10	-.1950-09	-.4233-09	.4661-09	.0126	155.2838
	11	-.1069-09	-.4618-09	.4740-09	.0128	166.9616
	12	-.8853-10	-.3708-09	.3812-09	.0103	166.5725
	13	-.6343-10	-.4597-09	.4641-09	.0125	172.1436
	14	-.2068-10	-.4199-09	.4204-09	.0114	177.1797
	15	-.6626-10	-.4352-09	.4402-09	.0119	171.3428
	16	-.2146-10	-.4554-09	.4559-09	.0123	177.3024
	17	-.4405-10	-.4282-09	.4305-09	.0116	174.1266
	18	-.1930-10	-.4779-09	.4783-09	.0129	177.6874
	19	-.1302-10	-.4523-09	.4525-09	.0122	178.3511
	20	-.3011-10	-.5015-09	.5024-09	.0136	176.5637
V817:	0	.0000	.3020-06	.3020-06	2.1403	.0000
	1	.5996-05	.1277-04	.1411-04	100.0000	-25.1477
	2	.2301-06	.1911-06	.2991-06	2.1198	-50.2823
	3	-.6963-08	-.1926-08	.7224-08	.0512	105.4586
	4	.4674-06	-.8730-07	.4755-06	3.3701	-100.5792
	5	-.9471-08	.3310-08	.1003-07	.0711	70.7340
	6	.2225-06	-.3995-06	.4573-06	3.2409	-150.8814
	7	-.2068-09	.4114-08	.4113-08	.0292	2.8781
	8	-.1825-09	-.5348-09	.5650-09	.0040	161.1563
	9	-.2982-11	-.1866-09	.1867-09	.0013	179.0847
	10	-.1268-09	-.1269-09	.1808-09	.0013	134.5672
	11	-.9699-10	-.1373-09	.1625-09	.0012	147.6362
	12	-.6962-10	-.8242-10	.1079-09	.0008	139.8150
	13	-.4887-10	-.1334-09	.1421-09	.0010	159.8811
	14	-.3497-10	-.1129-09	.1182-09	.0008	162.7867
	15	-.6208-10	-.1147-09	.1308-09	.0009	151.2673
	16	-.5121-10	-.1254-09	.1355-09	.0010	157.7884
	17	-.6389-10	-.1076-09	.1252-09	.0009	149.3039
	18	-.5669-10	-.1295-09	.1414-09	.0010	156.3643
	19	-.6132-10	-.1177-09	.1327-09	.0009	152.4877
	20	-.7521-10	-.1405-09	.1593-09	.0011	151.8328

Table 3. An Offset (0.25V) Floating Clock/Drain Buffer (PWCO-4-6)

```
TIME 1U 200U
RA 8 17 10
RB 9 17 10
C8 8 0 5P
C9 9 0 5P
C16 16 0 .5P
C17 17 0 5800U
C10 10 0 .5P
Q1 BP1 3 2 0 0 .7M .7M 0 0 .07P .07P
Q2 BP1 4 4 3 0 .7M .7M 0 0 .07P .07P
Q4 BP1 16 3 8 0 2.8M .7M 0 0 .28P .28P
Q5 BP1 16 10 9 0 2.8M .7M 0 0 .28P .28P
Q3 BP1 10 7 0 0 .7M .7M 0 0 .07P .07P
Q6 BP1 4 4 10 0 .7M .7M 0 0 .07P .07P
Q14 BP1 16 17 0 0 14M .7M 0 0 .07P .07P
Q15 BP1 17 17 0 0 14M .7M 0 0 .07P .07P
Q16 BP2 7 6 16 0 14M .7M 0 0 .07P .07P
Q17 BP1 7 7 17 0 14M .7M 0 0 .07P .07P
BP1 PMO VTO=-2 UB=250.6E4..15 COX=23N DNB=1E15 XJD=.3M GDS=2 CSS=.5P
BP2 PMO VTO=-2.25 UB=250.6E4..15 COX=23N DNB=1E15 XJD=.3M GDS=2 CSS=.5P
V4 4 0 -20
V7 7 0 -10
VSIN 6 0 .125V 6KHZ 0 -10
VSIN 2 0 .125V 30KHZ 0 -10
PLOT VOUT 8 9
PLOT VO 16 0
PLOT V3 3 0
PLOT V8 8 17
PLOT V6 3 10
PLOT V17 17 0
FOR 30U 196.667U 20
END
```

NODE VOLTAGES --

(0)	.0000	(2)	-10.0000	(3)	-8.7846	(4)	-20.0000
(6)	-10.0000	(7)	-10.0000	(8)	-4.4501	(9)	-4.4501
(10)	-8.7846	(16)	-4.3125	(17)	-4.4501		

TRANSISTOR OP. PT. --

NAME	TP	VGS	VDS	VSB	IDS(MA)
Q1	P	-10.0000	-8.7846	.0000	-.1291
Q2	P	-11.2154	-11.2154	-8.7846	-.1291
Q4	P	-4.3345	.1376	-4.4501	.0033
Q5	P	-4.3345	.1376	-4.4501	.0033
Q3	P	-10.0000	-8.7846	.0000	-.1291
Q6	P	-11.2154	-11.2154	-8.7846	-.1291
Q14	P	-4.4501	-4.3125	.0000	-.2980
Q15	P	-4.4501	-4.4501	.0000	-.2995
Q16	P	-5.6875	-5.6875	-4.3125	-.2914
Q17	P	-5.5499	-5.5499	-4.4501	-.3061

ORDER	HARM	DSINE	CODSINE	MAGNITUDE	REL MAG	PHASE
V89:	0	.0000	.1541-08	.1541-08	111.0164	.0000
	1	.8261-09	.1116-08	.1386-08	100.0000	-36.5218
	2	-.8756-09	-.1401-08	.1652-08	119.0382	148.0041
	3	-.7616-08	-.2560-08	.8035-09	578.8249	108.5779
	4	.4426-06	-.8350-07	.4504-06	32447.1410	-100.6830
	5	.1303-05	-.9419-06	.1608-05	115845.2490	-125.8525
	6	.2106-06	-.3787-06	.4333-06	31216.7599	-150.9263
	7	-.6241-09	.6808-08	.6837-08	492.5152	5.2372
	8	.1999-09	-.2778-09	.3423-09	24.6562	-144.2590
	9	-.1114-08	-.1837-08	.2149-08	154.7760	148.7535
	10	-.1492-08	-.1344-08	.2008-08	144.6763	132.0099
	11	-.2541-09	-.8337-09	.8715-09	62.7846	163.0474
	12	.8675-10	-.1011-08	.1014-08	73.0756	-175.0943
	13	-.1505-09	-.7970-09	.8111-09	58.4295	169.3083
	14	-.1652-09	-.7133-09	.7322-09	52.7488	166.9593
	15	-.1252-09	-.8848-09	.8936-09	64.3726	171.9439
	16	-.1996-09	-.9289-09	.9501-09	68.4407	167.8712
	17	-.1335-09	-.8999-09	.9098-09	65.5381	171.5591
	18	-.7761-10	-.8960-09	.8994-09	64.7899	175.0498
	19	-.1057-09	-.9522-09	.9580-09	69.0151	173.6658
	20	-.1225-09	-.9425-09	.9504-09	68.4649	172.5936
V817:	0	.0000	.3273-04	.3273-04	172.4026	.0000
	1	.8068-05	.1719-04	.1899-04	100.0000	-25.1478
	2	-.3012-07	-.2512-07	.3922-07	.2066	129.8229
	3	-.6221-07	-.1640-07	.6433-07	.3388	104.7673
	4	.4480-06	-.8402-07	.4558-06	2.4009	-100.6222
	5	.1231-05	-.8898-06	.1519-05	8.0013	-125.8571
	6	.1912-06	-.3432-06	.3929-06	2.0693	-150.8843
	7	-.1558-08	.2161-07	.2167-07	.1141	4.1238
	8	.5230-09	.6807-09	.8584-09	.0045	-37.5368
	9	-.6739-08	-.6865-08	.9620-08	.0507	135.5319
	10	-.3902-08	-.1825-08	.4307-08	.0227	115.0646
	11	.3743-08	-.9270-09	.3856-08	.0203	-103.9057
	12	.2486-08	-.2149-08	.3286-09	.0173	-130.8447
	13	-.1084-08	.1038-08	.1501-08	.0079	46.2547
	14	-.4834-09	.1880-08	.1941-08	.0102	14.4183
	15	-.2866-09	-.1064-08	.1102-08	.0058	164.9214
	16	-.1321-08	-.1752-08	.2194-08	.0116	142.9857
	17	-.1056-09	-.5098-09	.5206-09	.0027	168.3108
	18	.1013-08	-.5513-09	.1153-08	.0061	-118.5581
	19	-.2817-10	-.6324-09	.6330-09	.0033	177.4494
	20	-.6564-09	.1200-09	.6672-09	.0035	79.6417

Table 4. No Offsets; Higher Voltage Operation (PCWCO-4-2)

```
TIME 1U 200U
RA 8 17 10
RB 9 17 10
C8 8 0 5P
C9 9 0 5P
C16 16 0 .5P
C17 17 0 5800U
C10 10 0 .5P
Q1 BP1 3 2 0 0 .7M .7M 0 0 .07P .07P
Q2 BP1 4 4 3 0 .7M .7M 0 0 .07P .07P
Q4 BP1 1E 3 8 0 2.8M .7M 0 0 .28P .28P
Q5 BP1 16 10 9 0 2.8M .7M 0 0 .28P .28P
Q3 BP1 10 7 0 0 .7M .7M 0 0 .07P .07P
Q6 BP1 4 4 10 0 .7M .7M 0 0 .07P .07P
Q14 BP1 16 17 0 0 14M .7M 0 0 .07P .07P
Q15 BP1 17 17 0 0 14M .7M 0 0 .07P .07P
Q16 BP1 7 6 16 0 14M .7M 0 0 .07P .07P
Q17 BP1 7 7 17 0 14M .7M 0 0 .07P .07P
BP1 PMO VTO=-2 UB=250.6E4.15 COX=23N DNB=1E15 XJD=.3M GDS=2 CSS=.5P
BP2 PMO VTO=-2.25 UB=250.6E4.15 COX=23N DNB=1E15 XJD=.3M GDS=2 CSS=.5P
V4 4 0 -24
V7 7 0 -12
VSIN 6 0 .125V 6KHZ 0 -12
VSIN 2 0 .125V 30KHZ 0 -12
PLOT VOUT 8 9
PLOT V0 16 0
PLOT V3 3 0
PLOT V8 8 17
PLOT VG 3 10
PLOT V17 17 0
FOR 30U 196.667U 20
END
```

NODE VOLTAGES --

(0)	.0000	(2)	-12.0000	(3)	-10.6794	(4)	-24.0000
(6)	-12.0000	(7)	-12.0000	(8)	-5.4035	(9)	-5.4035
(10)	-10.6794	(16)	-5.4035	(17)	-5.4035		

TRANSISTOR OP. PT. --

NAME	TP	VGS	VDS	VSB	IDS(MA)
Q1	P	-12.0000	-10.6794	.0000	-.1975
Q2	P	-13.3206	-13.3206	-10.6794	-.1975
Q4	P	-5.2758	-.0000	-5.4035	-.0000
Q5	P	-5.2758	-.0000	-5.4035	-.0000
Q3	P	-12.0000	-10.6794	.0000	-.1975
Q6	P	-13.3206	-13.3206	-10.6794	-.1975
Q14	P	-5.4035	-5.4035	.0000	-.5546
Q15	P	-5.4035	-5.4035	.0000	-.5546
Q16	P	-6.5965	-6.5965	-5.4035	-.5546
Q17	P	-6.5965	-6.5965	-5.4035	-.5546

ORDER	HARM	DSINE	CODSINE	MAGNITUDE	REL MAG	PHASE
V89:	0	.0000	-.2959-10	.2959-10	2.2089	180.0000
	1	.6670-09	.1162-08	.1340-08	100.0000	-29.8581
	2	.2327-09	-.1611-10	.2333-09	17.4102	-93.9598
	3	-.1350-08	-.6318-09	.1490-08	111.2334	115.0053
	4	-.3898-06	-.7306-07	.3966-06	29600.9913	-100.6156
	5	-.4553-08	-.2802-10	.4553-08	339.8208	90.3526
	6	.1856-06	-.3334-06	.3816-06	28479.3551	-150.9007
	7	-.6174-10	.1165-08	.1167-08	87.0957	3.0332
	8	-.1975-09	-.6103-09	.6414-09	47.8777	162.0628
	9	-.4497-09	-.7580-09	.8820-09	65.8339	149.3453
	10	-.1196-09	-.2814-09	.3059-09	22.8235	156.9661
	11	-.6260-09	-.2536-09	.6772-09	50.5501	111.9908
	12	-.5751-10	-.2571-09	.2634-09	19.6639	167.3899
	13	-.4784-10	-.3124-09	.3161-09	23.5924	171.2942
	14	-.1880-10	-.2855-09	.2861-09	21.3575	176.2324
	15	-.5048-10	-.2958-09	.3001-09	22.3994	170.3161
	16	-.2025-10	-.3098-09	.3104-09	23.1711	176.2607
	17	-.3612-10	-.2914-09	.2936-09	21.9145	172.9341
	18	-.1962-10	-.3254-09	.3260-09	24.3308	176.5494
	19	-.1607-10	-.3082-09	.3086-09	23.0332	177.0152
	20	-.2834-10	-.3423-09	.3434-09	25.6344	175.2675
V817:	0	.0000	.2087-06	.2087-06	.8116	.0000
	1	.1093-04	.2328-04	.2572-04	100.0000	-25.1454
	2	.1585-06	.1320-06	.2063-06	.8021	-50.2035
	3	-.2497-09	-.5290-09	.2592-08	.0099	101.9603
	4	.3615-06	-.6716-07	.3677-06	1.4297	-100.5246
	5	-.5324-08	.6422-09	.5362-08	.0209	83.1217
	6	.1722-06	-.3086-06	.3534-06	1.3743	-150.8398
	7	-.1632-10	.1953-08	.1953-08	.0076	.4786
	8	-.5398-10	-.1452-09	.1549-09	.0006	159.6017
	9	-.3329-09	-.3082-09	.4994-09	.0019	128.1132
	10	-.3032-10	.1219-09	.1256-09	.0005	13.9656
	11	-.5647-09	.1872-09	.5950-09	.0023	71.6535
	12	-.3330-10	.1367-09	.1407-09	.0005	13.6935
	13	-.2837-10	.1345-09	.1375-09	.0005	11.9097
	14	-.4053-10	.1338-09	.1398-09	.0005	16.8484
	15	-.4687-10	.1425-09	.1500-09	.0006	18.2052
	16	-.6385-10	.1420-09	.1557-09	.0006	24.2057
	17	-.6526-10	.1470-09	.1609-09	.0006	23.9321
	18	-.7307-10	.1522-09	.1688-09	.0007	25.6485
	19	-.8490-10	.1493-09	.1717-09	.0007	29.6283
	20	-.9223-10	.1521-09	.1778-09	.0007	31.2367

Table 5. Summary of MSINC Run Data:
PMOS Correlator with Complementary Operation (PCWCO)

"PCWCO" Run No.	Differential Output				Single-Ended Output			
Item	4–3	4–5	4–6	4–2	4–3	4–5	4–6	4–2
Absolute Currents (na.) Drain Freq.	.0236	370.1	.1388	.1340	1757	1411	1899	2572
Gate Freq.	.7467	.8176	160.8	.4553	.9232	1.003	151.9	.5362
(Gate - Drain) Freq.(Desired Signal)	48.40	50.88	45.04	39.66	45.24	47.55	45.58	36.77
(Twice Drain) Freq.	.0312	2.292	.1652	.0233	26.95	29.91	3.922	20.63
(Gate - Twice Drain) Freq.	.3145	.3779	.8035	.1490	.6451	.7224	6.433	.2552
Distortion Rejection (dB): Drain Freq.*	66.3	-17.2	50.2	49.4	-31.8	-29.4	-32.4	-36.9
Gate Freq. * †	36.2	35.9	-11.1	38.8	33.8	33.5	-10.4	36.7
(Twice Drain) Freq.	63.8	26.9	48.7	64.6	4.5	4.0	21.3	5.0
(Gate - Twice Drain) Freq.	43.7	42.6	35.0	48.5	36.2	36.4	17.0	43.2
Power (mW): Drain Buffer	3.026	3.026	2.914	6.655				
Gate Buffer	2.582	2.582	2.582	4.740				
Total	5.608	5.608	5.496	11.395				
Loading: g_{m14} (micromhos)	245.8	245.8	243.3	325.9				
g_{DS4}(micromhos)	22.8	17.5	25.3	35.9				
Ratio: $(g_{m14} \div g_{DS4}) = \lambda$	11.1	14.1	9.6	9.1				
g_{m1} (micromhos)	32.3	32.3	32.3	39.5				
Multiplier Drives: V_{DS4} (mV)	0	0	137.6	0				
V_{GS4} (V)	4.322	4.322	4.335	5.276				
V_{SB4} (V)	4.462	4.462	4.450	5.404				
AC Signals: V_{ds4} (mV.)	79.59	80.69	75.16	71.74				
V_{gs4} (mV.)	65.69	65.69	65.69	63.43				
Buffer Gain: Drain (%) = A_D	63.7	64.6	60.1	57.4				
Gate (%) = A_G	52.6	52.6	52.6	50.7				
Multiplier Efficiency: $\frac{\mu a}{V^2}$								
$v\ (f_g - f_D) \div (V_{ds4} \times V_{gs4})$	9.26	9.60	9.12	8.72				

Run No. Key:
PCWCO–4–3: Perfect Uniform Array, No Offsets.
PCWCO–4–5: An Offset (0.25 V) Multiplier Threshold (or Floating Clock/Gate Buffer)
PCWCO–4–6: An Offset (0.25 V) Floating Clock/Drain Buffer
PCWCO–4–2: No Offsets; Higher Voltage Operation

* Distortion Rejection Values Prior to Four-Quadrant Sequential Multiplication Operation.

† This Model Circuit Makes no Provision for Gate-Frequency Cancellation.

76-0971-TA-2

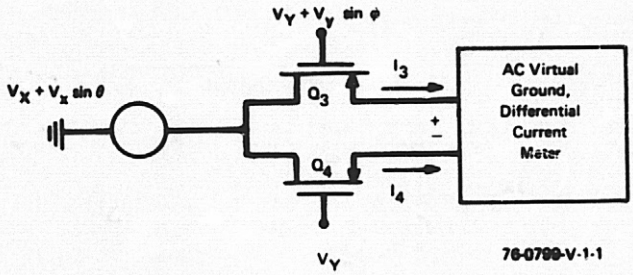

Figure 1. Conceptual Multiplier Circuit

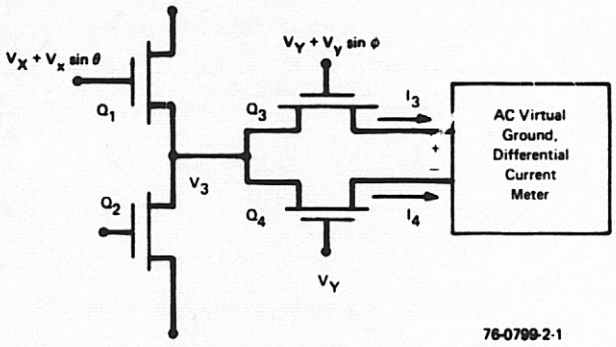

Figure 2. Drain-Buffer Multiplier Circuit

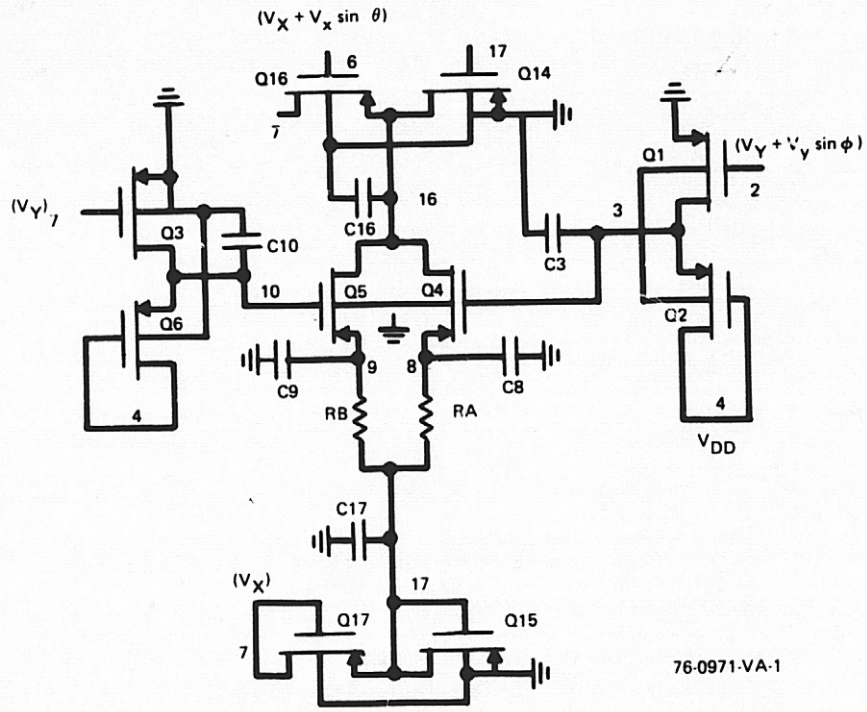

Figure 3. CAD Modeling Circuit for Fully Buffered Multiplier

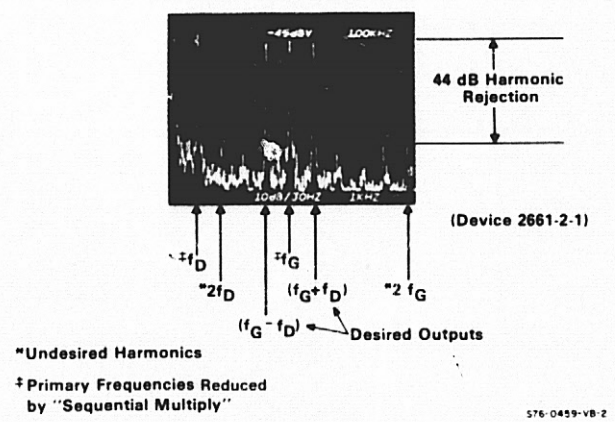

Figure 4. MOS Analog Multiplier Output

METAL-INSULATOR-SEMICONDUCTOR STUDIES OF LEAD TELLURIDE

D. A. Lilly, D. E. Joslin, and H. K. A. Kan

The Aerospace Corporation
El Segundo, California 90245

ABSTRACT

The capacitance and conductance-voltage characteristics were measured on metal-insulator-semiconductor capacitors fabricated with zirconium dioxide films on single-crystal lead telluride. At 77 K, on both n- and p-type substrates, evidence of surface potential control was obtained. Comparison of the measured capacitance-voltage characteristics with those calculated from the equilibrium solution of the one-dimensional Poisson equation indicates qualitative agreement, although the slope (dC/dV) of the measured capacitance in the region near the capacitance minimum is less steep than calculated. The high-frequency response of the capacitance and position of the capacitance minimum were used to deduce the presence of an inversion layer on some n-type substrates of charge density approximately 5.0×10^{13} cm^{-2}. This layer was found to be dependent on surface preparation treatment prior to insulator deposition. Results of surface chemical studies indicate that inversion may be due to oxide formation during chemical etching. Conductance data obtained confirm the existence of a large interfacial state density.

I. INTRODUCTION

The metal-insulator-semiconductor (MIS) structure was used in investigating the surface electronic properties of many semiconductors (Refs. 1-4). These properties are strongly determined by preparation and fabrication techniques and are revealed in measurements of the capacitance-voltage (C-V) and conductance-voltage (G-V) characteristics of MIS structures. In this paper the results of an investigation of the electronic properties at 77 K of MIS structures fabricated on monocrystalline lead telluride (PbTe) substrates are reported. Although several insulators and surface preparation techniques were investigated, the discussion here is limited to the results obtained for devices fabricated with zirconium dioxide (ZrO_2) and prepared with two different chemical treatments.

II. SAMPLE PREPARATION AND DEVICE FABRICATION

Wafers of p-type PbTe up to 1.5 mm thick were sliced and diced on a stainless steel wire saw (diamond impregnated blade of 0.010 in. diam) with a slurry of fine grit and glycerine. The crystal* was characterized by small-angle grain boundaries; etching (Ref. 5) revealed etch pit densities of 10^6 cm^{-2} and, near grain boundaries, as great as 10^8 cm^{-2}. Room-temperature carrier concentration and mobility of the as-received crystal were 2×10^{18} holes cm^{-3} (assuming $p = (eR_H)^{-1}$) and 735 cm^2 - V^{-1} - sec^{-1}, respectively. The normal to the sample surfaces was determined to be within 5 deg of <100>.

Sample carrier concentration was controlled by using an isothermal annealing technique that was described by Brebrick and Gubner (Ref. 6). Prior to annealing, the sample thickness was reduced to nominally 0.8 mm by lapping first on water-moistened 600 grit paper and then on a silk-covered wheel with 0.3 μm alumina powder moistened with a detergent-water solution. A final 1 to 5 μm of material was removed by lapping on a felt wheel with a solution of iodine and methanol (Ref. 7). Samples were then rinsed thoroughly in methanol and distilled water and sealed off in an annealing ampoule at a pressure of less than 10^{-6} Torr.

Following annealing and immediately prior to insulator deposition, one of two final surface treatments was used. In order to remove approximately 1 μm of material, all samples were again lapped on a felt wheel with a solution of iodine and methanol, rinsed in methanol and distilled water, and dried in a stream of argon gas. An additional 2 μm of material were removed from some of these samples during a second treatment that consisted of the following process (Ref. 8):

1. Immerse for 10 s in a 9/1 solution of potassium dichromate and nitric acid
2. Rinse in distilled water
3. Immerse for 30 s in a solution of warm (40° C) 50% sodium hydroxide
4. Rinse in distilled water
5. Immerse in dilute HCl
6. Rinse in distilled water
7. Dry in a stream of argon gas.

Samples were immediately mounted in special holders for deposition of ZrO_2 in an oil-pumped, electron-beam evaporator system. Spectrographic grade ZrO_2 (pressed powder from Wah Chang Corporation or grey pellets from EM Laboratories, Inc.) was outgassed at a moderate temperature (a few hundred degrees centigrade) before being deposited in a controlled oxygen background pressure of 5×10^{-4} Torr at a rate of 20-25 Å/s. No effort was made to control the substrate temperature, which may have increased to approximately 40°C during the deposition. Deposition times were limited in order to obtain film thickness of approximately 1500 Å.

Circular field electrodes (30 Å chromium, 500 Å gold, and 2 μm indium) were evaporated through a hard mask with apertures of 4.2×10^{-4} and 1.4×10^{-4} cm^2 by standard electron beam procedures. This step required a brief exposure

*Purchased from Atomergic Chemical Company, Long Island, New York.

of the substrates to the ambient for placement of samples in the mask holders.

III. C-V AND G-V RESULTS

For a basis of comparison with experimental results, calculated C-V characteristic curves are presented in Fig. 1 for the low- and high-frequency response of a PbTe MIS capacitor following the full statistical treatment of Marcus (Ref. 9). Results are shown for n-type substrates with temperature = 77 K, carrier concentration = 5×10^{17} cm^{-3}, ratio of insulator dielectric constant to thickness = 10^{-2} $Å^{-1}$. PbTe band and material parameters were taken from a review article by Dalven (Ref. 10). It is clear from Fig. 1 that small capacitance changes are to be expected experimentally, and that insulator dielectric strengths in excess of 10^6 $V\text{-}cm^{-1}$ are required in order to obtain surface potential control.

C-V characteristic curves obtained at 77 K for MIS structures fabricated on n- and p-type substrates are shown in Fig. 2. On most devices, insulator breakdown voltages were greater than 5×10^6 $V\text{-}cm^{-1}$; the film dielectric constant was determined to be approximately 15. These C-V characteristics are typical of those obtained on devices that received the iodine-methanol surface treatment prior to insulator deposition. The capacitance minima appear at a positve (negative) voltage for p-type (n-type) substrates, as expected. The small changes in capacitance, of the order of 3%, are consistent with calculations, but the slope (dC/dV) of the measured capacitance in the region near the capacitance minimum is less steep than calculated. It should be noted that these curves were obtained after the structures were baked for 65 h in air at 80°C, which dramatically reduced hysteresis effects in the iodine-methanol polished samples.

The C-V characteristic curves obtained for the n-type device shown in Fig. 2 at 1, 10, and 100 kHz are shown in Fig. 3. The variation in capacitance at different frequencies can be attributed to the frequency dependence of the ZrO_2 capacitance that was observed in measurements of metal-insulator-metal (MIM) capacitors fabricated with the MIS capacitors. The closed points were obtained by subtracting a small voltage-dependent MIM capacitance (Fig. 4) from the total measured MIS capacitance. The primary effect of such a calculation is to flatten the characteristic at large applied bias such that the attainment of the accumulation capacitance at $V_b \approx 20$ V is implied.

In Fig. 3, the transition to high-frequency behavior occurs near 100 kHz. This frequency is much greater than the high-frequency limit (approximately 100 Hz for a minority carrier lifetime of 5 ns) calculated from bulk considerations (Ref. 11). It is concluded, therefore, that interfacial states determine the frequency response of the device up to approximately 100 kHz. The contribution of these interfacial states to the capacitance depends on frequency and bias, as can be seen in the region of negative bias for curves A and B (Fig. 3). This interfacial behavior is reflected by the G-V characteristics that were obtained on this device (Fig. 5). Such overall behavior indicates the presence of an equivalent interfacial state capacitance comparable in magnitude to the depletion layer capacitance ($\approx 8 \times 10^{-7}$ F/cm^2).

The C-V characteristic curves in Fig. 6 were obtained for an MIS structure whose surface was treated with the potassium dichromate-nitric acid solution as described in Section II. These curves are typical of those obtained with this surface treatment and show large hysteresis effects. Neither a bake for 24 h in air at 80°C nor bakes for 1 h in flowing hydrogen gas at 80°C and 3 h at 150° C reduced the hysteresis or altered the C-V and G-V characteristics. Evidently, this highly oxidizing treatment results in the creation of an interfacial trap level (or levels) that is stable with respect either to further oxidation (air-bake) or reduction (hydrogen bake). Furthermore, the position of the capacitance minimum at positive gate bias in Fig. 6 indicates that the surface of the n-type substrate is inverted and becomes somewhat less inverted with increasing frequency. For inversion to occur, a negative charge layer of magnitude approximately $1/q\,(C\Delta V) \approx 9.0 \times 10^{13}$ e^-/cm^2 is required. The presence of this layer may also be the result of the surface treatment.

On several devices prepared with the second treatment, however, the capacitance minimum moved across the $V_B = 0$ axis for sufficiently large voltage excursions (Fig. 7). Such effects have been reported on MIS structures of anodic oxides on p- and n-type indium antimonide (2) and may be due to interfacial traps for majority as well as minority carriers. Since this capacitance minimum shift did not occur over a ± 80 V range of similarly prepared p-PbTe, however, it appears that interfacial traps for majority carriers only are sufficient qualitatively to explain such behavior.

In an effort to relate the chemical composition of the surface to the measured electrical properties, x-ray photoelectron spectra were obtained on samples that had received the surface treatments described. Preliminary spectra show a pronounced difference between the peak height ratios of two tellurium peaks (the $3d_{5/2}$ and $3d_{3/2}$) to their associated oxides. Identification of the peaks was aided by an independent run with pure tellurium and comparison with previously reported lead telluride and tellurium oxide spectra (Ref. 12). It is not now known, however, whether the tellurium peaks should be associated with neutral tellurium or a charged state. Nevertheless, these preliminary results indicate that the effect of the second surface treatment with potassium dichromate and nitric acid relative to the first with iodine and methanol is to increase the surface tellurium concentration relative to the tellurium-oxide concentration. We believe, therefore, that the electrical activity of the $PbTe\text{-}ZrO_2$ interface increases as the surface concentration of tellurium (perhaps Te^{2-}) increases relative to the concentration of TeO_2.

IV. CONCLUSIONS

These experimental results are important for assessing the suitability of PbTe for use as substrate material in charge-coupled devices. The results indicate that two initial requirements for such use have been met in (1) obtaining an

electrically stable insulator of high dielectric strength, and (2) demonstrating surface potential control from accumulation through inversion in a manner generally consistent with theoretical expectations. Such consistency, it should be noted, was not shown by previously reported C-V data obtained on PbTe films (Ref. 13). The most successful results have been obtained on substrates that were prepared with an iodine-methanol polish.

Interfacial state densities remain high, however, and must be reduced if efficient charge transfer or charge injection is to be realized. More work is required, particularly in surface preparation, in order to passivate the surface and develop the relationships between surface preparation and surface electrical properties.

REFERENCES

1. Nicollian, E. H., and Goetzberger, A., "The Si-SiO_2 Interface-Electrical Properties as Determined by the Metal-Insulator-Silicon Conductance Technique," Bell Syst. Tech. J., Vol. 46, No. 6, p. 1055, July-August 1967.

2. Kim, J. C., "InSb MOS Detector," Final Technical Report, Army Night Vision Laboratory, Contract No. DAAK02-73-C-006, General Electric Company, Syracuse, New York, February 1975.

3. Leonberger, F. J., McWhorter, A. L., and Harman, T. C., "PbS MIS Device for Charge-Coupled Infrared Imaging Applications," Appl. Phys. Lett., Vol. 26, No. 12, p. 704, June 1975.

4. Schwartz, R. J., Dockerty, R. C., and Thompson, H. W., Jr., "Capacitance Voltage Measurements on n-Type InAs MOS Diodes," Solid State Electron., Vol. 14, No. 2, p. 115, February 1971.

5. Houston, B. B., and Norr, M. K., "Dislocation Etch Pits on p-Type Lead Telluride," J. Appl. Phys., Vol. 31, p. 615, 1960.

6. Brebrick, R. F., and Gubner, E., "Composition Stability Limits of PbTe. II," J. Chem. Phys., Vol. 36, No. 5, p. 1283, March 1962.

7. Calawa, A. R., Harman, T. C., Finn, M., and Youtz, P., "Crystal Growth, Annealing, and Diffusion of Lead-Tin Chalcogenides," Trans. Metall. Soc. AIME, Vol. 242, No. 3, p. 374, March 1968.

8. Lorenz, M. R., "A Chemical Polish for Lead Telluride," Electrochem. Soc., Vol. 112, No. 2, p. 240, February 1965.

9. Marcus, Paul M., "Calculation of the Capacitance of a Semiconduction Surface with Application to Silicon," IBM J. Res. Dev., Vol. 8, No. 5, p. 496, November 1964.

10. Dalven, R., "A Review of the Semiconductor Properties of PbTe, PbSe, PbS, and PbO," Infrared Phys. Vol. 9, No. 4, p. 141, December 1969.

11. Hofstein, S. R., and Warfield, G., "Physical Limitations on the Frequency Response of a Semiconductor Surface Inversion Layer," Solid State Electron., Vol. 8, No. 3, p. 321, March 1965.

12. Grant, R. W., Paska, J. G., Long, J. T., and Andrews, A. M., "ESCA Surface Studies of $Pb_{1-x}Sn_xTe$ Devices," J. Vac. Sci. Technol., Vol. 13, No. 4, p. 940, July-August 1976.

13. Tao, T. F., Ellis, J. R., Kost, L., and Doshier, A., "Feasibility Study of PbTe and $Pb_{0.76}Sn_{0.24}Te$ Infrared Charge-Coupled Imager," Proceedings of the CCD Applications Conference, pp. 249-268, Naval Electronics Center, San Diego, September 1973.

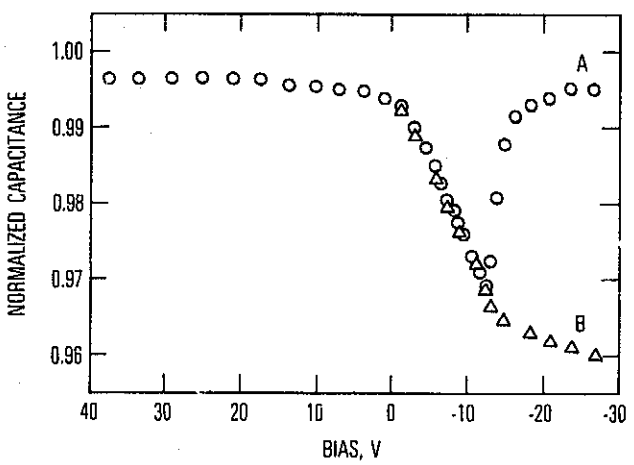

Fig. 1. Calculated low-frequency (A) and high-frequency (B) C-V characteristics for a PbTe MIS capacitor.

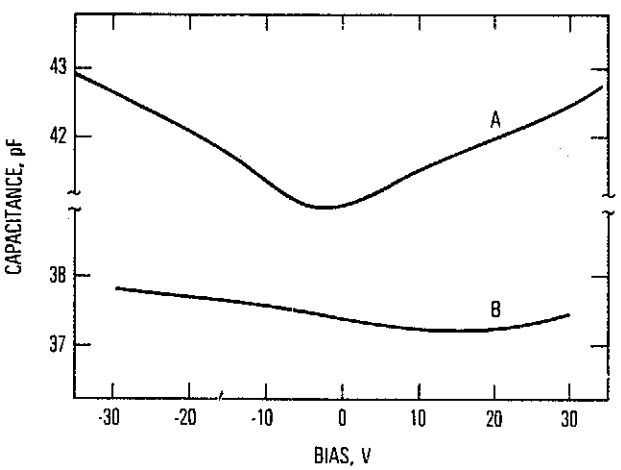

Fig. 2. Experimental C-V characteristics for an iodine-methanol treated PbTe MIS device. Curve A, $n = 2.0 \times 10^{17}/cm^3$; curve B, $p = 1.1 \times 10^{18}/cm^3$.

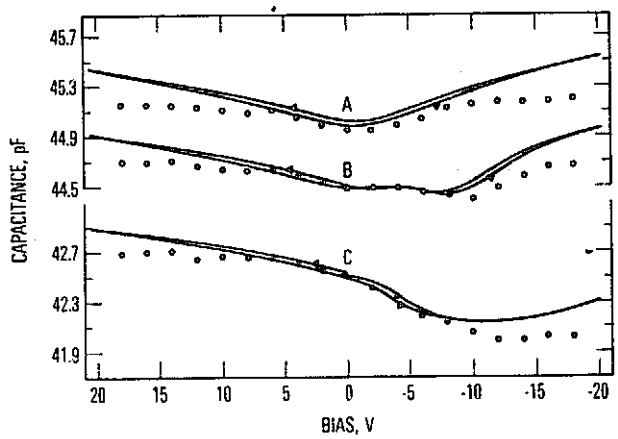

Fig. 3. Experimental C-V characteristics for the iodine-methanol treated PbTe MIS device in curve A of Fig. 2. Field plate area = 4.9×10^{-4} cm^2, insulator thickness = 1590 Å, voltage sweep rate = 40 V/min. Curve A, f = 10^3 Hz; curve B, f = 10^4 Hz; curve C, f = 10^5 Hz.

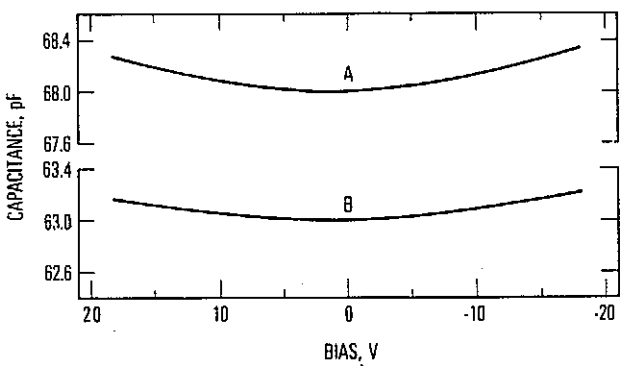

Fig. 4. Experimental C-V characteristics for a ZrO_2 MIM device. Curve A, f = 10^3 Hz; curve B, f = 10^5 Hz.

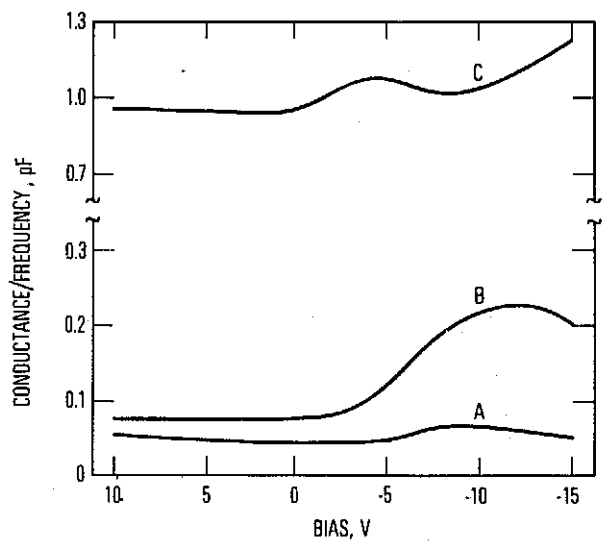

Fig. 5. Experimental G-V curves for the iodine-methanol treated device in Fig. 3. Curve A, f = 10^3 Hz; curve B, f = 10^4 Hz; curve C, f = 10^5 Hz. Voltage sweep rate = 40 V/min.

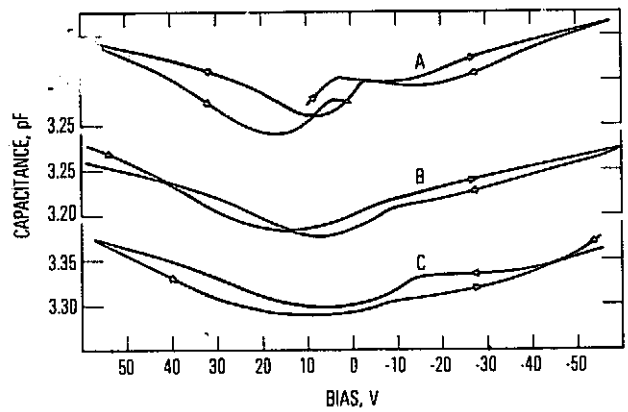

Fig. 6. Experimental C-V curves for a potassium dichromate-nitric acid treated PbTe MIS device. Carrier concentration = 5×10^{17}/cm^3 (n-type); insulator thickness = 1500 Å; field plate area = 4.5×10^{-5} cm^2. Curve A, f = 10^3 Hz; curve B, f = 10^4 Hz; curve C, f = 3×10^4 Hz.

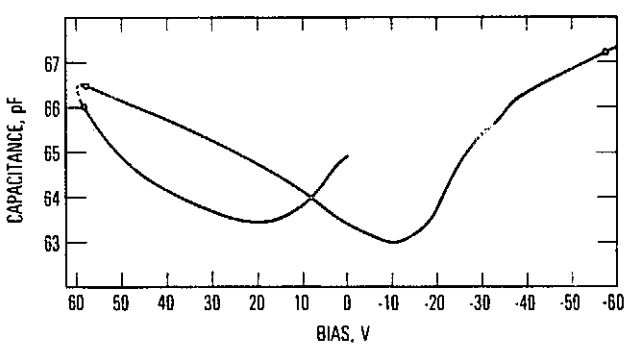

Fig. 7. Experimental C-V characteristics for a potassium dichromate-nitric acid treated n-type PbTe substrate. f = 10^3 Hz.

InSb ARRAYS WITH CCD READOUT FOR 1.0- TO 5.5-μm INFRARED APPLICATIONS*

J. D. Phillips, J. B. Scorso, and R. D. Thom
Santa Barbara Research Center
Goleta, California

ABSTRACT

The application of charge-coupled device (CCD) readout and signal processing techniques to infrared (IR) arrays is leading to a new generation of IR focal plane assemblies with significant improvements in performance. In this paper, two approaches for fabricating indium antimonide (InSb) arrays with CCD readout are discussed. The hybrid approach integrates InSb detectors and silicon CCDs in a modular assembly via an advanced interconnection technology. In the monolithic approach, the InSb infrared detectors and the CCD readout are integrated on the same InSb chip. Both approaches utilize intrinsic (band-to-band) photodetection with the attendant advantages over extrinsic detectors. The status of each of these detector readout concepts, with pertinent performance characteristics, is presented.

I. INTRODUCTION

The development of high-density two-dimensional IR focal plane arrays (FPAs) has been pursued extensively in recent years. The use of CCD readout and signal processing techniques has made possible the combination of detection and multiplexing functions on the focal plane with an attendant reduction in sensor power, size, and weight. Further, enhanced sensitivity can be obtained, if required, by implementing the time delay and integration (TDI) function in the CCD readout registers. The resulting IR array assemblies are ideally suited to, for example, earth resource and outer planet IR imaging applications.

Two distinct methods can be used to achieve IR detection on the focal plane — intrinsic and extrinsic photodetection. The extrinsic approach uses appropriately doped silicon, thus allowing device fabrication on silicon chips. The intrinsic mode of detection, however, utilizes band-to-band photodetection which provides significant operating advantages over the extrinsic approach. In particular, higher operating temperatures (≃ 77° to 100°K) are possible with intrinsic detectors as opposed to 50°K or less for extrinsic detector arrays. Further, the larger absorption coefficient of intrinsic materials provides not only higher quantum efficiencies but lower crosstalk between detector sites than is feasible for extrinsic detectors. The result is a decided systems advantage for intrinsic detectors.

Two concepts for implementing the advantages of intrinsic detectors are discussed in this paper for the case of InSb detectors. The hybrid concept utilizes an advanced interconnection technology to combine the maturity of silicon CCD technology with an array of backside-illuminated InSb photodetectors. The interconnection procedure for this approach is discussed in Section II along with performance data for the InSb detector arrays.

The alternate concept is a complete monolithic structure in which the IR detection and CCD signal readout functions are incorporated on the same InSb chip. This approach obviously eliminates the requirement of an interconnection technology, but it suffers from the relative lack of maturity in the processing of metal-insulator semiconductor (MIS) structures on intrinsic IR detector materials, for example InSb. A viable MIS process has been developed in this laboratory for InSb, and CCDs have been successfully operated. Four-element and 20-element imaging arrays have been designed with fabrication and testing of these devices proceeding at this time. The status of this CCD program will be discussed in Section III.

The possibility of achieving TDI in real time, within the imaging device itself, is an attractive feature of both the monolithic and hybrid InSb/CCD arrays which can significantly increase sensor signal-to-noise ratio (SNR). In Section IV, this performance improvement is illustrated by considering a future generation Landsat Sensor with a monolithic InSb TDI CCD 16 × 16 array operating at 95°K. A four-fold increase in detectivity over a conventional InSb detector array with discrete current-mode preamplifiers is estimated for the particular configuration and spectral bands considered.

II. HYBRID InSb ARRAYS

The demonstration of a 32-element solder bump interconnected FPA was the beginning of hybrid FPA development. Building on this initial success, significant advances in the interconnection technology have been made. In particular, a process was developed in 1974 by which InSb diode detectors could be solder bump connected to silicon CCDs, the resulting structure thinned and then illuminated from the back side. A schematic of such a structure (the BInSb structure) is shown in Figure 1.

The thinning of the back surface of the structure, to a thickness of a few μm, is necessary to achieve photoresponse in the InSb material. Since the silicon CCD readout circuitry is located below

*This work supported in part by NASA under Contracts NAS1-13937 and NAS1-14395.

the InSb in this device, a BInSb array can have virtually all the available FPA area photosensitive; i.e., a high filling factor is feasible. Taking advantage of this property, a 32 × 32 element backside-illuminated array is currently being fabricated. With 1024 detectors located on 0.1-mm (0.004-inch) centers, the device has a filling factor of 95%.

To ascertain the performance characteristics of backside-illuminated arrays, photovoltaic (PV) InSb detectors were assembled to silicon test substrates having metallized lead patterns. A primary measure of the array performance is the quantum efficiency (η) of the structure using backside-illuminated geometry. The quantum efficiency depends on the InSb thickness, the wavelength of incident radiation, and the intrinsic InSb properties. In particular, InSb possesses a high optical absorption coefficient (α) since it is an intrinsic IR detector. As a result, most incident radiation will be absorbed within a few μm of the back surface. The minority carriers (holes for p-on-n InSb diodes considered here) generated by this absorption must then diffuse through the InSb bulk to the diode depletion region. At this point, the carriers result in photocurrent in the usual manner. The importance of the diffusion process to the overall detector quantum efficiency is thus significant.

The process is governed by the continuity equation for minority carrier transport subject to the appropriate boundary conditions at the back surface and at the p-n junction depletion region edge. With this equation, a model using known material parameters has been found to predict the quantum efficiency of BInSb detectors. A curve based on this model is shown in Figure 2 where calculated values of η are shown versus substrate thickness. Two data points are also shown in the figure for different substrate thicknesses. The agreement with the model predictions is observed to be good.

The surface recombination velocity (s) at the back surface is also a critical property which can strongly affect the η, particularly at shorter wavelengths. If s is high ($>> 10^3$ cm/sec), then the majority of the photogenerated holes will recombine at the back surface with a corresponding decrease in quantum efficiency. To ensure a low back surface s value, a passivation process has been developed which yields, repeatedly, detectors with the ideal response of Figure 3. The quantum efficiency is observed to be $\eta \simeq 0.6$ and uniform across the response region of InSb. As noted, the uniformity at the shorter wavelengths demonstrates the success of the passivation process for low s structures.

Finally, the detectivity (D*) and responsivity (R_λ) of the BInSb structure are observed to be comparable to conventional InSb detectors. This point is illustrated by Figure 4 where these parameters are plotted for a BInSb array. It is clear from the figure that the structure is operating at close to BLIP (background limited performance) limit.

III. MONOLITHIC InSb CCD ARRAYS

Charge-coupled devices have been fabricated on InSb substrates and successfully operated. This success has prompted the design of full monolithic InSb arrays which combine InSb MIS detectors with InSb CCDs for signal readout. These arrays are now being fabricated and tested. Due to the importance of these developments for focal plane imagery, it is of interest to examine the status of InSb CCDs in some detail.

The devices fabricated thus far are four-phase (4ϕ) p-channel overlapping gate structures with six basic layers. A cross-sectional view of the device structure is shown in Figure 5. It is clear from the figure that the structure is conventional with the possible exception of the channel stop metal. This layer, used in lieu of the channel stop diffusion of silicon CCD structures, defines the active channel regions of the CCD. Note that the presence of this metal adds one additional layer to the CCD structure, thus complicating the topography of the device. The primary metal used in device fabrication is titanium with silicon monoxide (SiO) being the prime insulator. Typical dimensions of the device include 0.1 μm for the metals, 0.15 μm for the gate insulator, and 0.3 μm for the buried metal insulator.

The first device fabricated in this fashion utilized conservative design rules, due to the initial unknowns of InSb MIS processing, so that the CCD gate lengths were approximately 50 μm. It was a 4-bit device and was successfully operated early in 1975 at a clock frequency of 5 kHz. The proper 4-bit delay was observed using 4ϕ clocking, and the observed charge transfer efficiency (CTE) per transfer was 0.90.

This low CTE value is due primarily to the 50-μm gate lengths in the CCD register, and a shorter gate length device (≃ 25 μm) was designed. The new design includes a 2-bit 4ϕ CCD shift register and a 9-bit 4ϕ CCD with four InSb MIS detectors. A recently fabricated chip is shown in Figure 6. This four-element imager incorporates a transfer gate with the MIS detectors to control access of integrated signal charge into the CCD register. The result is a completely monolithic, albeit small, InSb imager. Already in fabrication with testing of some devices in progress, the successful demonstration of charge transfer from the MIS detectors into the CCD registers is expected shortly.

The 2-bit device has been successfully operated at a clock frequency of 10 kHz, again using 4ϕ operation of the device. The requisite 2-bit delay in the device output is shown in Figure 7 for the case of (a) a single charge packet, and (b) a pulse train

of six charge packets being electrically injected into the CCD register. The CTE can be obtained directly from this figure. Thus, for the single charge packet case, the magnitudes of the first and second output pulses (A and B, respectively) are related to the CTE by

$$N(1 - CTE) = N\epsilon = B/A \qquad (1)$$

where N is the number of transfers of the packet and ϵ is the transfer inefficiency of the device. Since one of a pair of output gates in the 2-bit structure was clocked in this operation, a value of N = 9 is appropriate in the present case. Using this result in equation (1) with the measured A and B values from Figure 7, the result is

$$\epsilon \cong 0.0214 \text{ or } CTE \simeq 0.978$$

A similar result is obtained using the pulse magnitudes of the multiple input pulse train. For this type of input, however, a different relationship between N, ϵ, and the pulse magnitudes must be used.

The expected improvement in the CTE due to the decreased gate length is shown in Table 1. This table was obtained by applying the charge control theory for CCDs as developed by Lee and Heller.[1] The basic assumptions of this model are that (a) the effects of interface states in the CCD can be treated by using an effective time constant (τ_s) for all states, and (b) that charge redistributes instantaneously during the transfer period of CCD operation. The τ_s value was obtained by fitting the CTE of the 50-μm gate length device to the Lee and Heller model. The resulting τ_s, 5 μsec, was then assumed to be valid for the shorter gate length devices and CTE values were computed on this basis.

It is evident that an additional parameter entering the model is the storage well depth of the CCD. The depth appropriate to the 25-μm structure is 1 volt, and for this value the projected CTE is 0.983. This CTE evidently compares favorably with the observed CTE of 0.978. It may thus be concluded that the projected CTE values for still shorter gate length devices are also accurate. Indeed, the tabulated values are the minimum CTE values expected since (a) no fringe field coupling, which increases with shorter gate lengths, is included in the analysis for Table 1, and (b) the continuing improvements in InSb MIS processing are expected to further increase the operating CCD well depth.

Due to these factors, both a 20-element imager with 13-μm gate lengths and a 2-element imager with 10-μm gate lengths are currently being processed along with the 25-μm 4-element imagers. From Table 1, the CTE for these structures should approach 0.999 with existing technology. Since programs to improve the InSb CCD processing sequence and interface state properties are in progress, the final CTE values obtained will be even higher. Some applications are possible even with CTE values of 0.995, however, and it is reasonable to consider a particular application configured around InSb CCD imagers on the focal plane.

IV. MONOLITHIC InSb CCD ARRAY FOR AN EARTH RESOURCES SENSOR

Several applications exist in the fields of remote earth sensing and planetary exploration for which the use of InSb CCD monolithic focal plane arrays with TDI would increase system performance. A partial list of potential applications includes forest fire surveillance and mapping, atmosphere temperature sounding in the 4.3-μm CO_2 band, pollution monitoring, mineral exploration and other geological uses, and distinguishing between clouds and water surfaces, all of which present mid-IR (1 to 5 μm) signatures. To estimate a representative level of performance improvement that should be realized with these arrays, a future generation Landsat Sensor has been considered using a monolithic InSb TDI CCD focal plane, and its performance has been calculated.

Such a future Landsat Sensor configuration is shown in Figure 8. This sensor system utilizes (intrinsic) silicon detectors on a warm focal plane for reflected light bands and one or more InSb TDI CCD arrays on a cold (95°K) focal plane for mid-IR bands. Other arrays may also be included on the cold focal plane for long-wavelength IR bands.

The Landsat spacecraft is assumed to be positioned in a sun-synchronous orbit at 705 km altitude. The IFOV of the system is 42 μrad giving a ground resolution of 30 meters, an improvement of a factor of 2.5 over the present multispectral scanner systems (MSS) now in orbit. A scan mirror (Figure 8) scans the linear arrays in the perpendicular-to-track direction to produce a 185 km swath width. This scan motion allows on-focal-plane TDI to be readily implemented without changing the basic sensor configuration.

The focal plane organization for the InSb TDI CCD array is shown in Figure 9. The number of detectors in TDI is 16; thus, the array is 16 × 16 or 256 elements total. The selection of a 16-element TDI subarray is not necessarily optimum; for this choice, the subarray detectivity in the ideal case is $\sqrt{16} = 4$ times the individual detector D*. Since the performance improvement is proportional to the square root of subarray length, relatively small gains are achieved by using numbers of detectors greater than about 30. The 16 subarrays are aligned with the perpendicular-to-track direction and staggered as shown in Figure 9 to provide contiguous coverage in the along-track direction.

The InSb CCD array parameters and the system parameters assumed for the future Landsat Sensor are given in Table 2. The two spectral bands

considered are a 1.55- to 1.75-μm band and a 3.6- to 4.1-μm (atmospheric window) band. Detectors are 0.05-mm (0.002-inch) square for the 42-μrad IFOV and telescope parameters assumed. The InSb CCD parameters are listed in the lower half of Table 2. These are based on typical design values and measured material parameters and represent presently achieved values or those predicted for the near future. Because of the relatively low backgrounds and scene radiances in these spectral bands and system dwell time, the CCD bit area required is not large, nor is it necessary to taper the CCD register in this case as needed in some TDI applications. This results in the compact array configuration shown in Figure 9.

Using these parameters, the results of D* calculations for the two spectral bands are given in Table 3. In each spectral band, detectivity is calculated for: (a) a conventional system configuration with a 16-element linear array (i.e., one detector/IFOV in the perpendicular-to-track direction); and (b) the 16 × 16 InSb TDI CCD array. The conventional system utilizes PV InSb detectors and current-mode preamplifiers. Noise and D* for this array were calculated using the usual noise current formalism. For the InSb TDI CCD, detectivity was calculated based on noise variance estimates for detector, CCD, and output circuit sources as tabulated in the second and fourth columns of Table 3.

In both bands, the InSb TDI CCD is shown to offer a significant detectivity improvement. For the conventional detector array, D* is amplifier/feedback resistance noise limited in both bands. In the 3.6- to 4.1-μm band, for example, D* is about 45% of the BLIP value for the PV InSb discrete amplifier case. For 16 elements in TDI, the ideal BLIP D* is four times higher. The estimated InSb TDI CCD D* in the 3.6- to 4.1-μm band is, with all noise variances considered, about 50% of this limit. Effective performance in this band is improved by a factor of 4 through use of the monolithic InSb TDI array.

In the 1.55- to 1.75-μm band, thermal background radiation is negligible and reflected sunlight dominates scene radiance. It is instructive to examine the improvement in system SNR in this band when InSb TDI CCDs are used. The minimum radiance N_{min} in this band is approximately 80 μw/cm^2-sr. Using a clear aperture area for the telescope equal to 85% of the primary mirror area and other optical parameters in Table 2, this radiance results in a power 7.8×10^{-11} watts, or 6.5×10^8 photons/sec, imaged on each detector. The summed signal charge at the TDI CCD output is $16 \times 0.75 \times 6.5 \times 10^8 \times 4.5$ μsec $= 3.5 \times 10^4$ charges. Including shot noise in signal, the total noise electron count is 604 electrons, yielding SNR = 58 at the minimum radiance level. For the single detector case, using R = 1 a/w, the noise current in Table 3, and including signal shot noise, the corresponding SNR at N_{min} is 19. These calculations illustrate the potential impact of InSb CCD arrays on future spacecraft sensor systems.

V. CONCLUSIONS

Two approaches to combine intrinsic IR detection and signal readout on the focal plane have been discussed. Hybrid arrays using InSb PV detectors solder bumped to silicon CCDs and backside illuminated have been successfully fabricated. The resulting structure exhibits uniform quantum efficiency ($\eta = 0.6$) and BLIP performance throughout the InSb response region.

Charge-coupled devices with 50-μm and 25-μm gate lengths have been fabricated directly on InSb and successfully operated. The observed charge transfer efficiencies (CTE) of 0.90 and 0.978, respectively, are in agreement with theoretical predictions for these gate lengths. Projected CTE values of 0.999 are expected for shorter gate length structures now being fabricated and tested. Among these structures is a 20-element imager with 13-μm gate lengths which completely integrates IR detection and CCD readout on the same InSb chip. An infrared system configured around the InSb CCD monolithic concept has been presented. A factor of 4 improvement over conventional detectors in system performance is predicted.

ACKNOWLEDGMENTS

The authors would like to thank J. H. Beeler and M. E. Dugger for the fabrication and characterization of the device structures reported in this paper.

REFERENCE

1. Lee, H. S., and Heller, L. G., "Charge-Control Method of Charge-Coupled Device Transfer Analysis," IEEE Trans. on Electron Devices, Vol. ED-19, 1270 (1972).

Table 1. Calculated Transfer Efficiency Versus Gate Length for InSb CCD

GATE LENGTH (μm)	WELL DEPTH (volts)	INTERFACE STATE LOSS	EFFICIENCY (CTE)
50	0.5	9.36×10^{-2}	0.90 (0.90)
25	1.0	1.65×10^{-2}	0.983 (0.978)
13	2.0	2.51×10^{-3}	0.997
10	2.0	1.61×10^{-3}	0.998
7.5	2.0	9.11×10^{-4}	0.999

f_c = 5 kHz; $\tau_s = 5 \times 10^{-6}$ sec; NO FRINGE FIELD; 4Φ CLOCK MODE

Table 2. InSb CCD Array Parameters and Representative System Parameters for Future Landsat Sensor

SYSTEM	InSb SPECTRAL BANDS		1.55 TO 1.75 μm 3.6 TO 4.1 μm
	ORBIT ALTITUDE		705 km
	ORBITAL PERIOD		98.5 minutes
	IFOV		42 μrad
	CROSSTRACK SWATH		0.26 rad
	f/NO.		f/3
	FOCAL LENGTH		1.2 meters
	OPTICAL EFFICIENCY		0.5
	DETECTOR AREA	A_D	2.58×10^{-5} cm^2
	SAMPLE RATE		1/RFOV
	FOCAL PLANE TEMPERATURE	T	95°K
	NO. OF DETECTORS PARALLEL-TO-TRACK		16
DETECTOR/ CCD	QUANTUM EFFICIENCY	η	0.75
	CCD BITS/DETECTOR		1
	BIT LENGTH		56 μm
	BIT AREA	A_B	1.42×10^{-5} cm^2
	THIN OXIDE CAPACITANCE		4×10^{-8} f/cm^2
	CLOCK VOLTAGE		5 volts
	DARK CURRENT (95°K)	J_D	10 μa/cm^2
	INTERFACE STATE DENSITY	N_{SS}	10^{11}/cm^2-eV
	INPUT/OUTPUT CAPACITANCE	(C_{IN}, C_O)	0.5 pF
	OUTPUT DEVICE NOISE AT 1 Hz	V_1	12.5 μV/$\sqrt{\text{Hz}}$

Table 3. Detectivity Calculations for Conventional and InSb TDI CCD Arrays

		SPECTRAL BAND (μm)			
		1.55 TO 1.75		3.6 TO 4.1	
RESPONSIVITY (a/w)	R	1.0		2.3	
BACKGROUND PHOTON FLUX (photons/sec cm^2)	Q_B	NEGLIGIBLE		7.4×10^{13}	
NUMBER OF DETECTORS PERPENDICULAR-TO-TRACK	N	1*	16**	1*	16**
SCAN EFFICIENCY		0.8	0.4	0.8	0.4
IFOV DWELL TIME (μsec)		9.0	4.5	9.0	4.5
BANDWIDTH (kHz)	Δf	55	110	55	110
CLOCK FREQUENCY (kHz)	f_c	---	220	---	220
DETECTOR TYPE		PV InSb	InSb CCD WITH PHOTOGATES	PV InSb	InSb CCD WITH PHOTOGATES
PREAMPLIFIER		CURRENT-MODE	NONE	CURRENT-MODE	NONE
DETECTOR DYNAMIC IMPEDANCE (Ω)		6×10^8	---	6×10^8	---
SHORT CIRCUIT CURRENT (a)		NEGLIGIBLE	---	2.3×10^{-10}	---
FEEDBACK RESISTANCE (Ω)		2×10^7	---	2×10^7	---
EXCESS NOISE CURRENT (a/$\sqrt{\text{Hz}}$)		3×10^{-15}	---	3×10^{-15}	---
TOTAL NOISE (a/$\sqrt{\text{Hz}}$)		1.7×10^{-14}	---	1.9×10^{-14}	---
NOISE ELECTRONS:					
PHOTON	N_P	---	NEGLIGIBLE	---	321
RESET	N_{RST}	---	130	---	130
DARK	N_D	---	385	---	385
FAT ZERO	N_{FZ}	---	130	---	130
INTERFACE STATE	N_{FIS}	---	358	---	358
OUTPUT DEVICE	N_{OUT}	---	140	---	140
TOTAL	N_T	---	574	---	658
D^*_λ (cm Hz$^{\frac{1}{2}}$/watt)		3.0×10^{11}	1.3×10^{12}	6.2×10^{11}	2.7×10^{12}
D^*_{BLIP} (η = 0.75)		---	---	1.4×10^{12}	5.5×10^{12}

$$N_P^2 = N\eta Q_B A_D T_C \qquad N_{FIS}^2 = 0.69 \frac{kT}{q} A_{CCD} N_{SS}$$

$$N_{RST}^2 = 2kTC_O/3q^2 \qquad N_{OUT}^2 = (V_1 C_O/q)^2 \ell n(1/T_C)$$

$$N_D^2 = \left[\frac{NJ_D T_C}{q}(A_D + \tfrac{1}{2}A_B)\right] \qquad D^*_\lambda = \left(\frac{A_D T_C}{2}\right)^{\frac{1}{2}} \frac{N\eta\lambda}{hcN_T}$$

$$N_{FZ}^2 = 2kTC_{IN}/3q^2$$

*CONVENTIONAL SYSTEM **TDI CCD

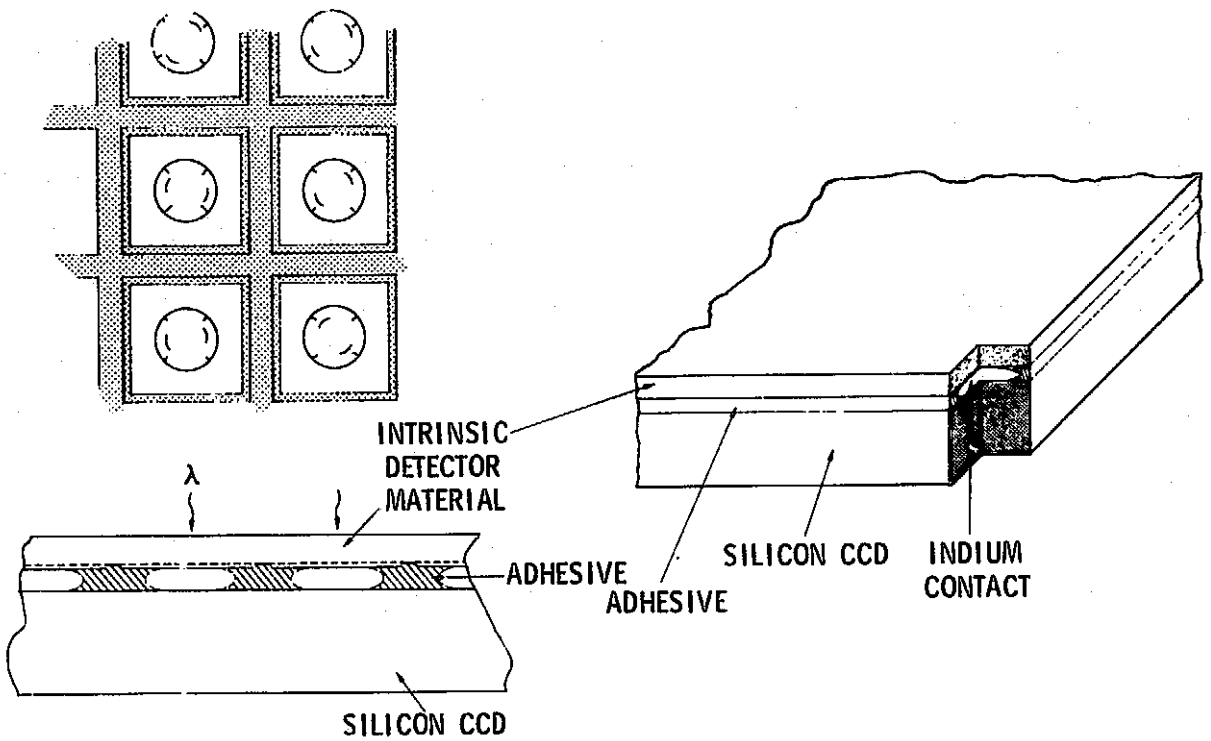

Figure 1. Schematic of Backside-Illuminated InSb Structure

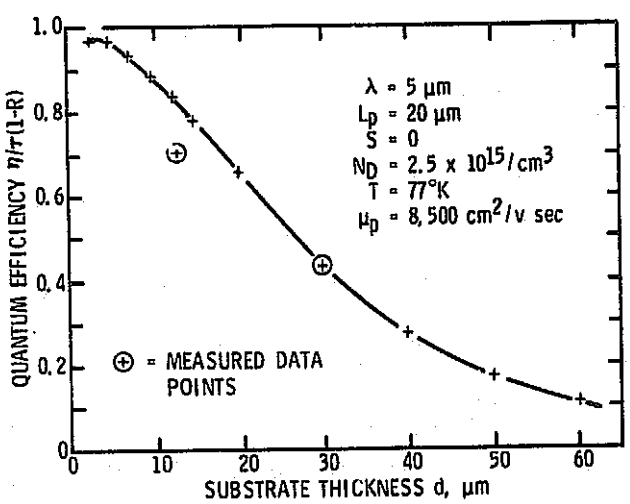

Figure 2. Quantum Efficiency Versus Substrate Thickness of Backside-Illuminated InSb (BInSb) Detectors

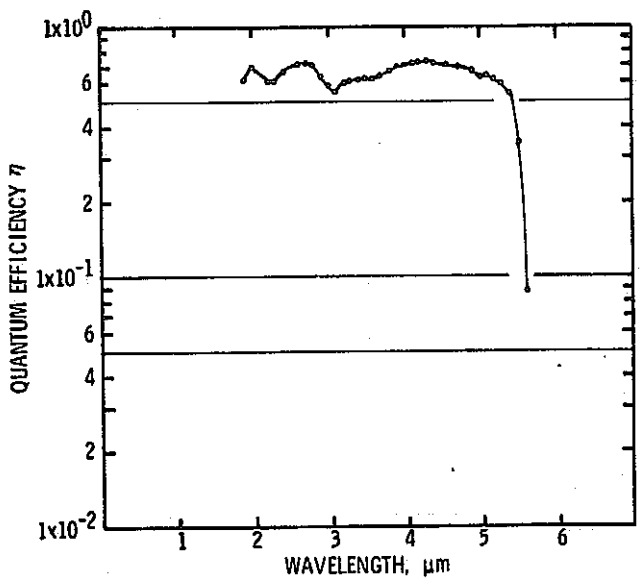

Figure 3. Measured Quantum Efficiency Versus Wavelength for Backside-Illuminated InSb (BInSb) Detectors

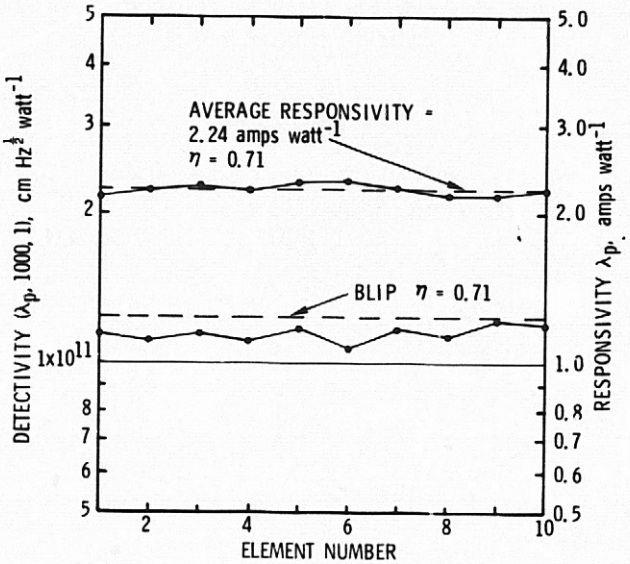

Figure 4. Performance Data on a Recently Measured Backside-Illuminated InSb (BInSb) Array ($Q_B = 1 \times 10^{16}$ photons/sec-cm^2; T = 77°K)

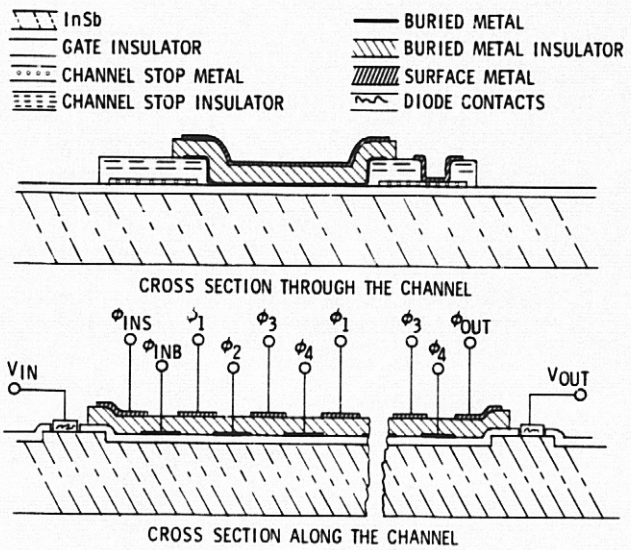

Figure 5. Cross-Sectional View of 4ϕ Overlapping Gate CCD

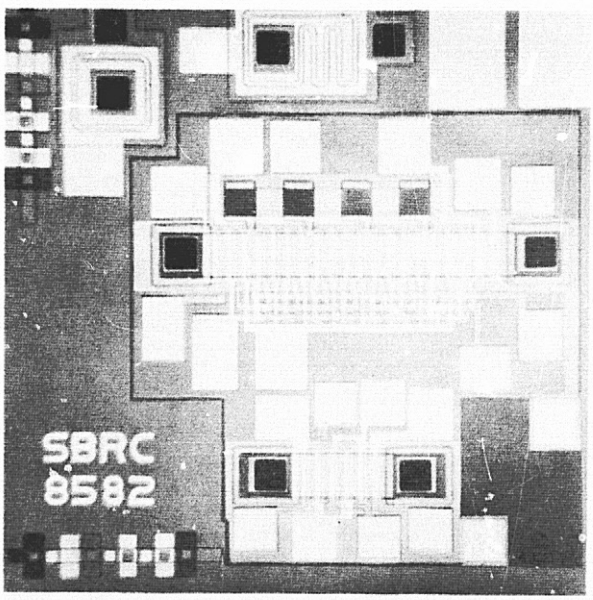

Figure 6. InSb CCD Test Chip with 9-Bit Linear Imager and 2-Bit CCD

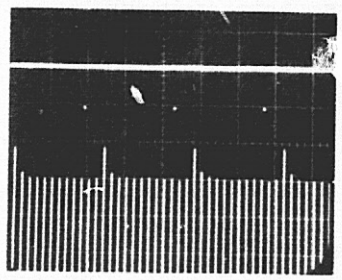

5 V / div

2 mv / div

(a) 500 µs/div

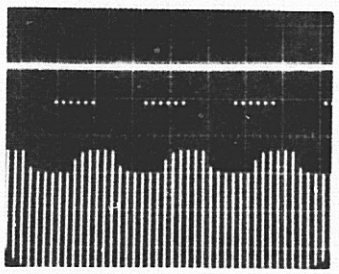

5 V / div

2 mv / div

(b) 500 µs/div

f_c = 10 kHz
4ϕ Clocking
T = 77°K
0° FOV

Figure 7. InSb CCD Output Waveform Two-Bit, 4ϕ CCD

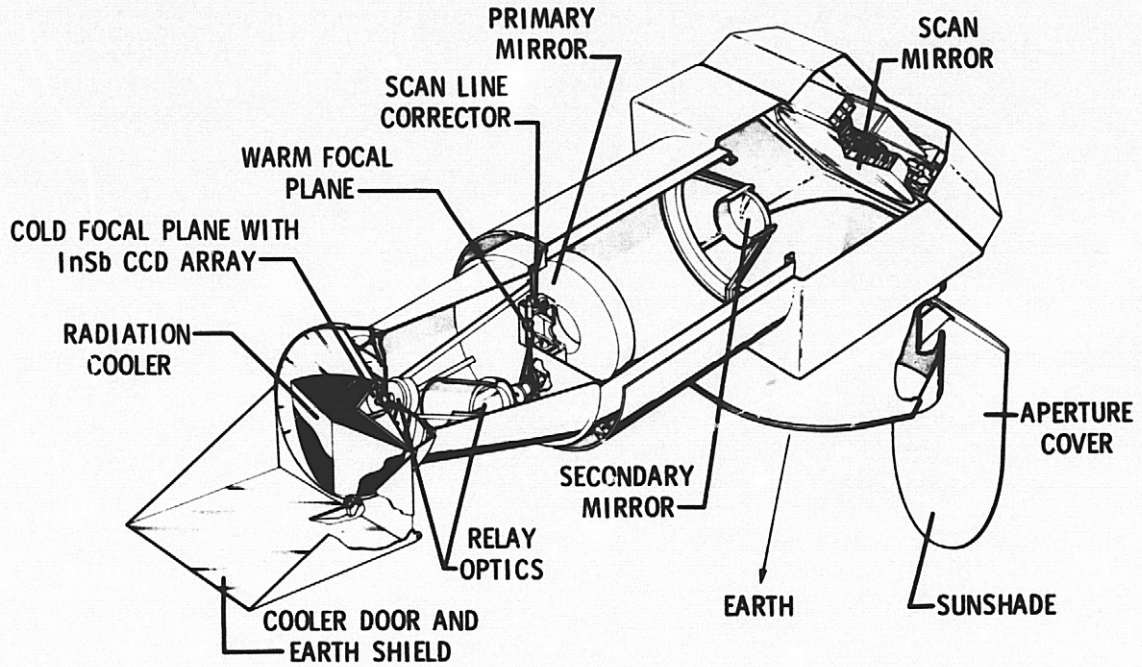

Figure 8. Future Generation Landsat Sensor with InSb CCD Focal Plane

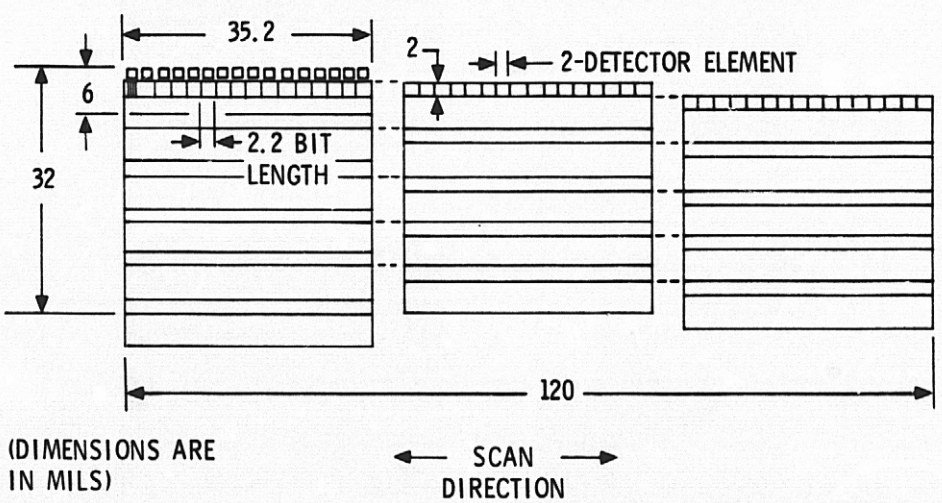

Figure 9. Focal Plane Organization for 16 x 16 InSb TDI CCD Array

COMPUTER-AIDED ANALYSIS OF CCD LINEAR IMAGE SENSORS

Steven S. Prince

The Perkin-Elmer Corporation
Optical Technology Division
100 Wooster Heights Road
Danbury, Connecticut 06810

ABSTRACT

This paper describes special test equipment and techniques to collect and process image information from charge coupled devices (CCDs) by digital computer. The video channel was traced from the CCD to the direct memory access bus of the Interdata Computer. Software was developed to evaluate and characterize a CCD for (1) dark signal vs temperature relationship, (2) calculation of temporal noise magnitude and noise shape for each pixel, (3) spatial noise into the video chain due to dark signal, (4) response vs illumination relationship (gamma), (5) response vs wavelength of illumination (spectral), (6) optimization of forcing functions, and (7) evaluation of an image viewed by a CCD. The basic software differences and specific examples of each program operating on real data are presented.

I. INTRODUCTION

The rapid growth of CCD technology presents a need to develop special test equipment for the timely measurement of critical CCD characteristics. These characteristics, such as dark signal and photoresponse, vary from lot to lot and device to device within a lot that is dependent on material purity, uniformity, and process control. Thus, a rapid evaluation system is required to expedite the screening of selected pieces from low yield processes to be used in an assembly and to assure a high probability of system success.

Perkin-Elmer's Optical Technology Division has responded to this need by developing Low Light Level (LLL) applications for CCDs; the CCD arrays are to be used as star trackers and fine guidance sensors. For these applications, the greatest uncertainty is in the selection and performance of the focal plane sensors. To determine and reduce this uncertainty, we have initiated a program to evaluate candidate sensors for the specific applications. Our computer experiments were conducted on Fairchild's CCDs 121. (Refer to Section III and see Fig. 1.)

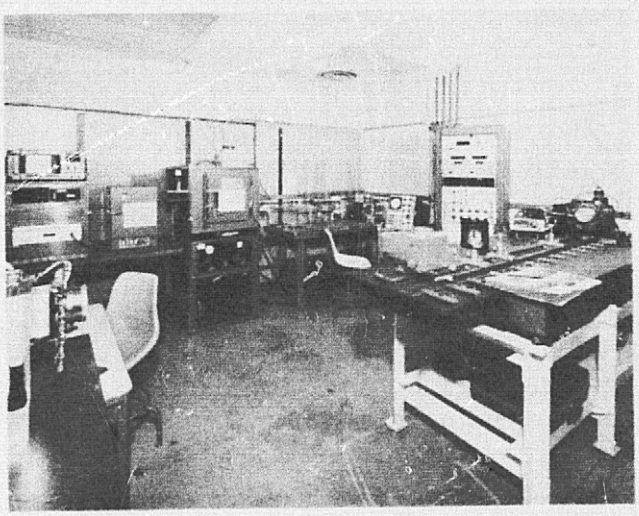

Fig. 1. Perkin-Elmer's Reliability Engineering Laboratory at OTD for CCD evaluation

The conditions of the applications were simulated with test equipment (thermoelectric cooler/vacuum chamber, translation table, etc.) so that the evaluation would be biased to the application requirements. Various light sources were used: a 2850°K, HeNe laser and monochromatic light from 400 - 1100 nm; color correcting filters were also used which resulted in a simulated 5000°K source.

The tests were configured to evaluate and characterize the CCD for the following phenomena:

- The effect on the output by varying the input electrical forcing functions.
- The functional dependence of dark signal to the temperature of operation.
- The spatial variations of the dark signal signature.
- The magnitude and shape of the temporal variation of each photoelement's (pixel) output.
- The linearity of photoresponse as a function of illumination level (gamma).
- The absolute photoresponse as a function of input light source wavelength (spectral response).

Data was recorded in initial tests by oscilloscope photographs which were capable of recording all pixels for each integration period, yet lacked the resolution of any individual pixel, precise measurement of magnitude, or information about the temporal noise magnitude. It was apparent from these photographs that the variations from pixel to pixel were greater than those budgeted for the system application. Dark signal subtraction was required to eliminate the "signature" of the array. Further, calibration was necessary to eliminate the "odd-even" output effect and nonuniformity of pixel responsivity. In addition, we had to quantify the temporal noise to assure the operation of the system in a favorable signal-to-noise ratio.

The measurement system must be capable of collecting data from the device under test at data rates up to 500K bytes per second. This data rate is necessary to allow the recording of every pixel for an integration period. The system must store data from multiple integration periods so that statistical averaging can be performed. Data from many different experiments must also be stored so that variations from experiment to experiment can be evaluated -- i.e., dark signal vs temperature at 9 temperatures, photoresponse vs illumination level at 11 illumination levels, and photoresponse vs wavelength at 29 wavelengths.

The number of tests, the detail of the measurements, and the required speed dictated the requirement for a computer to collect, store, and reduce the voluminous data. Once the need for the computer was established as the data recording system, this permitted additional features to be considered. Simulation of specific applications was now possible. The ability to translate images and point sources

by the array and record the output from the entire image was feasible. In addition, software was developed to simulate several algorithms of data compression that would be performed in the equipment of the final system configurations.

II. TEST EQUIPMENT

1. Drive Electronics

The applications for which this special equipment was designed required the use of multiple CCD line arrays operating with a common integration time and sequential readout. The electronics was designed to allow readouts from 1 to 16 arrays per integration period. The integration period could be altered by adjusting a master clock; all other required clocks track this master clock. All input clocks and voltage levels were adjustable so that the performance of the chip under test could be optimized.

The electronics timed the injection of the charge into the test points on the test array so that charge transfer efficiency (CTE) could be measured in the analog shift registers. This method of measurement eliminated the inherent difficulty of light spot alignment and focus for measurements from a single illuminated pixel, or the nonuniformity of photoresponse that interferes with the CTE measured by uniform illumination.

2. Thermoelectric Cooler/Vacuum Chamber Assembly

The device under test was mounted on a beryllium pedestal which, in turn, was mounted on a thermoelectric cooler. The cooler allowed the chip to be operated at temperatures as low as -40°C. The array clock drivers and first preamplifier were inside a vacuum chamber which could be either pumped down for vacuum operation or backfilled with dry nitrogen for atmospheric pressure tests.

The thermoelectric cooler/vacuum chamber assembly was mounted on a precision, three-axis translation table. (The X and Y directions have remotely controlled stepper motors that provide positional control in two tenths of micron steps. The Z-axis is manually controlled and used for focus.) This apparatus was used to perform simulated image motion on the detectors.

3. Video System

The signal output and the compensation output were subtracted in a low noise preamplifier inside the vacuum chamber. The signal was sent to two sample-and-hold amplifiers. One sample-and-hold amplifier sampled the waveform reference level just ahead of the video information; the other sampled the video output. The reference was then subtracted from the video in the next amplifier. This operation provided DC restoration to the signal and rejected time-correlated noise. Next in the video chain was an optional gain of ten amplifier. For low signal levels, it was necessary to increase the resolution of the following analog-to-digital converter (ADC) circuitry.

Two ADC's were available. Both have 8 bits and 1 MHz conversion time. One has 5 volts full scale; the other, 10V full scale and, combined with the optional times ten amplifier, yields full scale ranges of 0.5V, 1.V, 5.V and 10V. Timing of the conversion occurred after the video sample-and-hold had become stable. The eight data bits and the end of convert pulse were sent to buffer/drivers for transmission to the computer.

4. Computer

An Interdata 7/32 Minicomputer was selected to collect and process the video data from the CCD under test. A Universal Logic Interface (ULI) board was employed to aid data transfer. Note that the addition of line receivers and a flip-flop integrated circuit (to govern the "handshake" control) to the ULI makes the test bench look like just any other high speed peripheral to the computer. This arrangement transfers data at rates in excess of 2 megabytes per second. The computer, containing two 5 megabyte disks (one removable) and two tape drives for bulk storage, services two hardcopy and two video graphics terminals.

III. COMPUTER EXPERIMENTS

We are engaged in the performance evaluation and characterization of Fairchild CCDs 121, both the X and Y configuration. The test equipment described in Section II allowed flexibility in the configuration of specific tests. The tests of primary importance were highlighted in the Introduction of this paper.

1. Optimization of Parameters

The first operation was for the optimization of the electrical forcing functions (the manufacturer's device data sheet was the reference). The primary adjustments were to the "Photogate" voltage and the "Output Gate" voltage. These had the greatest impact on the "odd-even" effect. Fig. 2 illustrates this effect and the computer output most helpful in observing it. Fig. 3 is the same data as received by the computer and displayed in oscilloscope fashion. By iterating the adjustments, the effect could be eliminated. After the optimization procedure had been completed, all the parameters were entered and stored into the computer.

2. Dark Signal vs Temperature

The variation of dark signal vs temperature is a critical parameter for system applications since it provides an indication of device quality. Classical physics predicts the generation of electron hole pairs to diminish by approximately a factor of two for every 8°C reduction in temperature. This relationship does not hold at temperatures close to 0°C and lower. It is postulated that the variation from the theory is due to various trapping states. The lower bandgap and the lower density of these states make their effect noticeable only at lower temperatures. The density of the traps gives a quantitative measure of the quality of the device under test.

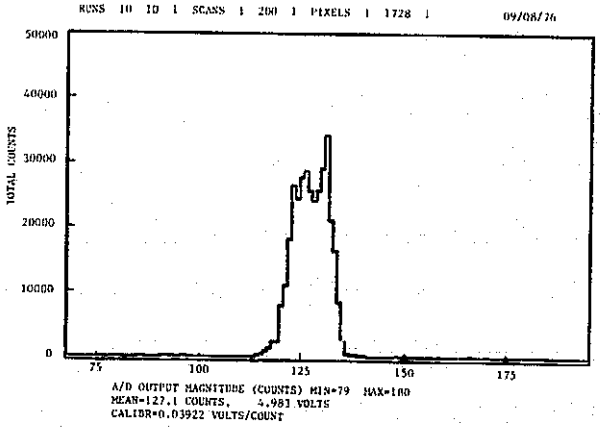

Fig. 2. Frequency distribution showing "odd-even" effect

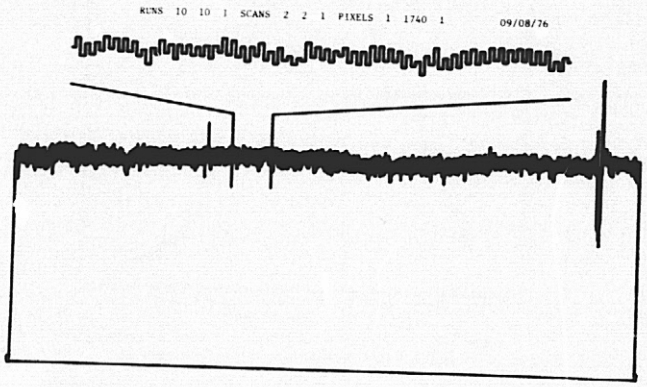

Fig. 3. Raw data in oscilloscope fashion showing "odd-even" effect

The first test that was performed on an array was for dark signal as a function of temperature. The test data was recorded by the computer at nine temperatures between -35°C to 10°C. A typical computer generated output is shown in Fig. 4. A theoretical model with provisions for both classical and trapping effects was drawn on the same figure.

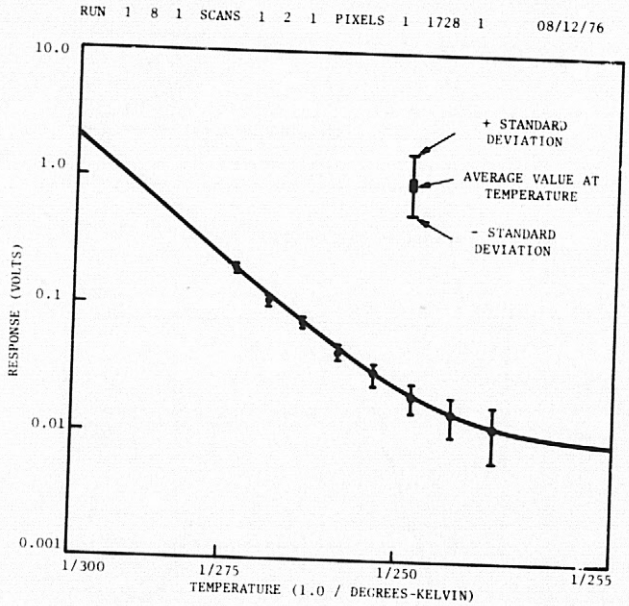

Fig. 4. Dark signal vs temperature functional relationship

3. Temporal Noise

The signal-to-noise ratio available for signal processing is a function of all the gains and added noise of each electronic stage in the video chain (Fig. 5). It has been proven that the most appreciable noise source is the device on the chip output amplifier.

Data collected for the dark signal vs temperature test consisted of 500 samples of each of the 1728 pixels of the array at each of the nine temperatures. The computer can use this data to calculate the shape, magnitude, and location of a three parameter Weibull distribution for each pixel (Figs. 6 and 7). A "composite" pixel was also calculated from the average of the 1728 shape, location, and scale parameters. This knowledge allowed determination of a threshold value for the video signal that will effectively reduce false hits while maximizing detection (Fig. 8).

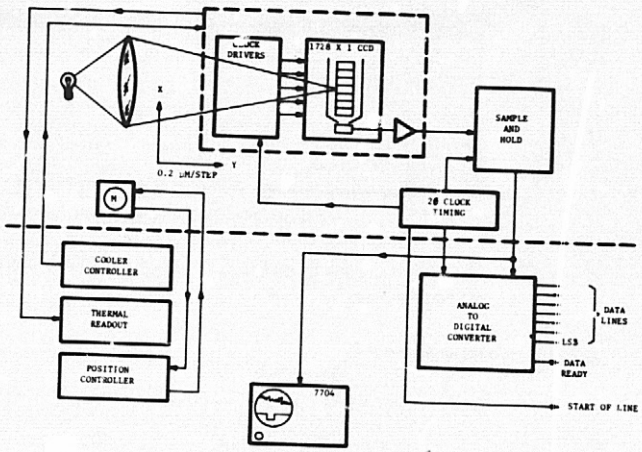

Fig. 5. CCD video chain to interdata computer

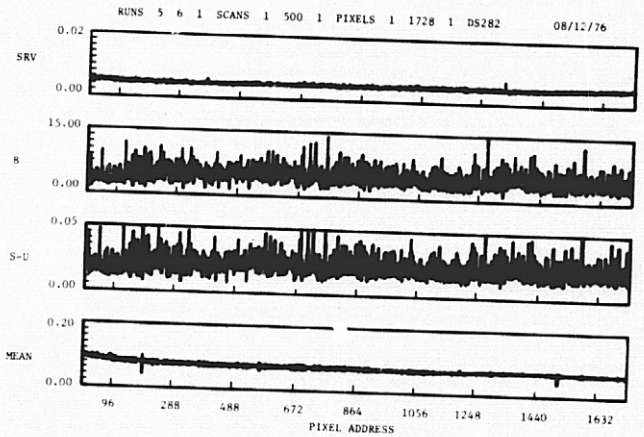

Fig. 6. Plots of three parameter Weibull values vs pixel number

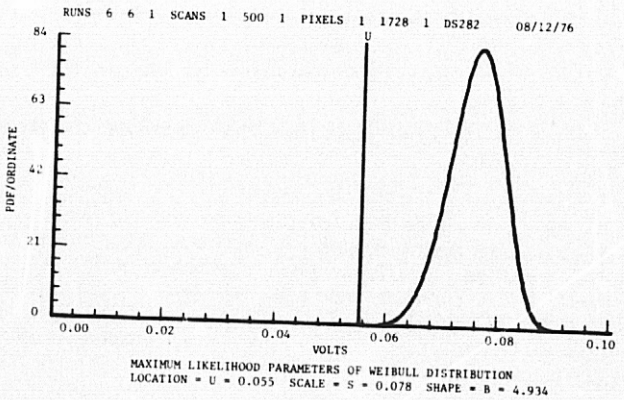

Fig. 7. Composite Weibull distribution of all pixels

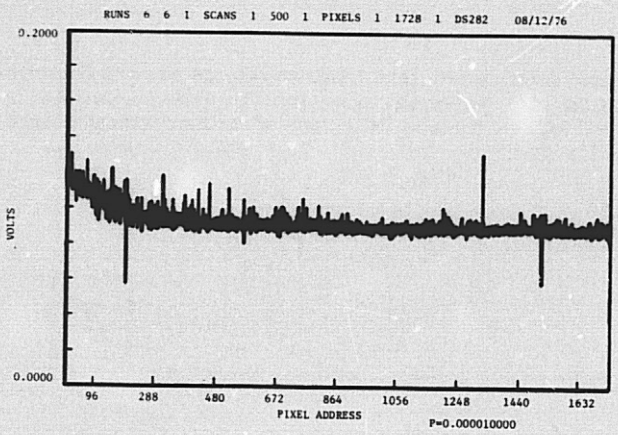

Fig. 8. Threshold voltage required for each pixel to assure a probability of false hits of 10^{-5}

4. Spectral Response

The response to light of different wavelengths is of prime importance to any detector application. The arrays tested exhibited response from 400 nm to 1100 nm. The method of the test involved the use of two monochrometers: one covered the range from 400 to 800 nm; the other, from 700 to 1100 nm; both in 25 nm steps. The overlapping points from 700 to 800 nm were used as a check for accuracy.

The computer collected dark signal data from the array and then data at 17 different wavelengths, using the visible region monochrometer. This was followed by another dark signal for reference and the monochrometer was changed. The procedure was repeated for the infrared region monochrometer.

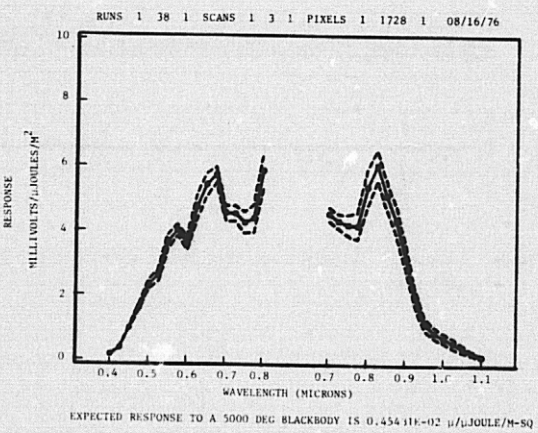

Fig. 9. Spectral response from the two monochrometers used

Fig. 9 shows the data from the two monochrometers and the standard deviation about the average. Fig. 10 folds the two together. The theoretical response to a light from a 5000°K full radiator was also calculated. The spectral response of any pixel or group of pixels could be calculated, and variations from end to end could be easily mounted (Figs. 11 and 12).

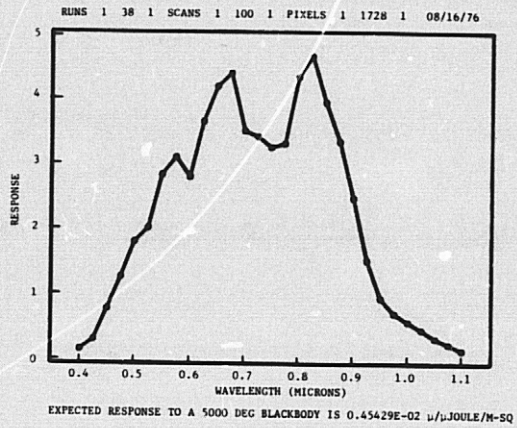

Fig. 10. Spectral response of all pixels averaged

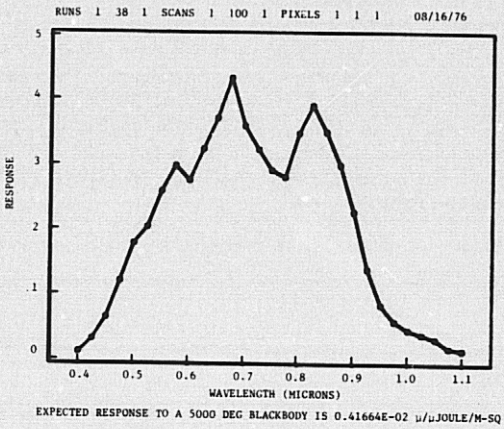

Fig. 11. Spectral response of pixel number one

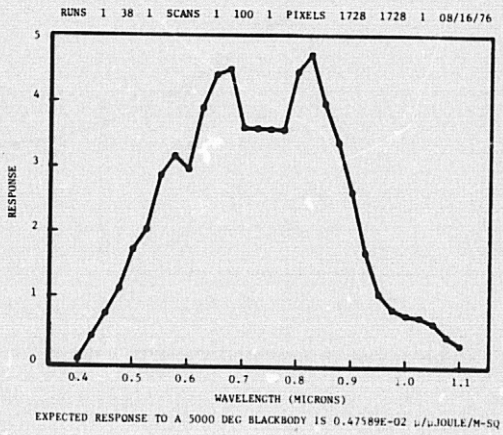

Fig. 12. Spectral response of pixel number 1728

5. Photoresponsivity and Linearity of Response (Gamma)

Particular interest has been placed on the linearity of response to different illumination levels. Film and television tubes both have an exponential response to light intensity. The theory for semiconductors predicts the exponent of Equation (1) to be 1.0.

$$\frac{\text{Illumination No. 1}}{\text{Illumination No. 2}} = \left(\frac{\text{Volts Response No. 1}}{\text{Volts Response No. 2}}\right)^{\gamma} \quad (1)$$

To evaluate this effect, the device was exposed to illuminations ranging from 2.μ j/square meter to 2600μ j/square meter (5000°K source, 80 msec integration time), and the data was collected by the computer. A dark signal reference level was collected before and after the complete range of illuminations; this approach ensured that the temperature of the array had not changed during the test. The dark signal data was also used for pixel-by-pixel subtraction of the dark signal before photoresponsivity calculations were made. A typical output (Fig. 13) produced the voltage output vs illumination level on log-log axes and the least-square-best-fit to the equation:

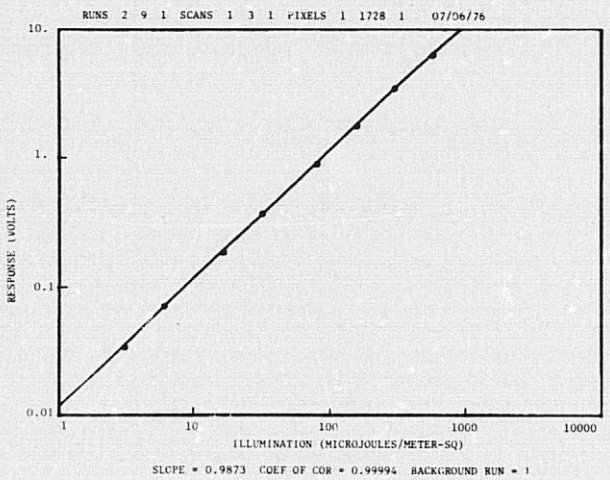

Fig. 13. Log response vs log irradiance curve

$$\log (Vi\text{-}DS) = \log B + \gamma \log (Hi) \quad (2)$$

where

Hi = the illumination of the ith level

Vi = voltage output at the ith level

DS = dark signal at test temperature

B = responsivity at 1μ j/m^2

γ = linearity exponent gamma

This test can be done for any pixel or group of pixels.

A measure of the charge transfer efficiency of a device could be made using the data available from the photoresponsivity and linearity test. It can be shown that:

$$\eta = \sqrt[M]{\frac{V_{N+2} - DS_{N+2}}{V_N - DS_N}}$$

where

η = charge transfer efficiency

M = number of transfers

N = last real pixel number

V_N = voltage from the last pixel

DS_N = dark signal from the last pixel

V_{N+2} = voltage two clock pulses after the last pixel

DS_{N+2} = dark signal two clock pulses after the last pixel

6. Image Analysis

The driving force behind the characterization of an imaging array was to be able to remove from the output signal spatial effects of the sensor and leave only effects of the image. The remaining temporal effects were the sole limitation on the devices with respect to LLL performance.

Operational differences between imaging and characterization were immediately apparent. The most obvious was that characterization tests must precede imaging. Second, for characterization, the image scene had to remain constant. The effect of temporal noise could then be used to smooth the transfer function of the ADC (multiple samples may be averaged together to obtain values between the assigned ADC codes). Imagers have a changing scene from integration period to integration period; they cannot time average the signal, and so were limited by the temporal noise and the ADC's least significant bit (LSB). One should be cautioned about using relative calculations below ADC code 5, as the error could be in excess of 10% of the assigned value with no temporal noise, and greater if noise is present. The probability of the value assigned by the ADC being less than ±1/2 LSB is a function of the code width to the standard deviation of the noise ratio (Fig. 14).

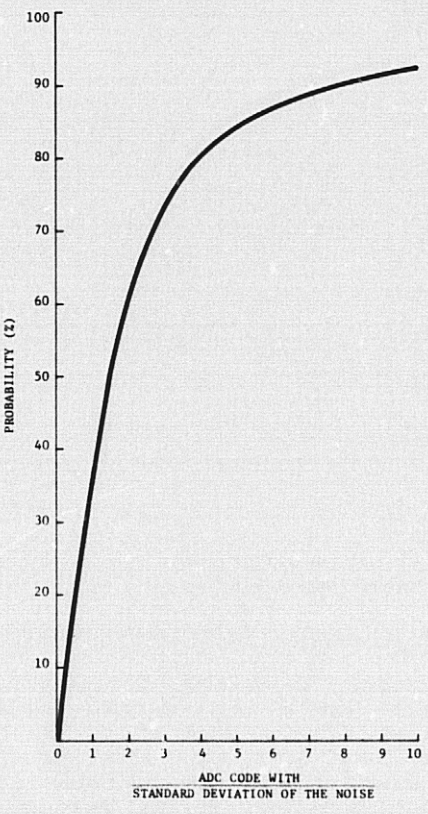

Fig. 14. Probability that the value the computer assigns to the signal is within ±1/2 least significant bit

There is no advantage in an imaging application to have the width to sigma ratio less than 1.5. This is the point at which the probability of an error greater than ±1/2 LSB equals 0.5. Lower ratios will favor the output not to be in the nearest conversion level to the signal.

In the simulation of our application, a spot generator was used to create a 20 μm diameter spot (5000°K blackbody). The X-axis stepper table was moved in two tenths of μm steps, 6.5 μm per integration time. The data could be plotted on the display screen. The options allowed for pixel-to-pixel dark signal subtraction, thresholding, and zoom magnification in any combination. Fig. 15 presents the results of thresholding alone. The required threshold dropped dramatically (for a 10 and 0.0049V RMS noise, 3 bit is sufficient) after background subtraction (Fig. 16). The centroid noted was the calculated prediction of the time and location of the spot's transit.

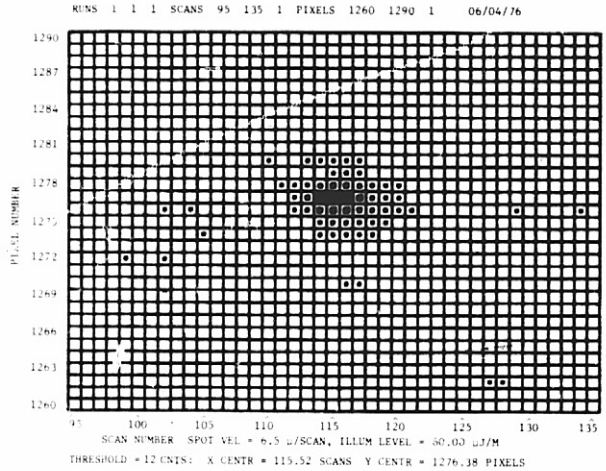

Fig. 15. Simulation star transiting array threshold of 12, no background subtraction

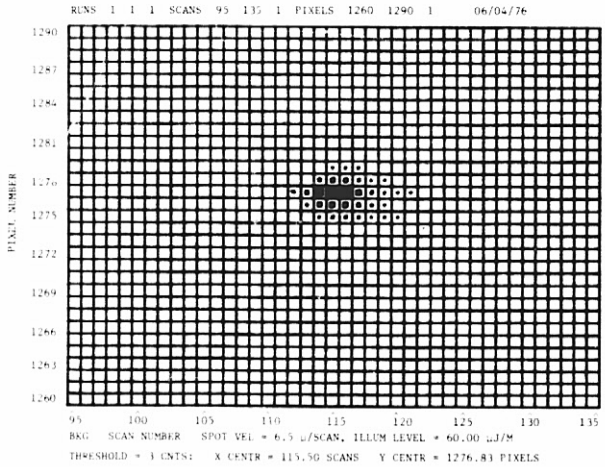

Fig. 16. Simulation of star transiting array threshold of 3 background subtracted

IV. RESULTS AND CONCLUSIONS

The computer is necessary for the comprehensive characterization and evaluation of CCDs. Not only does it measure and store the output of each pixel for each integration period, but its speed allows the collection of multiple array readouts during real time -- i.e., for our system, 500 successive samples in 40 seconds in which the array generated the information. It is the short time duration which maintains the integrity of the experiment. The temperature, clocking voltages, light sources, etc., cannot vary appreciably during the length of the experiment. The new data may be operated on immediately for verification purposes and/or stored on magnetic tape as a data base for multi-experiment comparisons or for future evaluations.

This software package is unique, extensive, and expanding. More than just data recording is provided. The data is reduced and fit to physical models such as:

- Dark signal vs temperature:

$$V_{DS} = A + BT^{3/2} e^{-EG/2KT} + CT^{3/2} e^{-EM/2KT}$$

- Photo response:

$$\log (V_{ILL} - V_{DS}) = \log B + \gamma \log (Hi)$$

The basic data is extended to make predictions:

- The probability of a false bit given a particular threshold voltage.
- The threshold voltage required to assure a particular probability of a false bit.
- The expected responsivity to any color temperature blackbody.

Application hardware and operation can be simulated in software to determine the most effective design algorithms for a particular system. Our system is not constrained to a particular device type. Three different video amplifiers in two different vacuum/thermo-electric cooler enclosures have been employed for both line and area arrays. The video chain can be broken at any point before the ADC, and other electronics can be substituted as necessary.

The overall results of testing (Table 1) reveal the dark signal for the Y configuration devices to be about 10 μ j/m^2 ; photoresponse: 54μ V/μ J/m^2 ; temporal noise equivalent signal: 0.9μ j/m^2 ; and saturation exposure in excess of 600μ j/m^2 .

By comparison, the X-configuration devices (which have an extra amplifier stage on the chip) exhibit 16 μ j/m^2 equivalent dark signal; 227μ V/ μ j/m^2 photoresponsivity; 1.1 μ j/m^2 noise equivalent signal; and saturation in excess of 2600 μ j/m^2 . They demonstrate dynamic ranges of 600 and 2000, respectively, for the Y and X types.

Table 1. CCD test results

S/N	Dark signal at -10°C	(mv/ μj/m^2) Responsivity	Noise
285040	0.1008v	11.2	
Y	9.8μ j	220 gain	
285044	0.1158	13.49	
Y	11.μ j	220 gain	
285054	0.08068	12.2	
Y	6.6μ j	220 gain	
285055	0.0452v	16.1	
Y	2.8μ j	220 gain	
226263	0.08337	5.32	
X	16μ j	20 gain	
256282	0.07545	4.54	4.9mv
X	16μ j	20 gain	1.07μ j
276347	0.04096	4.53	5.37mv
X	9μ j	20 gain	1.18μ j

D7

TESTING THINNED, BACKSIDE ILLUMINATED CCD AREA IMAGE SENSORS

George Root

Jet Propulsion Laboratory
Pasadena, California

ABSTRACT

During the last two years, Texas Instruments, Inc., has, with support from NASA, developed thinned, backside illuminated CCD area image sensors. Arrays of 100 x 160 and 400 x 400 elements have been produced. During this time a facility to test and evaluate these sensors has been assembled at JPL. For a typical space application the CCD sensor will be cooled, exposure will be controlled by a shutter and the video signal will be read-out at a slow rate compatible with spacecraft data systems. This mode of operation enhances some of the performance parameters of the CCD but also causes problems in device testing primarily due to the long frame times involved. In order to overcome these difficulties some novel test techniques have been developed making use of computer processing of the video data. This paper presents the results of testing device noise and nonuniformity. Read-out noise levels of 25-50 electrons rms and uncorrected nonuniformity of response of about 1-3% have been measured. A simple technique for linearly correcting nonuniformity is described and examples given. The technique is shown to be successful in reducing nonuniformity to the level of random noise.

I. INTRODUCTION

During the last two years Texas Instruments, Inc., with support from NASA, has developed thinned, backside illuminated CCD area image sensors. The design and fabrication of these sensors has been described (Ref. 1 and 2) and will not be repeated here except to note that arrays of 100 x 160 picture elements (pixels) and 400 x 400 elements have been produced. Figure 1 is a photo of the "front side" of a 400 x 400 array. The "back side" of the silicon substrate is etched until the thickness of the active area ia approximately 10 μm. The image to be sensed is focussed on the thinned "backside" eliminating losses and interference effects caused by light passing through the "frontside" gate structure. Examples of some astronomical images taken using a 400 x 400 array are presented in another paper in these proceedings (Ref. 3).

For a typical space imaging application the CCD sensor will be cooled to reduce dark current, the exposure will be controlled by a shutter, and the video signal will be read-out at a slow rate compatible with spacecraft data systems. This mode of operation has at least two advantages in sensor performance. Since the exposure is controlled by a shutter, it is not necessary to reserve part of the sensor area for an opaque buffer, the entire array can be used for imaging. The second advantage stems from the slow read-out rate. It will be shown later that the slow read-out permits low noise operation of the on-chip precharge amplifier. However, the operating mode described also causes some problems in device testing. A means for cooling the sensor must be provided, and the test procedures must take into account the long frame times caused by slow read-out. At a typical rate of 100 k pixel/sec it takes 1.6 seconds to read out a 400 x 400 element image.

Figure 2 is a photo of the CCD test facility developed at JPL. The CCD sensor is mounted within a double walled vacuum dewar where it is cooled to a temperature in the range -40° C to -90° C by circulating cold nitrogen gas which is boiled off from a dewar of liquid nitrogen. The video data read-out from the CCD is amplified and digitized to 12 bit accuracy. This digital data is recorded on magnetic tape for subsequent computer processing. High resolution video monitors can be used to observe the data coming directly from the CCD in real time or to display data read back from digital tapes after computer processing.

This paper will describe some of the results of tests to measure the noise and nonuniformity associated with these CCD sensors, and a simple but effective method for removing nonuniformity in order to achieve noise limited performance.

II. NOISE

The Texas Instruments' CCDs incorporate an on-chip precharge amplifier. An off-chip correlated double sampler is used to reduce the reset noise associated with this type of preamplifier which would otherwise amount to some 200 electrons rms. Figure 3 shows the results of a theoretical analysis of the minimum possible noise for this type of signal extraction technique. Only two sources of noise were considered in this analysis, thermal noise associated with the "off" resistance of the on-chip FET reset switch, R_{OFF}, and thermal noise associated with an equivalent noise resistance, R_N, representing the actual load resistor combined with "white" noise generators in the output source follower and the input stage of the off chip amplifier, all divided by the gain of the source follower squared. As shown, the output noise is a function not only of the parameters R_{OFF} and R_N, but also on the time between the samples of the reset voltage (clamp) and the signal voltage (sample). It is assumed that as the time between the clamp and the sample is varied, the bandwidth of the signal chain is correspondingly changed to retain optimum performance. The optimum relationship between clamp to sample time and video bandwidth is indicated by the two scales at the bottom of the figure. The curves of Figure 3 indicated that very low values of read out noise can be achieved with this type of amplifier, but only if R_{OFF} is large, R_N is small, and the time between clamp and sample can be made relatively large, say in the range of 1 μs to 10 μs. Since a typical spacecraft data system would require a relatively slow read out rate anyway, the performance of this type of signal chain is nicely matched to the requirements. Although the TI CCDs have been operated at read out rates of several million pixels per second,

noise measurements at JPL have all been done at a rate of 100 K pixel/sec and with a clamp to sample time of 2 μs. The vertical bar near the center of Figure 3 indicates the range of readout noise measured for current CCDs using buried channel source follower FETs, 25 to 50 electrons rms. Earlier CCDs with surface channel FETs exhibited noise levels of about 100 electrons rms.

One common technique for measuring the noise of CCDs is to sample the output of a single pixel on successive frames and to measure the standard deviation of a large set of such samples. This technique is not suitable for slow read out rates; at 100 K pixel/sec it would take nearly 3 minutes to collect 100 samples. Any drift in lamp output or irregularities in exposure time during this period would be measured as noise. A more accurate as well as faster technique is made possible by computer processing of the recorded video data. To measure the output noise at any exposure level, two consecutive frames taken about 2 seconds apart are recorded. A small area, typically 20 pixels square is selected from both frames and the difference between output levels is taken on a pixel by pixel basis. The mean value of these 400 differences is near zero and is an indication of the drift in the system during the 2 seconds between frames. This mean difference is largely due to slight variations in exposure time and is ignored. However, the standard deviation of the 400 differences is just $\sqrt{2}$ times the noise in either of the frames, assuming the noise is uncorrelated frame-to-frame. Since the differences are taken pixel by pixel, nonuniformity in output from pixel to pixel does not appear in the measured noise. Figure 4 is a typical plot of noise versus output measured by this technique. This particular curve is for a 400 x 400 array identified as JPL 12. At high output levels the measured noise tends toward shot noise in the output as would be expected, confirming the validity of the technique. It should be noticed that this technique does not respond to low frequency noise components which effect primarily the mean value of the differences rather than their variance.

To demonstrate the low noise capabilities of these CCDs, the series of photos in Figure 5 were made. The area shown is a portion of the same 400 x 400 array whose measured noise is shown in Figure 4. The photos are of raw video without processing and each photo is a single exposure. The peak signal level for the brightest bars is shown below each photo. Nonuniformity in response causes the signal level near the top and bottom of the array to be less than shown. Light and dark bands running horizontally across the photos are 60 Hz pickup. Since the full well capacity of this CCD is over 3×10^5 elec/pixel, the 50 electron photo represents a sensor dynamic range of over 6000. Figure 5 demonstrates that quite usable images are possible with these sensors with only a few hundred electrons of signal. Combined with the high quantum efficiencies possible with "backside" illumination this results in a very useful low light sensor.

The photos in Figure 5 demonstrate low signal performance where, for cooled sensors, performance is limited by temporal noise. At high signal levels, however, performance is limited by pixel to pixel nonuniformity in response. This will be discussed in the next section.

III. NONUNIFORMITY

CCD image sensors, as do all discrete photo sensor arrays, exhibit pixel to pixel variation or nonuniformity of response. Figure 6 shows computer generated pseudo-three-dimensional plots of sensor output for dark and uniform illumination at 700 nm for a 100 x 160 element CCD identified as JPL 10. Note the 4X difference in scale factors for the two plots. The unit DN is just the digital number the A/D converter assigns to each pixel's output. In the dark plot, except for the blemish in the lower right corner, the variations visible are due to random temporal noise, that is if the same test were done again the pattern would be different. However, for the illuminated case the variations are large compared to the noise and are quite repeatable. These plots show good uniformity of response across the array which indicates a uniformly thinned sensor. Current 400 x 400 arrays exhibit more large scale variation in response associated with variation in the thickness of the finished sensor. The measured pixel to pixel nonuniformity is about the same for both sensor sizes.

The pixel to pixel sensor nonuniformity is measured by calculating the standard deviation of outputs for a uniform exposure for a small area, again typically 20 x 20 pixels. Figure 7 is a plot of the results of such a nonuniformity test on the same sensor as shown in Figure 6. As can be seen the output nonuniformity increases in direct proportion to the output. The proportionality constant, the slope of the line, is a measure of response nonuniformity, in this case ±2.6%. The zero response, i.e. dark, intercept is a measure of dark nonuniformity, in this case ±97 electrons. This is an older device with a measured noise of about 100 electrons rms again indicating that at low temperatures variations in dark output are due to temporal noise.

The plot in Figure 7 demonstrates the problem of achieving noise limited performance at high signal levels. For example, at an output of 10^5 electrons, Figure 7 shows a nonuniformity of about ±3000 electrons/pixel. Referring back to Figure 4 it is seen that the noise at this output level is only about 300 electrons, so to achieve noise limited performance requires the removal or correction of a nonuniformity about 10 times larger than the noise. A simple technique for accomplishing this will be discussed next.

IV. NONUNIFORMITY CORRECTION

Measurements of the linearity of CCD and signal chain have shown them to respond linearly within the resolution limit imposed by the 12 bit A/D converter. Since this is true, the response of each individual pixel can be characterized by two parameters indicating the slope and offset of that pixel's light transfer curve. Those two parameters can be measured by using uniformly illuminated calibration frames. In order to reduce the uncertainty in the calibration coefficients, each calibration frame is repeated several times,

typically four times, and the results averaged pixel by pixel. For each pixel a least mean squares straight line fit of the form y = a + bx is made using the averaged data where y= the individual pixel's output and x= the mean output of all pixels. The coefficients a and b are such as to correct each individual pixel's response to be equal to the average of all pixels. The set of coefficients, a and b, represents the calibration data. At some later time a set of raw image data can be corrected using the relationship (corrected data) = (raw data-a)/b. To assess the efficacy of this correction, the standard deviation of the corrected data is found and compared to the standard deviation of the raw data, and to be random noise level. A "perfect" correction would be indicated by a standard deviation equal to about 1.12 times the random noise, i.e. the rms sum of the noise in the data and the residual noise in the calibration coefficients. This could supposedly be reduced to just the random noise by repeating each calibration frame more than four times.

Figure 8 shows the results of such a test using an area of 30 x 30 pixels. Again a partial area is used to reduce processing cost, and in this case to eliminate blemishes from the area tested. A 700 nm spectral filter was used to prevent spectral shifts as the lamp intensity was varied. The standard deviation of the raw data is similar to that shown in Figure 7, again indicating an uncorrected nonuniformity of about ±2.8%. The standard deviation of the linearly corrected data is slightly above the random noise level as expected indicating that simple linear correction is quite effective in reducing output nonuniformity. In fact, the rightmost data point shows a residual nonuniformity of about ±5 DN for an output signal of about 2500 DN or a residual error of ±0.2%.

Figure 9 shows the results of using linear decalibration to correct response nonuniformity in a 100 x 160 pixel image. The contrast has been enhanced to accentuate the results, both photos have the same contrast enhancement. Most of the spots in the prints are due to chemical processing of the film and not the CCD. It should be noted that although this decalibration process removes nonuniformity of response, it does not change the signal to noise ratio and in the photos shown the S/N ratio is lower in the top left corner because that area of the array had lower sensitivity. It may be possible to see the slightly more "noisy" appearance of that area of the corrected photo.

In order for this technique of correcting sensor nonuniformity to be of practical usefulness, the pattern of nonuniformity must be stable and repeatable. To determine if this is the case, a one week stability test was conducted. The results are shown in Figure 10. The calibration data were taken at time =0 and then this single set of data were used to decalibrate test frames taken over a period of one week. The vertical axis is the residual dispersion in the data after being corrected as described above. The three curves are for dark output and two light levels corresponding to about half and one third of full well. It should be noted that the tests were done at room temperature to avoid problems of frost and dew collecting on the dewar windows. This accounts for the high level of dark output and dark noise. The three arrows at the right of the figure indicate the expected level of residual nonuniformity (1.12 times the random noise) expected for each curve. As can be seen the residual dispersion is again due essentially entirely to random noise, that is, the fixed nonuniformity pattern has been "completely" removed. These curves also show that the pattern of nonuniformity is stable over a period of at least one week within the level of random noise.

V. MEMBRANE INTERFERENCE

When thinned CCD sensors are used to image in nearly monochromatic light, interference fringes are generated within the silicon membrane and are visible in the video output. This effect is noticeable only for wavelengths long enough that the light can make at least one double pass through the membrane (λ greater than about 600 nm) and for spectral bandwidths narrow enough to produce well defined fringes ($\Delta\lambda$ less than about 50 Å). One application where this effect is apparent is methane band imaging at 890 nm. The index of refraction of silicon is so high, approximately 4, that light travels through the silicon essentially perpendicular to the surface regardless of incidence angle. Thus, at least to first order, the interference pattern generated in the silicon wafer is a function only of the thickness variation of the wafer and not of the incidence angle of the light, nor of the nature of the image focussed on the CCD surface. For a constant temperature, the thickness variations of the wafer should be fixed and so the interference pattern should appear to be another form of fixed pattern response nonuniformity which can be corrected using the technique described above. To test this hypothesis, a 100 x 160 element CCD was illuminated by tungsten light passed through an 890 nm methane band filter (half power bandwidth 40 Å). Figure 11 shows the results of this test. The left photo is the "flat field" containing the interference pattern used for decalibration. The image used is that of a medium contrast bar target. The peak to peak signal amplitude is about the same as the peak to peak amplitude of the interference pattern. Again the simple linear decalibration is quite effective in correcting for sensor response nonuniformity.

REFERENCES

1. Antcliffe, G. A., L. J. Hornbeck, J. M., Younse, J. B. Barton, and D. R. Collins, "Large-Area CCD Imagers for Spacecraft Applications", Symposium on Charge-Coupled Device Technology for Scientific Imaging Applications, Pasadena, California, March 6-7, 1975.

2. Antcliffe, G. A., L. J. Hornbeck, W. C. Rhines, W. W. Chan, J. W. Walker, and D. R. Collins, "Development of a 400 x 400 Element, Backside Illuminated CCD Imager", 1975 International Conference on the Application of Charge-Coupled Devices, San Diego, California, October 29-31, 1975.

3. Smith, B. A., "Astronomical Imaging Applications for CCDs", Paper 5 of Session Five of these Proceedings.

Acknowledgment. This paper presents the results of one phase of research carried out at the Jet Propulsion Laboratory, California Institute of Technology, under Contract NAS7-100, sponsored by the National Aeronautics and Space Administration.

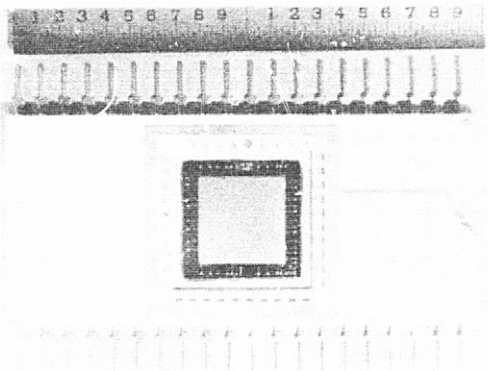

Figure 1. Texas Instruments 400 x 400 Element CCD Image Sensor

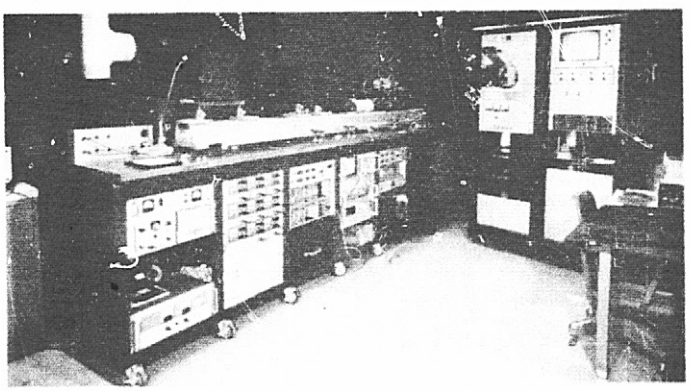

Figure 2. CCD Test Facility at JPL

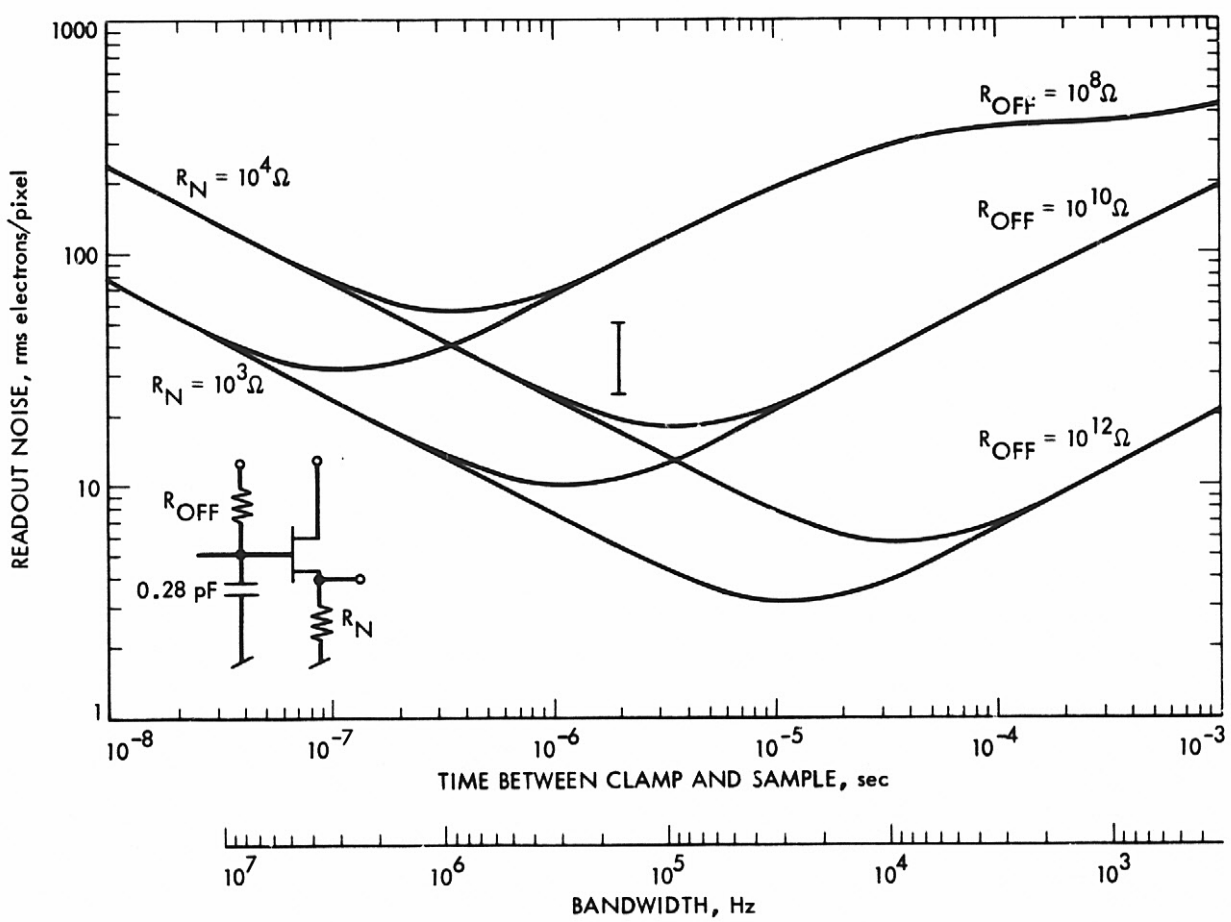

Figure 3. Minimum Read Out Noise for Precharge Amplifier-Correlated Double Sampler Combination

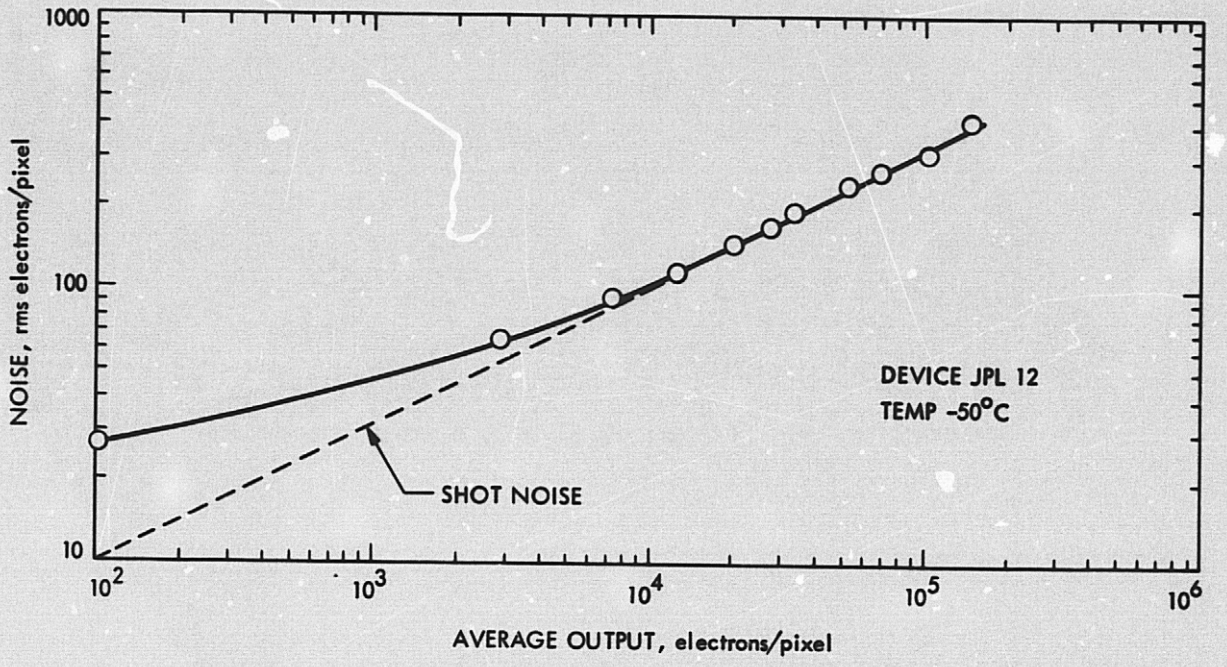

Figure 4. Measured Output Noise

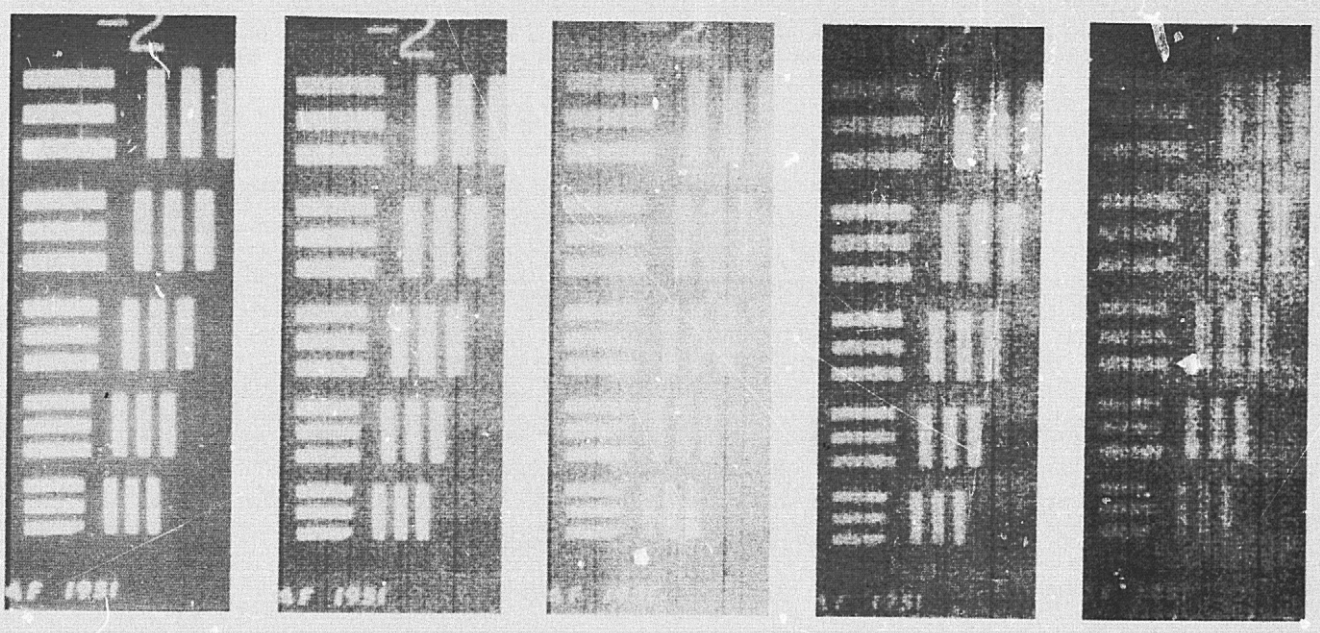

Figure 5. Examples of Low Light Level Images

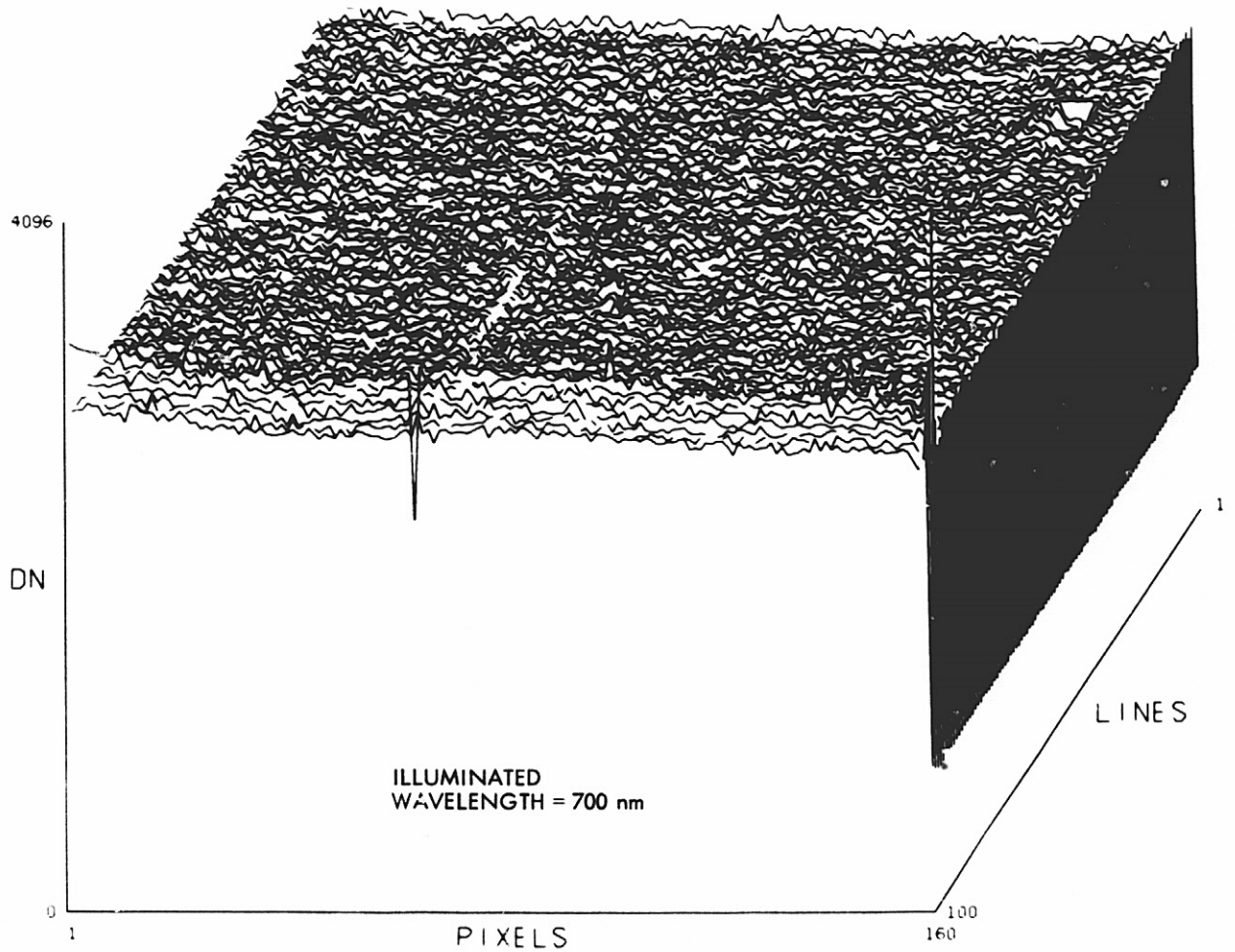

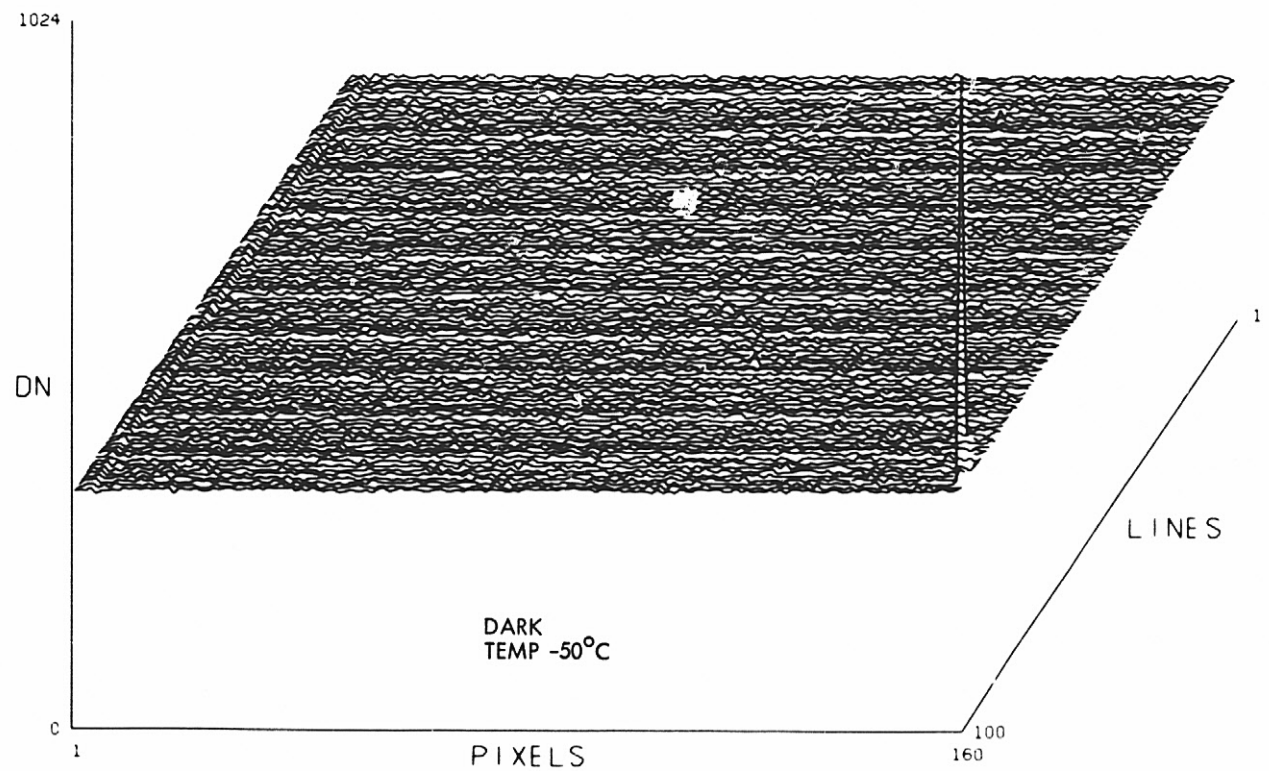

Figure 6. Computer Generated Plots of 100 x 160 Element CCD Output

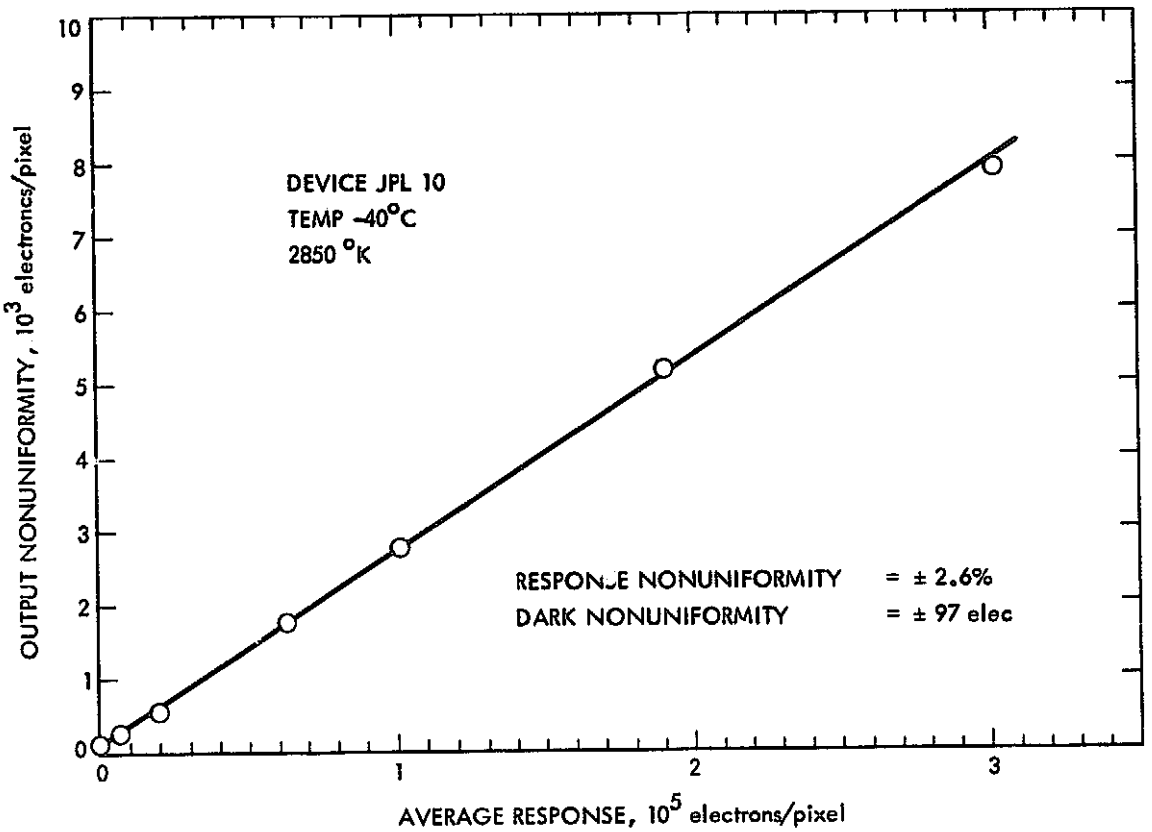

Figure 7. Measured Output Nonuniformity

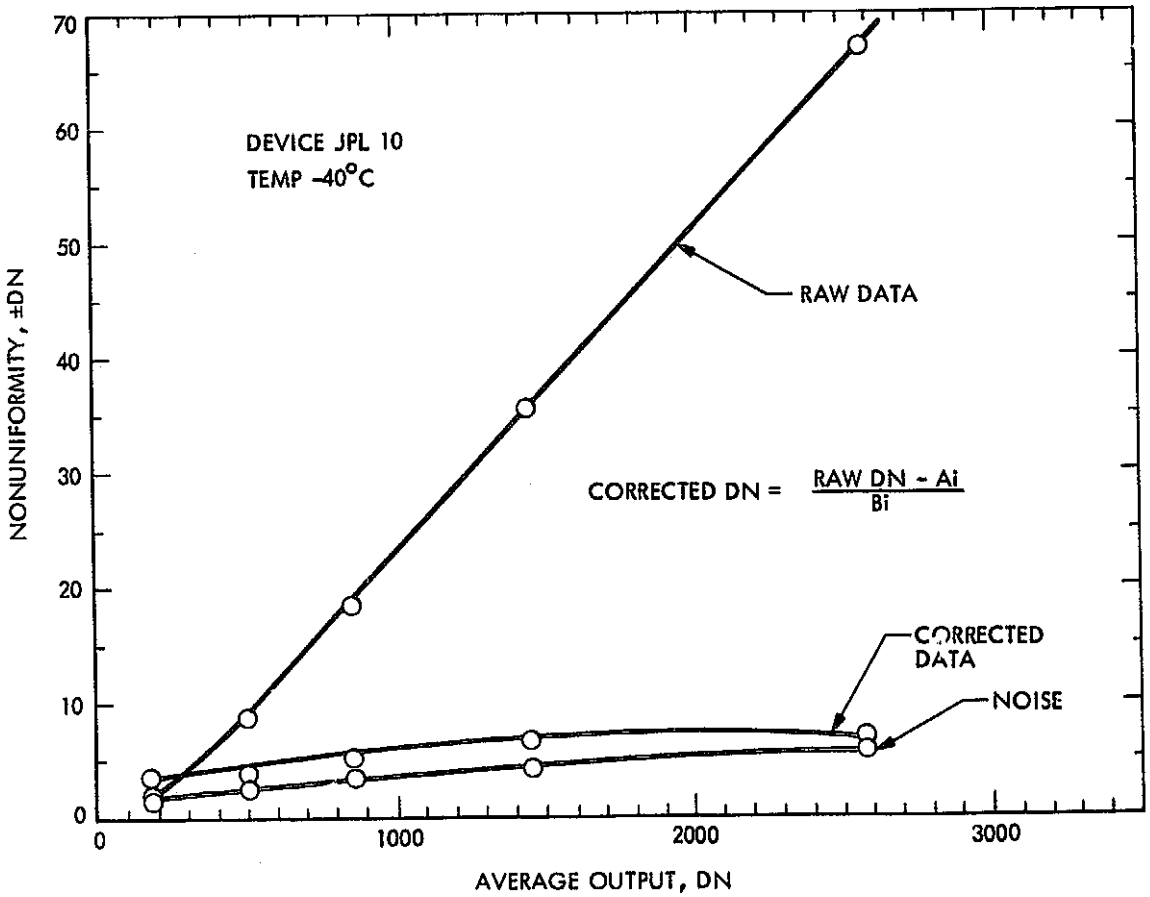

Figure 8. Nonuniformity of Raw Data and Linearly Corrected Data

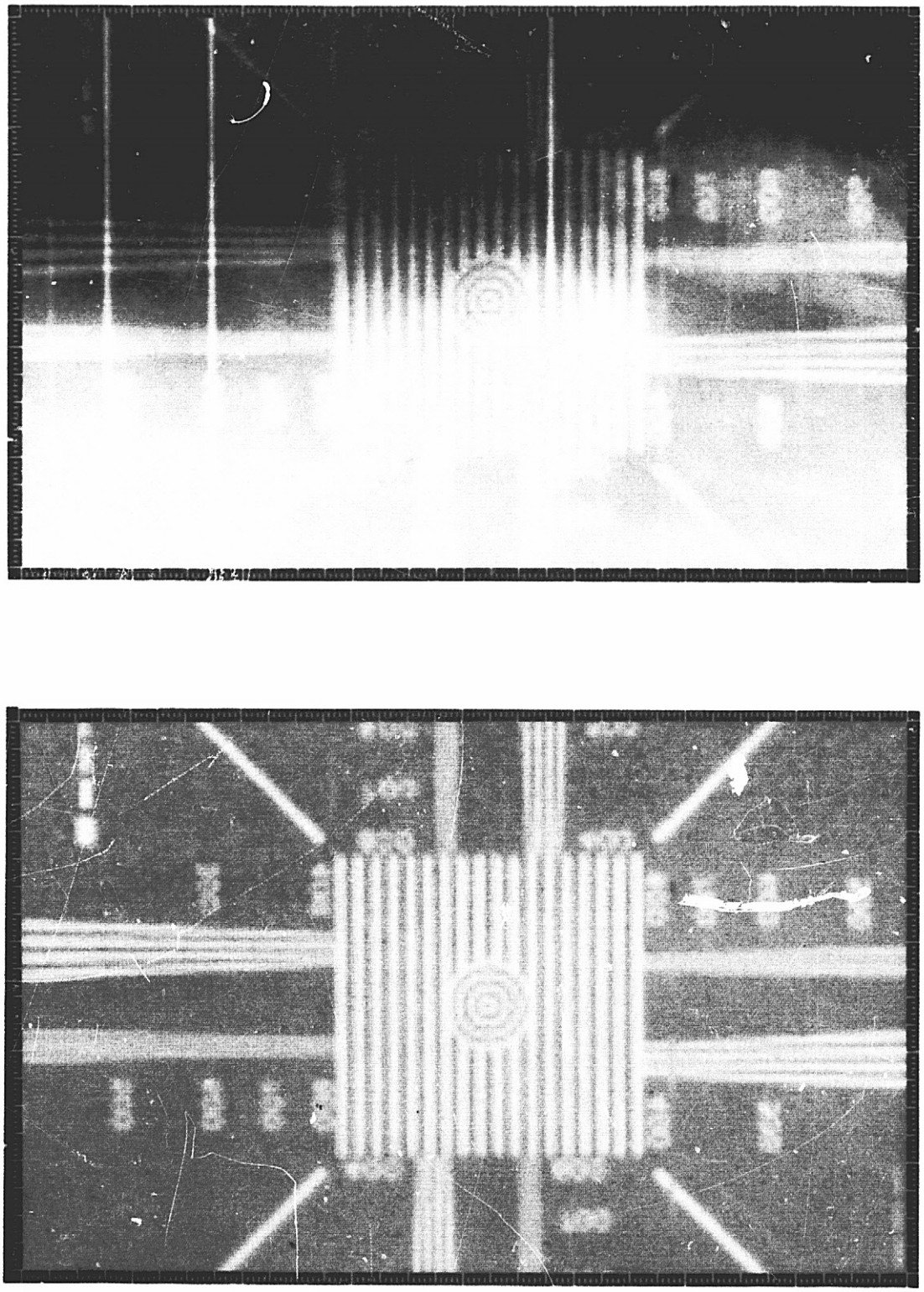

Figure 9. Raw and Corrected Images from 100 x 160 Element CCD

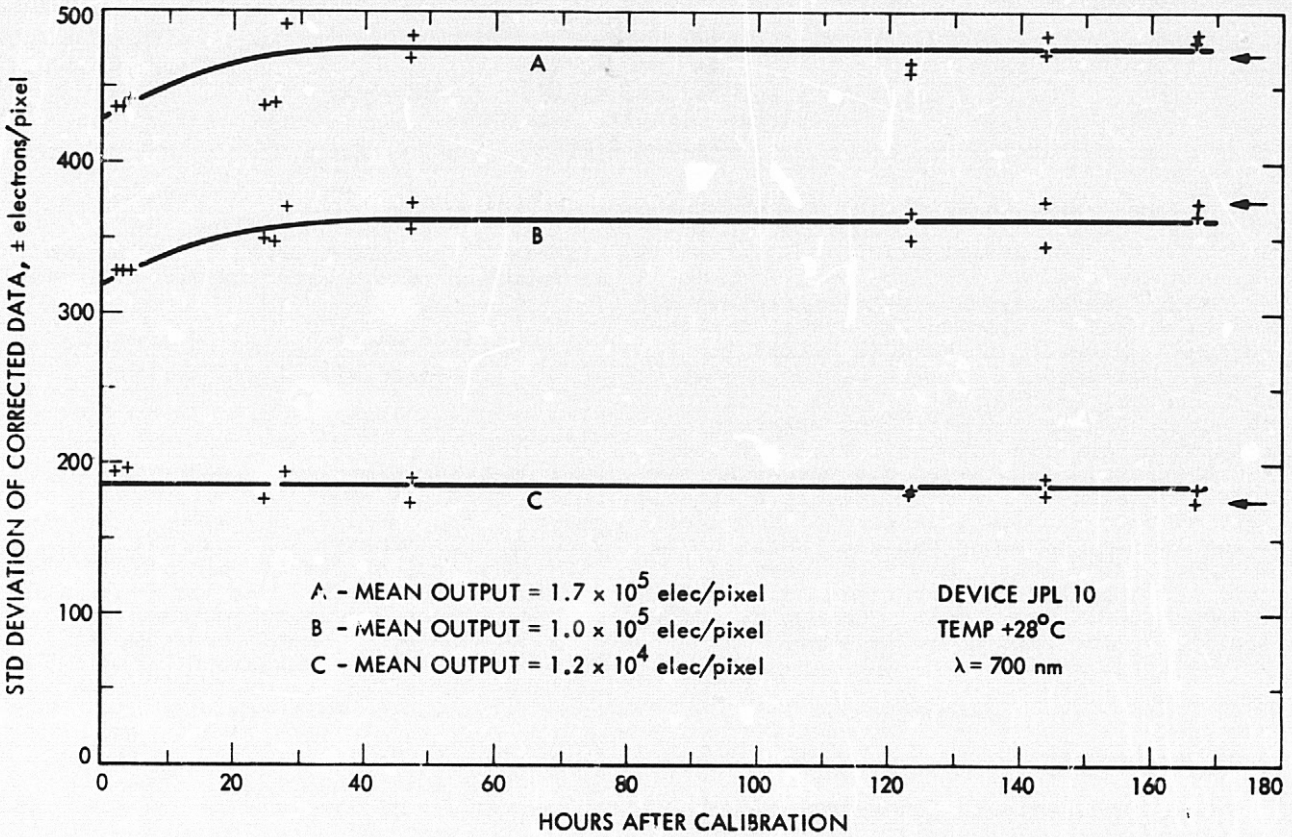

Figure 10. Stability of Nonuniformity Correction

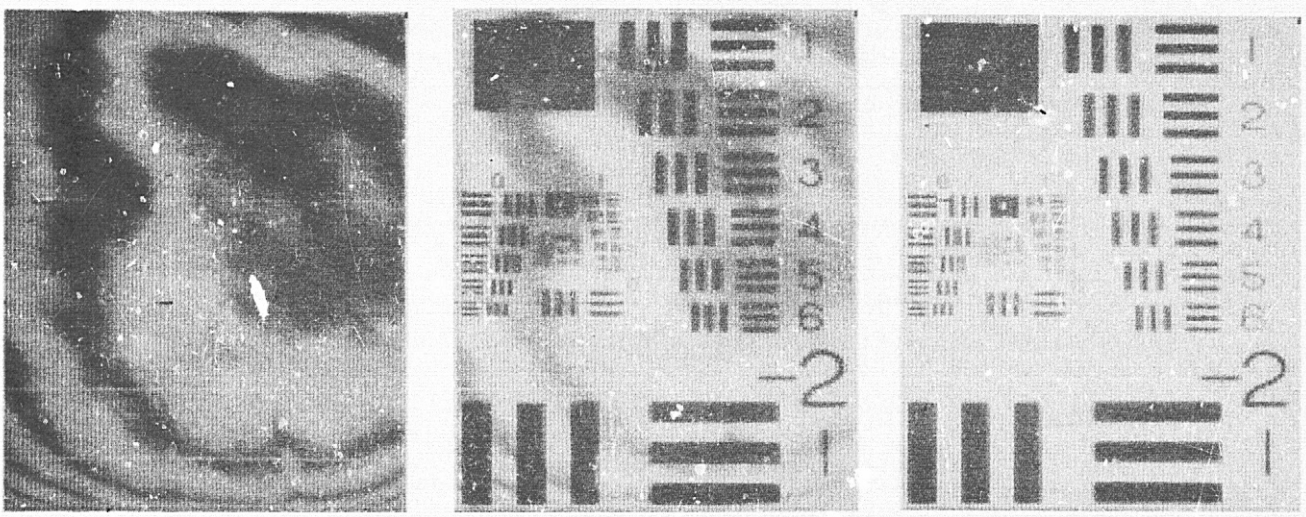

FLAT FIELD USED FOR DECALIBRATION

RAW IMAGE

CORRECTED IMAGE

Figure 11. Correction of Interference Pattern Caused by Imaging through Narrow Band Filter at 8900 A

HIGH DATA RATE PERFORMANCE OF A BCCD FOR RAPID SCAN IMAGING

David E. Schmieder and Stanley P. Buchanan
Martin Marietta Aerospace
Orlando, Florida

ABSTRACT

BCCD line arrays are very attractive for use in visual simulation and aerial mapping systems. However, to be most useful in these applications, it must be shown that such devices are capable of data rates to 16 MHz or higher and that they maintain high resolution and low noise operation at these higher rates. This paper discusses the results achieved when a commercially available 1728 element shallow bulk channel CCD line array is clocked at output data rates up to 30 MHz. The results show that temporal noise is near 200 electrons and is largely independent of clock rate. Charge transfer efficiency is found to be in excess of 0.9999 at 30 MHz.

I. INTRODUCTION

A. APPLICATIONS

Long, bulk channel CCD (BCCD) line arrays promise the capability to outperform area sensors in many applications which require low cost, but high resolution and jitter free imagery. This potential makes the BCCD line array very attractive for use in visual simulation and aerial mapping systems. For instance, visual simulation systems typically must cover wide fields of view at high resolution, often in a dynamic environment. Area sensors have difficulty meeting the resolution requirements and then often require video bandwidths above 80 MHz (Ref. 1). In addition, a dynamic environment smears the imagery due to the long 33 ms frame exposure periods. Solid state line sensors promise to overcome some of these problems with their higher resolution, potential for parallel operation, and shorter useful exposure periods. Similar benefits can be realized in aerial surveillance where the line array sensor can now replace film and provide real time imagery. The short exposure periods allow gimbal stabilization requirements to be relaxed and W/H effects to be minimized.

B. REQUIREMENTS

To be most attractive for these applications it is necessary to show that such devices are capable of high data rates and that they maintain high resolution and low noise operation. This is readily seen from a cursory examination of the data rates required in visual simulation. Here it is desired to provide wide 120° x 60° fields of view while maintaining resolution comparable to that of a human observer - near 1.5 arc minutes per resolution element. Interlaced frame rates should be no less than 30 frames/second to avoid flicker effects. The output sample rate (S) which corresponds to these requirements is simply.

$$S = \frac{(120 \text{ deg})(60 \text{ deg})(30 \text{ frames/sec})}{(1.5 \text{ arc min})^2 (1/60 \text{ arc min deg}^{-1})^2}$$

$$= 346 \text{ MHz}$$

Such data rates are well beyond the capabilities of a single vidicon or solid state sensor. But parallel operation of many side by side sensors can potentially provide this or even higher data rates. The difficulty is in achieving the focal plane sensor packaging density required for lower data rate sensor operation and low cost. The problems with packaging a vidicon for parallel operation are obvious. However, studies at Martin Marietta with the commercially available Fairchild Semiconductor 1728 element CCD line array (CCD121-DC) have shown that packaging densities of near 12 arrays per focal plane can be achieved in a scanning configuration with a reasonable focal plane size. This density then requires that each CCD line array be capable of output sample rates near 30 MHz. At this data rate the line exposure time is approximately

$$t_\ell = \frac{1728 \text{ elements}}{30 \text{ MHz}} \approx 60 \text{ µs.}$$

With such a short exposure time signal levels will be low and the utility of low noise as well as high speed operation is apparent.

A similar high speed, low noise operating requirement is apparent when the application of line arrays to aerial mapping is examined. In the past (Ref. 2) line arrays have been implemented in the "push-broom" configuration where vehicle motion is used to scan a continuous strip. The push-broom approach has generally not required high speed device operation but has required a complex optical system. The complexity has resulted when wide fields of view, combined with high resolution requirements, necessitated long focal planes of optically butted line arrays. An attractive alternative to the push-broom scheme in some applications is the "windshield wiper" implementation illustrated in Fig. 1. While this approach requires a moving gimbal to scan the array and a high device data rate, a single 1728 element line array can provide complete coverage over a wide field of view with a simple optical design.

The output data rates required in the windshield wiper scheme are exemplified by an aircraft operating at an altitude of 1200 feet and traveling at approximately Mach

0.6. The windshield wiper could be oriented to sweep out a wide 160° horizontal field while subtending 8° in the vertical direction. A continuous map of the ground would result if the array were scanned about once every 3.5 seconds with the gimbal oriented to scan the center of field at a down range distance of near 12 kft. The resolution provided would be a respectable

$$\frac{(8°)(17.4 \text{ mr/deg})(12 \text{ kft})}{1728} = 1 \text{ ft.}$$

However, the output data rate required of the 1728 element CCD array is high with a nominal requirement of:

$$\frac{(160°)(8°)(17.4 \text{ mr deg}^{-1})^2}{(3.5 \text{ sec})(1 \text{ ft}/12 \text{ kft})^2} \approx 16 \text{ MHz.}$$

This data rate corresponds to a "line" exposure time of approximately 110 μs and again points to the need for low noise operation if adequate signal to noise ratios are to be maintained.

These and other line array applications, such as helicopter obstacle avoidance, satellite surveillance, and laser beam pointing and tracking, potentially require the high resolution, high speed operation promised by large BCCD line arrays. This paper provides some of the data required to implement one such device at high data rates. Measured characteristics include noise levels, transfer efficiency, and resolution.

C. RESULTS SUMMARY

To date, commercially available, shallow bulk channel CCD line array characteristics have not been published for device operation above the 1-7 MHz regime (Refs. 2, 3). This paper presents the results achieved when a commercially available 1728 BCCD line array is clocked at output data rates up to 30 MHz. The more significant noise sources are identified; they include GCD (gated charge detector) reset noise, GCD thermal channel noise, and coherent clock pulse feedthrough. The results show that the total noise level from all sources is near 200 electrons and is nominally independent of clock rate. These results are shown to be in agreement with predictions.

Charge transfer efficiency and MTF (modulation transfer function) performance data are also presented for device operation at high data rates. Charge transfer efficiency is found to be in excess of 0.9999 at 30 MHz. This transfer efficiency allows high MTF performance.

II. DESCRIPTION OF THE 1728 ELEMENT ARRAY

Figure 2 shows a circuit representation of the 1728 element line array. This sensor was first described less than two years ago by C. K. Kim (Ref. 4). A complete description of the sensor can be found in the "Fairchild Charge Coupled Device · CCD 121" 1975 data sheet.* Some of the more significant device features are repeated here only to help in the understanding of the device performance data presented.

As shown in Figure 2, two 864 element, 2 phase, CCD shift registers are used to transport charge from the central photosites to a gated charge detector on-chip preamplifier. The photosites, spaced 13 μm apart, are separated by diffused channel stops and covered by a polysilicon photoelectrode.

In operation, charge packets from alternate photosites are transferred simultaneously to the CCD shift registers and clocked out. Interleaving, or recombining, occurs at the output gate to return the pulse train to its original sequence. Charge packets are detected in the GCD with a precharged diode whose potential changes in proportion to the quantity of charge delivered. This potential is applied to the gate of an output MOSFET (Fig. 2) which produces an output signal at OS. A reset FET is driven by a reset clock so as to recharge the diode capacitance before the arrival of each new charge packet from the transport registers. Operation of the GCD preamplifier is matched by a dumby compensation amplifier which provides an output similar in wave shape to the reset transient contained in the output signal. This compensation output can be used to partially cancel the rest transient in the video.

III. SPECIAL CONSIDERATIONS FOR OPERATION AT HIGH DATA RATES

A. INTERFACE, WAVEFORM, AND PHASING REQUIREMENTS

The major requirements for successful operation at rates up to 30 MHz were found to include:

1) Output rise and fall times of $\leq$ 10 ns on the output shift register drivers when loaded with 560 pf,

2) Driver output voltages of 0 to +12V with the low state to be held to no less than -0.4V to prevent charge injection into the substrate,

3) A 14V peak excursion on the GCD reset pulse with a 4 ns pulse width (at half maximum).

Selection and careful use of the National Semiconductor LH0033 Driver was sufficient to meet the above shift register requirements. Figure 3 shows oscilloscope pictures of the shift register drive waveforms produced by the LH0033 at a device output data rate of 30 MHz. It is to be noted that these waveforms more closely approximate a sine wave than the square wave being strived

*An improved version of this device has recently been introduced and called the CCD 121H.

for. This is an indication of the shift registers' insensitivity to drive wave shape. In fact, the sine wave was found to be preferable in that less clock pulse feedthrough was apparent in the output video than with sharper waveforms.

Other considerations for successful device operation at high data rates include provision for overall frequency stability and careful phase adjustment of the reset pulse.

B. CLOCK PULSE SUPPRESSION

The suppression of clock pulse coupling to the output video was found to be a major consideration at output data rates (f_c) above approximately 8 MHz. This coupling manifested itself in two forms: (1) GCD reset pulse feedthrough, and (2) digital logic transient coupling. The latter effect was most bothersome since it appeared as a fixed pattern noise at frequencies less than half the output data rate and thus occurred within the device's effective information passband. This noise source is discussed in more detail in section IV. Careful attention to board wiring consistent with good RF design techniques was the principal means used to reduce these effects. Reset pulse feedthrough was reduced to less than 5 mV relative to the advice's 170 mV maximum output with such techniques. It has been found that such reset pulse feedthrough, which occurs at the output clock frequency, can be reduced to insignificant levels when a lowpass filter with a sharp cut off at $f_c/2$ is employed in the video output circuit.

IV. MEASURED NOISE LEVELS

A. TEST SETUP

Figure 4 illustrates the sensor electrical operating configuration and output circuitry employed for high clock rate evaluation. Output circuitry operates the on-chip output MOSFET (Fig. 3) in a source follower configuration with a 1 kΩ load resistance (R_L). This produces a large current gain but results in a voltage gain of only 0.5. The voltage gain A_V is given by the expression

$$A_V = \frac{g_m R_L}{1 + g_m R_L} \qquad (1)$$

where g_m, the MOSFET transconductance, is 1 mmho. This configuration results in an output signal (at OS) saturation voltage (V_{SAT}) of approximately 170 mV when measured across Rl. Since the manufacturer claims that V_{SAT} corresponds to approximately 5×10^5 electrons per pixel, the amplifier charge detection responsivity at the device output is

$$Rq = \frac{5 \times 10^5 \text{ electrons}}{170 \times 10^3 \ \mu V} \qquad (2)$$

$$= 2.94 \text{ electrons}/\mu V$$

Output video is connected to the base of a buffer amplifier before being connected to the input of the first off-chip voltage boosting amplifier, the μA733. The buffer arrangement isolates the signal from loading effects of the μA733.

Noise measurements were made with an HP 8553B/8552B spectrum analyzer. This spectrum analyzer provides a CRT plot of the envelope detected rms noise level in a selectable measurement bandwidth swept over the frequency range from 0 to 100 MHz. The noise Wiener spectrum can be computed by squaring the rms CRT reading and dividing by the measurement bandwidth. Integration of the Wiener spectrum over frequencies from dc to $f_c/2$ is then the noise variance in the device's information passband. This measurement technique was felt to provide very accurate random noise measurement data when proper accounting for the spectrum analyzer's envelope detection scheme and the measurement bandwidth was made.

Coherent noise such as the fixed pattern variation in the output video, thought to be caused primarily by logic switching transients, could not be reliably measured with the spectrum analyzer. This coherent noise occurred at precise frequencies that were found to be harmonics of the various timing frequencies of the clock waveform generating logic. Coherent noise appeared as a periodic waveform. It was measured from scope trace photographs of the peak to peak variations in the output video averaged over many line periods.

Noise measurements were performed on a total of three CCD 121 sensors; no difference in noise level between devices, either temporally warying or fixed, was detected.

B. NOISE MEASUREMENT RESULTS

Temporal noise Wiener spectra due to all sensor and external circuit noise sources are presented in Figure 5 for various output clock rates f_c ranging from 4 to 30 MHz. These measurements were taken at room temperature with no input illumination on the sensor. The measurement system noise level, consisting of spectrum analyzer and video output circuitry noise, is also shown in the figure. The latter system noise was measured with the CCD 121 clocks and bias voltage inputs disabled. All noise values are related to the sensor output at OS in Fig. 4. The Wiener spectra noise densities are seen to fall rapidly past the frequency $f_c/2$. Spectral noise densities are also seen to decrease with increasing clock rate. This result is consistent with the dominant role played by GCD reset noise. Reset noise variance should be independent of output clock rate since the reset FET noise bandwidth is independent of the clock rate. Thus the noise Wiener spectra must, and do, show lower spectral noise densities as the bandwidth, over which this noise is distributed, increases.

Table 1 summarizes the rms noise levels per pixel which result from the previous noise spectra. Here off-chip output circuit and spectrum analyzer noise contributions have been removed. The noise densities are converted to a standard deviation in electrons per pixel by integrating the Wiener spectrum over frequencies from dc to $f_c/2$, obtaining the square root, and using the amplifier charge responsivity calculated in equation (2). These "temporal" noise magnitudes do contain a small (<12 electrons rms) fixed pattern noise due to dark charge variations as discussed in section V. Also shown in Table 1 are the predicted total rms temporal noise levels as computed from the noise models to be given in section V. Good agreement between measured and predicted noise levels indicates that the major noise sources have been correctly identified. Nevertheless, the consistently (∿10 percent) lower measured noise magnitude is an indication of either a slight systematic measurement error or over estimation in the noise prediction.

Table 1. Summary of measured temporal noise magnitudes, measured fixed pattern noise, and predicted temporal noise.

Output Bit Rate	4MHz	8MHz	16MHz	30MHz
Measured rms temporal[a] noise (electrons)	212	188	197	201
Predicted rms temporal[a] noise (electrons)	226	225	225	225
Measured rms fixed pattern noise[b] (electrons)	∿47	∿47	59	472
Total measured rms noise from all sources (electrons)	217	194	206	513

[a] Includes a small fixed pattern noise due to dark charge variations.
[b] rms = peak-to-peak/5

Finally, Table 1 indicates the measured fixed pattern noise found at the various output clock rates. This is believed to be primarily the result of either inductive or capacitive coupling of clock logic and driver transients to the output video. The drive and output circuitry employed in the test is seen to be susceptible to significant levels of fixed pattern noise at the higher clock rates. In principle this external noise source can be essentially eliminated, but to do so will require careful attention to proven RF design practices.

Figure 6 shows a representative noise spectrum for a 16 MHz output data rate as photographed from the CRT of the spectrum analyzer. The output data rate fundamental frequency can be clearly identified as can the line rate and line rate harmonics. Also clearly visible is an apparent coherent noise at $f_c/2$. This was found to be due to a slight difference in the shape of the reset feedthrough pulse between the two parallel shift registers shown in figure 2 and was not associated with a variation in the output video amplitude.

V. PREDICTED NOISE SOURCES AND MAGNITUDES

A. GCD RESET NOISE

The largest noise source in GCD type preamplifiers is due to the resetting of the precharged diode after each charge packet is shifted out. Thermal noise of the reset MOSFET channel resistance in parallel with the diode node capacitance (C) causes the amount of prechanging to vary each clock cycle. Thornber (Ref. 5) has shown this noise variance to be given by the expression:

$$N_r^2 \text{ (electrons}^2) = \frac{2\ KTC}{3\ q^2} \qquad (3)$$

where

$K = 1.38 \times 20^{-23}$ (J/K°)

T = temperature (°K)

$q = 1.6 \times 10^{-19}$ (Coul/electron)

The node capacitance can be determined from the relation:

$$C = \frac{q\ N_{SAT}\ G_V}{V_{SAT}} \qquad (4)$$

where

N_{SAT} = pixel saturation charge (∿5 x 10^5 electronics)

V_{SAT} = saturation output voltage (∿0.170V)

G_V = voltage gain at output (0.5)

Hence:

C = 0.23 pf.

Thus at 300°K the rms thermal noise of the reset MOSFET is

N_r = 157 electrons

However, both the signal GCD and the compensation GCD show reset noise. Since these noise sources are uncorrelated and combined in the μA733 amplifier (Fig. 4) they must be added in quadrature giving a total rms reset noise level of

N_r (total) = 223 electrons

B. OUTPUT MOSFET NOISE

The output noise (Ref. 6) of the on-chip MOSFET preamplifier consists of thermal

noise of the channel resistance and a thermal noise due to an effective shunt resistance between gate and source. At high clock rates ($\geq$ 1 MHz) the latter (Ref. 7) parallel resistance can be neglected. The expression for channel resistance thermal noise variance is

$$N_t^2 = \frac{4\ KT\ R_s\ \Delta f\ C^2}{q^2} \qquad (5)$$

where, from Reference 6, $R_s \simeq (2/3)\ (1/gm)$. Thus for a bandwidth Δf of half the output clock frequency $f_c/2$ = 15 MHz, and g_m = 1 mmho, the RMS thermal noise is N_t = 19 electrons. Addition of this amount in quadrature with that from the compensation GCD indicates a total rms thermal channel noise of N_t = 27 electrons.

C. BULK TRAPPING NOISE

Bulk channel CCD's show a signal fluctuation due to the filling and emptying (Ref. 8) of bulk states as the signal transfers along the channel. For a single level of bulk traps with density N_{tk} and interacting volume V_c per pixel the maximum variance associated with this transfer noise was shown (Ref. 7) to be

$$N_b^2 = 0.25\ V_c\ N_{tk} \qquad (6)$$

The magnitude of N_{tk} was indicated by Jack and Dyck (Ref. 9) to be consistent with a single level trap density near 1×10^{11} cm^{-3}. Volume V_c occupied by the signal packet at low signal levels will be at least an order of magnitude less than the volume of the pixel. The latter is that of a 13 µm x 17 µm area with a buried channel depth of approximately 1/4 to 1/2 µm (Ref. 10). Therefore the maximum signal packet volume should be no greater than 1.1×10^{-10} cm^3 and for small signal levels would be less than 10^{-11} cm^3. It is readily seen from equation (6) that bulk trapping noise levels are predicted to be insignificant.

D. DARK CURRENT SHOT NOISE

Thermal dark charge generation in CCD photosites and transfer registers gives rise to a dc background level. The generation process is random and known to obey Poisson statistics. Hence, the rms dark charge temporal noise can be thought of as a shot noise equal to the square root of the mean charge level. The average background charge N_d was measured at a 1 MHz output rate to be 5000 electrons per pixel at room temperature. Hence the dark level at output frequency f_c is nominally:

$$N_d = \frac{5000}{f_c\ (MHz)} \qquad (7)$$

The dc charge at 30 MHz is then 167 electrons and the associated rms shot noise is 13 electrons.

E. FIXED PATTERN NOISE

Fixed pattern, or temporally non-varying, noise has been found to originate from four potentially bothersome sources. These are non-uniformities in the dark charge generation rate, photoresponse non-uniformity, GCD reset pulse feedthrough, and clock pulse generation logic transients. The latter two can, in principle, be held to low levels.

Dark charge non-uniformity, according to the manufacturer's data sheet is typically 3 percent of saturation or ∿15000 electrons (zero-to-peak) at room temperature after a 1.94 ms integration time. Measured non-uniformities were much less and were found to be primarily manifested as a gradual change in the dc level across the array. Random dark charge variation between pixels was approximately 48 electrons rms at 1 MHz (1.94 ms integration time). This corresponds to ∿1 electron with the ∿60 µs integration time available at a 30 MHz clock rate. Only the random variations are believed to effectively contribute to the overall rms noise level.

Photoresponse non-uniformity is claimed to be typically ±6 percent of the signal level. Thus the final fixed pattern noise contribution from this source will depend upon the actual signal level available. Measurements on two devices have shown non-uniformities of ±3 percent with broadband irradiance but ±10 percent with 0.86 µm narrowband irradiance. This non-uniformity will generally not contribute a significant amount of fixed pattern noise under low light level operating conditions.

Table 2 shows a summary of the predicted noise from the various noise sources for f_c = 30 MHz. The total rms total noise of 225 electrons is clearly dominated by GCD reset noise. If this noise could be eliminated by the process of correlated double sampling (Ref. 11), without a large implementation noise penalty at these high clock rates, the total noise level could be reduced to significantly lower levels. Likewise, reduction of the reset node capacitance, already accomplished in the new CCD121H (Ref. 10) line array, is expected to produce a much reduced noise level.

Table 2. Noise source contributions (rms electrons) at f_c = 30 MHz

GCD Reset	Output MOSFET	Bulk Trapping	Dk. Chg. Shot	Dk. Chg. Fixed Pat.	Total
223	27	∿0	13	∿1	225

VI. CHARGE TRANSFER EFFICIENCY

A. MEASUREMENT APPROACH

Efforts to measure charge transfer inefficiency were made for CCD121 operation

at clock rates up to 30 MHz. The measurement technique consisted of focusing a HeNe CW laser on a single pixel of the array and measuring the charge lost to trailing charge packets in the output shift register. Charge levels employed in these tests were in the range from 50 to 100 percent of pixel saturation. Although the laser spot size employed in was only slightly less than the pixel center-to-center spacing, potential difficulties from spot spillover or diffusion, which could lead to erroneous results, were not encountered due to the devices alternate photosite transfer technique (Fig. 2). With this technique alternate sites are shifted to different output registers, hence spillover due to transfer inefficiency can occur only in alternate charge packets in the output data. This fact helps to distinguish transfer inefficiency effects from other spurious effects.

B. RESULTS

The experimental apparatus employed for transfer inefficiency measurements was too insensitive to measure the small inefficiencies encountered at $f_c < 30$ MHz. At 30 MHz, however, an $n\epsilon$ product of $\simeq 0.09$ was measured after 1330 transfers. Here $n\epsilon$ is the usual measure of transfer inefficiency where n is the number of transfers and ϵ is the fraction of charge not transferred per shift. The resulting transfer efficiency $(1-\epsilon)$ for the above $n\epsilon$ product is 0.99993. Figure 7 shows a photograph of the oscilliscope trace for the output pixel train at 30 MHz containing single pixel illumination.

In the process of arriving at a waveform for driving the CCD121 at high clock rates the authors measured transfer efficiencies much lower than the above. It was concluded that $n\epsilon$ is very sensitive to driving waveform shape and voltage swing. The shift register waveforms used for the above measurement are shown in figure 3. The present experimental results to not preclude the possibility that still higher transfer efficiencies can be obtained for different driving waveforms.

VII. MTF PERFORMANCE

In order for this sensor to be useful at high data rates it is important that the device maintain high resolution as well as low noise. High transfer efficiency, as reported in the previous section, should provide resolution comparable to that available at lower clock rates. The measurements reported in this section support that conclusion at a data rate of 30 MHz.

A. APPROACH

The objective of resolution performance measurements here is to obtain an estimate of the CCD121's sine wave response at the output data rate of 30 MHz. While the square wave response is much easier to measure, it is awkward for the system designer to use when attempting to predict the combined performance of many cascaded subsystems. The normal procedure is to measure square response and then simply transform it to a sine wave response. The problem with using this approach is that the transform requires accurate square wave response data at frequencies several multiples higher than the frequency of interest. With sampling devices, such as CCD's, response data above the basic Nyquist limited spatial sampling rate is ambiguous. Its use in the transform would likely lead to an ambiguous conclusion. To skirt this problem a reverse approach is taken. The BCCD's sine wave response is first predicted from basic principles, the sine wave response is transformed to a square wave response, and finally, the predicted square wave response is compared to measured square wave response data.

B. PREDICTED SINE WAVE RESPONSE

The sine wave response can be computed for a sampled CCD image plane by assuming the individual receiving apertures (pixels) are always geometrically aligned with a sine wave input pattern to obtain the maximum amplitude response. This amplitude response at any given spatial frequency is the device's "in-phase" Modulation Transfer Function (MTF). The term Modulation Transfer Function is defined here as the amplitude of the optical transfer function (OTF) and can assume negative values. The MTF is converted to a square wave response (H_{sq}) at spatial frequency v by the relationship (Ref. 12)

$$H_{sq}(v) = \frac{4}{\pi}\left[MTF\ (v) - \frac{MTF\ (3v)}{V} + \frac{MTF\ (5v)}{5} - \ldots\right] \quad (8)$$

The MTF of the 1728 element BCCD is predicted from the individual response functions of three known resolution degrading phenomena. These include the response (M_a) due to a finite aperture, the response (M_t) due to transfer inefficiency and the response (M_d) due to carrier diffusion in the substrate. The one dimensional aperture response is given by the well known relation

$$M_a = \frac{\sin \pi dv}{\pi\ dv} \quad (9)$$

where d is the pixel aperture size (13 μm). Joyce and Bertrum (Ref. 13) have determined that the response due to transfer inefficiency can be expressed as

$$M_t = (1-\epsilon)^{n_e}\ n\epsilon\ \cos(2\ \pi v/N_p) \quad (10)$$

where Np is the device's spatial sampling frequency (76.9 pixels/mm). Figure 8 shows a plot of the aperture function and transfer inefficiency response for n = 1040 transfers and $\epsilon = 0.99993$. Finally Sieb (Ref. 14) has shown that the response function due to charge carrier diffusion is

$$M_d = C\left(1 - \frac{e^{-\alpha L_D}}{1 + \alpha L}\right) \qquad (11)$$

where

C = normalization constant,

α = optical absorption coefficient of silicon,

L_D = depletion width

$$L = \left(\frac{L_o^2}{1+L_o^2 K^2}\right)^{1/2}$$

L_o = diffusion length

$K = 2\pi v$ (lp/mm)

The M_d expression is also plotted in figure 8 for an α characteristic of silicon at a wavelength of 0.862 µm and at 300°K taken from reference 15. This wavelength was selected to correspond with the measurements taken with a narrow bandpass filter centered at 0.862 µm. The other parameters were assumed as follows:

$L_D \approx 0.01$ mm

$L_o \approx 0.1$ mm

per values indicated in reference 16 for BCCD devices of similar architecture. Figure 8 shows a plot of the total resulting CCD121 sine wave response as predicted from the relation

$$MTF = M_a \cdot M_t \cdot M_d \qquad (12)$$

C. MEASURED SQUARE WAVE RESPONSE

The 1728 element BCCD square wave response was measured by imaging a standard 4 bar, 7:1 aspect ratio resolution chart on the array through an f2.5 Angenieux lens. Chart illumination was filtered with a 0.03 µm bandpass filter centered at 0.862 µm. The lens MTF was measured on an Optics Technology model K-III MTF analyzer with a 0.09 µm bandpass filter. This, slightly larger lens measurement passband tended to under rate the lens MTF actually available in the CCD resolution tests by a small amount. Figure 9 shows the measured lens MTF, the predicted CCD121 MTF from figure 8, and their product. This combined MTF, when transformed to a square wave response, should compare to the measured square wave response data.

Figure 10 illustrates the combined CCD121 and test lens measured square wave response at 30 MHz and the corresponding predicted square wave response as computed from equation (8). It is seen that the predicted response compares favorably with measured data. This favorable comparison supports the use of the CCD121 MTF shown in figure 8 as the device's sine wave response up to the cutoff frequency of 38.4 lp/mm for the stated conditions.

VIII. SUMMARY AND CONCLUSIONS

Long CCD line arrays are believed to promise advantages over area type sensors in several applications. These include flight simulation and aerial surveillance. To be suitable for these applications in the implementation schemes presented it must be shown that the long line arrays maintain low noise levels and high resolution when clocked at output data rates to 30 MHz. Results presented in this paper show that a commercially available 1728 element bulk channel CCD line array does indeed meet these requirements.

ACKNOWLEDGEMENT

The authors wish to acknowledge the contributions of Mr. Henry E. Helms of Martin Marietta Aerospace whose circuit design expertise led to successful CCD121 operation at high data rates. They also wish to thank Drs. David D. Wen and Rudolph H. Dyck of Fairchild Semiconductor for their helpful discussions and device operating suggestions.

REFERENCES

1. Irish, Kenneth M., et. al., "Visual Simulation Video Processing Techniques," AFHRL-TR-74-76. p.25, December, 1974.

2. Vicars-Harris, M., "Slow-Scan Operation of Long Linear CCD Arrays," Proceedings of the Symposium On Charge-Coupled Device Technology for Scientific Imaging Applications, Pasadena, CA., March 1975.

3. Hunt, J, and Sadowski, H., "Diverse Electronic Imaging Applications for CCD Line Image Sensors," Proceedings of the 1975 International Conference on the Application of Charge-Coupled Devices, San Diego, CA., October 1975.

4. Kim, C. K., "Two Phase Charge Coupled Linear Imaging Device with Self-Aligned Implanted Barrier," IEDM Technical Digest, December 1974.

5. Thornber, K. K., "Noise Suppression in Charge Transfer Devices," Proc. IEEE, Vol. 60, P. 1113, 1972.

6. Motchenbacker, C. and Fitchen, F., Low Noise Electronic Design, John Wiley and Sons, Inc. 1973.

7. Sequin, C. H., and Tompsett, M. F., Charge Transfer Devices, Academic Press, 1975.

8. Moshen, A. M., and Tompsett, M. F., "The Effects of Bulk Traps on the Performance of Bulk Channel Charge-Coupled Devices," IEEE Trans. on Elec. Devices, Vol. ED-21, No. 11, Nov. 1974.

9. Jack, M. D., and Dyck, R. H., "Charge-Transfer Efficiency in a Buried-Channel

Charge-Coupled Device at Very Low Signal Levels," IEEE Trans. on Elec. Devices, Vol. ED-23, No. 2, Feb. 1976.

10. Wen, David D. Private Communication, July 8, 1976.

11. White, M. H., et. al., "Characterization of Surface Channel CCD Image Arrays at Low Light Levels," IEEE Journal of Solid State Circuits, Vol. SC-9, No. 1, Feb. 1974.

12. Coltman, John W., "The Specification of Imaging Properties by Response to a Sine Wave Input," JOSA, Vol. 44, No. 6, June 1954.

13. Joyce, W. B., and Bertrum, W. J., "Linearized Dispersion Relation and Green's Function for Discrete-Charge-Transfer Devices with Incomplete Transfer," BSTJ, Vol. 50, No. 6, July-August 1971.

14. Sieb, David, "Carrier Diffusion Degradation of Modulation Transfer Function in Charge Coupled Imagers," IEEE Transactions on Electron Devices, Vol. ED-21, No. 3, March 1974.

15. Dash, W. C., and Newman, R., "Intrinsic Optical Absorption in Single-Crystal Germanium and Silicon at 77°K and 300°K," Physical REview, Vol. 99, No. 4 August 15, 1955.

16. "Low Light Level Charge-Coupled Imaging Devices (Phase I)" Final Report, Oct. 1973, AD915 544L.

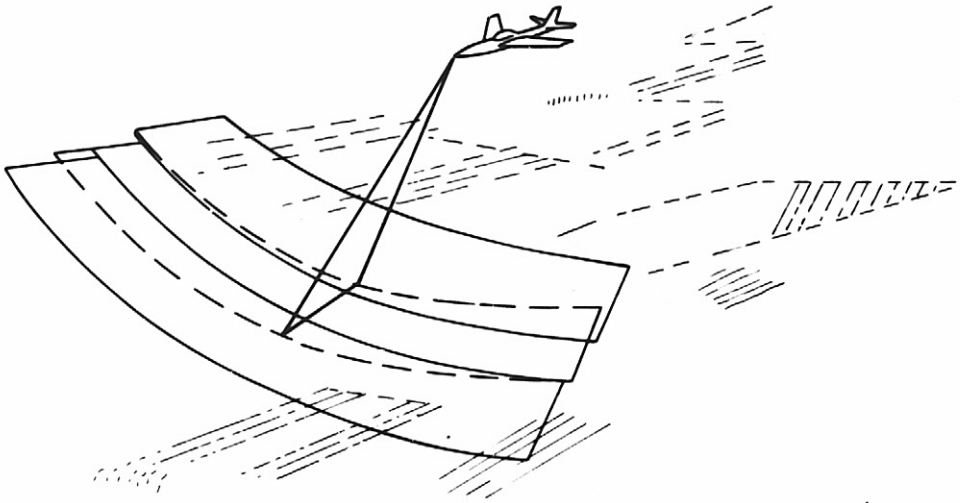

Fig. 1. Illustration of "windshield wiper" scan pattern in aerial mapping.

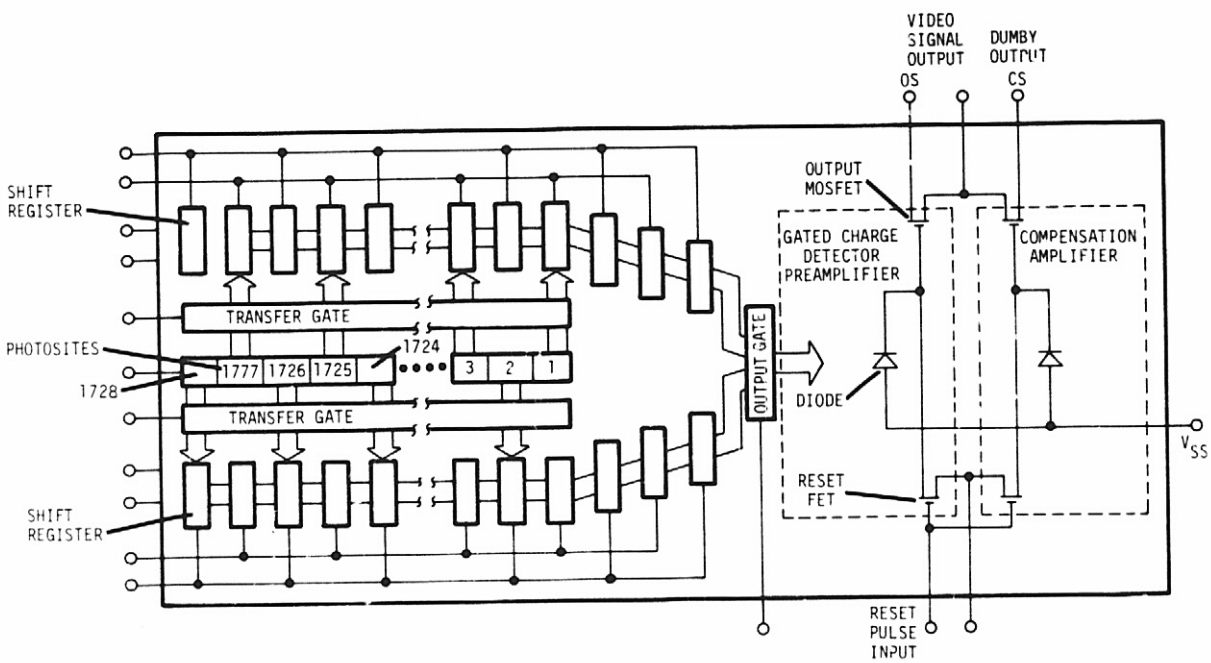

Fig. 2. CCD 121 circuit representation

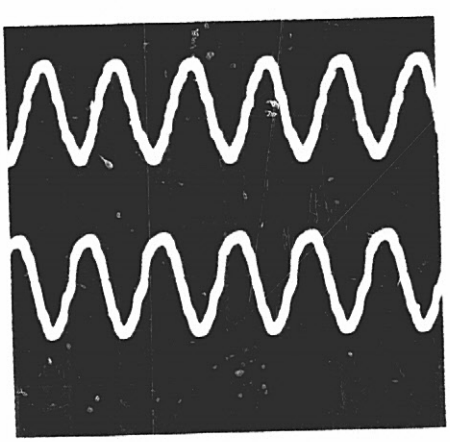

Fig. 3. Driver waveforms supplied to one of the two phase, parallel output shift registers at 30 MHz output data rate when loaded with 560 pf capacitance. Vertical scale is 5V/div, horizontal scale is 50 ns/div, scope bandwidth is 150 MHz.

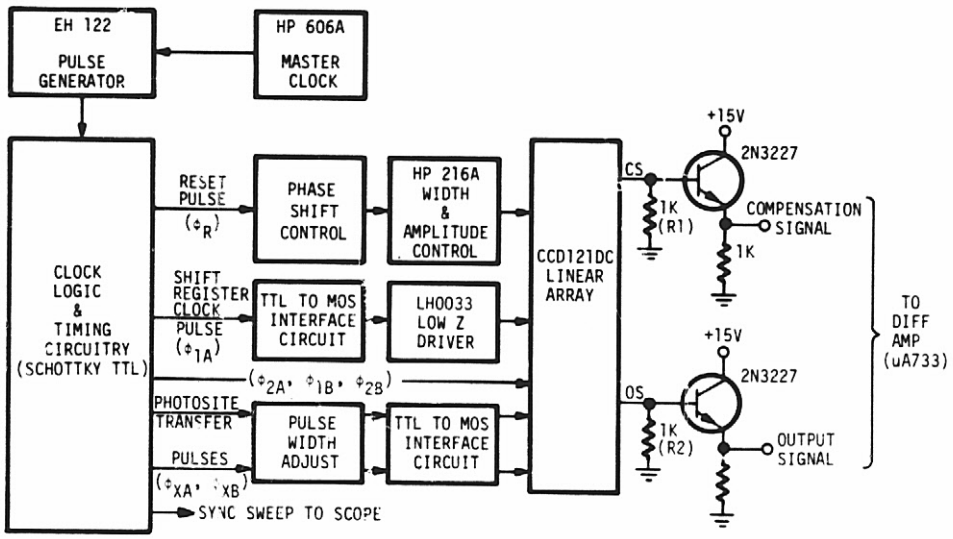

Fig. 4. Line array drive configuration and output circuitry for high speed evaluation.

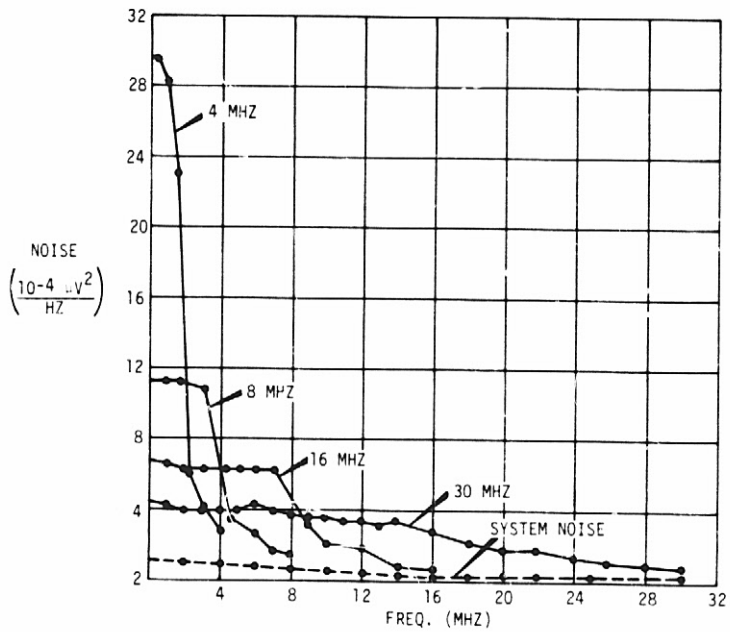

Fig. 5. Wiener spectra of CCD 121 and measurement circuit temporal noise for various output data rates.

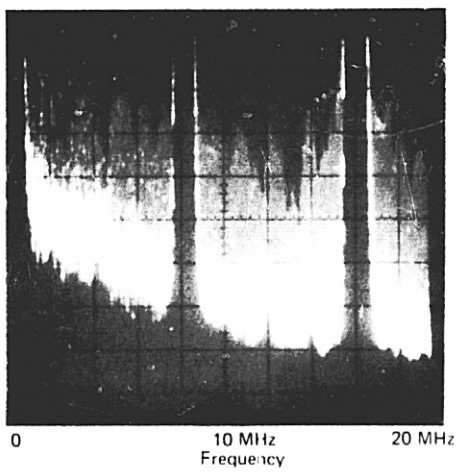

Fig. 6. Representative noise spectrum display at a 16 MHz output data rate. Scale is 20 μv/div vertical and 2 MHz/div horizontal. System gain is 5.0. Evidence of fixed pattern noise at frequencies $<f_c/2$ can be seen at 2 and 4 MHz.

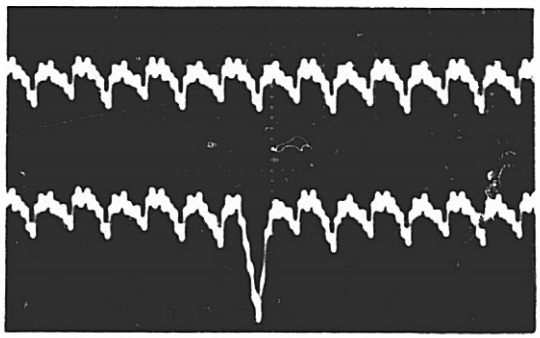

Fig. 7. Output wave train from CCD 121 at 30 MHz with an offset between the parallel output registers. The top trace shows output with no input illumination on the device. The bottom trace shows pixel number 1330 illuminated with some stray light falling on the preceding pixel. (Scale: 0.2 V/div vertical, 50 ns/div horizontal).

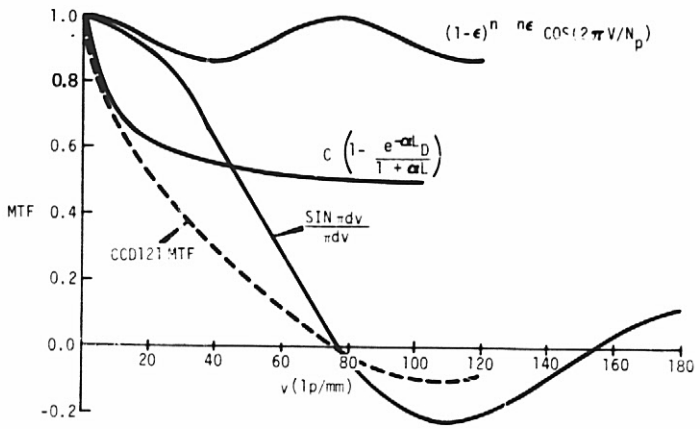

Fig. 8. Plot of total CCD 121 MTF and constitutent response functions for a 30 MHz clock rate and 0.862 um narrowband illumination.

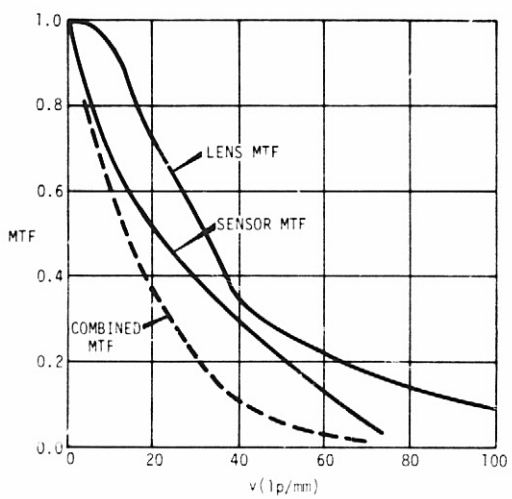

Fig. 9. Measured test lens MTF and combined sensor and lens MTF response.

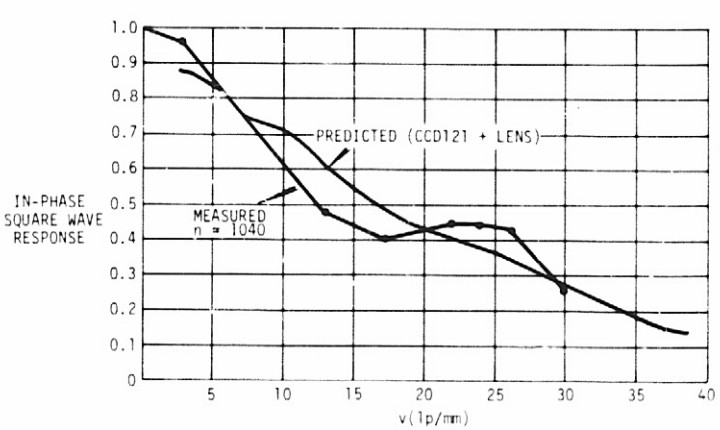

Fig. 10. Comparison of predicted and measured square wave response for a clock rate of 30 MHz and narrowband illumination centered at 0.862 u m.

LOW-NOISE VIDEO AMPLIFIERS FOR IMAGING CCD'S

Frank Scinicariello

The Perkin-Elmer Corporation
Optical Technology Division
100 Wooster Heights Road
Danbury, Connecticut 06810

ABSTRACT

This paper describes various techniques developed by The Perkin-Elmer Corporation which will enable the CCD (charge coupled device) imaging array user to obtain optimum performance from the device. A CCD video channel is described, and detector-preamplifier interface requirements are examined. A noise model for the system is discussed at length and laboratory data presented and compared to predicted results. The paper concludes with a new preamplifier configuration that will yield improved performance.

I. INTRODUCTION

A typical CCD video channel (Fig. 1) can be broken down into two major components: on-chip and off-chip electronics. The on-chip electronics comprises the inner elements of the CCD detector, i.e., the detector elements, charge transport registers, bias electrodes, and output amplifier. The off-chip electronics contains a preamplifier and signal processing electronics. The preamplifier provides sufficient gain to amplify the detector's output to a level well above the inherent noise of the processing electronics, while the processing electronics extracts the video information and enhances the signal-to-noise ratio (S/N). Processing techniques to improve S/N consist of bandwidth control and synchronous sampling. Minimizing channel bandwidth prior to any signal sampling reduces the contribution of frequency-dependent noise sources. Sampling techniques, such as correlated double sampling (Ref. 1), can suppress correlated noise sources, among which are reset noise, dc offsets, slowly varying baselines, and 1/f noise.

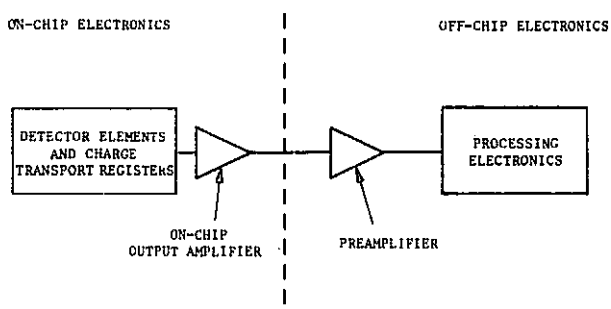

Fig. 1. Typical CCD video channel

Since the interface between the detector and preamplifier can be critical if low-noise performance is required, the characteristics of the on-chip amplifier, the preamplifier, and any processing electronics must be established. To determine the combined effects of all noise sources in the channel, this paper covers various types of noises and provides a noise model block diagram to locate each source; methods to reduce their effects are also discussed. Laboratory results are presented and compared to the predicted values. Finally, based on the results obtained, this paper concludes with a new preamplifier configuration which will yield improved performance.

II. DETECTOR/PREAMPLIFIER INTERFACE COMPATIBILITY

The output amplifier commonly used on commercially available CCD detectors (Ref. 2) is the gated charge amplifier (GCA) which consists of two MOS (metal oxide semiconductor) transistors (Fig. 2a). One is used as a switch to reset the charge sensing capacitor (C_o), while the other is connected as a source follower to buffer the output. The signal present at the output of the detector is a three-level waveform approximately 0.2V to 0.3V peak-to-peak impressed upon a dc level of several volts. The three levels are defined as (1) reference level, (2) signal level, and (3) reset clock feedthru (Fig. 2b). The video information is equal to the difference in magnitude of the signal and reference levels.

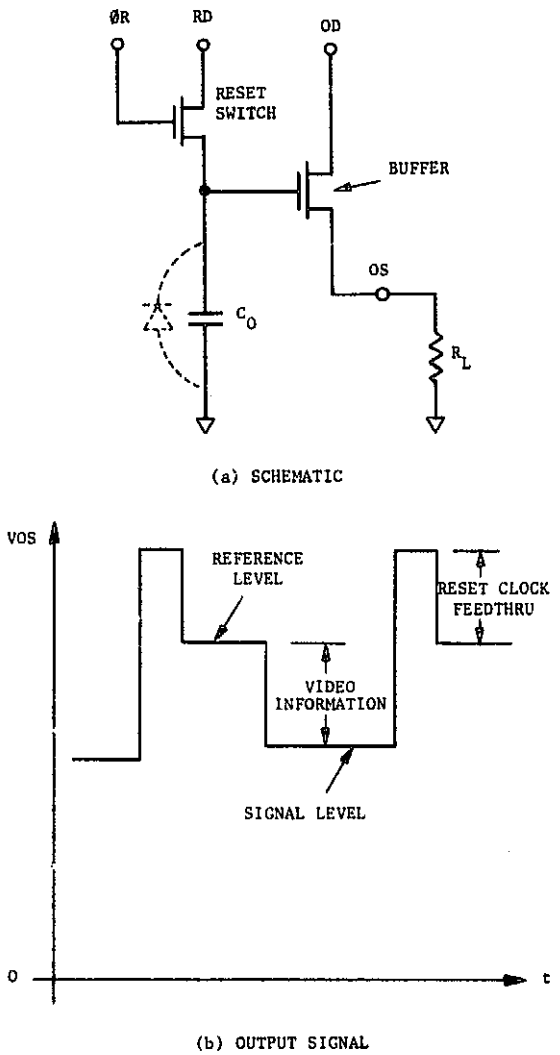

Fig. 2. Gated charge amplifier

The reset clock feedthru signal presents a processing problem in low-noise applications due to its large amplitude, typically 200 mv. In amplifying the signal, the reset clock feedthru becomes amplified and this could possibly overload the preamplifier. To alleviate the problem, it is common to find another output available from the detector, known as the compensation output (Ref. 2). By using a differential input preamplifier, it is possible to cancel the reset clock feedthru at the preamplifier's input. Since the dc levels at the signal and compensation outputs may be different, direct subtraction of the two signals is not possible. A coupling capacitor must be used to block the dc component at each output. The functional schematic representing the detector-preamplifier interface is shown in Fig. 3, which includes a CDS (correlated double sampling) implementation.

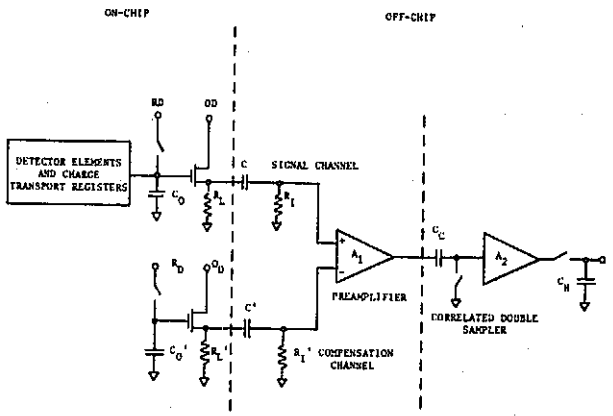

Fig. 3. Video channel functional schematic

III. NOISE MODEL

The noises likely to be found in the video channel are generated both in the detector and the off-chip electronics. A noise model block diagram locating each source is shown in Fig. 4.

A. DETECTOR NOISE SOURCES

1. Dark Current

Dark current noise is a result of thermally generated hole-electron pairs within a CCD cell. The magnitude of dark current noise, in electrons, is given by

$$N_d = \left[\frac{JA\tau}{q}\right]^{1/2} \quad (1)$$

where

J is the average dark current density

A is the total collection area

τ is the integration time

q is the magnitude of an electronic charge.

Dark current is generated in both the detector elements and analog transport registers. J is a function of temperature, doubling approximately in value for every 10°C rise.

2. Reset Noise

A GCA requires precharging the collection capacitor C_o prior to receiving each new signal charge packet from the CCD registers. The noise associated with this resetting mechanism is given by:

$$N_r = \frac{1}{q}\left[k\,T\,C_o\right]^{1/2} \quad (2)$$

where K is Boltzmann's constant and T is the absolute temperature. Reset noise is correlated within a detector element period.

3. Bulk State Noise

Bulk state noise is produced by trapping states in the bulk of the silicon. At low light levels, the worst case magnitude of this noise source, according to Barbe (Ref. 3), is

$$N_b = 0.28\sqrt{M} \quad (3)$$

where M is the number of transfers experienced by the charge packet.

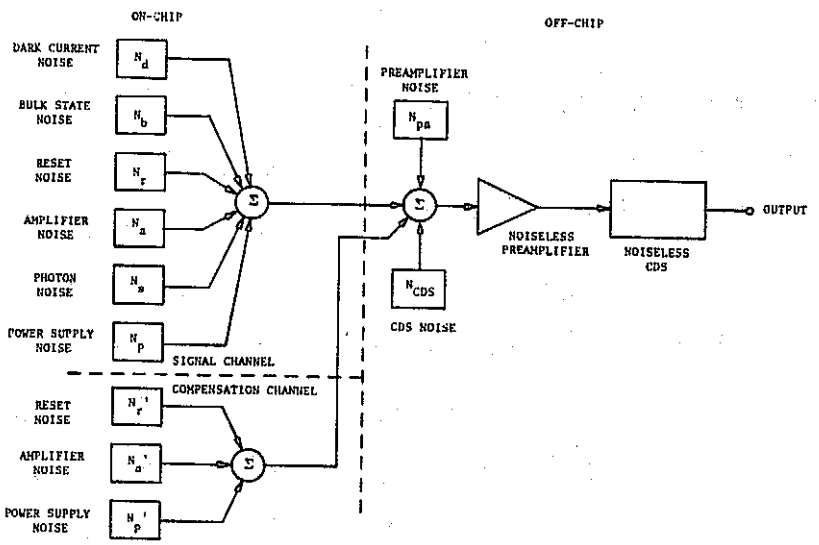

Fig. 4. Noise model block diagram

4. Photon Noise

The emission of photons from any source obey Poisson's statistics. Thus, the noise inherent to the signal to be detected is

$$N_p = \sqrt{N_s} \tag{4}$$

where N_s is the number of signal electrons generated at the pixels.

5. Amplifier Noise

The on-chip amplifier consists of an MOS transistor connected as a source follower. The principal noise source associated with this FET (field-effect transistor) is a noise voltage in series with the gate terminal. The midband value for this voltage (above the 1/f knee) is given by (Ref. 4):

$$e_n^2 = \frac{4kTB}{g_m} K \tag{5}$$

where g_m is the FET's transconductance, B the noise bandwidth and K a factor which depends upon operating conditions and transistor design and processing. The value of K can be as low as 2/3. Thus, the minimum expected noise, in electrons, at the collection capacitor C_o due to the transistor is:

$$N_a = \frac{C_o}{q}\sqrt{\frac{8kTB}{3g_m}} \tag{6}$$

It must be noted that this is the midband value and does not account for any 1/f noise components. Therefore, it is important to know the spectral content of the FET noise and the frequency band of interest in order to include all the noise introduced by the FET. The contribution of input noise current for the FET amplifier is suppressed by the chopping action of the reset switch (Ref. 5) and can, therefore, be neglected.

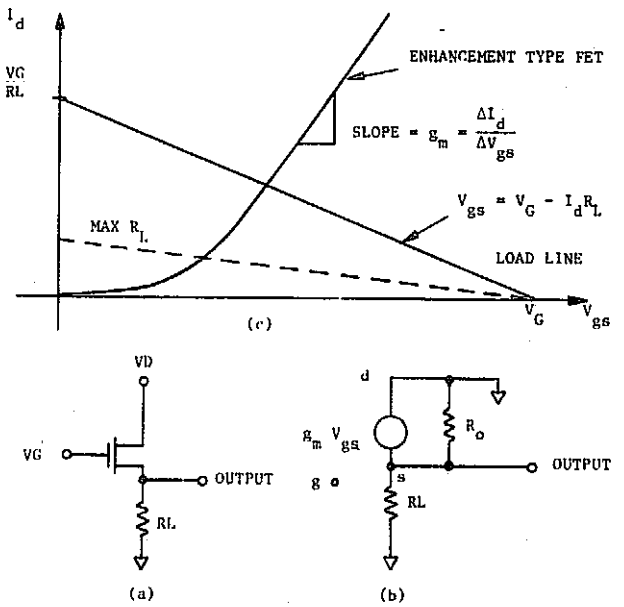

(a) SCHEMATIC
(b) SMALL SIGNAL EQUIVALENT CIRCUIT
(c) TRANSFER CHARACTERISTIC WITH DC LOAD LINE

Fig. 5. FET source follower

6. Power Supply Noise

Noise present on the drain of the output or reset transistor can perturbate the output signal; noise on the reset drain is directly impressed on the collection capacitor during the reset period. The equivalent noise electrons introduced are

$$N_{RD} = \frac{C_o}{q} e_{RD} \tag{7}$$

where e_{RD} is the rms noise at the reset drain.

The equivalent noise at the collection capacitor C_o due to variations at the output drain terminal is given by:

$$N_{OD} = \frac{C_o}{q}\frac{e_{OD}}{g_m R_o} \tag{8}$$

where e_{OD} is the rms noise present at the output drain and R_o is the output resistance of the FET (Fig. 5b). The total power supply noise component is:

$$N_p = \frac{C_o}{q}\left[\left(\frac{e_{OD}}{g_m R_o}\right)^2 + e_{RD}^2\right]^{1/2} \tag{9}$$

B. OFF-CHIP ELECTRONICS NOISE SOURCES

1. Preamplifier Noise

The preamplifier is characterized by its own equivalent input noise voltage and current sources, e_{npa} and i_{npa}, respectively. They are a function of the preamplifier's design. The equivalent noise contributed by these sources at C_o is equal to:

$$N_{pa} = \frac{C_o}{q}\left[\frac{1+g_m R_L}{g_m R_L}\right]\left[e_{npa}^2 + (i_{npa} R_s)^2\right]^{1/2} \tag{10}$$

where R_L is the dynamic load seen by the output source follower and R_S is the equivalent source resistance seen by the amplifier.

2. Correlated Double Sampler (CDS) Noise

Since CDS requires the charging of a capacitor through a switch of finite impedance, the noise produced is identical to the reset noise associated with the GCA. Thus, the noise contributed by the capacitors in the CDS at C_o is given by:

$$N_{CDS} = \frac{C_o}{q A_1}\left[\frac{kT}{C_c} + \frac{kT}{A_2^2 C_H}\right]^{1/2} \tag{11}$$

where

A_1 is the gain of the preamplifier

A_2 is the gain of the buffer within the CDS

C_C is the clamping capacitor

C_H is the holding capacitor.

C. SYSTEM NOISE

Combining each of the component parts described above, two expressions for noise are obtainable. For the system not utilizing the double correlated sampler, the equivalent noise at C_o is given by:

$$N_T^2 = N_d^2 + 2N_r^2 + N_b^2 + N_s^2 + 2N_a^2 + N_{pa}^2 \qquad (12)$$

Using CDS, the equivalent noise at C_o is:

$$N_{T_{CDS}}^2 = N_s^2 + N_b^2 + N_s^2 + 2N_a^2 + N_{pa}^2 + N_{CDS}^2 \qquad (13)$$

In each case, power supply noise N_p was not included since it can be adequately suppressed by proper power supply bypassing.

D. OPERATING CONSIDERATIONS

A review of the on-chip noise source (Equations 1, 2, and 5) indicates that both time and temperature can affect the total noise generated within the CCD detector. Cooling the detector to -10°C will reduce the reset and on-chip amplifier noise components by a small amount. However, dark current noise will be reduced significantly. Assuming that the dark current halves for every 10°C drop in temperature, the dark current noise at -10°C will be 35% of the room temperature value.

Since the detector elements operate independently of the CCD transport registers, it is possible to control the time parameter in the dark current noise expression (Equation 1). Dark current (and the noise associated with it) is generated both in the detector elements and the transport registers. The available intensity level of the object will, in general, set the integration time required for the detector elements to accumulate sufficient signal charge. During the same interval, the detector elements are also accumulating dark current charge. For low light level operation, integration times of 0.1 second are common. Cooling is the only means of reducing dark current under these conditions. However, it is not necessary for the transport registers to also accumulate dark current charge during this time. Depending on the rate at which the register is clocked, it is possible to output all detector element data before the end of an integration period (transfer command). Operation in this mode presents the video information at the output in the form of a burst immediately following a transfer command. The signal present for the remainder of the period is merely the zero signal level of the transport register. This level is a function of clock rate and dark current density. In the case of long integration time systems, the burst readout mode offers three advantages:

- Minimization of noise due to dark current in the transport registers.
- Increased dynamic range since dark signal is less, leaving more well capacity for signal charge.
- Increased suppression of 1/f noise components by CDS due to higher frequency operation.

E. NOISE MEASUREMENTS

To determine the validity of the noise model, we conducted an experiment using a commercially available 1728 element linear array. Since the effect of all external (off-chip) noise sources is divided by the gain of the on-chip source follower, it is important to know this gain. Using the small signal model shown in Fig. 5b, the gain of the on-chip amplifier is:

$$G = \frac{g_m R'}{1+g_m R'} \qquad (14)$$

where R' is the equivalent parallel resistance of R_L and R_o. It is expected that g_m is on the order of 1 mmho. Thus if R' is 1 kΩ, the gain G will be 1/2. This gain, being less than unity, will effectively increase the contribution of all off-chip noise sources. The characteristics of the output FET were measured in order to account for its effect.

1. Measurement of FET Characteristics

The FET characteristics may be measured using the following technique. Bias the output drain (OD) and reset drain (RD) terminals (refer to Fig. 2a) at their normal operating levels as recommended by the manufacturer. Ground all clock inputs except the reset clock (ØR). Apply a bias to the ØR electrode equal to the "high" level recommended by the manufacturer. These bias conditions keep the reset transistor "on", setting the gate potential of the output FET to VRD. By varying R_L, the voltage at the output source (OS) will change according to the FET characteristics. The drain current (I_d) is given by VOS/R_L and VGS is equal to VRD-VOS. This procedure was used to obtain the output FET characteristics of the test detector. The results are plotted in Fig. 6. The measured value of g_m is 0.85 mmho. It is interesting to note that it appears that g_m is relatively constant down to a drain current of 1 ma. This indicates that this device may be operated with a bias resistor of 10 kΩ. This would reduce on-chip power dissipation to under 10 mw.

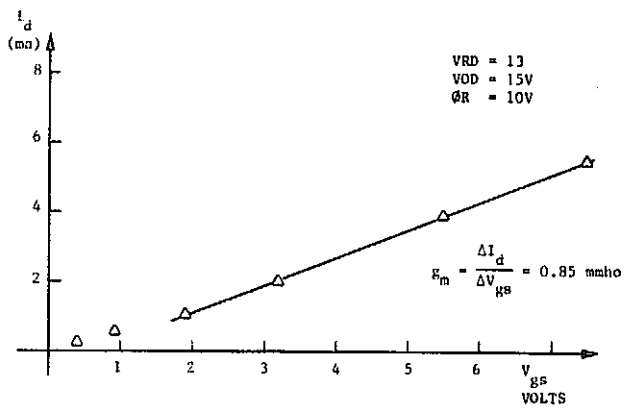

Fig. 6. Output FET characteristics

In a similar fashion, the noise of the on-chip output FET was measured. With the output FET statically biased, the noise in a 5 MHz bandwidth was found to be 38 nV/$\sqrt{Hz}$. Although larger than that predicted by Equation 5 (3.6 nV/$\sqrt{Hz}$), it is not an unusual value. As previously mentioned, Equation 5 predicted only the midband value and did not account for any 1/f contributions. Similar results were reported in Ref. 6.

2. Dynamic Test

A preamplifier having a total equivalent input noise of 4.8 nV/ Hz was used. The detector was cooled to -10°C. The magnitude of the individual noise components is given in Table 1. The entry for N_d is an estimate; however, its contribution is small and will not effect the results significantly. N_{CDS} and N_p were also small and could be neglected; N_s was omitted since noise was measured under dark conditions.

Table 1. Noise contributors

Source		Magnitude (electrons)
N_r	Reset	188
N_a	On-chip amplifier	132
N_d	Dark current	10
N_b	Bulk state	12
N_{pa}	Preamplifier	56
N_{CDS}	CDS	-
N_p	Power supply	-
N_s	Signal	-

A noise prior to CDS was predicted to be (using Equation 12) 330 electrons and 196 electrons after CDS processing (using Equation 13). Measured results (Fig. 7) indicate 472 and 235 noise electrons before and after CDS, respectively. The large discrepancy between pre-CDS noise is most likely due to the value of the on-chip collection capacitance being larger than expected and significant 1/f noise components of the output amplifier. However, being correlated, this additional noise was rejected by the CDS as demonstrated by the measured noise after CDS.

Since the on-chip amplifier is a dominant contributor to the total noise signal, improved performance could be obtained if the off-chip preamplifier did not use the compensation signal. The compensation source was used only to eliminate front end overload in the preamplifier by canceling the reset clock feedthru. A preamplifier configuration that does not require the compensation signal is presented in section IV. Elimination of this noise source would yield improved performance.

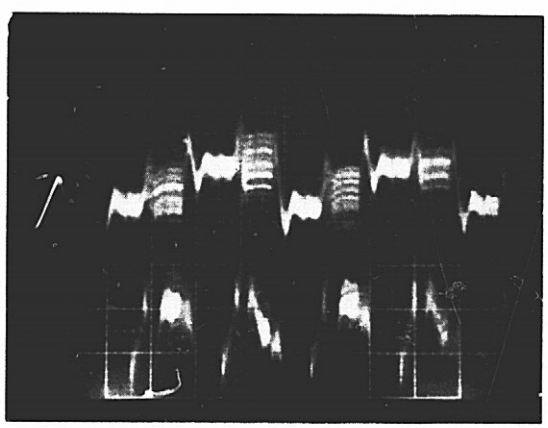

2 μs/DIV

Fig. 7. Measured noise: pre- and post-CDS
(a) Output of CDS - off chip electronics gain of 200
(b) Input to CDS - off chip electronics gain of 100

IV. NEW PREAMPLIFIER CONFIGURATION

The proposed preamplifier configuration (Fig. 8) is a clamped input amplifier. Operation of the circuits is as follows. By selectively closing switch S while the detector's output is at the reference level (Fig. 2), capacitor C will charge towards this level with a time constant equal to

$$\tau_c = (R_S + R_{SW})\, C$$

where R_S is the source impedance and R_{SW} is the "on" switch resistance. With C charged to the reference level, the output of the amplifier will swing negatively for signal levels and positively for reset feedthru's when the switch is opened. The signal level will be amplified by 1+(R2/R1), but the reset feedthru will be limited to one diode drop. The result is that the amplifier's input will not be overdriven and the reset feedthru is limited.

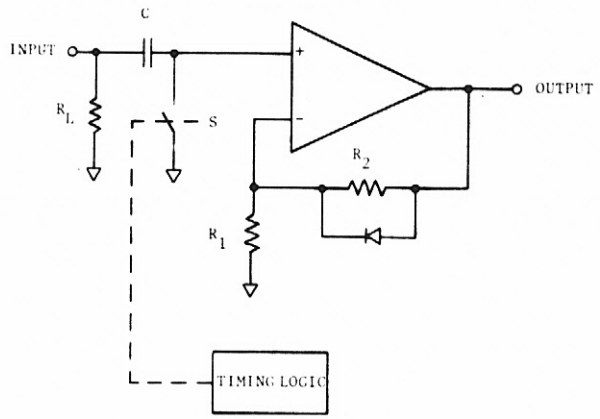

Fig. 8. Clamped input amplifier

The clamping can be done on an element or line basis. However, line clamping is preferable since no extra switching transients are injected into the signal during the video output period. The charging of capacitor C need not be completed in one reference level interval either if line clamping is elected. Several periods may be used. When the switch is opened, an error due to the amplifier's input bias current will be produced, manifesting itself in the form of a ramp. The magnitude of this error at the last pixel is

$$\varepsilon = \frac{I_b\, Ne}{C\, f_d} \qquad (15)$$

where Ne is the number of elements in the array and f_d is the data rate.

The action of charging the coupling capacitor through a finite impedance does introduce another source of reset noise at the preamplifier's input. The amount of noise produced, referred to the collection capacitor within the detector, is

$$N_e = \frac{C_o}{q}\left[\frac{kT}{C}\right]^{1/2}\left[\frac{1+g_m R_L}{g_m R_L}\right] \qquad (16)$$

However, it is correlated noise, that is, on a line-by-line basis. By utilizing the CDS at the preamplifier's output, N_e can be suppressed.

Input clamping provides an additional benefit. By performing a dc restoration immediately at the input, the floating baseline present in a capacitively coupled configuration is eliminated.

V. CONCLUSIONS

During our investigation of a typical imaging CCD video channel, particular attention was paid to the detector's on-chip output amplifier and the off-chip low-noise preamplifier interface compatibility, including the need for the compensation output. A noise model, incorporating the

detector and processing electronics noise sources, was developed for the video channel, and the experimental results demonstrated the validity of the model. The concept of "burst readout" operation to yield improved performance by reducing dark current noise and increasing dynamic range was introduced as a result of the noise analysis. A method to measure the detector's on-chip output FET characteristics also warranted the activity. Data obtained from a 1728 element linear CCD array indicated the following:

- the value of the dc load resistance could be increased to 10 kΩ.
- the noise contributions of the FETs associated with the signal and compensation output amplifiers were significantly higher than predicted by theory.

This being the case, a new preamplifier configuration, allowing the detector to operate with a higher load resistance and not requiring the compensation output from the detector, was our result. Operation with a higher load resistance reduces the effect of all off-chip noise sources by increasing the gain of the on-chip amplifier. Elimination of the need for the compensation output eliminates the noise associated with it, thus increasing the overall signal-to-noise ratio.

REFERENCES

1. White, M. H., Lampe, D. R., Blaha, F. C., and Mach, I. A., "Characterization of Surface Channel CCD Imaging Arrays at Low Light Levels," IEEE Trans. Solid State Circuits, Vol. SC-9, pp. 1-13, February 1974.
2. Fairchild Semiconductor MOS/CCD Data Book, Section 5, Fairchild Camera and Instruments Corporation, Semiconductor Components Division, Mountain View, Calif., 94042, 1975.
3. Barbe, D. F., "Imaging Devices Using the Charge Coupled Concept, " IEEE Proc., Vol. 63, No.1, pp. 38-67, January 1975.
4. Hall, J. A., "Amplifier and Amplifier Noise Considerations," Solid State Imaging (NATO Advanced Study Institutes Series), pp. 535-559, Published by Noordhoff, Leyden, Netherlands, 1976.
5. Buss, R. R.,Tanaka, S. C., and Weckler, G. P., "Principles of Low Noise Signal Extraction from Photodiode Arrays," Solid State Imaging (NATO Advanced Study Institutes Series), pp. 561-599, Published by Noordhoff, Leyden, Netherlands, 1976.
6. Brodersen, R. W. and Emmons, S. P., "The Measurement of Noise in Buried Channel Charge Coupled Devices," International Conference on the Applications of Charge Coupled Devices, pp. 331-349, San Diego, Calif. 29-31 October, 1975.

ACKNOWLEDGMENTS

The author wishes to thank Messrs. J. Shamaly, F. Krausz and J. Savarese of The Perkin-Elmer Corporation for their assistance.

A SUB-NANOSECOND CCD

Y. T. Chan

Rockwell International
Electronics Research Division
Anaheim, California

ABSTRACT

A 32-cell silicon n-channel PCCD was fabricated and tested for charge transfer efficiency vs. transfer time. Results showed that a charge transfer time of 550 picoseconds with a 0.9998 transfer efficiency could be obtained when operated in the uni-phase mode. These conditions correspond to an operating rate of 900 MHz when operated as an analog data or digital device.

I. INTRODUCTION

The CCD is becoming a very significant electronic device and is finding uses in many digital, analog and imaging applications. As with most electronic devices, the frequency of operation is one of the most important features. In the case of the CCD, the ability to transfer data at a rapid rate is one of its paramount features. Surface or buried channel CCD's which are presently available have been limited to operating speeds below 20 MHz. This is due to the limitations of the materials and photolithographic technology. Esser (Ref. 1), however, introduced the modified bulk channel CCD (peristaltic CCD) which transfers charge deep within the material where the transverse electrical field is large and the transfer efficiency is, therefore, higher. Theoretically, it has been estimated that charge transfer in a Si PCCD is sufficiently fast that it can be operated into the GHz range (References 2 and 3).

Lately, PCCD's have been operated over 200 MHz with good transfer efficiency when operated in the fast/slow mode (Ref. 4). The purpose of this present work was to determine quantitatively how rapid charge transfer can be in a silicon PCCD. The devices used in these experiments were made on n-type, epitaxial silicon grown on p-type substrate material. These devices showed extremely good transfer efficiency with charge transfer times between gates as short as 550 picoseconds.

II. EXPERIMENTAL DEVICE

The devices which were tested were 32-cell PCCD's. These devices had the same basic structure and design parameters as reported before (References 1 and 4), and as shown here in schematic detail in Figure 1. The devices were fabricated on a 5-micron epi layer which was grown on a (100) silicon substrate doped with 5×10^{14} boron/cm^3. The epi layer was doped 1×10^{15} phosphorous/cm^3. After the channel stop, input and output diffusions were grown; the CCD channel region was implanted with a phosphorous implant at a dosage of 1×10^{-2}/cm^2.

The post-implant anneal and drive-in was performed for one hour at 1000°C. By means of spreading resistance measurements, it was shown that 80 percent of the implanted phosphorous ions were activated. The profile of the substrate wafer after the anneal stage is shown in Figure 2. Two layers of aluminum were used to form the four-phase CCD drive gates. For the gate structure, which consisted of 5 micron wide gates, a 2200 A layer of Silox was used as insulation between the two gate layers. The overlap between gates was designed to be 0.5 microns. This overlap was used to minimize intergate capacitance and to reduce the probability of gate shorts due to pinholes in the Silox in the overlapping areas.

The completed devices were packaged in 16-pin TO-8 cans. A packaged device is shown in Figure 3. Notice that all four driving gate pads are bonded to the package with two 1-mil aluminum wires in order to reduce lead inductance and its effects at the higher frequencies. In addition, one more lead was wire-bonded to gate 3 in order to provide access in monitoring the gate waveform at the device itself.

III. DEVICE OPERATION

Although the initial intent was to operate this device in a two-phase mode, it was found that operation in the uni-phase mode was much simpler to implement since only one driving pulse was required and there were no synchronization problems which could be difficult at high speeds. The timing for uni-phase operation is illustrated in Figure 4. Initially, at $t = t_o$ the potential well configuration is biased like a staircase and the charges are stored under gate 4. When a pulse arrives, the gate potential increases. At $t = t_1$ the potential barrier of gate 1 is still high and no transfer of charge occurs, even though the potential profile under the gates has changed. When the (negative) gate voltage increases further, charges start to move from under gate 4 to a position under gate 2 as shown in the potential diagram for $t = t_2$. At the peak of the pulse, the charge transfer is in its final stages. As the gate voltage is reduced, a potential bucket will be formed after time $t = t_2$ but before $t = t_4$, as shown in the sketch for $t = t_3$. As the potential drops, a well starts to form under a gate 4 and the charge stops flowing. Any residual charges will remain in that well. As the potential drops further, a second transfer occurs as illustrated for $t = t_4$ and t_5. This process completes the charge transfer. Although the actual charge transfer time, T, is less than the width

of the driving pulse (i.e., t_4-t_1), this value is more easily defined and more convenient. In the case of two-phase operation the corresponding clock frequency is 1/2T.

IV. EXPERIMENTAL SETUP

As in most high frequency experiments, difficulties are always encountered in driving a large capacitance to high voltages with short pulses. One of the solutions to this problem is to reduce the load resistance of the line so that the RC time constant is smaller than the rise time of the applied pulses. Under these conditions the driver will require more power. In order to overcome these requirements for vhf large amplitude drive pulses, a Tektronix-type 109 line discharge pulse generator with low repetition rate was used. This pulse generator can reproduce pulses at a 700 Hz rate. The pulses which are generated have a 250 picosecond rise and fall time and can have an output voltage as high as 50 volts into a 50-ohm line using the internal voltage source in the instrument. Because of the high power output of this generator, a large attenuation can be tolerated. This feature makes it very desirable for this experiment. Since this type of pulse generator uses a mercury relay switch to discharge the pulse generating line, the output is not stable and has a large amount of time jitter associated with it. Pulses from the generator were stepped down on the CCD test circuit board into 8 ohms by means of a resistor attenuator. The total driven capacitance for each CCD gate was approximately 15 picofarads. This resulted in an RC time constant of 120 picoseconds. The equivalent circuit of the gate structures and the associated drivers is shown in Figure 5. In order to determine the exact pulse width as it was actually applied to the CCD gates, an additional bond was made to the phase 3 pad and a wire taken out in order to monitor the gate 3 waveform. This additional bonding wire can be seen in Figure 3. A 500-ohm attenuator was used so that a 50-ohm coaxial cable could be connected to the signal of the gate to the scope, without loading the driving signal to the gate. Additional signals were also picked off at the input side of the circuitry in order to provide triggering for the sampling scope and a clock signal to the CCD tester. The CCD test boards provided all the CCD bias voltages to the CCD, the reset pulses required for the output operation and a countdown of 256 which was used to synchronize the signal and to trigger the input signal pulse generator. A block diagram of the overall setup is shown in Figure 6.

V. TESTS AND RESULTS

Because of the low repetition rate of the Tektronix 109 pulse generator and the thermal leakage current of the CCD's, the device had to be cooled down to -150°C. Before the device was operated at the lower temperature, a preliminary configuration using another pulse generator with higher repetition rate was used for the initial setup. After the initial operation at room temperature and adjustment of all bias voltages, the entire CCD test board with the 32-cell CCD was lowered into a liquid nitrogen transfer dewar. The driver circuits remained above the liquid nitrogen level because operation at nitrogen temperature was not required of these circuits. The temperature of the device was monitored at the back of the CCD using a platinum resistor thermometer and bridge. The driving pulses were applied to gate 3 and 4. The waveform is shown in Figure 7. The amplitude of the pulse was 9 volts and the pulse width was 500 picoseconds. Both input with and without fat zero had been tested. The transfer efficiency was about the same.

The output without fat zero is shown in Figure 8. The number of total charge transfers was 31 and the transfer efficiency was demonstrated to be better than 0.9998 per transfer.

VI. CONCLUSIONS

We have demonstrated that charge can be transferred within the silicon n-channel PCCD's in less than 550 picoseconds with a 0.9998 transfer efficiency. These results suggest the feasibility of operating the PCCD at 1/2T = 900 MHz for uni- or two-phase mode of operation. For four-phase mode of operation, the wave of the potential well is a continuous propagated movement; hence, the operating frequency will be doubled, i.e., 1/T = 1.8 GHz. At these transfer times we have not observed any degradation of the transfer efficiency. It is thought that this performance may be due to higher carrier mobility in the silicon at the lower temperatures at which the device was operated. This will be the basis for future investigations. The CCD input and output has not been investigated in detail. The highest rate of operation for the input has been 200 MHz. It is clear that the input circuitry may have less difficulty in operating at higher speeds because the higher power signal can be used to overcome the stray capacitance. The output circuitry does not have this advantage. Therefore, the output amplifier may be the most important factor which governs the maximum speed of the CCD. It should be noted, however, that since gigahertz FET operation has been achieved, the incorporation of gigahertz FET's into the CCD process and their utilization as an output device for the CCD makes a gigahertz PCCD feasible.

VII. ACKNOWLEDGMENT

The author would like to thank Dr. Barry T. French for discussions and General American Research Division and Sandia who sponsored the design of the high speed CCD used by the author.

REFERENCES

1. Esser, L. J. M. "Peristaltic CCD: A New Type of CTD", Electronic Letters, Vol. 8, p. 620, Dec. 1972.

2. L. J. M. Esser, M. G. Collet and J. G. Van Santen, "The Peristaltic CCD" IEDM, Washington, pp. 17-20, Dec. 1973.

3. H. El-Sissi, and R. S. C. Cobbold, "Potentials and Fields in Buried-Channel CCD's: A Two-Dimensional Analysis and Design Study", IEEE Trans. Electron Devices, Vol. ED-22, No. 3, March 1975.

REFERENCES (Continued)

4. Y. T. Chan, B. T. French, and P. E. Green, "Extremely High Speed CCD Analog Delay Line", Inter. Conf. on the Application of CCD's, p. 29-31, Oct. 1975, San Diego, CA.

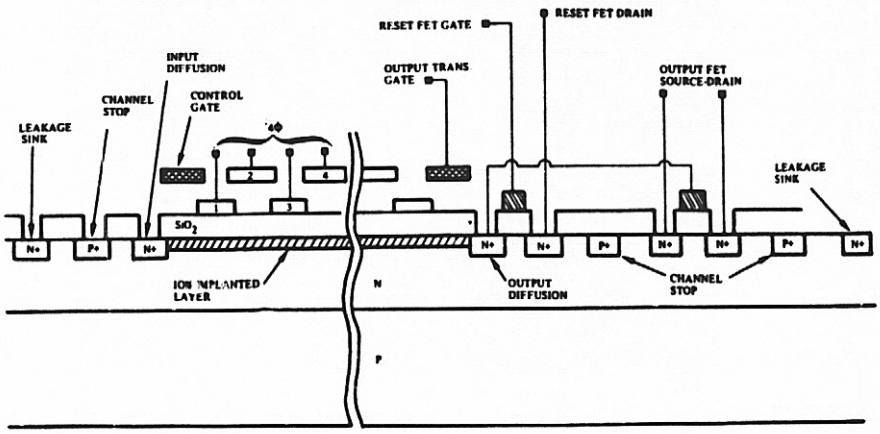

Figure 1. Peristaltic CCD - Cross Section (in Direction of Charge Propagation)

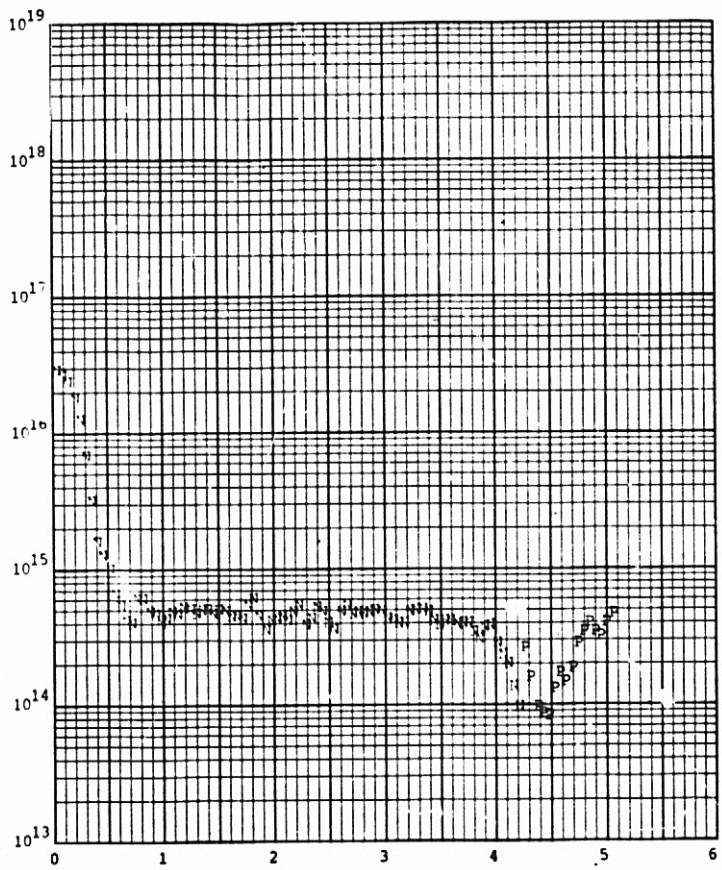

Figure 2. Device Doping Profile

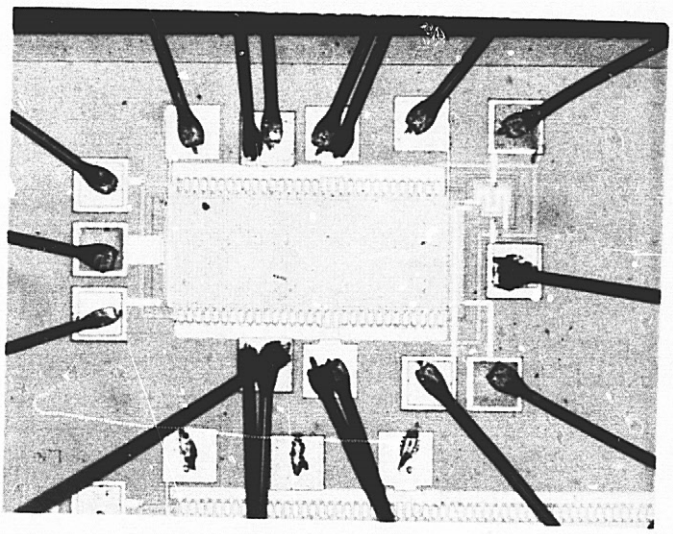

Figure 3. Photograph of a Tested Device

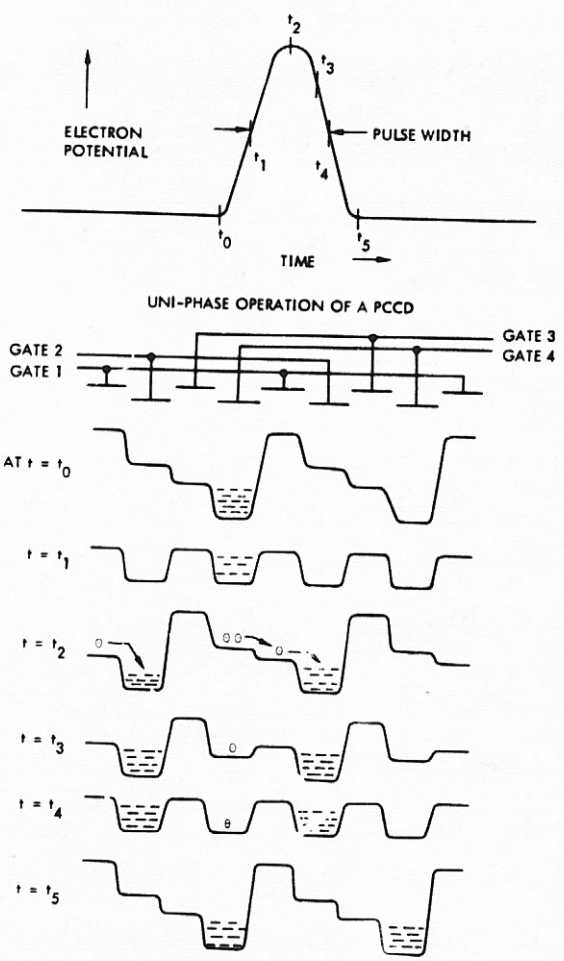

Figure 4. Uni-Phase Operation of a PCCD

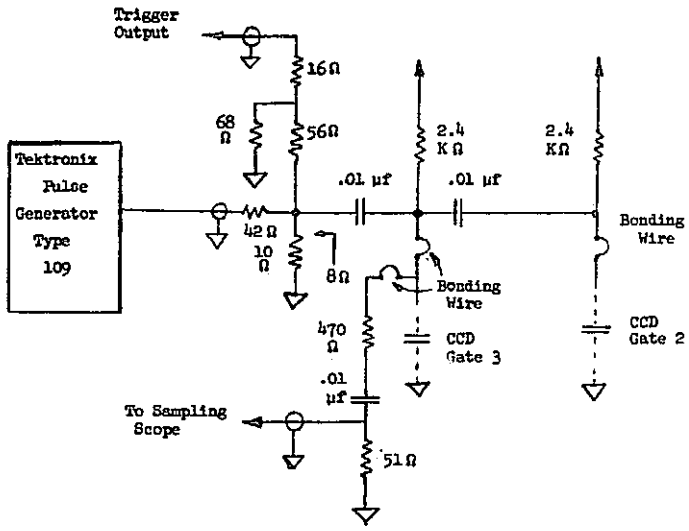

Figure 5. PCCD Driving Circuit

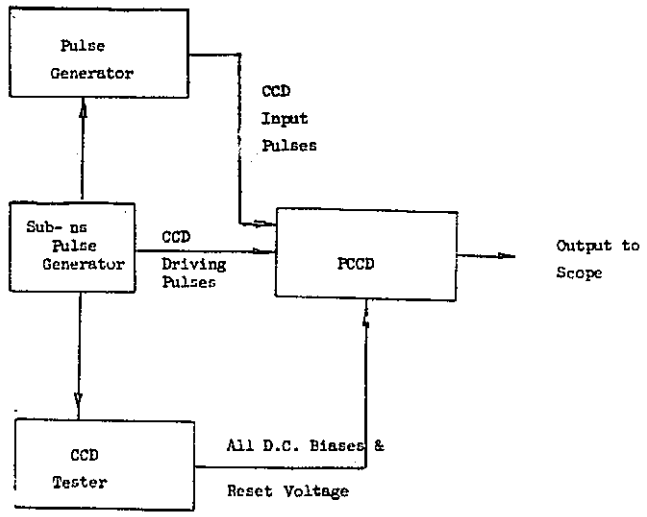

Figure 6. Block Diagram for Charge Transfer
Time Measurement Using Uni-Phase

Figure 7. Waveform of CCD Driving Pulse

Vertical Scale: 2v/div.
Horizontal Scale: 500 ps/div.

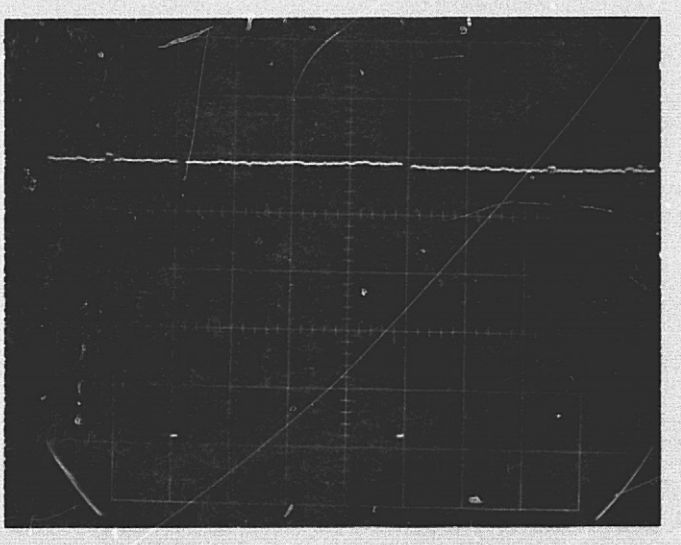

Figure 8. Output of PCCD at -142°C

D11

ELECTRON BEAM IRRADIATION OF THINNED BACKSIDE ILLUMINATED CCDs

G. M. Borsuk, J. A. Green, and R. F DeWitt
ITT Avionics Division, Electro-Physics Laboratories
Columbia, Maryland

J. M. Killiany
Naval Research Laboratory
Washington, D. C.

ABSTRACT

The physical properties of backside illuminated 64 x 64 pixel surface channel CCD arrays and a 160 x 100 pixel buried channel CCD array when bombarded with electrons have been studied. The devices were mounted in a high vacuum system and irradiated with electrons generated by an electron gun. Basic measurements of EBS gain, dead voltage, transfer efficiency and dark current were performed to verify proper device operation. The surface channel devices were then irradiated with electrons of up to 8 keV energy for up to 98 hours while the buried channel device was irradiated with electrons of up to 20 keV energy for up to 134 hours. After localized prolonged irradiation at 8 keV, the surface channel devices exhibited a reversible (by temperature annealing) decay of responsivity to both electrons and photons and an increase in dark current. The buried channel device did not suffer a measurable loss of responsivity in irradiated areas after bombardment by 20 keV electrons for 134 hours. However, dark current did increase by a factor of approximately two in the irradiated region. If the dark current continued increasing at that rate, the wells would fill with dark current for an integration time of ~35 milliseconds after the device had been operating for ~3000 hours. These phenomena are attributed to soft X-rays generated by the impact of the electrons upon the silicon substrate which cause a change in the fixed charge in the oxide and an increase in the surface states at the silicon dioxide-silicon interface. Verification of an increase of interface states in the irradiated region of the 160 x 100 buried channel device was made by charge transfer efficiency measurements. The input threshold voltage of the lower serial register was measured before and after that area of the device was irradiated with 10 keV electrons. Threshold shifts were measured which were coincident with an increase in dark current in that region of the array. An estimate of the radiation dose deposited in the oxide was made using TLD detectors, yielding ~1600 rads (SiO_2).

I. INTRODUCTION

The use of a thinned backside illuminated CCD as the electron sensor of an image intensifier has been demonstrated by several groups of researchers (Refs. 1, 2, 3, 4). The advantage of such an imaging CCD-tube combination is that photoelectric gain of the order of several thousand can be achieved because one electron-hole pair may be created in the silicon substrate for every 3.5 eV of energy of the incident electron. Consequently, the inherent noise of the CCD can be overcome by this gain mechanism, allowing photon shot noise limited performance at room temperature. Another aspect of this type of sensor is that the spectral response of the photocathode can be optimized for a given application.

This paper describes the results of measurements made to determine the physical properties of thinned backside illuminated CCDs when irradiated with electrons for prolonged periods of time (tens of hours). Both surface channel and buried channel devices were tested. The devices tested were not sealed in an image intensifier and did not undergo any stages of intensifier tube fabrication. Consequently, only physical effects generated by the electron beam itself were measured. Both kinds of devices were manufactured by Texas Instrument, Inc. The 160 x 100 buried channel device is of the same type which has been successfully operated in intensifier tubes Refs. 1, 2).

II. EXPERIMENTAL DESCRIPTION

The experimental arrangements used to make measurements were somewhat different for the two types of devices tested. The 64 x 64 surface channel device was completely mounted within the high vacuum system. Clock lines and other inputs and outputs were coupled into the system via a feed-through port. The 160 x 100 buried channel device had already been mounted to a vacuum header, which in turn was mounted to a vacuum system port using a mechanical o-ring pressure fitting. Several electron guns were used during these experiments. All guns were mounted on a port directly opposite the devices irradiated. A current monitoring Faraday bucket was mounted directly to the side of the CCDs. The electron beam could be steered into this pocket, permitting direct measurement of total beam current. An aluminum shield of 0.16 cm thickness with a pin hole was placed directly in front of all devices while in the system so that only a small area of the array was bombarded by the electron beam at any given time. This technique offered a high degree of control

and safety from inflicting accidental damage to the arrays under test.

The 64 x 64 CCDs tested were three-phase n-channel devices capable of frame storage. The gate structure of these devices included single metalization non-overlapping electrodes. The electrode size was 0.3 x 1.2 mils with 0.1 mil gaps between transfer electrodes. The active area was 0.038 cm^2. A single diode-gate structure ran the entire length of the parallel registers across the top of the device and enabled the loading of fat zero into the parallel registers. A serial shift register at the bottom of the parallel array facilitated readout. A diode-gate input was provided on this register to allow fat zero and other electrical waveforms to be entered. A conventional two transistor pre-charge and float output circuit was employed for signal extraction. The thickness of the arrays was 11.4 microns $\pm$ 2.5 microns as measured by manufacturer. The thinned backsides were accumulated. Substrate doping was 1 to 2 x 10^{15} cm^{-3} while the surface orientation was <100>. The devices were operated in the frame storage mode during irradiation by an exerciser built specifically for the purpose.

The 160 x 100 buried n-channel array is identical to those used by Williams (Ref. 1) and Caldwell, et al. (Ref. 2) and described in detail elsewhere (Ref. 5). The device is a three-phase overlapping gate CCD without frame storage capability. Serial registers are provided on the top and bottom of the parallel registers allowing the parallel registers to be uniquely probed by inserting an electrical pulse in a serial register, transferring it through the parallel register under investigation and subsequent readout through the other serial register. The device is a nominal 10 μm thick and the backside is accumulated. The quantum efficiency of the device as measured by the manufacturer was 12% at 0.45 μm, 52% at 0.8 μm, and 2.5% at 1.1 μm. The device was operated in the full frame mode during irradiation by an exerciser built specifically for the purpose.

III. EXPERIMENTAL RESULTS

A. RESULTS WITH A SURFACE CHANNEL IMAGER

Experimental results obtained for four 64 x 64 surface channel devices are presented first. The devices were operated in the frame storage mode at a clock rate of 500 kHz corresponding to a frame integration period of 4 milliseconds. In this mode the integration area consisted of 64 x 32 pixels. The transfer efficiency of the serial register with 20% fat zero ranged between .9969 and .9973 for all devices tested. The dark current density of the devices was on the order of 12 nA/cm^2 measured at 26°C. All devices exhibited well defined dark current pattern noise. All signal measurements were made by the use of an oscilloscope. Care was taken to isolate the output signal cable from CCD clock lines to minimize clock pickup. The typical maximum full well signal amplitude from photo sites was 1.4 volts. Measurement of electron gain for one of the devices tested is plotted in Fig. 1. The plot indicates a dead voltage of 3.2 kV. Fig. 2 shows a plot of irradiation response versus time for 8 keV electrons. The electrons were illuminating a 7 x 7 matrix of elements for about 100 hours. An initial beam current per element of 16 picoamperes corresponded to a condition of 50% full well. No fat zero was used in the parallel register while 20% fat zero was injected in the serial register for all measurements. As the responsivity of the irradiated area decayed with time, it was noted that addition of parallel register fat zero immediately restored some response. However, after prolonged irradiation all response to electrons and photons was lost regardless of fat zero level. A curious phenomenon observed was a return of some responsivity to devices after they were left unclocked and not irradiated for some time ranging from 10 to 48 hours. However, when the electron bombardment was resumed, degradation proceeded at a much faster rate. A small increase in dark current was also observed in those areas irradiated by electrons.

The decay of responsivity to both electrons and photons occurred simultaneously with a similar inability to obtain charge transfer through regions which had been irradiated. This phenomenon was observed in the inability to transfer fat zero charge through parallel registers which had part of their structure illuminated. Fig. 3a shows one line output of a tested device before irradiation. The bottom output trace shows the signal level with 20% serial register fat zero. The upper trace shows the signal distribution when 00% parallel register signal is added. The location of the electron beam within this line when incident upon the device is shown in Fig. 3b. After all responsivity to the electron beam and the light was lost, an attempt was made to transfer full wells of charge through the affected area. This failed, resulting in a pronounced notch in the output as shown in Fig. 3c. The device was then removed from the vacuum system and heated in air to 85°C for three hours with all of its pins shorted together. It was then replaced in the vacuum system and found to be sensitive to both photons and electrons in the previously insensitive area. Attempts were again made to transfer full wells of charge through the affected area, and these were successful, as is shown in Fig. 3d.

B. RESULTS WITH A BURIED CHANNEL IMAGER

The 160 x 100 buried channel device was operated in the full frame mode at a clock rate of 500 kHz, an integration period of 108 milliseconds, and a read-out period of 36 milliseconds. The transfer efficiency

of the lower and upper serial registers at 25% full well signals were 0.99906 and 0.9993, respectively. When signals that nearly filled wells were entered, efficiency decreased dramatically as expected because this increased the probability of transitions to interface states. The dark current density of the device was measured as 16 nA/cm^2 which was in good agreement with the manufacturer's data. The full well signal obtained from the parallel array was 0.375 volts. The energy efficiency, η, is plotted as a function of bombarding electron energy in Fig. 4. The plot shows a dead voltage at about 3 keV. Electron beam energies below this level caused a small response in the form of an increase in dark current apparently caused by local heating of the substrate which was coincident with the application of the electron beam. The energy efficiency of 0.5 at 20 keV corresponds to an EBS gain of ~2800.

The device was bombarded with 20 keV electrons for a prolonged period of time at one location of the array and with 10 keV electrons for a shorter period of time at another location. The irradiated region was uniformly bombarded through a circular aperture of 13.5 mils which corresponded to a diameter encompassing about 15 pixels. The electron beam current was set to achieve a signal 50% of a full well and corresponded to a beam current density of 0.075 nA/cm^2 at 20 keV. No dark current increase due to localized heating was noted at these current densities. Measurements were made by reading the wells out through the upper serial register. Fig. 5 shows the normalized increase in dark current signal for the irradiated region (20 keV electrons) as a function of irradiation time, which was accumulated intermittently over about three weeks. After 134 hours of bombardment, the increase in dark current in the region of irradiation could clearly be seen in the output of one line as shown in Fig. 6. This oscillograph shows a relative increase in dark current of about a factor of two over the pre-irradiation level. An increase in surface state density in the region of irradiation was observed by probing this area of the device with an electrically inputted pulse that filled one line of the raster. Fig. 7 shows the increased loss because of surface state trapping for a near full well signal and also shows the laggard charge in the following lines. As expected for operation in the buried channel mode (that is, no interface state trapping), this transfer inefficiency disappeared, as shown in Fig. 8. A second area of the array was subsequently illuminated with 10 keV electrons. At the end of an accumulated time of 25 hours, a very slight but perceptible increase in dark current was noted in this area as compared to pre-irradiated levels.

Another experiment was carried out to determine if a shift in the threshold voltage of one of the serial input gates could be observed. The aperture was placed over the input structure of the lower serial register. The electron beam also irradiated part of the parallel array. A series of pre-irradiation curves were made at different input diode voltages by plotting input gate voltage as a function of reset drain current on an x-y recorder. The region was then bombarded with 10 keV electrons until a noticeable increase in dark current was observed in the irradiated array region. At no time during irradiation was there noted an increase in dark current due to localized heating caused by the electron beam. An input gate voltage shift for constant input drain voltage was then observed as shown in Fig. 9. Continued irradiation of the area increased this shift toward lower gate voltages as shown in Fig. 9.

IV. ANALYSIS

Ionizing radiation causes a buildup of positive charge in the oxide of a MOS structure and an increase in the density of states at the oxide semiconductor interface. The trapped charge in the oxide produces a negative shift in the flat-band voltage of the device. However, a carefully designed and properly operated CCD can function satisfactorily after several volts of flat-band shift, since the charge transfer process in a CCD is fairly insensitive to flat-band voltage shift (Ref. 6). Of course, a potential-equilibration type input technique has to be employed to compensate for the input gate threshold voltage shift (Ref. 7). The buildup of interface states during ionizing irradiation causes an increase in transfer loss for surface channel devices and an increase in the dark current density for both surface and buried channel devices.

The changes in the dark current density and input gate threshold voltage observed after an electron beam irradiated CCD had been operated for over 100 hours can be attributed to the x-rays generated by the electrons incident on the silicon. Few bombarding electrons can reach the silicon-silicon dioxide interface because the range of 20 keV electrons in silicon is only 2.2×10^{-4} cm while the substrate is 10×10^{-4} cm thick (Ref. 8). However, x-rays are generated and a significant fraction of these penetrates to the oxide. Several experimentors have reported radiation damage in MOS devices which were exposed to the x-rays produced by electron beam bombardment of low Z materials (Refs. 9 and 10).

The x-radiation produced by electron bombardment of the silicon consists of two components, the continuous or bremsstrahlung radiation, distributed in energy from zero up to the electron beam energy, E_o, and the characteristic x-rays of the silicon which are sharply defined in energy. Because the absorption cross section of x-rays in a material is a function of the x-ray energy, a calculation of the fraction of the

x-radiation which reaches the CCD oxide requires a knowledge of the entire spectrum. However, an estimate of this fraction can be made by considering the absorption of the characteristic x-ray. The intensity I of the K_α x-rays reaching the CCD oxide is related to the intensity I_o generated at the back of the CCD by

$$I = I_o e^{-\mu x} \qquad (1)$$

where $\mu = 8.34 \times 10^2$/cm is silicon's absorption coefficient for its K_α x-rays and x is the thickness of the silicon substrate.(Ref. 11). I/I_o is equal to a .435 for $x - 10 \times 10^{-4}$cm.

An estimate of the x-ray intensity at the silicon-silicon dioxide interface of the electron bombarded CCD was made by using square calcium fluoride (CaF_2:Mn) thermoluminescent dosimeters (TLDs) $.079 \times 10^{-3}$ cm thick and $.3175 \times 10^{-3}$cm on a side. The dosimeters were covered with 10×10^{-4} cm of aluminum foil and exposed to 10 keV electrons. The dose deposited in the detectors was used to determine the energy per unit area of the x-ray field at the detector's surface. The distribution of the absorbed energy in the TLD detector was considered in making the x-ray intensity calculation (i.e., most of the x-rays are absorbed within a few microns of the detector's surface).

The absorption coefficient for the silicon K_α x-ray in silicon dioxide was calculated from the tablulated values for silicon and oxygen using the expression (Ref. 9).

$$\mu_{SiO_2} = 0.47\mu_{Si} + 0.53\mu_{O_2} \qquad (2)$$

Using this absorption coefficient in equation (1), one finds that the 1000 A° thick film of silicon dioxide will absorb 1.7% of the incident energy from a beam of 1.738 keV electrons.

Finally, the dose deposited in the CCD oxide layer will be approximated by using the measured x-ray energy per unit area that penetrated the aluminum foil and the absorption coefficient for silicon K_α x-rays in silicon dioxide. The dose accumulated in the oxide of the thinned CCD which had been bombarded with 20 keV electrons for 134 hours is calculated to be 1,600 rads. The damage observed is what one would expect from a dose of 1,600 rads on the basis of previous experimental irradiation of similar devices that are reported in the literature (Ref. 7 and 12).

V. CONCLUSION

Surface channel and buried channel backside illuminated devices have been irradiated with controlled electron beams for prolonged periods of time (>100 hours). A small but consistent increase in dark current was observed in those areas irradiated. A measurement of charge transfer efficiency as a function of signal level was made with the buried channel device, which indicated an increase in the interface state density in the irradiated regions. The input of a serial register of the buried channel device was irradiated after which a negative shift in input gate threshold voltage was observed. These results are attributed to the generation of soft x-rays by the bombarding electron beam. A measurement of the dose was made by irradiation of TLD detectors. The effects noted above were consistent with those reported earlier (Refs. 7, 12) in which similar devices made by the same manufacturer were damaged by comparable doses of radiation.

VI ACKNOWLEDGEMENTS

The authors thank Mr. Jack Williams of NASA Greenbelt for the loan of the buried channel CCD and Dr. Dean Baker of the Naval Research Laboratory for the loan of the surface channel CCDs. We also thank Mr. John Cuny, ITT-EOPD for the loan of the exerciser used to operate the buried channel CCD. We thank Mr. Stephen Gorbes of NRL for making the dosimetry measurements and Mr. James Rapece of NRL for useful discussions concerning the use of dosimeters. Finally, we thank Dr. Walter Slusark for monitoring the test apparatus.

VII. REFERENCES

1. Williams, J., "The Intensified Charge-Coupled Device as a Photon Counting Imager," Proc. 21st Annual Meeting. Amer. Astronaut. Soc., Denver, CO, 1975.
2. Barton, J., Cuny, J., and Collins, D., "Performance Analysis of EBS-CCD Imaging Tubes/Status of ICCD Development," Proc. of Int. Conf. on Charge-Coupled Devices, October 27, 1975, San Diego, CA.
3. Caldwell, L., Boyle, J., and Smith,E., "Operation of CCDs in the Electron Bombarded Mode," Proc. of Int. Conf. on Charge-Coupled Devices, Sept. 26, 1976, Edinburgh, Scotland.
4. Brown, H., Gray,P., and Pool, P., "An EBS-Mode CCD for Low Light Imaging Applications," Proc. of Int. Conf. on Charge-Coupled Devices, Sept.26, 1976, Edinburgh, Scotland.
5. Antcliffe, G., "Low Light Level Performance of CCD Imagers for Spacecraft Applications," Proc. of the Symp. on Charge-Coupled Device Tech. for Scientific Imaging Applications, JPL, March, 1975, Pasadena, CA.
6. Killiany, J., Saks, N. and Baker, W.," Effects of Ionizating Radiation on a 256 Stage Linear CCD Imager," I.E.E.E. Trans. Nuc. Sci., NS-22,p2634, 1975.
7. Killiany, J. and Baker, W., "Limitations of a Threshold Insensitive Input Technique in a Total Dose Radiation Environment," Proc. of Int. Conf. on Charge-Coupled Devices, October 27, 1975, San Diego, CA.

8. Burger M. and Peltzer S., "Energy Spectra and Angular Distribution of Electrons Transmitted Through Saphire (Al_2O_3) Foils," NASA SP-3008, 1964.

9. Thomas, A., Butler, S.,Goldstein, and Parry, P., "Electron Beam Irradiation Effects in Thick-Oxide MOS Capacitors, I.E.E.E. Trans. Nuc. Sci., NS-21, No.4 p. 14, 1974.

10. Mayo, S., Galloway, K.,and Leedy, T.," Radiation Dose Due to Electron Gun Metalization Systems," Presented at 1976 I.E.E.E. Nuc. and Space Radiation Effects Conference, July, 1976.

11. Robinson, J., Editor, CRC Handbook of Spectroscopy, Vol.1, CRC Press, Cleveland, Ohio, 1974.

12. Hartell, G., "Radiation Hardness of Surface and Buried Channel CCDs," Proc. od Int. Conf. on Charge-Coupled Devices Oct.27. 1975, San Diego, CA.

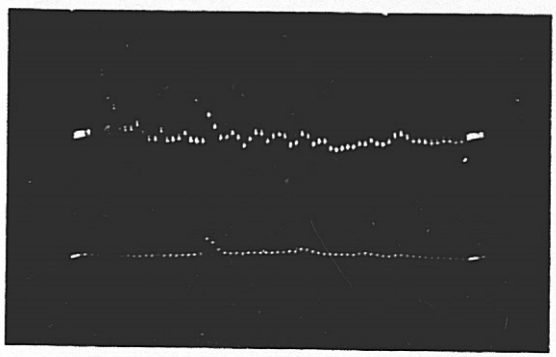

3a

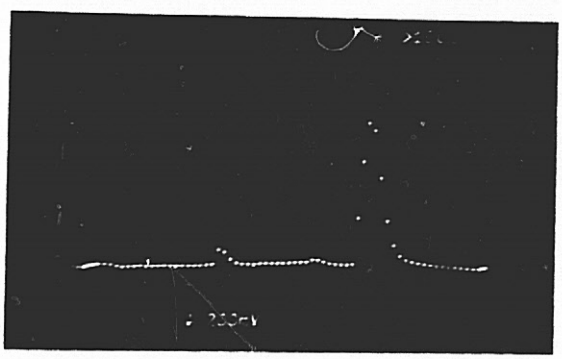

3b

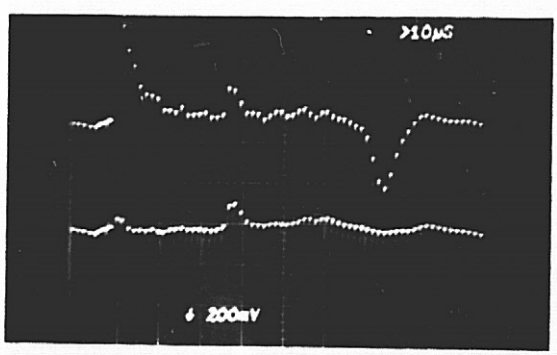

3c

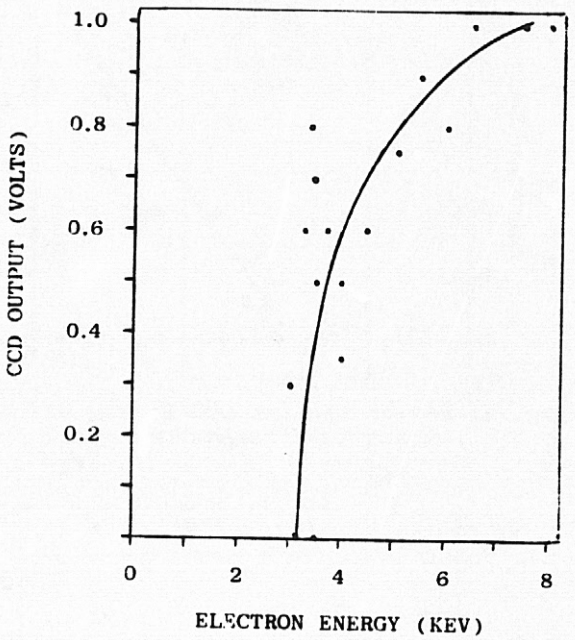

Fig. 1. EBS Gain versus electron energy for 64x64 Surface Channel CCD.

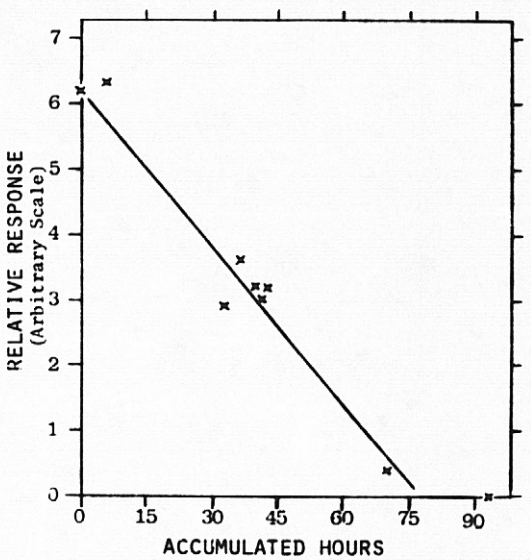

Fig. 2. EBS Response versus time for 8 keV electrons- Surface Channel CCD.

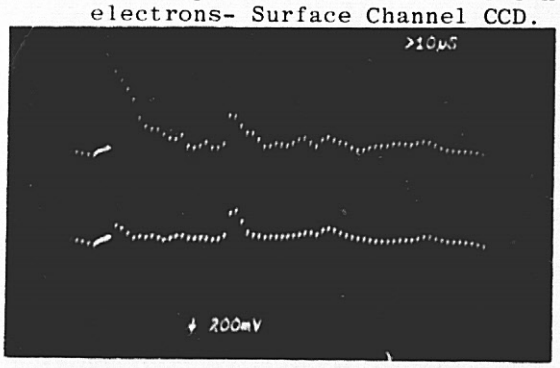

Fig. 3. Line output of Surface Channel CCD Before, During, and After Irradiation and After Temperature Anneal.

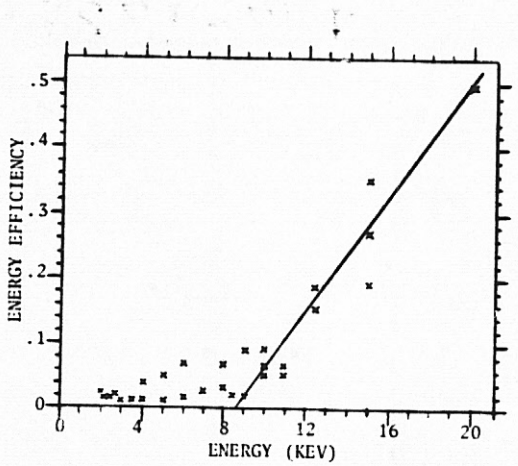

Fig. 4. Buried Channel CCD Energy Eff. versus electron beam energy.

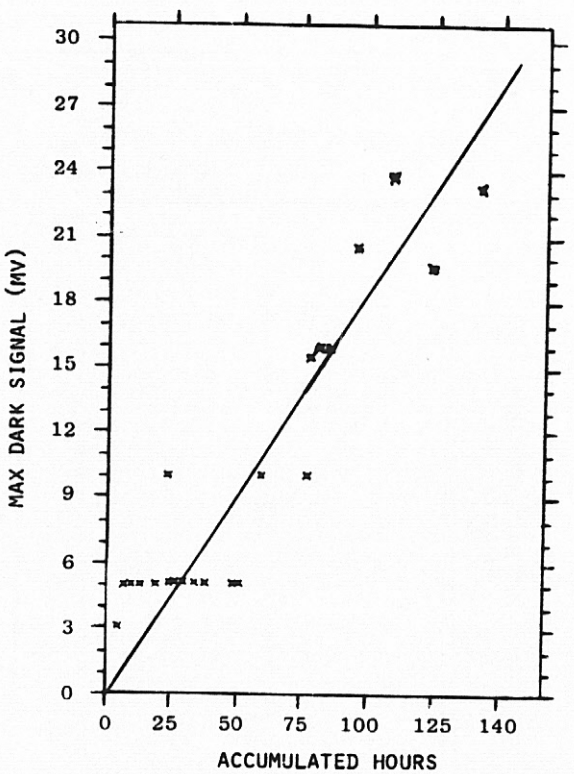

Fig. 5. Normalized increase in dark current versus time for 20 keV irradiation.

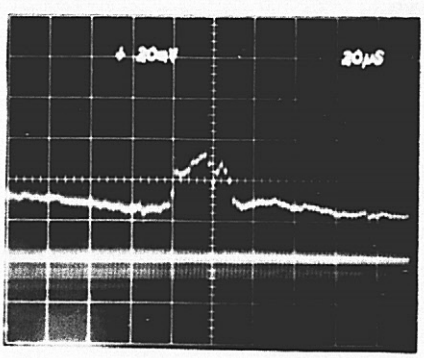

Fig. 6. Dark current irregularity due to prolonged electron beam irradiation.

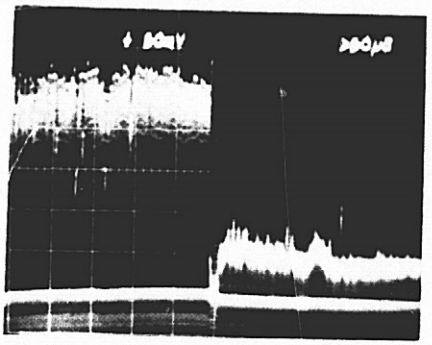

Fig. 7. Surface state trapping due to electron beam irradiation.

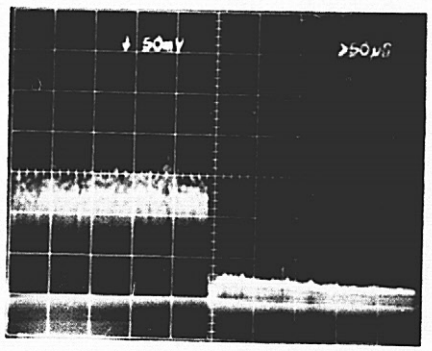

Fig. 8. Mitigation of trapping by buried channel operation.

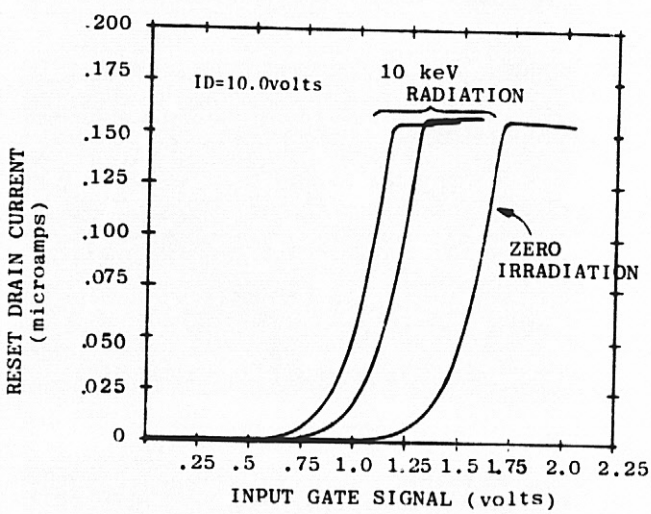

Fig. 9. Input Gate Threshold Voltage Shift as a Function of Irradiation.

N77-17275

RECENT PROGRESS IN PHOTOELECTRON IMAGE DETECTION WITH CCDs

John P. Choisser

Electronic Vision Company
A Division of Science Applications, Inc.
San Diego, California

ABSTRACT

During the past year, additional intensified CCDs (ICCDs) have been built and operated. These ICCDs are electrostatically and magnetically-focussed image tubes which use CCDs as anodes. The ICCDs have been shown to detect single photoelectrons, and have electron gain very near that which was predicted. This paper will present the first single-pixel pulse-height distributions, and will show the leakage current increases as a function of photoelectron irradiation. The advantages and disadvantages of front-and rear-illuminated designs will be discussed in light of differing applications requirements.

I. INTRODUCTION

A number of electrostatically-focussed ICCD Digicons have been fabricated at EVC during the past two years, and test results have been published as they have become available (1,2,3). These tubes initially used the Fairchild 100x100 CCD-201, and later the replacement array CCD-202.

Figure 1 shows the tube envelope used in the ICCD construction. The body is alumina, with copper flanges at each end for attaching the array header and photocathode by cold welds. We believe the combination of external photocathode processing and the use of molecular beam photocathode activation methods are responsible for minimizing the alkali metal damage to the semiconductor. Out of eight ICCDs only one CCD failed to operate after tube processing, and even that was an array whose operation had been intermittent before tube processing. Figure 2 shows a CCD mounted on the EVC Digicon tube header.

Figure 3 shows the first magnetically focussed Digicon ICCD-202, built recently and delivered to Dr. Robert Hobbs of NASA Goddard Space Flight Center. This tube was processed like a standard Digicon, using standard Digicon tube parts, except for an adapting flange at the anode end to make the one-inch diameter ICCD header fit the two-inch diameter tube body. This tube will be used for experimental astronomical imaging photon counting by Currie, of the University of Maryland, and Hobbs.

Two of the recent Digicon ICCDs have been built with UV-transmitting faceplates, to show a further advantage over unintensified CCDs. These first UV tubes, which use sapphire faceplates, will be followed by tubes using quartz and magnesium fluoride faceplates. A gated magnetically-focussed Digicon ICCD using the Fairchild ICCD-211 (190x244 picture elements) is now under construction.

II. SINGLE PHOTOELECTRON DETECTION

Last year, using one of the first EVC Digicon ICCDs, Currie (3) took pulse-height distributions of single and multiple photoelectron arrivals, accumulated over the central 3,000 pixels of the ICCD-201. These data, which included pixel-to-pixel dark signal variations, showed that the ICCD could be used for photon counting with reasonable photometric accuracy even without subtracting fixed-pattern noise. It would be expected, of course, that a better pulse height distribution exists at each pixel, and would be evident if the fixed pattern noise in the array were stored and subtracted from the output.

In EVCs demountable vacuum system, a CCD on its header was installed to make photoelectron bombardment damage tests, to be described later in this paper. During the experiment, a single pixel was monitored to determine both the pulse height distribution and the photoelectron incident flux rate for calibration of the overall experiment. The resulting pulse height distribution is shown in Figure 4.

The distribution represents a 100 second accumulation of outputs from a single pixel. In that time, there were a total of 7,847 events, approximately 4,319 of which were zeros (dark events), 2,783 were single photoelectron arrivals, 597 were doubles, 131 were triples, and 17 were quadruples. The average flux level was 43.5 photoelectrons per second, which is 0.56 electrons per scan at 77 scans per second. The single photoelectron arrivals were also clearly evident by visually monitoring the video signal. In the dark, the zero peak was perfectly symmetrical, except for an occasional thermal electron arrival. The data indicate that an ICCD may be used in a photon-counting mode to provide accurate multi-channel photometry at very low input flux levels.

III. ELECTRON BOMBARDMENT DAMAGE

The primary damage mechanism observed so far is an increase in leakage current as a result of electron bombardment. The 18KV electrons used in this test caused observable increases in leakage current in many of the pixels irradiated. These data were taken very recently and have not

yet been fully analyzed. A cursory examination of the data, however, indicates that the anlysis will not be a simple task. For example, as dosage increases, some pixels have been observed to have their leakage current change reverse direction and begin decreasing, even to a level below that of non-irradiated pixels, in some cases. The data analysis problem is further complicated by the fact that each of the two interlaced fields exhibited different characteristics in leakage current changes. In an irradiated spot, pixels belonging to one field had increasing leakage currents while the other field had decreasing leakage currents. This caused a very pronounced striped effect in the leakage current pattern. It was subsequently discovered,however, that modifying the photogate voltage on the CCD could cause the high leakage current pixels to appear in the other field and vice versa. The average of the high and low leakage currents, however, is still higher that the leakage currents before irradiation.

Figure 5 shows some data taken very recently on two adjacent pixels in one column (so the pixels are in different fields). The variations in leakage current for the two pixels as a function of dose shows their different behavior, as well as the dependence on the photogate voltage.

The abcissa shows the accumulated dose in the number of 18KV electrons per pixel, and the ordinate the leakage current as a fraction of saturation at room temperature. The error in the vertical scale is probably significant, however,and a better vertical reference is shown by the 10 photoelectron equivalent signal shown at the right. Unfortunately the amplitude of the output signal is also somewhat dependent on the photogate voltage; this is one of several reasons why these very recent data are not yet thoroughly analyzed.

Irradiation-caused leakage current increases in some arrays have been shown to be a reversable process. At EVC, for example, we have, on numerous occasions, been able to decrease the leakage current in damaged diodes by irradiation of generally lower-energy electrons. Gordon(4) and Tull (5) have also shown that leakage currents in Reticon arrays can be reduced by electron irradiation. At EVC, we are beginning to determine whether damage effects on the CCDs may also be reversible. Hopefully we will have results over the next few months.

In summary, we have shown that image tubes can be built using the Fairchild CCDs and that the CCDs can survive the image tube processing schedules. We have also shown that CCDs with low noise electronics are capable of detecting single photoelectron arrivals. The present tubes may be suitable for applications at very low light levels, or when short array lifetimes can be tolerated. The currently available front-illuminated devices are being studied to learn more about their characteristics in hopes that periodic electron bombardment annealing may increase the array lifetime for more applications. It is also anticipated that in the future tubes will be built using thinned CCDs for rear bombardment which may preclude the electron bombardment damage from happening at all. Premiminary work by others using thinned devices has begun (6,7) and when either we or they are successful, devices will then be available that are useful in a wider range of applications.

REFERENCES

1. Choisser, J.P., "Experiments on the Use of CCD's to Detect Photoelectron Images" presented at Symposium on Charge Coupled Device Technology for Scientific Imaging Applications, 6 March 1975, p. 150, JPL SP 43-21.

2. Currie D.G., "An Intensified Charge Coupled Device for Extremely Low Light Level Operation", presented at the 1975 International Conference on the Application of Charge Coupled Devices, sponsored by the Naval Electronics Laboratory Center, 29, October 1975.

3. Currie, D.G., Choisser, J.P.,"A photon Counting Array Photometer",Proceedings of the SPIE, Vol. 78, Reston, Virginia, March 1976.

4. Gordon, R.L., "Annealing Procedure for Self-Scanned Diode Arrays", Applied Optics, Vol. 15, No. 8, p.1909, August 1976.

5. Tull, R.G., private communication.

6. Sobieski, S., "ICCDs for Ultra Low Light Level Imaging", Proceedings of the SPIE, Vol. 78, Reston, VA., March 1976.

7. Williams, J., "Test Results on Intensified Charge Coupled Devices", Proceedings of the SPIE, Vol. 78, Reston, Va., March 1976.

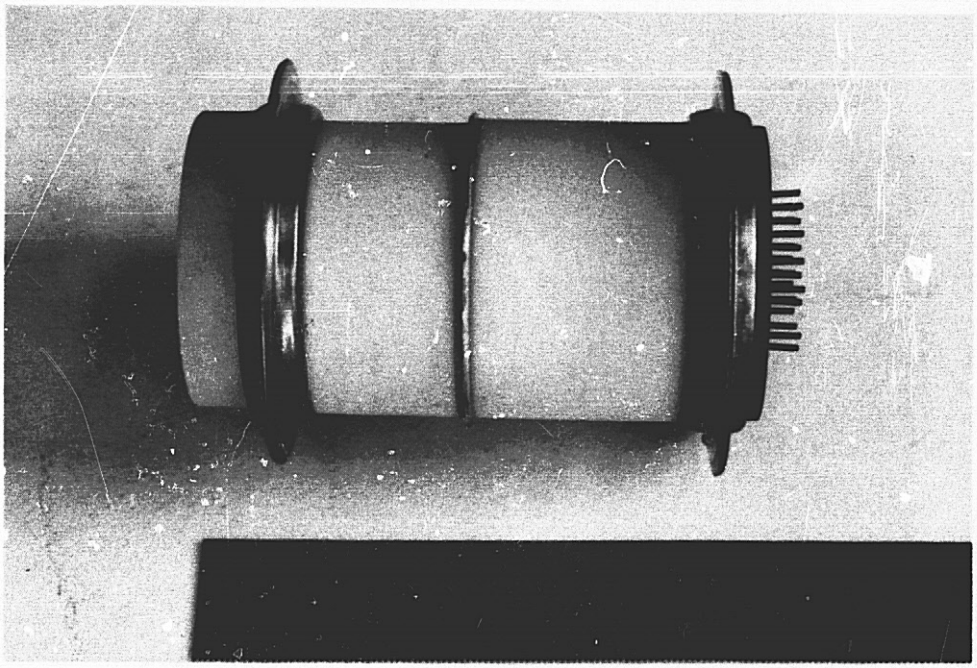

Figure 1. Electrostatically-focussed Digicon

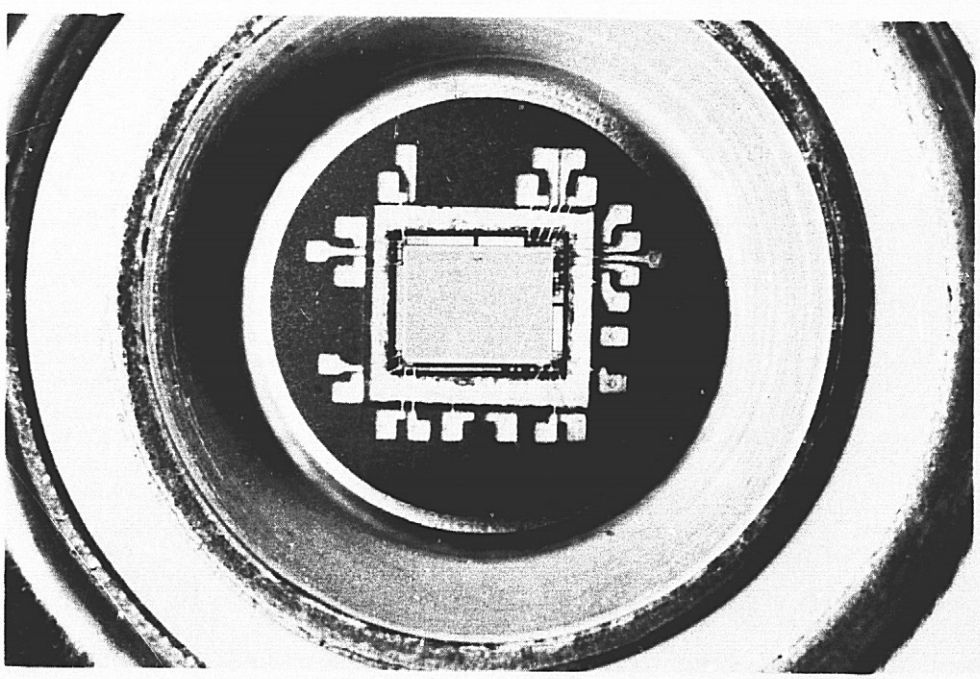

Figure 2. CCD-202 on Digicon header

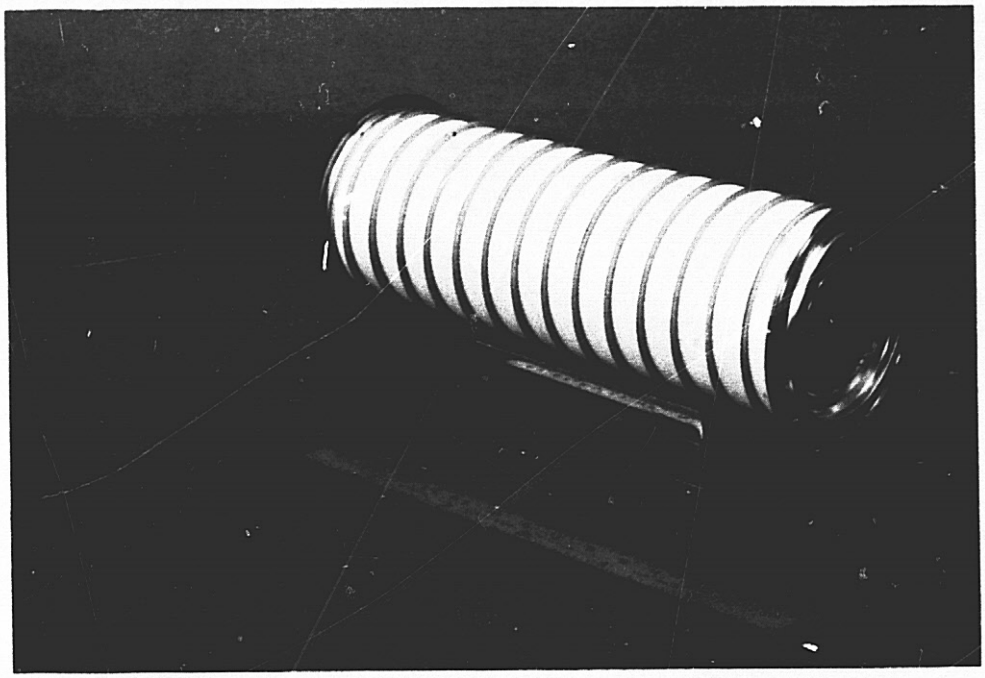

Figure 3. Magnetically-focussed Digicon IC[illegible]-202

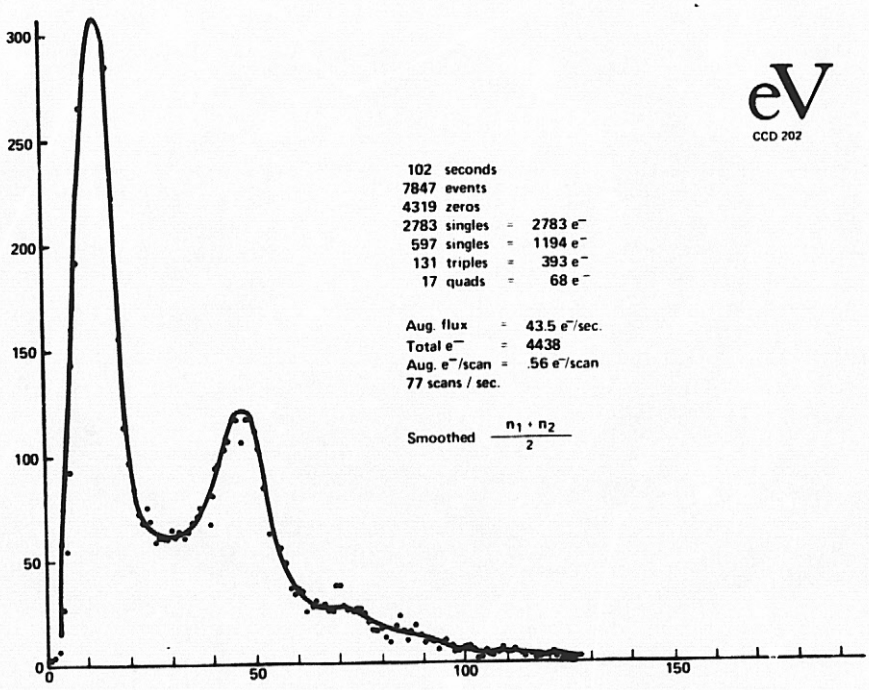

Figure 4. Photoelectron pulse height distribution for ICCD-202

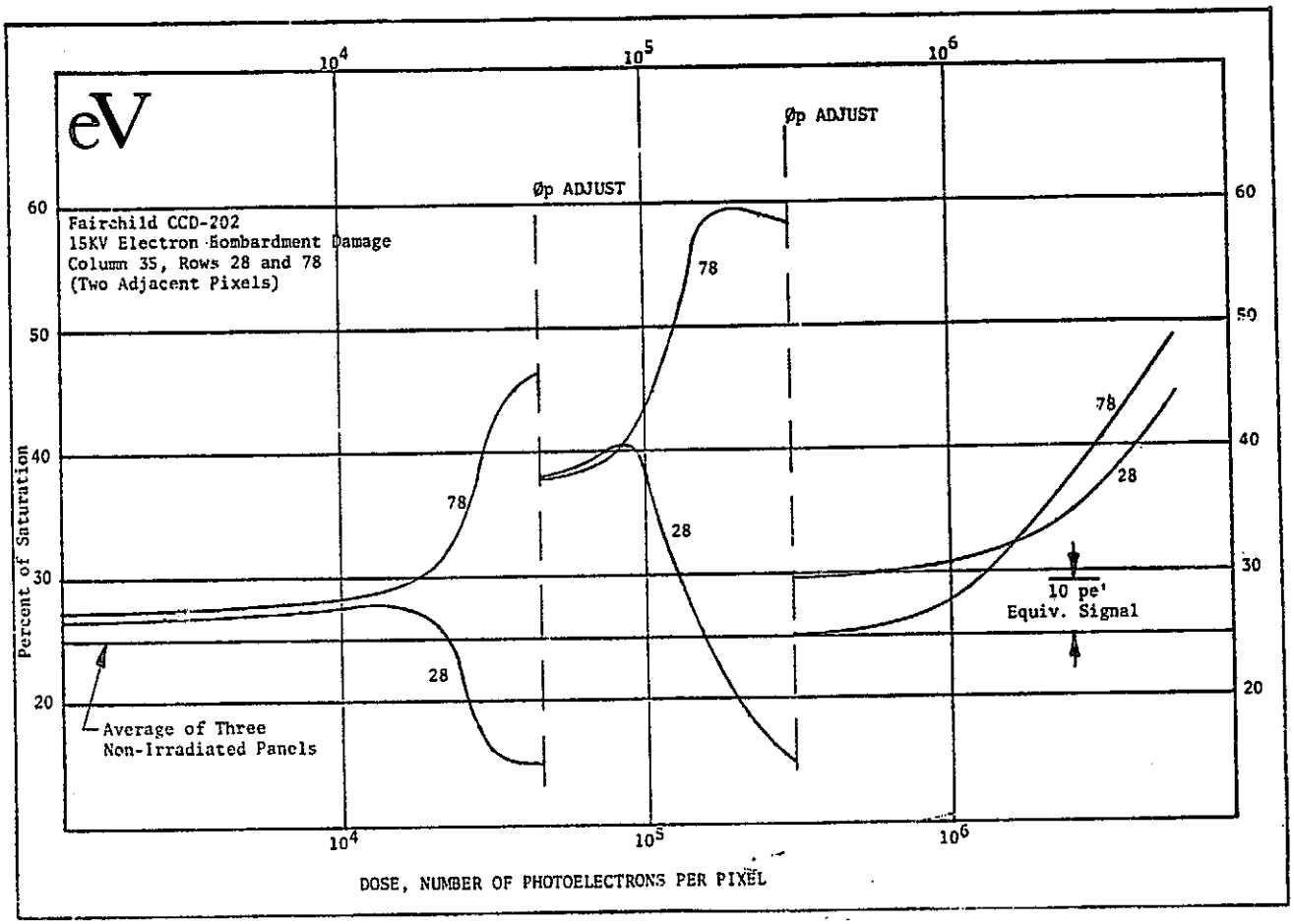

Figure 5. ICCD-202 photoelectron bombardment damage

D/3

N77-17276

X-RAY QUANTUM EFFICIENCIES OF CCD'S*

Martin Peckerar
Westinghouse Electric Corporation
Baltimore, Maryland 21203

W. D. Baker and D. J. Nagel
Naval Research Laboratory
Washington, D.C. 20375

ABSTRACT

All of the X-ray energy incident on a CCD does not contribute to the formation of charged carriers which show up as signals in external circuitry. There are three reasons why this is so. First, some energy is absorbed in insensitive insulating layers above the sensitive silicon bulk. Second, carriers released beneath the device depletion layer may recombine before collection. Third, high energy photons may escape the device entirely without the creation of charged carriers. As a result, the X-ray quantum efficiency is less than 100%. It is demonstrated that the X-ray quantum efficiency of a CCD is still high enough to obtain good X-ray imaging with this device. The range and response of the CCD to incident X-rays in the 5 - 14.1 KeV range are determined experimentally. Knowledge of this range and response allows direct measurement of quantum efficiency. Quantum efficiency decreases monotonically from 82% to 35% in the range studied. Comparison of experimental and theoretical quantum efficiencies allows a determination of silicon bulk electron diffusion length. For the device studied the electron diffusion length was 75μm.

INTRODUCTION

Charge-coupled devices (CCD's) are of great potential use in the quantitative study of X-ray intensity distributions.[1] The usefulness of CCD's in the field rests on the ability of these devices to convert X-ray energy efficiently into collectible charged carriers. There are three reasons why CCD's are not 100% efficient in converting X-rays into collectible charge. Some X-ray energy is lost in metallization and dielectric "dead" layers over the sensitive silicon surface. Second, high energy photons may pass through the device without creating any ionizations. Finally, carriers introduced in the CCD bulk below the depletion region may recombine before they can show up as signal in external circuitry.

In this paper, it is demonstrated that the conversion of X-rays to collectible carriers in CCD's is efficient enough to produce good X-ray images. The range and response of an X-irradiated CCD is then presented. A discussion of the method whereby range and response functions can be converted to quantum efficiency follows. It is further shown that a comparison of theoretical and experimental quantum efficiency allows a direct determination of electron diffusion length in the CCD bulk silicon.

EXPERIMENTAL

A standard CCD imager, the Fairchild CCD 201 array, was used in this study. This is a 100 x 100 picture element (pixel) array. Photosensitive sites are 30μm by 20μm squares located on 30μm centers in the vertical and on 40μm centers in the horizontal directions. Appropriate clocks were provided to read out the array in a 100 line TV-type format with 2:1 interlace and a frame rate of 8 msec. The on chip pre-amplifier was followed by an off chip amplifier with gain 100. To reduce array dark current, the devices were cooled to about 150K. The image was displayed on a conventional oscilloscope. The CCD amplifier output provides oscilloscope beam intensity modulation.

The CCD was placed in the experimental setup as indicated in Figure 1. The X-ray beam was created by fluorescence of five materials (vanadium, iron, nickel, germanium, and strontium) with an MO-targeted X-ray tube. These fluorescers provided fairly monochromatic beams of 5, 6.4, 7.5, 9.9 and 14.1 KeV respectively.

To provide X-ray images, a nickel mesh with a 1 mm grid spacing was placed 1/2 cm from the surface of the CCD array. The shadow of this mesh is recorded by the CCD. To get a quantitive measure of the CCD response as a function of incident X-ray energy, the CCD was removed and Kodak no-screen X-ray film was substituted. The films were then read with a modified Leed and Northrup densitometer. The film data was converted to X-ray intensities using the computer program of Brown, Criss and Birks.[2]

RESULTS

In Figure 2 we see the shadow image of the grid, made with Germanium Kα photons. The image is distinct and no blooming is observed. In Figure 3, the response of the CCD (i.e., the voltage the stored pixel charge produces in external circuitry) is plotted as a function of X-ray fluence for the 5 different photon energies used. The response is linear from 0.8 volts to 4.0 volts. In Figure 4, the CCD response to germanium Kα photons is compared with the photographic response of Kodak no-screen film.

In Figure 5 the quantum efficiency of the CCD is plotted as a function of incident photon energy. Quantum efficiency is here defined as the ratio of the number of electrons which create a signal to the total number of electron hole pairs which would be formed if all the incident X-ray energy were converted to electron-hole pairs (expressed as percent). The solid curves are theoretical curves obtained assuming infinite 75μm and 10μm electron diffusion lengths in bulk silicon. The method used to calculate these curves is discussed below. The points are experimentally derived. Measured quantum efficiency decreases monotonically from 82% at 5.0 KeV to 35% at 14.1 KeV.

DISCUSSION

The above results indicate that X-ray intensity distributions can be imaged with CCD's.

* Work performed when author was with the Naval Research Laboratory. This work was supported by the Office of Naval Research.

Figure 3 shows that for all 5 photon energies used in this study, the response is linear over a range of about 3 volts. The upper limit of the response curve is defined by the potential well saturation of the CCD. That is, each pixel will hold at most 5.0×10^{-14} coulombs of charge. Once this number of charges fills the well, further X-ray exposure will not lead to more stored charge. Hence, the response saturates. The 0.8 volt threshold limit in response is determined by the amplifier-preamplifier chain. The chain employed was not designed for low noise performance. Thus, the system was not sensitive to the smaller changes in voltage created by the lower fluences of incident X-rays. An amplifier-preamplifier designed for low noise performance would extend the CCD response curve to lower fluences.

Figure 4, however, shows that the threshold limit of the CCD is about the same as that of Kodak no-screen film. The saturation limit of the CCD response, though, is lower than that of film. The range of film response is about 20 times that of the CCD.

Knowledge of the CCD geometry also allows a determination of resolving power. The CCD used here has a resolving power of 160 line pairs/cm vertically and 120 line pairs/cm horizontally. Previous work in X-ray film[3] indicates the resolving power of Kodak no-screen film can be estimated at about 500 line pairs/cm.

As indicated in Figure 5, quantum efficiencies can be derived from the experimental data. First, the amount of charge in X-ray exposed pixels is calculated. This is done by assuming that when the saturation voltage is reached the full 5×10^{-14}C saturation charge is present in the cell. At lower voltages the amount of charge in the cell is the saturation charge multiplied by the ratio of the observed response voltage to the saturation voltage. Next the number of electron-hole pairs the incident X-ray beam would create if all X-rays were converted to electron-hole pairs is calculated. This is gotten by dividing the total X-ray incident energy by the energy needed to form an electron hole pair (3.6 eV). This number is converted to coulombs. The quantum efficiency is the ratio of the amount of charge in this well to the number of electron-hole pairs the X-ray beam would create if all X-rays were converted to electron-hole pairs (expressed as a percent).

The quantum efficiency of the CCD for a given photon energy incident can be calculated from first principles. To do this, one must understand why all the X-ray incidents are not converted to collectible electron-hole pairs. There are three sources of X-ray energy loss. The first is loss in oxide-metal dead layers above the sensitive silicon surface. X-rays absorbed in these dead layers will not produce electron-hole pairs. Second, some X-rays (particularly high energy X-rays) may pass through the device without being stopped by the material. Finally, electrons released below the depletion layer of the device may recombine before reaching the silicon surface. There electrons will not be collected. It is this last source of carrier loss that makes X-rays so useful as a probe of semiconductor material properties in the CCD bulk.

To perform the calculation, the device is broken into 3 layers: The metal-oxide dead layer above the active silicon; the depletion layer; and the bulk silicon beneath the depletion layer. The amount of energy absorbed in each layer is easily calculated from the formula:

$$I = I_o \exp -\mu\rho x$$

where:

I_o = incident intensity,

I = intensity emerging from the layer,

μ = mass absorption coefficience of the layer for the X-ray photon,

x = depth of the layer,

ρ = layer density.

No electron-hole pairs are collected from the dead layer. All electrons released in the depletion layer are assumed to be collected. In the bulk beneath the depletion layer, not all electrons released reach the surface. These recombined electrons will not show up as signal in external circuitry. The number of released electrons which reach the surface is gotten by breaking the bulk up into incremental thicknesses. The number of electrons released in each thickness (i.e., the X-ray energy absorbed divided by 3.6 eV) is calculated.

To account for recombination, a one-dimensional diffusion model is chosen. In this model, the number of electrons released in each incremental thickness is multiplied by $\exp(-x/D_e)$, where x is the depth of the incremental thickness below the surface. D_e is the electron diffusion length. The contribution from each incremental thickness is added to find the total number of electrons collected. The resulting curves are shown as solid lines in Figure 5.

This figure indicates that theory predicts an initial increase in quantum efficiency as photon energy increases. This is followed by a quantum efficiency decline at higher energies. Initially, there is considerable energy loss in dead layers. As the photons become more energetic, they penetrate more deeply and less energy is expended in the dead layer. As the penetration depth increases more energy is deposited beneath the depletion layer. Thus, for higher energies, the curves become sensitive to electron diffusion length. The apparent "anomaly" occurring at about 2.8 KeV is due to the silicon absorption edge. The experimental results are, for the most part, in agreement with the theory, assuming 75μm electron diffusion length. The one apparent exception to this occurs at 14.1 KeV (Strontium Kα X-rays). At this energy a considerable amount of energy passes through the material. There is a possibility that these high energy X-rays ionize the CCD flat pack and yield an apparently high efficiency by injecting electrons from the rear.

A final word must be said about radiation damage. It has been shown in the past that X-rays do damage CCD's. Based on the total dose tolerance

of these devices the useful imaging life of a CCD for 10 KeV X-rays is 15 hours. Devices specifically designed for operation in ionizing radiation ambient (i.e., fabricated with particular care to provide radiation hard dielectric layers) should easily have an order of magnitude longer life. If X-rays are to be used to ascertain material parameters, such as electron diffusion length, the beam can be shuttered to give minimum exposure.

CONCLUSION

In this paper it was shown that CCD's convert X-ray quanta to electrical signals with sufficient efficiency to image X-ray intensity distributions. The threshold response for CCD imaging is similar to that of film, but the range is about 20 times less. Spatial resolutions is also somewhat poorer.

It was further demonstrated that X-rays can be a useful probe of the material properties of the CCD's. A comparison of observed quantum efficiencies allows a determination of bulk electron diffusion lengths.

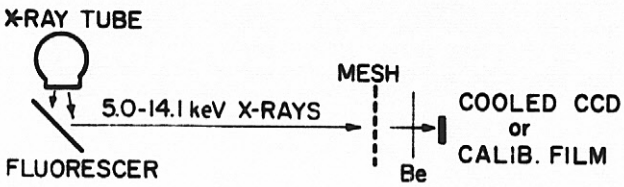

Figure 1. Schematic of the experimental arrangement. The mesh used to produce an X-ray pattern was removed to measure the response of the CCD and to calibrate the X-ray intensity with a photographic film of known response.

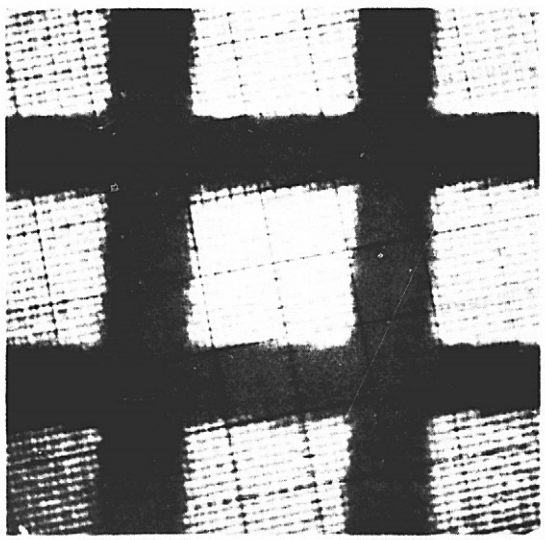

Figure 2. Shadow cast on a CCD array by a metal mesh in a beam of 9.9 keV X-rays. Wires in the mesh are 1 mm center-to-center. Individual picture elements (and the scale marks of the oscilloscope used to record this picture) are visible.

REFERENCES

1. G. Renda, J. Lowrance, "Symposium On Charge-Coupled Device Technology for Scientific Imaging Applications," JPL SP 4-21, 91 (1975).

2. D. B. Brown, J. W. Criss, L. S. Birks, "Journal of Applied Physics," 47, 3722 (1976).

3. K. Rossmann, B. Luberts, "Radiology," 86, 235 (1966).

4. J. M. Killiany, W. D. Baker, N. S. Saks, D. F. Barbe, "IEEE Trans. Nuc. Sci.," NS-21, 193 (1974).

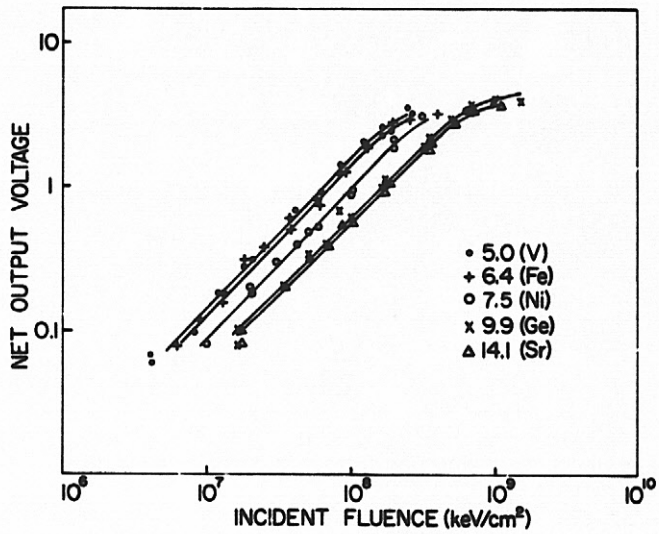

Figure 3. Measured CCD response (above a 80 mv noise level) for five Kα X-ray energies produced using the fluorescent elements indicated in parentheses.

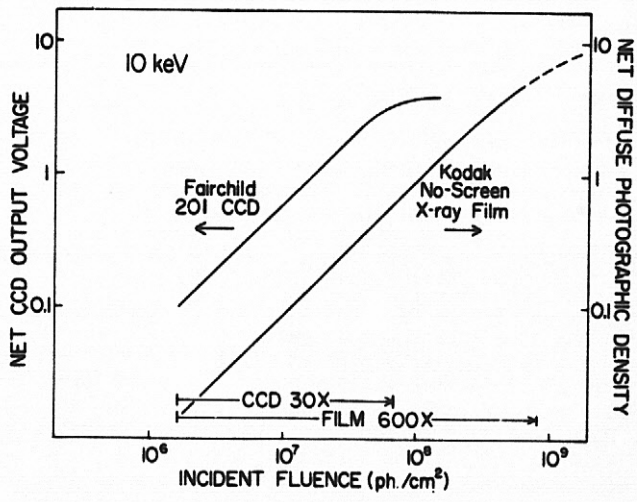

Figure 4. Empirical net responses of a CCD array (this work) and no-screen X-ray film[3] at 10 keV.

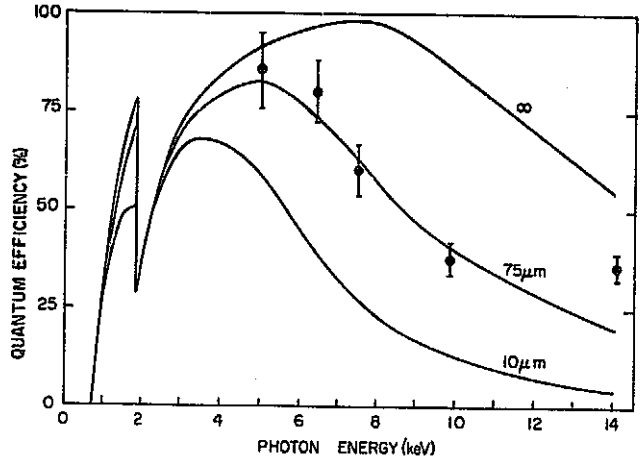

Figure 5. Quantum efficiency as computed for 10, 75μm and infinite carrier diffusion lengths and measured at five energies.

N77-17277

EFFECTS OF NEUTRON IRRADIATION ON THE CHARACTERISTICS OF A BURIED CHANNEL CCD AT 80°K AND 295°K

N. S. Saks
J. M. Killiany
W. D. Baker

Naval Research Laboratory
Washington, D. C.

ABSTRACT

Buried channel CCD shift registers have been irradiated with 15 MeV (average energy) neutrons in steps to $3x10^{13}$ n/cm^2. The irradiations were performed at 80°K and 295°K on operating devices with normal clocks and bias voltages applied. Dark current increased from the pre-irradiation value of 7 nA/cm^2 to 1600 nA/cm^2 at $1x10^{13}$ n/cm^2. The input gate threshold shift observed at 80°K was -0.9 volts per 10^{13} n/cm^2, a factor of 4 less than that predicted from a first-order calculation of the equivalent ionization dose of neutrons in the oxide. Transfer efficiency measurements yield a bulk electron trap creation rate for neutron irradiation ($\Delta N_t/\Delta\phi$) of 14.0 cm^{-1} at 295°K with a trap emission time constant of 25μs. At 80°K, the trap creation rate is 2.0 cm^{-1} with an emission time constant of 100 ms.

I. INTRODUCTION

Charge-coupled device (CCD) structures are attractive for application in space and strategic systems. Since these systems generally operate in a radiation environment, the behavior of CCDs is such environments must be characterized. The effects of both ionizing and displacement damage must be understood and controlled.

As in all MOS structures, ionizing radiation results in a build-up of positive charge in the oxide and an increase in the surface states of a CCD.[1] Since the charge transfer process in a CCD is relatively insensitive to flat-band voltage shifts, a carefully designed and properly operated CCD can function satisfactorily with as much as several volts of shift.[2] Some of the device properties which may be affected by ionizing radiation are (1) input threshold voltage, (2) dark current, (3) on-chip output amplifier gain, and (4) transfer loss to surface state trapping.

In addition to ionization effects, particle radiation can deposit energy in an MOS structure via displacement damage. In the silicon substrate this results in the creation of bulk traps which cause a reduction in the minority carrier lifetime and the removal of free carriers. The effects of bulk damage in CCDs tend to be obscured by ionization effects for charged-particle radiation. High energy neutrons, however, cause a large amount of displacement damage with relatively little ionization.[3]

In this work we report the effects of high energy neutrons on the properties of an unhardened CCD. The devices were irradiated while operating with all normal clocks and biases applied in order to simulate real conditions. Several devices were irradiated while operating at 80°K to reproduce conditions for proposed low temperature CCD applications. Buried channel CCDs with high preirradiation transfer efficiency were used to minimize the effects of surface state and preirradiation bulk defect trapping relative to neutron induced defect trapping.

II. EXPERIMENTAL CONDITIONS

The devices irradiated are 150-bit 4-phase buried n-channel CCD shift registers.[4] Pertinent structural parameters are: 0.3x5.0 mil phase gates, 1500 Å gate oxide, 6000 Å buried n-channel with implant dose $1.5x10^{12}$ phosphorus. The shift registers were operated at 500 KHz with 15 volt clock swing at a 60% duty cycle. When measuring transfer efficiency, the signal charge in each 'one' was kept at .375 or less of a full well to insure there was no trapping of signal charge by surface states. The fill-and-spill input technique was used to inject a burst of ones which are of equal magnitude to very high precision.[5]

The neutron irradiations were performed at the NRL cyclotron. The energy spectrum of the neutrons is a Gaussian distribution 0 to 35 MeV with a broad peak at 15 MeV. The maximum neutron flux employed was $5x10^9$ n/cm^2-sec. The amount of gamma radiation in the neutron beam was calculated to be 10^3 rad (Si) per 10^{13} n/cm^2.

The CCDs were operated with all normal biases and clocks applied during the irradiation. Device BC 57-7-7, which was irradiated at liquid nitrogen temperature, was maintained at 84°K throughout the entire sequence of alternating irradiations and measurements. Device BC 57-7-3 was irradiated at 84°K but room temperature measurements of device characteristics were made after each irradiation.

III. EXPERIMENTAL RESULTS

The CCD shift registers were irradiated through a sequence of doses to a maximum of 1 or $3x10^{13}$ n/cm^2. Device characteristics which were measured after each dose were (1) input gate threshold voltage, (2) full well capacity, (3) output voltage to output charge gain of the on-chip output amplifier, (4) CCD dark current, and (5) transfer efficiency. At $3x10^{13}$ n/cm^2, about a 7% decrease in the gain of the output amplifier was observed. There was no change in the full well capacity up to the maximum dose.

Measured values of the input gate threshold voltage shift for devices at 295°K and 84°K are shown in Figure 1. The magnitude of the threshold shift is larger at 84°K than at 295°K as expected from results on the effects of ionizing radiation

in MOS structures at 77°K.[6] The observed threshold voltage shift is approximately -0.9 volt per 10^{13} neutrons/cm^2 at 84°K and is most likely due to the relatively small ionization effect of high energy neutrons in SiO_2. An approximate value for the effective rate of energy deposition by ionization for 15 MeV neutrons in silicon is 10^4 rad (Si) per 10^{13} n/cm^2.[3] Using this value for the neutron energy spectrum used in this work, and assuming the same ionization rate in SiO_2 as silicon, the maximum expected threshold voltage shift for 1500 Å oxide thickness is -4.0 volts per 10^{13} n/cm^2.[7] However, the average field in the oxide beneath the input gate is approximately 0.5×10^6 volt/cm which is considerably less than the field required to produce the calculated maximum threshold shift.[7] Also, the long elapsed time between irradiation and threshold measurement, up to 48 hrs at the largest dose, may have permitted some annealing of radiation-induced charge to take place.

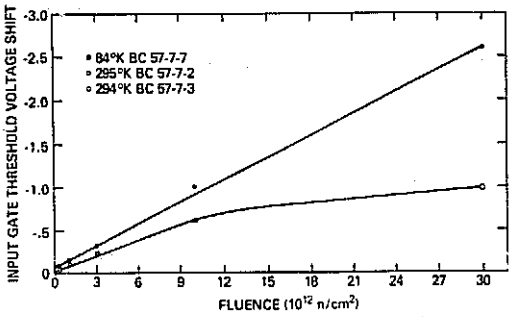

Fig. 1. Input gate threshold shift vs. neutron fluence, showing the expected greater shift at 84°K compared to the 295°K values

The effect of neutron irradiation on CCD dark current at 300°K is shown in Figure 2. The dark current for this CCD increased from the preirradiation value of 7 nA/cm^2 to 1600 nA/cm^2 at 10^{13} n/cm^2, in qualitative agreement with data published previously.[8,9] The surface generation component of the dark current was measured with an on-chip gated diode. During irradiation, the same biases applied to the CCD buried channel and one phase gate were applied to the gated diode implanted channel and gate, respectively. These results are also given in Figure 2 and show that the surface component of the dark current did not increase significantly with fluence. Therefore, the approximately linear increase in CCD dark current with neutron fluence is due to bulk generation within the CCD depletion region.

Measurements of the charge transfer inefficiency (CTI) for a CCD irradiated to 3×10^{13} n/cm^2 at 294°K are shown in Figure 3 for different amounts of signal charge. For this dose, the CTI is on the order of 1% which would make the device useless for most applications. As shown in Figure 3, the CTI is a function of the size of the signal packet. This effect can be attributed to non-uniform doping in the buried n-channel layer.[10]

The CTI is measured using the double pulse technique.[11] Briefly, a burst of 20 charge packets of equal magnitude (ones) is input to

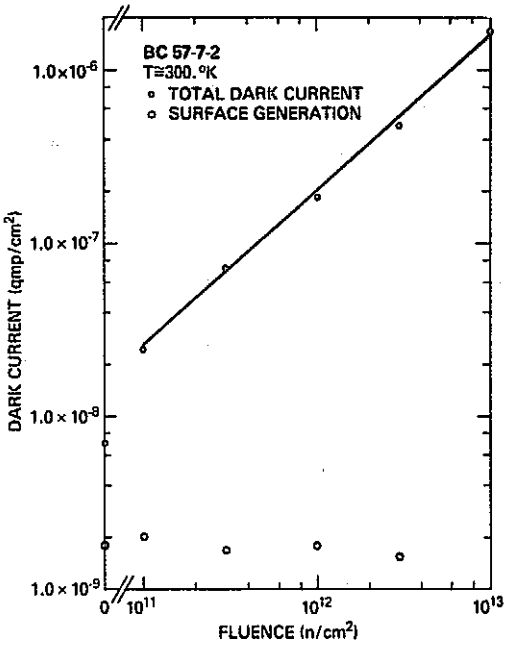

Fig. 2. Dark current density at 300°K as a function of neutron fluence, illustrating the linear relation between J_D and the neutron fluence.

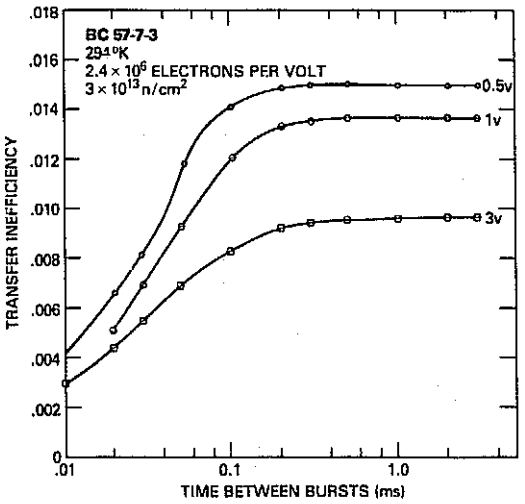

Fig. 3. Transfer inefficiency for a CCD at 294°K after 3×10^{13} n/cm^2 vs. time between bursts for three different signal levels. The dependence of inefficiency on signal level indicates non-uniform doping in the buried channel.

the CCD, followed by a number N_Z of empty packets (zeros). Then a second burst of ones is input to the CCD and the loss in the leading ones is measured as a function of the time between bursts, $N_Z T_C$, where T_C is one clock period (2μs). The effect of high energy neutron radiation is to create a number of bulk trapping levels in the buried channel layer. When a packet of signal charge electrons occupies the volume of semiconductor surrounding an empty trap, the trap

captures an electron from the signal packet in a time which is usually short compared to a clock period. As the signal packet is transferred along the CCD to the next potential well, what happens to the trapped electron is a function of the electron emission time of the trap, τ_i: (1) If $\tau_i \ll T_c$ (the clock period), the trapped electrons will rejoin the signal packet and no effects of trapping will be observed. (2) If $\tau_i \gg N_z T_c$ then the traps remain filled; consequently, the traps will not remove charge from the signal packet and no effect on CTI will be observed. (3) If $T_c < \tau_i < N_z T_c$ then the traps will remove electrons from the signal packet and will re-emit them too late to rejoin the signal packet. This will be observed as loss in the signal packet at the output. For a single level of traps, the total loss in number of electrons is given by:[10,11]

$$N_{loss} = M\, V_{SIG}\, N_t\, e^{-T_t/\tau_i}\, (1-e^{-N_z T_c/\tau_i}) \qquad (1)$$

where M is the number of transfers, V_{SIG} is the volume occupied by the signal packet, N_t is the density of traps, and $T_t \simeq T_c/4$. If there is more than one level of traps, Equation (1) must be summed for all traps. Equation (1) shows that buried channel CCDs are relatively sensitive to bulk traps because every signal charge packet encounters traps under each phase gate. This increases the effective trap density by the number of transfers M, which for these devices is 600.

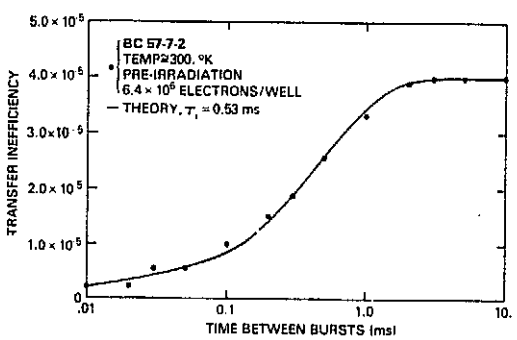

Fig. 4. Fit of the preirradiation transfer inefficiency data as a function of time between bursts to the theoretical loss curve for a single trap level (Eq. 1).

A curve of CTI vs. time between bursts for a typical sample at 300°K before irradiation is shown in Figure 4. The solid line is a best fit of Equation (1) to the data and shows a good fit between data and theory for a single level of electron traps with emission time 0.53 ms at 300°K. For long times between bursts, $N_z T_c \gg \tau_i$, and for $\tau_i \gg T_t$, Equation (1) reduces to

$$N_{loss} = M\, V_{SIG}\, N_t \qquad (2)$$

where N_{loss}/M is given by CTI multiplied by the number of electrons per well. Using Equation (2) with M = 600, $V_{SIG} = 2.25\times10^{-10}$ cm^3, and N_{loss}/M = 262 electrons, we obtain $N_t = 1.2\times10^{12}$ traps/cm^3 (preirradiation).

In this calculation we have assumed that the volume occupied by the signal charge is 3/8 of the thickness of the buried channel (a 3 volt signal divided by the 8 volt full well signal). This is equivalent to the assumption of uniform doping in the buried channel layer. As shown by the CTI measurements as a function of packet size in Figure 3, small packets occupy a larger volume than assumed in the linear approximation. This is a major source of error in this and the following trap density calculations.

Data showing N_{loss} as a function of time between bursts for a sample irradiated to 3×10^{12} n/cm^2 at 295°C is shown in Figure 5. The solid line shows the best fit of Equation (1) to the data. The data does not fit Equation (1) nearly as well as in the preirradiation case. A better fit would be obtained if a distribution in electron emission times of the traps is assumed. Similar effects have been observed with fast neutron induced bulk defects in JFETS by Gregory et.al.[12] They suggest that, because fast neutrons create defect cluster perhaps with many defects in each cluster, the properties of a individual defect may depend on its local environment within the cluster.

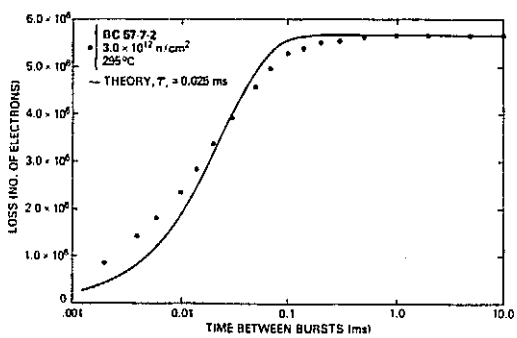

Fig. 5. Fit of the post-irradiation transfer inefficiency data as a function of the time between bursts to the theoretical loss curve indicating a broadening of the trap energy level.

The density of bulk electron traps created by high energy neutrons can be obtained from Equation (2) and the data in Figure 5 when $N_z T_c \gg \tau_i$. The calculated trap density is 4.2×10^{13} cm^{-3} at 3×10^{13} n/cm^2, or a bulk electron trap creation rate $(\Delta N_t/\Delta\phi)$ of 14.0 cm^{-1} at 295°K. Data for the same sample at 10 ms between bursts is shown in Figure 6 plotted as Δ CTI (measured value of CTI minus the preirradiation value). vs. neutron fluence. Figure 6 shows an excellent linear relationship between Δ CTI, or number of bulk electron traps created, versus fluence. The data in Figure 6 shows a larger increase in CTI than was reported by Hartsell for similar devices using 1 MeV neutrons for the irradiation. Because the ratio of bulk displacement damage of 14 MeV neutrons to 1 MeV neutrons is 2.5, a larger increase in CTI is expected in this work.[3]

The CTI of a CCD at 84°K as a function of neutron fluence is shown in Figure 7. The data presented illustrate the fact that at fluences greater than 10^{12} n/cm^2, significant degradation

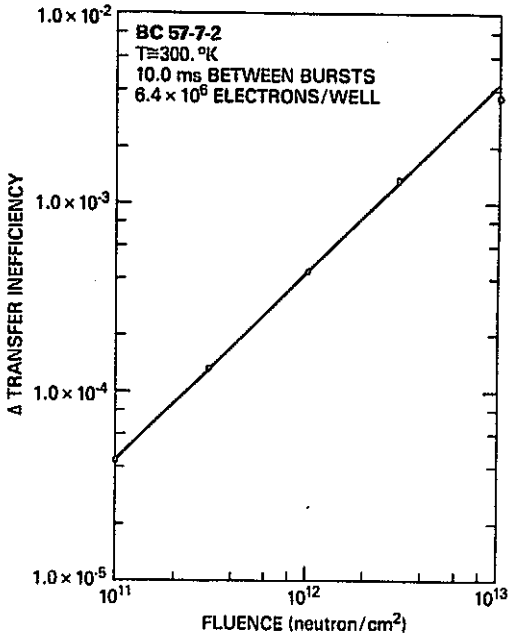

Fig. 6. Change in transfer inefficiency at 300°K as a function of neutron fluence, illustrating the linear relation between the increase in transfer inefficiency due to bulk trapping and the neutron fluence.

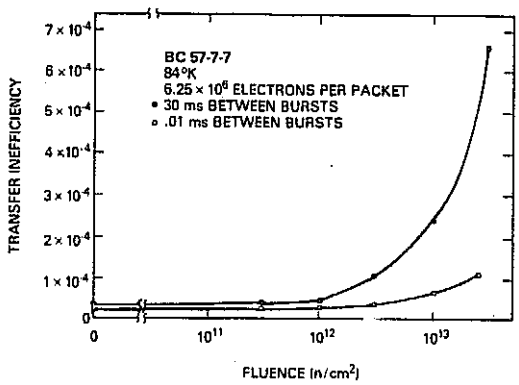

Fig. 7. Transfer inefficiency at 84°K as a function of neutron fluence for two times between bursts, demonstrating the importance of stipulating the time between bursts employed in transfer inefficiency measurements.

of the transfer efficiency occurs. The figure demonstrates the importance of exactly stipulating the conditions under which the CTI measurements are performed.

In Figure 8, the CTI of a CCD irradiated and measured at 80°K for a dose of 3×10^{13} n/cm^2 is shown vs. time between bursts (lower curve). The temperature of the device was then raised to 294°K and the data remeasured (upper curve). From Figure 8, the electron emission time at 294°K is approximately 25 μsec and the calculated trap creation rate $\Delta N_t/\Delta\phi$ is 10.4 cm^{-1}. Within experimental error, these values are the same as for the CCD irradiated at 294°K, and the conclusion is that lowering the temperature to 80°K

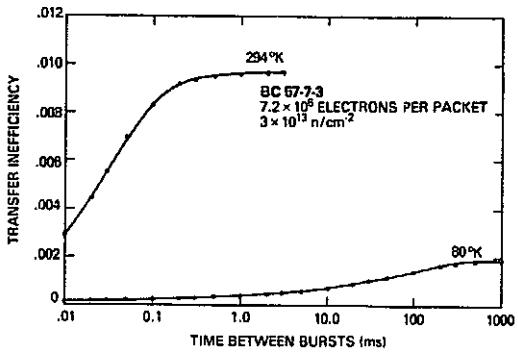

Fig. 8. Transfer inefficiency vs. time between bursts at 294°K and 80°K for a CCD irradiated to 3×10^{13} n/cm^2. At 80°K, the electron traps with emission times between 2μs and 1 sec have a smaller density than the traps effective at 294°K, which results in a smaller CTI at 80°K.

during the irradiation had no effect on the creation of these bulk traps.

The data in Figure 8 illustrates the temperature dependence of the electron emission time of bulk traps. At 80°K the emission time of the trap level which is seen at 295°K has increased to a time much longer than 1 second. Consequently, these traps are always filled during the double pulse measurements and do not affect the CTI. Instead, second level of electron traps appears at 80°K with a density of approximately a factor of 5 less than the 295°K traps ($\Delta N_t/\Delta\phi \approx 2.0$ cm^{-1}) and an electron emission time on the order of 100 ms.

Assuming that the two levels of electron traps observed at 295°K and 80°K are the major fast neutron electron traps in bulk n-type silicon, the sum of the trap creation rates for these levels would give the carrier removal rate for electrons, or $\Sigma \Delta N_t/\Delta\phi = 12.4$ cm^{-1} for BC 57-7-3. This value is larger than the values of carrier removal rate measured by Stein and Gereth which range from about 6 to 10 cm^{-1} for approximately 1 MeV (average energy) neutrons.[13] The value measured in this work is expected to be higher due to the larger damage constant of 15 MeV neutrons. In addition, the major source of error here is in the charge packet volume approximation discussed previously, which tends to overstate the actual trap density.

IV. SUMMARY

Buried channel CCD shift registers have been irradiated with high energy neutrons to a fluence of 3×10^{13} n/cm^2 at 80°K and 295°K with the devices operating. CCD characteristics measured were input gate threshold voltage, full well capacity, output voltage to output charge gain of the on-chip output amplifier, dark current, and transfer efficiency. There was no observable change in the full well capacity and only about 7% decrease in the output amplifier gain at 3×10^{13} n/cm^2. The dark current increased substantially to 1600nA/cm^2 at 300°K for 10^{13} n/cm^2 dose.

The input gate threshold shift was observed to depend on the temperature of the CCDs during irradiation and was larger at 80°K than 295°K, similar to the effects of ionizing radiation in MOS structures at liquid nitrogen temperatures. However, the observed threshold voltage shift was approximately a factor of 4 less than would have been predicted from a rough estimate of the ionization equivalent dose for high energy neutrons.

At 295°K, fast neutrons cause a substantial degradation in the charge transfer efficiency of the CCDs. At 3×10^{13} n/cm^2, the transfer inefficiency is about 1%, which would make the CCD unsuitable for most applications. At 295°K, the observed defect introduction rate for an average of 3 devices is 12.8 cm^{-1}, and the electron emission time of these bulk traps is about 25 μsec. At 84°K, the effect of neutron induced bulk defects on transfer efficiency is not nearly as severe due to the temperature dependence of the electron emission time constant.

ACKNOWLEDGEMENTS

The authors would like to thank Dr. L. August and Mr. G. Miller for their help at the NRL cyclotron, and Mr. J. Modolo for his help with the electronics.

REFERENCES

1. Barbe, D. F., Killiany, J. M., and Hughes, H.L. "Effects of Gamma Radiation on Charge-Coupled Devices", Appl. Phys. Letts., 23, pp. 400-402, October 1973.

2. Killiany, J. M., Baker, W. D., Saks, N. S., and Barbe, D. F., "Effects of Ionizing Radiation on Charge-Coupled Device Structures", IEEE Trans. Nucl. Sci. NS-21, pp. 193-200,(1974)

3. Poll, R. A., "Electronic System Hardening Approaches", IEEE Trans. Nucl. Sci., NS-18, pp. 100-103, Dec. 1971.

4. Devices were fabricated by Texas Instruments, Inc., Central Research Laboratories, Dallas, Texas.

5. Killiany, J. M., and Baker, W. D., "Limitations of a Threshold-Insensitive CCD Input Technique in a Total Dose Radiation Environment", Proc. Int. Conf. Appl. CCDs (29-31 October 1975), pp. 369-374.

6. Harari, E., Wang, S., and Royce, B.S.H., "Low Temperature Irradiation Effects in SiO_2 Insulated MIS Devices", J. Appl. Phys. 46, pp. 1310-1317, March 1975.

7. Boesch, H. E., Jr., McGarrity, J. M., and McLean, F. B., "Charge Yield and Dose Effects in MOS Capacitors at 80°K", presented at 1976 IEEE Nuclear and Space Radiation Effects Conference, July 1976.

8. Hartsell, G., "Radiation Hardness of Surface and Buried Channel CCDs", Proc. Int. Conf. Appl., CCDs (29-31 Oct. 1975), pp. 375-382.

9. Williams, R. A., and Nelson, R. D., "Radiation Effects on Charge-Coupled Devices", IEEE Trans. Nuclear Science NS-22, pp. 2639-2644, (1975).

10. Mohsen, A. M., and Tompsett, M. F., "The Effects of Bulk Traps on the Performance of Bulk Channel CCDs", IEEE Trans. Elec. Dev. ED-21, pp. 701-712, November 1974.

11. Broderson, R. W., and Emmons, S. P., "The Measurement of Noise in Buried Channel CCDs", Proc. Int. Conf. Appl. CCDs (29-31 Oct. 1975), pp. 331-349.

12. Gregory, B. L., Naik, S. S., and Oldham, W. G., "Neutron Produced Trapping Centers in JFETS", IEEE Trans. Nucl. Sci. NS-18, pp. 51-59, December 1971.

13. Stein, H. J., and Gereth, R., "Introduction Rates of Electrically Active Defects in n- and p-Type Silicon by Electron and Neutron Irradiation", J. Appl. Phys. 39, pp. 2890-2904, May (1968).

A CCD INTEGRATED CIRCUIT FOR TRANSIENT RECORDERS

Joseph W. Balch
Charles F. McConaghy

Lawrence Livermore Laboratory
Livermore, California

ABSTRACT

A 50 MHz CCD integrated circuit is described that has been developed for use in transient analog signal recorders to sample and time expand transient signals. The integrated circuit achieves an effective 200 MHz sample rate by using four 32 stage peristaltic CCDs to sample the transient signal four times each clock period. Dual frequency, 4ϕ clocking is used to sample and time expand the sampled data. The output signals of the four CCDs are multiplexed on-chip into a single low frequency output data line. When operated with 50 MHz/165 KHz 4ϕ clocks, this circuit has a 200 MHz sample rate, a record length of 640 nanoseconds, a time expansion factor of 303, and overall signal to noise ratio of 40:1. The signal to noise ratio is limited by fixed pattern noise of the four CCDs.

I. INTRODUCTION

A 50 MHz peristaltic CCD integrated circuit has been developed for use in transient analog signal recorders to sample and time expand transient signals before they are processed by a low speed A/D converter and digital memory. CCDs have previously been shown to be a useful element in this application (Ref. 1-3). This integrated circuit uses four CCDs to sample the transient signal four times each clock period to achieve a 200 MHz sampling rate. The time expansion operation involves clocking the electrical transient into the four CCDs at a 4ϕ clock frequency of 50 MHz and after some desired record length, switching the clock frequency to 100 to 200 KHz to read out the sampled data. The output signals of the four CCDs are multiplexed on-chip into a single output line.

II. CHIP DESIGN AND FABRICATION TECHNOLOGY

A. BURIED CHANNEL CCD TECHNOLOGY

Figure 1 shows the chip which consists of four 32 stage peristaltic CCDs positioned side by side so as to utilize a common 4ϕ clock structure. Each CCD is isolated from its neighbor and the rest of the chip by a 10 μm wide P+ channel stop diffusion. The devices have been constructed in a 4 μm thick N type epitaxial layer deposited on a P type substrate to achieve the very high speed charge transfer via large fringing fields (Ref. 4). The doping concentrations are 4×10^{14} and 6×10^{14} cm^{-3} for the epitaxial layer and substrate respectively. The 4ϕ clock electrodes are double layer polysilicon gates 11 μm long and span the four 250 μm wide channels. The channel oxide thickness under all the polysilicon gates is 0.15 μm. The overall chip dimensions are 2 mm by 2.8 mm.

B. INPUT STRUCTURE

Four N+ input diffusions and a common aluminum input gate comprise the input structure of the circuit as shown on the left side of Figure 1. The input gate is aluminum to allow it to overlap the first clocking electrodes which are on different levels of polysilicon for the four CCDs. The diffusions are staggered on a diagonal so that the first clocking electrode of each CCD is connected to a different clock phase to achieve four data samples per clock period. The transient signal can be applied to either the input gate or the diffusions. Most of our high speed measurements were made with the transient applied to the input gate and the input diffusions pulsed low for a very short time each clock period to inject a charge packet into the first potential well of each CCD. The input structure was d.c. biased to operate in a pulsed dynamic injection method with the transient signal on the input gate modulating the size of the charge packets introduced into the CCDs (Ref. 5). Figure 2 is a timing diagram of the significant input clocks for one representative CCD. The input diffusion clocks were phased so that they would inject a charge packet into the four CCD channels when a potential well existed under the first two clocking electrodes of each CCD.

C. OUTPUT STRUCTURE

The output section of the chip detects the charge packets in the four CCD channels and multiplexes the four parallel data signals into one output signal. Each of the four CCD channels uses a gated charge integrator consisting of a reset FET and an output source follower FET to detect the charge packets. The four floating N+ diffusions used for sensing the charge packets in the channels are staggered diagonally so that the last clocking electrode is a different phase for each of the CCDs. This organization, shown on the right side of Figure 1, permits each of the output FETs to sense the charge packets in different quarter segments of a clock period. The floating diffusions are separated from their respective last clocking electrode by a common aluminum output gate.

Aluminum was used in the same manner as for the input gate to permit overlapping of both levels of polysilicon used in the clocking structure with the common output gate. To multiplex the four output signals, the source terminals of the four output FETs were connected together on chip to a common bond pad and to an off-chip load resistor. Although this connection simplifies off-chip circuitry, the maximum voltage gain of the four output source followers operated in parallel is one quarter rather than unity. In addition, the reset gates were bonded together on chip and driven by a single reset gate clock operating at four times the frequency of the low frequency 4ϕ clock. The timing diagram for this common reset gate clock and the 4ϕ clocks operating at low frequency is shown in Figure 3. The timing of the reset gate signal was adjusted so that all reset gates were reset and turned off immediately before any clock phase goes to a low voltage state.

III. EXPERIMENTAL RESULTS

A. TEST CIRCUITS

Figure 4 shows a block diagram of the test circuits used for the time expansion mode of operation. For device diagnostic purposes the transient test pulse generator supplies a test signal to the input gate of the four CCDs in sync with the 50 MHz 4ϕ clock. The sync pulse is provided by a gate output pulse of a commercial oscilloscope. This sync pulse also starts a counter that counts the desired number of 50 MHz clock cycles before sending a trigger pulse to the frequency control and 4ϕ clock circuit that then switches the clock frequency from 50 MHz to a lower readout frequency. The frequency control and 4ϕ clock circuit uses a divide by four emitter coupled logic circuit (ECL) to generate the 4ϕ clock signals from a master clock signal supplied by either the f_{Hi} oscillator or the f_{Lo} oscillator. The ECL circuit maintains the phase integrity of all four clock phases at the instant of switching from 50 MHz to the readout frequency. Commercial pulse amplifiers increase the 4ϕ ECL level clock signals to 6 volts before the clock signals are applied to the CCD. Also, the 4ϕ ECL clock signals are used to trigger four additional clock generators that supply the input diffusion clock signals. The reset gate clock generator is synchronized to the f_{Lo} master oscillator so as to operate at four times the low frequency of the 4ϕ clock signals.

B. CCD PERFORMANCE

The performance of the CCD circuit when operated in the time expansion mode has been characterized by examining its response to rectangular pulse and linear ramp waveforms. Figure 5 shows an input pulse about 190 nanoseconds wide and the sampled output pulse time expanded to about 60 microseconds wide. The CCD clock frequency was switched from 50 MHz to 165 KHz for this result. The output signal voltage of this pulse is 34 mV with no fat zero having been introduced. The full well output signal voltage for the CCDs is about 55 mV. This corresponds to a measured full well charge packet of 0.23 picocoulomb. The charge transfer efficiency (CTE) of the CCDs has been measured to be greater than 0.9998 per transfer for a total of 128 (4 x 32) high speed transfers at 50 MHz. This CTE is sufficiently large that no output voltage difference can be seen between a single packet having 128 transfers at 50 MHz and a packet having only four transfers at 50 MHz and 124 low frequency transfers.

The response of the circuit to a linear ramp is shown in Figure 6. Figure 6a shows the input ramp applied to the common input gate electrode of all four CCDs and Figure 6b the time expanded output signal. As seen from the output signal waveform, the response of the circuit becomes increasingly nonlinear for low level charge packets. Consequently, we have found it necessary to bias the device into a more linear region of operation by introducing a background charge corresponding-to about 7 to 10 mV of output signal. For Figure 6b a 7 mV background signal was introduced to improve its linearity.

To obtain waveforms like those of Figures 5 and 6, we found it necessary to compensate any fixed pattern noise due to unequal response of the four CCDs by adjusting the individual d.c. bias levels of the four input diffusions. Some of the causes of unequal response of the four CCDs include (1) different clock voltages and waveshapes of the 4ϕ clocks and input diffusions clocks, (2) different electrode areas of the first clocking electrodes of the four CCDs and (3) different voltage gains of the four gated charge integrators. We have been able to compensate for these differences to the extent shown by the results of Figures 5 and 6 by individually adjusting the d.c. biases of the four input diffusions to obtain a smoothed output response to a linear ramp input. It has been possible to reduce this fixed pattern noise so that the ratio of the peak signal to the peak fixed pattern noise is about 40:1.

The fixed pattern noise among the four CCDs is much larger than the intrinsic noise of a single CCD channel as measured by a pulse height analyzer (PHA). The PHA was used to sample and record the output voltage distribution of a full well charge packet repeatedly injected into a single CCD channel. The noise distribution was nearly Gaussian and the signal to noise ratio was calculated as the ratio of the maximum signal to the full width half maximum. This number was repeatedly measured to be greater than 90:1. For this measurement, no prefiltering was done to remove any noise of the output FET or reset FET.

IV. CONCLUSION

Sampling of transients at a 200 MHz rate and their subsequent time expansion to output sample periods greater than 5 µs has been accomplished by operating four CCDs on a single chip at a 50 MHz 4ϕ clock frequency. The output signal amplitude, linearity and noise has been described. Further improvements are needed in the input and output sections of the CCDs to reduce the fixed pattern noise and improve the linearity of the circuit.

ACKNOWLEDGEMENTS

This work was performed under the auspices of the U.S. Energy Research and Development Administration under contract number W-7405-Eng-48.

The authors wish to acknowledge the fabrication assistance of F. Cook, K. Mayeda, W. Tindall and J. Trevino and the electronics assistance of L. Mendonca.

REFERENCES

1. Chan, Y. T., French, B. T., and Green, P. E., "Extremely High Speed CCD Analog Delay Line," Proceedings of 1975 International Conference on the Application of Charge-Coupled Devices, pp. 389-398, San Diego, CA, October 29-31, 1975.

2. Gradl, D. A., Groenwald, R. A., and Flanagan, T. J., "High Speed Operation of CCDs," ibid., pp. 399-412.

3. Linnenbrink, T. E., Monahan, M. J., and Rea, J. L., "A CCD-Based Transient Data Recorder," ibid., pp. 443-453.

4. Esser, L. J. M., Collet, M. G., van Santen, J.G., "The Peristaltic Charge Coupled Device," International Electron Devices Meeting, pp. 17-20, Washington, D.C., Dec. 3-5, 1973.

5. Sequin, C. H. and Mohsen, A. M., "Linearity of Electrical Charge Injection into Charge-Coupled Deivces," IEEE J. Sol. St. Circuits, Vol. SC-10, No. 2, pp. 81-92, April 1975.

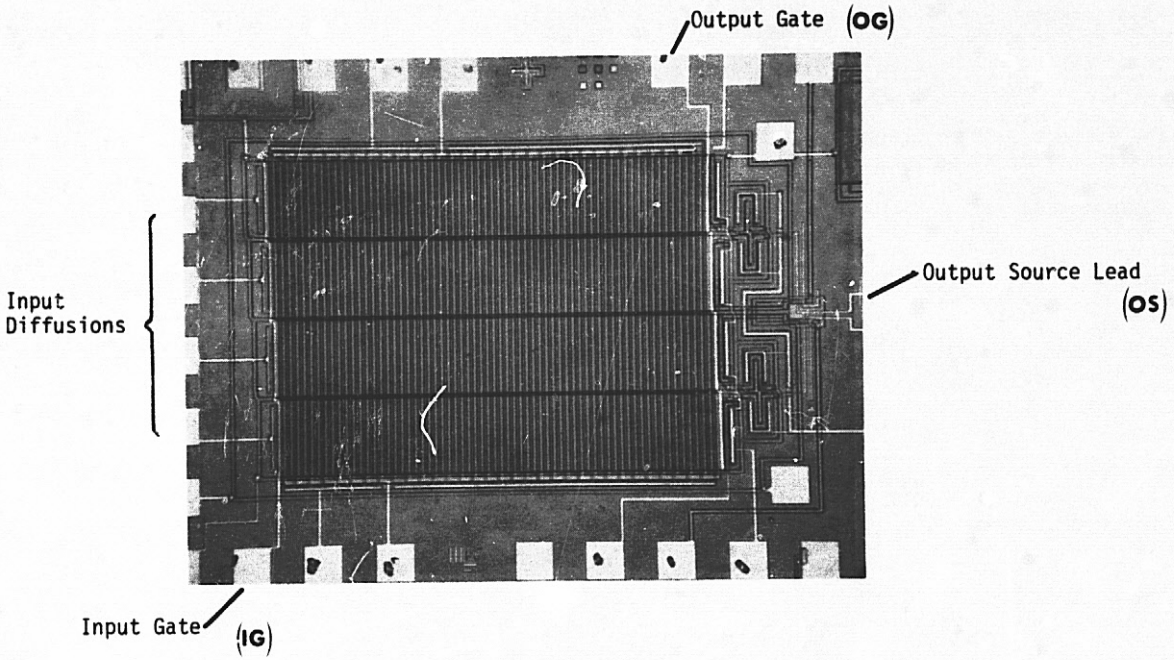

Fig. 1. Photomicrograph of Transient Recorder Chip

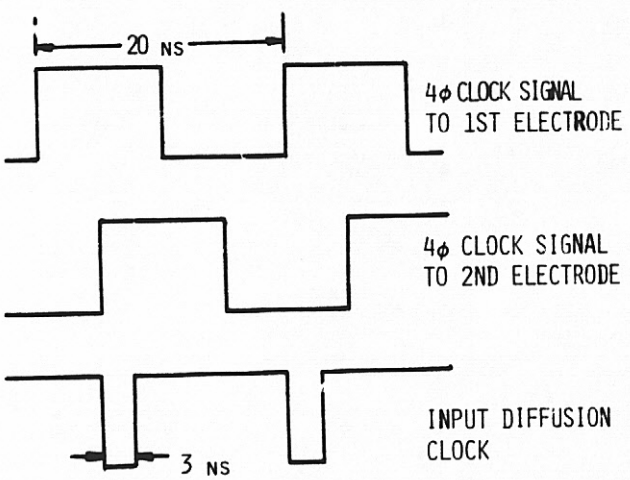

Fig. 2. Timing diagram of significant clocks at input structure of one CCD channel.

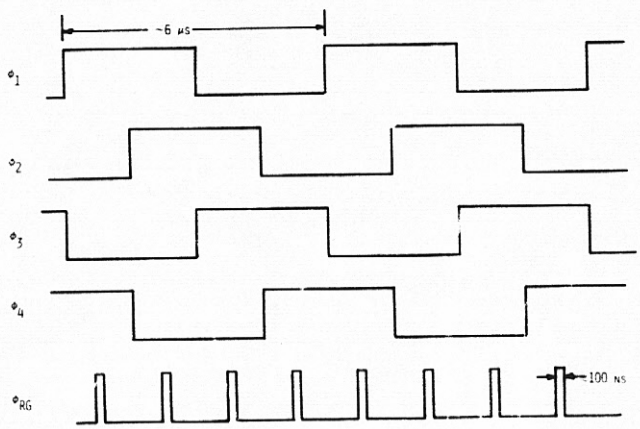

Fig. 3. Timing diagram of reset gate and 4 φ clocks operating at low frequency.

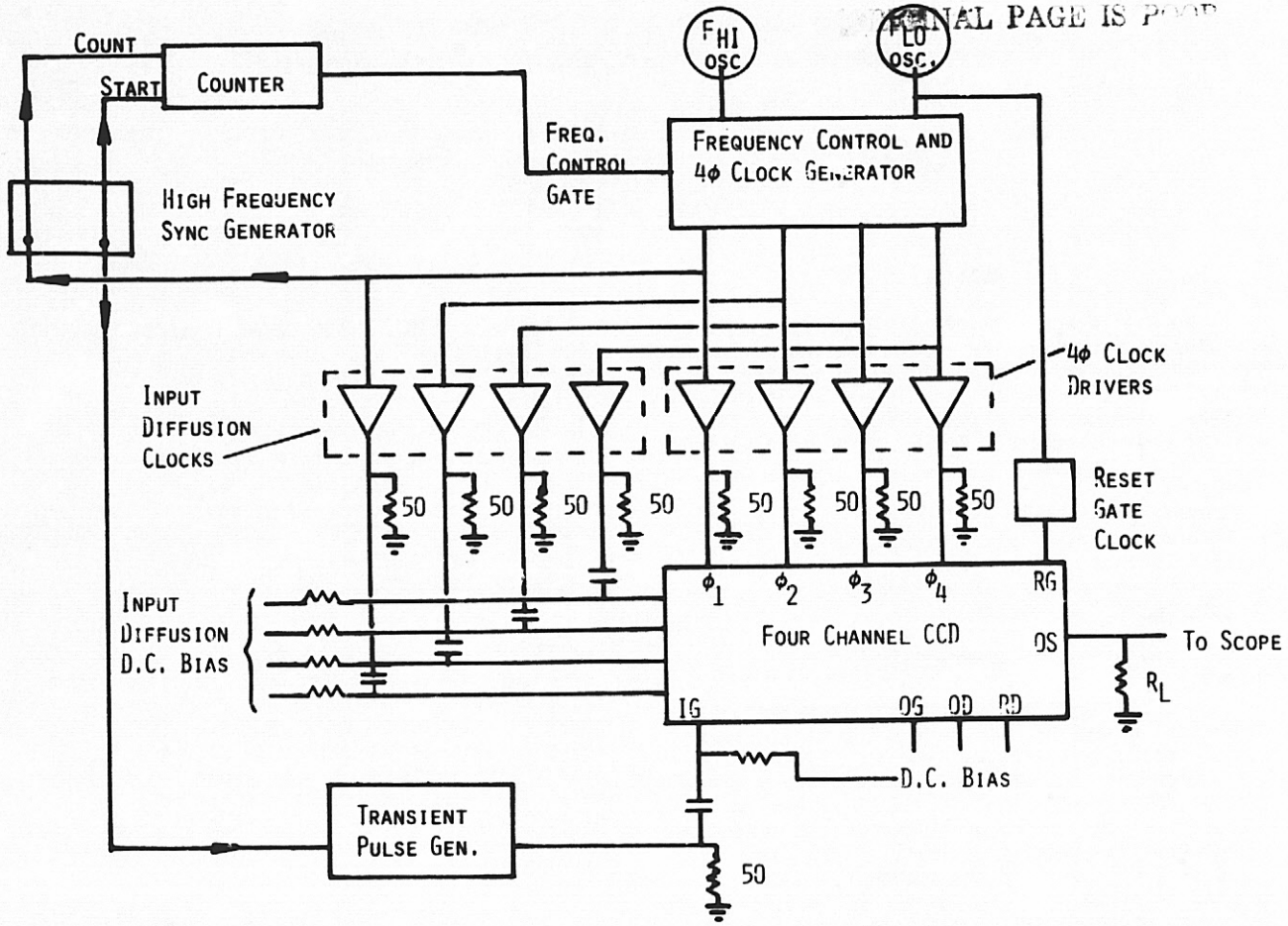

Fig. 4. Test Circuit for Time Expansion Operation

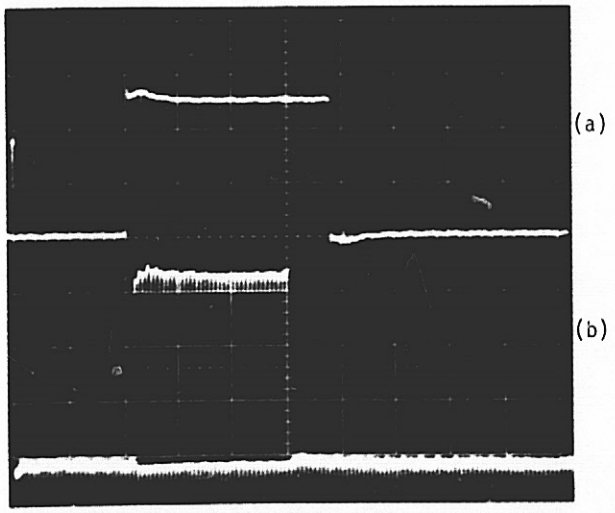

Fig. 5. Pulse response
(a) Input: 2V/DIV., 50 NS/Div.
(b) Output: 10 mV/DIV., 20 µs/DIV.

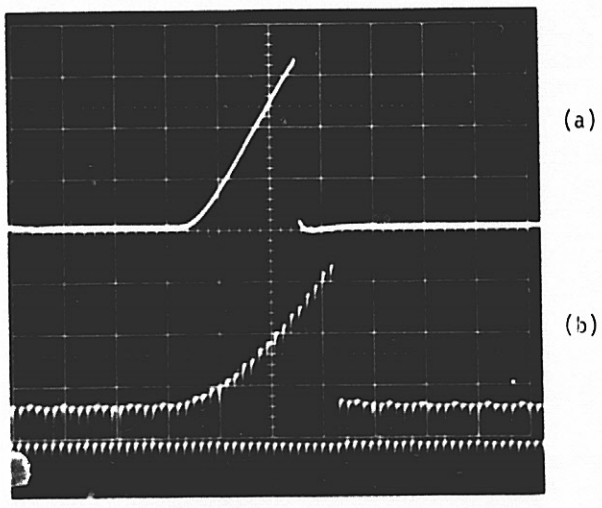

Fig. 6. Ramp response
(a) Input: 1V/DIV., 50 NS/DIV.
(b) Output: 10 mV/DIV., 10 µs/DIV.

916

N77-17279

LINEAR CHARGE COUPLED DEVICE DETECTOR ARRAY FOR IMAGING LIGHT PROPAGATING IN AN INTEGRATED THIN-FILM OPTICAL WAVEGUIDE*

C.L. Chen and J.T. Boyd
Solid State Electronics Laboratory
Department of Electrical and Computer Engineering
University of Cincinnati
Cincinnati, Ohio 45221
(513) 475-4461

ABSTRACT

We will discuss device design, fabrication, and operation of a linear charge coupled device (CCD) detector array integrated with a thin-film optical waveguide and applications of this structure to integrated optical signal processing and fiber optical communications. A two-phase, overlapping-gate CCD is connected in parallel by means of a series of gates to an array of photodiodes. The photodiode provides an electrode-free surface region so that a highly-efficient waveguide-detector coupling technique can be implemented. A thermally-oxidized layer of SiO_2 forms an effective substrate for the optical waveguide.

I. INTRODUCTION

A CCD linear imaging array integrated with an optical waveguide structure has been fabricated and successfully operated. In this integrated device guided optical waves propagate along the wafer surface entering the imaging device laterally as opposed to from the top or bottom of the device as in conventional imaging devices. Light can be confined in a thin-film in the transverse dimension perpendicular to the film surface by having a film thickness on the order of the optical wavelength and a refractive index greater than that of the substrate. As a thick layer of SiO_2 having refractive index n = 1.46 serves as the effective substrate for the thin-film waveguide, a wide variety of thin films having a larger refractive index can be utilized to form optical waveguides. If the film is uniform along the direction parallel to the axis of the detector array, a slab waveguide exists and the function of the CCD linear detector array is to image light in this transverse direction. This light variation could be the result of parallel optical signal processing performed at another location in the optical waveguide. Alternately, a number of parallel channel waveguides could be defined photolithographically with each channel waveguide coupling to a single array element. Although both types of structures are expected to find applications in signal processing and optical communications, the present discussion will generally be confined to the slab waveguide structure.

II. DEVICE STRUCTURE AND OPERATION

The integrated optical waveguide and CCD linear image array are formed on a common silicon substrate with the optical waveguide being formed on a layer of SiO_2. This layer is sufficiently thick (typically $\sim$ 1 μm.) so that evanescent coupling of light from the waveguide to silicon is negligible, except in the detector region. In the detector region, the SiO_2 layer tapers to zero thickness so that light in the waveguide is coupled into the silicon substrate.[1] A taper which minimizes optical scatter is formed by allowing a carefully controlled amount of undercutting to occur during etching in device processing. A profile of the integrated waveguide - CCD detector structure is shown in Figure 1. Note in Figure 1 that the waveguide is continuous along the diode region instead of directed and terminated onto this region. Such a configuration causes the light reflected from the waveguide-silicon interface to be totally-internally reflected from the waveguide surface and incident again on the waveguide-silicon interface. Since the waveguide continues along the detector region, this process repeats itself many times. The resulting multiple refraction of light into the detector minimizes detector loss due to reflection.

The detector array in Figure 1 consists of an array of photodiodes formed in n-type silicon connected in parallel by means of a series of gates to a CCD shift register. The charge transfer portion of the device utilizes a two-phase, overlapping-gate structure consisting of one level of polysilicon electrodes insulated by an additional layer of SiO_2 from a second level of overlapping aluminum electrodes.[2] One CCD unit cell corresponds to each photodiode. Channel isolation is maintained through the series of gates by the presence of channel stopping n+ regions. The detector array integrates the optical signal incident on the array of photodiodes as the potentials of the control and integration gates are adjusted so that charge excited by incident light collects underneath the integration gate. At the end of the integration period T, the transfer gate is turned on so that the collected charge is transferred into the shift register. This charge transfer occurs simultaneously for each array element and in a time less than 1/2 of the CCD clock period. Once this charge has transferred into the shift register, the transfer gate is turned off and the charge is shifted along the register to the end where a serial, discrete-time signal emerges representing the spatial light distribution. As soon as the transfer gate is turned off, the photosensors begin integrating

* Research sponsored by the Air Force Office of Scientific Research, Air Force Systems Command, USAF, under Grant No. AFOSR-76-3032 and under a subcontract from Rockwell International as prime contractor for the Air Force Avionics Laboratory. The United States Government is authorized to reproduce and distribute reprints for Governmental purposes notwithstanding any copyright notation hereon.

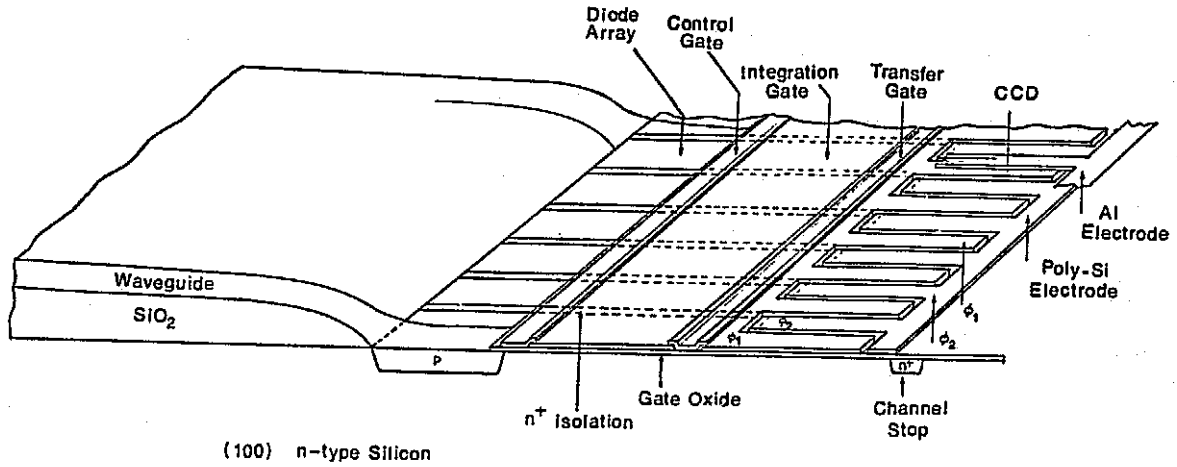

Figure 1. Integrated optical waveguide and CCD detector array.

charge and the cycle is repeated. The integration time is thus N times the lock period where N is the number of CCD cells equal to the number of array elements. Because charge integration can occur while CCD readout takes place, sensing takes place essentially 100% of the time.[3] For many applications of the integrated waveguide - CCD detector array, minimizing the array element center-to-center spacing allows the information handling capability to be maximized.[4] Such spacings will generally be limited by lithography considerations. Large aspects ratios of the rectangular photodiode region are generally undesirable. The question thus arises as to whether the extent of the photodiode in the direction of light propagation L can be chosen sufficiently large so that nearly all light incident can be multiply refracted into the detector region. To examine this question, we consider the decay of light intensity along the photodiode surface in the direction of light propagation I(z), given as

$$I(z) = I_0 e^{-\alpha_e z} \qquad (1)$$

In (1) α_e is an effective decay constant accounting for light coupled into the photodiode region given as

$$\alpha_e = \frac{1-R}{d \tan \theta}, \qquad (2)$$

where d is the waveguide thickness and θ is the waveguide mode characteristic angle with respect the waveguide surface normal. R in (2) is the appropriate Fresnel reflection coefficient at the waveguide-silicon interface for the mode characteristic angle and polarization in question.[6] We will restrict our present discussion to the TE_0 mode. For a thin SiO_2 layer in the photodiode region evanescent wave coupling will occur causing the field in the waveguide to decay according to (1) and (2), but with R interpreted more generally as a composite reflection coefficient. As evanescent coupling is weaker than multiple refractive coupling, multiple refraction is preferred as it allows minimization of the photodiode length L required for efficient coupling. An analysis of photodiode quantum efficiency for the type of waveguide coupling described herein has shown that for a variety of situations the quantum efficiency increases with $\alpha_e L$ until $\alpha_e L \sim 3$.[1] Since further increase of $\alpha_e L$ causes no significant increase in quantum efficiency, an optimum value of detector length L_0 can be defined as

$$L_0 = 3/\alpha_e. \qquad (3)$$

The magnitude of the device quantum efficiency for detector lengths greater than (3) saturates at a value determined by the silicon absorption coefficient at the wavelength of interest, depletion region depth, carrier diffusion lengths, and depth of the surface recombination region.

We have calculated the optimum detector length L_0 for the TE_0 mode as a function of waveguide thickness d for a waveguide refractive index of $n_g = 1.61$. This refractive index is characteristic of the KPR photoresist waveguides used in the experiments described herein, as well as characteristic of 7059 sputtered glass waveguides. The result of the calculation is shown in Figure 2 for $\lambda = .9$ μm and .6 μm. The portions of the curves to the left of the dotted vertical lines are the regions in which only a single TE mode can exist. In the single mode regions the optimum detector lengths would allow fabrication of efficient photodiodes with reasonable aspect ratios and with center-to-center spacings approaching photolithographic limits. However, for multimode waveguides the corresponding optimum detector lengths become quite long. It is fortunate that in many signal processing applications use of a single-mode waveguide is advantageous in view of other considerations.[4] In Fourier optical processing utilizing optical waveguide lenses the integrated waveguide-detector array described herein would find application in focal imaging. If L_0 exceeds

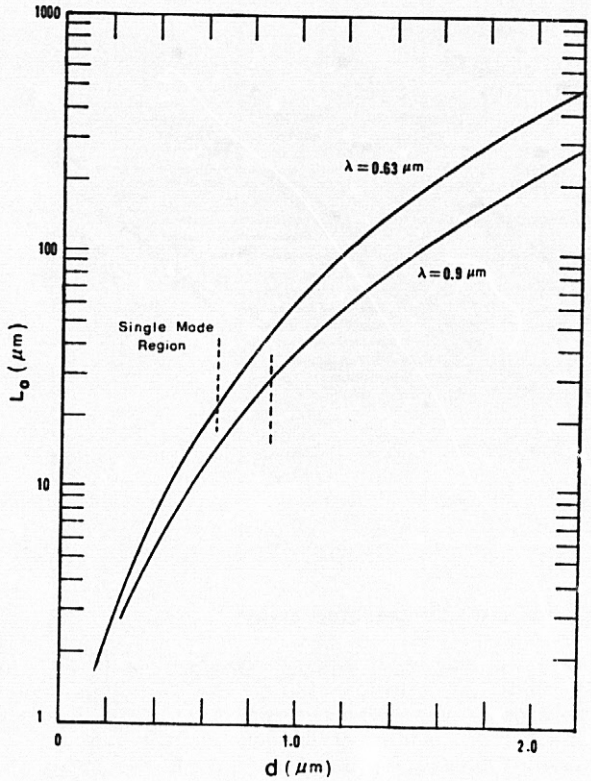

Figure 2. Detector length for efficient coupling of light from waveguide to detector as a function of waveguide thickness for a waveguide refractive index n = 1.61.

the depth of focus for such applications, then an array of channel waveguides, one passing directly over each photodiode would be required to preserve signal integrity.

The integrated waveguide-CCD detector array configuation shown in Figure 1 was fabricated using n type silicon having resistivity of 8 ohm-cm. and 100 orientation. The detector portion of the resulting device is shown in Figure 3. This device contains 19 array elements with the photodiodes measuring 25 μm x 115 μm with 7 μm of isolation between adjacent elements. In view of Figure 2, the photodiode length of 115 μm is quite sufficient for effective coupling for the KPR photoresist waveguide employed in our experiments. However, this length would be somewhat long if we were to attempt to reduce the center-to-center spacing to the photolithographic limit. The two-phase overlapping gate CCD has a conventional charge collection diode for signal output and a charge injection diode for serial input. The latter allows for electronic evaluation of the CCD and for serial injection of bias charge.

After initial probe testing of fabricated devices, individual arrays were mounted and bonded in dual-in-line packages. The packages employed were specifically altered so they could accomodate a sufficiently large piece of silicon that would allow space for prism coupling of light into the waveguide and for waveguide propagation. Once packaged the devices could then be inserted in a

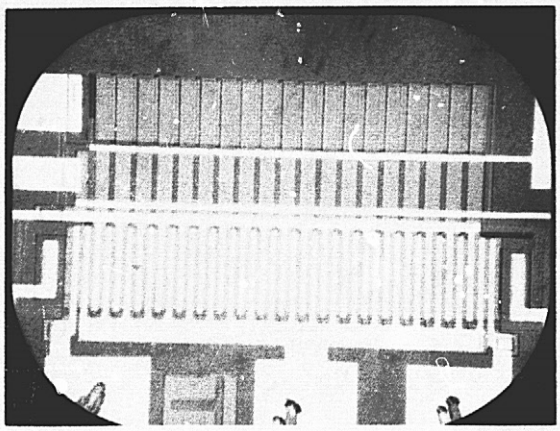

Figure 3. Linear photodiode imaging array coupled to a two phase, overlapping gate CCD.

socket attached to a standard prism coupling optical mount. A macroscopic view of HeNe laser light coupled into the optical waveguide through a prism coupler[5] is shown in Figure 4-a. The bright area on the left is a top view of the prism illuminated by scattered light, while the dark area in the center is a clamp pressing the prism against the surface. The streak of scattered light is approximately 125 μm wide and corresponds to the light beam which had been externally focused propagating until it reaches the detector region. Bonding wire leading from bonding pads on silicon to connections on the package is illuminated by scattered light. The detector array is located between the termination of the streak of light and the bonding pads. Because the magnification in Figure 4-a is considerably less than that in Figure 3, details of the CCD detector array are not resolvable. Note that there is no visible indication of excess scatter occuring in waveguide-detector coupling. Figure 4-b is an oscilloscope trace of the signal emerging from the CCD corresponding to the laser excitation in Figure 4-a. Differential amplification of the signal was used to eliminate some of the pickup from the clock pulses.

The device was operated with a two-phase clock producing overlapping pulses in the 100 KHz frequency range. Counter circuitry synchronized to the clock was used to control pulsing of the transfer gate so that this gate was turned on only after charge in the CCD shift register had been completely shifted out. Counter circuitry was also employed to provide a suitable electronic input for electronic evaluation of charge transfer efficiency. Charge transfer efficiency can be evaluated by serially injecting several low duty-cycle rectangular pulses with each separated by one clock period.[7] By carefully noting the degradation of the leading and trailing edges of the pulse train, information regarding transfer efficiency can be inferred. For the devices fabricated we determined a transfer efficiency of .993 per double transfer. Although this value is adequate for performance of our 19 stage device, higher values can be obtained. Good charge transfer efficiency requires very sharp lateral potential barriers.[8] Although the purpose of the channel stop diffused regions is to provide such

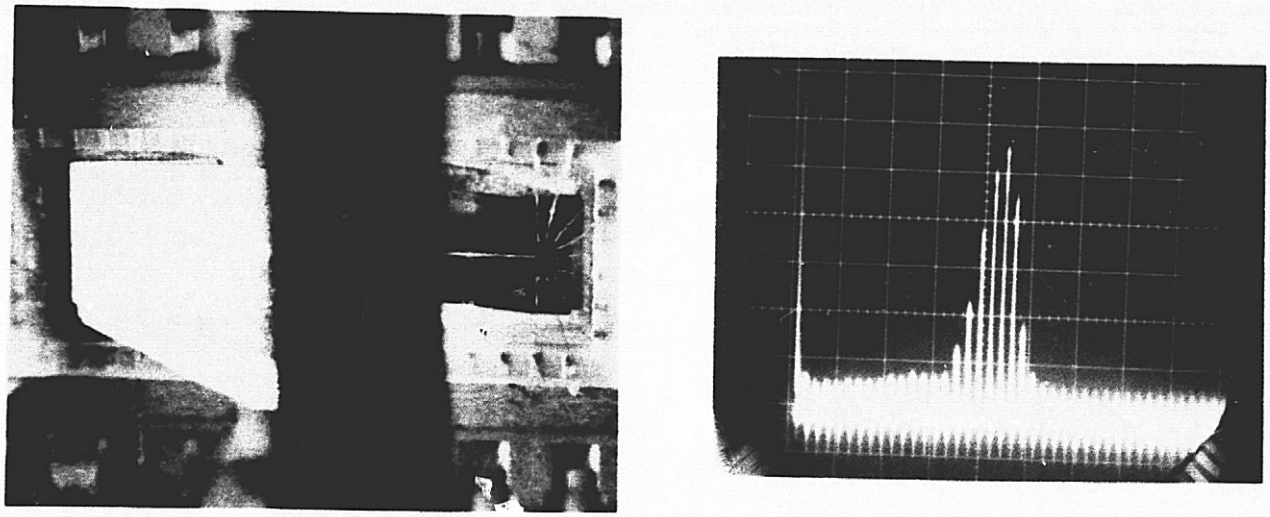

Figure 4. (a) Light propagating in an optical waveguide from the prism coupler to the integrated CCD detector array. (b) CCD output signal corresponding to illumination shown in (a).

n+ barriers, the device processing sequence we employed involved a high temperature thick gate oxide growth step after the channel stop diffusion. Further diffusion thus would occur during the oxide growth, resulting in more gradual lateral barriers. Evidence that this was indeed occuring was obtained from the transfer efficiency measurements in that larger values of bias charge than usual were required to eliminate fixed transfer loss.[7] The problem can be overcome by using ion implantation for channel stop doping and altering the processing sequence.

III. APPLICATIONS

The integrated optical waveguide and charge-coupled device (CCD) linear imaging array structure is expected to find many applications in integrated optical signal processing device structures. Optical signal processing using an integrated optical format combines the advantages of parallel processing with those present in an efficient, compact, and economical device. Parallel processing occurs when information is imparted to the transverse spatial distribution of an optical wave. Appropriate modulation and processing techniques include highly-efficient and wide band acoustooptic deflection,[9] electrooptic deflection,[10] and one-dimensional spatial Fourier transformation performed by an optical waveguide lens.[11]

For example, integrated optical acoustooptic deflection, optical waveguide lenses, and an integrated waveguide-detector such as described herein can be used to perform wide band spectrum analysis of electronic signals by employing the configuration shown in Figure 5.[4]

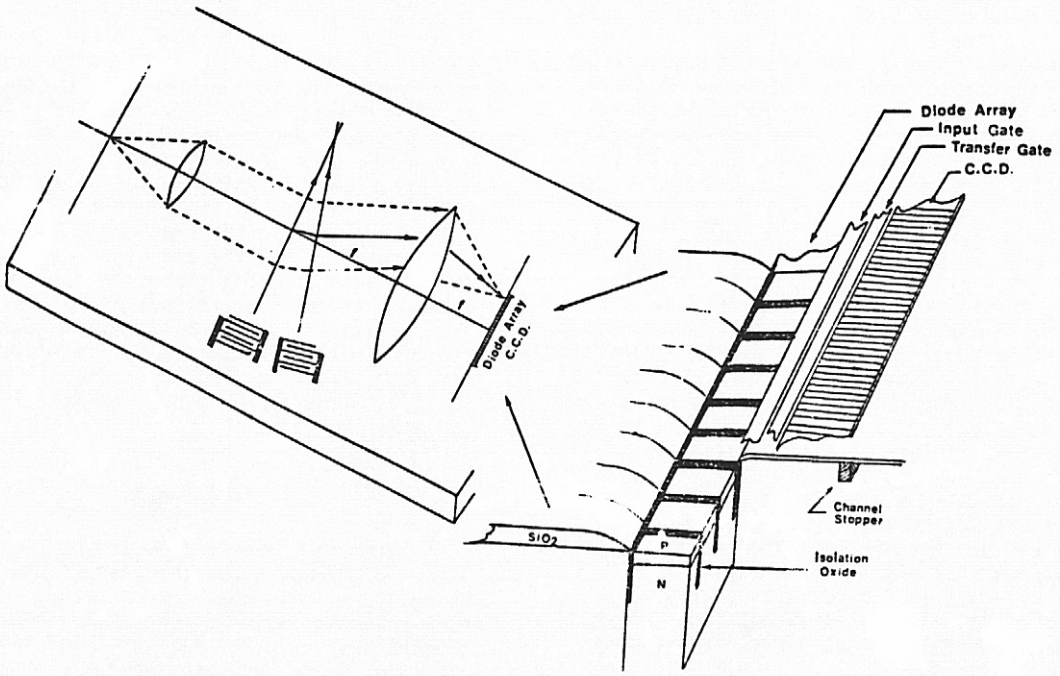

Figure 5. Integrated optical spectrum analyzer configuration.

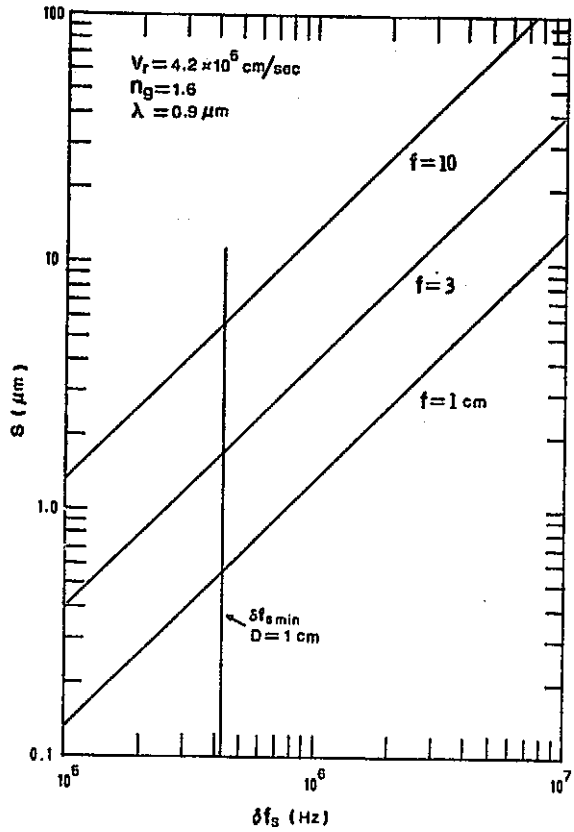

Figure 6. Detector array center-to-center spacing as a function of spectrum analyzer frequency resolution.

Coherent laser light propagating in a thin-film waveguide is expanded and collimated prior to being incident on a surface elastic wave which has been excited by the incoming signal. Surface elastic waves can be excited efficiently on silicon using a ZnO film in the transducer region.[12] Diffraction of light by the surface elastic wave occurs in such a way that light is diffracted at different angles corresponding to different signal frequency components. The signal frequency range of the spectrum analyzer corresponds to the bandwidth of the surface elastic wave transducer configuration. For a range of signal frequencies and wave intensities, the deflection angle is linearly proportional to the signal frequency and the diffracted light amplitude is linearly proportional to the signal surface elastic wave amplitude. A waveguide lens is then positioned so as to perform a one-dimensional Fourier transform. Signal spectral information which is represented by the angular composition of light emerging from the surface elastic wave region then becomes represented by the transverse spatial variation of light in the Fourier transform plane. The intensity of the light spatial distribution in the transform plane corresponds to the signal power density spectrum and can then be converted to an electrical signal by means of a detector array. With the presence of a CCD in the detector array, transformation of the electrical signal from a parallel format into a serial format occurs in a natural and simple way.

Information capacity of integrated optical signal processing devices will be limited by beam diffraction or array resolution and detector dynamic range.[4] In particular, the nature of acoustooptic deflection and of the Fourier transform property of lenses causes the optical diffraction pattern in the lens transform plane to be displaced by a distance s for a signal frequency deviation δf_s, where [4]

$$s = \frac{f\lambda}{n_e v_r} \delta f_s \ . \qquad (4)$$

In (4) f is the lens focal length, λ is the optical wavelength, n_e is the waveguide mode effective refractive index, and v_r is the Rayleigh wave velocity. If the detector array in Figure 5 is spacing of s, then λf_s is the frequency difference which can be resolved by the spectrum analyzer. The relationship between center-to-center spacing and frequency resolution is illustrated in Figure 6 for several focal lengths and typical parameters. As expected, smaller center-to-center spacings are required to resolve smaller frequency differences. The vertical ine in Figure 6 corresponds to the diffraction-limited frequency resolution for a 1 cm. aperture. Once this assymptote has been reached, further reduction in detector center-to-center spacing cannot improve frequency resolution. As the presence of optical scattering will reduce both spectrum analyzer frequency resolution and dynamic range, integration of the array into the optical waveguide, and thereby minimizing scattering occuring in waveguide-detector coupling, will allow superior performance as compared with the use of an external detector array.

The integrated waveguide-CCD detector array may find additional applications based on its inherent property of parallel entry of signal information into a CCD shift register. Optical injection of parallel signals into CCDs offers significant advantages over electrical injection techniques, in that for the latter sophisticated stabilized charge injection circuits would likely be required for each entry tap. Furthermore, capacitive coupling limits both the proximity of adjacent taps and the maximum usable signal frequency for parallel electrical injection. Parallel optical signal injection using bulk optical waves along with a mask to implement a fixed tap weight transversal filter has previously been demonstrated[13] We anticipate that the use of integrated optical channel waveguide-detector structures could yield a programmable device with potentially a large channel density and almost complete channel isolation. Parallel integrated optical signal injection into CCDs may also find application in multiplexing, other types of programmable filtering, and memory devices.

IV. SUMMARY

Successful fabrication and operation of a linear CCD image array integrated into an optical waveguide structure have been described. Data have been presented with regard to the optimum array element size required for the light wave to be efficiently coupled into the detector region. Minimal excessive scattering in the region where

coupling of light from the waveguide to the detector occurs was observed. The integrated structure that has been described herein is expected to serve as a basic element in integrated optical signal processing devices and to provide a method for parallel entry of information into CCDs.

We would like to acknowledge J. T. Garrett for providing technical assistance, S. G. Garg for performing the polysilicon deposition, and A. J. Van Velthoven of the NCR Microelectronics Division for supplying the device packages. Helpful discussions with D. B. Anderson and M. C. Hamilton are also appreciated.

REFERENCES

1. J. T. Boyd and C. L. Chen, "Integrated Optical Silicon Photodiode Array," Appl. Opt. Vol. 15, pp 1389-1393, 1976.

2. W. F. Kosonocky and J. E. Carnes, "Two Phase Charge-Coupled Devices with Overlapping Polysilicon and Aluminum Gates," RCA Rev. Vol. 34, pp 164-202, 1973.

3. M. F. Tompsett, G. F. Amelio, W. J. Bertram, R. R. Backley, W. J. McNamara, J. C. Mikkelsen, and D. A. Sealer, "Charge Coupled Imaging Devices: Experimental Results," IEEE Trans. Electr. Dev. Vol. ED-18, pp 992-996, 1971.

4. D. B. Anderson, J. T. Boyd, M. C. Hamilton, and R. R. August, "Integrated Optics Approach to the Fourier Transform," to be published.

5. P. K. Tien, and R. Ulrich, "Theory of Prism-Film Coupler and Thin Film Light Guides," J. Opt. Soc. Am. Vol. 60, pp 1325-1337, 1970.

6. M. Born and E. Wolfe, Principles of Optics, Second Edition, Pergamon Press, 1964.

7. R. W. Brodersen, D. D. Buss, and A. F. Tasch, "Experimental Characterization of Transfer Efficiency in Charge-Coupled Devices," IEEE Trans. Electr. Dev. Vol. ED-22, pp 40-46, 1975.

8. C. H. Sequin and M. F. Tompsett, Charge Transfer Devices, Academic Press, 1975.

9. C. S. Tsai, M. A. Alhaider, L. T. Nguyen, and B. Kim, "Wideband Guided-Wave Acoustooptic Bragg Diffraction and Devices Using Multiple Tilted Surface Acoustic Waves," Proc. IEEE, Vol. 64, pp 318-328, 1976.

10. C. S. Tsai and P. Saunier, "Ultrafast Guided-Light Beam Deflection/Switching and Modulation Using Simulated Electro-optic Prism Structures in $LiNbO_3$ Waveguides," Appl. Phys. Lett. Vol. 27, pp 248-250, 1975.

11. R. Shubert and J. H. Harris, "Optical Guided Wave Focusing and Diffraction," J. Opt. Soc. Amer., Vol. 61, pp 154-161, 1971.

12. F. S. Hickernell, "Zinc Oxide Thin-Film Surface Wave Transducers," Proc. IEEE, Vol. 64, pp 631-635, 1976.

13. M. A. Copeland, D. Roy, J. D. E. Beynon, anc F. Y. K. Dea, "An Optical CCD Convolver," IEEE Trans Electr. Dev. Vol. ED-23, pp 152-155, 1976.

N77-17280

TELEVISION CAMERAS EMPLOYING SOLID-STATE IMAGING SENSORS FOR MANNED SPACECRAFT APPLICATIONS

Bernard C. Embrey, Jr.

NASA, Johnson Space Center
Houston, Texas

ABSTRACT

In past manned spacecraft programs, particularly since the advent of Apollo, on-board television systems have served a key role in the transfer of information concerning in-space activities as they occur. The next generation of manned space programs will expand the television usage from its primarily public information role to a whole host of operational support activities that will require exacting performance capabilities. The Space Shuttle television system will incorporate a versatile complement of TV equipment which will allow the positioning, quantity, and performance capabilities of the multiple TV cameras to vary as dictated by the particular mission. However, current TV camera technology employing glass-enclosed, vacuum processed image sensors results in a bulky device that restricts its location and versatility. This paper addresses these problems and discusses the potential solutions that can be achieved through the employment of solid-state image sensors - for both monochrome and color applications.

I. INTRODUCTION

Television has continually grown in its importance for manned space flight since its early use in the Apollo Program. Beginning with Apollo 7 and continuing throughout the Apollo, Skylab, and ASTP (Apollo Soyuz Test Project) programs, more and more demands have been made resulting in expanded capabilities of the inflight TV systems. Black-and-white television was replaced by color. Television on the lunar surface evolved from a slow-scan (10 frames per second) black-and-white to an EIA-compatible field-sequential color output. Control and use of the camera system transferred from strictly crew-operated manual control to almost independently remote control operation by the mission controllers in Houston. Environmental requirements expanded from the relatively simple in-cabin situation to the very uncompromising environments of outer space and on the lunar surface. The number of cameras employed for a mission grew from one during the early Apollo flights to two for later Apollo missions and Skylab, and to four for ASTP (plus four Russian TV cameras for their system). The uses of the system and its product has also increased in complexity - initially, the TV was used practically solely for purposes of increasing the public's awareness of the space program and information dissemination. Later, support of the experimental aspects of the missions was provided, and finally experiments were conducted that employed television as an integral part of the program.

However, the next generation of manned space programs will greatly broaden the scope of television usage and the attendant demands for more exacting performance. Those activities that comprise the Space Shuttle program can best be grouped into three areas of operation - within the crew compartment, within the payload bay (an area approximately 60 feet long and 15 feet in diameter), and mounted on the remotely-controlled manipulator arms. Included in the scope of tasks that television will play a key role in supporting will be general Shuttle operations and crew activities, the onboard experimental activities, the entire spectrum of remote manipulative functions - payload inspection, deployment and retrieval, servicing, repositioning, etc., and the operations concerning the attached payload (e.g., Spacelab) programs. In a large percentage of these tasks, the success of the operation will greatly depend on the performance of the television system. Such parameters as resolution, extreme ranges of light levels, high linearity with minimum distortion, wide dynamic range, and high blooming resistance are among the key performance demands for which the Shuttle television system must be optimized.

II. PRESENT SYSTEM

The Shuttle Orbiter closed-circuit television (CCTV) system is being designed and implemented to be a versatile and flexible complement of TV equipment. This will allow the positioning, quantity, and performance capabilities of the multiple TV cameras and their associated hardware to vary as dictated by the specific requirements of a particular mission. The CCTV system as is presently baselined for use on the Shuttle program is composed of a total of five TV cameras - one portable, color camera for use in the crew compartment; one black-and-white camera mounted on the forward payload bay bulkhead and another on the aft bulkhead; and one black-and-white camera each mounted on the port and starboard remote manipulator arms. There are additional camera mounting locations being provided throughout the Orbiter for use when needed. The latter four TV cameras have a remotely-controlled pan and tilt capability which allows them practically unlimited viewing range within the restrictions of the mounting location. A variety of lenses, both fixed-focal length and zoom, with remote-control capability will be used as required to support the specific mission requirements. A small, monochrome monitor which connects to the portable, color TV camera is provided to assist the crewman in adjustments and pointing of the camera. Two console-type monochrome monitors will be mounted at the rear of the crew compartment to support the crewman as he performs a task which requires TV viewing. The CCTV system control and distribution functions are performed by two units called the video switching unit and the remote control unit which for simplicity shall be referred to herein as the video control unit (VCU).

The multitude of functions of the video control unit serves well to illustrate the

complexity of the Shuttle CCTV system. The VCU generates the master composite sync signals for all of the TV cameras, monitors, etc. It generates a color frame sync for each camera (this is in keeping with the philosophy that each camera will be designed such that conversion from monochrome to color capability, and vice versa, can be made simply thus resulting in a commonality of camera equipment), a camera location identification code, and a full field test signal (or signals) to be used in monitor setup and downlink transmission checkout. The VCU recognizes inputs from both the onboard control panel and ground uplink sources as commands to control camera, lens, pan and tilt, monitor, etc., functions which must be remotely controlled. These control messages are then amplitude-time division multiplexed with the sync signals and sent to the selected locations. Switching of all the various video inputs to the various selected outputs (including the monitors, the downlink signal processors, and payloads operating in the payload bay) is done by the VCU. Also, the VCU supplies a split-screen capability for both of the console-type monitors.

One major area of concern within the currently envisioned CCTV system configuration is the fact that the current state-of-the-art television camera - those previously proven by experience and use in space - incorporates a glass enclosed, vacuum processed image sensor. This type of sensor is highly susceptible to vibration and thermal damage thus requiring bulky protection which results in large devices and high program cost. This bulky size and its correspondingly excessive weight in many instances may prove to be very marginal if not in fact actually unusable for certain potential Shuttle mission situations. Television operations in some portions of the crew compartment will be severely hampered due to the close proximity of the candidate camera positions to the subjects of interest. The size of certain payloads; the necessary close proximity of the payload cameras to some payload extremities; the constraining nature of the volume required for a large size camera to be panned and/or tilted over a wide range; the size, weight, and volume constraints of mounting a TV camera with pan and tilt capability on a manipulator arm (whose own volume for operation and stowage represent highly restrictive problems in themselves); the need for precise, extremely accurate TV viewing of alignment cue markings used in payload manipulations... these all reflect the types of problem areas that must be addressed during the life of a multi-mission, multi-year space program, particularly with the present TV camera image sensor technology.

III. ADVANCED SYSTEMS

A television camera that employs a solid-state imaging device (SSID) as the image sensor if adaptable to the specialized performance and environmental requirements that will be encountered on manned space missions appears to offer the needed versatility. Such a camera should be much smaller than its tube-type equivalent (possibly as much as 90% smaller) since the sensor itself requires only a small fraction of the tube-required space and much of the electronic circuitry can be made an integral part of the sensor chip. A corresponding substantial reduction in camera weight estimated to be as much as 80% less than current tube sensor cameras should be attainable. Power consumption. a third highly important factor in all space flight applications, is estimated to approach an 85% reduction from the current technology.

Prototype development work by JSC with a variety of SSID technologies has produced extremely encouraging results. All indications point to the possibilities of relatively early incorporation of a solid-state TV camera into the Shuttle CCTV program as being both very feasible and quite advantageous. Solid-state TV cameras appear to offer significant improvements in certain performance parameters over those currently attainable. The linearity characteristics of the SSID appear to be significantly better than those attainable with image tubes. Lag (residual imaging) is not present with solid-state imaging devices. Low light level operation as well as designs for a wide dynamic range are progressing satisfactorily. The signal-to-noise and vertical and horizontal resolution capabilities of SSID cameras appear to be capable of achieving at least performance comparable to the commercial industry tube-type cameras. At this time, there do not appear to be any insurmountable problems associated with these SSID cameras being operated in a space environment. However, a more detailed investigation into this aspect of SSID camera development still remains to be conducted.

In terms of a long range, multi-mission program such as the Shuttle, it has been estimated that substantial cost savings can be realized. It is anticipated that the space-type version of the solid-state TV camera will result in a weight reduction of 10 pounds per camera and an approximate 90% size reduction will result in decreased mounting structure weight. Furthermore, the use of a solid-state camera will result in reduced development costs for camera thermal controls and vehicle structure/camera loading requirements. The unit cost of a solid-state camera designed for space environments is expected to be possibly one-third that of a tube-type camera. The number of tube-type cameras that have been estimated to be needed to support the Shuttle program through 1992 has been based on a limited shelf and operating life which dictates a periodic refurbishing and/or discarding of the cameras from flight status. It is estimated that the lifetime of the current image-tubes is such that they will require periodic replacement throughout the program while the SSID may need no replacement. The solid-state camera should be much less susceptible to operating life limitations and should have a greatly increased shelf life. Thus, the quantities of solid-state cameras need be much less for the program duration.

Thus far, practically all of the government and industry efforts related to solid-state TV camera development has disregarded the need for color capability. The present market potential for solid-state cameras has been concentrated in areas where black-and-white cameras are quite

adequate. However, the manned space program has identified a significant set of requirements that necessitate color. Some of these prime uses thus far identified include providing additional precision and parts discrimination information for manipulative tasks in space; providing subtle, discrete color changes for use in inspection operations, e.g., to evaluate the effects of environmental exposure of heat shields; and, enhancement of the downlinked spacecraft video pictures so as to increase their acceptance potential as an information transfer medium to the public. Essentially the same program cost reduction considerations as have been mentioned above would apply for the color solid-state TV camera case with a greater percentage unit cost reduction possibly being realized.

Intensification of emphasis for development of a color solid-state TV camera suitable for use on manned space missions is currently being undertaken. Certain major design considerations must be addressed in order to be acceptable as a replacement for the currently employed tube-type color TV camera. The primary problem area concerns the attainment of a balanced spectral response for the three primary colors (red, green and blue) of the visible spectrum. The current SSID technology exhibits a relatively low blue response. Another consideration is achieving operating performance characteristics approaching, if not comparable to, the monochrome camera version. Certain techniques that could be employed to achieve a color capability as well as balancing the spectral response might lead to a color camera but with a severely reduced overall performance capability. Lastly, an evaluation is required to determine whether, for space applications, the full NTSC (National Television System Committee) or a quasi-field-sequential mode (field sequential color is presently employed for manned spacecraft transmission systems) of color generation should be used.

In summary, solid-state television cameras most certainly will figure prominently in future manned space programs. Intensified development work is currently progressing with the goal of incorporating low cost, high performance SSID cameras into the Shuttle program during the early phases to effect substantial program cost reductions.

D/8

RECON 6 - A REAL-TIME, WIDE-ANGLE, SOLID-STATE RECONNAISSANCE CAMERA SYSTEM FOR HIGH-SPEED, LOW-ALTITUDE AIRCRAFT

Richard L. Labinger

The Perkin-Elmer Corporation
Optical Technology Division
100 Wooster Heights Road
Danbury, Connecticut 06810

ABSTRACT

The maturity of self-scanned, solid-state, multielement photosensors makes the realization of "real time" reconnaissance photography viable and practical. This paper discusses a system built around these sensors which can be constructed to satisfy the requirements of the tactical reconnaissance scenario. The concept chosen by Perkin-Elmer is the "push broom" strip camera system -- RECON 6, which represents the least complex and most economical approach for an electronic camera capable of providing a high level of performance over a 140 degree wide, continuous swath at altitudes from 200 to 3000 feet and at minimum loss in resolution at higher altitudes.

I. INTRODUCTION

Low-altitude, visible imaging reconnaissance missions require wide field of view (FOV) cameras capable of producing imagery with resolution adequate for tactical scenarios. In the past, this requirement was met by using frame or panoramic film cameras. The maturity of self-scanned, solid-state, multielement photosensors now makes it practical to realize "real-time" photography for this application. This paper discusses Perkin-Elmer's RECON 6, a system built around these sensors which can be constructed to satisfy the requirements of the tactical reconnaissance scenario. Typical real-time camera specifications are:

Platforms:	RF-4, RF-14, RF-15, RF-16, and RF-111, remotely piloted vehicles (RPV's), etc
Altitude range:	200 to 2000 ft AGL (Above ground level)
v/h range:	0.25 to 4.0 rad/sec
Roll angle:	$\pm 30^{\circ}$
Roll rate:	$\pm 30^{\circ}$/sec
Cross-track FOV:	140° (5500 ft at 1000 ft + AGL)
Target illumination:	3000 to 100,000 lumen/meter^2
Target contrast:	1.4: 1 to 100:1
Required resolutions:	1.5 to 2.5 ft at 1000 ft AGL
Data link bandwidth:	15 MHz
Size, Weight, Power, Cost, Unreliability, Maintenance	*Minimal!*
Output:	Hard copy on dry processed material in essentially real time.

II. MECHANIZATION OF THE RECON 6

The concept chosen by Perkin-Elmer to mechanize a system to meet the above requirements was the "push broom" strip camera system which we call RECON 6. Self-scanned, solid-state detector arrays provide electronic cross-track scanning, while the platform's forward motion provides in-track scanning (see Fig. 1). Thus, the camera can be realized with no moving parts. This had decided cost and reliability advantages over panoramic or flying spot-type implementations.

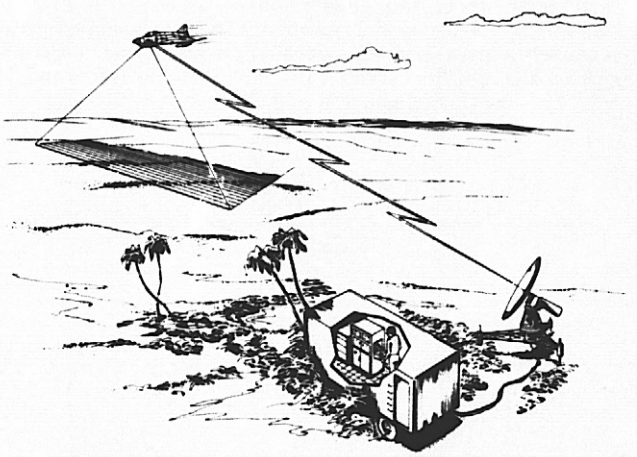

Fig. 1. RECON 6 - Electronic solid-state, wide-angle camera system

The resolution requirement of 1.5 feet resulted in a ground sampled distance (GSD) of 0.75 foot, assuming the generally accepted criterion of two samples per line pair for a sampled data system. Dividing this into the cross-track coverage that is required resulted in the need for a minimum of 7500 detector elements. Since linear charge coupled device (CCD) photodetectors and multielement photodiode arrays are available with 1728 and 1872 elements, respectively, it can be seen that multiple arrays will be required to cover the cross-track swath.

Next in order of consideration was the optical system. The most straightforward lens system for this application is the flat field mapping type. These have been built with field angles approaching 140 degrees (with difficulty). They also suffer from off axis illumination degradation in accordance with $\cos^4$ of the field angle. Additionally, they are expensive to manufacture. For these reasons, this type of lens was discarded.

Another interesting single lens which can cover the 140 degree field is the "Ball Lens" shown schematically in Fig. 2. Illumination through this lens falls off only as $\cos^1$; this made it more attractive than the mapping lens. However, its focal plane is curved. This would require curved detectors or fiber optic interfaces, both considered prohibitively expensive for this application.

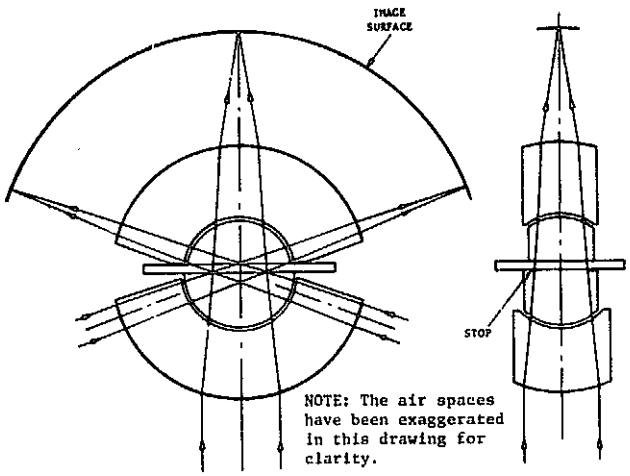

Fig. 2. Spherical focal plane 73.1 mm f/3 ball lens with 140° FOV

Finally, then, the choice narrowed down to multiple lenses to cover the field. For today's visible-to-near infrared silicon sensors, double gaussian and telephoto refractive designs result in the best performance at minimum cost (see Figs. 3, 4 and 5).

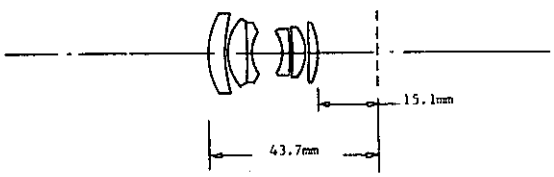

Fig. 3. 28.28 mm f/3 lens, 43.32° FOV

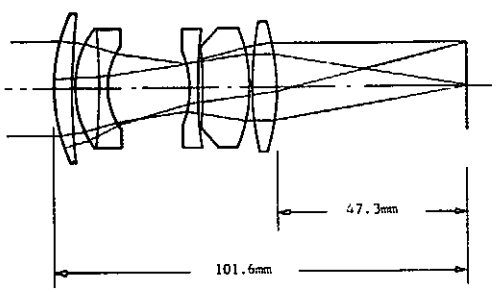

Fig. 4. 72 mm f/3 lens, 17.7° FOV

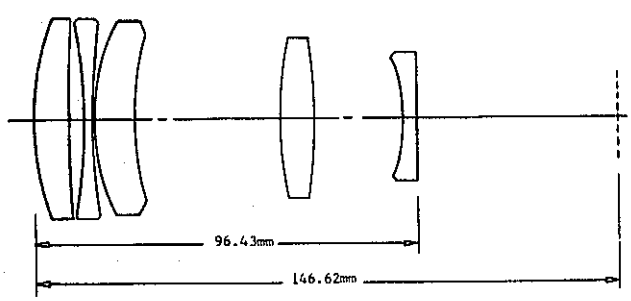

Fig. 5. 145 mm f/3 lens, 8.8° FOV

III. PERKIN-ELMER'S RECON 6

Fig. 6 is a block diagram of the RECON 6 wide-angle, electronic, solid-state, real-time camera system. It consists of an airborne sensor subsystem containing a six camera assembly, a video processing electronics assembly and data link transmitter. Alternatively, the transmitter could be replaced by an onboard recorder. The video data can be transmitted to a ground station containing a receiver, reconstruction electronics, laser beam recorder, and film processor.

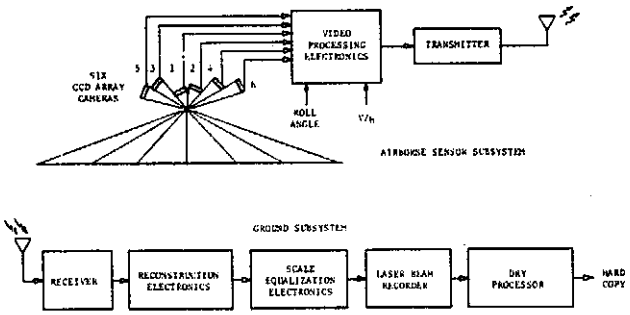

Fig. 6. RECON 6 system block diagram

A. AIRBORNE SENSOR SUBSYSTEM

The RECON 6 airborne sensor subsystem represents the least complex and most economical approach for an electronic camera capable of providing a high level of performance over a 140 degree wide. continuous swath at altitudes from 200 to 3000 feet and at minimum loss in resolution at higher altitudes.

1. Six Camera Assembly

This is a segmented six-lens strip camera where each lens provides an image to a single line array, 1728 elements wide. Fig. 7 shows the six camera assembly model of RECON 6. The total airborne sensor subsystem weight is 42.6 pounds. Each detector element is 0.013 mm wide and 0.017 mm long. The array length is 0.013 x 1728 = 22.46 mm. The focal lengths of the lenses were selected to provide equal worst-case, cross-track, ground resolved distance (GRD) of 1.5 feet at the edges of the field (see Fig. 8). The cross-track coverage of the six lenses is ±70 degrees, and the system is operated nominally at 0 degree pitch angle. The focal lengths and field angles of the three lenses covering 0 degree to 70 degrees are as follows:

Focal length (mm)	Field angle (degrees)	Nominal cross-track pointing angle (degrees)
28.3	±21.67	21.67
72.1	± 8.86	52.18
145.3	± 4.42	65.45

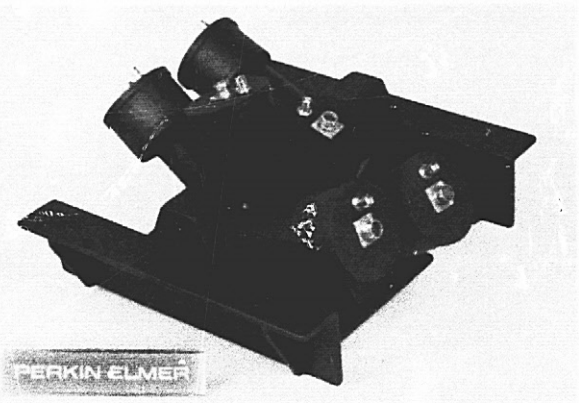

Fig. 7. Photograph of RECON 6 model

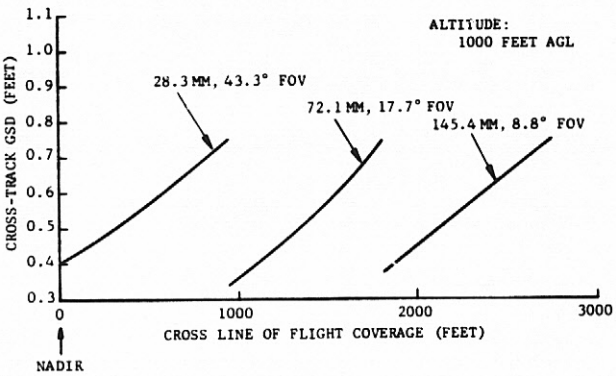

Fig. 8. Cross-track ground sampled distance versus cross line of flight coverage

A second set of three identical lenses provides coverage from -70 degrees to 0 degree. The relative f/3 aperture of the lenses was selected to provide a high level of image illuminance at minimum complexity in optical design. The individual camera assemblies consist of a lens cell assembly and a detector array assembly. The three different focal length lens cells are unique in their optical design, but a common interface between the three lens cells and the detector array is maintained, thus providing universal interchangeability between subsystems. Perkin-Elmer's designs for these lenses provide for a weighted polychromatic MTF (modulation transfer function) in the spectral region of the detectors of 0.6 at 40 line pairs/mm over the entire field.

The configuration of the camera is such that the strip image plane is tilted with respect to the ground across the track. Therefore, the projection of the detectors on the ground is variable, producing undesirable scale changes in the imagery. However, the RECON 6 system rectifies the image electronically in the ground subsystem and thus provides uniformity of scale.

Fig. 9 shows the design layout of the six camera assembly. Pointing and alignment of the individual cameras, to provide contiguous coverage of the broad FOV, are provided through alignment and locating keys at the interface between the camera assemblies and the main frame. The interface between the airborne sensor subsystem and the aircraft is through passive elastomeric vibration isolators. Power, control signals, and video signals are processed in the common electronics package to interface the airborne sensor subsystem to the aircraft power bus and data link.

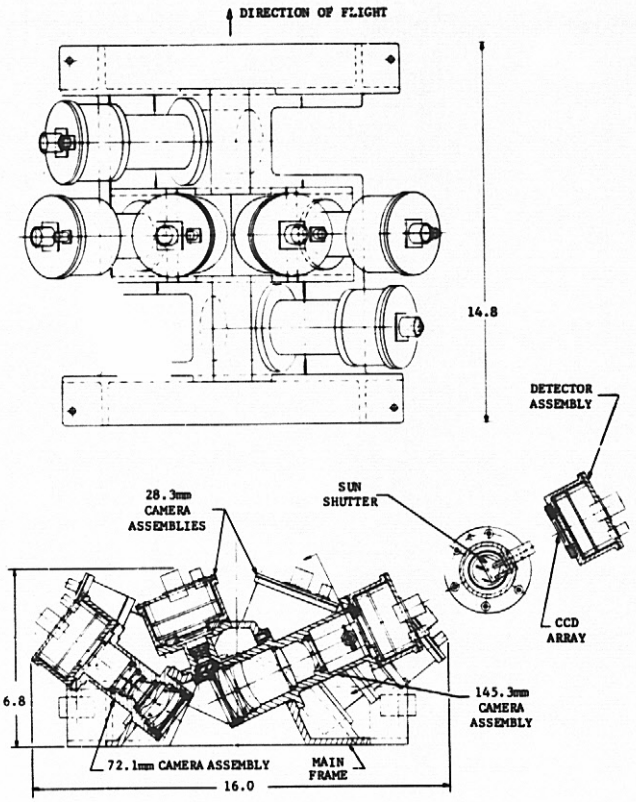

Fig. 9. Design layout of six camera assembly

2. Video Processing Electronics Assembly and Data Link Transmitter

The detector array and its first stage analog electronics are packaged in an enclosed aluminum housing. During assembly, the array is aligned and positioned with reference to the interface flange and locating pin. This technique assures alignment when the electronics housing is mounted to the lens assembly. Since the minimum amount of electronics are located adjacent to the detector array, noise generation related to thermal dissipation is minimized, and simple heat sink techniques are sufficient to maintain the detector assembly at its optimum temperature.

The airborne electronics system consists of six identical detector assemblies (one in each camera), a data processor which is common to all six cameras, and interfacing cabling. Each detector assembly contains a single 1728 element CCD array (Fairchild CCD 121H). A functional block diagram of the RECON 6 airborne sensor subsystem electronics is shown in Fig. 10. The camera video outputs are processed in contiguous pairs, requiring three subcarrier channels. The video data processing is simultaneous among the three pairs because the cameras operate in parallel. The serial channel data will modulate a selected subcarrier frequency, and the three channels will be summed at the input to the link transmitter. Video signals from cameras 1 and 2 will modulate the link transmitter directly, i.e., the subcarrier frequency is zero. Video signals from cameras 3 and 5 will modulate a 6.5 MHz subcarrier; the video signals from cameras 4 and 6 will modulate a 13 MHz subcarrier. During a blanking period, digital synchronizing and fiducial data will be generated and inserted by the composite video generator into the main data stream.

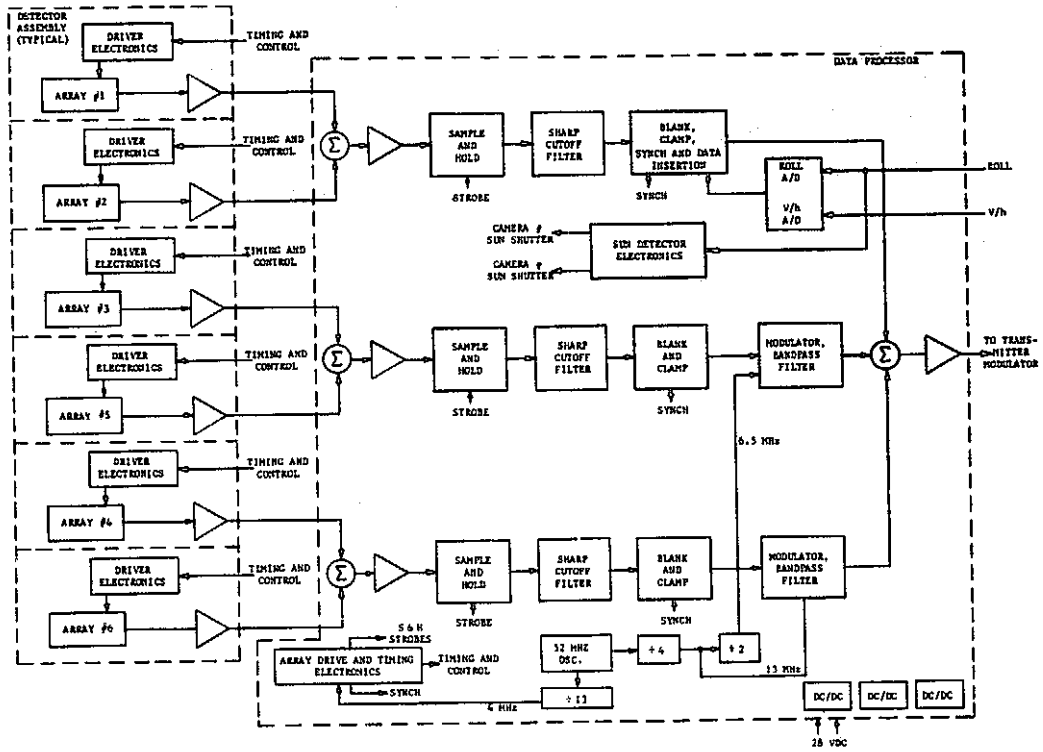

Fig. 10. RECON 6 airborne sensor subsystem electronics block diagram

B. GROUND SUBSYSTEM

Any part of the system that is not absolutely required to be in the airborne sensor subsystem is placed in the ground subsystem. The MTF of the ground subsystem is expected to be in the order of 0.6 at 38.5 line pairs/mm. Fig. 11 is a block diagram of the RECON 6 ground subsystem. The composite data from the data link receiver contains two channels of direct video data, four channels of video data superimposed on two subcarriers, and synchronization data. These data subsets are separated by appropriate filters. The subcarriers are routed to demodulators, the direct video data are routed to temporary storage, and the synchronization information is used to provide reference points for the timing electronics. Factory-generated calibration corrections of dark current for each pixel are added to the scene data after digitization as appropriate. The scene data is commutated from the three sources and fed to the laser recorder. Scale equalization and roll compensation take place within the temporary storage area of the laser recorder. All of the timing and control signals for this function are generated within the ground subsystem electronics.

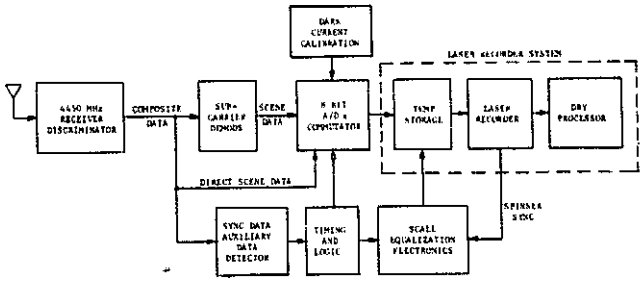

Fig. 11. Block diagram of RECON 6 ground subsystem

Stabilization of the image with roll angle requires that the data be shifted with respect to the scanning beam. Therefore, if the starting address for the data output is modified as a function of roll angle, the data is shifted with respect to the beam position. A simple PROM (programmable read only memory) is used to generate starting address values as a function of roll angle over the range of ±30 degrees.

Equalization of the imagery scale is accomplished by modulating the rate at which the data is written by the laser recorder. The scanner speed is not changed; only the clocking rate of the data which has been stored in the recorder memory is changed.

CCD and photodiode arrays exhibit variations in dark current from pixel to pixel. If this variation were not compensated, fixed pattern noise would be apparent in the imagery gathered during very low light-level operation. Perkin-Elmer calibrates each detector array and stores the pixel-by-pixel dark current values in PROM. These chips, one per array, are installed in the ground subsystem electronics in positions consistent with the array's position in the camera. The correction is then subtracted pixel-by-pixel from the video data after digitization.

IV. SYSTEM PERFORMANCE PREDICTION

To predict system performance, the effects of the basic RECON 6 elements (which are the airborne sensor subsystem, the data transmission link, and the ground-based image reconstitution system) had to be considered. The principal source of image degradation is noise at the detector preamplifier. Video signal amplification will greatly amplify both the detector signal as well as the detector preamplifier noise prior to the addition of other sources of noise developed in the transmission and image reconstitution link. These latter sources of noise will have a very small effect on the reconstituted imagery. Similarly, the signal reduction of the image recorder will be

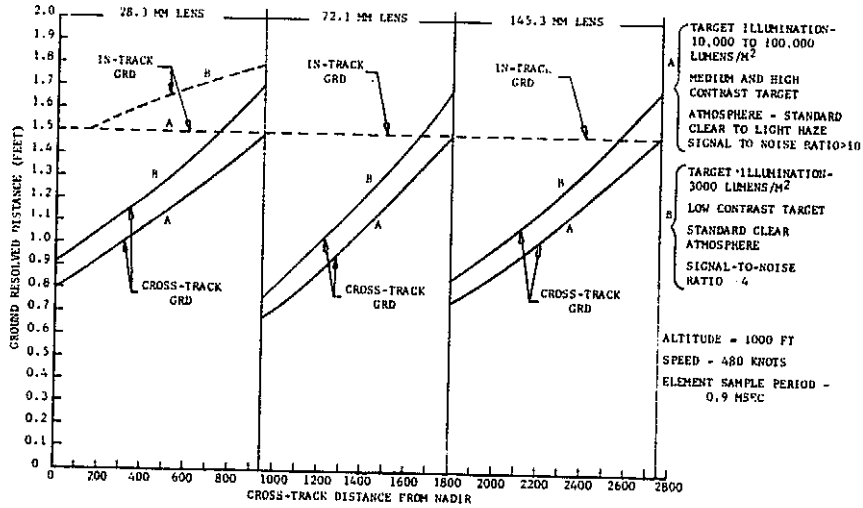

Fig. 12. RECON 6 system performances versus cross-track distances

neglected, primarily because both signal and noise are reduced by the recorder characteristics. Signal pre-emphasis may also be utilized to regain modulation loss at the higher spatial frequencies. Gain control is included in the ground subsystem to maximize the dynamic range of the video for the specified scene brightness levels.

Fig. 12 shows predicted system performance as a function of distance from nadir at 1000 feet AGL. Note that GRD varies between 0.8 feet to 1.8 feet in the cross-track direction and between 1.5 feet and 1.75 feet in the in-track direction, depending on the position in the field as well as illumination conditions. It should be noted that Fig. 12 shows equivalent object resolution at the output of the transmission link. The scale of the image is rectified electronically prior to reconstitution.

Performance criteria for electro-optical imaging systems have long been the subject of experimental and theoretical study at Perkin-Elmer. The principle evaluation criteria revolved around minimum signal-to-noise requirements. One of our studies had shown that, in the presence of white noise, 3-bar targets may be detected with signal-to-noise ratios between 0.5 and 0.8 provided that the targets are viewed at a magnification optimized for the MTF of the eye. However, at these low signal-to-noise ratios, the pictorial information is not "pleasing" to the eye. Simulated imagery provides a subjective criteria for acceptable levels of signal-to-noise.

Typical imagery produced on the Perkin-Elmer Line Scan Image Generator (LSIG), at simulated signal-to-noise ratios of 4:1 and 10:1, is shown in Fig. 13. Reasonably good imagery results for signal-to-noise ratios as low as 4:1.

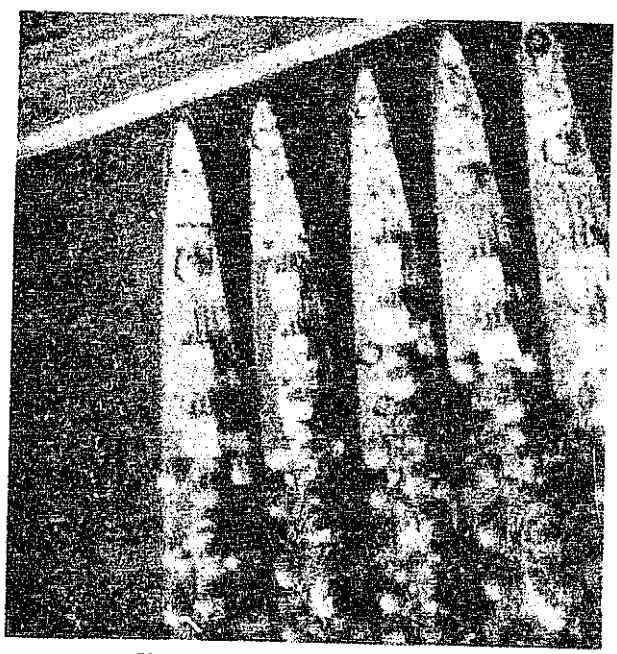

PROJECTED SPOT SIZE = 1.5 FT

$$\frac{\text{SIGNAL}_{(\text{PEAK-PEAK})}}{\text{NOISE}_{\text{RMS}}} = 10{:}1$$

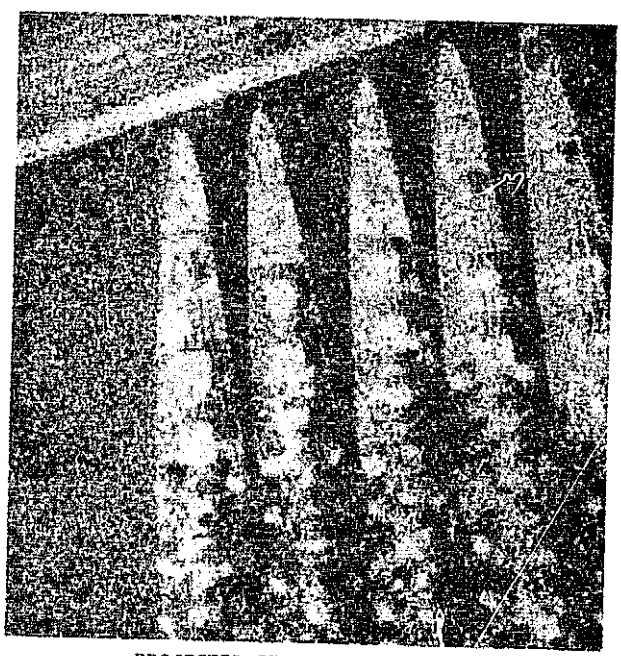

PROJECTED SPOT SIZE = 1.5 FT

$$\frac{\text{SIGNAL}_{(\text{PEAK-PEAK})}}{\text{NOISE}_{\text{RMS}}} = 4{:}1$$

Fig. 13. Typical simulation imagery produced by Perkin-Elmer's LSIG

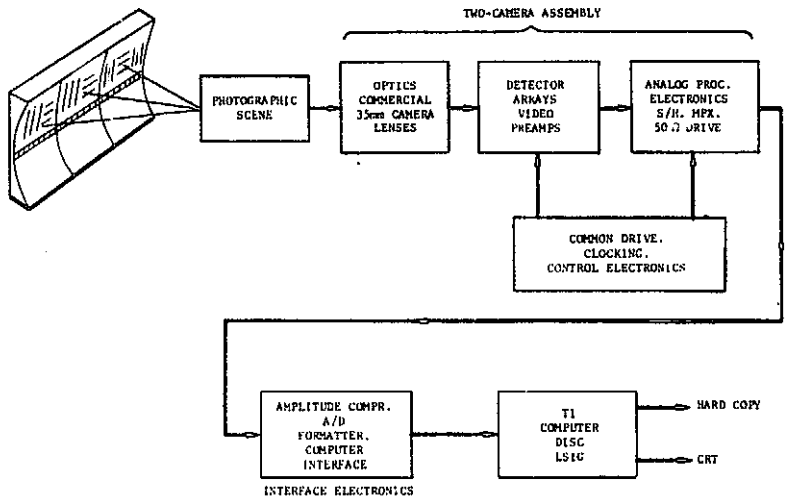

Fig. 14. RECON 6 breadboard

V. BREADBOARD TESTING

In order to demonstrate the salient features of the RECON 6 system, Perkin-Elmer constructed and tested a breadboard of a portion of the system. Two of the RECON 6 cameras, covering about 60 degrees, comprised the breadboard camera system.

Fig. 14 is a block diagram of the RECON 6 breadboard. Each of the two cameras consists of a lens purchased from a selection of off-the-shelf 35 mm camera lenses, a Fairchild 1728 element CCD imaging line array, a video preamplifier, and a sample-and-hold circuit. The two cameras were mounted in a common housing and contain the drive, clocking, control, multiplex, and drive electronics necessary to make the two cameras perform as an imaging system. In-track image motion is provided by a mechanism. The LSIG made the hard copy imagery. The LSIG, its TI computer, and disk memory offered the ability to perform a scale equalization demonstration.

A montage shown in Fig. 14 was constructed with linear dimensions of 6 ft x 9 ft and curved about a horizontal axis to a radius of 5 ft. Imagery and targets with a scale of 1 inch = 16.67 ft were provided.

Hard copy output photographs obtained from the breadboard are shown in Figs. 15 and 16. Fig. 15 shows the scale distortion inherent in the camera, requiring scale equalization. Scale equalized imagery is shown in Fig. 16.

VI. SUMMARY AND CONCLUSIONS

The maturity of self-scanned, solid-state, multielement photosensors makes the realization of "real time" reconnaissance photography viable and practical. This paper has shown that a system built around these sensors can be constructed to satisfy the requirements of the tactical reconnaissance scenario.

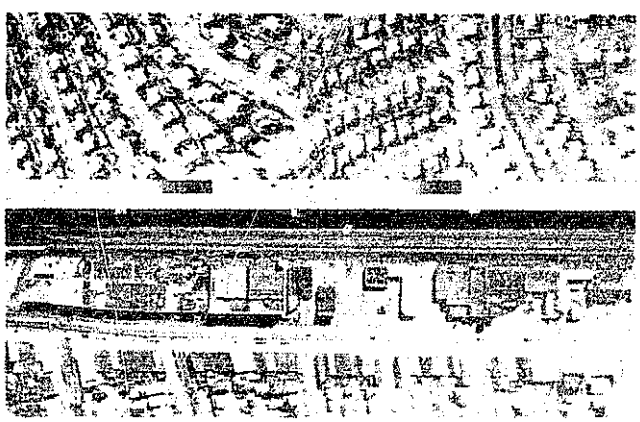

Fig. 15. RECON 6 breadboard (output as photographed)

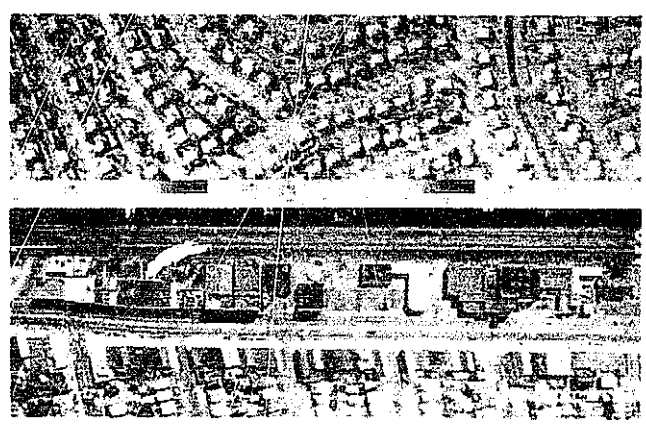

Fig. 16. RECON 6 breadboard (Output from breadboard - after electronic rectification)

ASTRONOMICAL IMAGING APPLICATIONS FOR CCDS

Bradford A. Smith

Lunar and Planetary Laboratory
Department of Planetary Sciences
University of Arizona
Tucson, Arizona

ABSTRACT

Preliminary testing of a back-illuminated, buried-channel CCD camera for astronomical telescopic imaging applications has already demonstrated an enormous research potential for this device. Images of several planets and both galactic and extragalactic objects were obtained using a 400 x 400 element TI CCD in a JPL developed camera on the University of Arizona's 154 cm telescope on Mt. Lemmon. The high quantum efficiency and relatively low noise of this CCD, along with the inherently high photometric and geometric stability, opens up new opportunities for astronomical research, especially in the spectral range from 0.8 to 1.0 μm. For example, images of Uranus obtained in the 0.89 μm absorption band of methane clearly reveal for the first time markings on the disk of this remote planet. Applications for both ground-based and near-earth orbiting telescopes are discussed.

I. INTRODUCTION

Shortly after the 1965 NASA/JPL symposium on the technology and application of charge-coupled devices, we were successful in employing a thinned, back-illuminated, buried-channel CCD for telescopic imaging of astronomical objects. The results which we obtained are most promising, and suggest that CCD's will attain widespread use in astronomical research as soon as they become more readily available. The superior photometric characteristics of CCD's in the visible and far-red spectral regions give them a distinct advantage over other currently employed electronic detectors (such as SIT and SEC devices), especially where precise area photometry is desired. Although CCD's are presently unable to compete with photographic emulsions for their high-density, data-storage capacity, or with various other photodetectors for short-wavelength response, their special characteristics as applied to many current astrophysical problems assure them a major role in astronomical research over the coming decade, both from the ground and from space.

II. CHARACTERISTICS OF BACK-ILLUMINATED CCD'S

Those characteristics of the thinned, back-illuminated CCD which so intrigue the observational astronomer are, by no means, properties which are peculiar to astrophysical research interests alone. Nevertheless, I will call specific attention to them here because, in several instances, they represent major breakthroughs when compared to currently employed area detectors.

(a) Spectral Range - covers the visible spectrum and the far red out to 1100 nm. The extended red sensitivity at relatively high quantum efficiency opens up an important spectral region for studies of planetary atmospheres and strongly redshifted galaxies and QSO's.

(b) Quantum Efficiency - only slightly less than unity in the red and still very high in the far red. At 1000 nm the quantum efficiency is approximately 200 times higher than its only competitor, the S-1 photocathode.

(c) Dynamic Range - approximately 2700 from S/N = 5 to saturation. This is equal to 8.5 stellar magnitudes, the approximate brightness range of the stars in many globular clusters.

(d) Linearity - better than 3×10^{-4}. The CCD, therefore, can be used for more than just an imaging device; both linearity and stability combine to produce an excellent area photometer.

(e) Dark Current - negligible.

(f) Readout Noise - less than 10 electrons per pixel. The negligible dark current and low readout noise make the CCD a sky-limited detector throughout its spectral operational range. All other area detectors are noise-limited in the far red.

III. ASTRONOMICAL OBSERVATIONS

Preliminary testing of a thinned, back-illuminated CCD on an astronomical telescope began in April and May 1976 at the University of Arizona's Mt. Lemmon Observatory, 30 miles north of Tucson. The detector was a Texas Instruments 400 x 400-element, thinned, back-illuminated, buried channel CCD (JPL-11) incorporated into a

breadboard camera* designed and fabricated by the Jet Propulsion Laboratory. Throughout the observing runs the CCD chip was cooled to 210°K by a thermostatically regulated flow of cold gas from a liquid-nitrogen Dewar. Although the camera system contained a 10-bit A/D converter, the recording of the CCD readout was limited to only eight of the ten bits (the most and/or least significant bit(s) could be dropped), and we were correspondingly constrained in the operational dynamic range.

The CCD camera was mounted at the f/13 Cassegrainian focus of the Mt. Lemmon 154-cm reflector. The f/13 focus has a focal-plane scale of 9.4 arcsec/mm, so that each 23 μm element (pixel) of the CCD array subtended an angle of 0.22 arcsec or a solid angle of 0.047 arcsec^2. The total array projected onto an area of the sky approximately 85 arcsec on the side. The breadboard camera had the capability for mounting optical filters, but contained no provisions for visual focusing. Although focusing could be and was accomplished by successive approximation using a 6-second readout display mode, the procedure was awkward and time consuming.

Two observing runs of approximately one week each were scheduled in mid-April and mid-May 1976. Unseasonable snows and poor image quality hampered the April run, but better conditions prevailed in May. A number of solar system and deep-space objects were recorded, primarily in several narrow spectral passbands in the far red, i.e., in the range from 800 to 1000 nm. Of particular interest are images of Uranus obtained in the 890 nm absorption band of metnane. These images clearly reveal for the first time cloud structure high in the atmosphere of Uranus (Fig. 1). Until a CCD became available for far-red methane-band imaging of this remote planet, no features had ever been recorded (with any degree of confidence) on the tiny 4-arcsec disk. Although the analysis is still incomplete, the results indicate that Uranus possesses a thin cirrus-type cloud layer composed of methane-ice crystals and that the diameter of the planet is somewhat greater than was previously thought. The Uranus images were recorded at an exposure time of 2 minutes, quite long compared to the nominal exposures for typical planetary images. The reflectivity of Uranus in the 890-nm methane band, however, is less than 0.01 and thus presents a surface brightness too faint for other detectors to reach within reasonable exposure times. Other objects looked at during these observational tests were Saturn, Neptune, Comet West, a globular cluster (M3), a large elliptical galaxy with a jet (M87/Virgo A) and a QSO (3C273). Although some of the faint-object imaging was hindered by bright moonlight, we were very pleased with the observations of both solar system and deep-space objects and are anxious to try again under better observing conditions.

The brief astronomical tests carried out to date have already demonstrated the enormous research potential for CCD's in both groundbased and space applications. We will look now at the capabilities of this detector when used on large groundbased telescopes and on the orbiting Space Telescope (ST).

IV. FUTURE PROSPECTS

The future for CCD's in astronomical research is now well established, particularly (but not exclusively) in problems requiring imaging or area-photometry in the far-red regions of the spectrum. Although the device is competitive with other area detectors throughout the visible portion of the spectrum, I will direct my remarks to the region from 800 to 1100 nm, referred to variously as the "far red" by some, and as the "near infrared" by others. Figure 2 shows the signal-to-noise ratio for both stellar (S) and extended sources (E) in a 100 nm bandpass centered on 1000 nm and computed for 3000 second exposures with a large groundbased telescope (the 4-m telescopes of the Kitt Peak National Observatory) and the ST (a 2.4-m space telescope to be launched in 1983). The focal ratio of the 4-m telescope (4M) is f/8 and the ST is f/24. The brightness of stars and extended sources are given in visual magnitudes and visual magnitudes per square arcsecond, respectively. Differences in detectability of faint objects are related to relative aperture, focal length and resolution and to the fact that the night sky at 1000 nm is 75 times brighter as seen from the earth's surface than when viewed from space. The bright night sky in the far red is caused by primarily airglow emission from OH molecules in the earth's atmosphere.

Objectives for future astronomical research with CCD's include studies of the atmospheres of the outer planets using images obtained in narrow molecular absorption bands. Much of the emphasis would be placed on Uranus and Neptune,

*I should state very clearly at this point that the JPL camera was designed for use as a laboratory test instrument and was never intended for operation in the inhospitable environment of an astronomical observatory dome. The success of the operation can be attributed directly to Jim Janesik and Larry Hoveland of JPL, who accompanied the instrument to Mt. Lemmon.

about which so little is now known, but we would also include studies of the dynamical properties of the atmospheres of Jupiter and Saturn.

Among deep-space objects of interest, we would certainly want to include highly redshifted galaxies and quasi-stellar objects (QSO's). The extreme red sensitivity of the CCD is particularly important in this application. Figure 3 shows the redshifted energy curve of giant elliptical galaxies together with the quantum efficiency curves of the CCD and the S-20 photocathode (the quantum efficiency of the S-1 photocathode is too low to appear on this diagram). The redshift parameter, Z, is defined as:

$$Z = \frac{\Delta\lambda}{\lambda} = \left(\frac{1 + v/c}{1 - v/c}\right)^{\frac{1}{2}} - 1$$

where λ equals wavelength, v is the recession velocity and c the velocity of light. Note that the S-20 photocathode does not retain adequate response in the far red to record giant elliptical galaxies redshifted beyond Z = 0.5. This is a serious limitation for those who want to study the very fringes of our universe.

The two areas of astronomical interest given above are only examples of the research problems in which one could use CCD detectors to excellent advantage. Many other problems of current astrophysical concern could be similarly identified, e.g., spectroscopy of highly redshifted objects.

The astronomical research in which CCD's will play a large role can be and, undoubtably, will be done with large or moderate-size groundbased telescopes. However, many of those studies which will be worked from the ground can be done better with a space telescope orbiting above the earth's atmosphere. Not only will angular resolution be higher than can be achieved under the very best conditions at the earth's surface, but the airglow of the night sky, which severely limits observations in the red beyond 800 nm, will be absent. I would hope that a CCD camera would be included as a prime instrument when NASA places the first large space telescope (ST) in orbit in 1983.

Fig. 1. Uranus in the 890-nm CH_4 absorption band.

ACKNOWLEDGEMENTS

I want to thank J. Janesik and L. Hoveland of JPL and S. Larson and J. Fountain of LPL for their assistance in making the observations at Mt. Lemmon. I am especially grateful to F. Landauer (JPL) for making the CCD camera available. This work was supported in part by NASA Grant NGL-03-002-002 and University of Arizona/JPL Contract 954057.

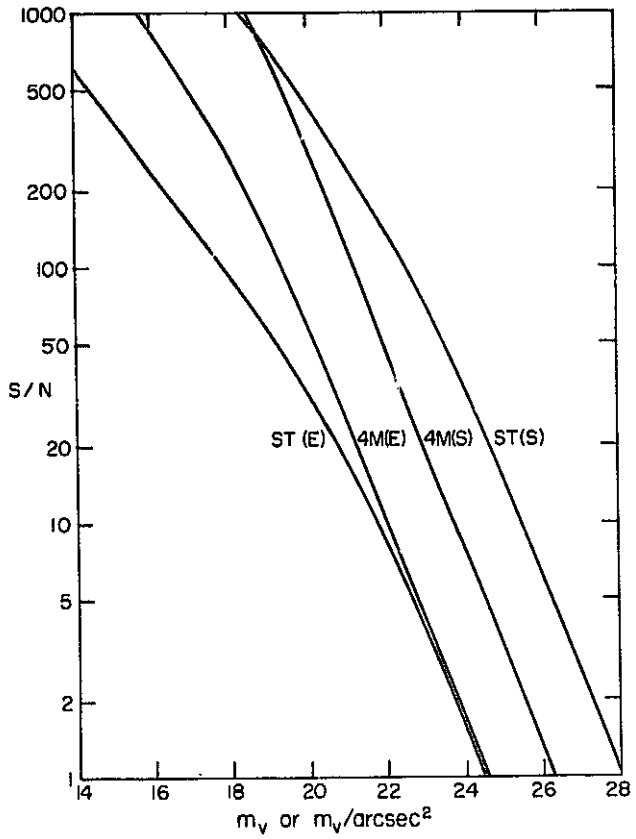

Fig. 2. S/N for stellar and extended sources exposed for 3000 seconds at 1000 nm (Δ = 100 nm) with a 4-m telescope and Space Telescope (see text).

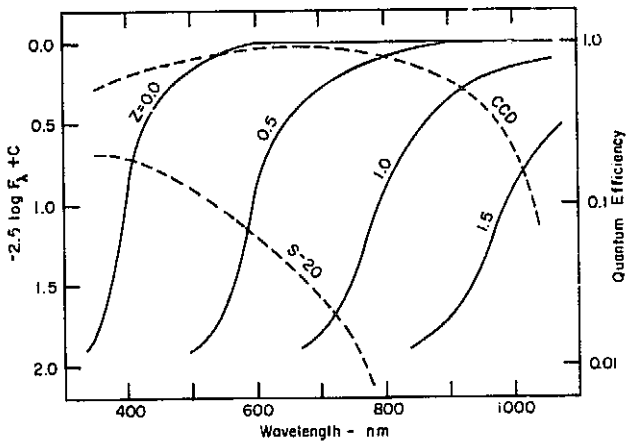

Fig. 3. Energy curves for redshifted giant elliptical galaxies and quantum efficiencies for CCD and S-20 photocathode.

D20

CHARGE-COUPLED DEVICE INTEGRATION-TIME CODING FOR DETECTION OF IMAGES MOVING WITH UNKNOWN VELOCITIES

J. M. White
G. W. Lynch

IBM Thomas J. Watson Research Center
Yorktown Heights, New York 10598

ABSTRACT

Existing techniques for the detection of a moving low light level image by a CCD array have required velocity synchronism between the image and the photogenerated charges. This was necessary to prevent blurring during the long duration of charge integration. A new detection scheme is described which causes the image to be convolved with a clock modulation signal as the photocharges are collected. The charge accumulating from each image point will now be spread over many photoelements due to the absence of velocity synchronism, but the output is not blurred in the usual sense. Instead the charge is distributed through the array in a controlled way so that the image can be reconstructed.

I. INTRODUCTION

The applications of charge coupled devices (CCD's) and other charge transfer devices have burgeoned into areas such as image sensing, electronic signal processing, and digital memories [Ref. 1]. One particular area of interest unique to charge transfer devices is image processing in which functions of sensing and processing may be effectively combined. One example of this combination is time delay and integration (TDI) [Ref. 2,3] in which the detection of an optical image moving at known velocity is improved by being averaged over many photocells as a result of synchronization of the motion of the charges in the CCD with the motion of the image for the duration of a long integration period. Also, Lagnado and Whitehouse [Ref. 4] have described ways of combining multiplication with the functions of time delay and optical integration so that image convolution can be achieved with CCD circuitry. Extending these ideas, we describe the use of a CCD linear scanner array to obtain the convolution of a moving optical image with discretely sampled linear FM chirps. This allows reconstruction of the image even though it was originally scanned while moving at an unknown velocity.

II. CONCEPTS OF OPERATION

Two primary ideas have been combined in our detection technique. The first concept gives a means for recording the convolution of the optical image with an electronic reference signal. An important part of this first concept is that the image is always moving relative to the accumulated charge packets. Synchronization of image and charge motion (as in TDI) is not needed and, in fact, must be avoided. The second concept relies on unique properties of the linear FM chirp as a reference signal. These properties have been studied in detail for applications such as RADAR signal processing (Ref. 5). The results of such studies can be used to give an indication of the ultimate capabilities of the chirp convolution detection technique.

A. CONVOLUTION VIA INTEGRATION CLOCK TIMING MODULATION

It is possible to take a slowly varying reference signal $r(t)$, sample its amplitude, and use this value to control the integration timing cycle of a CCD photoarray. Furthermore, with two storage cells at each photoelement, it is possible to assign positive and negative values to the weighting function $r(t)$. In this case, the integration periods are split, based on the value of $r(t)$. After the first part of each cycle the charge in a particular photoelement is put into one cell, and after the remainder of the cycle, the additional charge is put into the other cell. The difference between charge collected in the arrays of cells during one integration cycle then represents the product of the image intensity $i(x,t)$ and the reference signal. If the photocharge is collected for many cycles without being shifted out of the storage cells, the difference between the linear charge per unit length in the "positive" and "negative" arrays becomes

$$q(x,t) = w \int_{-\infty}^{t} i(x-v_i t')\, r(t')\, dt' \quad . \qquad (1)$$

Image intensity distribution i is moving with constant velocity v_i and is in units of photocurrent collected per unit area. w is the transverse width of the photoarray. The dimensionless weighting function r and the array elements are assumed to be suitably approximated by the continuous limit so that the charge may be written as an integral instead of a sum of discrete elements. Equation (1) is recognized as the convolution of the image and reference functions within the spatial and temporal limits of the device.

The convolutional distribution of charge may be collected as described in the above paragraphs, and the integrated values then shifted, or read, out of the array. However, the shifting can also be accomplished simultaneously with the collection of photocharge. This mode of operation is somewhat similar to TDI, but one important difference is that the image velocity v_i and the velocity of the collected charge v_c are unequal. The shift of charge along the array during the integration process is equivalent to replacing x by $x - v_c \cdot (t - t')$ in integrand of Eqn. (1), which gives

$$q(x,t) = w \int_{-\infty}^{t} i[(x-v_c t)-(v_i-v_c)t']\, r(t')\, dt' \quad . \qquad (2)$$

The variable of integration can be changed,

$t' \rightarrow \frac{x'}{\Delta v}$ where $\Delta v = v_i - v_c$, to give

$$q(x,t) = \frac{w}{\Delta v} \int_{-\infty}^{\Delta v \cdot t} i[(x-v_c t)-x'] \; r[\frac{x'}{\Delta v}] \; dx'. \qquad (3)$$

Equation 3 represents the convolution of the image function with a modified version of the reference signal. Moving the charge during the integration process is seen to be equivalent to expanding or shrinking the scale of the reference function.

B. THE LINEAR FM CHIRP AS THE REFERENCE SIGNAL

If the reference signal $r(t)$ is chosen to be a linear FM chirp, then the image $i(x)$ can be reconstructed from the convolved charge distribution which was recorded in the CCD. The reconstruction is achieved by passing the CCD output through an appropriate matched filter having a compensating linear dispersion. This is straightforwardly demonstrated by an analysis in the frequency (Fourier transform) domain.

The frequencies associated with the linear FM chirp are linearly and uniformly dispersed in time; therefore, a matched filter having a compensating linear dispersion will cause the chirp to be compressed into a narrow spike, or delta function.

In complex analog notation, the linear FM chirp, called r for "reference" signal, is

$$r(t) = \exp j \; [(\omega_0 + \frac{\mu t}{2}) \; t] \qquad (4)$$

which has an instantaneous frequency described by constants ω_0 and μ. The Fourier transform of this $r(t)$ is

$$R(\omega) = \sqrt{\frac{\pi}{|\mu|}} \exp -j \left[\frac{(\omega-\omega_0)^2}{2\mu}\right] . \qquad (5)$$

A capitalized function name indicates frequency domain representation of the respective lower-case time domain function name. If the above signal $R(\omega)$ is passed through a filter having a transfer function

$$H(\omega) = \sqrt{\frac{\pi}{|\mu|}} \exp j \left[\frac{(\omega-\omega_0)^2}{2\mu}\right] \qquad (6)$$

(i.e., identical to $R(\omega)$ but with opposite sign of dispersion, $\mu \rightarrow -\mu$) then the output will be constant in the frequency domain:

$$R(\omega) \cdot H(\omega) = \frac{\pi}{|\mu|} . \qquad (7)$$

Thus, in the time domain, the output will be a spike, or delta function.

The output of the CCD described in section II A is the convolution of the image function and the reference function. In the frequency domain, the convolution becomes a multiplication:

$$Q(\omega) = I(\omega) \cdot R(\omega). \qquad (8)$$

When passed through the filter $H(\omega)$, the final output $G(\omega)$ is

$$G(\omega) = I(\omega) \cdot R(\omega) \cdot H(\omega) = I(\omega) \cdot \frac{\pi}{|\mu|} . \qquad (9)$$

Thus, the output of the filter equals the input image function except for an amplitude constant. The image function is recovered even though it had been spread out due to the difference in velocities between image and charge motions.

Of course, the above analysis is idealized. In actuality, the length of the CCD and the time scales used are bounded and discrete, and the functions $i(x)$ and $r(t)$ are real. The use of a real, finite length, sampled chirp restricts the resolution and quality of the final compressed image which is recovered [Ref. 5] and the frequency range which may be utilized [Ref. 6]. However, the analysis indicates the essential concepts of operation.

III. EXPERIMENTAL DEVELOPMENT

The demonstration of our convolution techniques in a commercially available product, the CCD110 (Fairchild Semiconductor Components Arrays, Fairchild Camera and Instrument Corporation, Mountainview, California) required construction of circuitry to provide a set of waveforms, Fig. 1., which are different from those used for the CCD110 in normal image scanning operations.

Convolution of the spatial variation of the optical signal with the temporal variation of a discrete sampled analog reference signal requires multiplication of the optical signal by the reference signal. Multiplication is accomplished by converting the amplitude of the sampled analog reference into a clocking sequence where charge integration time is proportional to the reference amplitude. The reference analog signal is sampled with period $T = 20$ μS in our experiment; $V_{ref}(n) = r(nT)$. The sampled amplitudes are denoted as $V_{ref}(n)$ and are indicated in Fig. 1(a). These amplitudes are converted into delay times

$$\tau^B(n) = \left[\frac{V_{ref}(n) - V_{ref}^{min}}{V_{ref}^{max} - V_{ref}^{min}}\right] \cdot (T - 2T_c) \qquad (5)$$

with the remaining time in each sample cycle denoted as $\tau^A(n)$. These delay periods are shown in Fig. 1 on the time scale between (b) and (c).

The charge accumulated during $\tau^A(n)$ is transferred into the "negative" A shift register (shown in the device diagram, (Fig. 2) and similarly $\tau^B(n)$ charges are transferred into the "positive" B register. When the CCD output is processed, the difference represents both positive and negative excursions of the accumulated product.

Because the charge is shifted past two photogates during each shift register clock cycle of ϕ_1 and ϕ_2, double transfer pulses, shown in Fig. 1 (b) and (c), must be used to completely empty the photocharge into the shift registers during each time T_c.

Note that one set of clock pulses occurs at a fixed interval T. At times $t = nT + T_c + \tau^B(n)$, there is another sequence which is not periodic; therefore, the term "semisynchronous" is coined to describe the method of clocking.

Following each shift ϕ_1, ϕ_2 (Fig. 1(d) and (e)), an output level set occurs (Fig. 1(f)). In our experimental system, a signal XTB (Fig. (8)) loads this output level into a waveform recorder (Model 805, Biomation, Cupertino, California). The waveform recorder samples, digitizes (8 bits), and buffers 2048 consecutive bytes, or output level samplings, from the CCD. The B and A outputs are interleaved in the recorded data.

For many applications, the speed of a dedicated analog processor (perhaps other CCD filters) would be preferable to digital processing. However, for our demonstration, we interfaced the 2048 bytes into a digital computer for simulation and freedom of data manipulation. The interleaved B and A register output generated by two spots of light being swept along the CCD with FM chirp convolution is shown in the graphical output from the computer, Figure 3.

Once in the computer, it is straightforward to take the difference between the alternate CCD outputs, thereby providing the negative-going waveforms previously discussed. This leaves us with 1024 bytes of information representing the time sequence of the convolution of the input image and the reference voltage signal. The output has some undesirable low frequency fluctuations. These appear to be related to an inability to separate charges into B and A registers as a function of position along the device. The "high" level of the transfer voltages, ϕ_{XA} and ϕ_{XB}, had some effect on these fluctuations and was chosen to minimize this problem. It must be appreciated that the particular CCD used was fabricated for use as an image sensor and that a design eliminating alternate photogates [Ref. 4] would simplify the requirements on the clocking waveforms and improve performance for convolver operation.

The low frequency fluctuations were removed by converting the time sequence into the frequency domain using a 1024-point Fast Fourier Transform (FFT) [Ref. 7] and then multiplying the real and imaginary parts of the discrete frequency representation by the function

$$M(k) = \begin{cases} \sin\left(\frac{\pi \cdot k}{50}\right); & k = 1, 2, \ldots, 50 \\ 1 \quad ; & k = 50, \ldots, 976 \\ \sin\frac{\pi \cdot (1026-k)}{50} \quad ; & k = 976, \ldots, 1024. \end{cases} \tag{10}$$

M(k) is shown in Figure 4 and the subsequent signal $q(x_o,t)$ is shown in Figure 5.

To obtain the double spots of the original image from the data shown in Fig. 5, we simulated a bank of filters h_ℓ with varying amounts of compensating dispersion. In the discrete frequency domain representation,

$$H_\ell(k) = \begin{cases} \exp[j2\pi(k-1)^2 \ell \times 10^{-5}] \\ \qquad \text{for } k=1, 2, \ldots, 512; \\ 0 \quad \text{for } k=513; \\ \exp[j2\pi(1025-k)^2 \ell \times 10^{-5}] \\ \qquad \text{for } k=514, \ldots, 1024 . \end{cases} \tag{11}$$

The inverse transform of the CCD output using these filter functions was calculated for a variety of values ℓ; i.e., the calculated term was

$$F^{-1}\{Q(k) \cdot M(k) \cdot H_\ell(k)\} , \tag{12}$$

where F^{-1} is the inverse Fourier transform operator, and where Q(k) is the discrete transformed version of the CCD output signal. The inverse transform with maximum peak output and contrast was for ℓ = 135. Figure 6 shows the magnitude (absolute value) of the final output. The existence of this output confirms the basic concept of operation of the input convolution.

For the experiment, the two spots of light were visually adjusted to give a separation of roughly half the length of the 256 element array. In Figure 6, the two peaks are about 70 units apart. Each unit corresponds to two photogate elements (due to the transfer/shift/transfer combination) so the two spots were actually separated by about 140 photogate spacings.

Maximum resolution, or the minimum width of the output spot, is essentially the inverse of the bandwidth of the recorded chirp. A reference chirp with a bandwidth of 0 to 25 kHz was used in order to provide at least two samples per cycle where each sample is T = 20 μS. The speed of the rotating mirror used to deflect the double spot was such that the image was on the CCD for only part of the chirp. This limited the recorded bandwidth to about 56% of the full chirp bandwidth. If we neglect negative frequencies, which arise since the Fourier transform of a real function is symmetric, and if we allow for 20% bandwidth compression between R(k) and $R(\Delta v \cdot k)$, for $v_c \approx 0.2\ v_i$, then we expect the bandwidth to be about 230 units in the transformed domain. For each spot individually, a bandwidth of about 160 units was observed. This corresponds to the 6 or 7 units of width in the compressed pulses of Figure 3. Poor focusing and perhaps nonuniform velocity effectively widened the input image and caused rolloff in the transform domain in our experiment. Although the experimental setup was sufficient to demonstrate the basic principle of operation, it was not optimized to give quantitative results on resolution.

In addition to permitting the recording of images moving at an unknown velocity, there are several other attractive features which arise from this type of scanning. For example, saturation occurs not because of the brightness of an individual spot, but rather because of the average brightness of the image. Thus, effects of blooming from isolated bright spots would be reduced. Also, localized sources of dark current, which are not moving with the velocity of the image, would be smeared out. Images, whether real or created by

dark currents, that have different Δv's will have different optimum matched filter functions, and will not compress concurrently.

In order to obtain the compressed image using Equation (11) and (12), many filters H_ℓ had to be simulated and the optimum image selected. The auto-correlation of the image is more easily and directly obtained. The transformed output of the CCD is $Q(\omega) = I(\omega) \cdot R(\omega)$ as described in Equation 8. From this, we can easily compute

$$|Q(\omega)|^2 = Q(\omega) \cdot Q^*(\omega) = I(\omega) \cdot R(\omega) \cdot R^*(\omega) \cdot I^*(\omega) \quad (13)$$

but since $R(\omega) \cdot R^*(\omega)$ is a constant (in the ideal case), it can be omitted. Thus, Equation (13) gives the transformed image autocorrelation $I(\omega) \cdot I^*(\omega)$. Because the linear chirp drops out of the autocorrelation, the relative velocity Δv does not enter into the final result. The cross-correlation between two images separately scanned at the same velocity also possesses this characteristic of dropout of velocity information when processed; i.e., $I_1(\omega) \cdot R(\omega) \cdot R^*(\omega) \cdot I_2^*(\omega) = I_1(\omega) \cdot I_2^*(\omega)$.

The role of the image function as input and of pulse-position modulation voltage as reference could be reversed, in which case the optical image can be used as a tap weighting function for a transversal filter acting on the sampling voltage input signal. For this application, the images should be spatially fixed. An optical transparency could be used to mask the array to provide fixed tap weights, or LED's individually focussed onto the sensors could be used to electronically vary the taps.

IV. CONCLUSIONS

The concept of performing convolution by modifying clocking waveforms in a charge coupled device image sensor has been illustrated experimentally. The mathematical implications of encoding an image by convolving it with a linear FM chirp point out several interesting capabilities: (1) Images can be integrated over long times even though moving with respect to the accumulating charge packets. A set of filters can be used to retrieve the original image. (2) The autocorrelation of such images is simply derived in spite of the motion. (3) Images moving with different velocities can be simultaneously recorded and subsequently separated with different compression filters subject to limitations in contrast and number of resolvable spots. Electro-optically controlled transversal filters can also be configured for a variety of applications using "semisynchronous" clocking.

We appreciate the direction of S. C.-C. Tseng at the start of this work, the help from A. J. Stein, A. A. Guido, S. Krasney, and C. G. Powell with the graphics terminal system and the computer interface, the design aid from T. R. Perry on the clocking circuits, and the comments on the manuscript from L. Kuhn.

REFERENCES

1. Séquin, C. H., and Tompsett, M. F., CHARGE TRANSFER DEVICES, Academic Press, New York, 1975.

2. Erb, D. M., and Nummedal, K., "Buried Channel Charge Coupled Devices for Infrared Applications," CCD Application Conf. Proc., Naval Electronics Laboratory Center, San Diego, pp. 157-167, September, 1973.

3. Texas Instruments, Inc., "Moving Target Sensor," Contract Report N00039-73-C-0070, October, 1973.

4. Lagnado, I., and Whitehouse, H. J., "Signal Processing Image Sensor Using Charge Coupled Devices," Int. Conf. Tech. and Appl. of CCD's, University of Edinburgh, pp. 198-205, September, 1974.

5. Cook, C. E., and Bernfeld, M., RADAR SIGNALS, Academic Press, New York, pp. 5-17, 130-172 (1967).

6. Rabiner, L. R., Schafer, R. W., Rader, C. M., "The Chirp Z-Transform Algorithm," IEEE Trans. Audio and Electroacoustics, AU-17, pp. 86-92, June, 1969.

7. McAuliffe, G. K., "APL Fast Fourier Program," RC 2832, IBM Thomas J. Watson Research Center, Yorktown Heights, N. Y. (1970).

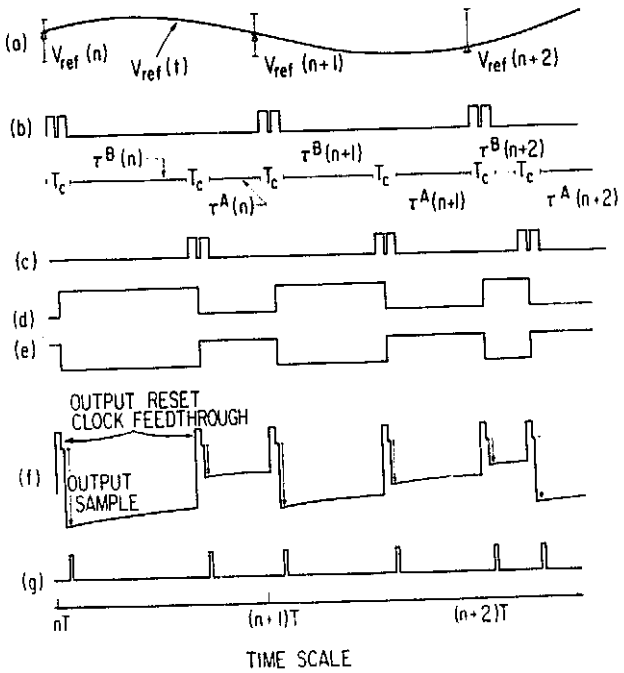

Figure 1. Semisynchronous waveforms for driving the CCD. (a) is the reference voltage waveform r(t) which is sampled at regular intervals. (b) and (c) are the transfer voltages, ϕ_{XA} and ϕ_{XB} respectively. (d) and (e) are the voltages ϕ_1 and ϕ_2, respectively, which control the shift registers. (f) appears at the output stage of the CCD. The output information is sampled as indicated by the arrows occurring shortly after the reset. (g) is the external time base (XTB) control which advances the waveform recorder.

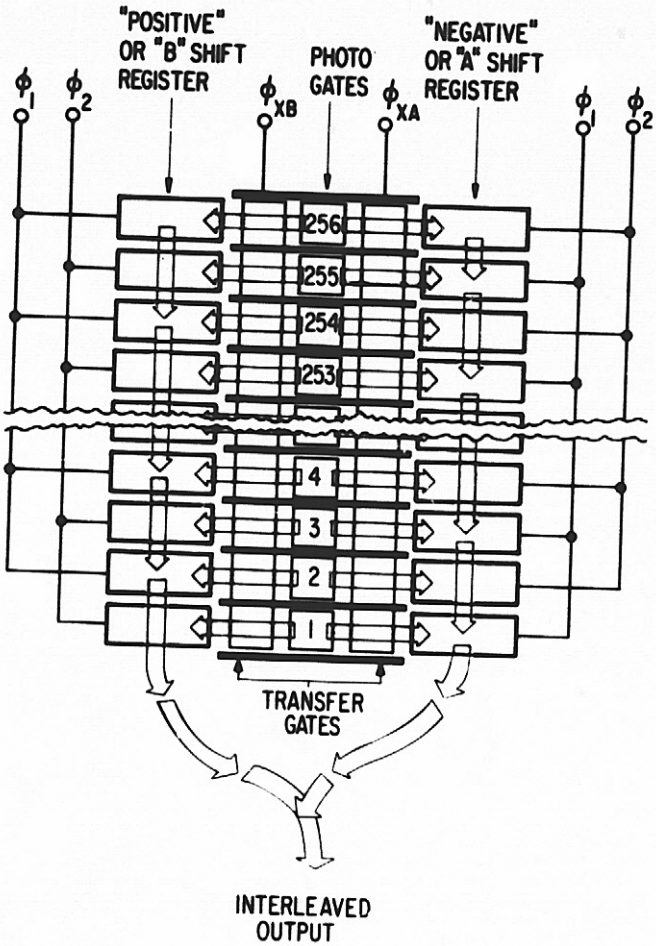

Figure 2. Schematic layout of the type of CCD used to sense and convolve images with reference voltage waveforms.

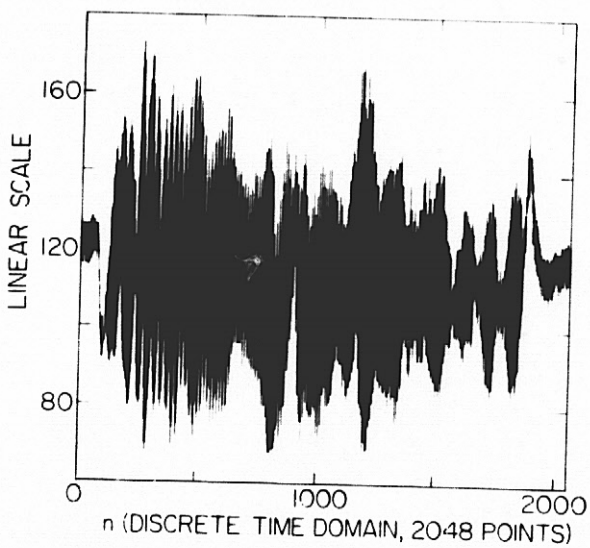

Figure 3. Output from the CCD after digital recording and as displayed on computer graphics system. Note that 2048 samples are shown. The "positive" and "negative" outputs are interleaved and will be later subtracted to provide 1024 samples of useful output.

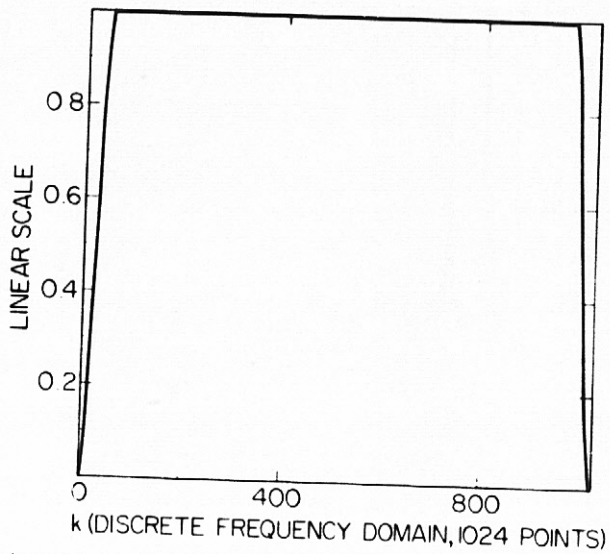

Figure 4. Transformed low frequency rejection filter M(k). Due to cyclic behavior of the discrete Fourier transform, negative low frequencies appear at right end of the scale.

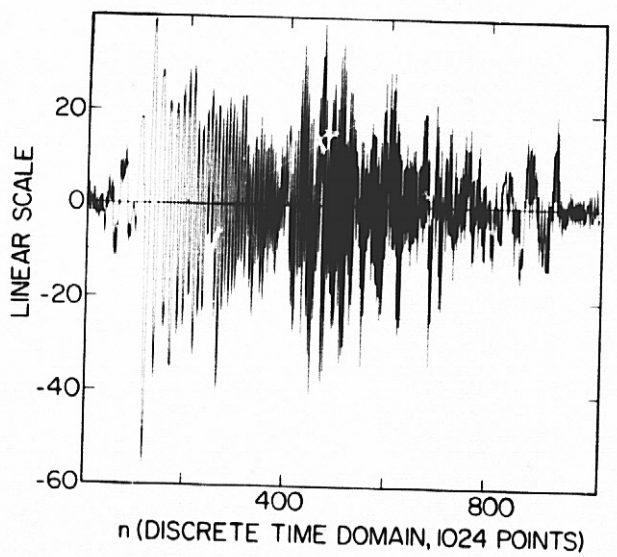

Figure 5. CCD output after "positive" and "negative" terms are combined and low frequency components have been removed.

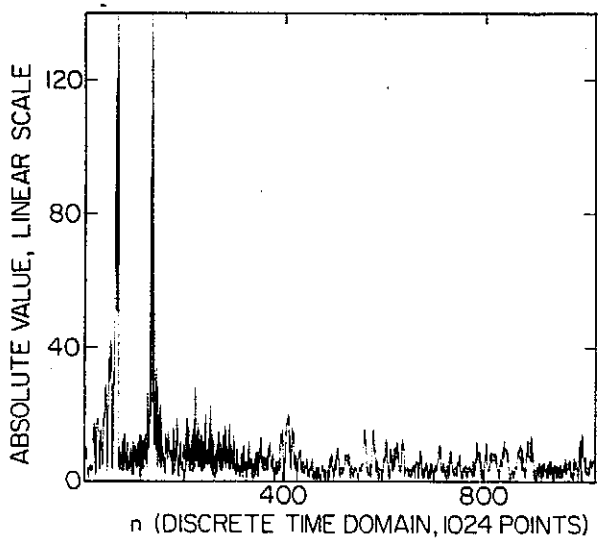

Figure 6. Magnitude of the output after final compression by simulated matched chirp filter. The two peaks correspond to the two spots originally scanned along the CCD sensor.

A HIGH SPEED IMAGING SYSTEM FOR NUCLEAR DIAGNOSTICS*

Harold H. Eyer

Lawrence Livermore Laboratory, University of California
Livermore, California 94550

ABSTRACT

A high speed imaging system based on state-of-the-art photosensor arrays has been designed for use in nuclear diagnostics. The system is comprised of a front-end rapid-scan solid-state camera, a high speed digitizer, and a PCM line driver in a downhole package and a memory buffer system in an uphole trailer. The downhole camera takes a "snapshot" of a nuclear device created flux stream, digitizes the image and transmits it to the uphole memory system before being destroyed. The memory system performs two functions: it retains the data for local display and processing by a microprocessor, and it buffers the data for retransmission at slower rates to the LLL computational facility (NADS). In the talk, the impetus for such a system as well as its operation will be discussed. Also discussed will be new systems under development which incorporate higher data rates and more resolution.

I. INTRODUCTION

All nuclear devices designed at Lawrence Livermore Laboratory are subjected to extensive field testing during their design and development phase. This is performed primarily to confirm that the actual device performance conforms to that predicted during device design. A secondary, but perhaps just as important, reason for testing, however, is to develop new experimental techniques capable both of answering some of the chronic problems of nuclear design and of testing more sophisticated design concepts.

Since the device to be tested must be sealed in the ground during test, the only method the designer has of observing its performance is by monitoring the various radiation and particle fluence emitted from the device during its detonation, particularly the neutrons, gamma rays, and x-rays. Device parameters that are of particular interest to the designer are:

1. The intensity of the flux.
2. The energy of the flux.
3. The spatial distribution at the birth of the flux.
4. The intensity, energy, and spatial distribution of the flux as a function of time.

II. NEW DIAGNOSTIC DEVELOPMENTS

Almost all of the available data are from two-parameter measurements. That is they are space or time averages over the entire device. Spatial distribution of the intensity of the neutron flux has commonly been obtained by using pinhole camera techniques with a recoverable film plane. The x-ray energy spectrum is usually obtained by using a recoverable film plane to record the intensity as deflected by a bent crystal. Time distribution is normally recorded by using radiation detectors to drive an uphole oscilloscope.

The new experimental techniques which are being developed are multi-parameter measurements. In these, source parameters such as intensity and energy are measured as functions of space and time. To affect this, the experiment must be placed in close proximity to the device under test and, in order to insure complete data retrieval, the data must be recorded and readout within several milliseconds. Solid state photosensor arrays provide the fast record/readout capability that is essential for these multi-parameter measurements. They also improve some of the existing experimental techniques by making them cheaper and safer. Some of these experiments are briefly described below.

A. TIME-INTEGRATED ELECTRONIC PINHOLE EXPERIMENT

Figure 1 illustrates the concept. X-rays, gamma rays, and neutrons from the device stream through the assembly of pinholes to excite a plastic scintillator. The intensity patterns are "photographed" with a solid state camera system. The x-ray or gamma ray image can be distinguished from the neutron image with a fast shutter that is opened at the appropriate time. For redundancy and/or economy, images can be multiplexed onto more than one camera by using fiber optics or mirrors. This diagnostic has two unique advantages over the existing method: (1) It eliminates problems (mostly containment) and hardware associated with recovery of radioactive plates, and (2) it can obtain both x-ray and gamma ray images.

B. TIME-INTEGRATED HIGH RESOLUTION X-RAY SPECTROMETER

Figure 2 illustrates the concept. X-rays from the device are diffracted by a crystal onto a scintillator that is optically coupled to a linear solid state camera system. The x-ray emission and absorption characteristics of elements of the device can be differentiated.

C. ULTRAFAST DOWNHOLE SIGNAL RECORDING

1. Solid State Transient Recorder

By taking advantages of the analog shift register property of charge coupled devices, ultrafast shifting (i.e., signal sampling) can lead to a very economical downhole oscilloscope with >1 GHz bandwidth. This exceeds the bandwidth of existing detector-cable-equalizer-oscilloscope systems by a decade or more. Such a capability would allow downhole recording of the signal at places where subnanosecond time resolution is most important.

*This work was performed under the auspices of the U. S. Energy Research and Development Administration, under contract No. W-7405-Eng-48.

2. Streaking Camera Recording

The concept is illustrated in Figure 3. Fast scintillators are coupled through fiber optics to a streaking camera. Routine data with high dynamic range can be obtained with one detector. Time resolution with newly developed fast scintillators or Čerenkov radiators is approximately 0.1 nsec.

D. LASER TIME-RESOLVED PINEX (LTRP)

Figure 4 illustrates the concept. The experiment will obtain device x-ray, gamma ray, or neutron images that are continuous in space and discrete in time. Ultimate time resolution is less than 100 psec. Radiation streams through a pinhole and interacts in a cell containing a fast-response ($\tau \lesssim 100$ psec) scintillator producing a time-dependent optical opacity that is proportional to the instantaneous flux. The scintillator is strobed during irradiation by a long sequence of mode-locked pulses that are spatially uniform upon entering the cell, but which are spatially non-uniform upon exit. The resulting non-uniform pattern contains the desired image information. The laser pulses propagate about 50 to 100 feet, are collected by telescopes and are fed through gated image intensifier tubes to solid state camera systems. The image intensifiers serve as fast shutters to prevent the many spatially uniform pulses containing no information from activating the solid state cameras. Spatial profiles recorded on each camera (images are multiplexed for economy) are read out in <3 msec, before ground shock arrives.

E. STREAKING CAMERA IMAGING

Figure 5 illustrates the concept. This experiment will obtain images that are discrete in space and continuous in time. X-rays, gamma rays and neutrons stream through a pinhole and interact in the fast scintillator. The time-dependent opacity pattern is focused onto a 2-dimensional fiber optic array. As the 2-dimensional image information passes through the array, it is converted into a time-dependent 1-dimensional pattern. The streaking camera converts this into a 2-dimensional pattern that is recorded on a solid state camera. A movie of the device emission is constructed from this pattern. With adequate signal to background ratios, spatially resolved alpha data can be obtained from a gamma-ray movie.

F. TIME-RESOLVED HIGH RESOLUTION X-RAY SPECTROMETRY

By focusing the scintillator intensity pattern obtained in crystal diffraction onto the streaking camera photocathode, time resolved x-ray spectra can be obtained.

III. HIGH SPEED IMAGING SYSTEM

The performance requirements for a nuclear diagnostics imaging system differ from those for a TV system or a low light level imaging system. Basicly, the requirements imposed on a nuclear diagnostics imaging system are:

1. A linear response to light durations as short as 5 ns.
2. A dynamic range of at least 200:1.
3. No blooming at ten times saturation.
4. No lag.
5. Capability of a scan rate as high as 5 MHz.
6. Capability of being reset within 1 μs and of being held reset for up to one hour.

A 45 megabits/second system (Figure 6) which satisfies most of these performance requirements has been developed at Lawrence Livermore Laboratory. It consists of two subsystems: An expendable downhole system (Figure 7) and an uphole buffer system (Figure 8).

A. DOWNHOLE CAMERA SYSTEM

The photosensor array is scanned at a 5 MHz rate thereby producing a 5 MHz video signal which is then sampled and held. The sampled and held video is then submitted to a high speed digitizer/serializer where it is converted into an eight bit data word. Parity is added and the data is serialized and transmitted uphole in the form of a 45 megabits/second BiΦ PCM bit stream.

B. UPHOLE BUFFER SYSTEM

Images transmitted uphole are received and stored in an uphole buffer system prior to transmission to the computational facility. The need for a forward area buffer stems from two considerations. First, the uphole transmission rate exceeds the maximum rate capability of the computational facility. Second, the images must usually be encrypted prior to microwave transmission, further reducing the maximum bit rate to 154 kilobits/second.

The uphole buffer system consists of a synchronizer and a memory system. the synchronizer receives the serial digital bit stream from the downhole camera and converts it to parallel digital words for the memroy. The memory system determines when the uphole image is valid and then stores it in a matrix identical to the sensor array (i.e., Row 4, column 33 of the sensor is stored at address row 4, column 33 of the memory). This makes it simple to select a specific area or location of the image for close examination.

A local readout system (Figure 9) is included in the bunker design to aid in system setup. This capability allows images to be displayed both as buffered by the memory system and in real time. The buffered display allows wide range gray scale hard copy reproduction of images as they are stored in the memory system. The real time display allows for viewing the camera output while focusing, setting light levels, etc.

The image stored in the uphole memory system is encrypted and transmitted (or directly transmitted when encryption is not required) to computational facility where it is recorded to await entry into the computer. Upon ingestion into the computer, software routines correct the data for

dark current noise and other calibrated variables and then produce half tone dot plots, isometric projections, contour plots, gray level photographs, and data tables.

IV. RESULTS

The 45 megabits/second system is presently based on the Reticon 50 X 50 and 100 X 100 photodiode arrays. However, both the Fairchild 100 X 100 CCD (CCD 201) and the General Electric CID, both epitaxial and bulk, have been field tested in the past.

The CCD suffered from two serious problems: first, they produced "ghost" images as a result of crosstalk between pixels and adjacent shift registers during illumination; and secondly, they exhibited serious line blooming.

The problems associated with the epitaxial CID camera were a result of using short light pulses. These problems resulted from the high currents produced in the thin epitaxial layer causing a loss of bias and the resultant collapse of the pixel depletion regions. This resulted in a nonlinearity and nonuniformity across the chip. The bulk CID arrays, on the other hand, exhibited none of the light pulse problems associated with the epitaxial arrays but did suffer from a serious crosstalk problem.

The Reticon photodiode arrays have, in tests to date with pulsed light sources, exhibited none of the problems that degraded the performance of the photosensors.

Acknowledgements

The design and development of this system required the expertise of many people of several different disciplines. The Electro-Optics and Digital Systems Group headed by T. Wieskamp, the L Division R&D Group headed by P. Ebert, the L Division Data Analysis Group headed by R. Neifert, and the Mechanical Technician Section of the Nuclear Test Engineering Division headed by L. Talbot were all necessary for the success of the project.

Work performed under the auspices of the U.S. Energy Research & Development Administration under contract No. W-7405-Eng-48.

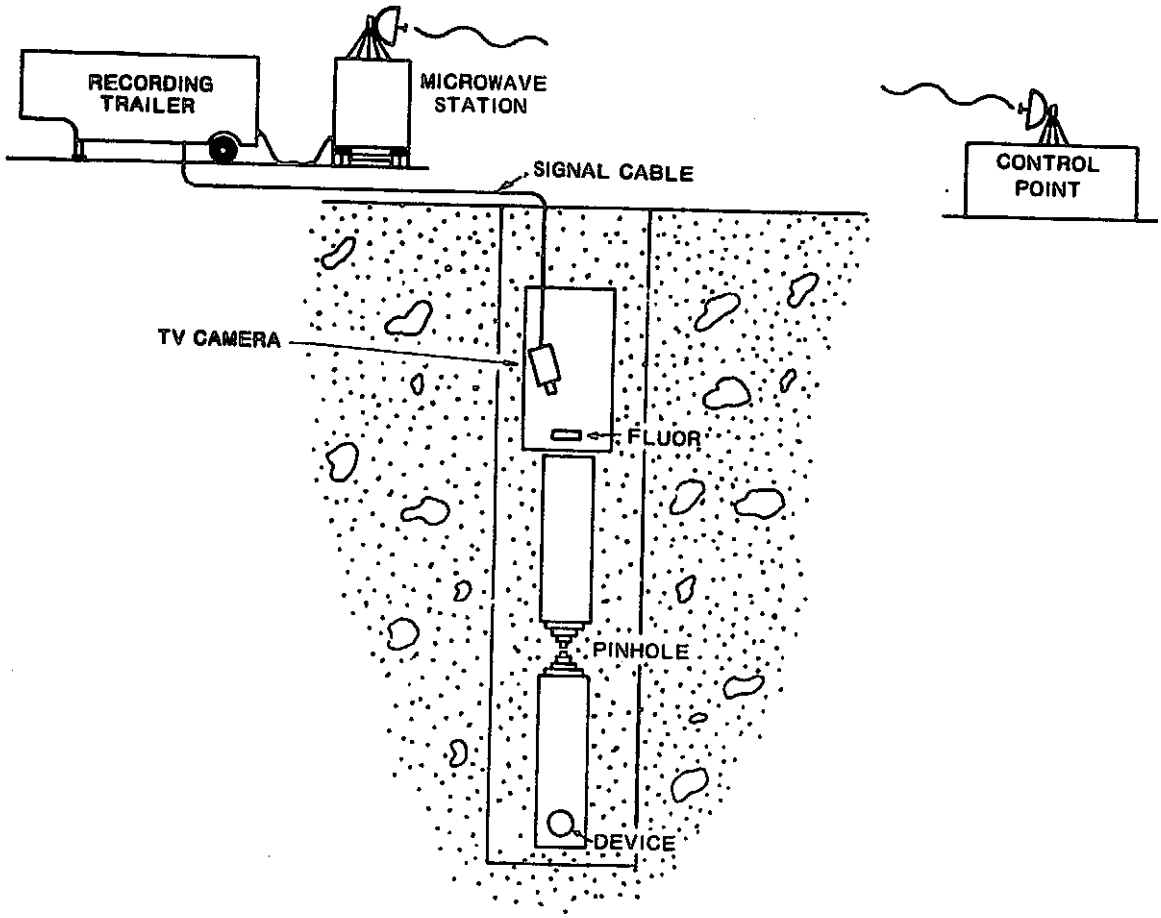

FIGURE 1 TIME–INTEGRATED ELECTRONIC PINHOLE EXPERIMENT

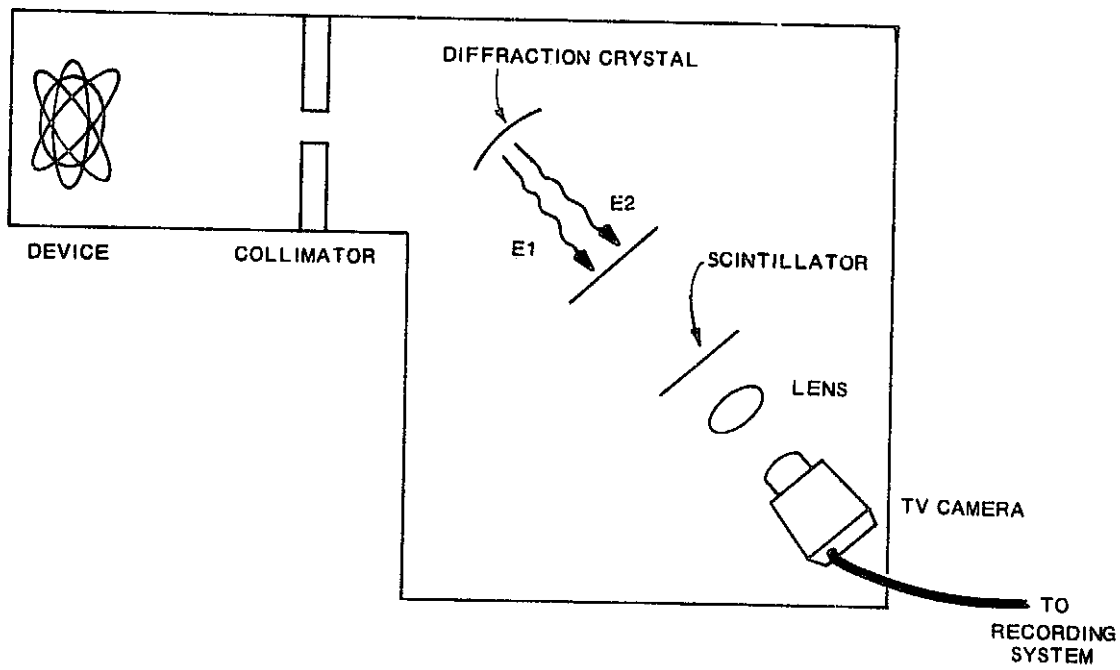

FIGURE 2 TIME– INTEGRATED HIGH RESOLUTION X–RAY SPECTROMETER

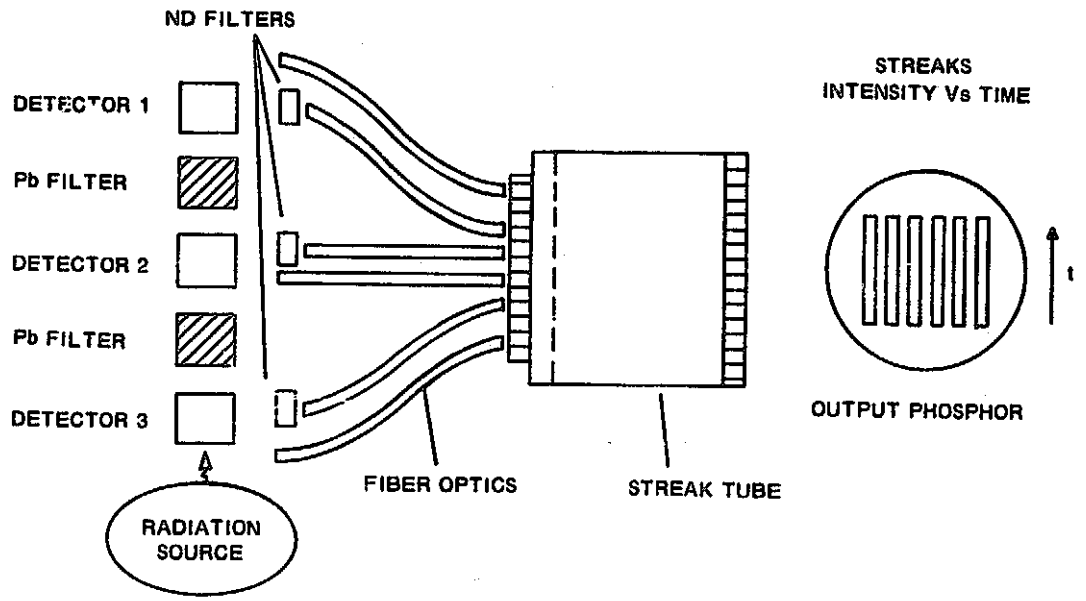

FIGURE 3 STREAKING CAMERA RECORDING

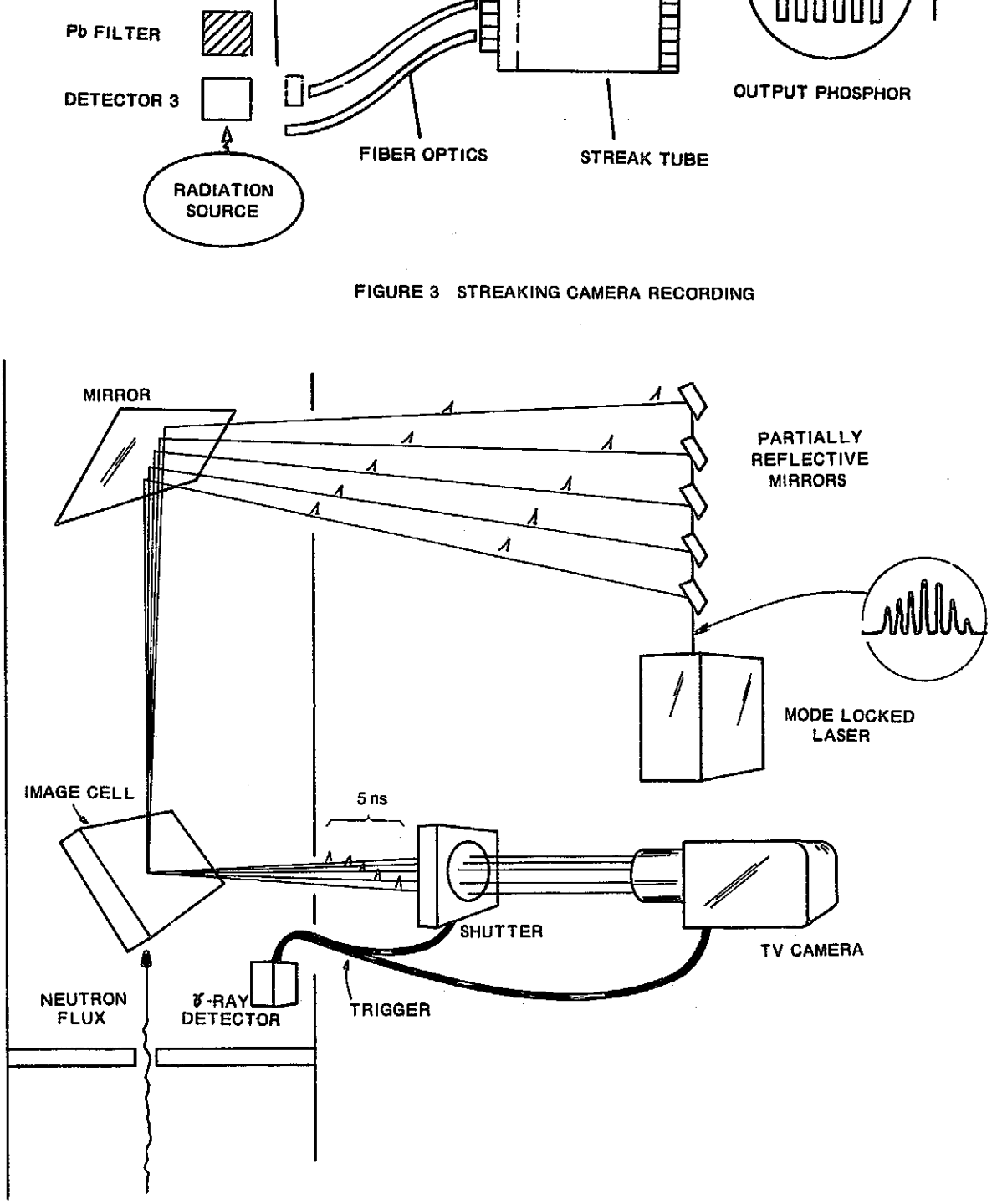

FIGURE 4 LASER TIME-RESOLVED PINEX (LTRP)

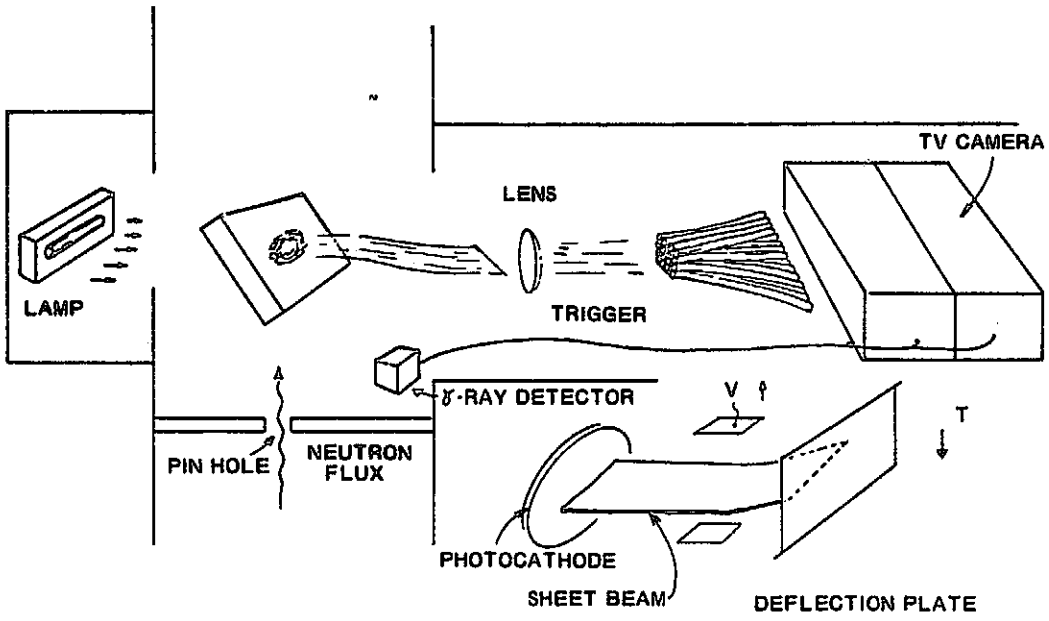

FIGURE 5 STREAKING CAMERA IMAGING

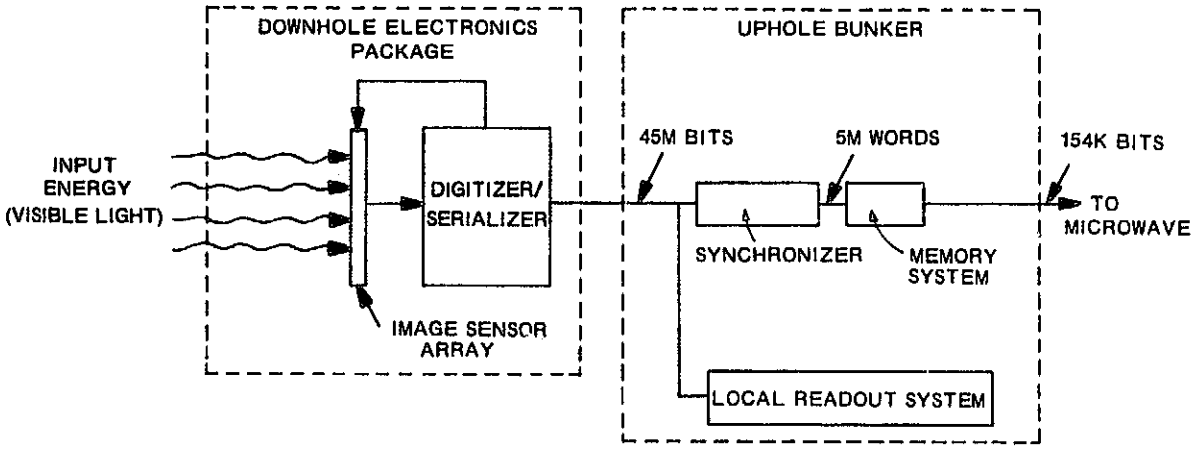

FIGURE 6 45 MEGABITS/SECOND IMAGING SYSTEM

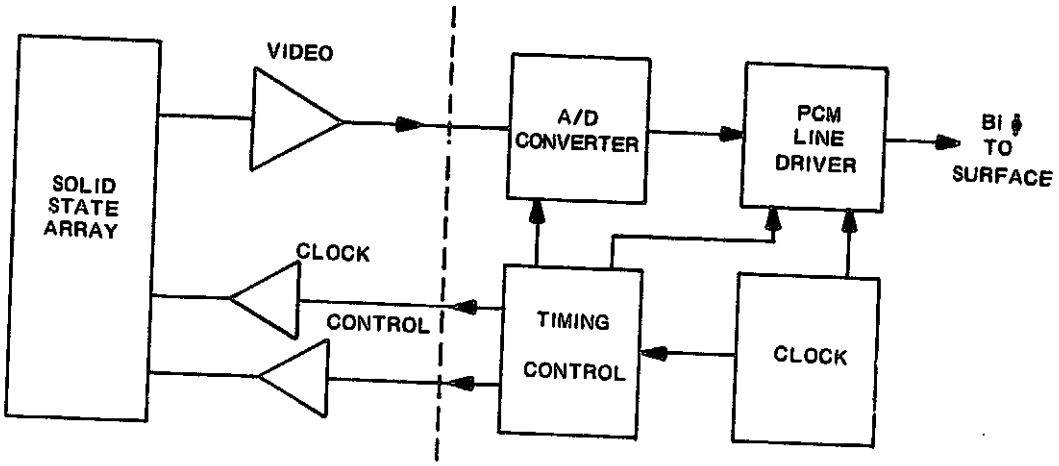

FIGURE 7 DOWNHOLE BUFFER SYSTEM

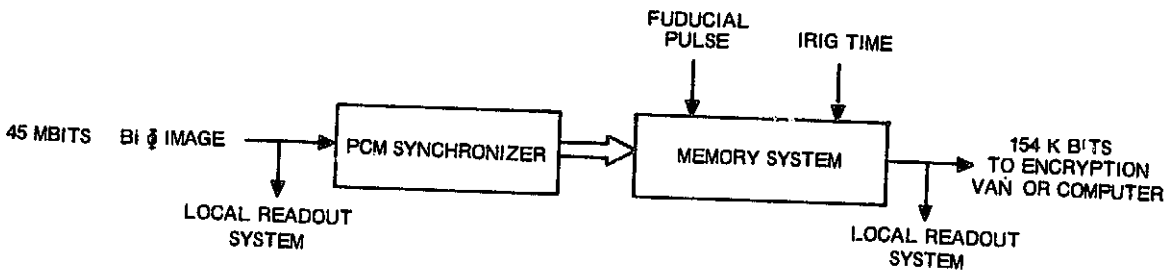

FIGURE 8 UPHOLE BUFFER SYSTEM

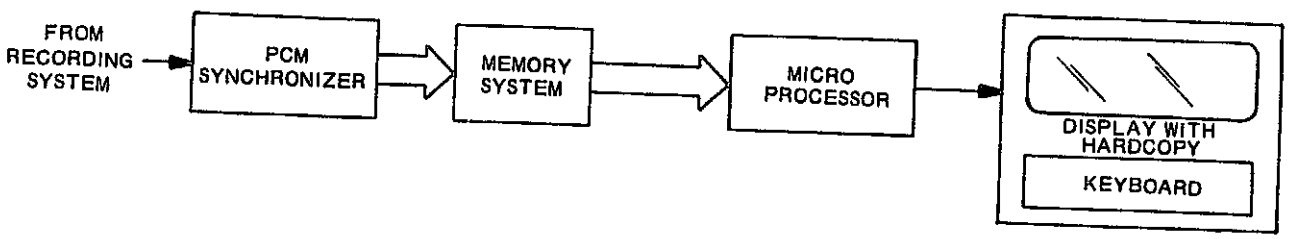

FIGURE 9 LOCAL READOUT SYSTEM

N77-17285

TELEVISION APPLICATIONS OF INTERLINE-TRANSFER CCD ARRAYS

Kenneth A. Hoagland

Fairchild Camera & Instrument Corporation
Fairchild Imaging Systems
300 Robbins Lane
Syosset, New York 11791

ABSTRACT

The design features and characteristics of interline-transfer (ILT) CCD arrays with 190 x 244 and 380 x 488 image elements are reviewed, with emphasis on optional operating modes and system application considerations. It is shown that the observed horizontal resolution for a TV system using an ILT image sensor can approach the aperture response limit determined by photosensor site width, resulting in enhanced resolution for moving images. Preferred camera configurations and read-out clocking modes for maximum resolution and low-light sensitivity are discussed, including a very low light level Intensifier-CCD concept. Several camera designs utilizing ILT-CCD arrays are described. These cameras demonstrate feasibility in applications where small size, low-power/low-voltage operation, high sensitivity and extreme ruggedness are either desired or mandatory system requirements.

I. INTRODUCTION

Charge-coupled area image sensors can be classified by the arrangement of sensing, storage and transport functions defining the flow of signal charge packets to the output detector. These functional arrangements or "readout organizations" have been selected to achieve interface compatibility with existing television system equipment requiring sequential video signals comprised of two interlaced fields at the conventional rates of 60 fields and 30 frames per second. Two readout organizations have been used to achieve interface compatibility. For the approach known as "frame-transfer" the sensor is divided horizontally to form an image sensing array and a separate light-shielded storage array. For the organization known as "interline-transfer", the image sensing, storage and transport functions are integrated within a single format region, with light-shielded vertical transport registers interleaved between columns of photosensor elements. Details of the frame-transfer organization and its application as a TV image sensor have been described elsewhere (Ref. 1); this paper is primarily concerned with the interline-transfer (ILT) device and its application as an image sensor or video signal processor component in television systems.

II. INTERLINE TRANSFER ARRAYS AS TV IMAGE SENSORS

The interline-transfer organization has been adopted for a family of charge-coupled image sensor designs with 100 x 100, 190 x 244 and 380 x 488 elements/frame (Ref.2). Features common to each of these designs are illustrated in Figure 1. The unit cell for these arrays contain one photosensor site and an adjacent light-shielded site which is one-half stage of a two-phase vertical transport register. In the normal readout mode alternate cell rows are uniquely assigned to each of the two fields comprising a TV frame, resulting in higher vertical MTF than for beam-scanned or frame-transfer type image sensors. An implanted barrier at the photosite/transfer site interface inhibits transfers to the vertical column register except when the photogate electrode potential (ϕ_p) is LOW and the adjacent transfer gate potential (ϕ_{V1} or ϕ_{V2}) is HIGH. Thus, 2/1 interlace can be achieved by pulsing ϕ_p low during each vertical blanking interval and applying complementary ϕ_{V1}, ϕ_{V2} waveforms with high states during alternate vertical blanking periods. At the start of the ODD field readout, elements corresponding to odd number rows are first shifted in unison into adjacent ϕ_{V1} sites for row transport along the column registers to the output register. The even field sequence is similar except the initial shift is into ϕ_{V2} sites. Three basic waveforms are sufficient for all charge transport functions prior to signal detection, since complementary waveforms can be used for both vertical and horizontal clock drives.

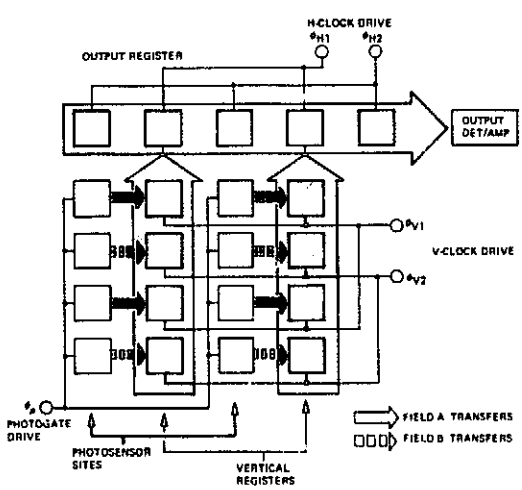

Figure 1. Interline-Transfer CCD Schematic

ILT area image sensors have characteristics which make these devices particularly useful for applications requiring high resolution display of moving image information:

1. The signal readout for each field does not contain the lag or residual signal effects from previous fields typically observed with beam-scanned image sensors.

2. All vertical transfers occur at the display line rate, thus field readout rates can be much higher than for frame-transfer type CCD sensors.

3. Since the integration period for photosensor sites is simultaneously defined for the entire field by the application of the appropriate ϕ_p and ϕ_v gate potentials, the information contained in the readout of a given field is analogous in spatial and temporal precision to the information recorded by an ideal "snapshot" camera with a fast-acting lens shutter. Thus image motion effects during a field integration period will be essentially similar for all photosensor sites, which is not the case with X-Y addressed solid-state sensors or beam-scanned image sensors where the process of sequential readout results in timing displacements of up to one field period across the vertical direction of the image format.

A unique feature of the ILT organization is its adaptability to an alternate readout mode which trades off static vertical resolution for improved moving image resolution. The normal mode for the 380 x 488 element sensor provides 2/1 field/frame interlaced readout with separate photosensor rows for addressing each active line of the displayed TV frame. Photosite integration time for the normal mode is 1/30 second and the Nyquist-limit vertical resolution is 488 TV lines. The alternate readout clocking mode is useful when it is desired to shorten the integration time to 1/60 second. In this mode charge packets from vertically adjacent sites along the even and odd field rows are added together in the vertical shift register before the start of the normal readout clocking sequence. Although the alternate mode has less vertical resolution than the normal mode, the difference can be minimized by performing the addition differently on alternate fields. For example, during the first field sensor rows 1 and 2, 3 and 4, 5 and 6, etc., are added together; during the next field sensor rows 2 and 3, 4 and 5, 6 and 7, etc., are added, with the row-addition sequence for subsequent fields alternating at field rate.

Because of the digital nature of charge transport functions, relatively simple circuit modifications can be used to change the clocking system from normal to alternate mode operation. The TV monitor test pattern photographs, (Figure 2), were obtained using a prototype 380 x 488 element CCD camera equipped with a selector switch to enable operation in either mode. Figure 2(a) shows the full screen display of a wedge-type target used for resolution tests. Figures 2(b) and 2(c) illustrate resolution effects for static imaging with normal mode 1/30 second integration and for the alternate mode with 1/60 integration, respectively. Nyquist limit resolutions for the normal mode are 488 TV lines/picture height (vertical) and 285 TV lines/picture height (horizontal). Alternate mode operation reduces the useful vertical resolution to 350-400 TV lines/picture height, i.e., comparable with the performance of frame-transfer CCD and beam-scanned image sensors in 525-line television applications.

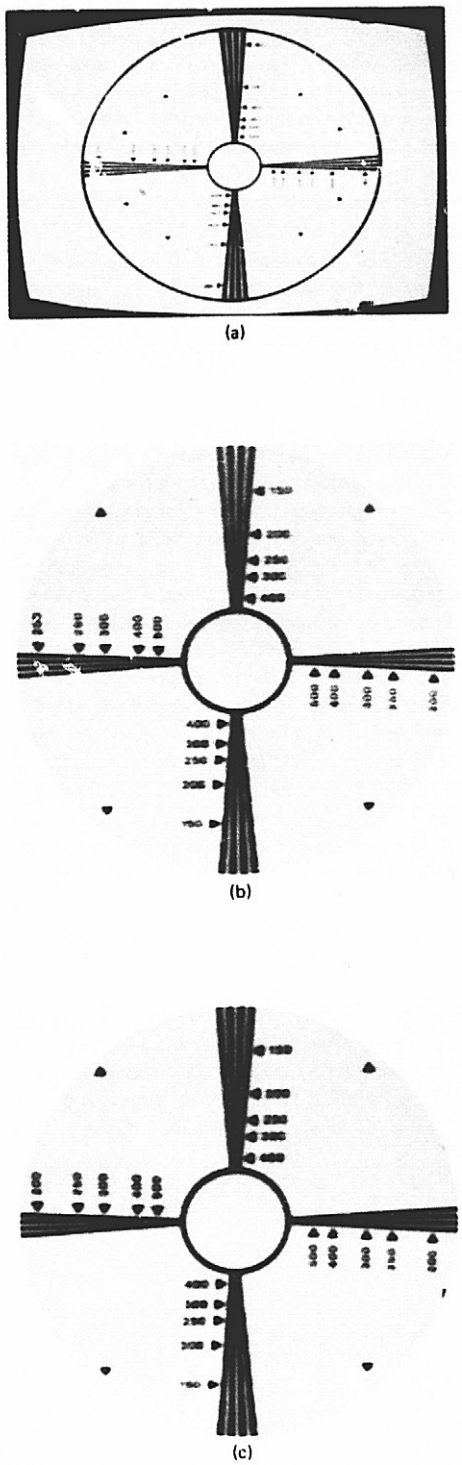

Figure 2. Resolution Test Target Imaging, 380 x 488 ILT-CCD Camera
(a) Full screen monitor display.
(b) Normal readout mode with 1/30 second integration.
(c) Alternate mode with 1/60 second integration.

One method to measure the performance of a TV camera viewing moving scene information is to expose the camera to resolution test patterns of vertical black and white bars which are moved at a uniform rate across the horizontal format direction. The observer tracks the moving information on the monitor screen and records the highest resolved spatial frequency as a function of viewfield traverse periods in the range of 5 to 20 seconds. A number of industrial and government laboratories perform tests of this type to determine the degradations in moving-image resolution caused by signal lag effects which can be particularly severe for certain types of beam-scanned image sensors (Ref. 3). Quite the opposite effect is observed with interline-transfer CCD-TV sensors. Evaluation tests of a 60 frame/second CCD camera using a 190 x 244 element array in the normal readout mode have resulted in moving image horizontal resolution observations approximately 2-1/2 times the Nyquist-limit for stationary image viewing.

The resolution enhancement observed for the moving image case is due to a combination of effects including negligible lag, precise spatial and temporal field exposure conditions, and the unique aperture response characteristics of the interline transfer organization. Figure 3 illustrates the latter characteristic. The unit cell dimensions for 190 x 244 and 380 x 488 arrays define 18 um high photosites, contiguous in the vertical direction, with 30 um center to center spacing in horizontal direction. Thus the vertical and horizontal Nyquist-limit sampling frequencies for stationary images are 27.8 lp/mm and 16.7 lp/mm respectively. The nominal photosite width dimension is 14 um , as determined by the width of aluminum stripes which opaque the adjacent vertical register sites. The output from an array pair can be optically and electrically multiplexed to double horizontal resolution as indicated in Figure 3 (b) and described in Reference (4). Figure 3(c) illustrates the sampling aperture geometry for a single-sensor camera where the effect of image motion is to displace the set of sampling apertures to new positions (with respect to the image) for each field period. In this case the observer tracking the displayed information is presented with three video frames sampling three overlapped regions of the total image space during each 0.1 second eye integration period. For preferred rates of image motion determined by (a) frame rate, (b) motion-smear effects during integration, and (c) the ability of the observer to track image motion, resolution enhancement to a limiting value fixed by MTF effects and the photosensor aperture width dimension can be achieved.

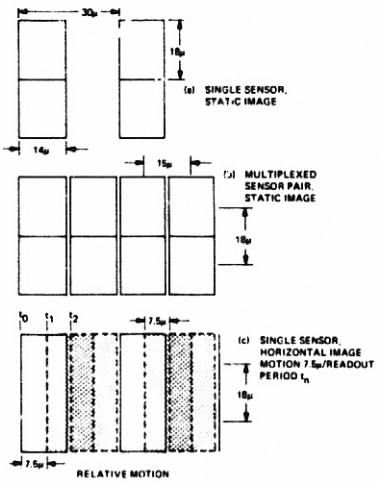

Figure 3. ILT-CCD Sampling Geometry

III. CAMERA AND TV SYSTEM APPLICATIONS

Since the development of the first CCD image sensors significant emphasis has been placed on demonstrating the advantages of these devices as replacements for conventional beam-scanned sensors in television system applications. The first commercially available device, with 100 x 100 elements, was used in the Fairchild MV-101 camera illustrated in Figure 4 (a). A subsequent design, the Fairchild MV-201 utilizing the higher resolution 190 x 244 array, is shown in Figure 4 (b). These cameras, with the exception of optics and an external power supply, are contained in small, lightweight packages of less than 17 cubic inches.

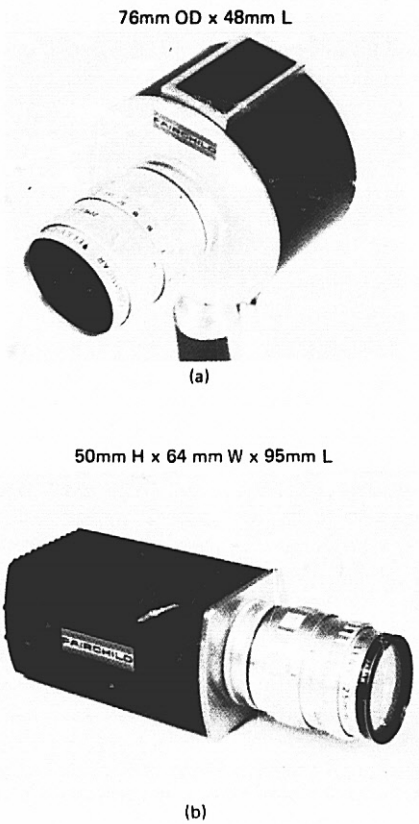

Figure 4. CCD Television Cameras Using Interline-Transfer Image Sensors
(a) Type MV-101 with 100 x 100 array.
(b) Type MV-201 with 190 x 244 array.

Variants of the MV-201 design have been developed for applications where the use of a beam-scanned image sensor is either undesirable or not feasible. An MV-201 camera has been incorporated in a camera system to be used for underground inspection in the event of a mine disaster. In this situation a long 2-1/2 inch diameter cylinder containing the camera, a slow-scan converter, and a battery pack is lowered into a borehole which has been drilled to reach the site. Single frame slow-scan video is then transmitted along a connecting cable to an observation site at ground level. Due to the possibility of explosive atmospheres at the mine site a standard vidicon system, with its associated high voltages, cannot be used without a large diameter explosion-proof housing. The CCD approach overcomes this limitation.

A development program, now is progress, utilizes a parachute deployed ILT-CCD camera and RF link in an artillery-launched projectile to provide real-time observation of selected areas (Ref. 5). The program makes use of the M485-A2 illuminating round for the 155 mm howitzer where the illuminant is replaced with a ballistically matched package (See Figure 5). In operation, the TV frames are simultaneously displayed in real time on a monitor and recorded on video tape. During the projectile launching, the camera system is required to endure setback accelerations of over 14,000 G's. A completely solid-state image sensor is clearly essential for operation in such an environment.

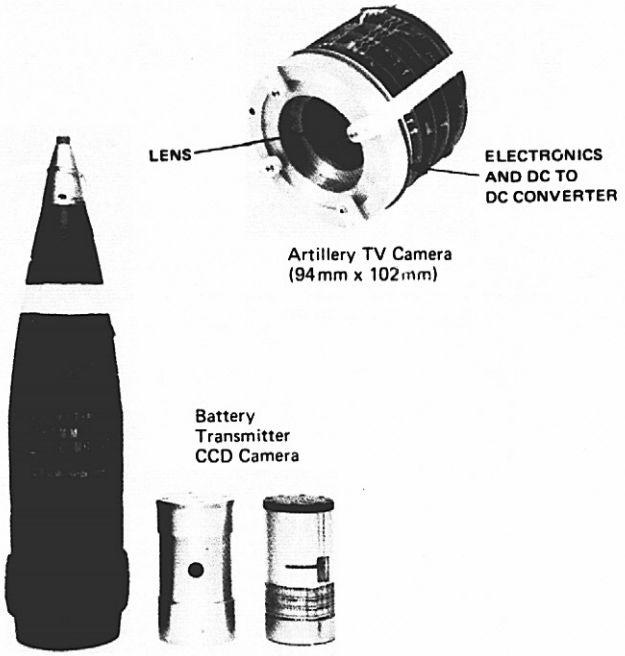

Figure 5. Artillery TV System

Recently concluded study programs have established feasibility for imaging systems consisting of a camera and video processor employing three electrically identical CCD area arrays, one of which functions as an imaging sensor supplying single-frame video on command to two opaqued area arrays operating as electrical-in/electrical-out analogue storage arrays (Ref. 6). The storage arrays are identical to the imaging array except an additional horizontal register, designed to accept analogue video signals at line rate, is used to inject charge packet information samples into column register sites on the side of the array opposite the output register. Control logic, arranged to select a particular frame of video from the imaging sensor output, is then used to load or "write-in" information into the vertical register sites of the storage arrays. Two arrays are required, each accepting one of the two fields comprising the complete frame. The frame information contained in the storage arrays can then be readout at the same rate as the input rate, or at a higher or slower rate, i.e. the two storage arrays perform a scan-rate conversion function. However, unlike other forms of electrical storage devices, the CCD array reads out the stored signal completely and therefore an erasure and priming cycle is not required. Write cycles can follow read cycles immediately with no need for dead time in between.

A major goal of CCD sensor research and development is to develop imaging devices suitable for use at very low light levels. Means for achieving this goal have been included in the 190 x 244 and 380 x 488 arrays; laboratory tests have yielded threshold imaging performance with sensor illumination levels of the order of 10^{-4} lx, 2854K (10^{-5} fc, Ref. 2, 4). The level of operating sensitivity achieved exceeds that of most beam-scanned image sensors with the exception of large-format camera tubes utilizing a form of image intensification prior to signal readout.

An approach which is conceptually similar is the subject of a current program to develop compact low-power Image Intensifier-CCD (I^2-CCD) TV cameras. In this case, the image sensor consists of a microchannel-plate image intensifier coupled by fiber optics to a buried-channel ILT-CCD array. Figure 6 illustrates preliminary test results for an assembly consisting of a 25 mm intensifier coupled through a 25/18 fiber-optic minifier to a 190 x 244 array, operating at a readout rate of 60 frames/sec. The smallest test patterns in these photographs correspond to 16.7 lp/mm resolution at the horizontal Nyquist limit. Threshold imagery was observed with sensor highlights near 10^{-5} lx, however the experimental system was gain limited at these levels. With additional gain, the threshold for the centrally located 1/2 Nyquist bars is expected to approach 10^{-6} lx, where the system would be intensifier-noise limited (Ref. 7).

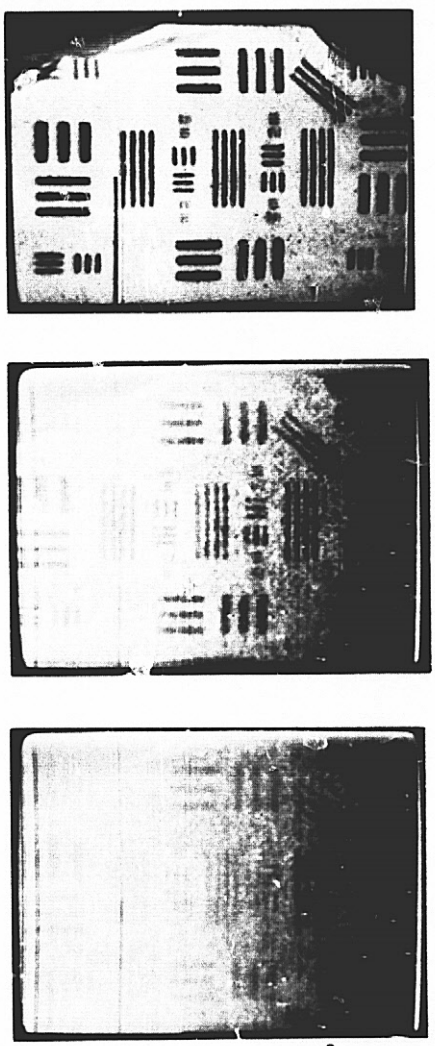

Figure 6. Image Intensifier-CCD(I^2-CCD) TV Camera Images, 190 x 244 Array

The I^2-CCD configuration does not require modification or redesign of either the Image Intensifier or CCD structure. Intensifier designs now in production for other night vision applications can be used. The CCD does not require "back-side" thinning for direct electron bombardment, nor is it necessary to operate the array within a vacuum envelope; each imaging device can be operated in an independent environment optimized for maximum reliability and operational life. Also, the use of an intensifier of the micro-channel-plate type provides an effective means for the suppression of CCD column blooming effects caused by intense point source overloads at the input photo-surface.

IV. CONCLUSIONS

CCD area arrays of the interline-transfer type are being utilized in a variety of television system applications. The number and complexity of drive waveforms necessary for charge transport have been minimized, thus simplifying the design of TV cameras where very small size, low power/low voltage operation and extreme ruggedness are required. Operating modes providing enhanced resolution of moving image information are feasible. Arrays with 190 x 244 and 380 x 488 elements exhibit sensitivity characteristics which make these devices useful as very low light level TV image sensors, either with or without image intensification. The devices also have a unique capability for accepting information from an electrical input register for video signal processing applications, including scan rate conversion.

REFERENCES

1. Sequin, C.H. and Tompsett, M.F., In Charge Transfer Devices, Chapter V, Academic Press, New York, 1975.

2. Steffe, W., Walsh, L., and Kim, C.K., "A High Performance 190 x 244 CCD Area Image Sensor Array", Proc. of the Int'l Conf. on the Application of Charge Coupled Devices, pp 101-108, San Diego, CA, October 1975.

3. Anderton, H., and Beyer, R.R., "Dynamic Imaging with Television Cameras", In Advances in Electronics and Electron Physics, pp 229-Vol 28A, Academic Press, London, 1969.

4. Hoagland, K.A., and Balapole, H.L., "CCD-TV Cameras Utilizing Interline-Transfer Area Image Sensors", Proc. of the Int'l Conf. on the Application of Charge Coupled Devices, pp 173-180, San Diego, CA, October 1975.

5. Ohlhoff, E., Vicars-Harris, M., and Bashe, R., "Artillery Launched Television", Proc. of the 1976 SPIE Technical Symposium/East, Vol. 79, Reston, VA, March 1976.

6. Hirschberg, I., "CCD Sensors, A Candidate for Precision Mappers", American Society of Photogrammetry Convention, Washington, D.C., February 1976.

7. Hoagland, K.A., "Low Light Level Performance Analysis for Charge Coupled Device TV Cameras", Proc. of the 1976 SPIE Technical Symposium/East, Vol. 78, Reston, VA, March 1976.

BIBLIOGRAPHY OF CHARGE-COUPLED DEVICE TECHNOLOGY

C. K. Sterkin
Jet Propulsion Laboratory

1. Ablassmeier, U., and Doering, E., "CCD Circuits of High-Storage Density in Al-Si Gate Technology," Siemens Forschungs- und Entwicklungsberichte, Vol. 4, No. 4, pp. 226-230, 1975. (In German)

2. Altman, L., "Charge-Coupled Devices Move in on Memories and Analog Signal Processing," Electronics, Vol. 47, No. 16, pp. 91-101, Aug. 8, 1974.

3. Amelio, G. F., "Physics and Applications of Charge-Coupled Devices," in 1973 IEEE Intercon Technical Papers, proceedings of the Institute of Electrical and Electronics Engineers International Convention and Exposition, New York, N. Y., March 26-30, 1973, Vol. 6, Paper 1/3.

4. Ando, K. J., "MTF and Point-Spread Function for a Large-Area CCD Imager," in proceedings of the Symposium on Charge-Coupled Device Technology for Scientific Imaging Applications, Pasadena, Calif., March 6-7, 1975, pp. 192-215.

5. Antcliffe, G. A., et al., "Large-Area CCD Imagers for Spacecraft Applications," in proceedings of the Symposium on Charge-Coupled Device Technology for Scientific Imaging Applications, Pasadena, Calif., March 6-7, 1975, pp. 125-136.

6. Antcliffe, G. A., et al., "Operation of CCD's with Stationary and Moving Electron-Beam Input," IEEE Transactions on Electron Devices, Vol. ED-22, No. 10, pp. 857-861, Oct. 1975.

7. Antcliffe, G. A., "Development of CCD Imaging Sensors for Space Applications, Phase 1," Final Report. NASA-CR-148193. Texas Instruments, Inc., Dallas; Jet Propulsion Laboratory, Pasadena, Dec. 15, 1975.

8. Arens, W. E., "Charge-Coupled Device Data Processor for an Airborne Imaging Radar System," Patent Application. US-Patent-Appl-SN-589119. National Aeronautics and Space Administration, Pasadena; Jet Propulsion Laboratory, Pasadena, June 23, 1975.

9. Autio, G. W., and Bafico, M. A., "Gamma Noise in CCD's," Infrared Physics, Vol. 15, pp. 249-258, Nov. 1975.

10. Baker, R. T., "CCD Array Forms Random-Access Memory," Electronics, Vol. 48, No. 23, pp. 138-139, Nov. 1975.

11. Baker, W. D. and Michels, D. J., "Imaging Performance of a CCD Array at 200°K," in proceedings of the Symposium on Charge-Coupled Device Technology for Scientific Imaging Applications, Pasadena, Calif., March 6-7, 1975, pp. 186-191.

12. Bankowski, W. F., Kumar, V. R., and Tartamella, J. D., "Charge-Coupled Devices Optical Sensor Storage Device," IBM Technical Disclosure Bulletin, Vol. 16, No. 9, pp. 2915-2916, Feb. 1974.

13. Barbe, D. F., "Imaging Devices Using the Charge-Coupled Concept - for Remote Sensing," IEEE Proceedings, Vol. 63, pp. 38-67, Jan. 1975.

14. Barbe, D. F., "Charge-Coupled-Device Imagers," in Technical Digest, proceedings of International Electron Devices Meeting, Washington, D. C., Dec. 1-3, 1975, pp. 60-65.

15. Barbe, D. F., and Baker, W. D., "Signal Processing Devices Using the Charge-Coupled Concept," Microelectronics, Vol. 7, No. 2, pp. 36-45, Dec. 1975.

16. Barbe, D. F., "Charge-Coupled Device and Charge-Injection Device Imaging," IEEE Transactions on Electron Devices, Vol. ED-23, No. 2, pp. 177-182, Feb. 1976.

17. Beaumont, J., "Performance Evaluation of the CCD450 Digital Memory," M. S. Thesis. AD-A019810. Air Force Institute of Technology, Wright-Patterson AFB, Ohio, Dec. 1975.

18. Benz, H. F. and Husson, C., "Charge-Coupled Device (CCD) Analog Signal Processing," IEEE Proceedings, Vol. 63, No. 5, pp. 822-823, May 1975.

19. Berger, J., "Comparaison des Performances des Dispositifs BBD et CCD Appliques aux Senseurs Optiques (Performance Comparison of CCD and BBD Working as Optical Sensors)," L'Onde Electrique, Vol. 54, No. 7, pp. 331-342, Aug.-Sept. 1974. (In French)

20. Bertram, W. J., et al., "Three-Level Metallization Three-Phase CCD," IEEE Transactions on Electron Devices, Vol. ED-21, No. 12, pp. 758-767, Dec. 1974.

21. Beynon, J. D. E., "Charged-Coupled Devices - Concepts, Technologies and Applications," Radio and Electronic Engineer, Vol. 45, No. 11, pp. 647-656, Nov. 1975.

22. Beynon, J. D. E., "Basic Principles of Charge-Coupled Devices," Microelectronics, Vol. 7, No. 2, pp. 7-13, Dec. 1975.

23. Bharat, R., "On the Feasibility of Slow-Wave-Structure Clocking of High-Frequency Charge-Coupled Devices," AD-768786. Denver University, Denver, Colo.; Battelle Columbus Laboratories, Columbus, Ohio, Oct. 1973.

24. Bharat, R., "A Frequency Divider Using a Charge-Coupled Device - for Timing Devices," AD-774253. Army Electronics Command, Fort Monmouth, N. J., Dec. 1973.

25. Bleier, S. A., "A Quantum Mechanical Description of Charge Injection Devices (CID)," M. S. Thesis. AD-A013496. Monmouth College, July 1975.

26. Board, K., Shannon, J. M., and Gill, A., "C.C.F.E.T.: An Active Charge-Coupled Device," Electronics Letters, Vol. 11, No. 19, pp. 452-453, Sept. 18, 1975.

27. Borsuk, J., and Bordoloi, K., "Charge-Coupled Devices: A Review," in Proceedings of the IEEE Southeast-Con, Region 3 Conference, Louisville, Ky., Apr. 30-May 2, 1973, Paper T-5.

28. Boudreaux, N. A., III, "Design Optimization of Metal-Insulator Semiconductor Devices for Infrared Solid State Imaging," M. S. Thesis. AD-A005472. Naval Postgraduate School, Monterey, Calif., Dec. 1974.

29. Bower, R. W., Zimmerman, T. A., and Mohsen, A. M., "Two-Phase Offset Gate CCD," IEEE Transactions on Electron Devices, Vol. ED-22, No. 2, pp. 70-72, Feb. 1975.

30. Bower, R. W., Zimmerman, T. A., and Mohsen, A. M., "Performance Characteristics of the Offset-Gate Charge-Coupled Device," IEEE Transactions on Electron Devices, Vol. ED-22, No. 2, pp. 72-74, Feb. 1975.

31. Brodersen, R. W., Buss, D. D., and Tasch, A. F., Jr., "Experimental Characterization of Transfer Efficiency in Charge-Coupled Devices," IEEE Transactions on Electron Devices, Vol. ED-22, No. 2, pp. 40-46, Feb. 1975.

32. Brodersen, R. W., Hewes, C. R., and Buss, D. D., "A 500-Stage CCD Transversal Filter for Spectral Analysis," IEEE Transactions on Electron Devices, Vol. ED-23, No. 2, pp. 143-152, Feb. 1976.

33. Brodersen, R. W., and Emmons, S. P., "Noise in Buried Channel Charge-Coupled Devices," IEEE Transactions on Electron Devices, Vol. ED-23, No. 2, pp. 215-223, Feb. 1976.

34. Brotherton, S. D., and Singh, M. P., "Influence of Clock Waveforms on the Performance of Charge Coupled Devices," Solid State Electronics, Vol. 17, No. 9, pp. 981-984, Sept. 1974.

35. Brown, R. W. and Chamberlain, S. G., "Quantum Efficiency of a Silicon Gate Charge-Coupled Optical Imaging Array," Physica Status Solidi (A) Applied Research, Vol. 20, No. 2, pp. 675-685, Dec. 1973.

36. Browne, V. A., and Perkins, K. D., "A Nonoverlapping Gate Charge-Coupling Technology for Serial Memory and Signal Processing Applications," IEEE Transactions on Electron Devices, Vol. ED-23, No. 2, pp. 271-275, Feb. 1976.

37. Burt, D. J., "Charge-Coupled Devices and Their Application," Electronics and Power, Vol. 21, No. 2, pp. 93-97, Feb. 6, 1975.

38. Burt, D. J., et al., "Development of a CCD Image Sensor, Phase 1," Final Report. Rept-16194C. General Electric Co., Ltd., Wembley (England), Nov. 1975.

39. Buss, D. D., Bailey, W. H., and Collins, D. R., "Analysis and Applications of Analogue CCD Circuits," in Digest Papers, proceedings of the International Symposium on Circuit Theory, Toronto., Ont., Apr. 9-11, 1973, pp. 3-7.

40. Buss, D. D., Holmes, J. D., and Rosser, L. A., "Investigation of Semiconductor Charge Devices, Part 1," Final Report. RADC-TR-73-259-PT-1. AD 772637. Texas Instruments, Inc., Dallas, Tex, Oct. 1973.

41. Buss, D. D., et al., "Signal Processing Applications of Charge Coupled Devices," in proceedings of the Western Electronic Show and Convention, Los Angeles, Calif., Sept. 10-13, 1974, Paper 2/2.

42. Buss, D. D., et al., "Application of Charge-Coupled Devices to Radar Signal Processing," in NEREM 74 Record, proceedings of the Northeast Electronics Research and Engineering Meeting, Boston, Mass., Oct. 28-31, 1974, pp. 83-98.

43. Buss, D. D., and Hewes, C. R., "Tunable Filters Using Charge Transfer Devices," Interim Technical Report, 16 July 1973 - 16 Mar. 1974. AD-782818. Texas Instruments, Inc., Dallas, Tex., June 1974.

44. Buss, D. D., and Hewes, C. R., "Tunable Filters Using Charge Transfer Devices - Computerized Simulation," Interim Report, 17 Mar. - 15 July 1974. AD-A000846. Texas Instruments, Inc., Dallas, Tex., Oct. 1974.

45. Buss, D. D. and Hewes, C. R., "Tunable Filters Using Charge Transfer Devices," Interim Report, 16 July 1974 - 16 Mar. 1975. AD-A012358. Texas Instruments, Inc., Dallas, Tex., June 1975.

46. Buss, D. D., et al., "Applications of Charge-Coupled Device Transversal Filters to Communication," in Conference Record, Vol. 1, proceedings of the International Conference on Communications, 11th, San Francisco, Calif., June 16-18, 1975, pp. 2-4 to 2-9. Institute of Electrical and Electronics Engineers, Inc., New York, N.Y., 1975.

47. Buss, D. D., et al., "Charge Transfer Device Transversal Filters for Communication Systems," Microelectronics, Vol. 7, No. 2, pp. 46-53, Dec. 1975.

48. Campana, S. B., and Barbe, D. F., "Tradeoffs Between Aliasing and MTF - for Charge Coupled Device Imagers," in Proceedings of the Technical Program, Electro-Optical Systems Design Conference - 1974 West, San Francisco, Calif., Nov. 5-7, 1974, pp. 1-9.

49. Carnes, J. E., Kosonocky, W. F., and Levine, P. A., "Measurements of Noise in Charge-Coupled Devices," RCA Review, Vol. 34, No. 4, pp. 553-565, Dec. 1973.

50. Carnes, J. E., and Kosonocky, W. F., "Charge-Coupled Devices and Applications," Solid State Technology, Vol. 17, No. 4, pp. 67-77, Apr. 1974,

51. Carnes, J. E., et al., "Charge-Coupled Devices for Computer Memories," in Conference Proceedings, Vol. 43, 1974, for AFIPS National Computer Conference and Exposition, Chicago, Ill., May 6-10, 1975, pp. 827-837.

52. Carnes, J. E., et al., "Effects of Radiation on Charge-Coupled Devices," in proceedings of the Symposium on Charge-Coupled Device Technology for Scientific Imaging Applications, Pasadena, Calif., Mar. 6-7, 1975, pp. 243-251.

53. Chamberlain, S. G., Copeland, M. A., and Ibrahim, A. A., "Some General Experimental Studies on Charge-Coupled Device Circuits," International Journal of Electronics, Vol. 35, No. 6, pp. 833-846, Dec. 1973.

54. Chamberlain, S. G., and Woo, B. Y., "Transient Analysis of Electrical Charge Injection into Charge-Coupled Devices," International Journal of Electronics, Vol. 40, pp. 569-586, June 1976.

55. Chambers, J. M., Sauer, D. J., and Kosonocky, W. F., "CCD's as Drum and Disc Equivalents," in proceedings of the Western Electronic Show and Convention, Los Angeles, Calif., Sept. 10-13, 1974, Paper 6/1.

56. Chan, C. H., Chamberlain, S. G., and Colton, D. R., "Charge-Coupled Serial to Parallel Shift Register," in Conference Digest, proceedings of the International Electrical, Electronics Conference and Exposition, Toronto, Ont., Oct. 1-3, 1973, Paper No. 73234, pp. 140-141. Institute of Electrical and Electronics Engineers, New York, N. Y., 1973.

57. Chan, C. H., and Chamberlain, S. G., "Numerical Methods for the Charge Transfer Analysis of Charge-Coupled Devices," Solid-State Electronics, Vol. 17, No. 5, pp. 491-499, May 1974.

58. Chien, R. T., and Snyder, W. E., "Hardware for Visual Image Processing," IEEE Transactions on Circuits and Systems, Vol. CAS-22, pp. 541-551, June 1975.

59. Choisser, J. P., "Experiments on the Use of CCD's to Detect Photoelectron Images," in proceedings of the Symposium on Charge-Coupled Device Technology for Scientific Imaging Applications, Pasadena, Calif., Mar. 6-7, 1975, pp. 150-162, June 1975.

60. Chou, S., "Design of a 16 384-Bit Serial Charge-Coupled Memory Device," IEEE Transactions on Electron Devices, Vol. ED-23, No. 2, pp. 78-86, Feb. 1976.

61. Chynoweth, A. G., "Electronic Materials - Functional Substitutions, " Science, Vol. 191, pp. 725-732, Feb. 20, 1976.

62. Clough, G. A., Kotyczka, W., and Erb, D. M., "Experimental Observation of Signal Degradation in Recirculating Charge-Coupled Devices," in Technical Digest, proceedings of the International Electron Devices Meeting, Washington, D. C., Dec. 9-11, 1974, pp. 251-252. Institute of Electrical and Electronics Engineers, New York, 1974.

63. Collet, M. G., and Vliegenthart, A. C., "Calculations on Potential and Charge Distributions in the Peristaltic Charge-Coupled Device," Philips Research Reports, Vol. 29, No. 1, pp. 25-44, Feb. 1974.

64. Collet, M. G., "Experimental Method to Analyse Trapping Centres in Silicon at Very Low Concentrations," Solid-State Electronics, Vol. 18, No. 12, pp. 1077-1083, Dec. 1975.

65. Collet, M. G., "The Influence of Bulk Traps on the Charge-Transfer Inefficiency of Bulk Charge-Coupled Devices," IEEE Transactions on Electron Devices, Vol. ED-23, No. 2, pp. 224-227, Feb. 1976.

66. Collins, D. R., et al., "Development of a CCD for Ultraviolet Imaging Using a CCD Photocathode Combination," in proceedings of the Symposium on Charge-Coupled Device Technology for Scientific Imaging Applications, Pasadena, Calif., Mar. 6-7, 1975, pp. 163-174.

67. Cooper, D. C., et al., "Reducing the Effect of Charge Transfer Inefficiency in a C.C.D. Video Integrator," Electronics Letters, Vol. 11, No. 16, pp. 384-385, Aug. 7, 1975.

68. Copeland, M. A., et al., "An Optical CCD Convolver," IEEE Transactions on Electron Devices, Vol. ED-23, pp. 152-155, Feb. 1976.

69. Corsi, C., et al., "Thin Film Infrared Detector Arrays for Integrated Electronic Structures - Based on Narrow-Gap Semiconductors Multicathode RF Sputtering Technique," Infrared Physics, Vol. 16, pp. 37-45, Jan.-Mar. 1976.

70. Currie, D. G.,"On a Photon-Counting Array Using the Fairchild CCD-201," in proceedings of the Symposium on Charge-Coupled Device Technology for Scientific Imaging Applications, Pasadena, Calif., Mar. 6-7, 1975, pp. 80-90.

71. Curtis, D. A., Granger, R. J., and Ross, M. H., "The Status, Development and Applications in Space of Solid-State Imaging Systems - Noting Charge-Coupled and Charge Injection Devices," Final Report. ESRO-CR(P)-416, April 1974. Cambridge Consultants Ltd. (England)

72. Daimon, Y., Mohsen, A. M., and McGill, T. C., "Charge Transfer in Buried-Channel Charge-Coupled Devices," in Digest of Technical Papers, proceedings of the IEEE International Solid State Circuits Conference, University of Pennsylvania, Philadelphia, Pa., Feb. 13-15, 1974, pp. 146-147, 245.

73. Daimon, Y., Mohsen, A. M., and McGill, T. C., "Final State of the Charge-Transfer Process in Charge-Coupled Devices," IEEE Transactions on Electron Devices, Vol. ED-21, No. 4, pp. 266-272, Apr. 1974.

74. Dale, B., "The Validity of the Depletion Approximation Applied to a Bulk Channel Charge-Coupled Device," IEEE Transactions on Electron Devices, Vol. ED-23, No. 2, pp. 275-282, Feb. 1976.

75. Dearnaley, G., "Ion Implantation in Semoconductor Fabrication Technology," Nature, Vol. 256, pp. 701-705, Aug. 28, 1975.

76. DeClerck, G. J., et al., "Experimental Results on Three-Phase Polysilicon CCD's with a TCE-SiO_2/Si_3N_4 Gate Insulator," IEEE Transations on Electron Devices, Vol. ED-23, pp. 297-299, Feb. 1976.

77. El-Sissi, H., and Cobbold, R. S. C., "One Dimensional Study of Buried-Channel Charge-Coupled Devices," IEEE Transactions on Electron Devices, Vol. ED-21, No. 7, pp. 437-447, July 1974.

78. El-Sissi, H., and Cobbold, R. S. C., "Potentials and Fields in Buried-Channel CCD's: A Two-Dimensional Analysis and Design Study," IEEE Transactions on Electron Devices, Vol. ED-22, No. 3, pp. 77-90, Mar. 1975.

79. El-Sissi, H., and Cobbold, R. S. C., "On the Decay of Small Amounts of Signal Charge in Surface-Channel CCD's," IEEE Transactions on Electron Devices, Vol. ED-22, No. 3, pp. 154-156, Mar. 1975.

80. El-Sissi, H., and Cobbold, R. S. C., "Influence of Signal Charge on the Final Decay Characteristics of Surface-Channel Charge-Coupled Devices," Solid-State Electronics, Vol. 18, No. 10, pp. 867-870, Oct. 1975.

81. Emmons, S. P., and Buss, D. D., "Noise Measurements on the Floating Diffusion Input for Charge-Coupled Devices," Journal of Applied Physics, Vol. 45, No. 12, pp. 5303-5306, Dec. 1974.

82. Emmons, S. P., Tasch, A. F., Jr., and Caywood, J. M., "Low Noise CCD Input with Reduced Sensitivity to Threshold Voltage," in Technical Digest, proceedings of the International Electron Devices Meeting, 20th, Washington, D.C., Dec. 9-11, 1974, pp. 233-235.

83. Emmons, S. P., et al., "A Study of Noise in Charge-Coupled Devices," Final Technical Report, 1 Apr. 1974 - 31 Mar. 1975, AD-A015365. Texas Instruments, Inc., Dallas. May 1975.

84. Epifanov, A. A., Frolov, O. S., and Derkach, Iu. P., "Theoretical Analysis of the Kinetics of Free Charge Transport in Charge-Coupled Devices," Poluprovodnikovaia Tekhnika I Mikroelektronika, No. 22, pp. 18-29, 1976. (In Russian)

85. Esser, L. J. M., "Peristaltic Charge-Coupled Device for High-Speed Charge Transfer," in Digest of Technical Papers, proceedings of the IEEE International Solid-State Circuits Conference, University of Pennsylvania, Philadelphia, Pa., Feb. 13-15, 1974, pp. 28, 29, 219.

86. Fairchild Camera and Instrument Corp., Mountain View, Calif., "Charge Coupled Device Image Sensor Study," Final Report. NASA-CR-136937. Feb. 1974.

87. Fairchild Space and Defense Systems, Syosset, N. Y., "Distributed Floating-Gate Amplifier (DFGA)," Final Report, Aug. 1973 - Aug. 1974. AD-A002474. Oct. 1974.

88. Fang, T.F., and Liu, H. K., "Fabrication and Measurements of a Silicon Charge-Coupled Device," in Proceedings of the IEEE Southeast-Con, Region 3 Conference, Louisville, Ky., Apr. 30 - May 2, 1973, Paper T-6.

89. Feth, G. C., "Memories - Smaller, Faster, and Cheaper," IEEE Spectrum, Vol. 13, pp. 36-43, June 1976.

90. Fishman, G. J., et al., "An X-Ray Shadowgraph to Locate Transient High-Energy Celestial Sources," in proceedings of the Symposium on Charge-Coupled Device Technology for Scientific Imaging Applications, Pasadena, Calif., Mar. 6-7, 1975, pp. 4-13.

91. Fraser, J. C., et al., "Extrinsic Silicon Charge Coupled Device for Detecting Infrared Radiation," in Technical Digest, proceedings of the International Electron Devices Meeting, 20th, Washington, D.C.. Dec. 9-11, 1974, pp. 442-445.

92. French, D. E., Sekula, J. A., and Hartman, J. M., "Off-Focal-Plane Time Delay and Integration (OTDI) Using Charge Coupled Devices," in Technical Digest, proceedings of the International Electron Devices Meeting, 20th, Washington, D.C., Dec. 9-11, 1974, pp. 437-441.

93. Galema, S. D., Schwartz, R. J., and Gunshor, R. L., "Acoustic Surface Wave Interaction Charge-Coupled Device," Applied Physics Letters, Vol. 29, pp. 82, 83, July 15, 1976.

94. Gassaway, J. D., "LSI Arrays for Space Stations," Interim Report. NASA-CR-144166. Missippi State University, Miss., Feb. 1976.

95. Gassaway, J. D., "Electrostatic Analysis of Charge-Coupled Structures - Numerical Analysis of Electrostatics for Shift Registers," NASA-CR-144175. Mississippi State University, Miss., Feb. 1976.

96. Gelberger, P. P., and Salama, C. A. T., "Moat-Etched Two-Phase Charge-Coupled Devices," Solid-State Electronics, Vol. 17, No. 3, pp. 301-305, Mar. 1974.

97. Goss, W. C., "CCD Star Trackers," in proceedings of the Symposium on Charge-Coupled Device Technology for Scientific Imaging Applications, Pasadena, Calif., Mar. 6-7, 1975, pp. 31-45.

98. Gunsagar, K. C., Guidry, M. R., and Amelio, G. F., "A CCD Line Addressable Random-Access Memory (LARAM)," IEEE Journal of Solid-State Circuits, Vol. SC-10, pp. 268-273, Oct. 1975.

99. Gunshor, R. L., "The Interaction Between Semiconductors and Acoustic Surface Waves - A Review," Solid-State Electronics, Vol. 18, pp. 1089-1093, Dec. 1975.

100. Gupta, B. B., "Engineering - in Charge Coupled Devices," Electronic Engineering (London), Vol. 47, No. 573, pp. 41-46, Nov. 1975.

101. Haken, R. A., Baker, I. M., and Beynon, J. D. E., "Simple Driving and Frequency Characterization Technique for Two-Phase Charge-Coupled Devices," IEEE Journal of Solid-State Circuits, Vol. SC-8, No. 4, pp. 199-203, Aug. 1974.

102. Haken, R. A., "Supply Charge Isolation - A Simple Surface Potential Equilibrium Charge-Injection Technique for Charge-Coupled Devices," IEEE Transactions on Electron Devices, Vol. ED-23, No. 2, pp. 257-264, Feb. 1976.

103. Hamaoui, H., Amelio, G., and Rothstein, J., "Application of an Area-Imaging Charge-Coupled Device for Television Cameras," IEEE Transactions on Broadcast and Television Receivers, Vol. BTR-20, No. 1, pp. 78-85, Feb. 1974.

104. Hartsell, G. A., and Kmetz, A. R., "Design and Performance of a Three-Phase, Double-Level Metal 160x100 Element CCD Imager," in Technical Digest, proceedings of the International Electron Devices Meeting, 20th, Washington, D.C., Dec. 9-11, 1974, pp. 59-62.

105. Hartsell, G. A., Robinson, D. A., and Collins, D. R., "Effects of Ionizing Radiation on CCD's" in proceedings of the Symposium on Charge-Coupled Device Technology for Scientific Imaging Applications, Pasadena, Calif., Mar. 6-7, 1975, pp. 216-227, June 1975.

106. Hense, K. R., and Collins, T. W., "Linear Charge-Coupled Device Signal-Processing Techniques," IEEE Transactions on Electron Devices, Vol. ED-23, No. 2, pp. 265-270, Feb. 1976.

107. Hewes, C. R., Brodersen, R. W., and Buss, D. D., "Frequency Filtering Using Charge Coupled Devices," in Proceedings of Annual Symposium on Frequency Control, 29th, Atlantic City, N. J., May 28-30, 1975, pp. 77-87.

108. Hirschberg, T., "CCDs and the Imaging Metamorphosis -- Applications of Charge Coupled Devices," Optical Spectra, Vol. 9, pp. 28-30, 32, 33, Nov. 1975.

109. Hoffman, C. P., et al., "Camera Memory Study for Large Space Telescope - Charge Coupled Devices," Final Report. Apr. 1974 - Jan. 1975. NASA-CR-143815. Westinghouse Electric Corporation, Baltimore, Md., Feb. 1975.

110. Hosack, H. H., and Dyck, R. H., "Transfer Inefficiency Effects in Parallel-Transfer Charge-Coupled Linear Imaging Devices," IEEE Transactions on Electron Devices, Vol. ED-22, No. 3, pp. 152-154, Mar. 1975.

111. Iamsa-Ad, V., "Charge-Coupled Devices for Analog Signal Processing Recursive Filter Study," M. S. Thesis. AD-A005469. Naval Postgraduate School, Monterey, Calif., Dec. 1974.

112. Ibrahim, A., et al., "CCD's for Transversal Filter Applications," in Technical Digest, proceedings of the International Electron Devices Meeting, 20th, Washington, D.C., Dec. 9-11, 1974, pp. 240-243.

113. Ionescu, N., "The Distribution of Mobile Carriers in a Surface CCD (Ideal Insulator)," Revue Roumaine de Physique, Vol. 21, No. 3, pp. 317-322, 1976.

114. Jack, M. D., and Dyck, R. H., "Charge-Transfer Efficiency in a Buried-Channel Charge-Coupled Device at Very Low Signal Levels," IEEE Transactions on Electron Devices, Vol. ED-23, No. 2, pp. 228-234, Feb. 1976.

115. Jacobson, R. A., "Charge Coupling - A Remarkable New Way to Manipulate Information," Machine Design, Vol. 46, No. 12, pp. 120-125, May 16, 1974.

116. Killiany, J. M., et al., "Effects of Ionizing Radiation on Charge-Coupled Imagers," in proceedings of the Symposium on Charge-Coupled Device Technology for Scientific Imaging Applications, Pasadena, Calif., Mar. 6-7, 1975, pp. 228-242.

117. Kim, C. K., and Dyck, R. H., "Low-Light Level Imaging with Buried Channel Charge-Coupled Devices," IEEE Proceedings, Vol. 61, No. 8, pp. 1146-1147, Aug. 1973.

118. Kim, C. K., "Two-Phase Charge Coupled Linear Imaging Devices with Self-Aligned Implanted Barrier," in Technical Digest, proceedings of the International Electron Devices Meeting, 20th, Washington, D.C., Dec. 9-11, 1974, pp. 55-58.

119. Kirk, J. C., Jr., "Digital Synthetic Aperture Radar Technology," in Record, proceedings of the International Radar Conference, Arlington, Va., Apr. 21-23, 1975, pp. 482-487.

120. Kleefstra, M., "First Experimental Bi-Polar Charge-Coupled Device," Microelectronics, Vol. 7, No. 2, pp. 68-69, Dec. 1975.

121. Kohn, E. S., and Schultz, M. L., "Charge-Coupled Scanned IR Imaging Sensors," Semiannual Technical Report, 29 June - 28 Dec. 1973. AD-780546. AFCRL-TR-74-0056. Radio Corporation of American, Princeton, N. J., Jan. 14, 1974.

122. Kohn, E. S., and Schultz, M. L., "Charge-Coupled Scanned IR Imaging Sensors," Semiannual Technical Report, 29 Dec. 1973 - 30 June 1974. AD-A003342. AFCRL-TR-74-0375. Radio Corporation of America, Princeton, N. J., July 15, 1974.

123. Kohn, E. S., "Charge Coupled Scanned IR Imaging Sensors," Semiannual Report, 1 July 1974 - 30 Apr. 1975. AD-A018057. AFCRL-TR-75-0284. Radio Corporation of America, Princeton, N. J., May 15, 1975.

124. Kohn, E. S., "A Charge-Coupled Infrared Imaging Array with Schottky-Barrier Detectors," IEEE Transactions on Electron Devices, Vol. ED-23, No. 2, pp. 207-214, Feb. 1976.

125. Kosonocky, W. F., "Charge-Coupled Devices - An Overview," in proceedings of the Western Electronic Show and Convention, Los Angeles, Calif., Sept. 10-13, 1974, Paper 2/1.

126. Kosonocky, W. F., and Sauer, D. J., "ABC's of CCD's," Electronic Design, Vol. 23, No. 8, pp. 58-63, Apr. 12, 1975.

127. Kosonocky, W. F., and Carnes, J. E., "Basic Concepts of Charge-Coupled Devices," RCA Review, Vol. 36, pp. 566-593, Sept. 1975.

128. Kosonocky, W. F., and Sauer, D. J., "Consider CCDs for a Wide Range of Uses," Electronic Design, Vol. 24, No. 6, pp. 70-78, Mar. 15, 1976.

129. Krambeck, R. H., et al., "Conductively Connected Charge-Coupled Device," IEEE Transactions on Electron Devices, Vol. ED-21, No. 1, pp. 70-72, Jan. 1974.

130. Krambeck, R. H., Retajczyk, T. F., Jr., and Yau, L. D., "Transfer Efficiency of E-Beam Fabricated C4D's," in Technical Digest, proceedings of the International Electron Devices Meeting, 20th, Washington, D.C., Dec. 9-11, 1974, pp. 248-250.

131. Krambeck, R. H., Retajczyk, T. F., Jr., and Yau, L. D., "Low Frequency Transfer Efficiency of E-Beam Fabricated Conductively Connected Charge-Coupled Device," IEEE Transactions of Electron Devices, Vol. ED-23, pp. 239-248, Feb. 1976.

132. Lancaster, A. L., and Hartman, J. M., "Recirculating CCD with Novel Input and Output Structures," in Technical Digest, proceedings of the International Electron Devices Meeting, 20th, Washington, D.C., Dec. 9-11, 1974, pp. 108-111.

133. Langan, L. J., "Solid State Mini-RPV Color Imaging System," AD-A018909. General Electric Company, Utica, N. Y., Sept. 12, 1975.

134. Lee, R.N., Scharnhorst, P.K., and Schoolar, R.B., "Preparation and Properties of PbS-Si Heterojunctions for Infrared Charge Coupled Imaging," Final Report, May 1972 - Nov. 1973. AD-775895. Naval Ordnance Laboratory, White Oak, Md., Jan. 17, 1974.

135. Leonberger, F. J., McWhorter, A. L., and Harman, T. C., "PbS MIS Devices for Charge-Coupled Infrared Imaging Applications," Applied Physics Letters, Vol. 26, pp. 704-707, June 15, 1975.

136. Lobenstein, H., and Ludington, D. N., "A Charge Transfer Device MTI Implementation," in Record, proceedings of the International Radar Conference, Arlington, Va., Apr. 21-23, 1975, pp. 107-110.

137. Lutin, E. A., Teliatnikov, L. I., and Shkalikov, V. N., "Phase Characteristics of a Two-Circuit Frequency Multiplier Employing a Charge-Storage Diode," Radiotekhnika, Vol. 30, pp. 60-63, Oct. 1975. (In Russian)

138. MacLennan, D. J., "Charge-Coupled Devices - 3. Signal Processing," Wireless World, Vol. 81, No. 1470, pp. 61-65, Feb. 1975.

139. MacLennan, D. J., and Mavor, J., "Novel Technique for the Linearisation of Charge-Coupled Devices," Electronics Letters, Vol. 11, No. 10, pp. 222-223, May 15, 1975.

140. Maines, J. D., and Paige, E. G. S., "Surface-Acoustic-Wave Devices for Signal Processing Applications," IEEE Proceedings, Vol. 64, pp. 639-652, May 1976.

141. Margraff, T. C., "Design and Performance of a CCD Memory System," M. S. Thesis. AD-A008657. Air Force Institute of Technology, Wright-Patterson Air Force Base, Ohio, Dec. 1974.

142. Martin, F. C., "Advanced Mail Systems Scanner Technology," Annual Report, 22 Oct. 1974 - 21 Oct. 1975. AD-A020175. Naval Electronics Laboratory Center, San Diego, Calif., Oct. 22, 1975.

143. Mattern, J., and Lampe, D. R., "A Reprogrammable Filter Bank Using Charge-Coupled Device Discrete Analog-Signal Processing," IEEE Transactions on Electron Devices, Vol. ED-23, No. 2, pp. 156-161, Feb. 1976.

144. Mayer, G. J., "The Chirp Z-Transform — A CCD Implementation," RCA Review, Vol. 36, No. 4, pp. 759-773, Dec. 1975.

145. Mayer, G. J., "Split-Gate CCD Sensing," RCA Technical Note No. 1148, Apr. 1976.

146. McCord, T. B., and Bosel, J. P., "Potential Usefulness of CCD Imagers in Astronomy," in proceedings of the Symposium on Charge-Coupled Device Technology for Scientific Imaging Applications, Pasadena, Calif., Mar. 6-7, 1975, pp. 65-69, June 1975.

147. McKenna, J., and Schryer, N. L., "Potential in a Charge-Coupled Device with No Mobile Minority Carriers," Bell System Technical Journal, Vol. 52, No. 10, pp. 1765-1793, Dec. 1973.

148. McKenna, J., Schryer, N. L., and Walden, R. H., "Design Considerations for a Two-Phase, Buried-Channel, Charge-Coupled Device," Bell System Technical Journal, Vol. 53, No. 8, pp. 1581-1597, Oct. 1974.

C-3

149. McKenna, J., and Schryer, N. L., "Analysis of Field-Aided Charge-Coupled Device Transfer," Bell System Technical Journal, Vol. 54, No. 4, pp. 667-685, Apr. 1975.

150. McNutt, M. J., and Sah, C. T., "High Frequency Space Charge Layer Capacitance of Strongly Inverted Semiconductor Surfaces," Solid-State Electronics, Vol. 17, No. 4, pp. 377-385, Apr. 1974.

151. Meindl, J. D.,"Implantable Integrated Electronics - in Biomedical Telemetry," in Biotelemetry II: Proceedings of the Second International Symposium, Davos, Switzerland, May 20-24, 1974, pp. 32-36.

152. Michels, D. J., "A CCD Image Transducer and Processor Suitable for Space Flight - Satellite Borne Solar Telescope Instrumentation," in proceedings of the Symposium on Charge-Coupled Device Technology for Scientific Imaging Applications, Pasadena, Calif., Mar. 6-7, 1975, pp. 14-29.

153. Michon, G. J., Burke, H. K., and Brown, D. M., "Recent Developments in CID Imaging - Using Charge Storage Capacitors," in proceedings of the Symposium on Charge-Coupled Device Technology for Scientific Imaging Applications, Pasadena, Calif., Mar. 6-7, 1975, pp. 106-115.

154. Mohsen, A. M., Bower, R., and McGill, T. C., "Overlapping-Gate Buried-Channel Charge-Coupled Devices," Electronics Letters, Vol. 9, No. 17, pp. 396-398, Aug. 23, 1973.

155. Mohsen, A. M., Diamon, Y., and Mead, C. A., "Numerical Simulation of Charge Coupled Device Operation, Abbreviated Form," Final Report. AD-A010915. California Institute of Technology, Pasadena, Calif., October 31, 1974.

156. Mohsen, A. M., and Tompsett, M. F., "Effects of Bulk Traps on the Performance of Bulk Channel Charge-Coupled Devices," IEEE Transactions on Electron Devices, Vol. ED-21, No. 11, pp. 701-712, Nov. 1974.

157. Mohsen, A. M., and Morris, F. J., "Measurements on Depletion-Mode Field Effect Transistors and Buried Channel MOS Capacitors for the Characterization of Bulk Transfer Charge-Coupled Devices," Solid-State Electronics, Vol. 18, No. 5, pp. 407-416, May 1975.

158. Mohsen, A. M., Tompsett, M. F., and Sequin, C. H., "Noise Measurements in Charge-Coupled Devices," IEEE Transactions on Electron Devices, Vol. ED-22, pp. 209-218, May 1975.

159. Mohsen, A. M., and Retajczyk, T. F., Jr., "Fabrication and Performance of Offset-Mask Charge-Coupled Devices," IEEE Transactions on Electron Devices, Vol. ED-23, No. 2, pp. 248-256, Feb. 1976.

160. Mohsen, A. M., et al., "16-KBit Block Addressed Charge-Coupled Memory Device," IEEE Transactions on Electron Devices, Vol. ED-23, pp. 108-116, Feb. 1976.

161. Mohsen, A. M., et al., "A 64-KBit Block Addressed Charge-Coupled Memory," IEEE Transactions on Electron Devices, Vol. ED-23, No. 2, pp. 117-126, Feb. 1976.

162. Nicastro, L. J., "Sinewave Clocking of CCDs at High Frequencies," RCA Engineer, Vol. 21, No. 4, pp. 76-77, Dec. 1975 - Jan. 1976.

163. Ong, D. G., and Pierret, R. F., "Approximate Formula for Surface Carrier Concentration in Charge-Coupled Devices," Electronics Letters, Vol. 10, No. 1, pp. 6-7, Jan. 10, 1974.

164. Ong, D. G., "Characterization and Modeling of Carrier Generation in Charge-Coupled Devices Operated at Low Frequency - Shift Registers," PhD. Thesis. Purdue University, Lafayette, Inc., 1974.

165. Ong, D. G., and Pierret, R. F., "Thermal Carrier Generation in Charge-Coupled Devices," IEEE Transactions on Electron Devices, Vol. ED-22, No. 8, pp. 593-602, Aug. 1975.

166. Otto, O. W., "Theoretical Comparison of Space-Charge-Enhanced Acoustic Surface Wave Convolvers," in proceedings of the Symposium on Optical and Acoustical Micro-Electronics, New York, N. Y., Apr. 16-18, 1974, pp. 511-528.

167. Parks, C. M., and Salama, C. A. T., "V. M. O. S. Conductively Coupled Charge-Coupled Device," Electronics Letters, Vol. 9, No. 25, pp. 593-594, Dec. 13, 1973.

168. Parks, C. M., and Salama, C. A. T., "V-Groove (VMOS) Conductively Connected Charge Coupled Devices, Solid-State Electronics, Vol. 18, No. 12, pp. 1061-1067, Dec. 1975.

169. Parrish, E. A., and McVey, E. S., "An Investigation of Potential Applications of OP-SAPS Operational Sampled Analog Processors," Semiannual Report. NASA-CR-143303. Virginia University, Charlottesville, Va., Feb. 1976.

170. Peek, H. L., "Twin-Layer PCCD Performance for Different Doping Levels of the Surface Layer - Peristaltic Charge Coupled Device Transfer Efficiency," IEEE Transactions on Electron Devices, Vol. ED-23, pp. 235-238, Feb. 1976.

171. Perkins, K. D., and Browne, V. A., "Sub-Microm Gap Metal Gate Technology for CCDs," Microelectronics, Vol. 7, No. 2, pp. 14-22, Dec. 1975.

172. Phillips, J. D., "Development of InSb Charge-Coupled Infrared Imaging Devices - Linear Imager," Final Report. NASA-CR-145003. Santa Barbara Research Center, Goleta, Calif., Apr. 1, 1976.

173. Powers, J. P., "Analysis of a Multipurpose Electro-Optical Signal Processor," Final Report, 1 May 1973 - 1 Jul. 1974. NPS-52P07411. AD-787475. Naval Postgraduate School, Monterey, Calif., June 20, 1974.

174. Reilly, T. H., and Herring, M., "CCD Imaging Instruments for Planetary Spacecraft Applications," in proceedings of the Symposium on Charged-Coupled Device Technology for Scientific Imaging Applications, Pasadena, Calif., Mar. 6-7, 1975, pp. 46-64.

175. Renda, G., and Lowrance, J. L., "Soft X-Ray Detection with the Fairchild 100 by 100 CCD," in proceedings of the Symposium on Charge-Coupled Device Technology for Scientific Imaging Applications, Pasadena, Calif., Mar. 6-7, 1975, pp. 91-105.

176. Renzelman, R. F., Jr., "Study of Infrared Solid State Images Using Charge Transport Devices," M. S. Thesis. AD-A005736. Naval Postgraduate School, Monterey, Calif., December 1974.

177. Riedl, J. L., "Charge Coupled Sensor Array Application to Tracker Systems, Information Display, Vol. 11, pp. 5-7, June 1975.

178. Roberts, J. B. G., "Radar Doppler Processing Using CCD and SAW Devices," Electronics Letters, Vol. 11, No. 22, pp. 525-526, Oct. 30, 1975.

179. Roberts, J. B. G., et al., "A Processor for Pulse-Doppler Radar," IEEE Transactions on Electron Devices, Vol. ED-23, No. 2, pp. 168-172, Feb. 1976.

180. Roberts, P. C. T., Singh, M. P., and Lamb, D. R., "Identification of Loss Mechanisms in 3-Phase Surface-Channel Charge-Coupled Devices," IEEE Proceedings, Vol. 122, No. 10, pp. 1089-1091, Oct. 1975.

181. Rodgers, R. L., III, "Silicon Intensifier Target Charged Coupled Device (SIT-CCD)," Final Technical Report, 28 Mar. 1973 - 7 Jan. 1974. AD-A018083. Radio Corporation of America, Lancaster, Pa., May 1974.

182. Rodgers, R. L., III, and Giovachino, D. L., "Cooled Slow-Scan Performance of a 512 by 320 Element Charge-Coupled Imager," in proceedings of the Symposium on Charge-Coupled Device Technology for Scientific Imaging Applications, Pasadena, Calif., Mar. 6-7, 1975, pp. 116-124, June 10, 1975.

183. Rosenbaum, S. D., et al., "A 16 384-Bit High-Density CCD Memory," IEEE Transactions on Electron Devices, Vol. ED-23, No. 2, pp. 101-108, Feb. 1976.

184. Sakaue, T., et al., "Improved Charge-Coupled Analog Delay Line," in proceedings of the Conference on Solid State Devices, 6th, Tokyo, Japan, Sept. 2-3, 1974, pp. 181-187.

185. Salomon, P. M., and Gorss, W. C., "A Microprocessor-Controlled CCD Star Tracker," in proceedings of the AIAA Aerospace Sciences Meeting, 14th, Washington, D. C., Jan. 26-28, 1976. AIAA Paper 76-116, January 1976.

186. Samuelsson, H., "Space Application of CCD Image Sensors," ESA Scientific and Technical Review, Vol. 1, No. 3, pp. 219-226, 1975.

187. Schechter, D., and Nelson, R. D., "Calculation of Potential Profiles in CCD's Using Green's Function Techniques," IEEE Transactions on Electron Devices, Vol. ED-23, No. 2, pp. 293-296, Feb. 1976.

188. Schmieder, D. E., "Seeker Lock-On Model and Performance Projections with CCD Sensors - Charge Coupled Devices for Missile Guidance," in NAECON'75: Proceedings of the National Aerospace and Electronics Conference, Dayton, Ohio, June 10-12, 1975, pp. 343-349.

189. Schneider, P., and Witte, J., "CCD Memories in a Working Memory System," Siemens Forschungs- und Entwicklungsberichte, Vol. 4, No. 4, pp. 231-237, 1975.

190. Sealer, D. A., et al., "Design and Characterization of Charge-Coupled Devices for Analog Signal Processing," in Conference Record, Vol. 1, proceedings of the International Conference on Communications, 11th, San Francisco, Calif., June 16-18, 1975, pp. 2-1 to 2-3.

191. Sealer, D. A., and Tompsett, M. F., "Dual Differential Charge-Coupled Analog Delay Device," IEEE Transactions on Electron Devices, Vol. ED-23, No. 2, pp. 173-176, Feb. 1976.

192. Sei, H., Miura, S., and Sakai, H., "Charge-Coupled Devices - 1. Fabrication Process." Fujitsu Scientific and Technical Journal, Vol. 11, No. 3, pp. 79-100, Sept. 1975.

193. Seib, D. H., "Carrier Diffusion Degradation of Modulation Transfer Function in Charge Coupled Imagers," IEEE Transactions on Electron Devices, Vol. ED-21, No. 3, pp. 210-217, Mar. 1974.

194. Seib, D. H., "Carrier Diffusion Degradation of CCD (Charge-Coupled Devices) Image MTF (Modulation Transfer Function) for Broadband Optical Sources," SAMSO-TR-76-25. AD-A020600. Aerospace Corporation, El Segundo, Calif., Jan. 29, 1976.

195. Sequin, C. H., et al., "Charge-Coupled Image-Sensing Devices Using Three Levels of Polysilicon," in Digest of Technical Papers, proceedings of the IEEE International Solid-State Circuits Conference, University of Pennsylvania, Philadelphia, Pa., Feb. 13-15, 1974, pp. 24-25, 218.

196. Sequin, C. H., "Experimental Investigation of a Linear 500-Element 3-Phase Charge-Coupled Device," Bell System Technical Journal, Vol. 53, No. 4, pp. 581-610, Apr. 1974.

197. Sequin, C.H., Shankoff, T.A., and Sealer, D.A.,"Measurements on a Charge-Coupled Area Image Sensor with Blooming Suppression," IEEE Transactions on Electron Devices, Vol. ED-21, No. 6, pp. 331-341, June 1974.

198. Sequin, C. H., and Mohsen, A. M., "Linearity of Electrical Charge Injection into Charge-Coupled Devices," in Technical Digest, proceedings of the International Electron Devices Meeting, 20th, Washington, D. C., Dec. 9-11, 1974, pp. 229-232.

199. Sequin, C. H., and Mohsen, A. M., "Linearity of Electrical Charge Injection into Charge-Coupled Devices," IEEE Journal of Solid-State Circuits, Vol. SC-10, No. 2, pp. 81-92, Apr. 1975.

200. Sequin, C. H., and Tompsett, M. F., "Charge Transfer Devices," Advances in Electronics and Electron Physics, Supplement 8, 1975, 309 p.

201. Shannon, J. M., et al., "Charge Coupled F.E.T. Devices (C.C.F.E.T.)," in Technical Digest, proceedings of the International Electron Devices Meeting, Washington, D.C., Dec. 1-3, 1975, pp. 320-323.

202. Simms, T., "Application of CCD's to Document Scanning," Microelectronics, Vol. 7, No. 2, pp. 60-63, Dec. 1975.

203. Simpson, P. I., "CCD Transversal Filters with Fixed Weighting Coefficients," Microelectronics, Vol. 7, No. 2, pp. 54-59, Dec. 1975.

204. Singh, M. P., and Brotherton, S. D., "Influence of Clocking Waveform on Charge Transfer in Three Phase Charge Coupled Devices," Solid-State Electronics, Vol. 19, No. 4, pp. 279-287, Apr. 1976.

205. Steckl, A. J., et al., "Application of Charge-Coupled Devices to Infrared Detection and Imaging," IEEE Proceedings, Vol. 63, pp. 67-74, Jan. 1975.

206. Steckl, A. J., "Infrared Charge Coupled Devices," Infrared Physics, Vol. 16, No. 1-2, pp. 65-73, Jan.-Mar. 1976.

207. Steigerwalt, S. T. and Lagnado, I., "CCD as a Test Structure for Semiconductor Process Control," Microelectronics, Vol. 7, No. 2, pp. 23-29, Dec. 1975.

208. Suzuki, N., and Yanai, H., "Analysis of Surface-Charge Transfer in a Charge-Coupled Device," Electronics and Communications in Japan, Vol. 57, No. 3, pp. 93-100, Mar. 1974.

209. Tanigawa, H., and Ando, T., "Nonlinear CCD Lumped Model and its Application to Output Stage Performance Analysis," IEEE Transactions on Electron Devices, Vol. ED-22, No. 8, pp. 575-581, Aug. 1975.

210. Tanikawa, K, Arakawa, I, and Ohtsuki, O., "Charge-Coupled Devices - 2. Charge Transfer Characteristics," Fujitsu Scientific and Technical Journal, Vol. 11, No. 3, pp. 101-119, Sept. 1975.

211. Tao, T. F., "Narrow Gap Semiconductors PbSnTe and PbSnSe," Final Report, 1 Jan. 1972 - 30 Sept. 1973. AFML-TR-74-162. AD-A005702. Naval Postgraduate School, Monterey, Calif., Nov. 1974.

212. Tasch, A. F., Jr., Fry, R. C., and Fu, H. S., "Charge-Coupled Ram Cell Concept," IEEE Transactions on Electron Devices, Vol. ED-23, No. 2, pp. 126-131, Feb. 1976.

213. Tchon, W. E., et al., "4096-Bit Serial Decoded Multiphase Serial-Parallel-Serial CCD Memory," IEEE Transactions on Electron Devices, Vol. ED-23, No. 2, pp. 93-101, Feb. 1976.

214. Terman, L. M., and Heller, L. G., "Overview of CCD Memory," IEEE Transactions on Electron Devices, Vol. ED-23, No. 2, pp. 72-78, Feb. 1976.

215. Theunissen, M. J. J., "Charge Transfer Devices. II.- Applications," L'Onde Electrique, Vol. 54, pp. 405-413, Oct. 1974.

216. Tompsett, M. F., et al., "Charge Coupled Image Sensing State of the Art," in 1973 IEEE Intercon Technical Papers, proceedings of the Institute of Electrical and Electronics Engineers International Convention and Exposition, New York, N. Y., Mar. 26-30, 1973, Vol. 6, Paper 1/4.

217. Tompsett, M. F., "Surface Potential Equilibration Method of Setting Charge in Charge-Coupled Devices," IEEE Transactions on Electron Devices, Vol. ED-22, No. 6, pp. 305-309, June 1975.

218. Upton, L. O., and Mayer, G. J., "Charge-Coupled Devices and Radar Signal Processing," RCA Engineer, Vol. 21, pp. 30-34, June-July 1975.

219. Vanstone, G. F., Roberts, J. B. G., and Long, A. E., "Measurement of the Charge Residual for CCD Transfer Using Impulse and Frequency Responses," Solid-State Electronics, Vol. 17, No. 9, pp. 889-895, Sept. 1974.

220. Varshney, R. C., et al., "Byte Organized NMOS/CCD Memory with Dynamic Refresh Logic," IEEE Transactions on Electron Devices, Vol. ED-23, No. 2, pp. 86-92, Feb. 1976.

221. Vicars-Harris, M., "Slow-Scan Operation of Long Linear CCD Arrays," in proceedings of the Symposium on Charge-Coupled Device Technology for Scientific Imaging Applications, Pasadena, Calif., Mar. 6-7, 1975, pp. 175-185.

222. Wallinga, H., and Van Ruyven, H. L. M., "Diagnostic Analysis of the Charge Transfer in CCDs," in Digest of Technical Papers, proceedings of the IEEE International Solid-State Circuits Conference, University of Pennsylvania, Philadelphia, Pa., Feb. 13-15, 1974, pp. 148-149.

223. Walsh, L. R., "A 190 by 244 Charge-Coupled Area Image Sensor with Interline Transfer Organization," in proceedings of the Symposium on Charge-Coupled Device Technology for Scientific Imaging Applications, Pasadena, Calif., Mar. 6-7, 1975, pp. 137-149.

224. Wang, S. T., Royce, B. S. H., Russell, T. J., "The Effect of Ion Implantation on Oxide Charge Storage in MOS Devices," IEEE Transactions on Nuclear Science, Vol. NS-22, pp. 2168-2173, Dec. 1975.

225. Weckler, G. P., "Solid State Image Sensing with Photodiode Arrays," in 1973 IEEE Intercon Technical Papers, proceedings of the IEEE International Convention and Exposition, New York, N. Y., Mar. 26-30, 1973, Vol. 6, Paper 1/2.

226. Weiss, H., "Physics and Technology of Data Storage - Comparison of Magnetic, Semiconductor and Optical Memories with Respect to Bit Density and Cycle Time," Solid-State Electronics, Vol. 19, pp. 347-356, May 1976.

227. White, M. H., et al., "Characterization of Surface Channel CCD Image Arrays at Low Light Levels," IEEE Journal of Solid-State Circuits, Vol. SC-9, No. 1, pp. 1-13, Feb. 1974.

228. White, B. J., "Edge-Triggered Charge-Coupled Device (CCD)," IEEE Transactions on Electron Devices, Vol. ED-23, pp. 299-300, Feb. 1976.

229. White, M. H., and Webb, W. R., "Study of the Use of Charge-Coupled Devices (CCDs) in Analog Signal Processing Systems," Final Report, 15 Sept. 1973 - 15 Mar. 1974. AD-783703. Westinghouse Defense and Electronic Systems Center, Baltimore, Md., April 1974.

230. Whitehouse, H. J., and Means, R. W., "Signal Processing Using Charge Coupled Devices and Surface Wave Devices," in proceedings of the IEEE Ultrasonic Symposium, Monterey, Calif., Nov. 5-7, 1973, pp. 572-577.

231. Willett, E., and Forst, H., "Artillery-Launched Charge-Coupled Device (CCD) - Aerial Reconnaissance Using Parachute Dropped Television Equipment," Final Report, 3 Dec. 1973 - 15 Apr. 1974. AD-786697. Fairchild Space and Defense Systems, Syosset, N. Y., June 1974.

232. Williams, J. T., "The Intensified Charge Coupled Device as a Photon Counting Imager," in proceedings of the AAS, AIAA, IEEE, ORSA, and IMS Meeting on the Space Shuttle Missions of the 80's, Denver, Colo., Aug. 26-28, 1975. AAS Paper 75-208.

233. Williams, R. A., and Nelson, R. D., "Radiation Effects in Charge Coupled Devices," IEEE Transactions on Nuclear Science, Vol. NS-22, pp. 2639-2644, Dec. 1975.

234. Williams, T. R., "Charge-Coupled Devices - 4. Imaging Applications," Wireless World, Vol. 81, No. 1471, pp. 133-138, Mar. 1975.

235. Wupper, H., "An Application of Charge-Transfer Devices to Filter Networks," Archiv fuer Elektronik und Uebertragungstechnik, Vol. 29, pp. 289-295, July-Aug. 1975.

236. Yau, L. D., "Scaling of Surface-Channel Charge-Coupled Devices," IEEE Transactions on Electron Devices, Vol. ED-23, No. 2, pp. 282-287, Feb. 1976.

237. Yeow, Y. T., and Mavor, J., "Influence of Charge-Transfer Inefficiency on CCD Recursive-Filter Performance," Electronics Letters, Vol. 12, pp. 125-127, Mar. 4, 1976.

238. Zimmerman, T. A., Charge Coupled Devices in Signal Processing Systems - The Analog and the Digital Approach," in Record, proceedings of the National Telecommunications Conference, San Diego, Calif., Dec. 2-4, 1974, pp. 254-258.

239. Zimmerman, T. A., and Miller, C. S., "Charge Coupled Devices in Signal Processing Systems. Volume 1. Digital Signal Processing." Final Report, Oct. 1973 - Apr. 1974. AD-782574. TRW Systems Group, Redondo Beach, Calif., July 1974.

240. Zimmerman, T. A., and Miller, C. S., "Charge Coupled Devices in Signal Processing Systems. Volume 2. Analog Signal Processing," Final Report, Apr. - Oct. 1974. AD-A011499. TRW Systems Group, Redondo Beach, Calif., Dec. 1974.

NASA—JPL—Coml., L.A., Calif.

ATTACHMENTS FOR JPL SP43-40

CONFERENCE ON CHARGE-COUPLED DEVICE TECHNOLOGY AND APPLICATIONS

Nov. 30 - Dec. 2, 1976

Sheraton Park Hotel
Washington, D. C.

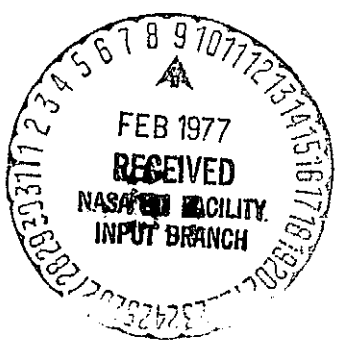

Sponsored by

National Aeronautics and Space Administration
Office of Aeronautics and Space Technology and
Jet Propulsion Laboratory
California Institute of Technology

DEVELOPMENT OF LARGE AREA CCD IMAGERS

G. W. Taylor, G. A. Antcliffe, and G. L. Streckmann

Texas Instruments Incorporated
Dallas, Texas 75222

ABSTRACT

High performance CCD imagers with 800 x 50 resolution elements have been fabricated using a coplanar, double polysilicon, electrode system. The imager was developed as a prototype to demonstrate the feasibility of an 800 x 800 array for application to deep space photography where data rates of $10K^2$ and operating temperatures of -40°C are required. The performance is discussed and comparisons made to the existing 400 x 400 imager.

I. INTRODUCTION

Large area CCD imagers having 400 x 400 resolution elements have been fabricated in the past[1] for the purposes of planetary imaging either from a ground based telescope or from a deep space probe. These devices were fabricated with a two-level, three-phase anodized aluminum technology[2] and exhibited excellent performance parameters including a high CTE and a high degree of uniformity across the array. This technology is restricted mainly by two limitations. Firstly, there is a prevalence of intra-level shorts defined as electrode shorts between two metal lines on the same level of metal. This is a fatal failure on the 400 x 400 because each phase occurs alternately on different levels of metallization. It occurs mostly because of imperfect definition of photoresist or becauseof imperfections in the photomasks themselves. These shortcomings can be alleviated only by improved methods of photomask inspection and production and by more scrupulous methods in slice cleaning and handling during the photoresist and etch stages. Secondly, the size of the resolution element is too large to allow the fabrication of an imager having more than 400 x 400 resolution elements using conventional optical photolithographic techniques.

Due to the demand for a higher resolution sensor and because of the difficulties in fabrication of the existing 400 x 400 imager, other technologies were investigated. To alleviate the problem of intra-level shorting failures a coplanar structure was chosen in which each level of metallization is used for only one clock phase. The size of the picture resolution element was reduced to the smallest possible consistent with the minimum design rule specifications of the standard N channel optically defined technology. In order to evaluate the capability to fabricate photomasks with sufficiently small tolerances and to hold these tolerances during the processing across the long distances of 500 mils, it was decided to build an imager having 800 pixels in one dimension and only 50 pixels in the other. This size of prototype imager is a convenient vehicle for the investigation of the limitations and advantages of the new technology. It allows one to concentrate on the problems of a very long chip dimension without the yield problems that would be associated with a very large area imager.

The imager was designed for thinning and backside illumination in the same fashion as used previously.[2-5]

II. DESIGN AND FABRICATION

A 2ϕ, two-level structure using polysilicon electrodes was chosen to implement the 800 x 50 imager. A cross-section of the device in the long dimension is illustrated in Fig. 1 and shows the critical dimensions. The device is a buried channel device typically fabricated on 10-15 ohm-cm p-silicon. The resolution element size is 0.6 x 0.6 mil^2 which requires that each parallel and serial electrode be 0.15 mil in width. However, we have used offset-gate alignment techniques so that the actual electrode width is 0.3 mil.[6] The channel width and channel stop regions in the central section are 0.4 mil and 0.2 mil, repectively, providing a total active area of 480 x 30 $mils^2$. Three of these arrays are positioned on a 502 x 502 mil^2 chip of silicon, one at each end and one in the central section. First and second polysilicon electrodes are isolated by 1300Å of SiO formed by thermal oxidation of the first level of polysilicon. Hence, the two clock phases, shown schematically in Fig.1, are actually isolated electrically by a high quality thermal oxide.

The phase-two electrodes overlap the phase-one electrodes by 0.1 mils to ensure a totally covered structure. This size of overlap was considered necessary to compensate for errors in mask making and processing over a 480 mil distance. However, no problems are created by the failure to completely separate second level electrodes during patterning, since this level does not require any separation for successful operation if one can tolerate somewhat more capacitance between ϕ_1 and ϕ_2. This approach has alleviated some of the formidable difficulties in photomask generation and slice processing formerly encountered with the 400 x 400. Nevertheless, the CCD processing used requires nine levels of photomasks with several critical alignments and so extreme care is required in both areas to achieve a reasonable yield. The devices were processed on 2" diameter silicon slices and seven bars (21 devices) are usable per slice.

The growth of a gate oxide with a low probability of defects also constitutes an important yield loss. This problem was encountered with the 400 x 400 and is still a problem of concern here. We are using the best available technology for the growth of high quality thermal SiO_2 but with the increasingly larger sizes of arrays, this problem will still create a significant yield loss.

The 800 x 50 is designed to operate in the serial parallel serial (SPS) mode. It has an upper and a lower serial register to allow continuous electrical operation for characterization purposes. The output of the CCD is a simple precharge amplifier using a buried channel reset switch and source follower. However, a second source follower is also provided to allow a cascade operation if desired. Off chip load resistor values of 10K - 50K are reasonable to achieve low levels of noise and low power dissipation. A photograph of part of the array including the output amplifiers is shown in Fig. 2.

The bond pads are located 45 mils from the active area so that the edges of the thinned silicon can extend outside this area and leave a 25 mil rim for membrane support. Thinning is performed by a chemical etching technique in either a chip or slice form. The membrane can be coated with an antireflective passivating layer and the performance of the membrane over a wide temperature range is stable. It will be noted that because of our polysilicon electrode structure it is also possible to illuminate the device from the front. The response of the device in this mode is expected to be degraded due to absorption in the polysilicon and internal reflections at the interfaces.

A buried channel structure is used to ensure a high CTE. Using a 0.5 to 1 μm deep phosphorous implanted channel yields a CTE > 0.9999 as determined by electrical injection through the array. With the exception of the buried channel implant a conventional MOS n channel technology is used throughout. After completion of the active imager area, contact windows are opened and the device is metallized. The metal is patterned and sintered and the device is then ready for a protective overcoat and thinning.

III. IMAGER PERFORMANCE

A high performance imager must meet a number of operating criteria independently. Among these are a low dark current, a high uniformity of response, and a maximum spectral responsivity to optical radiation. The uniformity of response is a significant parameter because large pixel-to-pixel nonuniformity in response may require excessive data reduction techniques to maximize the resultant information.

The uniformity of response is measured typically with a multichannel analyzer by sampling a group of resolution elements on several successive frames and displaying the total number of pixels that fall within a particular voltage window ("bin") as a function of voltage level. For the 800 x 50 we used all available pixels and divided the full well level into 1024 bins to obtain the results shown in Fig.3(a) for the imager at average well populations of 0% (in the dark), 50%, and 100%. The distributions are very sharp and close in shape to the normal distribution curve. Using a response figure of the standard deviation devided by the mean yields 7.9%, 3.3% and 3.8%, respectively. The corresponding flat field response is also shown in Fig.3(b). Inspection of the figure shows an angular pattern superimposed on the image. This effect is caused by the blanking feature of the random raster sampler which samples every 20th pixel of the array on each frame starting from pixel one on the first frame, pixel two on the second, and so on. This technique is necessary to form a representative sample of all the pixels in the array and yet to supply the information to the MCA at a rate which it can accept (40 kHz). The dark lines crossing the image are due to bond wires crossing the array since we are illuminating from the front side.

The dark current of the array is in the range of 5 - 10 na/cm^2 for typical arrays. The dark current pattern which is obtained by integrating with the device in the dark and then reading out the data at 1.0 MHz is shown in Fig. 4. The integration time is 2 sec and the dark current pattern is seen to be very uniform with the exception of the bottom line of the array. This section shows premature blooming due to the proximity of the serial register.

Imagery with the 800 x 50 is shown in Fig. 5 at a data rate of 1.0 MHz and using strobed illumination.

The image shows very high resolution and a relatively defect-free image. The resolution in this image is sufficiently high that it is no longer possible to detect pixel-to-pixel variations in the x direction on a typical monitor display. It is noted in the figure that the density of lines in the centre of the picture has exceeded the imager Nyquist frequency of 32.8 line pairs/mm.

IV. CONCLUSIONS

Very long, high resolution, low dark current CCD arrays with uniform response have been demonstrated. The performance of the prototype imager has shown the feasibility of constructing an 800 x 800 resolution element sensor for application

in a spacecraft environment. Operation at low data rates and low temperatures (-40°C) have already been successful with thinned backside illuminated imagers. Improvements in this technology are continuing and it is expected to be compatible with the very large CCD array.

REFERENCES

1. Antcliffe, G. A., Hornbeck, L. T., Rhines, W. C., Chan, W. W., Walker, J.W., and Collins, D. R., International Conference on the Application of CCD's, San Diego, 1975.

2. Collins, D. R., Shortes, S. R., McMahon, W. R., Bracken, R. C., and Penn, T. C., J. Electrochem. Soc. 20, 521 (1973).

3. Shortes, S. R., Chan, W. W., Rhines, W. C., Barton, J. B., and Collins, D. R., Appl. Phys. Lett. 24, 565 (1974).

4. Antcliffe, G. A., Hornbeck, L. T., Younse, J. N., Barton, J. B., and Collins, D. R., Symposium on Charge-Coupled Device Technology for Scientific Imaging Applications, Jet Propulsion Laboratory, Pasadena, 1975.

5. Hartsell, G. A., and Kmetz, A. R., 1974 IEDM, Digest of Technical Papers, p. 59 (1974).

6. Tasch, A. F. Jr., to be published.

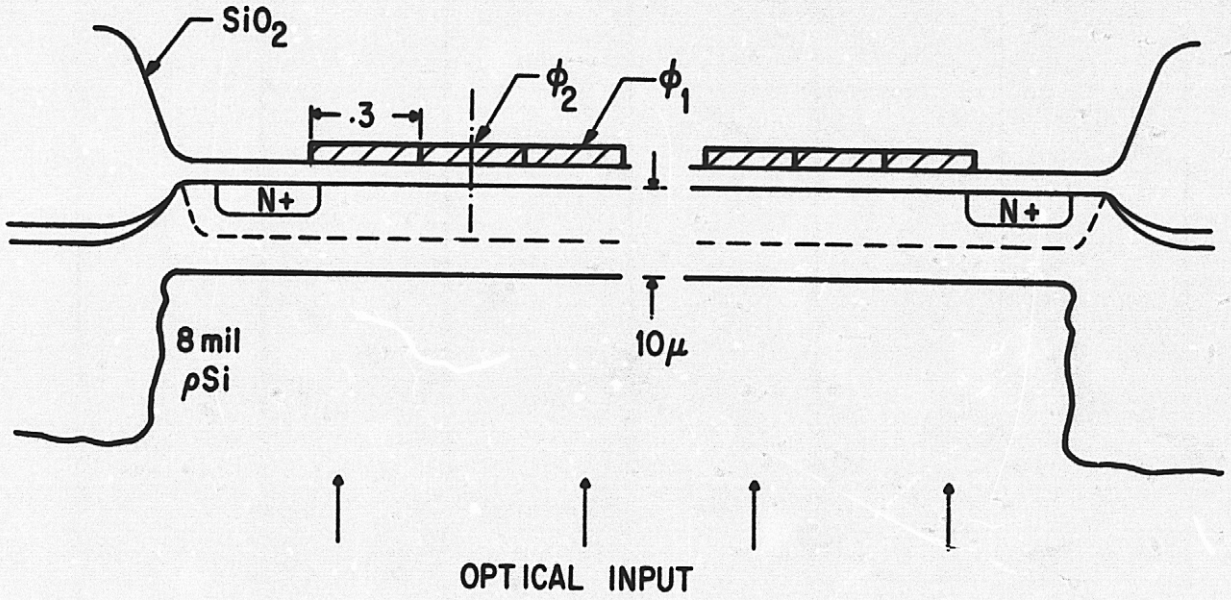

Fig. 1. Cross-section of an 800 x 50, 2φ coplanar polysilicon imager showing critical dimensions.

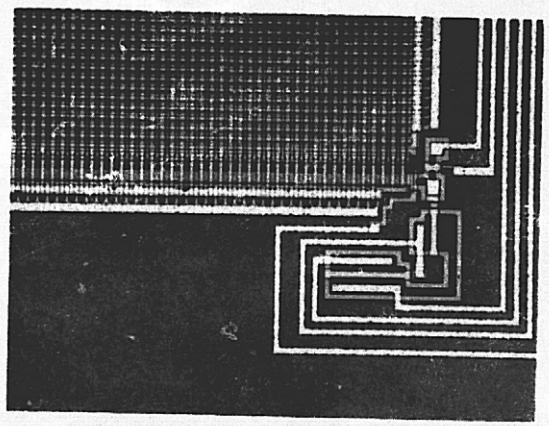

Fig. 2. Enlarged view of output section of imager.

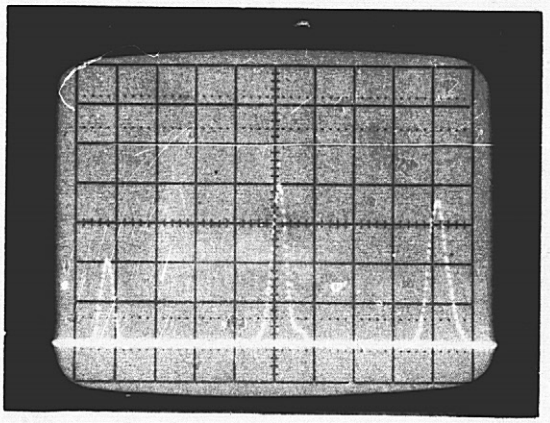

Fig. 3(a). Uniformity of response data accumulated by sampling over all 800 x 50 elements in the dark, at 50% and 100% of full well.

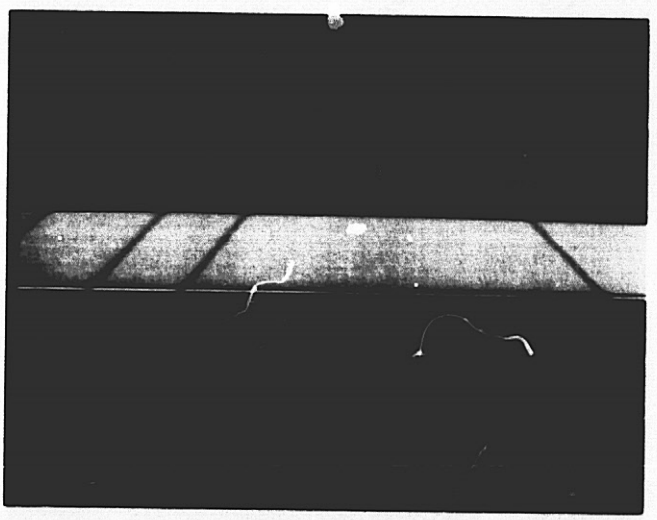

Fig. 3(b). Response of imager to flat field illumination (2854°K) at 50% of full well.

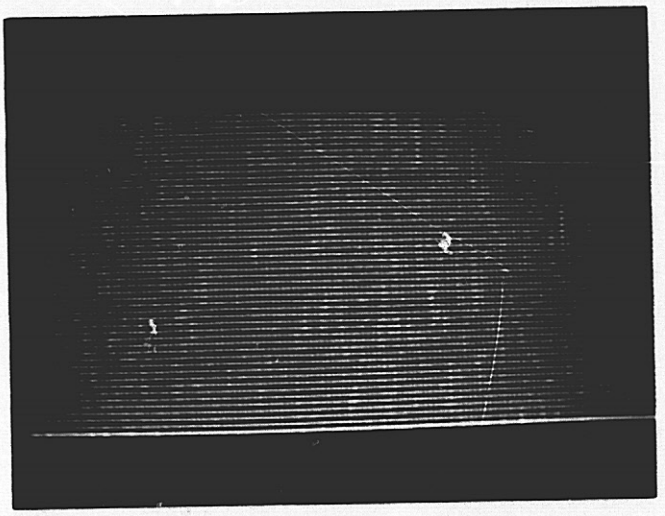

Fig. 4. Dark current variation in the 800 x 50 array after integration in the dark for 1 second and readout at 1.0 MHz.

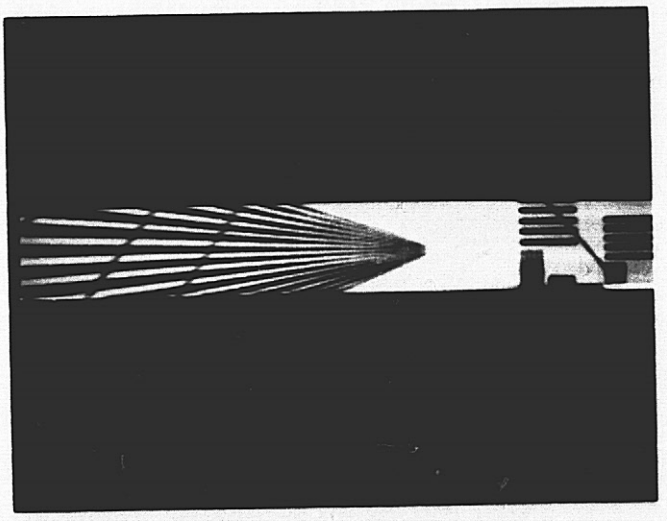

Fig. 5. Imagery at 1 MHz with the 800 x 50 using strobed illumination to avoid streaking.

THEORY AND APPLICATIONS OF SAMPLED ANALOG RECURSIVE CTD COMB FILTERS

T. F. Tao, S. Holmes, A. Ejaz,
F. Piazza, L. Saetre, and B. Freund
Naval Postgraduate School
Monterey, California 93940

Sampled analog comb filter using a recursive filter implementation is studied. Charge transfer device delay lines are used as the delay elements. The similarities and differences between sampled analog recursive filter and digital recursive filter are pointed out. Both canceller type and integrator type comb filter using the first order or the second order canonical circuits are studied. Experimental results of frequency response are presented to show their difference from that of digital filters. A theoretical analysis is presented based essentially on the digital filter theory but modified to take into account the differences described above. The usefulness of this theory in analyzing the comb filter characteristics is discussed. Several applications of both the canceller type comb filter and the integrator type comb filter are demonstrated.

1. INTRODUCTION

Several sampled analog recursive filter studies using charge transfer devices (CTD) as delay elements have been reported. BBD recursive filters were first studied.[1-2] Later, a three poles[3] and a two poles/one zero[4] CTD recursive filters and a one pole CTD recursive integrator[5] were reported. We presented the results of a different type of recursive filter which emphasized the comb feature of its frequency characteristics.[6] A first order comb filter was studied using one CTD delay line of eight delay stages. A modified digital recursive filter theory was used to account for the major features of the sampled analog comb filter. However, several deviations between experimental results and theoretical calculations were reported. This paper will present more recent results of our continuing study of the recursive comb filters. Second order comb filters have been more extensively studied. The theory was improved and can analyze some of the characteristics unaccounted for by the earlier analysis. In section 2, the principle and general characteristics of comb filters are presented. The difference between sampled analog recursive filters and digital recursive filters is pointed out. In section 3, experimental results are presented to highlight the major features of the frequency characteristics. In section 4, a theory is presented which is able to analyze most of the features. It is based essentially on the digital recursive filter theory but modified to take into account the differences pointed out in section 2. In section 5, several applications of both the canceller type comb filter and the integrator type comb filter are demonstrated.

2. COMB FILTER AND SAMPLED ANALOG RECURSIVE IMPLEMENTATION

Comb filters are characterized by their periodic transfer characteristics in the frequency domain. They can be classified into two general types. The first one is the canceller or bandstop type shown in Figure 1(a). It has large attenuation in a narrow neighborhood of a series of periodically separated frequencies and good transmission in between. The second one is the integrator or bandpass type shown in Figure 1(b). It has good transmission in a narrow neighborhood of a series of periodically separated frequencies and strong attenuation in between. In order for the comb teeth to separate from each other, it is desirable to have zero transmission at certain frequencies between neighboring teeth.

Both analog comb filters and digital comb filters have been developed before using several different implementation techniques such as the feedforward circuits, frequency sampling, fast Fourier transform, recursive filter circuits, etc. All use delay devices in some manner. In the analog case, quartz delay lines are the major candidates. In the digital case, implementation has been mainly carried out by software programs on computers. However, using the family of charge transfer device delay lines, sampled analog comb filters are being developed using several implementation techniques: feedforward circuits,[7] chirp Z transform[8] and recursive filter implementations.[3,4,6,9]

The recursive filter approach is used in our study. The circuit configuration is shown in Figure 2 for the special case of second order filters. It is similar to the canonical circuit used in the digital recursive filters but with four basic differences.

(1) Delay elements of multiple delay stages:

The delay element used in the sampled analog recursive filter circuit is implemented by CTD delay lines which usually consists of N delay stages. In digital filters, the delay is accomplished either by memory or by shift registers and consists of one delay stage. The presence of N delay stages in one delay line is instrumental in providing the comb feature of its frequency characteristics. The reason for this important property can be explained qualitatively as follows. Since the signal is delayed by N clock periods before it is processed, the frequency of recursive filter operation (f_r) is not the sampling frequency (f_s) but is only one Nth of f_s. Therefore, frequency characteristics of this type of filter are not only periodic with respect to f_s but also periodic with respect to f_r. Since $f_r = f_s/N$, there are $N/2$ comb teeth within the Nyequist frequency range from 0 to $f_s/2$. This is in contrast to the situation for digital recursive filters where the recursive filter operations take place after each delay stage, resulting in only one comb tooth within the Nyquist range.

(2) Special relation among the feedforward coefficients a_0, a_1 and a_2:

A good comb filter requires that two neighboring comb teeth should be clearly separated from each other in frequency domain. In other words, the transfer function should be zero at a series of periodically separated frequencies starting either at f_r or $f_r/2$ and repeating at its multiples. These zeroes provide ideal separation between two neighboring teeth. Since there are now N/2 periods within the Nyquist frequency range for this type of filters, a proper design of the "zero" locations of the singularities of H(Z) can meet that requirement. This is accomplished by designing the values of the feedforward coefficients a_0, a_1 and a_2 according to the ratio of 1:±2:1. Consequently, a series of "zeroes" of the transfer function will occur at frequencies periodically separated by the period of f_s/N and started either at f_r or $f_r/2$. In digital filters, the delay element has only one delay stage. The frequency characteristics will also become zero at a series of periodically separated frequencies. But they are separated by the period f_s and started either at f_s or $f_s/2$ which is beyond the useful signal frequency range. Therefore, in digital filters, the requirement of keeping a_0, a_1 and a_2 at the ratio of 1:±2:1 never did take

place.

(3) Frequency dependence of filter coefficients:

In sampled analog comb filters, the filter coefficients are implemented by potentiometers. The summation operations are implemented by operational amplifiers with feedback. Both components have finite bandwidth and introduce frequency dependence. The signal is sampled and delayed by the CTD device which also introduces other frequency dependences due to two effects:

{ sampled and hold effect
{ charge transfer inefficiency effect.

Consequently, it is difficult to maintain a set of properly designed values of filter coefficients throughout the frequency range from 0 to $f_s/2$. In digital filters, the coefficients are set in memory and do not vary with frequency.

(4) Mixed processing of sampled and unsampled signals:

The input signal in this type of filter is usually analog. It is sampled by the CTD device. When the delayed signal is fedback and processed at the input summer, a mixing of the continuous and analog input signal with the sampled analog feedback signal takes place. Because a sampled signal has a $\sin x/x$ type of frequency dependence while an unsampled signal does not, the same processing operation can not be maintained throughout the Nyquist frequency range.

Because of these four differences, the frequency characteristics of the sampled analog comb filter are substantially different from that of the digital recursive filter even when their circuit configurations are the same canonical type. This will be shown by some experimental results in the next section.

3. EXPERIMENTAL RESULTS

Two types of CTD delay lines are used in the experimental studies:

{ 8 bits CCD delay line
{ 96 bits Reticon SAD-100 delay line

In Fig. 3, the frequency characteristics of a second order canceller type comb filter are shown. A theoretical calculation is included in the same figure and will be explained in the next section. The filter information is:

{ 8 bits CCD delay line
{ f_s = 20 kHz
{ Filter coefficients: a_0=1, a_1=2, a_2=1
b_1=-0.3, b_2=+0.3

The major features of a comb filter are clearly shown:

° Frequency characterists is periodic with respect to a frequency of 2.5 kHz which is equal to f_s/N.

° There are four comb teeth in the Nyquist frequency range from 0 to 10 kHz.

However, it is different from the ideal comb filter characteristics in three ways:

- Two neighboring teeth are not separated by infinite attenuation as in an ideal comb filter. The attenuation is more than -50 db at the first null frequency, but deteriorated to -42 db at the second null frequency and to -34 db and so on.
- The peak amplitude of each comb tooth does not remain constant as in an ideal comb filter. For this filter, it first decreases and then rises at the fourth tooth.
- The shape of the comb tooth changes with frequency.

These major features of sampled analog recursive comb filters are further demonstrated by the following frequency characteristics of comb filters using 96 bits Reticon delay line. The filter information is given as follows:

Fig. 4. { Canceller type comb filter
{ f_s = 400 kHz
{ Filter coefficients: a_0=1, a_1=2, a_2=1
b_1=-0.973,
b_2=+0.334

Fig. 5. { Integrator type comb filter
{ f_s = 390 kHz
{ Filter coefficients: a_0=1, a_1=2, a_2=1
b_1=-0.2, b_2=-0.6

The periodic feature of the comb filter again is clearly shown. However, the variations among the first twelve to thirteen teeth are much smaller than among the first four teeth shown in Fig. 3. This difference can be qualitatively explained as follows. In the previous section, it was explained that in sampled analog recursive filters, several factors give rise to frequency dependences of the processing operations. They become more pronounced as the frequency is approaching the Nyquist frequency. In Fig. 3, an 8 bits CCD was used. There are only four comb teeth within the Nyquist range. Therefore, noticeable changes take place from the first tooth to the fourth tooth. On the other hand, a 96 bits recursive comb filter was studied in Fig. 4 and 5. There are 48 comb teeth within the Nyquist range. The first twelve to thirteen comb teeth cover only one-fourth of the Nyquist range. Their frequency dependence should be less pronounced. However, if the frequency range is extended to cover all 96 comb teeth, as shown in Fig. 6, strong frequency dependence is clearly seen. The filter information is:

96 bits Reticon SAD 100 delay line
f_s = 400 kHz
Filter coefficients: $a_o=1$, $a_1=2$, $a_2=1$
$b_1=+0.2$, $b_2=+0.2$

It is an integration type comb filter. In this case, all three types of deviations from an ideal comb filter can be detected. As the frequency or the order of comb teeth is increased, the attenuation between two neighboring teeth deteriorate, the peak amplitude decreases and the tooth shape changes. These behaviors do not exist in digital recursive filters. Therefore, digital recursive filter theory should be properly modified to account for these features.

4. THEORY

Since the circuit configuration of the sampled analog recursive comb filter is the same as the canonical circuit of digital recursive filter except for four differences pointed out in section 2, it is reasonable to expect that the digital recursive filter theory should apply to the sampled analog case if proper modifications are made.

The transfer function of a second order digital recursive filter is

$$H(Z) = \frac{a_o + a_1 Z^{-1} + a_2 Z^{-2}}{1 + b_1 Z^{-1} + b_2 Z^{-2}}$$

The modifications needed to account for the four differences are discussed as follows:

(1) To take into consideration the presence of N delay stages, Z^{-1} is changed to Z^{-N}.

(2) To provide zero between two neighboring teeth: $a_o = 1$, $a_1 = \pm 2$, $a_2 = 1$

- The "-" sign of a_1 is for the canceller type comb filter.
- The "+" sign of a_1 is for the integrator type comb filter.

(3) Filter coefficients are no longer constant and vary with frequency. The exact frequency dependence could be complicated because there are several factors contributing to the frequency dependence simultaneously.

(4) The effect due to the mixing of unsampled input signal and sampled feedback signal at the first summer is more difficult to model by a frequency dependence. Instead, a change of the circuit configuration should be considered to avoid this problem.

Combing these modifications, the transfer function for a sampled analog recursive comb filter is

$$H(Z) = \frac{a_o(f) + a_1(f) Z^{-N} + a_2(f) Z^{-2N}}{1 + b_1(f) Z^{-N} + b_2(f) Z^{-2N}}$$

where $a_o(f) = 1$, $a_1(f) = \pm 2$, $a_2(f) = 1$
for $f \ll f_s/2$

The agreement between this theoretical analysis and measured result has been investigated. For the 8 bits CCD recursive comb filter shown in Fig. 3, theoretical calculations have been made by considering two factors contributing to the frequency dependence.

- Sample and hold effect.
- Charge transfer inefficiency effect.

The calculated result is also plotted in Fig. 3. It can be seen that all three trends of deviation have been accounted for qualitatively:

- Deterioration of attenuation between neighboring comb teeth.
- Change of peak amplitude of each comb tooth.
- Change of shape of comb tooth.

However, quantitative agreement has not been accomplished. The same situation is found for the 96 bits CTD recursive comb filters shown in Fig. 4 through 6. A theoretical calculation considering only the effect of sampled and hold operation is shown in Fig. 7 for the filter of Fig. 6. Again, the major features of this comb filter have been accounted for only qualitatively.

It can be concluded that the basic consideration of the theoretical analysis is complete. Flaws in both calculations and measurements have contributed to the lack of perfect agreement. In the theoretical calculation, the frequency dependences of filter coefficients were only approximations. In the experinental results, measurement can be improved in high frequency range close to the Nyquist frequency. It is believed also that the circuit configuration can be improved, such as by the use of a sampled and hold circuit in front of the comb filter, to provide frequency characteristics closer to that of an ideal comb filter. However, major features of a comb filter have been accomplished such that meaningful investigation of their applications can be carried out. They will be presented in the next section.

5. APPLICATIONS

The periodic nature of the comb filters makes them well suited to process signals which are periodic in time and in frequency as in radar and sonar systems and many others. The canceller type comb filters can be used to reject periodic signals by aligning the null frequencies of the comb filter with the periodic frequency spectrum of the undesirable signal. Two applications have been investigated. The first is the cancellation of clutter spectrum in an MTI radar. The second is the cancellation of 60 Hz noise and its harmonics.

The integrator type comb filters can be used to enhance a periodic signal. Two applications have been investigated. The first is the separation of one periodic signal from another periodic signal of a different pulse repetition frequency, an application of interest to threat analysis. The second is the enhancement of signal to noise ratio of a periodic signal contaminated by noise. Some of their preliminary results will be presented.

(1) Canceller application:

In MTI radar, moving targets can be distinguished from clutters or stationary targets by using the Doppler shifts between their spectra in frequency domain. The clutter is characterized by a periodic spectra at d.c. and multiples of PRF. The moving target is characterized by another spectrum of the same period but shifted by its Doppler frequency. The clutter spectrum can be eliminated by a canceller type comb filter by aligning the null frequencies of the filter with the PRF frequencies of the radar return signal. Therefore, f_s/N = PRF. In addition to this canceller requirement, there are two other requirements in order for the comb filter to pass the radar pulse signal without too much distortion:

- Bandwidth requirement = BW $\geq \frac{1}{2\tau}$
- Sampling frequency requirement: $f_s \geq \frac{1}{\tau}$

where τ = radar pulse width.

These considerations are reported in more details recently.[10] Because of the limited length of the CTD device used in this study, the sampling frequency cannot be raised high enough to provide adequate bandwidth for processing real radar signal. Simulated MTI radar signals are used to demonstrate the application of canceller type comb filters as shown in Fig. 8 and 9. A stationary target is simulated by a pulse. A moving target is simulated by a train of pulses whose amplitudes

are modulated by the Doppler frequency, producing the so-called "butterfly" or "bipolar" signal shown in Fig. 8. The filter information is:

Canceller type comb filter
96 bits Reticon SAD 10 delay line
f_s = 400 kHz
Filter coefficients: $a_o=1$, $a_1=-2$, $a_2=1$
$b_1=-0.334$, $b_2=+0.334$

It can be seen that the stationary target pulse is eliminated at the output while the moving target "butterfly" signal passed the filter with small amount of attenuation and distortion. However, some glitches can be seen suggesting that high frequency components have not been cancelled. This probably is the consequence of deteriorated attenuations of the comb filter at high frequency range as described in section 2. This effect is tested in Fig. 9 which presents the same experimental situation as in Fig. 8 except that the simulated stationary target pulse is much narrower and has more high frequency components. It can be seen that the cancellation is not as complete as in Fig. 8.

(2) Integrator application:

An integrator type comb filter will only pass a periodic signal whose PRF matches the recursion frequency of the filter, i.e., f_s/N = PRF. Other noises and/or undesirable signals will be suppressed and accomplish an overall improvement of signal to noise ratio or signal to interference ratio. Fig. 10 and 11 demonstrate this ability. The filter information is the same as in Fig. 5. In Fig. 10, a 0.3 volt peak to peak pulse train is contaminated by random noise of 0.4 rms volt. In Fig. 11, another pulse train of 0.1 volt peak to peak is contaminated by random noise of 0.2 rms volt. The improvement of S/N ratio is clearly seen.

6. CONCLUSION

The basic concept, circuit configuration and theory of a sampled analog recursive comb filter are presented. Two CTD delay lines have been used in experimental studies. The measured results agree fairly well with the calculation suggesting that the basic understanding and a usable theoretical analysis have been obtained. Feasibilities of several applications were demonstrated. However, other performance criteria important to practical applications such as the dynamic range, bandwidth limit, sensitivity, stability, noise properties, etc. have not been investigated. They should be investigated if practical applications in real systems are to be considered.

ACKNOWLEDGEMENT

The authors wish to thank Professors S. R. Parker, R. Fossum for encouragement and support, Mr. P. Kopp for laboratory assistance and Ms. A. Schow for preparing the manuscript.

* Supported by Naval Electronic Systems Command and Naval Postgraduate School Research Foundation.

REFERENCES

1. D.A. Smith, C.M. Puckett and W.J. Butler, IEEE J. Solid State Circuits, SC-7, p. 421 (1972).
2. D.A. Smith, W.J. Butler and C.M. Puckett, IEEE Trans. Communications, COM-22, p. 921 (1974).
3. J. Bounden, R. Eames and J. Roberts, Proceedings 1974 International Conference on Technology and Applications of CCD, Edinburgh, Scotland, September 1974, p. 206.
4. J. Mattern and D. Lampe, ISSCC Technical Paper Digest, Philadelphia, February 1975, p. 148.
5. J. Roberts, M. Chesswas and R. Eames, Electronic Letters, 10, p. 169 (1974).
6. T.F. Tao, V. Iamsaad, S. Holmes, B. Freund, L. Saetre and T. Zimmermann, Proceedings, 1975 International Conference on CCD Applications, October 1975, San Diego, California, p. 257.
7. W. Butler, W. Engeler, H. Goldberg, C. Puckett and H. Lobenstein, IEEE International Symposium on Circuits and Systems, Boston, April 1975, IEEE Publication Advanced Solid State Components for Signal Processing, p. 30.
8. W. Bailey, R. Broderson, W. Eversole, L. Hite, M. Whatley, D. Buss and R. Sproat, Digest of Papers, 1974 Government Microcircuits Applications Conference, 5, p. 76 (1974).
9. M. Tompsett, A. Moshen, D. Sealer and C. Sequin, IEEE International Symposium on Circuits and Systems, Boston, April 1975, IEEE Publication Advanced Solid State Components for Signal Processing, p. 83.
10. T. F. Tao, L. Saetre, S. Holmes and A. Ejaz, Digest of Papers, 1976 Government Microcircuits Applications Conference, Orlando, Florida, November 9-11, 1976.

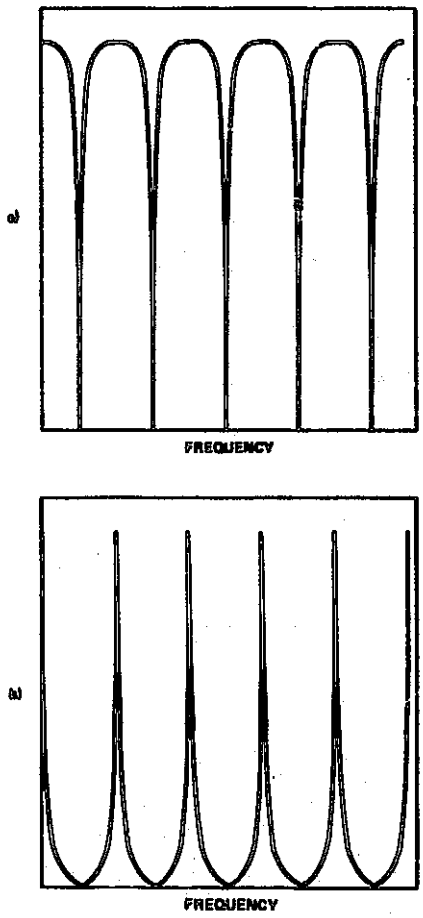

Fig. 1 Frequency Characteristics of (a) Canceller Type Comb Filter (b) Integrator Type Comb Filter

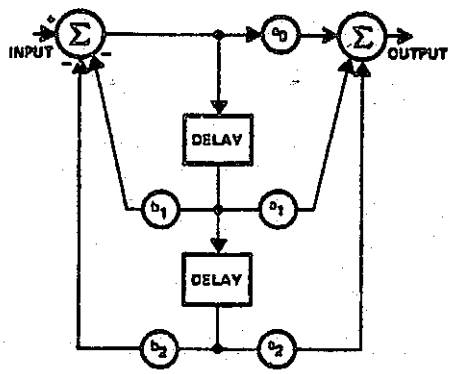

Fig. 2 Configuration of Second Order Canonical Circuit for Recursive Filter

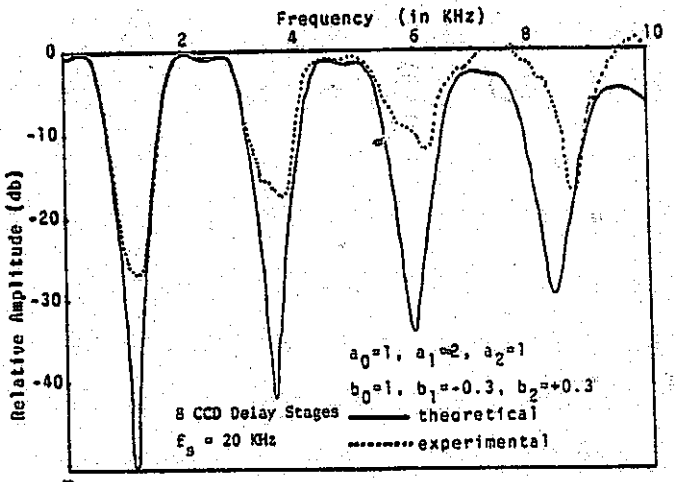

Fig. 3 Measured Frequency Characteristics of Canceller Type Comb Filter Using an 8 bits CCD Delay Line

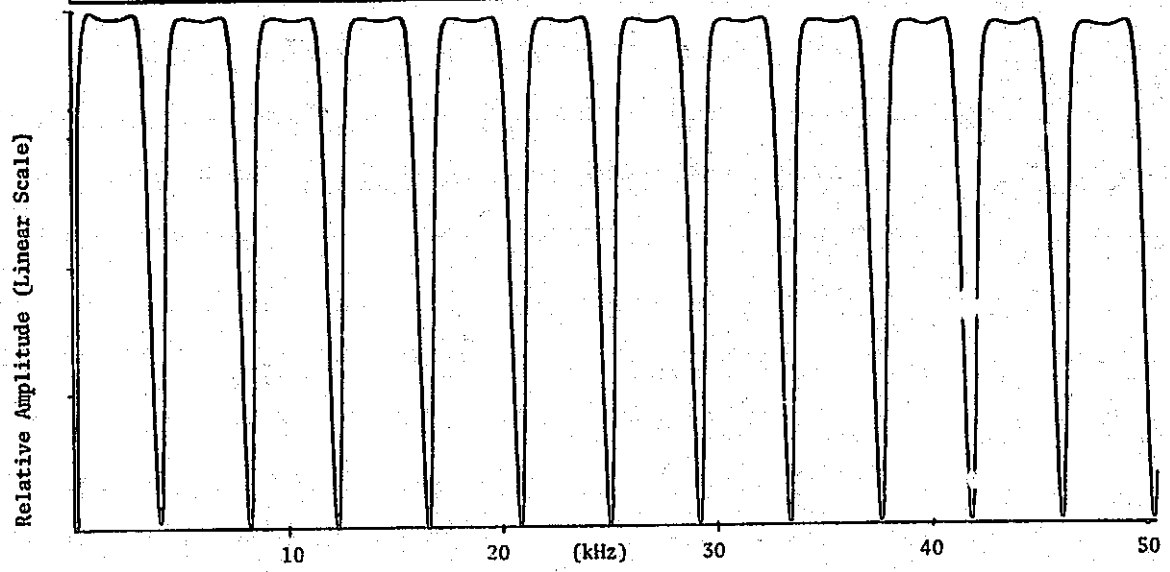

Fig. 4 Measured Frequency Characteristics of Canceller Type Comb Filter Using a 96 bits CTD Delay Line

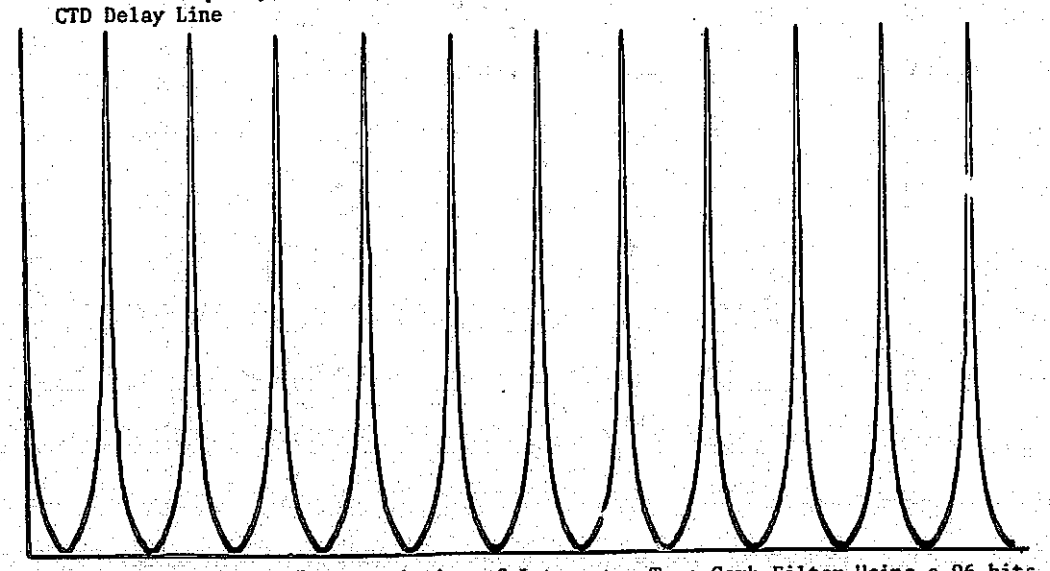

Fig. 5 Measured Frequency Characteristics of Integrator Type Comb Filter Using a 96 bits CTD Delay Line.

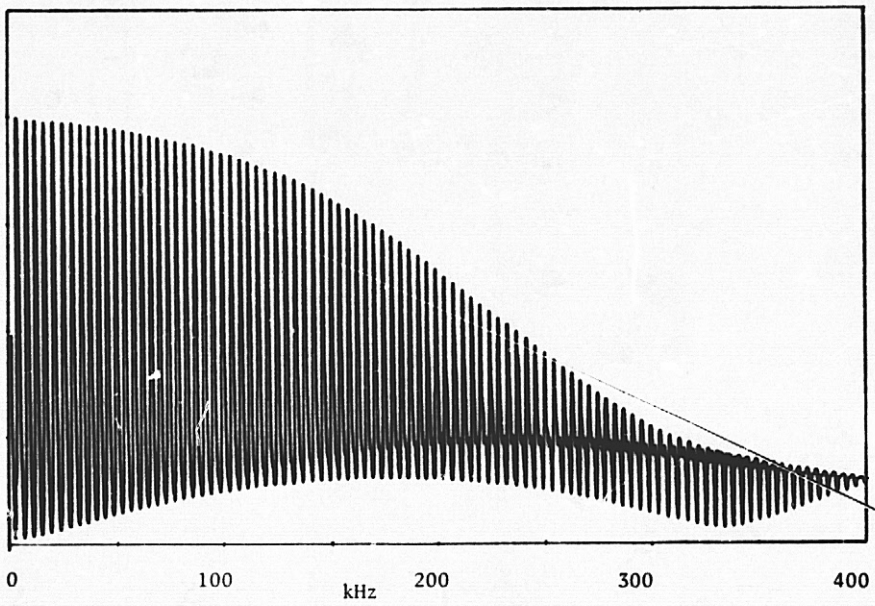

Fig. 6 Measured Frequency Characteristic of An Integrator Type Comb Filter Using 96 Bits CTD Delay Line

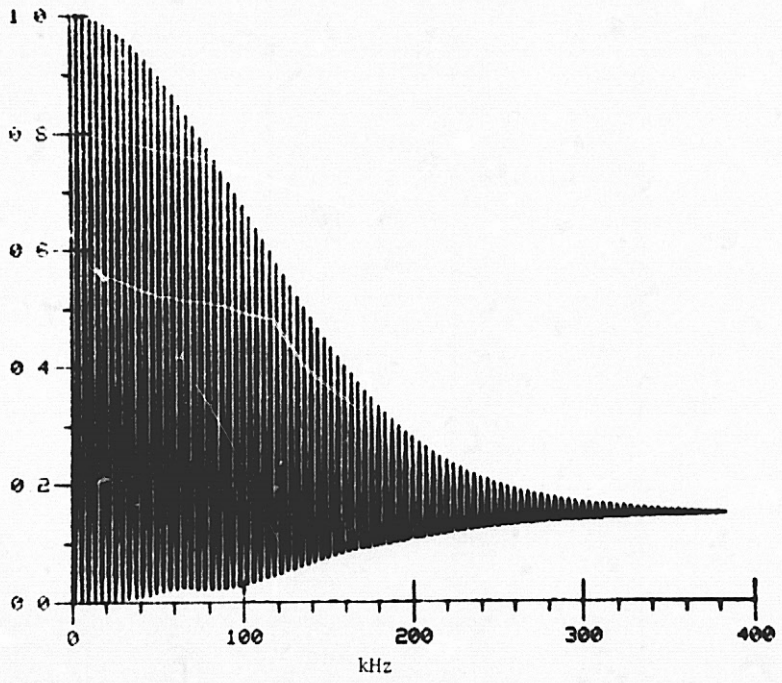

Fig. 7 Calculated Frequency Characteristic of An Integrator Type Comb Filter Using 96 Bits CTD Delay Line.

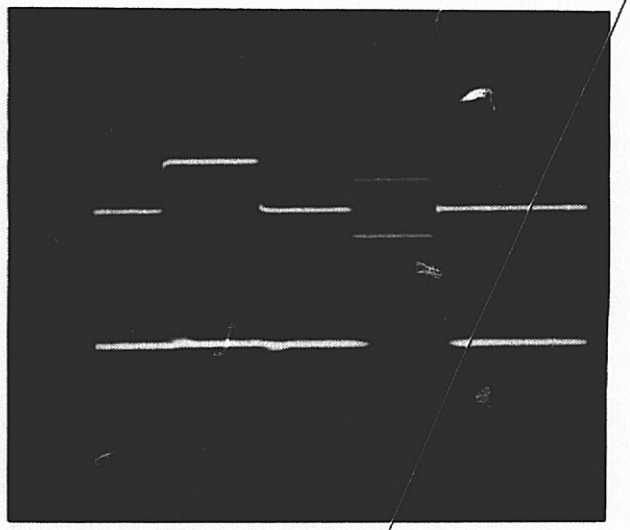

Fig. 8 Demonstration of Using Canceller Type Comb Filter for MTI Radar Applications

X scale: 10 μsec/division

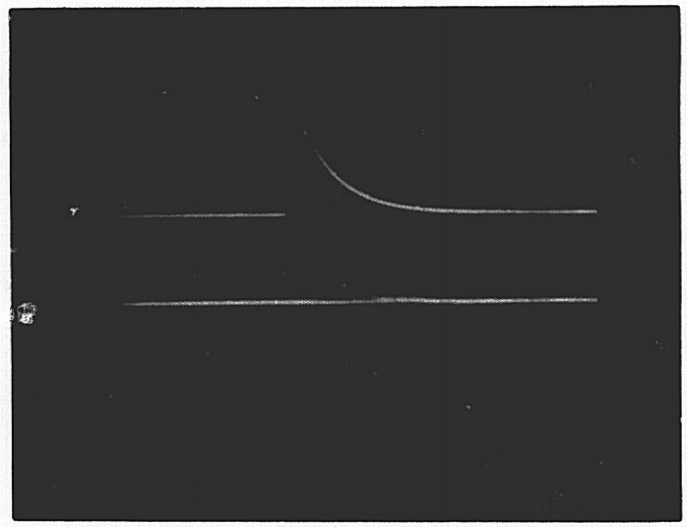

Fig. 9 Demonstration of Using Canceller Type Comb Filter for MTI Radar Applications

X scale: 1 μsec/division

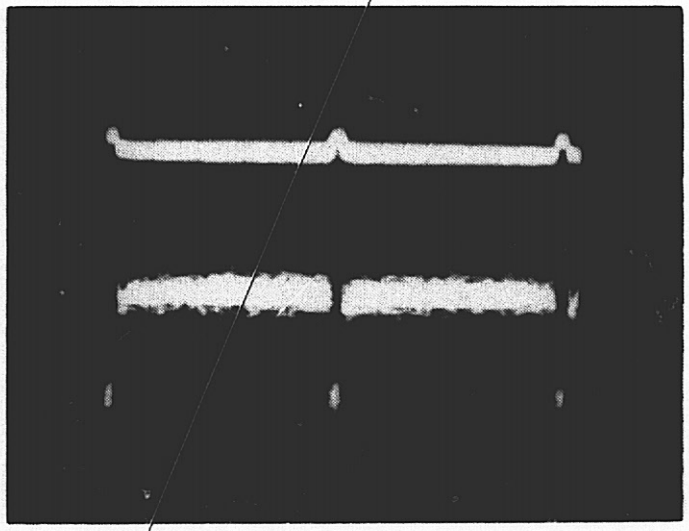

Fig. 10 Demonstration of Using Integrator Type Comb Filter for Enhancing Periodic Signal Contaminated by Noise

Signal = 0.3 volt P-P, Noise = 0.4 volt RMS

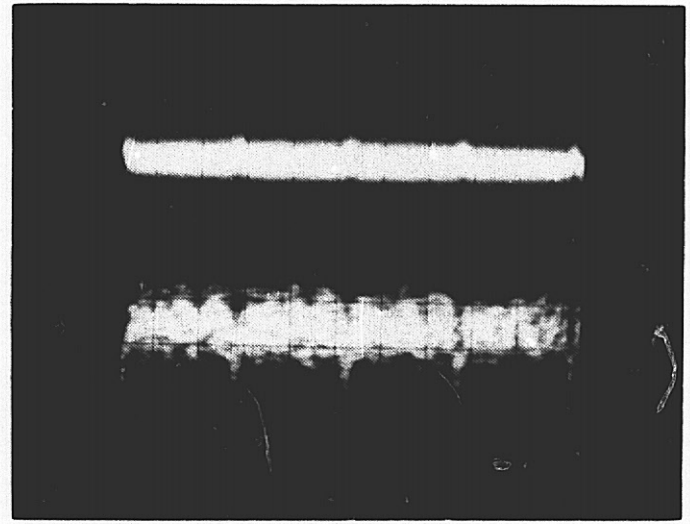

Fig. 11 Demonstration of Using Integrator Type Comb Filter for Enhancing Periodic Signal Contaminated by Noise

Signal = 0.1 volt P-P, Noise = 0.2 volt RMS

A PHOTON COUNTING ARRAY PHOTOMETER USING AN INTENSIFIED CHARGE COUPLED DEVICE

DOUGLAS G. CURRIE

University of Maryland, College Park, Maryland USA

ABSTRACT

An array photometer which uses an Intensified Charge Coupled Device has been developed at the University of Maryland. This system, the University of Maryland Array Photometer (UMAP) has the ability to discriminate single photoelectron events in real-time at a 4 Megahertz rate. The photosensor uses an S-20 photocathode and a Fairchild CCD202 with a 100 by 100 array of separate individual channels. This is an electrostatically focused device fabricated by the Electronic Vision Company. The overall system has demonstrated a noise level which permits single photoelectron discrimination, a scan rate of 400 frames per second, a very linear response, and very low lag. The UMAP system has a very large dynamic range exceeding 10,000 in the photon counting mode. A special technique to extend the dynamic range to 1,000,000 will be described. The performance parameters of this system, both in the laboratory and on the telescope will be discussed. It has already been operated in the photon counting mode on several different telescopes. Data from these observations will be discussed to illustrate the system sensitivity (which is at a level defined by the photocathode sensitivity and the spacial resolution), which is basically limited by the pixel size in the array, rather than the electro-optics.

I. Introduction

The University of Maryland Array Photometer consists of an array of photosensitive channels, each of which is capable of single photoelectron discrimination, or photon counting. This system, in its basic form, is not saturated by a uniform illumination of 400 photoelectrons per pixel per second, i.e., a photoelectron rate of 4×10^6 photoelectrons per second for the entire array. The photodetector of this system is an internally Intensified Charged Coupled Device fabricated by the Electronic Vision Company and built around a Fairchild CCD201/202. Several of these Intensified Charge Coupled Devices (ICCD) have been fabricated by the Electronic Vision Company (a division of Science Applications, Inc.) and tested at the University of Maryland. These tests have been conducted primarily using the Single Scan Data Recording System with some preliminary tests conducted using the full University of Maryland Array Photometer system.

General Properties of the Array Photometer

The University of Maryland Array Photometer (UMAP) system, using an ICCD, is an ultra-sensitive TV-type camera system which distinguishes individual photoelectrons in each of 10,000 channels. These channels are arranged in the form of an array of one hundred by one hundred elements. The time resolution in each channel is normally somewhat shorter than three milliseconds, which is the time required to scan one frame. The frame time, and thus the time resolution, may be much smaller if a shorter subarray is scanned. The array is sensitive to the incident light for essentially all of the observational period (i.e., greater than 98% of the time) and the expected dynamic range for each channel in the basic system is very large, about 250,000 for a ten minute observation. For the extended (analog) system, this expected dynamic range is 5×10^7.

Internally Intensified Charge Coupled Device

The basic photodetector for the University of Maryland Array Photometer (UMAP) system is the Intensified Charge Coupled Device (ICCD). In this device, an incident photon is converted to a photoelectron at the photocathode. In the current tubes, the photocathode has response similar to the S-20 response. The photoelectron is accelerated and focused, and then penetrates the region of active silicon in the Charge Coupled Device, where ionization produces a charge packet. The scanning circuitry of the CCD provides the parallel-to-serial conversion of the data, and the video signal is preamplified by circuitry on the CCD substrate.

History and Current Status

The development of the UMAP electronics and of the Single Scan Data Recording System (SSDRS) was started late in 1973. A preliminary set of electron bombardment tests of a CCD were preformed at the Electronic Vision Company in August of 1974 using the preliminary form of the SSDRS. The initial contract for tube fabrication from the University of Maryland to the Electronic Vision Company was let in October of 1974. ICCD-1 was received for testing at the University of Maryland in June of 1975. This tube proved to be gassy after an initial series of tests were completed. ICCD-3 was received at the University of Maryland in September of 1975, and has shown no problems with gas. ICCD-4 was received in February of 1976. The results of earlier tests have already been reported [1], and this report will primarily focus on the results obtained with ICCD-3.

The overall system is currently operating at a noise level which permits single photoelectron discrimination and permits the formation of images with discriminated single photoelectrons. The system has been operated in this fashion on a variety of astronomical telescopes. Although the UMAP system is not yet in full operation, and the results are quite preliminary, the various aspects of the system which have been carefully tested are in accord with the early theoretical predictions.[2]

II. Requirements for the Array Photometer

The development effort described in this report has been motivated by two different applications at the University of Maryland. These applications, although they are both astrophysical in nature, generate a significantly different set of requirements on the array photometer.

Amplitude Interferometer Requirements

The primary application of the UMAP system is to provide the basic photosensor for a new astronomical instrument, the Multi-Aperture Amplitude Interferometer (MAAI). This unique new system is a multi-channel version of the Amplitude Interferometer which has been used in an astronomical observation program over the last four years [3,4,5,6,7]. When used on a large telescope, the current instrument yields image information, through the earth's atmosphere, which has a resolution that is somewhat better than the diffraction limit of the telescope. The MAAI will have an angular resolution which is about the same as the currently operating instrument of i.e., 0.010 arc-seconds when used on the 200-inch telescope on Palomar Mountain. The precision of the measurements which have been made with the current instrument are about 0.002

arc-seconds [7]. This will be greatly improved with the new MAAI, which has a data rate which is larger by a factor of about 7,000 and which utilizes all of the light received by the telescope primary.

Basically, the MAAI application requires an array of individual photosensors, each of which has:

1. The ability to discriminate reliably among zero, one, two, and more than two photoelectrons per pixel per scan,
2. Very low lag, i.e., very little memory from one frame to the next frame,
3. Minimal cross talk between spacial channels (or pixels) and high geometric stability.

The requirements on the overall array are:

1. At least 100 by 100 elements,
2. The ability to complete the scan of a full frame in a few milliseconds, and subframes at a rate of much faster than the basic 400 frames a second.

Direct Imaging Camera Requirements

The other application in which the Array Photometer will be used consists of a Direct Imaging Camera in the focal plane of a large telescope. Although initially planned for use on an earth-based telescope in conjunction with the MAAI, the low weight, the electrostatic focusing, and low power requirement of the system make it very interesting for space applications. For one, most of the above requirements are important, but the imaging application has the additional requirements of:

1. Very large dynamic range,
2. Very low blooming.

Some of the electronic operating parameters of the system will be significantly different when the UMAP system is used in these two different applications.

III. Method of ICCD Operation

In this section, we briefly describe the theory of operation and the detailed design of the ICCD. Both of these areas have been previously described in more detail in the literature [2,8].

Theory of Operation of the ICCD

The incident photons are received on a semi-transparent photocathode, where they are converted into photoelectrons. On the current devices, this is an S-20 photocathode. As indicated in Figure 1, these photoelectrons are accelerated to an energy of about 15 Kev and electrostatically focused onto the front surface of a Fairchild Charge Coupled Device (CCD201, or the current and future ICCD's, the CCD202).

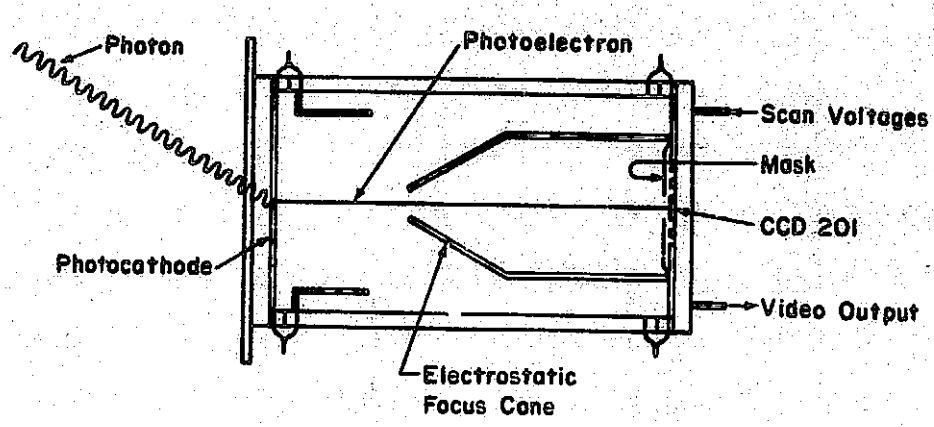

Schematic Diagram of Intensified Charge Coupled Device
Figure 1

The photoelectron penetrates the overlying layers of circuitry (where some energy is lost) and creates a packet of charge at one of the photosites by ionization of the silicon. This accumulation of individual packets of charge created by separate photoelectrons may continue until the end of the integration cycle. The charge packets which have accumulated during the integrating cycle (which is typically a few milliseconds) is then moved from the photosites to the transfer registers. The period during which the charge is transfered from the photosites to the shift registers is about 50 microseconds. During this period (about 2% of the integration cycle) the system is insensitive to light. The transfer registers move the charge line by line vertically from the two-dimensional array of photosensitive sites to the horizontal transfer register. Here one performs a parallel-to-serial conversion. The charge packets then go to the on-chip preamplifier. These transfer registers operate independently of the photosites and at the same time that the photosites are integrating the electrons produced by ionization for the next frame. Thus the transfers or "scanning" take place during the integration period, and the array is sensitive more than 98% of the time.

The transfer registers are protected by a layer of aluminum on the front surface of the CCD and the accelerating voltage is chosen so that those bombarding electrons which fall on the transfer sites do not reach the active silicon. Thus when operating in the direct imaging mode one loses a factor of two in effective quantum efficiency. The protection of the aluminum means that one does not have any ionization or "interline noise" in the transfer registers.

Electrical Operation of the CCD The scanning of the CCD is controlled by a set of control words in the Circulating Semiconductor Memory which will also store the data. In order to operate the light sensor on the telescope, a long cable from the electronics to the camera head is required. To handle this, a special camera head has been fabricated which minimizes the cross-talk and coherent noise. The pulse trains are transmitted to the telescope on high impendence lines. These are converted to the required high current pulses by clock drivers in the camera head. The camera head also contains amplifiers, a sample and hold circuit, and a discriminator.

Noise Sources in the Charged Coupled Devices There are three types of electronic noises which are most significant with respect to ideal photoelectron discrimination operation. These effects which will be defined in the following paragraphs are "random charge noise", "thermal leakage charge" and the variation of the thermal leakage current or the "thermal leakage noise".

The random noise is the variation of the voltage level, from one frame to the next, at a given pixel. For measurements of the random noise, the illumination is presumed to be constant, or as for most of these tests, there is no illumination. The random noise is characterized by the standard deviation of the voltage at a given pixel for a number of successive frames. This type of noise behaves as if it were Johnson noise dominated by the capacitive input of the on-chip preamplifier. The value of the random noise is essentially independent of temperature (more precisely it varies inversely as the absolute temperature). At a data rate of 0.5 MHz the random noise has been measured by Dyck and Jack[4] to be about 300 electrons per pixel per scan. We find about the same value at 0.5 MHz and about 1.0 MHz.

The "dark current" or thermal leakage current is due to thermally generated charge pairs which are created within the active silicon. The leakage current is parameterized by the average number of electrons which collect at a given pixel during the integration interval (usually this is equal to the scan or frame time). The value of the thermal leakage charge varies across the frame from pixel to pixel. It decreases by a factor of two when the temperature of the CCD is reduced by 6 or 7°C and decreases linearly as the integration time is decreased. The average leakage charge across the frame does not significantly effect the ICCD operation but its variation across the chip may create a problem. The variation of the thermal leakage charge from frame to frame (Poisson Statistics) in the leakage electrons would properly be a component of the random noise, but its value is negligible for normal ICCD operation.

The "thermal leakage noise" or fixed pattern noise is the variation of the thermal leakage charge across the array. This will be parameterized by the standard deviation of the thermal leakage charge across the array. More precisely, it is the variation of the mean (over many frames) thermal leakage charge across the array. This latter form of the definition removes the random noise as a component of the thermal leakage noise. It should decrease with temperature at the same rate as the thermal leakage charge and decrease in proportion to the increased data rates. This has been verified as will be discussed later. In order to permit single photoelectron discrimination without a change of discriminator level for each pixel, this filled pattern noise must be reduced to about 100 electrons. Although this should be satisfied at room temperature, it may safely be accomplished by cooling to approximately -20°C.

In order to study these quantities, an Image Processing System has been developed at the University of Maryland which permits computer processing of many scanned frames and the determination of these quantities by a standard procedure.

Operation of Intensified CCD

In this section we discuss the intensification of the CCD201 in more detail.

Theory of Intensification The photoelectrons provided at the photocathode are accelerated to 14.6 KeV prior to impact on the CCD. This value will provide sufficient charge by ionization to permit the detection of a single photoelectron, but is not sufficient to penetrate the aluminum (and other layers) which form the protection for the transfer registers. Since different regions covering the transfer registers ahve different thicknesses, the accelerating voltage is chosen so the photoelectron cannot penetrate the thinnest region. For a photoelectron which impacts the CCD over a photosite, some of the energy is lost in the layers of silicon and silicon dioxide which lies over the photosite. The 14.6 KeV electron will encounter either of two regions over the photosites which have different thicknesses. Therefore, the photoelectron may have either 8.5 or 9.6 KeV upon entry to the active silicon. These detailed calculations are based on a specific model of the CCD architecture which was obtained from R. Dyck of the Fairchild Corporation. For any given device from a particular run, it is expected that there will be significant variations. Thus these numbers may be considered as a sample calculation.

As a result of the energy of the photoelectron entering the active silicon, we will have the production of charge packets containing 2300 or 2600 electrons, depending on how many layers it has penetrated. The variation of these numbers is relatively small, especially when compared to noise in the on-chip amplifier of 300 electrons. Since the incident electrons may enter either area, we expect an ideal pulse height distribution of the electrons to have the form indicated by the vertical bars in Figure 2. For this case, the energy has been further reduced to 13.3 KeV so the photoelectron will not penetrate into the final layers of SiO_2 insulation above the active silicon of the transfer registers. The cross-hatched area represents the pulse height spectra for the case in which the noise of the on-chip preamplifier is included. The different values depend upon the energy of the accelerated electron, i.e., the accelerating voltage.

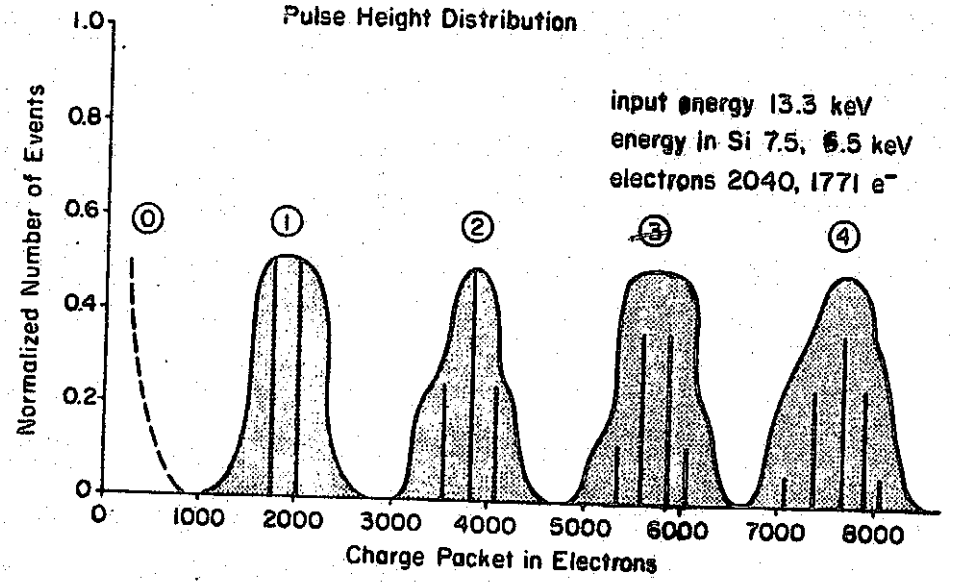

Theoretical Pulse Height Distribution
due to Ionization in the CCD by Accelerated Photoelectrons
Figure 2

Thus, for an incident energy of 13.3 KeV, and depending upon what region of the photosite the electron enters, a packet of either 1,770 or 2,040 ionization electrons is produced for each photoelectron. Since the noise in the on-chip preamplifier is about 300 electrons, one may easily discriminate between a single photoelectron or no photoelectrons.

ICCD Design

The design of the ICCD incorporates several features which enhance the ability to discriminate at the single photoelectron level. A special CCD201, on which most of the top layer of SiO_2 (the scratch protection) was not added, was mounted by the Fairchild Corporation on a ceramic header. This header, designed by the Electronic Vision Company, provides the required electrical contacts for the CCD in a circular pattern of pins. Thus it may be mounted in a socket in the camera head which was developed for the ICCD. The header also provides the support for the electrostatic focus cone and the mask which exposes the active array and protects the preamplifier and other circuitry on the chip from damage by the accelerated photoelectrons. The chip is bonded directly to the ceramic header so the CCD may be readily cooled using a probe which contacts the header directly below the CCD. This is an area which is clear of pins. The cooling may be required to reduce the thermally generated dark current on the chip.

IV. University of Maryland Array Photometer System

Since the UMAP system described in this section has been developed primarily as the photosensor for the Multi-Aperture Amplitude Interferometer, several aspects of the system are especially oriented toward this goal. In particular, there are several requirements on the system beyond those general requirements discussed in Section II which are related to operation at the Cassegrain or prime focus of a large telescope. These are:

1. Operation over a wide temperature range,
2. Photometer unit which is light weight, mechanically and optically rugged, and operable at all orientations.
3. High immunity to external RFI,
4. Proper operation with main electronics subsystems located 100 meters from photometer unit, i.e.,
   a. a minimum of cross talk between the signals transmitted on the cable
   b. proper sequencing of the various clocks in order to handle propogation delays which consist of several cycles,
5. Equipment packaging to permit the use of air freight in an "assembled" configuration.

The following discussion will center on the use of the ICCD as the photosensor for the UMAP system. However, the UMAP system is also designed to use bare CCD's as infrared sensors with a few minor additions. The use of the UMAP system within the MAAI involves a rather complex overall system. Thus to simplify the following discussion, we shall describe the use of the UMAP system with the Direct Imaging Camera. This will use part of the MAAI system, but the additional capabilities and complications involved in the MAAI system will be either ignored or mentioned only in passing in this discussion.

Block Diagram of UMAP System

The block diagram of the University of Maryland Array Photometer system, as it will be used in the "Direct Imaging Camera" mode, is shown in Figure 2.

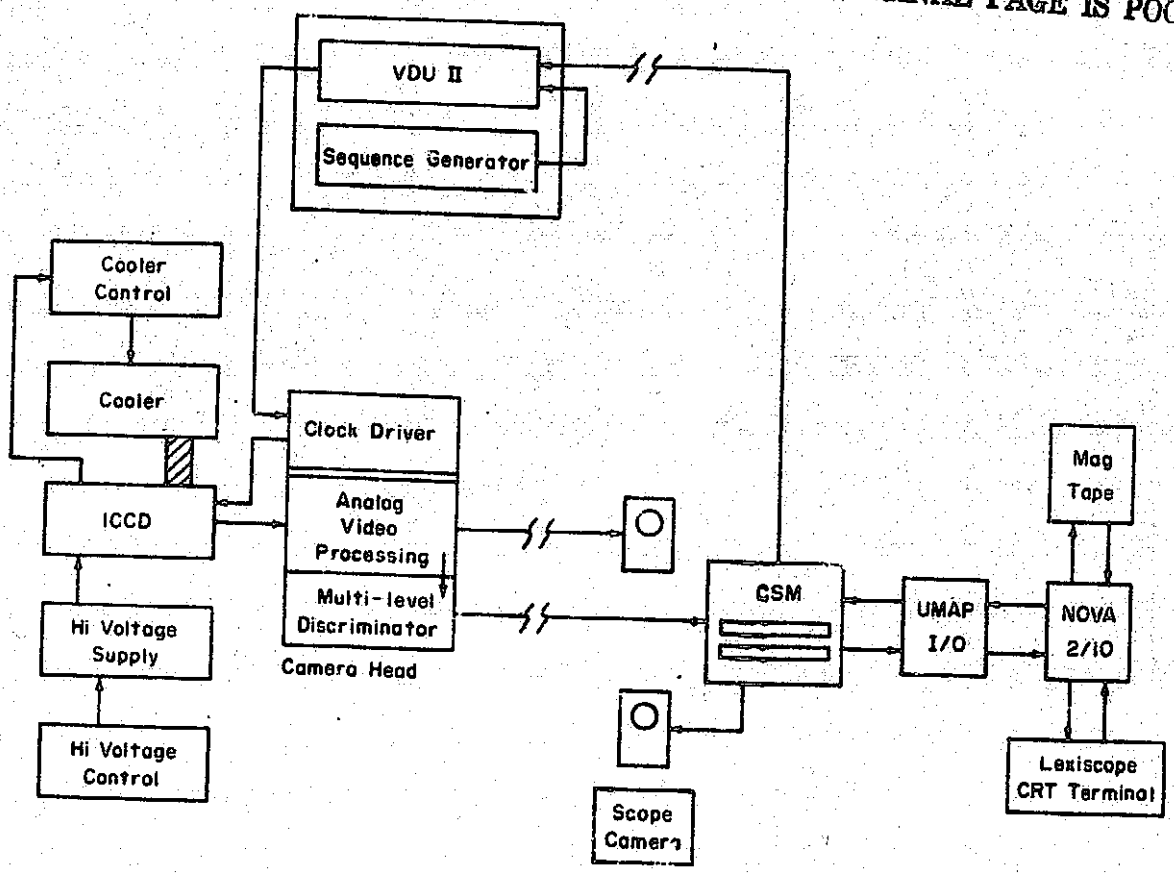

Block Diagram of UMAP System as Used in the Direct Imaging Camera Mode
Figure 3

We shall now proceed to describe the overall operation of the UMAP system. Depending on the particular requirements of the observations, the scan rate, the format and the size of the array to be scanned is chosen by the operator. The parameters which describe this subarray are typed into the lexiscope CRT interface. The NOVA mini-computer then generates the detailed instructions which are required for scanning the CCD in this particular fashion. The NOVA cannot operate at the speed required to directly control the CCD, so these commands are transferred and stored as special control words in the Circulating Semiconductor Memory. The Circulating Semiconductor Memory (CSM) is a special memory device which has been designed and fabricated for this application. It has five tracks (only one of which is used in the Direct Imaging Camera mode) each containing 12,288 words. The individual words are 16-bits deep. The total memory capacity of the CSM is 0.6 M bits and it currently operates with an input of 5, 3-bit words at a rate of 75 M bits per second. The CSM, which operates at a data rate as high as five megahertz, transmits these individual commands to the Video Drive Unit (VDU) which is located on the telescope near the photometer unit. The Video Driver Unit generates coded pulses to drive the CCD. The CCD may be cooled by a thermoelectric device to reduce the variations of the dark current across the chip to a value which is small compared to the random capacitive input noise on the on-chip preamplifier. This temperature is typically between 20°C and -20°C. The video output from the CCD, which contains the data, is brought to an electrically isolated portion of the camera head, i.e., separate from the chamber which contains the CCD drive circuitry. This configuration reduces the pick-up of coherent noise by the sensitive video electronics. The video signal is amplified and the signal divided for the two types of processing. On the one hand, the charge from each photosite is discriminated at various preset voltage levels for use in a photon-counting mode. On the other hand, an A/D conversion

is performed on the other portion of the signal. This permits the operation of the CCD in a linear or analog; rather than photon counting mode. The information, in digital form is transmitted from the telescope down to the Video Processing Unit. The Video Processing Unit has a very simple function for the Direct Imaging Camera. However, in the MAAI, it performs the on-line computations which are required to transfer the data into a structure in which one may add successive frames of data. From the Video Processing Unit, the data stream proceeds to the Circulating Semiconductor Memory, where this data is added, pixel by pixel, to the data of the previous scans. Thus one channel of the CSM records data at a five Megahertz rate for a three bit word. For all five channels the CSM accepts data at a rate of 75 megabits/sec and records them in a memory which totals 0.6 Megabits of storage. One may select, either by thumb wheel or by software, various different sizes of memory and various different rates of operation. For permanent storage of the data, the NOVA minicomputer slows down the CSM in a predetermined sequence, transfers a block of data from the CSM to the NOVA core storage, sets the registers in this block in the CSM to zero, and accelerates the CSM to the proper rate and reinitializes the CCD. The data is then transferred from the NOVA core storage to digital magnetic tape while new data from the CCD is being recorded in the CSM.

Projected System Performance of UMAP System

Let us now consider the predicted performance of the overall system. The intrinsic dynamic range for the UMAP system is extremely large (i.e. of the order of 5×10^7 per pixel for a ten minute integration). Since the overall system is not yet operating at this level, these predictions will be based on data from several sources, some of which will be discussed in later sections.

Operational Direct Imaging Performance In most applications, practical aspects of the application will prevent the use of such a large dynamic range. For example, when the system is used to record the direct images of faint objects with a wide spectral range on a large telescope, the effective dynamic range is defined by various parameters of the overall UMAP/telescope system and of the atmosphere. Thus to make a realistic projection for a given observational situation, we will consider the overall configuration which was to be used for quasar observations on the 200-inch telescope at Palomar Mountain in January of 1976. The photometer unit was installed at the prime focus, with Ross corrector lens system, and a set of spectral filters. However, to achieve the maximum performance in terms of the high dynamic range, none of these optics would be used. For the photocathode response, we use the measured quantum efficiency of the "S-20" photocathode of ICCD-1. For this illustrative calculation, we shall express the results in units of the image brightness expressed in stellar magnitudes per square arc-second. Thus we primarily address the study of an extended object, like a distant galaxy. We note, however, that if the seeing disc is slightly larger than one arc-second, the ordinate and absissa of Figure 4 may also be correctly interpreted in terms of the visual magnitude of an unresolved source. Thus this analysis permits a condensed presentation to both the observation of a quasi-stellar or unresolved object (expressed in stellar magnitudes) and to an extended object (i.e., a faint galaxy) where the surface brightness is expressed in stellar magnitudes per arc-second. A more complete discussion, including the dependence of this performance on the diameter of the seeing disk will be presented elsewhere.

Dynamic Range Extension by Use of Analog Mode There is no blooming until at least several hundred photoelectrons per pixel per scan are accumulated. Thus if we were to record data on the SSDRS at the same time as the photon counting data is recorded in the CSM, we would obtain an additional factor of, conservatively, 200 in the dynamic range. The current camera heads permit this but the improvements required for the rest of the equipment have not yet been implemented. Thus we see from the figure that the dynamic range for this configuration is 16.4 stellar magnitudes or about 3.5×10^6.

Thus this mode of operation includes the use of the data from regions bright enough to require operation in the analog region of the CCD. For this analog measurement, we have presumed that the limit in the accuracy of the measurement may not be the photon counting statistics, but the accuracy to which the systematic problems may be corrected. For the solid line in Figure 3, we have presumed that the systematic errors can be corrected to a level at which we have already found that we can perform this correction during some early tests at the University of Maryland (i.e. 0.3%). The dotted line indicates a correction at a level of 0.05%, which has been achieved during more recent tests. We note that Fairchild has published data claiming this may be corrected to a level of 0.025%.

This projected performance makes the UMAP system particularly interesting for use in observing objects which have a very large dynamic range over a relatively small field. Since the response of each individual pixel is independent at this signal level, one can expect operation here with very little blooming. For the configuration of the telescope and the UMAP system described in this section, the effect of the insensitive aluminum transfer registers on the photometric accuracy for observing unresolved objects is less than 0.05%. We are particularly interested in the study of Seyfert galaxy cores and quasars, with a determination of the type of the underlying galaxies in the latter case.

Assumptions for Limiting Performance. In the operation mentioned, the limiting magnitude is defined by the statistical noise in the night sky background. However, in the absence of the night sky, there are two effects which will limit the ultimate dynamic range. The first of these is the emission of thermal electrons from the photocathode in the absence of light (photocathode dark current) and the other is caused by large random noise excursions tripping the discriminator (electronic dark current).

The theoretical evaluation of the expected level of the electronic dark rate makes several assumptions.

1. The "random noise"[(2)] of the CCD has a standard deviation of 300 electrons,
2. The distribution of this random noise is indeed Gaussian to the required level. Preliminary data on this point will be discussed in a later section of this paper.
3. The chip architecture, and the resultant pulse height distribution have the form which has been described earlier [(2)],
4. The discriminator operating point is set at a level of .320 electrons to yield a collection efficiency of 93%.

This results in a limiting magnitude due to electronic dark current (in the 1-T sense) of $m_v = 32.4$ for a ten minute exposure.

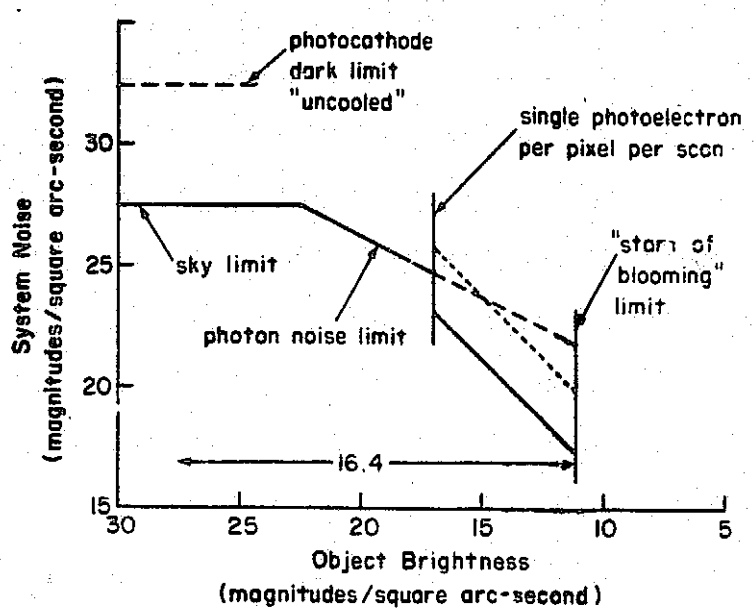

Limiting system noise of UMAP system, where the absissa describes the surface brightness expressed in magnitudes per square arc-second and the ordinate describes the equivalent brightness of the "noise" or uncertainty in an observation of a pixel expressed in stellar magnitudes.

Figure 4

In general, the figure describes the observation of an extended area for which the brightness of this object may be, for example, 20 magnitudes per square arc-second. In this case, the "system noise" will be about 26 magnitudes per arc-second, or it will have a standard deviation (if several observations of ten minutes are taken) of 0.4% which, in this domain, is due to the Poisson noise of the signal. Thus we might expect to see, at a "one-sigma" level, a feature with a brightness of 26 magnitudes per square arc-second overlying a region with a uniform brightness of 20 magnitudes per square arc-second.

For an object with a brightness between 16.9 and 22.5, this uncertainty in the intensity of the image (the "system noise") is due to the Poisson counting statistics in the signal from the object. This is based upon an assumed observation interval of ten minutes. This also assumes a visual brightness for the moon-less night sky at Palomar Mountain of 22.5 magnitudes/square arc-second. For objects fainter than 22.5 magnitudes, the dominant noise source is the Poisson statistics in the night sky. In the range from 16.9 to 11.2, the noise may be either Poisson or systematic as will be discussed in more detail later. We have presumed an "uncooled" photocathode. The plate scale is about 11"/mm, giving a field of 33" by 44". The UMAP system will discriminate among zero, one, two, and more photoelectrons [2]. Thus one may have a mean count rather close to the frame rate of 400 frames a second, and still have a reasonably small correction for four and more counts. We shall nominally assume a mean rate of 400 photoelectrons per second per pixel for the maximum rate which is still in the single photon counting rate. For the faint limit of the dynamic range, we obtain a brightness of 27.5 magnitudes which is equal to the statistical Poisson noise in the night sky, i.e., we have here a signal-to-noise ratio of one. Remaining in the photon counting mode, we then have a dynamic range of 10.6 magnitudes or 17,400.

The 'uncooled' dark current limit presumes that the system is operating at about 'observatory' temperature of 50°F which we have found to be representative of the dome temperature. This calculation is based upon dark current rates which we have observed in the field and at the University of Maryland on similar devices with S-20 surfaces. This is in accord with published S-20 data.[8] One then obtains a limiting magnitude of 32.2, or about one photoelectron in ten minutes which is indicated in Figure 3. The addition of a procedure for cooling the photocathode would reduce this noise source, but this is not particularly effective, since then the electronic dark noise would immediately dominate.

For applications in which one is not limited by sky noise (i.e., imaging with narrow spectral filters or for spectrophotometry), we would have a photon counting range of 6.3×10^5 and a total dynamic range of 1.3×10^8. However, the computations of these theoretical results are extremely sensitive to the assumption made on the electronic dark current.

VI. Laboratory Performance

In this section we consider various tests and evaluations which have been conducted in the laboratory.

Single Scan Data Recording System

In order to evaluate the performance of the various portions of the system prior to the full operation of the electronics of the UMAP system, a test system, the Single Scan Data Recording System[9] (SSDRS) was designed, fabricated, and put in operation in May of 1974. A block diagram of the SSDRS is shown in Figure 5.

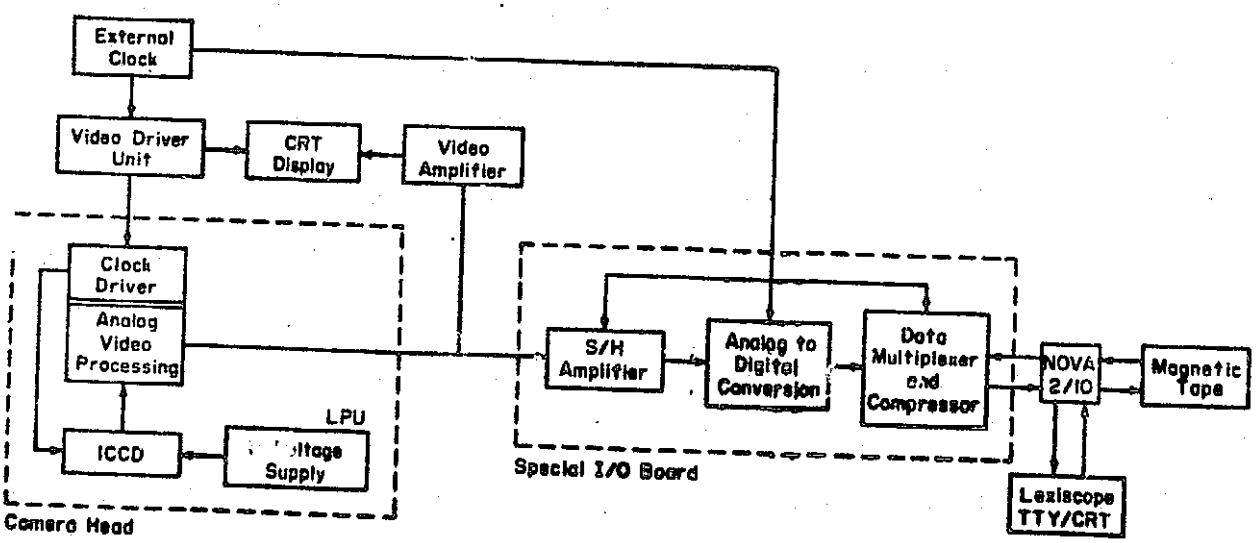

Block Diagram of the Single Scan Data Recording System
Figure 5

The basic mode of operation is to perform an A/D conversion for each pixel at a data rate which may be as high as four megahertz. A single frame of data words is then stored in the NOVA core. This stored frame of data is written onto digital magnetic tape. The rate at which frames may be recorded is limited by the magnetic tape writing speed to about three frames per second. Most of the laboratory and telescope data has been collected with this system. In several cases there appears to be some noise pickup which may dominate the effects of the noise in the CCD and in the camera head. In addition, we have recently discovered a one pixel shift in the recording of the data which has led to an apparent increase in the noise. Recent measurements, after fixing the jitter, on ICCD-4 which has a CCD202, indicate a random noise of about 300 electrons.

CCD System Noise Level

In this section we consider effects of "noise" which would degrade the system performance. The first of these effects to be considered here is the "random noise", followed by a consideration of the "fixed pattern noise".

We now consider the apparent random noise which one observes at the CCD. This has been measured in various laboratories including our own, to have a typical value of about 300 electrons.

In order to evaluate our data for this purpose, we shall use a pulse height distribution over many elements of the array. The pulse height distributions are formed by the following sequence of operations. One first records ten frames from the CCD with no illumination falling on the CCD or the photocathode (a "dark frame"). These are then averaged. Ten frames are then recorded during which the photocathode is illuminated (an "illuminated" frame). One then subtracts from a single illuminated frame, pixel by pixel, the averaged dark frame, and then performs a pulse height analysis of the remaining array. Usually this pulse height analysis is done over a central subarray, to reduce computer costs and to eliminate edge effects. The pulse height analysis consists of forming a pulse height distribution, i.e., the number of times one observes a given sized pulse or a given voltage for a pixel as a function of the pulse height or the voltage on the pixel. This analysis is repeated for each of the ten frames and the ten pulse height distributions which are produced are summed to produce a total pulse height distribution. This may be displayed directly (as seen in Figure 8) or we may normalize the peak of the pulse height distribution to unity and plot the upper side of this curve, which is relevant to photoelectron discrimination, as seen in Figure 6.

The random noise of the CCD is indicated in Figure 6 and is seen to be about 1.1 A/D Converter Units (ADU). The effect of turning on the high voltage is indicated by the pulse height distribution denoted with o. The difference is not significant, since differences of this magnitude occur for runs separated by an interval of time. As indicated above, more recent tests have demonstrated a standard deviation of 300 electrons.

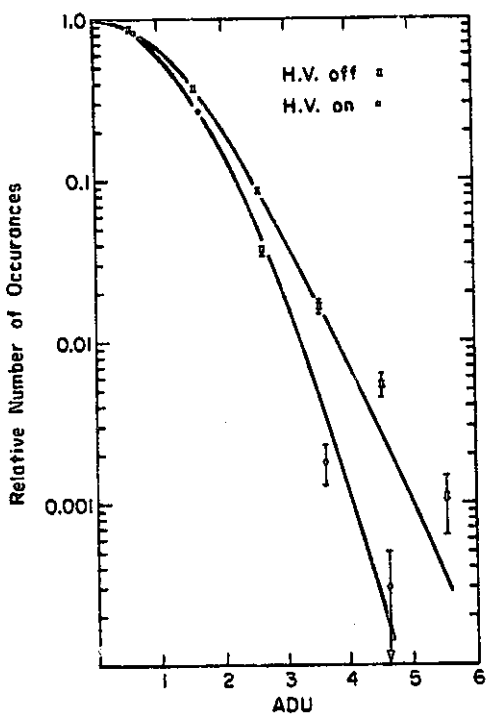

Pulse Height Distribution of Random Noise for ICCD-3. The ADU are each 0.124 millivolts at the CCD.

Figure 6

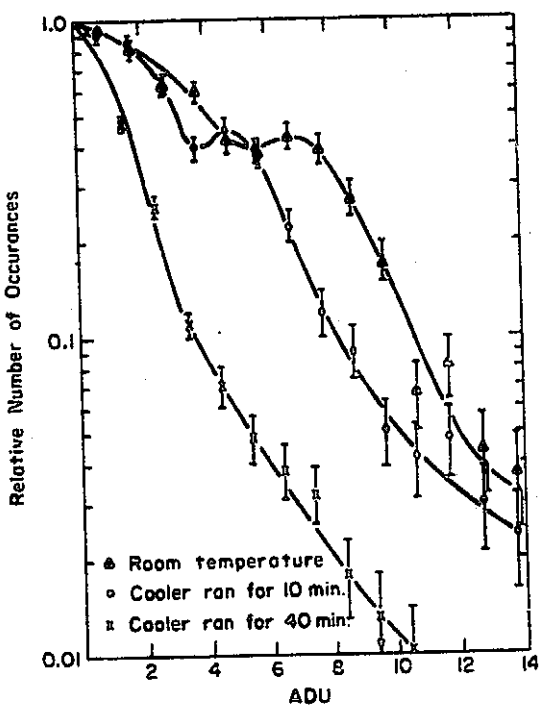

Pulse Height Distributions of Thermal Leakage at Three Different Temperatures.

Figure 7

The other source of noise is the "fixed pattern noise" or the spacial variations of the thermal leakage current in the silicon. The two types of noise are independent and combined in a simple manner, so they may be studied separately. The fixed pattern noise is then evaluated by averaging ten frames (to reduce the effect of random noise). A pulse height distribution is then obtained for the values expressed in the averaged frame. At room temperature and at a scan rate of 0.5 MHz, these variations in dark current are expressed in Figure 7 and are unacceptably large. The variation becomes much smaller and quite acceptable as the CCD is cooled. On the other hand, when the CCD is operated at 4 MHz, the width of the peak should be reduced by another factor of eight, which also makes the width quite acceptable.

Single Photoelectron Pulse Height Distribution

We now wish to evaluate the magnitude of the signal from a single photoelectron. In order to do this, the photocathode is illuminated with a uniform intensity and the recorded data is used to obtain the single photoelectron pulse height distribution. This has been done with various voltages and various light intensities. Three of these pulse height distributions are indicated in Figure 8.

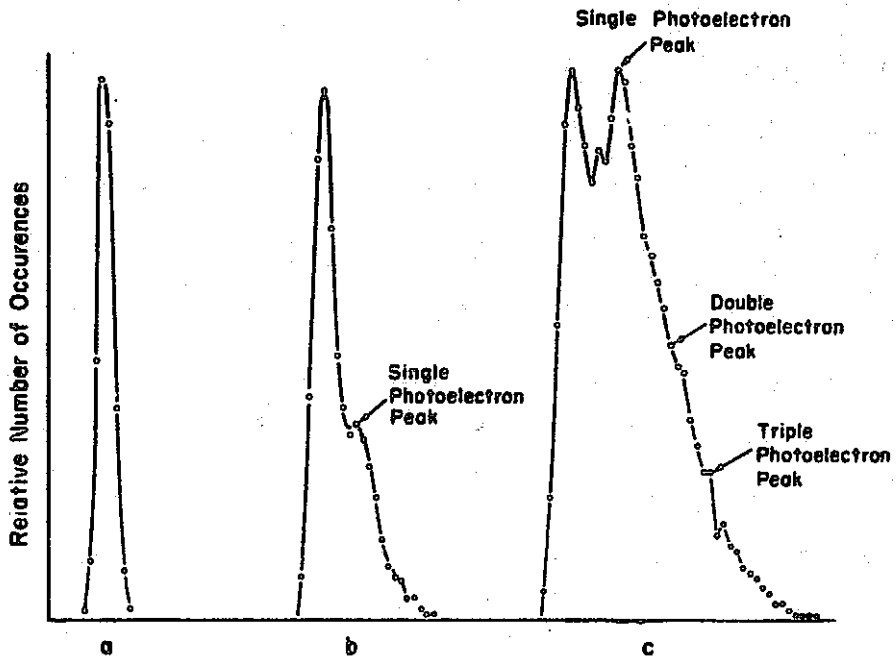

Pulse height distribution with 15 KV, 15 KV, and 18 KV, respectively and with no illumination, illumination, and illumination respectively.
Figure 8

Figure 8a illustrates the random noise of the CCD with no light input. This shows a relatively narrow peak with a standard deviation of 1.2 ADU. In Figure 8b, the photocathode is uniformly illuminated with an accelerating voltage of 15 KV. The peak due to the single photoelectrons can be seen. The peak due to zero photoelectrons is somewhat enlarged to about 1.5 ADU, and the mean magnitude of the single photoelectron signal is 5.3 ADU. In Figure 8c, where the accelerating voltage has been increased to 18 KV, the zero photoelectron peak is further broadened to about 2.0 ADU. This may be due to some penetration occuring at this (above nominal) accelerating voltage. The position of the single photoelectron peak (with respect to the ICCD photoelectron peak) is 7.5 ADU. Finally, the width of the single photoelectron peak is 3.0 ADU. In order to compare these values with the predictions, we must determine the gain of the on-chip preamplifier. The nominal value [10] is 1.5 Volts/picocoulombs, however, this may have wide variations [10]. Thus to determine the value for this present chip, we use the change in accelerating voltage and the change in peak position. This implies 380e^-/ADU or the gain of 2.0 Volts/picocoulomb, and implies the measured signal at 14.4 KV (which was calculated in an earlier work [2]) would be 1780e^- compared with the theoretical value of 1910e^-, well within the accuracy of this determination and knowledge of the various layers on the chip surface. The additional width of the singles peak is also in agreement with predictions [2]. That is, in Figure 8c, the singles peak is 1.0 ADU wider than the zero photoelectron peak and the prediction is that the additional width is 0.7 ADU.

The behavior of an individual channel or pixel in the ICCD is comparable to the performance of a conventional photomultiplier. Using the data expressed in Figure 8c, and setting the discriminator at a level to obtain a collection efficiency of 84%, one has a dark current rate of one count per second, which is a rather respectable performance, even at this preliminary stage.

Spacial Resolution

The spacial resolution of the electrostatically focused ICCD-3 was evaluated, using a microprojector to place a small spot of light (~7μm) on the photocathode. In the central region (out to a radius of about 1.3 mm in the 3mm by 4mm format), essentially all of the light fell within a single picture element. In this region, the diameter of the electron image of the incident light was less than 20 micrometers. This was determined by moving the incident light spot until the electron image fell on the aluminum transfer register between two photosites which has a width of 20 micrometers. No response was seen in either of the adjoining photosites where the sensitivity of this determination was at least 10% of the peak response. Thus in this region, the MTF of the UMAP system is basically the MTF of an array of discrete pixels. However, around the outer edge of the array the electron image spread to cover more than a single pixel.

VII. Field Operation

Operational tests using the Single Scan Data Recording System with the bare CCD's and the ICCD's have now been conducted on a variety of telescopes. The purpose of these tests have been to:

1. evaluate the field problems (low temperatures, transportation, "fool-proof operation")
2. determine the sensitivity of the system to external interference (TV and FM)
3. evaluate the system sensitivity

Some of these tests were conducted on the 36-inch telescope (which is operated by the Laboratory for Optical Astronomy) and the 48-inch telescope (operated by the Laser Technology Branch). Both of these groups are within the Goddard Space Flight Center and the telescopes are located at the Goddard Optical Research Facility (GORF). In addition, the photometer system was operated at the 60-inch and 100-inch telescopes at Mt. Wilson, and preliminary tests were also conducted on the 200-inch telescope at Palomar Mountain, which are operated by the Hale Observatories. A detailed list of these observations appears in Table I.

Field Configuration of System

The system configuration which has been used in these tests consists of the Single Scan Data Recording System. Although the CCD has not been cooled, the ambient temperature has ranged, on various observational runs, between 0°C and 20°C. A number of different objects have been observed in order to calibrate the sensitivity and to evaluate the general performance.

TELESCOPE	FOCUS	DATE	OBJECT	PHOTO-SENSOR	PLATE SCALE ARC-SEC/PIXEL	COMMENTS
100-inch Mt. Wilson	Cassegrain	8 July 1975	β Her, etc.	CCD	0".178	System operation Test of TVI sensitivity
Mt. Wilson	50 mm lens**	7 July 1975	Antares	CCD	146"	Sensitivity test & camera calibration
60-inch Mt. Wilson	50 mm lens	19 July 1975	Jupiter	CCD	146"	System operation Test of TVI sensitivity
36-inch GORF*	135 mm lens	24 Oct. 1975	Jupiter	ICCD-3	54"	Determination of the system QE
Sorrento Valley ††	135 mm lens		Pleiades	ICCD-3	54"	Blooming and resolution measured
48-inch GORF	Coude	November 1975	o UMa	ICCD-3	0".197	Determination of the system QE
36-inch GORF	Cassegrain	16 Nov. 1975	Jupiter, γ Ari, 30 Tau, Landolt 095-0206	ICCD-3	".56	Determination of the system QE
36-inch GORF	Cassegrain		Landolt 095-0206	ICCD-3	".56	System Sensitivity
36-inch GORF	Cassegrain	19 Nov. 1975	30 Ari, Saturn Trapezium	ICCD-3	".56	Evaluation of imaging
			Saturn		1".00	Evaluation of imaging
100-inch Mt. Wilson	Cassegrain	28-31 Dec. 1975	ξ UMa, α Per, 14 Aur, 39 Leo	ICCD-3	0".178	Star calibration of sensitivity and effects on TVI determined.
200-inch Palomar Mtn.	Prime Focus	8-10 Jan. 1976	Star	(ICCD-3)	0".39	†

* Goddard Optical Research Facility, Beltsville, Maryland

** 50 mm lens and 135 mm lens are camera lenses

†† Electronic Vision Co., Sorrento Valley, San Diego, California

† Due to power supply accident no observations performed with ICCD, however, some observations were made with a simulated ICCD. Alignment and operational procedures developed.

Table I
Operation of UMAP System on Astronomical Telescopes

Telescope Mounting of Photometer Unit

The photometer unit (which is about 4" by 5" by 6") was mounted in a different fashion at each of the telescopes. On the 36-inch telescope at GORF, this was mounted at the Cassegrain focus by means of an existing adapter, a 4" by 5" holder. The operation using the 48-inch telescope at GORF was at the Coude focus and the photometer unit was tripod mounted within the Coude room. The mounting on the 100-inch telescope was at an auxiliary focus at the Naismith Cassegrain position. This was formed with a bending mirror attached to the Amplitude Interferometry Mounting Adapter. The mounting on the 200-inch was at the prime focus using the Westphal bracket for the SIT camera while the Amplitude Interferometer was mounted at the Cassegrain focus. This dual configuration permitted rapid change over between the two instruments (approximately 15 minutes).

Results of Telescope Operation

We first consider Figure 9, which shows the random noise when the system is operated on the telescope at the Goddard Space Flight Center.

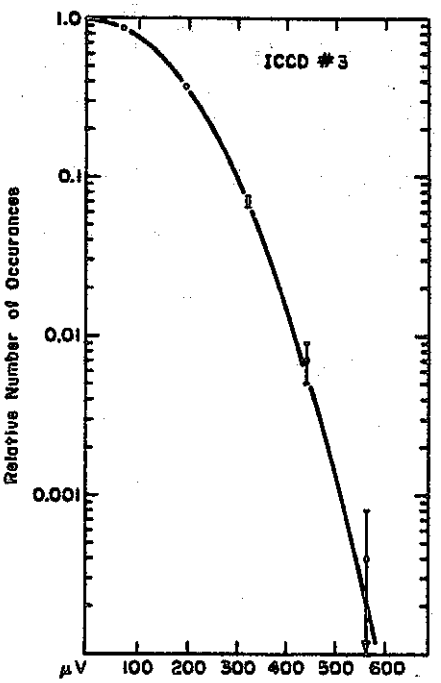

Pulse Height Distribution of Random Noise
Measured on 36-inch Telescope at GORF
Figure 9

For the calculation of the dynamic range, it was assumed that the statistical behavior of the random noise was Guassian over 4.5 orders of magnitude. In Figure 9, the Gaussian curve, fitted to the three highest points, is indicated by the solid line. Although this data does not cover the full range of five decades, this data is Gaussian, within the statistical error bars of the measurement. Even at Mt. Wilson, where 30 Megawatts of TV and FM power are emitted within one mile of the dome, and where the analog signal sent along 150 feet of cable, the apparent random noise was not excessive and the monitor display was quite acceptable. This apparent random noise due to external pickup should not be a problem when the discrimination is done within the camera head.

System Performance

We now discuss the results which were achieved with the SSDRS operating on the various telescopes. The general purpose of the stellar observations has been to calibrate the sensitivity of the system. As indicated in the table, the stellar observations have been conducted on the 36-inch, the 48-inch, and the 100-inch telescopes. Generally, these tests have indicated a system response within a factor of two or three of the predicted system response. A more precise comparison is difficult, since the quantum efficiency of the photocathode dropped by a factor of ten from the values measured during tube fabrication (about 20% at peak) to the values measured at the end of the tests. The reason for this decrease is being investigated. However, the system seems to behave as predicted using the value of the quantum efficiency measured

after the test. This assumes the loss was due to an event early in the tube lifetime. In addition to the stellar images, direct images of several objects were recorded. In particular, Saturn was observed with a neutral density filter to reduce the intensity by 100. This resulted in a multi-photoelectron signal per pixel per scan. The set of four stars which compose the Trapezium was observed with neutral density filters which reduced the light level by factors of 10 and 100. The first set of data has about ten photoelectrons per pixel per scan, while the second set of data on the Trapezium had about one photoelectron per pixel per scan, at the brightest region.

The Trapezium data was then discriminated in the computer. That is, the dark frames were averaged and subtracted from each frame with the image on it. Then each time a pixel had a signal as large as one photoelectron, a total frame was incremented by one unit. This "software discrimination" was applied to a set of 100 frames of data, and yeilded a reasonable image of the configuration. During exposure to normal (low) light intensity, there has been no obvious cumulative damage to the CCD by the accelerated electrons, either due to a lack of damage inflicted or due to self-annealing between exposures. When the tube (ICCD-3) was exposed to high levels of light, there has been obvious increases in dark current which have apparently not self-annealed. Similar affects due to high level illumination have already been reported[1]. However, these regions of increased dark current become negligible in magnitude when the CCD is cooled.

Conclusions

An array photometer using an ICCD as the photodetector has been designed, developed, and fabricated. It is currently being tested in the laboratory and on the telescope. The performance in the tests up to this time has been generally in accord with predictions.[2] The system has performed imaging on the telescope with discriminated single photoelectrons. The ICCD has operated reliably in the laboratory and in the field for five months. A test of the full system is expected shortly.

Acknowledgements

Many people and groups have aided this effort. We very much appreciate the generous amounts of telescope time which have been made available by the Hale Observatories and by the Goddard Space Flight Center, both for the ICCD work, and for the Amplitude Interferometry. At the University of Maryland I would especially like to thank Robert Braunstein, who has been responsible for the major effort in obtaining the operating data on the UMAP system and analyzing this data. The electronics of both the UMAP system and the SSDRS has been brought into reality by John Giganti and the Electronics Shop at the University of Maryland. Most of the development and programming of the NOVA and Eclipse system has been done by Al Buennagel. The programming and rather extensive computations which have been required for the data analysis have been performed by S. Kaisler, A. Blumenthal, and L. Bleau of our group. This was done on the UNIVAC 1108 of the University of Maryland Computer Science Center which is supported in part by NASA Grant NGR 398. I would also like to thank John Choisser, Jim McPherson and Peter Bertling for their work on the ICCD at Electronic Vision Company.

Various different aspects of the work on tube fabrication and system development have been supported by grants and contracts to the University of Maryland from the National Science Foundation (MPS-74-05890-001), National Aeronautics and Space Administration (NGR-21-002-444), Office of Naval Research (N00014-75-C-0343), and to Science Applications, Inc. from USAF Space and Missile Systems Organization (F04701-75-C-0068).

References

1. D. G. Currie, AN INTENSIFIED CHARGE COUPLED DEVICE FOR EXTREMELY LOW LIGHT LEVEL OPERATION, presented at the 1975 International Conference on the Application of Charge Coupled Devices, sponsored by the Naval Electronics Laboratory Center, 29 October 1975.

2. D. G. Currie, ON A PHOTON COUNTING ARRAY USING THE FAIRCHILD CCD201, presented at the symposium on Charge Coupled Device Technology for Scientific Imaging Applications, 6 March 1975, p. 80, JPL SP 43-21. This appears in somewhat extended form in University of Maryland Technical Report # 75-082.

3. D. G. Currie, ON A DETECTION SCHEME FOR AN AMPLITUDE INTERFEROMETER NAS-NRC, Woods Hole Summer Study on Synthetic Aperture Optics, Vol. II, p. 35, 1968.

4. D. G. Currie, ON THE ATMOSPHERIC PROPERTIES AFFECTING AN AMPLITUDE INTERFEROMETER, NAS-NRC Woods Hole Summer Study on Synthetic Aperture Optics, Vol. II, p. 79, 1968.

5. D. G. Currie, S. L. Knapp, and K. M. Liewer, FOUR STELLAR-DIAMETER MEASUREMENTS BY A NEW TECHNIQUE: AMPLITUDE INTERFEROMETRY, the Astrophysical Journal, Vol. 187, p. 1 January 1974.

6. S. L. Knapp, D. G. Currie, and K. M. Liewer, ON THE EFFECTIVE TEMPERATURE OF α HERCULIS A, Astrophysical Journal V 198, 561, 1975, University of Maryland Technical Report # 75-006, July 1974.

7. Stellar Disk Diameter Measurements by Amplitude Interferometry, 1972 - 1976, Currie, Knapp, Liewer and Braunstein, Technical Report # 76-125, submitted to Astrophysical Journal.

8. J. P. Choisser, EXPERIMENTS ON THE USE OF CCD'S TO DETECT PHOTOELECTRON IMAGES, presented at Symposium on Charge Coupled Device Technology for Scientific Imaging Applications, 6 March 1975, p. 150, JPL SP 43-21.

9. LARGE SPACE TELESCOPE, PHASE A, FINAL REPORT.

10. L. A. Buennagel, D. G. Currie, R. Braunstein, A PRELIMINARY DESCRIPTION OF THE SINGLE SCAN DATA RECORDING SYSTEM, University of Maryland Technical Report # 76-038.

11. R. H. Dyck, private communication.

N77-17289

CCD CORRELATION TECHNIQUES

C. R. Hewes, P.W. Bosshart*, W.L. Eversole
M. de Wit and D.D. Buss

Texas Instruments Incorporated
Dallas, Texas

ABSTRACT

Two CCD techniques are discussed for performing an N-point sampled data correlation between an input signal and an electronically programmable reference function.

1. Direct time domain correlation
2. Correlation by multiplication in the frequency domain.

The design and experimental performance of an implementation of the direct time correlator utilizing two analog CCDs and MOS multipliers on a single IC are discussed. The performance of a CCD implementation of the chirp z-transform is described and the design of a new CCD integrated circuit for performing correlation by multiplication in the frequency domain is presented. This new chip provides a discrete Fourier transform (DFT) or inverse DFT, multipliers, and complete support circuitry for the CCD CZT. The two correlation techniques are compared.

I. INTRODUCTION

The N-point correlation of two analog, sampled data signals x(n) and y(n) is given by

$$R_{xy}(m) = \frac{1}{N} \sum_{n=0}^{N-1} x(n)\, y(n-m) \qquad (1)$$

This operation is mathematically equivalent to the convolution of the signal y(-n) with the impulse response x(n). It is important in a number of military and NASA systems including classification of data in a satellite.

The operation of convolution in a fixed impulse response filter is easily implemented in a CCD split-electrode transversal filter.[1,2,3,4,5,6,7] However, correlation requires a convolution device in which the impulse response can be electronically programmed. This paper discusses two techniques for performing programmable convolution or correlation.

- Time domain correlation
- Frequency domain correlation

Section II discusses the direct time domain implementation of Eq.(1) with CCDs and analog MOS multipliers. Section III discusses the frequency domain implementation in which

- The discrete Fourier transform (DFT) of y(n) is performed using the CCD chirp z-transform (CZT)
- The DFT Y(z) is multiplied by X(z) which is the DFT of x(n)
- The inverse DFT is performed on X(z) Y(z).

Section IV concludes with the relative advantages of each approach.

II. TIME DOMAIN CORRELATION

A block diagram of a CCD, time domain, analog correlator is given in Figure 1.[8,9] It operates by first loading CCD1 with a reference signal and then clocking a second signal through CCD2. Since the charge is stored dynamically in CCD1, it decays due to thermal leakage and must be refreshed after 10 msec to 100 msec. The design and performance of an analog time domain correlator are discussed below.

A. DESIGN

Each stage of the CCD is tapped with a floating gate whose potential takes on a value approximately proportional to the signal charge, and four-quadrant multiplication is accomplished using the circuit of Figure 2. Transistors Q_3 and Q_4 act as voltage controlled resistors, and the balanced configuration overcomes the inherent nonlinearity of MOS transistors used as resistors. The output V_2 from CCD2 is applied to the gate of Q_4, and the gate of Q_3 is biased to V_{ref} which is equal to the value of V_2 when CCD2 has the zero level of charge (half full well). The output from CCD1 is buffered by a source follower whose output V_a is applied to the drain of Q_3 and Q_4. The sources of Q_3 and Q_4 are connected to virtual ground current busses Σ^- and Σ^+ whose currents are differenced in an off-chip differential amplifier.

The currents flowing in Q_3 and Q_4 are

$$I_3 = \beta(V_{ref} - V_t - \tfrac{1}{2}V_a)V_a, \qquad (2)$$

and

$$I_4 = \beta(V_2 - V_t - \tfrac{1}{2}V_a)V_a. \qquad (3)$$

The difference current

$$I_4 - I_3 = \beta(V_2 - V_{ref})V_a \qquad (4)$$

contains no nonlinear terms within the approximation of Eqs. (2) and (3).

B. PERFORMANCE

The multipliers are measured to have linearity within 1% with respect to V_a and V_2 for 2 V peak-to-peak signals. Two other sources of nonlinearity

*Patrick Bosshart is presently on leave of absence to MIT, Cambridge Massachusetts

exist, however. (1) Capacitive coupling between the gate and drain of Q_4 results in a modulation of V_2 by changes in V_1. This results in a 2% quadratic distortion which can be eliminated by the use of a source follower buffer between CCD2 and Q_4. (2) High output impedance of Q_1 results in distortion due to loading of the buffer by the resistor transistor Q_4. This effect can be minimized by making Q_1 wider.

A 20-stage correlator has been designed and tested.[8] Based upon these results, a new 32-stage correlator has been designed having the following improvements.

- Floating gate amplifiers tapping the CCD for improved charge transfer efficiency.
- Source follower buffer between CCD2 and Q_4.
- Lower impedance Q_1.

The redesigned correlator is expected to perform correlation at 5 MHz clock rate with an accuracy of better than 3% per stage at a power consumption of 100 mW.

The biggest limitation of the time domain correlation approach outlined above in Figures (1) and (2) is fixed pattern noise due to threshold offsets in the source followers which buffer the CCDs and the multipliers.[10] If a constant signal is applied to both CCD1 and CCD2, a dc output should result. However, threshold variations across the chip result in fixed pattern noise which limits the dynamic range of the device. If the signal at the output of the n^{th} stage (n=0, N-1) of the i^{th} shift register (i=1,2) is $v_i(n)$ and the offset is $\Delta v_i(n)$ the output will be proportional to

$$V_{out} = \frac{1}{N} \sum_{n=0}^{N-1} [v_1(n) + \Delta v_1(n)][v_2(n) + \Delta v_2(n)] \quad (5)$$

The maximum signal swing of the source follower output is approximately $v_1^p \approx v_2^p \approx \pm 2V$ and the threshold offset limits $\Delta v_1 \approx \Delta v_2 \approx \pm 50$ mV. The accuracy per stage is therefore approximately 2.5%.

The rms error which results can be estimated by assuming that the $\Delta v_i(n)$ are uncorrelated. If a maximum amplitude signal is applied to both CCD shift registers, the output signal is proportional to

$$V_{out}^{peak} = \frac{1}{N} \sum_{n=0}^{N-1} v_1(n)\, v_2(n) \approx 4V \quad (6)$$

and the rms error is proportional to

$$\Delta V_{out}^{rms} \propto \frac{1}{N} \sum_{n=0}^{N-1} v_1(n)\, \Delta v_2(n) + \Delta v_1(n) v_2(n)$$

$$\propto \frac{2}{N} \sum_{n=0}^{N-1} v_1^p\, \Delta v_2 \propto .2/\sqrt{N} \quad (7)$$

For a 32-stage correlator, the peak signal to rms error is approximately

$$\frac{V_{out}^{peak}}{V_{out}^{rms}} \approx 20\sqrt{N} \approx 113 \text{ (41 dB)} \quad (8)$$

III. FREQUENCY DOMAIN CORRELATION

A second approach to performing correlation with CCDs relies on the well known fact that correlation in the time domain can be accomplished by multiplication in the frequency domain. CCD technology is particularly well suited to performing the discrete Fourier transform (DFT) by means of an algorithm called the chirp z-transform (CZT).[6,11,12] CCD CZT technology is well established and is reviewed in Section III-A. A single chip 32-point CZT for use in performing CZT correlation has been designed and is discussed in Section III-B.

A. CCD CZT

The discrete Fourier transform (DFT) operation can be performed using the chirp z-transform (CZT) algorithm. The CZT gets its name from the fact that it can be implemented in an analog manner by (1) premultiplying the time signal with the chirp (linear FM) waveform, (2) filtering in a chirp convolution filter, and (3) postmultiplying with a chirp waveform.

When implemented digitally, the CZT has no advantages over the conventional fast Fourier transform algorithm. However, the algorithm lends itself naturally to implementation with CCD transversal filters.[11]

Starting with the definition of the DFT

$$F_k = \sum_{n=0}^{N-1} f_n e^{-i2\pi nk/N} \quad (9)$$

and using the substitution

$$2nk = n^2 + k^2 - (n-k)^2 \quad (10)$$

the following equation results.

$$F_k = e^{-i\pi k^2/N} \left[\sum_{n=0}^{N-1} \left(f_n e^{-i\pi n^2/N} \right) e^{i\pi (k-n)^2/N} \right] \quad (11)$$

This equation has been factored to emphasize the three operations which make up the CZT algorithm. It is illustrated in the block diagram of Figure 3.

Results of a 500-point CCD CZT are shown in Figure 4.[6] Figure 4a shows symmetric square wave input at 200 Hz. The CZT is clocked at 25 kHz and has 40 Hz resolution. The power density spectrum of the input is shown in Figure 4b. Harmonics of the output are shown at odd multiples of 200 Hz. Figures (4c) and (4d) show the output expanded by 10x and 100x. The arrow in Figure 4c indicates the trailing pulse which results from imperfect charge transfer efficiency.

B. CCD CZT CORRELATOR

The concept of the CCD CZT correlator is illustrated in Figure 5. Figure 5a shows the input signal x(n) being transformed, multiplied by the Fourier transform H(z) of the reference and inverse transformed to give the correlation function y(n). In Figure 5b, the DFT box and the inverse DFT box are replaced by the CZT equivalent. The post multiplication of the first CZT is seen to cancel the premultiplication of the second CZT to give the

simplified block diagram of Figure 5c.

The correlation which results from the system of Figure 5 differs from the direct time correlation in that the former is circular convolution, i.e., it is equivalent to the direct time domain correlation in which the samples of x(n) which exit the filter are fed back to the input. In some cases, circular convolution is required but in cases where linear convolution is required the direct time domain implementation is preferable. Another limitation of the CZT correlator is 50% duty cycle. For an N-point correlation, the N points are loaded into the first CCD and the data must be blanked for the next N clock periods. If continuous correlation is required, two identical units must be operated in parallel.

A CCD chip has been designed for use as a 32-point correlator. The block diagram of the correlator is shown in Figure 6 with a dashed line enclosing one CCD chip. The chip consists of the following functions:

- 4 63 stage CCD filters (two with cosine chirps and two with sine chirps),
- 4 multiplying digital to analog converters,[13]
- 2 ROMs (one with a cosine chirp and one with a sine chirp),
- 1 six stage counter and counter decode,
- clock logic and drivers,
- input/output buffer amplifiers.

As illustrated the CCD chip can be used for either the DFT or the IDFT. When the chip is used for the DFT the digital chirps which are stored on chip in the ROMs are applied to the input multipliers. The two output multipliers are used for part of the reference function multiplication. In the other mode (IDFT) the input multipliers of the chip are used to complete the reference function multiplication and the output multipliers are connected to the chirp ROMs to complete the IDFT.

IV. CONCLUSIONS

The direct time domain correlator discussed in Section II is useful for applications which require high speed but only limited accuracy. It has the further disadvantage that the reference is stored in analog form in the CCD and it must be refreshed every 10-100 msec depending upon the ambient temperature.

The CZT correlator has improved accuracy but requires more Si area to perform correlation than the time domain correlator. The CZT correlator is particularly advantageous when the reference in known in the frequency domain e.g. adaptive prewhitening, preemphasis, variable frequency bandpass or lowpass filtering. It is also useful for nonlinear prewhitening in the presence of narrow band jamming. If single frequency jamming or pick-up is present, the device can be operated in such a way as to limit any large single frequency component of the spectrum.

There exist two additional approaches to performing correlation or programmable convolution which are useful in certain applications

- Analog/digital correlator
- Sequentially addressed memory (SAM) correlator.[14,15]

A block diagram of the analog/digital programmable transversal filter is illustrated in Figure 7. Its operation is based on the fact that binary-weighted filters whose weighting coefficients take on one of two values (1 and 0 or +1 and -1) can be made to be electronically programmable. In the analog/digital weighting scheme, the weighting coefficients are digitized to M-bit accuracy, and the analog signal is clocked through M filters whose digital weighting coefficients represent the desired impulse response. The desired filter output is obtained by combining the outputs of the various filters with the appropriate power of two as shown in Figure 7. The analog/digital technique is well suited to adaptive filtering where the desired impulse response is calculated digitally and changes slowly with respect to the data rate. The technique is also important for realizing programmable pn-sequence filters in which case, only a one-bit representation of the weighting coefficients is required.

The SAM correlator is operationally similar to the analog/digital correlator. In this structure, the analog signals are stored on MOS capacitors, and a digital code is clocked past the analog samples performing a linear combination of analog signals each clock period. M-bit accuracy on weighting coefficients h_n is realized by appropriately combining the outputs of M surface charge correlators. This structure is useful for achieving high T_dW product at high speed because charge transfer efficiency has negligible effects.

The technology for making CCD filters with fixed impulse response has been well developed over the past few years. However, the technology for making programmable CCD correlators is not so well defined at the present time. Several competitive approaches exist, and the choice of technology depends upon the application. In the next year, increasing emphasis will be placed upon CCD programmable correlators.

ACKNOWLEDGEMENT

The authors are grateful to NASA for the support of this work and to Dr. Harry F. Benz of NASA Langley Research Center for its technical direction.

REFERENCES

1. D. D. Buss, D. R. Collins, W. H. Bailey and C. R. Reeves, "Transversal Filtering Using Charge-Transfer Devices," IEEE J. Solid-State Circuits, SC-8, pp 138-146, April 1973.

2. R. D. Baertsch, W. E. Engeler, H. S. Goldberg, C. M. Puckette and J. J. Tiemann, "Two Classes of Charge-Transfer Devices for Signal Processing, Proc. CCD Technology and Applications Conf., pp 229-236, Edinburgh, September 1974.

3. A. Ibrahim and L. Sellars, "CCDs for Transversal Filter Applications," IEEE Int. Electron Devices Meeting, Tech. Dig., Washington, DC, pp. 240-243, December 1974.

4. J. A. Sekula, P. R. Prince, and C. S. Wang, "Non-Recursive Matched Filters Using Charge-Coupled Devices," IEEE Int. Electron Devices Meeting, Tech. Dig., Washington, DC, pp 244-247, December 1974.

5. C. R. Hewes, "A Self-Contained 800-Stage CCD Transversal Filter," CCD '75 Proceedings, pp 309-318, San Diego, October 1975.

6. R. W. Brodersen, C. R. Hewes and D. D. Buss, "A 500-Stage CCD Transversal Filter for Spectral Analysis," IEEE J. Solid-State Circuits, SC-11, pp 75-84, February 1976.

7. R. D. Baertsch, W. E. Engeler, H. S. Goldberg, C. M. Puckett, IV, and J. J. Tiemann, "The Design and Operation of Practical Charge-Transfer Filters," IEEE J. Solid-State Circuits, SC-11, pp 65-74, February 1976.

8. P. Bosshart, "An Integrated Analog Correlator using Charge-Coupled Devices," 1976 IEEE International Solid-State Circuits Conf., Digest of Technical Papers, pp 198-199, Philadelphia, February 1976.

9. J. G. Harp, G. F. Vanstone, D. J. MacLennan, and J. Mavor, "Analogue Correlators using Charge-Coupled Devices," CCD '75 Proceedings, pp 229-235, San Diego, October 1975.

10. D. J. MacLennen, J. Mavor and Y. T. Yeow, "Errors in Programmable CCD Transversal Filters and Correlators," Proc. 3rd Int. Conf. Technology and Applications of Charge-Coupled Devices, pp 259-268, Edinburgh, September 1976.

11. H. J. Whitehouse, J. M. Speiser and R. W. Means, "High Speed Serial Access Linear Transform Implementation," presented at the All Applications Digital Computer Symposium, Orlando, Florida, January 1973, NUC TN 1026.

12. D. D. Buss, R. L. Veenkant, R. W. Brodersen and C. R. Hewes, "Comparison Between the CCD CZT and the Digital FFT," CCD '75 Proc., pp 267-281, San Diego, October 1975.

13. J. L. McCreary and P. R. Gray, "All-MOS Charge Redistribution Analog-to-Digital Conversion Techniques -- Part I," IEEE Journal of Solid State Circuits, Vol SC-10, pp 370-378 and R. E. Suarez, P. R. Gray and D. A. Hodges, "All-MOS Charge Redistribution Analog-to-Digital Conversion Techniques -- Part II," IEEE Journal of Solid State Circuits, Vol SC-10, pp 379-385.

14. J. J. Tiemann, W. E. Engeler and R. D. Baertsch, "A Surface-Charge Correlator," IEEE J. Solid-State Circuits, SC-9, pp 403-410, December 1974.

15. Y. A. Haque and M. A. Copeland, "An Electrically Programmable Transversal Filter," Proceedings of the International Electron Devices Meeting, Washington DC, December 1976 (to be published).

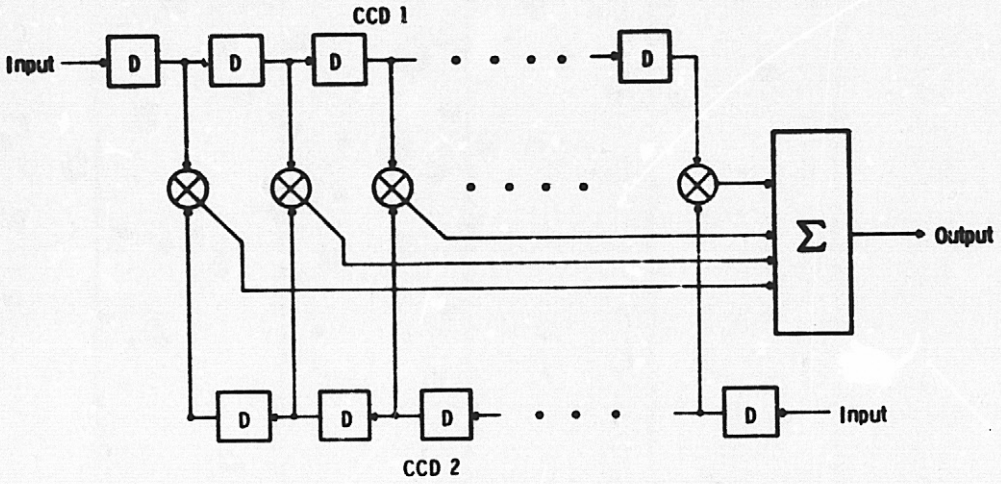

Figure 1. Block diagram of the CCD time domain correlator.

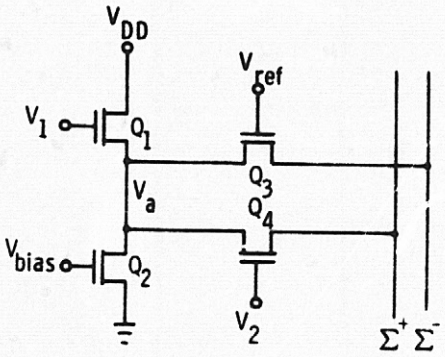

Figure 2. Schematic of dn NMOS 4-quadrant multiplier.

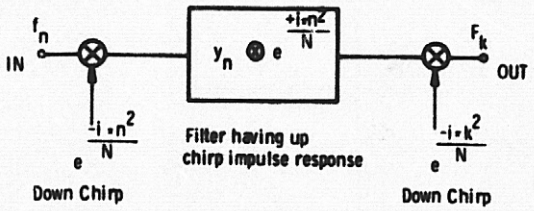

Figure 3. Schematic of the CZT algorithm.

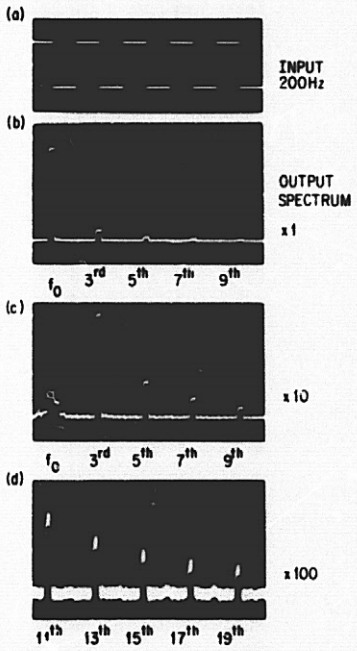

Figure 4. Power density spectrum of a 200 Hz square wave computed by a 500-point CCD CZT.

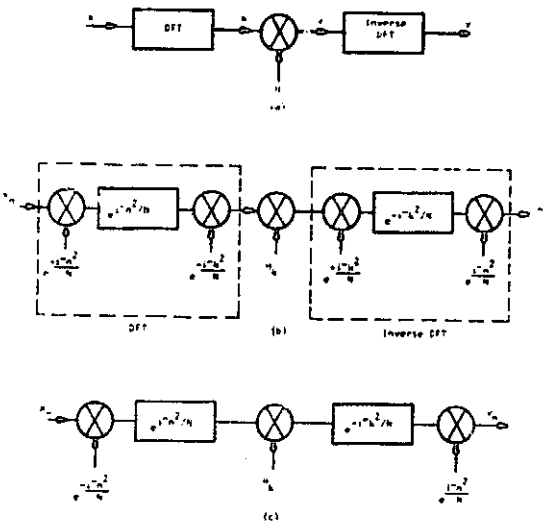

Figure 5. Block diagram of CCD frequency domain correlator.

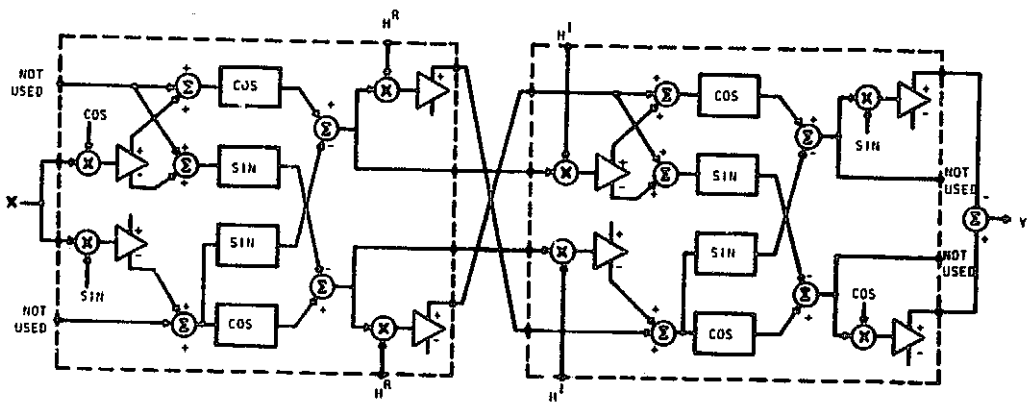

Figure 6. Block diagram of a CCD integrated circuit for use as a frequency domain correlator.

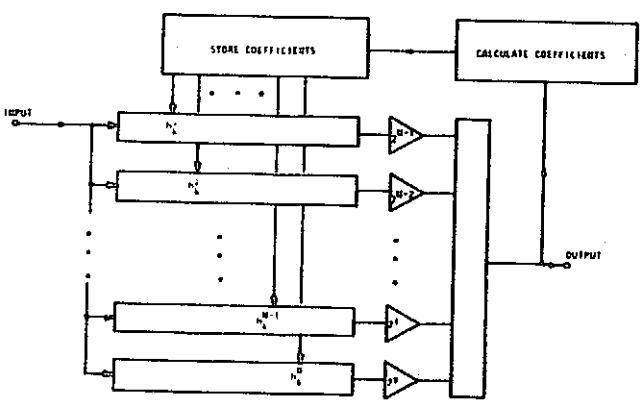

Figure 7. Analog/digital programmable transversal filter for use in adaptive filtering applications.

N77-17290

A CCD SCANNED (Hg,Cd)Te ARRAY FOR EARTH VIEWING APPLICATIONS

S. Iwasa and W.J. White

Honeywell Radiation Center
Lexington, Massachusetts

ABSTRACT

A 9-channel demonstration of 10-micrometer photoconductive mercury cadmium telluride detector array, bipolar preamplifiers, and a Si CCD multiplexer, integrated into a focal plane assembly and operating at 105°K and at 17 Hz is reported. An average $D^*_{\lambda peak} = 7.5 \times 10^9$ cmHz$^{\frac{1}{2}}$/W is obtained after the electronic scanning by the CCD. Reported also is the result of a direct coupling experiment between a 5-micrometer photovoltaic mercury cadmium telluride photodiode and a CCD. No appreciable degradation in the signal-to-noise ratio was experienced and $D^*_{\lambda peak} = 1.6 \times 10^{11}$ cmHz$^{\frac{1}{2}}$/W at 723Hz and at 77°K was obtained after the CCD.

I. INTRODUCTION

Present generation earth resources sensors flying in near earth orbit use a single infrared detector in each spectral region and scan by means of a moving mirror to obtain a full field of coverage in the direction orthogonal to the vehicle motion. In future systems it would be desirable to eliminate the need for the mirror, which is physically large and heavy, requires considerable drive power, and has the inherent reliability problems of mechanical devices.

Electronic scanning can be done simply by multiplexing, however, a large number of resolution elements (detectors) will be required. Any consideration of the benefits of electronic scanning must take into account not only relative system performance but also any tradeoffs between extra cooling power required for the extra elements, and operating power for the mirror. If low level radiative cooling is provided for example, then low power dissipation per element becomes a controlling factor.

Photoconductive (Hg,Cd)Te detectors are ideally suited for 10.5 to 12.5-micrometer earth resources applications. Detectors having $D^*(500, 3kHz, 1Hz) > 2 \times 10^{10}$ cmHz$^{\frac{1}{2}}$/W at 110°K are readily available. Recent advancements in 1/f noise reduction have been made also. Detectors operating at 82°K have shown $D^*(500, 17, 1)$ of 1.2×10^{10} cm Hz$^{\frac{1}{2}}$/W.

The resistance of these detectors has been improved to the 50-200 Ω range for square detectors, which results in power dissipations in the 100μW to 1mW range. Even with on focal plane parallel to serial conversion this amount of power may prove to be undesirable.

The (Hg,Cd)Te photodiodes, on the other hand would dissipate little or no power and would appear to be a better choice for the future earth resources, long life satellite applications. It will be shown in the text that (Hg,Cd)Te PV detectors can be direct coupled into buried channel CCD shift registers, thus providing the potential for an on focal plane parallel to serial conversion at power dissipation levels acceptable to radiative cooler requirements. Recent developments have been made in (Hg,Cd)Te photodiodes leading toward realization of such low power focal plane.[1]

In order to demonstrate the viability of on focal plane parallel to serial conversion using CCDs, a breadboard demonstration was made up and tested. This breadboard included current state of the art 9-element photoconductive (Hg,Cd)Te 10.5 to 12.5-micrometer detector array, a cryogenically cooled single stage bipolar preamplifier for each detector, and a 9-channel buried n-channel CCD multiplexer. These were all mounted on the cold pedestal of a variable temperature (80 to 110°K) dewar. Additionally clock drive, bias, and readout circuitry were built up to operate the breadboard. It was found that D* values in the detector were degraded only slightly at the CCD output.

As a demonstration of direct coupling (no preamplifier) the signal from a 5-micrometer (Hg,Cd)Te photovoltaic detectors was directly injected into a CCD multiplexer. Within the experimental error, no degradation in the S/N ratio was experienced in going through the multiplexer. This is an encouraging result towards the realization of a hybrid focal plane with low power consumption. An analysis is presented, taking into account the 1/f noise from the CCD.

II. BURIED CHANNEL CCD MULTIPLEXER

The parallel-to-serial multiplexer used in the IR/CCD experiment is a two-phase, n-channel CCD with 30 parallel inputs. The input MOSFET structure is surface channel. Each input stage consists of an independently accessible pair of source diffusion and control gate, followed by a storage gate and a transfer gate. The shift register is buried, and two adjacent inputs are separated by an empty bit for minimizing crosstalk. A transfer efficiency of 0.99995 has been measured at 1MHz clock frequency. The input/output characteristics of the CCD have been studied in depth for two types of signal injection, i.e., charge equilibration and current integration.[2] Figure 1 describes an I/O characteristic of the equilibration mode for 9 of the 30 available inputs, when signal is entered via the control gate. The relationship is described by

$$V_{out} = C_W(V_W - V_{in}) \times \frac{1}{C_{FD}} \times \alpha \qquad (1)$$

where C_W and V_W are respectively the capacitance and potential of the storage well, C_{FD} is the effective depletion capacitance of the floating diffusion and $\alpha = 0.7$ is the gain of the source follower.

From equation 1, the experimentally measured slope of 0.2 corresponds to $C_{FD} = 3.5\ C_W$, which is in agreement with the CCD geometry. The slope remains the same at 77°K. The channel nonuniformity is seen to be small.

Figure 2 depicts the I/O relationship for the current integration mode. For the range of the integration times shown, the channel under the control gate is strongly inverted and the I/O characteristic is given by

$$V_{out} = \frac{\mu C_{ox} Z\tau}{2L} [V_{in} - (V_G - V_T)]^2 \frac{1}{C_{FD}} \alpha \qquad (2)$$

where $\mu_n = 650\ cm^2/V\text{-}s$ at 300°K is the surface channel electron mobility, C_{ox} the gate oxide capacitance per unit area, Z/L the gate aspect ratio, τ the integration time, and V_{in}, V_G and V_T respectively refer to the source, gate and the threshold voltage. In the current integration mode, one has the option of signal entry either at the source diffusion or at the control gate, leading to an identical I/O relationship as given in equation 2. The input impedance is different for the two entries, however. In the source input case, the transconductance is given by

$$g_m = \sqrt{\frac{\mu C_{ox} Z}{2L} I_s} \qquad (3)$$

where I_s is the source diffusion current. The gate is nearly open except for a small capacitance. The nonuniformity among the 9 inputs originate mainly from variations in the threshold voltage of ΔV_T=20mV as evidenced by translation and not slope change in Figure 2. The effect of the integration time τ is a change in the slope. Figure 3 illustrates the I/O characteristic of the current integration mode at 300°K and at 77°K, where the major changes occur in V_T (translation) and in μ_n (slope change). The low frequency input referred noise of the two signal input techniques at 300°K and 77°K are shown in Figure 4.

III. PHOTOCONDUCTIVE (Hg,Cd)Te IR/CCD

A. 10-MICROMETER PHOTOCONDUCTIVE (Hg,Cd)Te ARRAY

The photoconductive (Hg,Cd)Te array used in the breadboard demonstration consists of 20 linear 5 mil by 5 mil detector elements separated by 1.5 mils. Their peak response is at 10.6 micrometers and the cutoff at 13 micrometers. They have an average resistance of 60Ω and are operated with best signal-to-noise ratios at approximately 0.3 volt bias. The $D^*_{\lambda peak}$ values of the array measured at 105°K are plotted in Figure 5 as a function of frequency. The average noise voltage of an element at 105°K at 17Hz is of the order of $40nV/\sqrt{Hz}$.

B. CRYOGENIC BIPOLAR PREAMPLIFIER

The input referred noise of the CCD MUX in current integration is of the order of $1.8\ \mu V/\sqrt{Hz}$ at 77°K and at 17Hz, and is 45 times larger than the detector noise. In order to make the detector a dominant noise source, a buffer amplifier must be inserted between the detectors and the CCD input. This buffer amplifier array must have 9 channels, have a voltage gain of about 100 times, and operate at focal plane temperatures in the vicinity of 105°K. Figure 6 gives a bipolar preamplifier version consisting of 2N3964 in a common gate and an ac coupled configuration. The gain bandwidth product of the present amplifier is 100MHz and the input referred noise is less than $10nV/\sqrt{Hz}$ at 77°K and at 17Hz. The selection of the transistor was a non trivial task. Most bipolars including the super betas, JFET and MOSFETs may operate perfectly at room temperature and at high frequencies but would fail at 77°K and at 17Hz.

C. PC (Hg,Cd)Te IR/CCD D*

The 10-micrometer PC (Hg,Cd)Te array, the bipolar preamplifier and the CCD MUX are mounted on a common pedestal block assembly. The pedestal block assembly is in (limited) thermal contact with the cold finger of a liquid nitrogen dewar, and an internal heater regulates the focal plane temperature in the range between 80°K and 120°K. Figure 7 illustrates the multiplexed output waveform as well as the sample/hold waveform of a selected channel, showing the chopped blackbody signal. The signal-to-noise ratios of the PC(Hg,Cd)Te IR/CCD at various stages, namely, that of the PC detectors, after the preamplifiers and after the multiplexer, are expressed as $D^*_{\lambda peak}$ and plotted in Figure 8. On the average, a 7% degradation in the S/N is experienced after the preamplifiers and 22% after the CCD multiplexer. The detector noise is $40nV/\sqrt{Hz}$ and the input noise of the amplifier $10nV/\sqrt{Hz}$, therefore, the expected average loss in the S/N is given by

$$\left[\left((10nV/\sqrt{Hz})^2 + (40nV/\sqrt{Hz})^2\right)/(40nV/\sqrt{Hz})^2\right]^{-\frac{1}{2}} = 0.97$$

which is to say a loss of 3% is accounted for. The S/N loss in going through the multiplexer is computed to be

$$\left[\left((40nV/\sqrt{Hz})^2 + (10nV/\sqrt{Hz})^2 + (1.8\mu V/\sqrt{Hz}/100)^2\right)/(40nV/\sqrt{Hz})^2\right]^{-\frac{1}{2}} = 0.89$$

There is an 11% discrepancy between the observed 0.78 and the calculated 0.89. The discrepancy is a direct result of the noise aliasing suffered when the CCD multiplexer samples the detector signal. In a sampled system, the noise spectrum beyond the integral multiple of the sampling frequency is reflected back into the base signal bandwidth. One method of minimizing aliasing is to reduce the noise bandwidth of the detector/amplifier to less than the sampling frequency. This can be achieved by adding a capacitor next to the collector resistance and forming a low pass filter. This was tried on one channel after which a near theoretical degradation has been observed.

D. POWER DISSIPATION OF PC(Hg,Cd)Te IR/CCD SYSTEM

The average power dissipation in the 10-micrometer PC(Hg,Cd)Te detector is of the order of 1.5mW per one element. Approximately 1mW is consumed in the bipolar preamplifier. In comparison, the power dissipation of the CCD is insignificant. Hence, the PC(Hg,Cd)Te IR/CCD consumes an average of 2.5mW per channel, or 23mW total for the 9 channels.

IV PHOTOVOLTAIC (Hg,Cd)Te IR/CCD

A. DIRECT COUPLING EXPERIMENT

The success of a hybrid focal plane ultimately depends on low power consumption and simplicity of the electronic and mechanical interface between the detector array and the silicon CCD. Photovoltaic (PV) detectors have high impedance and operate with minimal power consumption. It is of interest, then, to explore direct coupling between a PV detector and a CCD without a buffer amplifier.[3]

An experiment was carried out in which a 4.4-micrometer peak photovoltaic (Hg,Cd)Te detector was directly coupled to a source diffusion of a surface p-channel CCD. Within the experimental error, there was no observable degradation in the signal-to-noise ratio when the detector signal was retrieved after the CCD multiplexer. The coupling scheme is of such a simplicity that the preliminary result is an encouraging one towards the realization of a large array hybrid IR/CCD structure with low power dissipation.

Figure 9 describes the experimental setup. The n-type PV detector element and its p-type substrate were directly connected, respectively, to the substrate and a source diffusion of a surface p-channel CCD. Table 1 summarizes the detector specifications. A clock rate of 500 Hz with the aluminum diode gate connected to Ø1, and the polysilicon gate bias in the vicinity of -1 volt, are designed to allow an input current of 0.2 μA to match the background generated photocurrent of the PV detector, therefore assuring the zero bias operation. A 500°K blackbody was chopped at 723 Hz, and the modulation was extracted by a sample and hold amplifier and analyzed by a 304 Quantek Wave Analyzer at 10 Hz bandwidth. The CCD output noise was typically $6\mu V/\sqrt{Hz}$ at 723 Hz.

In these experiments, the PV HCT detector was operated with a S/N value of typically 600. When the detector was directly coupled to the CCD, the CCD output exhibited S/N values of 600 ± 100. These values correspond to the detector D* values of 1.6×10^{11} cm^2Hz/W. Signal and noise traces of the PV HCT detector only, and the PV HCT CCD output, are shown in Figure 10.

B. PV IR/CCD D* ANALYSIS

In the directly coupled PV IR/CCD system in Figure 9, the detector noise is in series with that of the CCD. The total detector noise voltage is given by

$$e_D^2 = \left(\frac{4kT}{R_o} + 2qI_\phi\right)R_o^2 \qquad (4)$$

where the first term in the bracket represents the detector Johnson noise current and the second the photon induced shot noise current. $I_\phi = \mu q \phi_B A$ is the diode photocurrent, where μ, ϕ_B, and A are, respectively, the quantum efficiency, photon flux and the photosensitive area of the diode. The CCD noise voltage is expressed by

$$e_{CCD}^2 = \frac{8kT}{3g_m} + e_{1/f}^2 \qquad (5)$$

where the first term is the Johnson noise of the strongly inverted channel region, and the second the 1/f noise. The transconductance gm is given in equation 3, in which I_s is to be replaced by I_ϕ.

The D* value of the IR/CCD is given by

$$D^*_{IR/CCD} = \frac{D^* \text{ DETECTOR}}{\sqrt{N.F.}} \qquad (6)$$

where the noise figure is defined as

$$\text{NOISE FIGURE} = \frac{\text{TOTAL NOISE POWER}}{\text{DETECTOR NOISE POWER}} = 1 + \frac{\text{CCD NOISE POWER}}{\text{DETECTOR NOISE POWER}} \qquad (7)$$

By substitution, one finds that

$$N.F. = 1 + \frac{\frac{8}{3}kT\sqrt{\frac{2L}{\mu C_{ox} Z I_\phi}} + e_{1/f}^2}{R_o^2\left(\frac{4kT}{R_o} + 2qI_\phi\right)} \qquad (8)$$

Using the values q R_o=20MΩ, I_ϕ = 0.2μA, T=77°K, $e_{1/f}$ = 18/f $\mu V/\sqrt{Hz}$ and the CCD parameters given as before, one finds N.F. = 1.00, namely, $D^*_{IR/CCD} = D^*_{DETECTOR}$. This is in agreement with the experiment. In fact, the experimental conditions can be relaxed quite a lot before the CCD starts to contribute a noticeable amount of noise. If for instance one can tolerate a 10% degradation in the system D* value, namely, $D^*_{IR/CCD} \geq 0.9\ D^*_{DETECTOR}$ this corresponds to a maximum noise figure of 1.23. Using equation 9, one can afford any one of the following relaxations when all else are assumed to remain the same.

1. R_o can be as low as 390 KΩ instead of 20MΩ.
2. Background photon flux can be as low as $5x10^{13}$ photons/cm^{2}sec instead of $9x10^{15}$ photons/cm^{2}sec.
3. Signal frequency can be as low as 5.4 Hz instead of 723 Hz.

The first condition suggests that the actual focal plane temperatures need not be as low as 77°K. It can be as high as when the diode impedance reduces to 390KΩ.

C. POWER CONSUMPTION

The PV(Hg,Cd)Te photodiode element is consuming $I_\phi^2 R_o$ = 0.8 microwatt, which is an insignificant amount compared with that of the PC(Hg,Cd)Te element.

V. SUMMARY

A 9-channel breadboard of 10.6 micrometer peak photoconductive (Hg,Cd)Te detector array, bipolar preamplifiers and a silicon CCD multiplexer, integrated on a focal plane, has demonstrated an electronic scanning. Operated at 105°K and at 17 Hz, the breadboard has yielded an average $D^*_{\lambda peak}$ = 7.5 x 10^9 cmHz$^{\frac{1}{2}}$/W, a 22% degradation from that of the detectors. The power dissipation is 2.5mW per channel.

A 4.4-micrometer peak photovoltaic (Hg,Cd)Te detector has been directly (no preamplifier) coupled to the source diffusion of a CCD. Operating at 77°K and at 723 Hz, the multiplexer has yielded $D^*_{\lambda peak}$ = 1.6 x 10^{11} cmHz$^{\frac{1}{2}}$/W, with no appreciable degradation from the detector value. The power dissipation was 0.8 μW. The latter configuration promises the realization of a large array hybrid focal plane.

VI. ACKNOWLEDGEMENT

The development of the breadboard demonstration of electronically scanned array was supported by NASA/Goddard Space Flight Center under Contract NAS 5-22339, monitored by K.L. Hallam.

The authors are indebted to D.E. Marshall and N.R. Butler for many helpful discussions. The 10.6-micrometer peak photoconductive (Hg,Cd)Te array was supplied by W.G. Rae, the 4.4-micrometer peak photovoltaic (Hg,Cd)Te array by T.J. Tredwell, and the CCDs by J.S.T. Huang. The hardware was assembled by A.R. Carson.

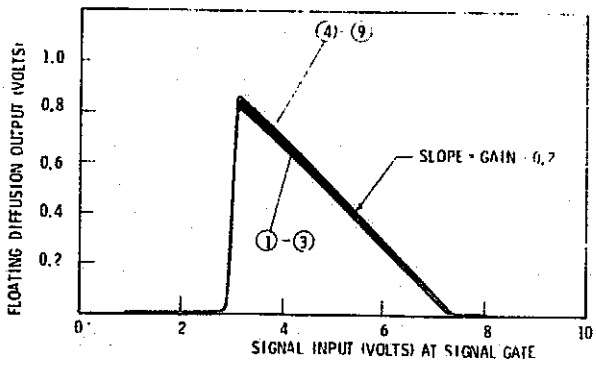

Figure 1. Channel uniformity for fill & spill

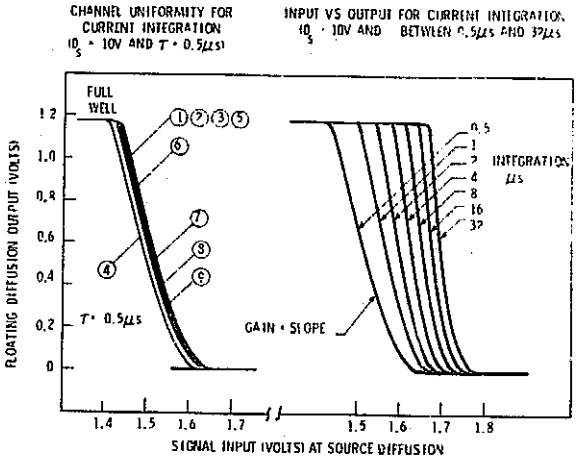

Figure 2. Channel uniformity and input vs output characteristics for current integration

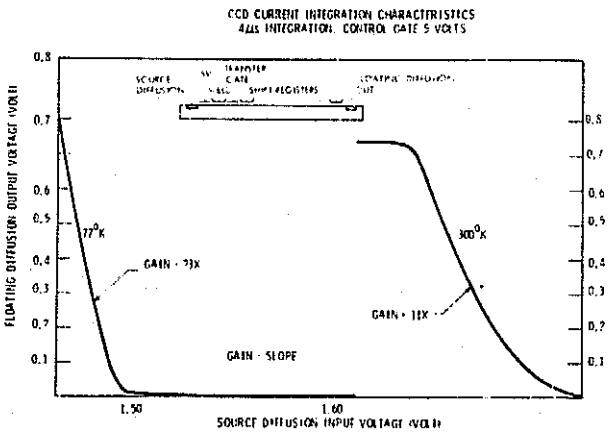

Figure 3. Current integration characteristics for T=300°K & T=77°K

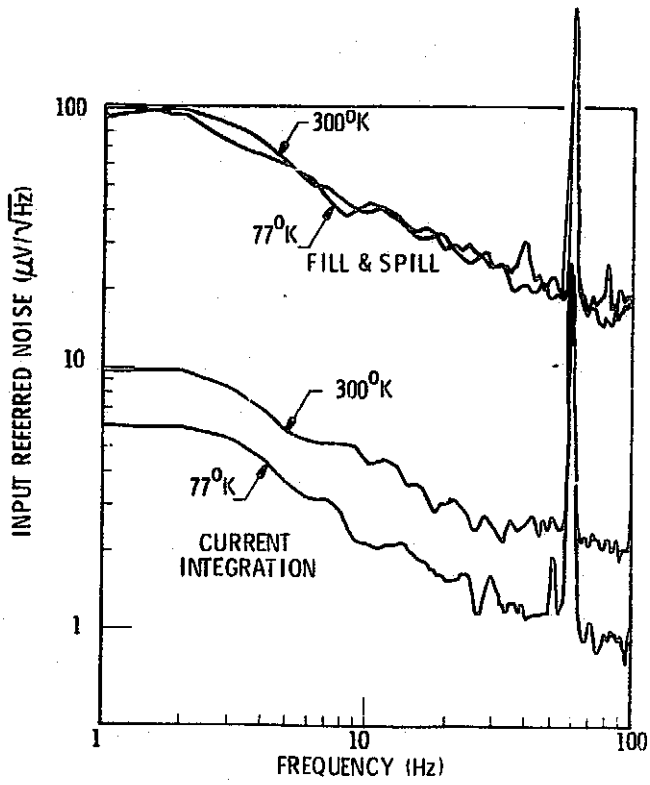

Figure 4. CCD input referred noise

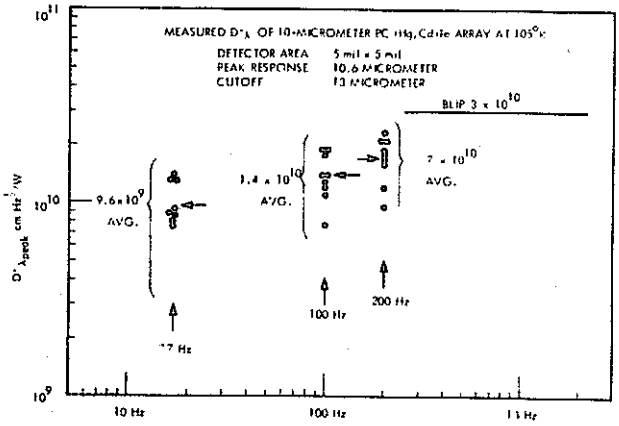

Figure 5. PC HCT array D* vs frequency

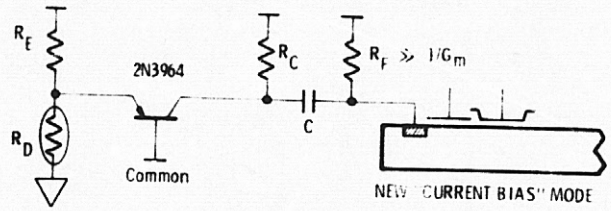

Figure 6. Cryogenic preamplifier configuration

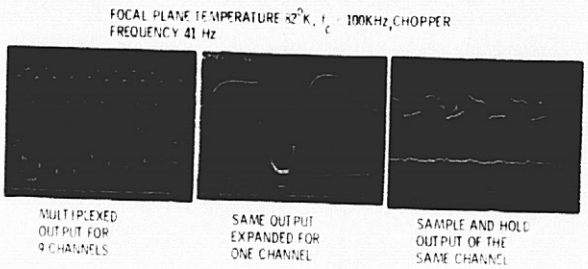

Figure 7. PC HCT IR/CCD MUX output waveforms

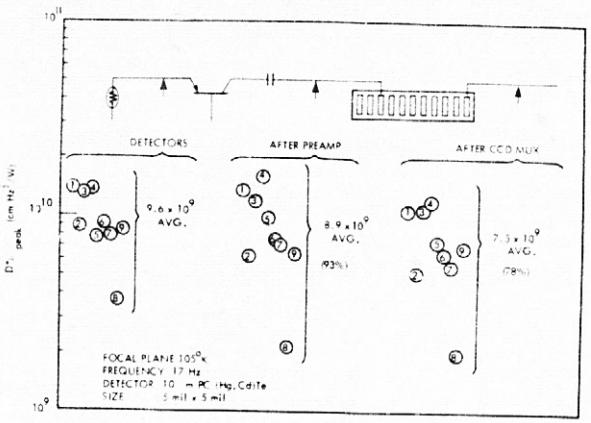

Figure 8. PC IR/CCD D*

Table 1. Photovoltaic (Hg,Cd)Te detector parameters

D* AT 180° FOV, 300°K BACKGROUND 1.6×10^{11} cm^2 Hz/W

D* AT 180° FOV, 77°K BACKGROUND 2.5×10^{12} cm^2 Hz/W

AREA:	1.82×10^{-4} cm^2
OPEN RESISTANCE R_0:	20MΩ at 77°K
RESPONSE MAXIMUM:	4.4 MICROMETERS
RESPONSE CUTOFF:	4.76 MICROMETERS
ZERO BIAS DETECTOR CURRENT:	0.2 μA
QUANTUM EFFICIENCY η:	0.74
R_0A:	3640 AT 77°K

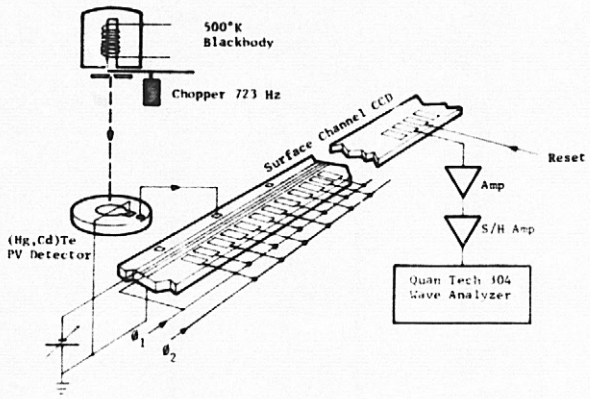

Figure 9. PV HCT direct coupling experiment

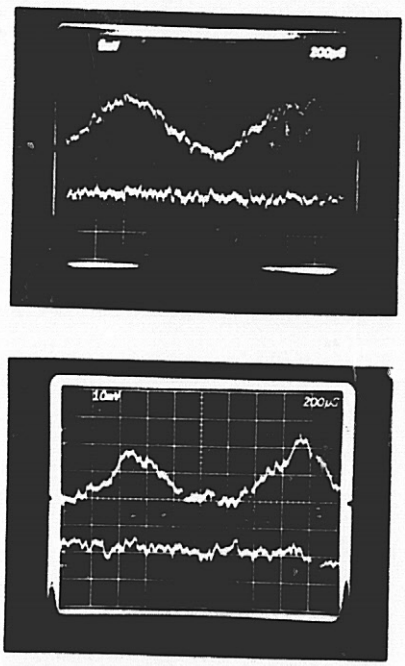

Figure 10. PV HCT detector coupled CCD

1. Tredwell, T.J., "(Hg,Cd)Te Photodiode Technology," to be published in proceedings of IEDM, December 1976.
2. Tompsett, M.F., "The Potential Equilibration Method of Setting Charge in CCDs," Electron Devices, Vol. ED-22, No. 6, p. 305; June 1975.
3. Steckl, A.J., Nelson, R.D., French, B.T., Gudmundsen, R.A., and Schechter, D; "Application of Charge-Coupled Devices to Infrared Detection and Imaging," Proc. IEEE, Vol. 63, No. 1, p. 67; January 1975.